

AD-A073 770

AIR FORCE WEAPONS LAB KIRTLAND AFB NM
ELECTROMAGNETIC PULSE INTERACTION NOTES -- EMP 3-38. (U)
MAY 79 C E BAUM

F/G 20/14

UNCLASSIFIED

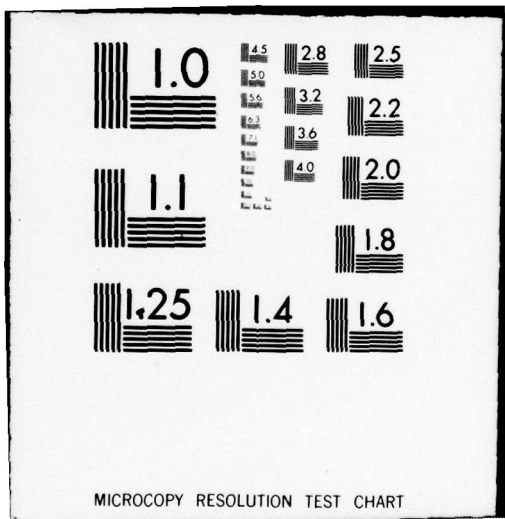
AFWL-TR-79-401

SBIE -AD-E200 329

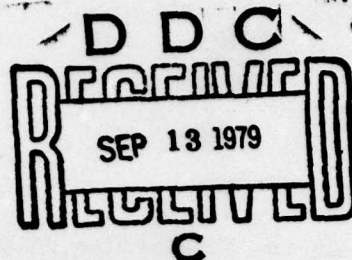
NL

1 OF 6
ADA
073770



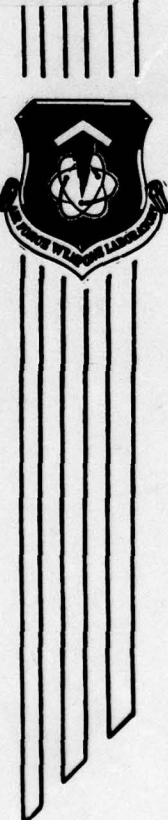


AFWL-TR-79-401



AFWL-TR-
79-401

ADA 073770



ELECTROMAGNETIC PULSE INTERACTION
NOTES — EMP 3-38

LEVEL ✓

DDC

May 1979

Final Report

Approved for public release; distribution unlimited.

DDC FILE COPY

AIR FORCE WEAPONS LABORATORY
Air Force Systems Command
Kirtland Air Force Base, NM 87117

79 08 20 066

This report is one in the Note Series on EMP and related subjects which is an EMP community-wide series or journal on EMP technology related matters. The editor is Dr Carl E. Baum (ELTE), who should be contacted concerning any matters related to this series. The Air Force Weapons Laboratory assists in the publication of this series as a service to the technical community.

When US Government drawings, specifications, or other data are used for any purpose other than a definitely related Government procurement operation, the Government thereby incurs no responsibility nor any obligation whatsoever, and the fact that the Government may have formulated, furnished, or in any way supplied the said drawings, specifications, or other data is not to be regarded by implication or otherwise as in any manner licensing the holder or any other person or corporation or conveying any rights or permission to manufacture, use, or sell any patented invention that may in any way be related thereto.

This report has been authored by an employee of the US Government. Accordingly, the US Government retains a nonexclusive royalty-free license to publish or reproduce the material contained herein, or allow others to do so, for the US Government purposes.

This report has been reviewed by the Office of Information (OI) and is releasable to the National Technical Information Service (NTIS). At NTIS it will be available to the general public, including foreign nationals.

This technical report has been reviewed and is approved for publication.

Carl E. Baum

DR CARL E. BAUM
Editor

Doland A. Dowler
DOLAND A. DOWLER
Col. USAF
Chief, Electromagnetic Division

FOR THE COMMANDER

Bruce H. Wheeler
BRUCE H. WHEELER
Col, USAF
Director of Nuclear Technology

UNCLASSIFIED

SECURITY CLASSIFICATION OF THIS PAGE (When Data Entered)

REPORT DOCUMENTATION PAGE		READ INSTRUCTIONS BEFORE COMPLETING FORM
1. REPORT NUMBER AFWL-TR-79-401	2. GOVT ACCESSION NO.	3. RECIPIENT'S CATALOG NUMBER
4. TITLE (and Subtitle) ELECTROMAGNETIC PULSE INTERACTION NOTES EMP 3-38		5. TYPE OF REPORT & PERIOD COVERED EMP NOTES
		6. PERFORMING ORG. REPORT NUMBER
7. AUTHOR(s) Dr. Carl E. Baum		8. CONTRACT OR GRANT NUMBER(s)
9. PERFORMING ORGANIZATION NAME AND ADDRESS Air Force Weapons Laboratory (ELTE) Kirtland Air Force Base, NM 87117		10. PROGRAM ELEMENT, PROJECT, TASK AREA & WORK UNIT NUMBERS 99960002
11. CONTROLLING OFFICE NAME AND ADDRESS Air Force Weapons Laboratory (ELTE) Kirtland Air Force Base, NM 87117		12. REPORT DATE May 1979
14. MONITORING AGENCY NAME & ADDRESS (if different from Controlling Office)		13. NUMBER OF PAGES
		15. SECURITY CLASS. (of this report) UNCLASSIFIED
		15a. DECLASSIFICATION/DOWNGRADING SCHEDULE
16. DISTRIBUTION STATEMENT (of this Report) Approved for public release; distribution unlimited.		
17. DISTRIBUTION STATEMENT (of the abstract entered in Block 20, if different from Report)		
18. SUPPLEMENTARY NOTES		
19. KEY WORDS (Continue on reverse side if necessary and identify by block number) EMP		
20. ABSTRACT (Continue on reverse side if necessary and identify by block number) This is a series of five notes on electromagnetic pulse interaction. Subjects covered in this volume are: electromagnetic shielding by advanced composite materials; fields in a rectangular cavity excited by a plane wave on an elliptical aperture; transient electromagnetic characterization of arbitrary conducting bodies through an aperture-perforated conducting screen; a comparison of stick model skin current predictions with scale model measurements for the E-4 and EC-135 aircraft; aperture excitation of a wire in a rectangular cavity.		

UNCLASSIFIED

SECURITY CLASSIFICATION OF THIS PAGE(When Data Entered)

UNCLASSIFIED

SECURITY CLASSIFICATION OF THIS PAGE(When Data Entered)

PREFACE

Much of the existing information on EMP is in the form of notes or semiformal reports and has not been adequately documented or distributed. In particular, there are several series of notes that act as technical journals for various areas related to EMP and other related subjects. These note series are not exclusively for one organization and are run much as technical journals with an editor, Dr. Carl E. Baum.

The Air Force Weapons Laboratory has undertaken to reissue these existing notes in convenient volume units. The present volume is Volume 38 of the Interaction Notes, one of the note series in the Electromagnetic Pulse Note Series. The Interaction Notes have the report designation EMP 3 in the EMP group of note series.

Contributions to this volume, EMP 3-38, have been made by the following individuals at the included organizations:

Air Force Weapons Laboratory

Carl E. Baum
Korada R. Umashankar

University of Arizona

David B. Seidel*
Donald G. Dudley

Dikewood Corporation

Gary Bedrosian

Eyring Research Institute

Harvey J. Fletcher
Alan K. Harrison

Kansas State University

Kendall F. Casey+

University of Mississippi

Chalmers M. Butler

Accession For	
NTIS GRA&I	<input checked="" type="checkbox"/>
DDC TAB	<input type="checkbox"/>
Unannounced	<input type="checkbox"/>
Justification _____	
By _____	
Distribution _____	
Availability Codes _____	
Dist.	Avail and/or special
PY	

* Currently at Sandia Laboratories
+ Currently at Dikewood Corporation

Research for these notes has been funded by the United States Air Force.

Contributions to the Note Series are encouraged from all organizations actively engaged in related research. Active participation throughout the community will build a collection of information useful to all. Contributions and questions regarding the Note Series should be directed to:

Dr. Carl E. Baum
Air Force Weapons Laboratory/ELT
Kirtland Air Force Base, New Mexico 87117.

TABLE OF CONTENTS

NOTE 341 ELECTROMAGNETIC SHIELDING BY ADVANCED COMPOSITE MATERIALS
K. F. Casey, Kansas State University

NOTE 342 FIELDS IN A RECTANGULAR CAVITY EXCITED BY A PLANE WAVE ON
AN ELLIPTICAL APERTURE
Harvey J. Fletcher and Alan K. Harrison, Erying Research
Institute

NOTE 343 TRANSIENT ELECTROMAGNETIC CHARACTERIZATION OF ARBITRARY
CONDUCTING BODIES THROUGH AN APERTURE-PERFORATED CONDUCTING
SCREEN
Korada R. Umashankar and Carl E. Baum, Air Force Weapons
Laboratory

NOTE 344 A COMPARISON OF STICK MODEL SKIN CURRENT PREDICTIONS WITH
SCALE MODEL MEASUREMENTS FOR THE E-4 and EC-135 AIRCRAFT
G. Bedrosian, The Dikewood Corporation

NOTE 345 APERTURE EXCITATION OF A WIRE IN A RECTANGULAR CAVITY
D. B. Seidel, and D. G. Dudley, University of Arizona and
C. M. Butler, University of Mississippi

NOTE 341

ELECTROMAGNETIC SHIELDING BY
ADVANCED COMPOSITE MATERIALS

by

K. F. Casey

Kansas State University

June 1977

ELECTROMAGNETIC SHIELDING BY ADVANCED COMPOSITE MATERIALS

ABSTRACT

The transmission of electromagnetic waves through planar sheets and cylindrical shells of advanced composite laminates is considered in both the frequency and time domains. Attention is concentrated on the frequency range characteristic of the nuclear electromagnetic pulse. The composite laminates are modeled for the purposes of this study by isotropic dielectric or conducting materials.

A new "boundary connection operator" is developed to describe the connection between the tangential electric and magnetic fields on either side of a general multilayer shield. An equivalent sheet impedance operator is developed to describe the bonded wire-mesh screen which is often incorporated in boron-epoxy composite laminates to improve their shielding effectiveness. These analyses are used to study the transmission of EMP signals through planar composite sheets and into cylindrical composite shells in the frequency and time domains. Both graphite-epoxy and "screened" boron-epoxy laminates are considered. Numerical results are presented to illustrate the analytical formulas which are derived.

It is found that the shielding effect of a screened boron-epoxy composite laminate is essentially that of the screen itself. The laminate only has an effect on the equivalent sheet impedance of the screen for parallel-polarized fields, and this effect is relatively minor over the EMP frequency spectrum.

The temporal behavior of the fields transmitted through a planar layer or penetrating a cylindrical shell of composite material is interpreted on the basis of the "low-pass" behavior of the graphite composite and the "high-pass" behavior of wire-mesh screens. Comparisons are made between the shielding effectiveness of the two types of composite materials which are discussed in the report, and it is noted that the screened boron-epoxy composites can be decidedly superior to graphite composites insofar as their shielding effectiveness with respect to EMP waveforms is concerned.

CONTENTS

<u>Section</u>		<u>Page</u>
I.	GENERAL INTRODUCTION	
1.	Composite Materials	341-8
2.	Electromagnetic Shielding Considerations	341-10
3.	Overview of the Report	341-12
II.	BOUNDARY CONNECTION SUPERMATRICES	341-16
1.	Introduction	341-16
2.	Single Layers and Admittance Sheets	341-16
3.	Special-Case Forms	341-24
III.	PLANAR GRAPHITE COMPOSITE SHIELDS	
1.	Introduction	341-31
2.	The Boundary Connection Supermatrix for a Planar Graphite Composite Layer in Free Space	341-32
3.	Plane-Wave Reflection and Transmission by a Planar Graphite Composite Layer	341-33
4.	EMP Transient Propagation Through a Planar Graphite Composite Layer	341-38
IV.	CYLINDRICAL GRAPHITE COMPOSITE SHIELDS	
1.	Introduction	341-45
2.	Formulation of the Problem: Frequency-Domain Results	341-46
3.	Time-Domain Shielding	341-60
V.	PLANAR WIRE-MESH COMPOSITE SHIELDS	
1.	Introduction	341-63
2.	Formulation of the Problem	341-64
3.	Grid Currents	341-72
4.	Equivalent Sheet Impedance of the Grid	341-80
5.	The Transmitted Field	341-90
6.	The "Perforated Screen" Model for a Wire Mesh	341-113
7.	Numerical Computation of Grid Currents	341-121
VI.	CYLINDRICAL WIRE-MESH COMPOSITE SHIELDS	
1.	Introduction	341-129
2.	Formulation of the Problem	341-129
3.	Time-Domain Shielding	341-133

TABLE OF CONTENTS (Continued)

VII. CONCLUDING REMARKS

1. Summary and Discussion	341-143
2. Conclusion	341-147
REFERENCES	341-149

31-140

31-141
31-142
31-143

31-144

31-145
31-146
31-147
31-148
31-149

31-150

31-151
31-152
31-153

31-154

31-155
31-156
31-157
31-158
31-159
31-160

31-161

31-162
31-163
31-164

ILLUSTRATIONS

<u>Figure</u>	<u>Page</u>
1.1 Standard EMP waveform vs. t	341-11
1.2a Standard EMP spectrum: magnitude vs. frequency	341-13
1.2b Standard EMP spectrum: phase vs. frequency	341-14
2.1 A general multilayer shield	341-18
2.2 A single-layer shield in free space with a sheet admittance in one surface	341-25
3.1 Reflection and transmission of a plane wave by a planar graphite composite layer: geometry of the problem	341-34
3.2 T'_o and T''_o vs. θ	341-39
3.3a Magnitude of $(1-j)x \csc(1-j)x$ vs. x	341-40
3.3b Phase of $(1-j)x \csc(1-j)x$ vs. x	341-41
3.4 Normalized transmitted EMP waveforms: graphite slab, normal incidence	341-44
4.1 Plane-wave penetration of, and scattering by, a cylindrical shell of graphite composite: geometry of the problem	341-47
4.2 Energy shielding ratio r_w vs. frequency with a as parameter; $d = 2\text{mm}$, $\sigma_g = 1.5 \times 10^4 \text{ mho m}^{-1}$	341-52
4.3 Energy shielding ratio r_w vs. frequency with σ_g as parameter; $d = 2\text{mm}$, $a = 1 \text{ m}$	341-53
4.4 Energy shielding ratio r_w vs. frequency with d as parameter; $a = 1 \text{ m}$, $\sigma_g = 1.5 \times 10^4 \text{ mho m}^{-1}$	341-54
4.5 Energy shielding ratio r'_w vs. frequency with a as parameter; $d = 2\text{mm}$, $\sigma_g = 1.5 \times 10^4 \text{ mho m}^{-1}$	341-57
4.6 Energy shielding ratio r'_w vs. frequency with σ_g as parameter; $d = 2\text{mm}$, $a = 1 \text{ m}$	341-58
4.7 Energy shielding ratio r'_w vs. frequency with d as parameter; $a = 1 \text{ m}$, $\sigma_g = 1.5 \times 10^4 \text{ mho m}^{-1}$	341-59

ILLUSTRATIONS (Continued)

4.8 (n_o) times internal magnetic field for graphite cylindrical shell vs. t ; $\rho_o = 1 \text{ m}$ 341-62

5.1 Reflection and transmission of a plane wave by a dielectric layer with embedded wire-mesh screen: geometry of the problem 341-65

5.2 Functions $f_a(x)$ and $g_a(x)$ vs. x 341-75

5.3a ϵ_{eqr} vs. d/a for $\epsilon_r = 2, 4, 6$; $r/a = 0.25$ 341-87

5.3b ϵ_{eqr} vs. d/a for $\epsilon_r = 2, 4, 6$; $r/a = 0.025$ 341-88

5.4a Curves of R_s and X_s ($Z'_s = R_s + jX_s$) vs. frequency; $r = 0.051 \text{ mm}$, $a = 0.212 \text{ mm}$ 341-91

5.4b Curves of R_s and X_s ($Z'_s = R_s + jX_s$) vs. frequency; $r = 0.127 \text{ mm}$, $a = 0.635 \text{ mm}$ 341-92

5.5a $|T'|$ vs. frequency; $a = 0.212 \text{ mm}$, $r = 0.051 \text{ mm}$, $\sigma_w = 1.1 \times 10^6 \text{ mho m}^{-1}$; $\theta = 0^\circ, 30^\circ, 60^\circ$ 341-96

5.5b $|T'|$ vs. frequency; $a = 0.212 \text{ mm}$, $r = 0.051 \text{ mm}$, $\sigma_w = 3.72 \times 10^7 \text{ mho m}^{-1}$; $\theta = 0^\circ, 30^\circ, 60^\circ$ 341-97

5.6a $|T'|$ vs. frequency; $a = 0.635 \text{ mm}$, $r = 0.127 \text{ mm}$, $\sigma_w = 1.1 \times 10^6 \text{ mho m}^{-1}$; $\theta = 0^\circ, 30^\circ, 60^\circ$ 341-98

5.6b $|T'|$ vs. frequency; $a = 0.635 \text{ mm}$, $r = 0.127 \text{ mm}$, $\sigma_w = 3.72 \times 10^7 \text{ mho m}^{-1}$; $\theta = 0^\circ, 30^\circ, 60^\circ$ 341-99

5.7a $|T''|$ vs. frequency; $a = 0.212 \text{ mm}$, $r = 0.051 \text{ mm}$, $\sigma_w = 1.1 \times 10^6 \text{ mho m}^{-1}$, $\epsilon_r = 1.0$; $\theta = 0^\circ, 30^\circ, 60^\circ$ 341-100

5.7b $|T''|$ vs. frequency; $a = 0.212 \text{ mm}$, $r = 0.051 \text{ mm}$, $\sigma_w = 1.1 \times 10^6 \text{ mho m}^{-1}$, $\epsilon_r = 4.5$; $\theta = 0^\circ, 30^\circ, 60^\circ$ 341-101

5.7c $|T''|$ vs. frequency; $a = 0.212 \text{ mm}$, $r = 0.051 \text{ mm}$, $\sigma_w = 3.72 \times 10^7 \text{ mho m}^{-1}$, $\epsilon_r = 1.0$; $\theta = 0^\circ, 30^\circ, 60^\circ$ 341-102

5.7d $|T''|$ vs. frequency; $a = 0.212 \text{ mm}$, $r = 0.051 \text{ mm}$, $\sigma_w = 3.72 \times 10^7 \text{ mho m}^{-1}$, $\epsilon_r = 4.5$; $\theta = 0^\circ, 30^\circ, 60^\circ$ 341-103

ILLUSTRATIONS (Continued)

5.8a	$ T'' $ vs. frequency; $a = 0.635 \text{ mm}$, $r = 0.127 \text{ mm}$, $\sigma_w = 1.1 \times 10^6 \text{ mho m}^{-1}$, $\epsilon_r = 1.0$; $\theta = 0^\circ, 30^\circ, 60^\circ \dots$	341-104
5.8b	$ T'' $ vs. frequency; $a = 0.635 \text{ mm}$, $r = 0.127 \text{ mm}$, $\sigma_w = 1.1 \times 10^6 \text{ mho m}^{-1}$, $\epsilon_r = 4.5$; $\theta = 0^\circ, 30^\circ, 60^\circ \dots$	341-105
5.8c	$ T'' $ vs. frequency; $a = 0.635 \text{ mm}$, $r = 0.127 \text{ mm}$, $\sigma_w = 3.72 \times 10^7 \text{ mho m}^{-1}$, $\epsilon_r = 1.0$; $\theta = 0^\circ, 30^\circ, 60^\circ \dots$	341-106
5.8d	$ T'' $ vs. frequency; $a = 0.635 \text{ mm}$, $r = 0.127 \text{ mm}$, $\sigma_w = 3.72 \times 10^7 \text{ mho m}^{-1}$, $\epsilon_r = 4.5$; $\theta = 0^\circ, 30^\circ, 60^\circ \dots$	341-107
5.9	$E_t(\tau)$ vs. τ ; $a = 0.212 \text{ mm}$, $r = 0.051 \text{ mm}$, $\sigma_w = 1.1 \times 10^6$, $3.72 \times 10^7 \text{ mho m}^{-1} \dots$	341-110
5.10	$E_t(\tau)$ vs. τ ; $a = 0.635 \text{ mm}$, $r = 0.127 \text{ mm}$, $\sigma_w = 1.1 \times 10^6$, $3.72 \times 10^7 \text{ mho m}^{-1} \dots$	341-111
5.11	Perforated screen geometry	341-114
5.12	Functions $(1/\pi) \ln(1 - e^{-2\pi r/a})^{-1}$ and α_m/a^3 vs. $r/a \dots$	341-118
5.13	α_e/α_m vs. $r/a \dots$	341-119
5.14	X_s' and X_s'' ($Z_s' = jX_s'$) vs. N ; $d/a = 1$, $\epsilon_r = 4.5$, $r/a = 0.01$, $\sigma_w = \infty$, $\theta = 60^\circ$, $\phi = 0^\circ$, $k_o a = 1.0 \dots$	341-124
5.15	X_s' and X_s'' ($Z_s' = jX_s'$) vs. N ; $d/a = 1$, $\epsilon_r = 4.5$, $r/a = 0.01$, $\sigma_w = \infty$, $\theta = 60^\circ$, $\phi = 45^\circ$, $k_o a = 1.0 \dots$	341-125
5.16	X_s' and X_s'' ($Z_s' = jX_s'$) vs. N ; $d/a = 1$, $\epsilon_r = 4.5$, $r/a = 0.01$, $\sigma_w = \infty$, $\theta = 60^\circ$, $\phi = 0^\circ$, $k_o a = 0.1 \dots$	341-126
5.17	X_s' and X_s'' ($Z_s' = jX_s'$) vs. N ; $d/a = 1$, $\epsilon_r = 4.5$, $r/a = 0.01$, $\sigma_w = \infty$, $\theta = 60^\circ$, $\phi = 45^\circ$, $k_o a = 0.1 \dots$	341-127
6.1	Plane wave penetration of, and scattering by, a cylindrical shell of boron-epoxy composite with a bonded wire-mesh screen in the outer surface: geometry of the problem	341-129

ILLUSTRATIONS (Continued)

6.2a	r_w vs. frequency; $a_m = 0.212$ mm, $r = 0.051$ mm, $\rho_o = 1$ m; $\sigma_w = 1.1 \times 10^6$ and 3.72×10^7 mho m^{-1}	341-134
6.2b	r_w vs. frequency; $a_m = 0.635$ mm, $r = 0.127$ mm, $\rho_o = 1$ m; $\sigma_w = 1.1 \times 10^6$ and 3.72×10^7 mho m^{-1}	341-135
6.3a	r'_w vs. frequency; $a_m = 0.212$ mm, $r = 0.051$ mm, $\rho_o = 1$ m; $\sigma_w = 1.1 \times 10^6$ and 3.72×10^7 mho m^{-1} ; $\epsilon_r = 4.5$	341-136
6.3b	r'_w vs. frequency; $a_m = 0.635$ mm, $r = 0.127$ mm, $\rho_o = 1$ m; $\sigma_w = 1.1 \times 10^6$ and 3.72×10^7 mho m^{-1} ; $\epsilon_r = 4.5$	341-137
6.4	$n_o H_{int}(t)$ vs. time; $a_m = 0.212$ mm, $r = 0.051$ mm, $\rho_o = 1$ m; $\sigma_w = 1.1 \times 10^6$, 3.72×10^7 mho m^{-1}	341-140
6.5	$n_o H_{int}(t)$ vs. time; $a_m = 0.635$ mm, $r = 0.127$ mm, $\rho_o = 1$ m; $\sigma_w = 1.1 \times 10^6$, 3.72×10^7 mho m^{-1}	341-141

SECTION I

GENERAL INTRODUCTION

1. COMPOSITE MATERIALS

Advanced composite materials have become increasingly important in recent years because of their great strength and relatively light weight. In fact, it is estimated that the F-18 aircraft will use advanced composites to the extent of nearly 40% by weight and 80% outer surface coverage [1].

Advanced composite materials are laminates, or multilayer "layups", of many individual laminae. A single lamina consists of a planar array of fibers (of boron/boron tungstate, graphite⁺, etc.) in an epoxy matrix. Typical lamina thicknesses are around 0.2 mm, and a typical aircraft skin panel comprises seven layers. The arrangement of the layers can be varied to suit the strength requirements of the laminate in given directions. Typically, however, a 0°-90° or 0°-45°-90° layup will be used, so that the laminate is nearly isotropic in its mechanical characteristics in directions parallel to its surfaces.

A review of the literature has shown that the basic electrical parameters (e.g., permittivity and conductivity) of advanced composites are only now beginning to be studied [1,2]. However, it seems generally to be agreed that graphite composites behave as good conductors (in the sense that conduction currents dominate displacement currents in the material) with conductivity roughly one-fourth that of pure graphite (7.14×10^4 mho m^{-1}), and that boron-epoxy composites behave as mildly lossy dielectrics.

⁺i.e., a pyrolyzed organic fiber such as polyacrylonitrile.

In this Note we shall assume that these materials are isotropic. It is clear from consideration of the physical structure of composite laminates that they are probably anisotropic, but for simplicity we shall for the present ignore this aspect of these materials. In a related study [3] it has been shown that the anisotropic conductivity of graphite composites is not of prime importance in characterizing the material, the transverse conductivity (i.e., that in the directions parallel to the laminate surface) being the descriptive parameter of principal interest. Furthermore, the anisotropy of boron-epoxy laminates appears to be weak.

Since boron-epoxy composite is such a poor conductor, it provides negligible shielding against penetration by electromagnetic fields. To improve the shielding effectiveness of a boron-epoxy composite laminate, a conducting screen may be embedded in one of its surfaces. In this study we shall assume that the wires in the screen are bonded at the junctions and develop an extension of the now classic theory of Kontorovich [4] in order to take into account the effect of the presence of a dielectric layer on the behavior of the screen.

The advanced composite materials we shall consider, therefore, are of two types: graphite composites, which are modeled as homogeneous, isotropic, conducting materials; and screened boron-epoxy composites, modeled as dielectric layers with a bonded wire-mesh screen in one surface. The conductivity of the graphite composites will be taken to be around 1.5×10^4 mho m^{-1} (roughly one-fourth the conductivity of pure graphite) and the relative permittivity of the boron-epoxy composites will be assumed to be in the range 4-5 [3]. Typical laminate thicknesses are in the range 1-3 mm and typical wire-mesh screen parameters are:

mesh size: 20×20 to 200×200 (per inch)
wire radius: 0.05 to 0.15 mm
wire conductivity: 1.1×10^6 mho m^{-1} (stainless steel)
 to 3.7×10^7 mho m^{-1} (aluminum)

2. ELECTROMAGNETIC SHIELDING CONSIDERATIONS

We shall concentrate in this study on the nuclear electromagnetic pulse (EMP) shielding characteristics of graphite and screened boron-epoxy composites. This restricts the frequency range of interest to $f < 10^8$ Hz. It should be noted that characterizations of advanced composite materials which are valid in this frequency range may not be useful, say, for studying the interactions of advanced composites with radar signals. The inhomogeneity and anisotropy of the materials, which may be neglected for EMP studies, may become critically important in dealing with higher-frequency interactions.

The standard EMP waveform which we shall use in this study is [5]

$$E(t) = E_p A (e^{-\alpha t} - e^{-\beta t}) \quad (1.1)$$

in which E_p denotes the peak amplitude of the electric field, and

$$A = \left(e^{-\alpha t_0} - e^{-\beta t_0} \right)^{-1} = 1.1373 \dots \quad (1.2a)$$

$$t_0 = \frac{1}{\beta - \alpha} \ln \frac{\beta}{\alpha} = 2.104 \times 10^{-9} \text{ sec.} \quad (1.2b)$$

$$\alpha = 4.80 \times 10^7 \text{ sec}^{-1} \quad (1.2c)$$

$$\beta = 1.76 \times 10^9 \text{ sec}^{-1} \quad (1.2d)$$

A plot of $E(t)/E_p$ vs. t is shown in Fig. 1.1[†]. The magnitude and phase

[†]The logarithmic time plot will be used throughout this report, in order best to display the detailed time history of the transient signals considered.

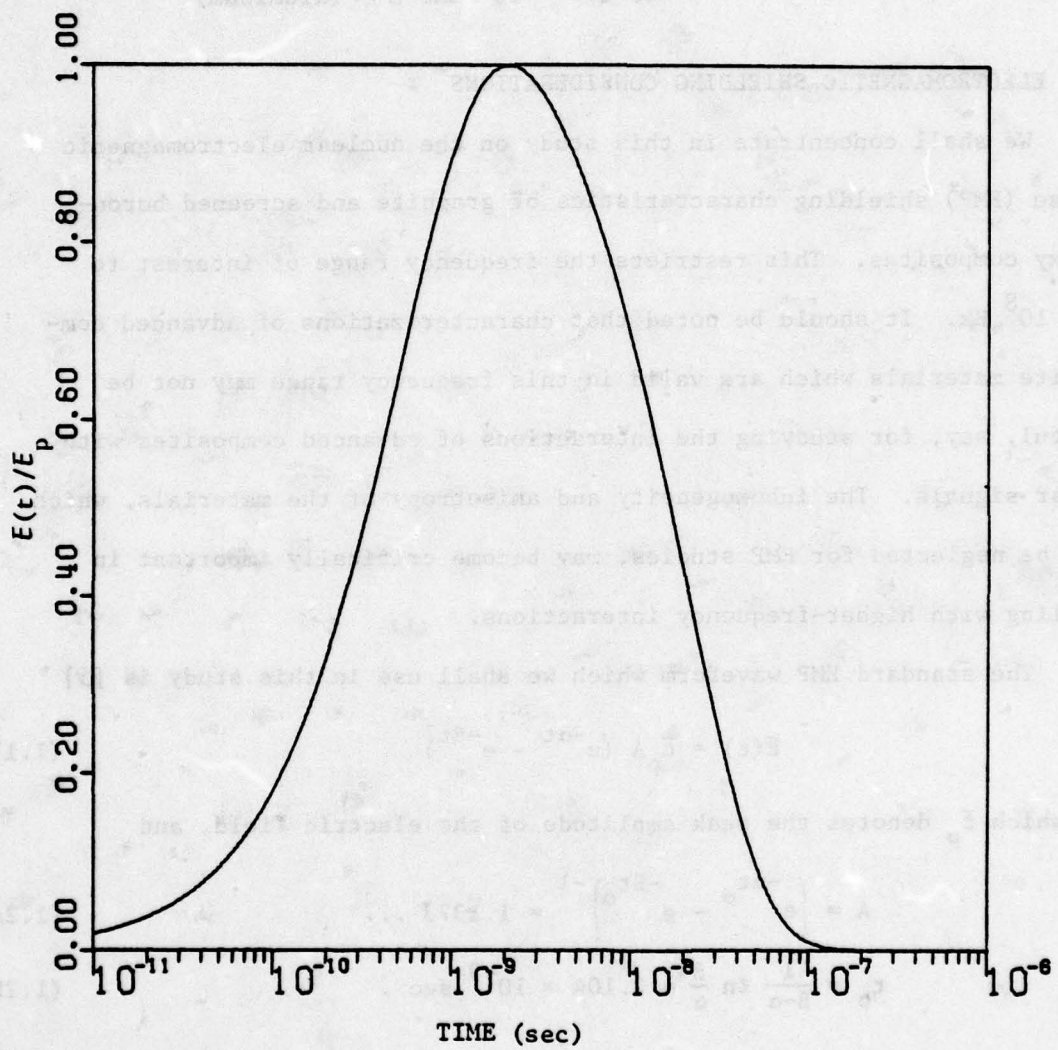


Figure 1.1. Standard EMP waveform vs. t

spectra of this EMP signal are shown in Fig. 1.2. The function $E(t)$ describes the electric field time history of an incident electromagnetic wave, which is assumed to be plane. The associated magnetic field $H(t) = E(t)/n_0$, in which n_0 denotes the intrinsic impedance of free space.

Two geometrical forms, the infinite sheet and the infinitely long cylindrical shell, are of principal interest to us. We shall address the problems of electromagnetic wave transmission through an infinite sheet of advanced composite and of electromagnetic wave penetration into the interior of a cylindrical shell of advanced composite. Both types of composites (graphite and screened boron-epoxy) will be considered and both frequency and time-domain calculations of the transmitted or penetrated field will be made, under the assumption that the incident field is as given above in (1.1) and (1.2).

3. OVERVIEW OF THE WORK

In Section II we shall develop a "boundary connection supermatrix" which relates the electromagnetic fields on either side of a multilayer shield of more or less arbitrary shape. In addition to its utility in non-separable geometries, it simplifies the analysis of separable problems in that the number of regions to be explicitly considered is reduced. This supermatrix is used in the problem formulations in Sections III-VI.

The interaction of plane electromagnetic waves with planar graphite composite laminates is discussed in Section III and the interaction with cylindrical graphite composite shells in Section IV. Both the frequency and the time domains are investigated (the latter via inverse Laplace transformation).

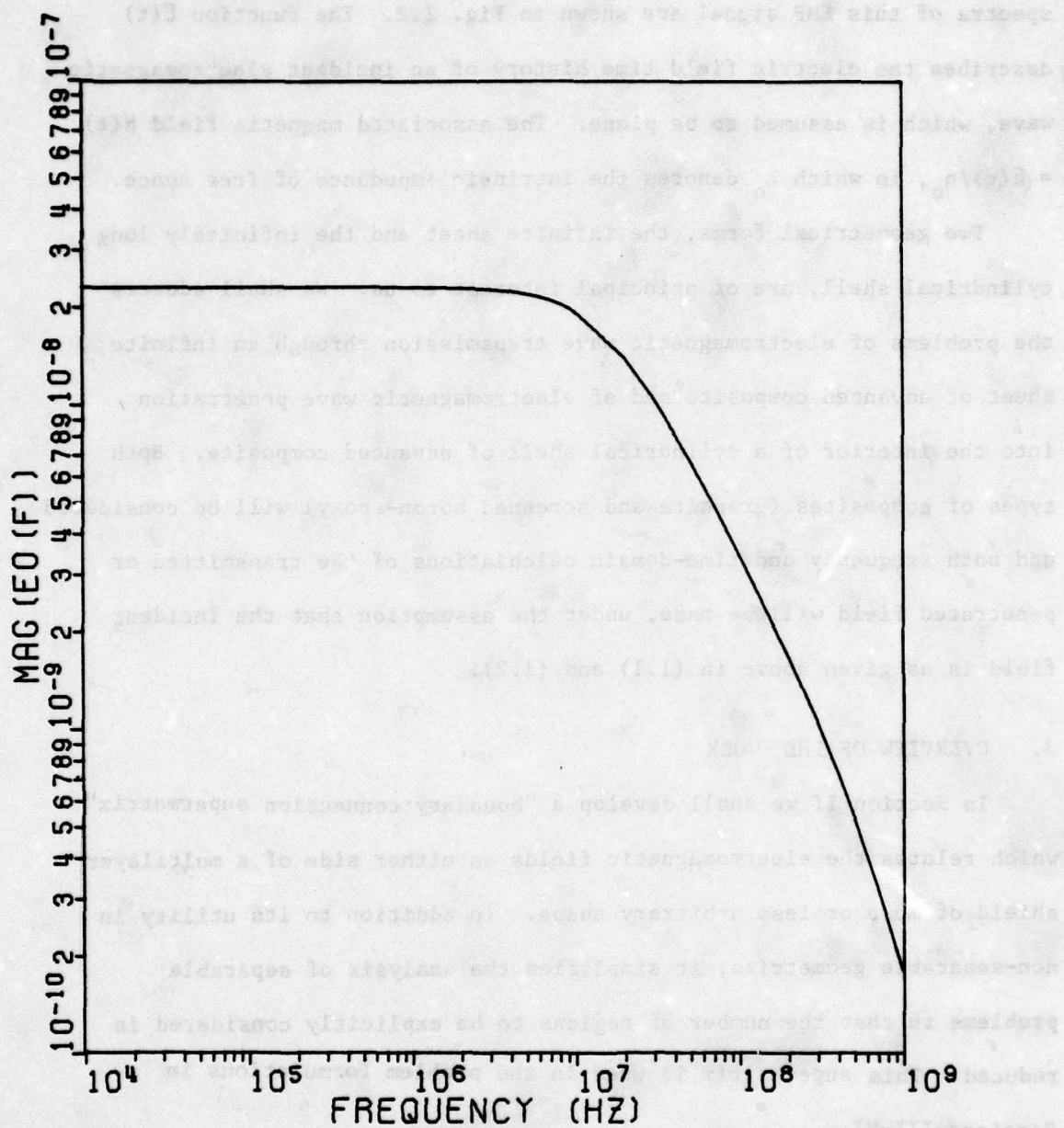


Figure 1.2a. Standard EMP spectrum: magnitude vs. frequency

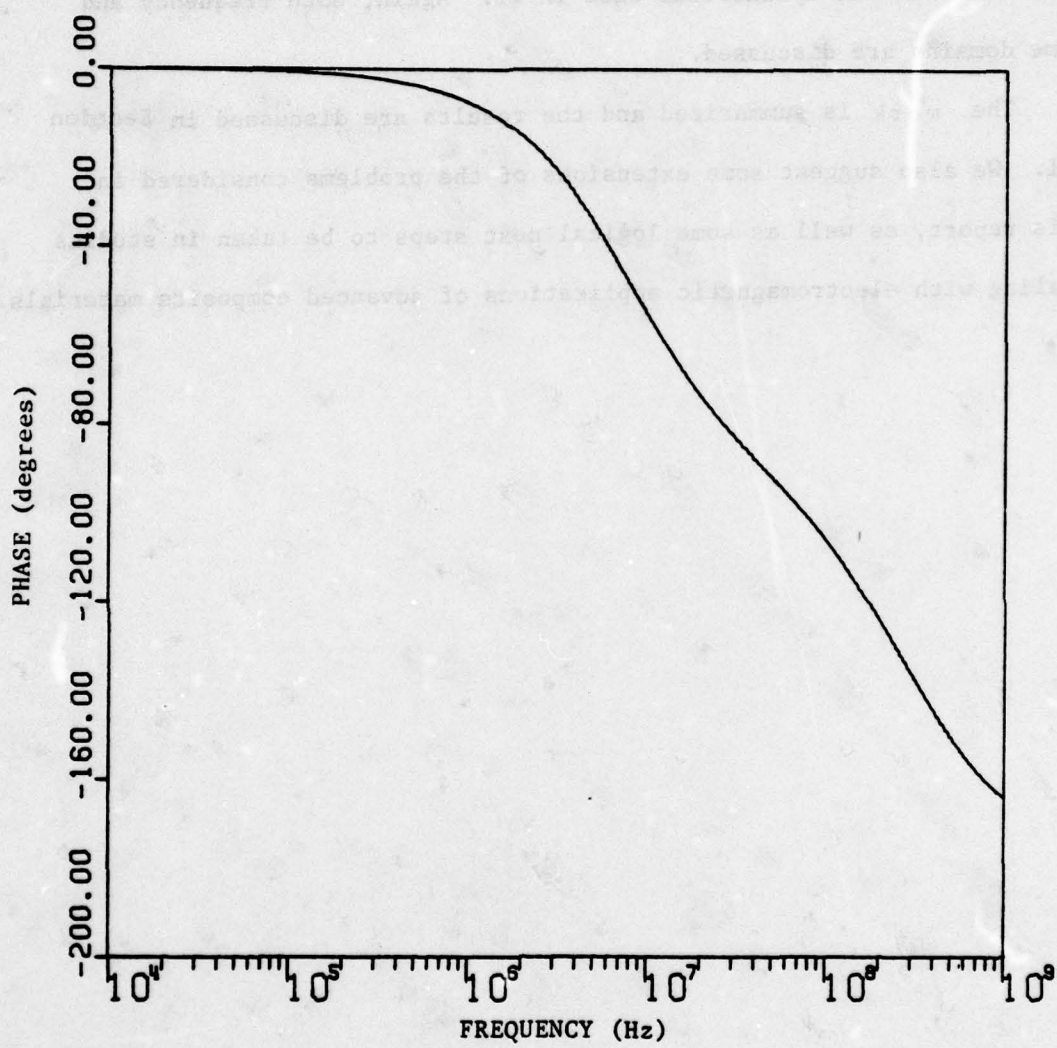


Figure 1.2b. Standard EMP spectrum: phase vs. frequency

Screened boron-epoxy laminates and their interactions with plane electromagnetic waves are considered in sections V and VI, the planar case in V and the cylindrical case in VI. Again, both frequency and time domains are discussed.

The work is summarized and the results are discussed in Section VII. We also suggest some extensions of the problems considered in this report, as well as some logical next steps to be taken in studies dealing with electromagnetic applications of advanced composite materials.

SECTION II

BOUNDARY CONNECTION SUPERMATRICES

1. INTRODUCTION

In order to assess the degree of electromagnetic shielding provided by a layer of a given material of specified shape, one must determine the relationship between the electromagnetic field on one side of the layer and that on the other. This fundamental mathematical problem is often complicated by the fact that the geometry of the shielding layer does not correspond to one in which the vector wave equation is separable. Therefore, in order to determine the relation desired, one must either develop exact solutions of such complexity and generality as to be of little use for practical purposes, or take advantage of whatever special circumstances exist in order to develop useful, albeit approximate, solutions to the problem.

Fortunately, such special circumstances occur in the type of problem in which we are primarily interested. They are that

- (a) the thickness of the material layer is usually much smaller than either of its two principal radii of curvature,
- (b) the wavelength in the material is usually much smaller than the wavelength outside, and
- (c) the shield is usually made of a lossy material.

We conclude from the second and third conditions above that the electromagnetic behavior of a shield is largely a local phenomenon, in that the fields at points $(\xi_1, \xi_2, \xi_3)^+$ and $(\xi_1 + \Delta\xi_1, \xi_2 + \Delta\xi_2, \xi_3)$ are not closely

[†] ξ_1 , ξ_2 , and ξ_3 are coordinates of a system whose origin lies in one surface of the layer, the other surface being at $\xi_3 = d$. ξ_1 and ξ_2 are therefore coordinates locally parallel to the shield surfaces.

coupled when $[(\Delta\xi_1)^2 + (\Delta\xi_2)^2]^{1/2} \gg d$, the thickness of the layer.

Therefore, the development of the "transfer characteristic" of the shield layer requires consideration not of the whole shield, but only of local portions of it. By virtue of the first condition listed above, we may consider these portions to be planar and utilize a planar model to determine the shield transfer characteristic. Having developed this characteristic, we may then apply the results to geometrical configurations which are nonplanar and for which the shield characteristics may even change with position, provided that these changes are sufficiently gradual.

The planar geometry which we shall consider in this chapter is shown in Fig. 2.1. The region $0 \leq z \leq d_s$ contains the shield material. This material may be arranged in layers of different thicknesses and electrical properties, and the layers may be separated by admittance sheets. We shall assume that the individual layers and admittance sheets are homogeneous, linear, and isotropic. In the following paragraphs, we shall develop a matrix of dyadics \bar{M} (the Boundary Connection Supermatrix or BCS) which expresses the relation between the tangential components of the electromagnetic fields on either side of the layer[†]. The BCS's for single layers and admittance sheets are derived in section B, and simplified forms of these BCS's applicable in special circumstances are discussed in paragraph 3.

3. SINGLE LAYERS AND ADMITTANCE SHEETS

We consider first the derivation of the single-layer supermatrix \bar{M}_g , which relates the tangential components of the electromagnetic field at $z = z_1 + d_g$ to those at $z = z_1$ in a homogeneous medium of permittivity

[†]The relations to be developed constitute an extension and modification of the ABCD matrix approach to the problem [6].

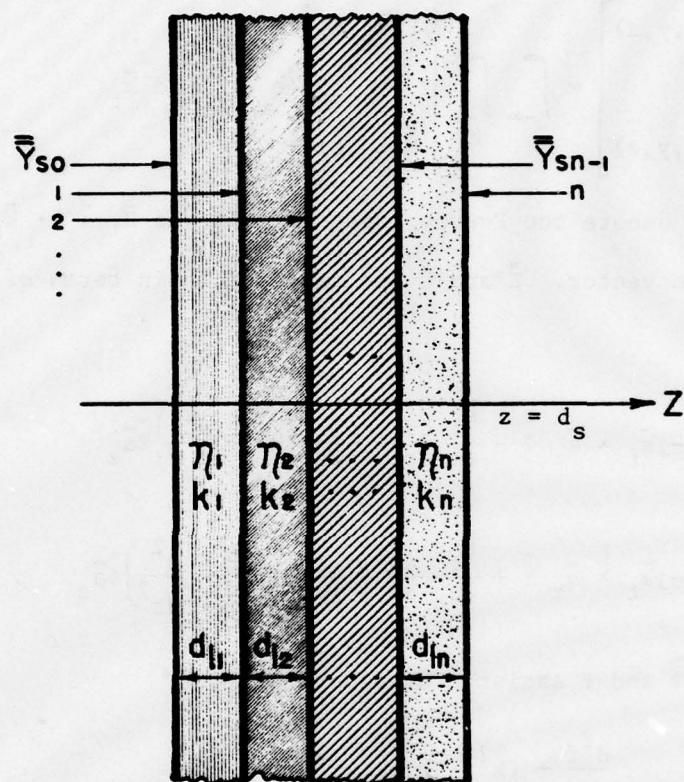


Figure 2.1. A general multilayer shield. η_i and k_i denote the intrinsic impedance and propagation constant of the i th layer. \bar{Y}_{si} denotes the sheet admittance operator on the right side of the i th layer.

ϵ^+ and permeability μ_0 . The time dependence $\exp(j\omega t)$ is assumed.

The relations which we seek are most conveniently developed in terms of the Fourier spectra of the electric and magnetic fields. Let us write the fields as follows:

$$\begin{bmatrix} \bar{E}(x, y, z) \\ \bar{H}(x, y, z) \end{bmatrix} = \int_{-\infty}^{\infty} \int_{-\infty}^{\infty} \begin{bmatrix} \tilde{\bar{E}}(\bar{k}_t, z) \\ \tilde{\bar{H}}(\bar{k}_t, z) \end{bmatrix} e^{-j\bar{k}_t \cdot \bar{r}} d^2 \bar{k}_t \quad (2.1)$$

in which $\tilde{\bar{E}}$ and $\tilde{\bar{H}}$ denote the Fourier spectra of \bar{E} and \bar{H} , $\bar{a}_z \cdot \bar{k}_t = 0$, and \bar{r} is the position vector. $\tilde{\bar{E}}$ and $\tilde{\bar{H}}$ are expressible in terms of two functions $\tilde{\phi}(z)$ and $\tilde{\psi}(z)$ as

$$\tilde{\bar{E}} = -j\bar{k}_t \times \bar{a}_z \tilde{\phi} - \frac{\bar{k}_t}{\omega \epsilon} \frac{d\tilde{\psi}}{dz} + \frac{1}{j\omega \epsilon} \left(k^2 + \frac{d^2}{dz^2} \right) \tilde{\psi} \bar{a}_z \quad (2.2a)$$

$$\tilde{\bar{H}} = -j\bar{k}_t \times \bar{a}_z \tilde{\psi} + \frac{\bar{k}_t}{\omega \mu_0} \frac{d\tilde{\phi}}{dz} - \frac{1}{j\omega \mu_0} \left(k^2 + \frac{d^2}{dz^2} \right) \tilde{\phi} \bar{a}_z \quad (2.2b)$$

$k^2 \equiv \omega^2 \mu_0 \epsilon$, and $\tilde{\phi}$ and $\tilde{\psi}$ satisfy the equation

$$\frac{d^2 f}{dz^2} + (k^2 - \bar{k}_t \cdot \bar{k}_t) f = 0 \quad (2.3)$$

Solving eq. (2.3) for $\tilde{\phi}$ and $\tilde{\psi}$ and inserting the solutions in eq. (2.2) yields expressions for the tangential field components (denoted by subscript t) as functions of $z' = z - z_1$:

$$\begin{aligned} \tilde{\bar{E}}_t(z') &= -j\bar{k}_t \times \bar{a}_z (A_\phi \sin k_z z' + B_\phi \cos k_z z') \\ &\quad - \frac{k_z}{\omega \epsilon} \bar{k}_t (A_\psi \cos k_z z' - B_\psi \sin k_z z') \end{aligned} \quad (2.4a)$$

[†]If the medium has finite conductivity σ , ϵ should be replaced by $\epsilon + j\omega/\sigma$.

$$\begin{aligned}\tilde{\tilde{H}}_t(z') &= -jk_t \times \bar{a}_z (A_\psi \sin k_z z' + B_\psi \cos k_z z') \\ &\quad + \frac{k_z}{\omega\mu_0} \bar{k}_t (A_\phi \cos k_z z' - B_\phi \sin k_z z')\end{aligned}\quad (2.4b)$$

The constants A_ϕ , B_ϕ , A_ψ , and B_ψ , which are the arbitrary constants associated with the solutions of eq. (2.3), are to be evaluated in terms of the tangential field components at $z' = 0$, and

$$k_z^2 = k^2 - \bar{k}_t \cdot \bar{k}_t \quad (2.5)$$

We have, setting $z' = 0$ in eq. (2.4),

$$\tilde{\tilde{E}}_t(0) = -jk_t \times \bar{a}_z B_\phi - \frac{k_z}{\omega\epsilon} \bar{k}_t A_\psi \quad (2.6a)$$

$$\tilde{\tilde{H}}_t(0) = -jk_t \times \bar{a}_z B_\psi + \frac{k_z}{\omega\mu_0} \bar{k}_t A_\phi \quad (2.6b)$$

from which we obtain

$$A_\psi = \frac{-\omega\epsilon}{k_z k_t^2} \bar{k}_t \cdot \tilde{\tilde{E}}_t(0) \quad (2.7a)$$

$$A_\phi = \frac{\omega\mu_0}{k_z k_t^2} \bar{k}_t \cdot \tilde{\tilde{H}}_t(0) \quad (2.7b)$$

$$B_\psi = \frac{1}{jk_t^2} \bar{a}_z \cdot [\bar{k}_t \times \tilde{\tilde{H}}_t(0)] \quad (2.7c)$$

$$B_\phi = \frac{1}{jk_t^2} \bar{a}_z \cdot [\bar{k}_t \times \tilde{\tilde{E}}_t(0)] \quad (2.7d)$$

where $k_t^2 \equiv \bar{k}_t \cdot \bar{k}_t$.

Now substitute eq. (2.7) into eq. (2.4) and set $z' = d_\ell$ ($z = z_1 + d_\ell$).

We find, after some simple manipulations, the compact relation

$$\begin{bmatrix} \tilde{\tilde{E}}_t(d_\ell) \\ \eta\tilde{\tilde{H}}_t(d_\ell) \end{bmatrix} = \begin{bmatrix} \bar{I} \cos k_z d_\ell & \bar{U} \sin k_z d_\ell \\ -\bar{U} \sin k_z d_\ell & \bar{I} \cos k_z d_\ell \end{bmatrix} \begin{bmatrix} \tilde{\tilde{E}}_t(0) \\ \eta\tilde{\tilde{H}}_t(0) \end{bmatrix} \quad (2.8)$$

where $\eta = \sqrt{\mu_0/\epsilon}$ denotes the characteristic impedance of the medium, \bar{I} is the identity operator, and

$$\bar{U} = -\frac{1}{jkk_z} \bar{a}_z \times (\bar{k}_t \bar{k}_t + k_z^2 \bar{I}) \quad (2.9)$$

Eq. (2.8) is the relation which has been sought. We define the single-layer connection supermatrix \bar{M}_ℓ as follows;

$$\bar{M}_\ell(z_1; k; z_2) = \begin{bmatrix} \bar{I} \cos k_z(z_1 - z_2) & \bar{U} \sin k_z(z_1 - z_2) \\ -\bar{U} \sin k_z(z_1 - z_2) & \bar{I} \cos k_z(z_1 - z_2) \end{bmatrix} \quad (2.10)$$

so that in general,

$$\begin{bmatrix} \tilde{\tilde{E}}_t(z_1) \\ \eta\tilde{\tilde{H}}_t(z_1) \end{bmatrix} = \bar{M}_\ell(z_1; k; z_2) \cdot \begin{bmatrix} \tilde{\tilde{E}}_t(z_2) \\ \eta\tilde{\tilde{H}}_t(z_2) \end{bmatrix} \quad (2.11)$$

The notation chosen for the arguments of \bar{M}_ℓ makes equations of the form of (2.11) read naturally from left to right. Note also that $\bar{M}_\ell^{-1}(z_1; k; z_2) = \bar{M}_\ell(z_2; k; z_1)$.

We now consider the connection between tangential field components across an interface. Such an interface may consist of a boundary between two different media, or of a sheet impedance, or both. We shall construct

the connection supermatrix for the general case; then, if the media on either side of the boundary are identical or if the admittance sheet is absent, the connection supermatrix will reduce to a simpler form.

Let the boundary be located at $z = z_s$. Then we require that

$$\tilde{\tilde{E}}_t(z = z_s+) = \tilde{\tilde{E}}_t(z = z_s-) = \tilde{\tilde{E}}_t(z = z_s) \quad (2.12a)$$

$$\bar{a}_z \times [\tilde{\tilde{H}}_t(z = z_s+) - \tilde{\tilde{H}}_t(z = z_s-)] = \bar{Y}_s \cdot \tilde{\tilde{E}}_t(z = z_s) \quad (2.12b)$$

\bar{Y}_s is an admittance operator which relates the surface current density $\tilde{\tilde{J}}_s$ at $z = z_s$ to the tangential electric field there:

$$\tilde{\tilde{J}}_s = \bar{Y}_s \cdot \tilde{\tilde{E}}_t(z_s) \quad (2.13)$$

It follows immediately from eq. (2.12) that if the characteristic impedance of the medium on the " z_s+ " side of the sheet is n_+ and that on the " z_s- " side is n_- , then

$$\begin{bmatrix} \tilde{\tilde{E}}_t(z_s-) \\ n_- \tilde{\tilde{H}}_t(z_s-) \end{bmatrix} = \begin{bmatrix} \bar{I} & \bar{0} \\ \bar{a}_z \times n_- \bar{Y}_s & \frac{n_-}{n_+} \bar{I} \end{bmatrix} \begin{bmatrix} \tilde{\tilde{E}}_t(z_s+) \\ n_+ \tilde{\tilde{H}}_t(z_s+) \end{bmatrix} \quad (2.14)$$

Eq. (2.14) is the relation which has been sought. We define the 2×2 matrix in eq. (2.14) to be the admittance-sheet connection supermatrix

\bar{M}_s and write

$$\bar{M}_s(n_-; \bar{Y}_s; n_+) = \begin{bmatrix} \bar{I} & \bar{0} \\ \bar{a}_z \times n_- \bar{Y}_s & \frac{n_-}{n_+} \bar{I} \end{bmatrix} \quad (2.15)$$

so that

$$\begin{bmatrix} \tilde{\tilde{E}}_t(z_s^-) \\ n_- \tilde{\tilde{H}}_t(z_s^-) \end{bmatrix} = \bar{M}_s(n_-; \bar{Y}_s; n_+) \cdot \begin{bmatrix} \tilde{\tilde{E}}_t(z_s^+) \\ n_+ \tilde{\tilde{H}}_t(z_s^+) \end{bmatrix} \quad (2.16)$$

The notation chosen for the arguments of \bar{M}_s makes equations of the form of (2.16) read naturally from left to right. Note also that $\bar{M}_s^{-1}(n_-; \bar{Y}_s; n_+) = \bar{M}_s(n_+; -\bar{Y}_s; n_-)$.

Now as an illustrative example, let us construct the boundary connection supermatrix for the configuration shown in Fig. (2.2). This is a material layer of parameters n and k in the region $0 \leq z \leq d_\ell$, having an admittance sheet on the surface $z = 0$. The medium outside the structure is free space, and we wish to connect the free-space fields at $z = 0-$ to the free-space fields at $z = d_\ell+$. We have the following relations:

$$\begin{bmatrix} \tilde{\tilde{E}}_t(0-) \\ n_0 \tilde{\tilde{H}}_t(0-) \end{bmatrix} = \bar{M}_s(n_0; \bar{Y}_s, n) \cdot \begin{bmatrix} \tilde{\tilde{E}}_t(0+) \\ n \tilde{\tilde{H}}_t(0+) \end{bmatrix} \quad (2.17a)$$

$$\begin{bmatrix} \tilde{\tilde{E}}_t(0+) \\ n \tilde{\tilde{H}}_t(0+) \end{bmatrix} = \bar{M}_\ell(0; k; d_\ell) \cdot \begin{bmatrix} \tilde{\tilde{E}}_t(d_\ell^-) \\ n \tilde{\tilde{H}}_t(d_\ell^-) \end{bmatrix} \quad (2.17b)$$

$$\begin{bmatrix} \tilde{\tilde{E}}_t(d_\ell^-) \\ n \tilde{\tilde{H}}_t(d_\ell^-) \end{bmatrix} = \bar{M}_s(n; \bar{0}; n_0) \cdot \begin{bmatrix} \tilde{\tilde{E}}_t(d_\ell^+) \\ n_0 \tilde{\tilde{H}}_t(d_\ell^+) \end{bmatrix} \quad (2.17c)$$

from which it is apparent that

$$\begin{bmatrix} \tilde{\tilde{E}}_t(0-) \\ n_o \tilde{\tilde{H}}_t(0-) \end{bmatrix} = \bar{\bar{M}}_t \cdot \begin{bmatrix} \tilde{\tilde{E}}_t(d_\ell+) \\ n_o \tilde{\tilde{H}}_t(d_\ell+) \end{bmatrix} \quad (2.18)$$

in which

$$\bar{\bar{M}}_t = \bar{\bar{M}}_s(n_o; \bar{\bar{Y}}_s; n) \cdot \bar{\bar{M}}_\ell(0; k; d_\ell) \cdot \bar{\bar{M}}_s(n; \bar{\bar{Y}}_s; n_o) \quad (2.19)$$

One will note that the arguments in eq. (2.19) read naturally from left to right, and correspond to the physical features of the shield structure, as is shown in Fig. 2.2. Furthermore, note that

$$\bar{\bar{M}}_t^{-1} = \bar{\bar{M}}_s(n_o; \bar{\bar{Y}}_s; n) \cdot \bar{\bar{M}}_\ell(d_\ell; k; 0) \cdot \bar{\bar{M}}_s(n; -\bar{\bar{Y}}_s; n_o) \quad (2.20)$$

Generalizations to arbitrarily complicated shield structures are obvious.

In many practical problems, the connection supermatrices which have been developed in this section can be simplified under certain conditions. We consider this problem in the next section.

3. SPECIAL-CASE FORMS

In this section we consider the forms taken by the connection supermatrices when

- (a) the electromagnetic field is either parallel-polarized or perpendicular-polarized
- (b) the (effective) permittivity of the shield material is large compared to that of the surrounding medium (usually free space)

We also consider the conditions which must hold for an electrically thin layer to be modeled as an equivalent admittance sheet.

$$\begin{bmatrix} \bar{Y}_s \\ 0 \end{bmatrix} = \begin{bmatrix} (-1) & 0 \\ 0 & 1 \end{bmatrix} \begin{bmatrix} \bar{Y}_s \\ 0 \end{bmatrix} + \begin{bmatrix} (-1) & 0 \\ 0 & 1 \end{bmatrix} \begin{bmatrix} 0 \\ 0 \end{bmatrix}$$

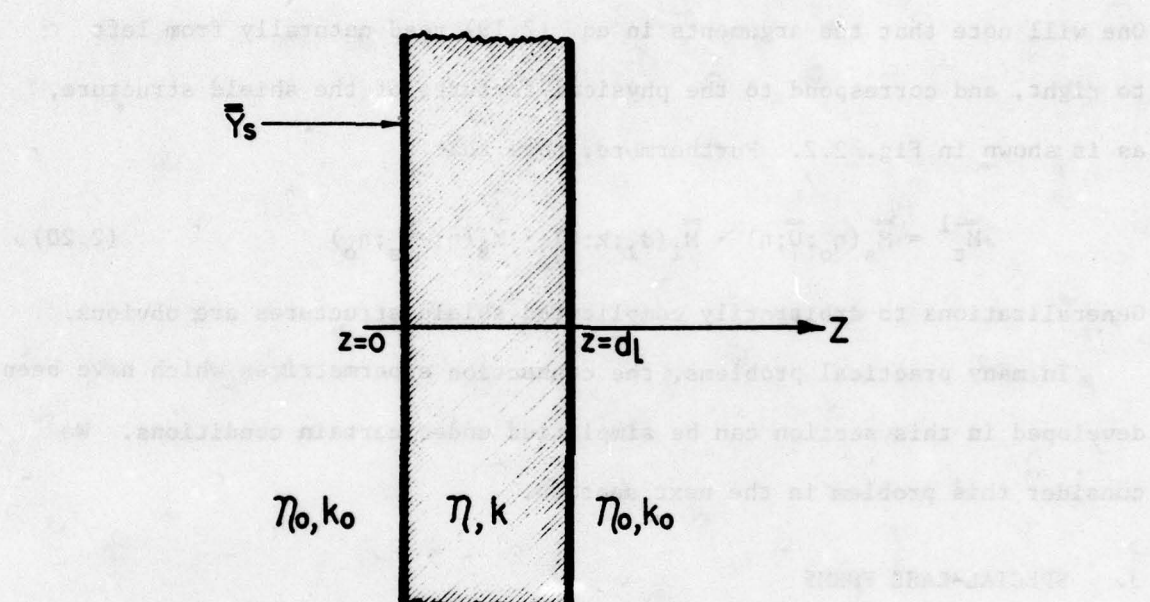
(1.1.5) $\text{Con-Dim } K = \text{Dim } \bar{Y}_s \text{, i.e., } K = 2$ 

Figure 2.2. A single-layer shield in free space with a sheet admittance \bar{Y}_s in one surface

The tangential fields $\tilde{\tilde{E}}_t$ and $\tilde{\tilde{H}}_t$ can be resolved into components parallel and perpendicular to \bar{k}_t as follows: denoting either $\tilde{\tilde{E}}_t$ or $\tilde{\tilde{H}}_t$ by $\tilde{\tilde{F}}_t$, we have

$$\tilde{\tilde{F}}_t = \tilde{\tilde{F}}'_t + \tilde{\tilde{F}}''_t \quad (2.21a)$$

$$\tilde{\tilde{F}}'_t = \left(\bar{I} - \frac{\bar{k}_t \bar{k}_t}{k_t^2} \right) \cdot \tilde{\tilde{F}}_t \quad (2.21b)$$

$$\tilde{\tilde{F}}''_t = \frac{1}{k_t^2} \bar{k}_t \bar{k}_t \cdot \tilde{\tilde{F}}_t \quad (2.21c)$$

in which $\tilde{\tilde{F}}'_t$ denotes the perpendicularly polarized part of $\tilde{\tilde{F}}_t$ and $\tilde{\tilde{F}}''_t$ denotes the parallel polarized part. Substituting representations for $\tilde{\tilde{E}}_t$ and $\tilde{\tilde{H}}_t$ of this form into eq. (2.11), we find that the resulting equations decouple into two sets:

$$\begin{bmatrix} \tilde{\tilde{E}}'_t(z_1) \\ \eta \tilde{\tilde{H}}''_t(z_1) \end{bmatrix} = \bar{M}'_l(z_1; k; z_2) \cdot \begin{bmatrix} \tilde{\tilde{E}}'_t(z_2) \\ \eta \tilde{\tilde{H}}''_t(z_2) \end{bmatrix} \quad (2.22a)$$

$$\begin{bmatrix} \tilde{\tilde{E}}''_t(z_1) \\ \eta \tilde{\tilde{H}}'_t(z_1) \end{bmatrix} = \bar{M}''_l(z_1; k; z_2) \cdot \begin{bmatrix} \tilde{\tilde{E}}''_t(z_2) \\ \eta \tilde{\tilde{H}}'_t(z_2) \end{bmatrix} \quad (2.22b)$$

where

$$\bar{M}'_l(z_1; k; z_2) = \begin{bmatrix} \bar{I} \cos k_z(z_1 - z_2) & \frac{jk}{k_z} \bar{a}_z \times \bar{I} \sin k_z(z_1 - z_2) \\ -\frac{jk_z}{k} \bar{a}_z \times \bar{I} \sin k_z(z_1 - z_2) & \bar{I} \cos k_z(z_1 - z_2) \end{bmatrix} \quad (2.23a)$$

$$\bar{M}_\lambda''(z_1; k; z_2) = \begin{bmatrix} \bar{I} \cos k_z(z_1 - z_2) & \frac{jk_z}{k} \bar{a}_z \times \bar{I} \sin k_z(z_1 - z_2) \\ -\frac{jk_z}{k} \bar{a}_z \times \bar{I} \sin k_z(z_1 - z_2) & \bar{I} \cos k_z(z_1 - z_2) \end{bmatrix} \quad (2.23b)$$

The supermatrices \bar{M}_λ' and \bar{M}_λ'' are substantially simpler than \bar{M}_λ .

We also consider the supermatrix \bar{M}_s in those cases in which the admittance operator \bar{Y}_s diagonalizes for perpendicularly-polarized and parallel-polarized fields:

$$\bar{Y}_s''' = Y_s''' \bar{I} \quad (2.24)$$

For such cases, the connection supermatrices \bar{M}_s are

$$\bar{M}_s'''(n_-; Y_s'''; n_+) = \begin{bmatrix} \bar{I} & \bar{0} \\ n_- Y_s''' \bar{a}_z \times \bar{I} & \frac{n_-}{n_+} \bar{I} \end{bmatrix} \quad (2.25)$$

When the effective permittivity of the shield material is large compared to that of the surrounding medium (which is usually free space), the condition $k_t^2 \ll |k|^2$ is valid for values of k_t corresponding to real angles of incidence. In such cases, the approximation $k_z \approx k$ holds and may be used to simplify \bar{M}_λ , \bar{M}_λ' , and \bar{M}_λ'' . We find that

$$\bar{M}_\lambda \approx \bar{M}_\lambda' \approx \bar{M}_\lambda'' \approx \begin{bmatrix} \bar{I} \cos k(z_1 - z_2) & j\bar{a}_z \times \bar{I} \sin k(z_1 - z_2) \\ -j\bar{a}_z \times \bar{I} \sin k(z_1 - z_2) & \bar{I} \cos k(z_1 - z_2) \end{bmatrix} \quad (2.26)$$

We conclude this section by considering the conditions under which an electrically thin layer may be modeled as an equivalent sheet admittance.

The connection supermatrix \bar{M}_t for a layer in free space is

$$\bar{M}_t = \bar{M}_s(n_o; \bar{0}; n) \cdot \bar{M}_l(0; k; d_l) \cdot \bar{M}_s(n; \bar{0}; n_o) \quad (2.27)$$

We define the equivalent sheet admittance \bar{Y}_{seq} by the relation

$$\bar{M}_s(n_o; \bar{Y}_{seq}; n_o) = \bar{M}_l^{-1}(0; k_o; d_l) \cdot \bar{M}_t \quad (2.28)$$

The factor $\bar{M}_l^{-1}(0; k_o; d_l)$ is inserted to account for the physical distance d_l occupied by the layer. Expanding the product in eq. (2.27) and substituting in eq. (2.28) yields the following four equations expressing the equivalence:

$$\bar{I} = C_o C_l \bar{I} + \frac{n_o}{n} S_o S_l \bar{U}_o \cdot \bar{U}_l \quad (2.29a)$$

$$\bar{0} = C_l S_o \bar{U}_o - \frac{n}{n_o} S_l C_o \bar{U}_l \quad (2.29b)$$

$$\bar{a}_z \times n_o \bar{Y}_{seq} = \frac{n_o}{n} C_o S_l \bar{U}_l - S_o C_l \bar{U}_o \quad (2.29c)$$

$$\bar{I} = C_o C_l \bar{I} + \frac{n}{n_o} S_o S_l \bar{U}_o \cdot \bar{U}_l \quad (2.29d)$$

in which

$$C_o = \cos k_{zo} d_l \quad (2.30a)$$

$$C_l = \cos k_{zd} d_l \quad (2.30b)$$

$$S_o = \sin k_{zo} d_l \quad (2.30c)$$

$$S_l = \sin k_{zd} d_l \quad (2.30d)$$

$$\bar{\bar{U}}_o = \frac{-1}{jk_o k_{zo}} \bar{a}_z \times (\bar{k}_t \bar{k}_t + k_{zo}^2 \bar{\bar{I}}) \quad (2.30e)$$

$$\bar{\bar{U}}_l = \frac{-1}{jkk_{zd}} \bar{a}_z \times (\bar{k}_t \bar{k}_t + k_{zd}^2 \bar{\bar{I}}) \quad (2.30f)$$

and $k_{zo}^2 = k_o^2 - k_t^2$, $k_{zd}^2 = k^2 - k_t^2$. Now if quantities of order $(kd)^2$ and higher are neglected, we find that eqs. (2.29a) and (2.29d) are satisfied as they stand; eq. (2.29c) yields the well-known result [7,8]

$$\eta_o \bar{\bar{Y}}_{seq} = jk_o d_l (\epsilon_r - 1) \bar{\bar{I}} \quad (2.31)$$

as we expect; but eq. (2.29b) reduces to

$$\bar{\bar{O}} = jk_o d_l \left(1 - \frac{\epsilon_o}{\epsilon} \right) \bar{a}_z \times \left(\frac{\bar{k}_t \bar{k}_t}{k_o^2} - \frac{k_t^2}{k_o^2} \bar{\bar{I}} \right) \quad (2.32)$$

which is not true in general. It is obviously true if $\bar{k}_t = 0$, i.e., at normal incidence.

The condition (2.32) is also true when the electromagnetic field is polarized perpendicular to the plane of incidence. This is so because (cf. eq. (2.21c))

$$(\bar{k}_t \bar{k}_t - k_t^2 \bar{\bar{I}}) \cdot \bar{k}_t \bar{k}_t \cdot \tilde{\tilde{H}}_t = 0 \quad (2.33)$$

as is apparent by inspection. We now inquire under what conditions the expression (2.31) is valid for parallel-polarized fields. We consider the problem of reflection and transmission of a parallel-polarized plane electromagnetic wave by an electrically thin dielectric layer and by a sheet admittance in free space. We readily obtain the following results:

$$\text{thin layer: } R'' = \left[\frac{jk_o d}{2} (\epsilon_r - 1) \cos \theta - \frac{jk_t^2 d}{2k_o} \sec \theta \left(1 - \frac{1}{\epsilon_r} \right) \right] T'' \quad (2.34a)$$

$$T'' = \left[1 + \frac{jk_o d}{2} (\epsilon_r - 1) \cos\theta + \frac{jk_t^2 d}{2k_o} \sec\theta \left(1 - \frac{1}{\epsilon_r} \right) \right]^{-1} \quad (2.34b)$$

admittance sheet: $R'' = \frac{\eta_o}{2} Y_s'' \cos\theta T'' \quad (2.34c)$

$$T'' = \left(1 + \frac{\eta_o}{2} Y_s'' \cos\theta \right)^{-1} \quad (2.34d)$$

where $k_t^2 = k_o^2 \sin^2\theta$. It is apparent upon comparison of (2.34a) and (2.34b) with (2.34c) and (2.34d) that if Y_s'' is given by eq. (2.31), then we must require that for the approximation of a thin layer by an admittance sheet to be valid,

$$\tan^2\theta \ll |\epsilon_r| \quad (2.35)$$

where, in general,

$$\epsilon_r \equiv \frac{1}{j\omega\epsilon_o} (\sigma + j\omega\epsilon) \quad (2.36)$$

We therefore conclude that the characterization of an electrically thin layer as an equivalent sheet admittance is valid for perpendicular-polarized fields generally, and for parallel-polarized fields in which

$$\frac{k_t^2/k_o^2}{1 - k_t^2/k_o^2} \ll |\epsilon_r| \quad (2.37)$$

where k_o^2 denotes $\omega^2 \mu_o \epsilon_{out}$, ϵ_{out} being the permittivity of the medium outside the sheet admittance.

SECTION III

PLANAR GRAPHITE COMPOSITE SHIELDS

1. INTRODUCTION

In this section we shall consider the problem of electromagnetic wave transmission through a planar layer of graphite composite in the frequency and time domains. A brief description of graphite composite materials has already been given in Section I of this report; we summarize here certain facts pertaining to these materials which are relevant to our electromagnetic analysis.

- (a) A layer of graphite composite is a layup of anisotropic laminae assembled into a "cross-ply" configuration. Therefore, the layer is itself probably anisotropic in behavior. However, some limited experimental data which has been previously mentioned [2] indicates that the anisotropy is weak. Therefore, we shall model the graphite composite as an isotropic material.
- (b) The conductivity of graphite composites appears to be roughly one-fourth that of pure graphite [1]. This value is 7.14×10^4 mho m^{-1} ; we shall use a value of conductivity equal to 1.5×10^4 mho m^{-1} for the composite material in our numerical work.
- (c) Graphite composite is nonmagnetic and we shall use a value for permeability equal to that of free space in our numerical work.

In the next section, we develop the boundary connection operator for a planar graphite composite layer in free space. Then in paragraph 3, the problem of electromagnetic wave reflection and transmission by such a layer is solved in the frequency domain. The transmission of a transient EMP signal through the layer is considered in paragraph 4.

2. THE BOUNDARY CONNECTION SUPERMATRIX FOR A PLANAR GRAPHITE COMPOSITE LAYER IN FREE SPACE

The conductivity of a graphite composite is sufficiently high that the material may be considered to be a good conductor for frequencies throughout and beyond the EMP spectrum. Consequently, displacement currents may be neglected in comparison to conduction currents in the material, so that

$$k^2 = \omega_g^2 \mu_g \epsilon_g - j\omega \mu_g \sigma_g \approx -j\omega \mu_g \sigma_g \quad (3.1)$$

in which μ_g , ϵ_g , and σ_g denote respectively the permeability, permittivity, and conductivity of graphite composite. Furthermore, since $\sigma_g \gg \omega \epsilon_0$ we neglect k_t^2 in comparison to k^2 in forming k_z^2 : thus

$$k_z d \approx k d = (1-j)d/\delta \quad (3.2)$$

where d is the thickness of the layer and $\delta = (2/\omega \mu_g \sigma_g)^{1/2}$ is the skin depth of the material. The boundary connection supermatrix for the graphite composite layer in free space is thus given by eq. (2.27), with $\bar{\bar{M}}_t$ given by eq. (2.26) and $k = (1-j)d/\delta$

$$\bar{\bar{M}}_t = \begin{bmatrix} \bar{I} \cos(1-j)d/\delta & -j \frac{n}{n_0} \bar{a}_z \times \bar{I} \sin(1-j)d/\delta \\ j \frac{n_0}{n} \bar{a}_z \times \bar{I} \sin(1-j)d/\delta & \bar{I} \cos(1-j)d/\delta \end{bmatrix} \quad (3.3)$$

in which $n = \sqrt{j\omega \mu_g / \sigma_g}$ is the characteristic impedance of the graphite composite.

In the low-frequency limit ($d/\delta \ll 1$)

$$\bar{\bar{M}}_t \approx \begin{bmatrix} \bar{I} & -jk_0 d \bar{a}_z \times \bar{I} \\ n_0 \sigma_g d \bar{a}_z \times \bar{I} & \bar{I} \end{bmatrix} \quad (3.4)$$

and when $d/\delta \gg 1$

$$\bar{M}_t = \frac{1}{2} e^{(1+j)d/\delta} \begin{bmatrix} \bar{I} & -\frac{n}{n_o} \bar{a}_z \times \bar{I} \\ \frac{n_o}{n} \bar{a}_z \times \bar{I} & \bar{I} \end{bmatrix} \quad (3.5)$$

Additionally, we note that

$$\frac{n_o}{n} = \sqrt{-j} \left[\frac{n_o \sigma d}{k_o d} \right]^{1/2} \quad (3.6a)$$

$$\frac{n}{n_o} = \sqrt{j} \left[\frac{k_o d}{n_o \sigma d} \right]^{1/2} \quad (3.6b)$$

3. PLANE-WAVE REFLECTION AND TRANSMISSION BY A PLANAR GRAPHITE COMPOSITE LAYER

The geometry of the problem to be considered in this section is shown in Fig. (3.1). A plane electromagnetic wave of frequency ω is incident upon a planar graphite composite layer of thickness d , from the region $z < 0$; the angle of incidence is θ . The medium outside the layer is free space. The reflected and transmitted fields are to be determined as functions of the wave frequency.

The incident wave in the region $z < 0$ is given by

$$\bar{E}_{\text{inc}} = [E'_0 \bar{a}_y + E''_0 (\bar{a}_x \cos \theta - \bar{a}_z \sin \theta)] e^{-jk_o(x \sin \theta + z \cos \theta)} \quad (3.7a)$$

$$n_o \bar{H}_{\text{inc}} = [E'_0 (\bar{a}_z \sin \theta - \bar{a}_x \cos \theta) + E''_0 \bar{a}_y] e^{-jk_o(x \sin \theta + z \cos \theta)} \quad (3.7b)$$

in which E'_0 and E''_0 denote the amplitudes of the perpendicular-polarized and parallel-polarized components of the incident-wave electric field.

The reflected wave in the region $z < 0$ is

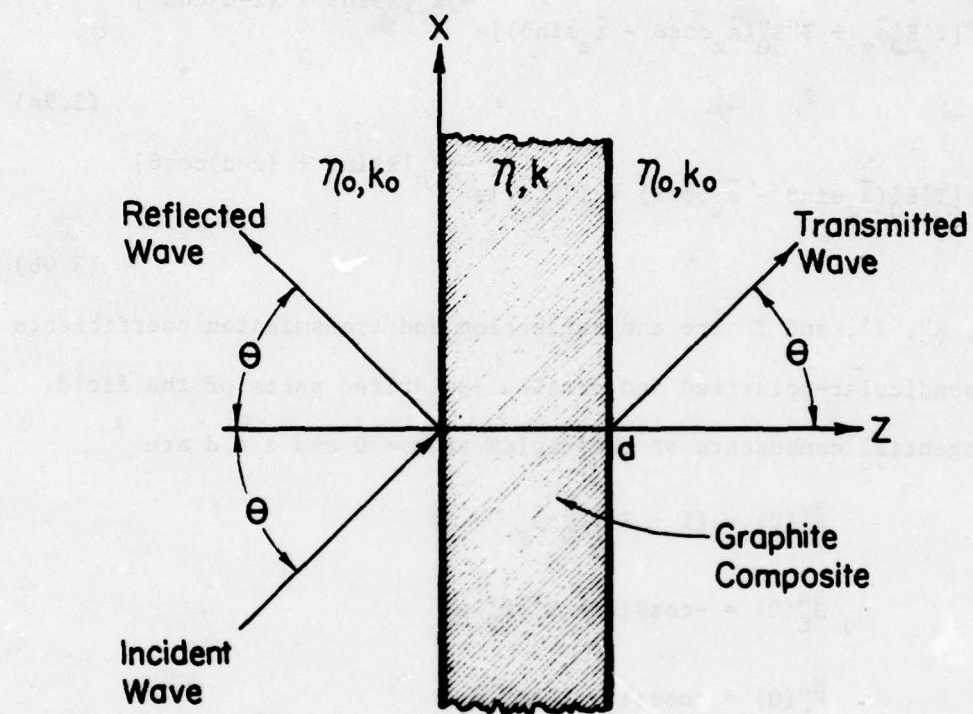


Figure 3.1. Reflection and transmission of a plane wave by a planar graphite composite layer: geometry of the problem

$$\bar{E}_{\text{ref}} = [R'E'_0 \bar{a}_y - R''E''_0 (\bar{a}_x \cos\theta + \bar{a}_z \sin\theta)] e^{-jk_o(x \sin\theta - z \cos\theta)} \quad (3.8a)$$

$$\eta_o \bar{H}_{\text{ref}} = [R'E'_0 (\bar{a}_x \cos\theta + \bar{a}_z \sin\theta) + R''E''_0 \bar{a}_y] e^{-jk_o(x \sin\theta - z \cos\theta)} \quad (3.8b)$$

and the transmitted wave in the region $z > d$ is

$$\bar{E}_{\text{trans}} = [T'E'_0 \bar{a}_y + T''E''_0 (\bar{a}_x \cos\theta - \bar{a}_z \sin\theta)] e^{-jk_o[x \sin\theta + (z-d) \cos\theta]} \quad (3.9a)$$

$$\eta_o \bar{H}_{\text{trans}} = [T'E'_0 (\bar{a}_z \sin\theta - \bar{a}_x \cos\theta) + T''E''_0 \bar{a}_y] e^{-jk_o[x \sin\theta + (z-d) \cos\theta]} \quad (3.9b)$$

in which R' , R'' , T' , and T'' are the reflection and transmission coefficients for the perpendicular-polarized and parallel-polarized parts of the field.

The tangential components of the fields at $z = 0$ and $z = d$ are

$$\tilde{E}'_t(0) = (1 + R') E'_0 \bar{a}_y$$

$$\eta_o \tilde{H}''_t(0) = -\cos\theta (1 - R') E'_0 \bar{a}_x$$

$$\tilde{E}''_t(0) = \cos\theta (1 - R'') E''_0 \bar{a}_x$$

$$\eta_o \tilde{H}'_t(0) = (1 + R'') E''_0 \bar{a}_y$$

(3.10)

$$\tilde{E}'_t(d) = T'E'_0 \bar{a}_y$$

$$\eta_o \tilde{H}''_t(d) = -\cos\theta T'E'_0 \bar{a}_x$$

$$\tilde{E}''_t(d) = \cos\theta T''E''_0 \bar{a}_x$$

$$\eta_o \tilde{H}'_t(d) = T''E''_0 \bar{a}_y$$

Connecting these fields across the graphite composite layer using the boundary connection supermatrix given in eq. (3.3) yields two sets of equations which may be solved for the reflection and transmission coefficients. We have

$$\begin{bmatrix} -C - j \frac{n}{n_o} \cos\theta S & 1 \\ \cos\theta C + j \frac{n_o}{n} S & \cos\theta \end{bmatrix} \begin{bmatrix} R' \\ T' \end{bmatrix} = \begin{bmatrix} C - j \frac{n}{n_o} \cos\theta S \\ \cos\theta C - j \frac{n_o}{n} S \end{bmatrix} \quad (3.11a)$$

$$\begin{bmatrix} \cos\theta C + j \frac{n}{n_o} S & \cos\theta \\ C + j \frac{n_o}{n} \cos\theta S & -1 \end{bmatrix} \begin{bmatrix} R'' \\ T'' \end{bmatrix} = \begin{bmatrix} \cos\theta C - j \frac{n}{n_o} S \\ -C + j \frac{n_o}{n} \cos\theta S \end{bmatrix} \quad (3.11b)$$

in which $C \equiv \cos(1-j)d/\delta$, $S \equiv \sin(1-j)d/\delta$. Solving eqs. (3.11), we obtain expressions for R' , T' , R'' , and T'' as follows:

$$R' = \frac{1}{D'} jS \left(\frac{n}{n_o} \cos^2\theta - \frac{n_o}{n} \right) \quad (3.12a)$$

$$T' = \frac{2}{D'} \cos\theta \quad (3.12b)$$

$$R'' = \frac{1}{D''} jS \left(\frac{n_o}{n} \cos^2\theta - \frac{n}{n_o} \right) \quad (3.12c)$$

$$T'' = \frac{2}{D''} \cos\theta \quad (3.12d)$$

in which

$$D' = 2\cos\theta C + jS \left(\frac{n}{n_o} \cos^2\theta + \frac{n_o}{n} \right) \quad (3.13a)$$

$$D'' = 2\cos\theta C + jS \left(\frac{n_o}{n} \cos^2\theta + \frac{n}{n_o} \right) \quad (3.13b)$$

Now, $|n/n_0|^2 = k_0/n_0 \sigma_g \ll 1$. Neglecting this quantity with respect to unity, which is consistent with neglecting the displacement currents with respect to the conduction currents in the graphite composite, we obtain the following expressions for the transmission coefficients:

$$T' = (C + \frac{j}{2} \frac{n_0}{n} \sec \theta S)^{-1} \quad (3.14a)$$

$$T'' = (C + \frac{j}{2} \frac{n_0}{n} \cos \theta S)^{-1} \quad (3.14b)$$

Further approximations to the transmission coefficients are useful. In particular, it is easy to show that for the graphite composite, the condition $d/\delta \ll n_0 \sigma_g d$ will hold for frequencies throughout and beyond the EMP spectrum. As a consequence, the approximation

$$T' \approx \frac{2\cos\theta}{n_0 \sigma_g d} (1-j) \frac{d}{\delta} \csc(1-j) \frac{d}{\delta} \quad (3.15)$$

is valid for all angles of incidence θ , and the approximation

$$T'' \approx \frac{2\sec\theta}{n_0 \sigma_g d} (1-j) \frac{d}{\delta} \csc(1-j) \frac{d}{\delta} \quad (3.16)$$

is valid for angles of incidence up to a point only a few hundredths of a degree from 90° . Eqs. (3.15) and (3.16) show that the effect on the transmission coefficients of changing the wave frequency (and thus d/δ) is almost completely separable from the effects of changing $n_0 \sigma_g d$ and θ . Therefore, we may express T' and T'' in terms of their values at $d/\delta = 0$ approximately, as follows:

$$\begin{bmatrix} T' \\ T'' \end{bmatrix} \approx \begin{bmatrix} T'_0 \\ T''_0 \end{bmatrix} (1-j) \frac{d}{\delta} \csc(1-j) \frac{d}{\delta} \quad (3.17)$$

in which

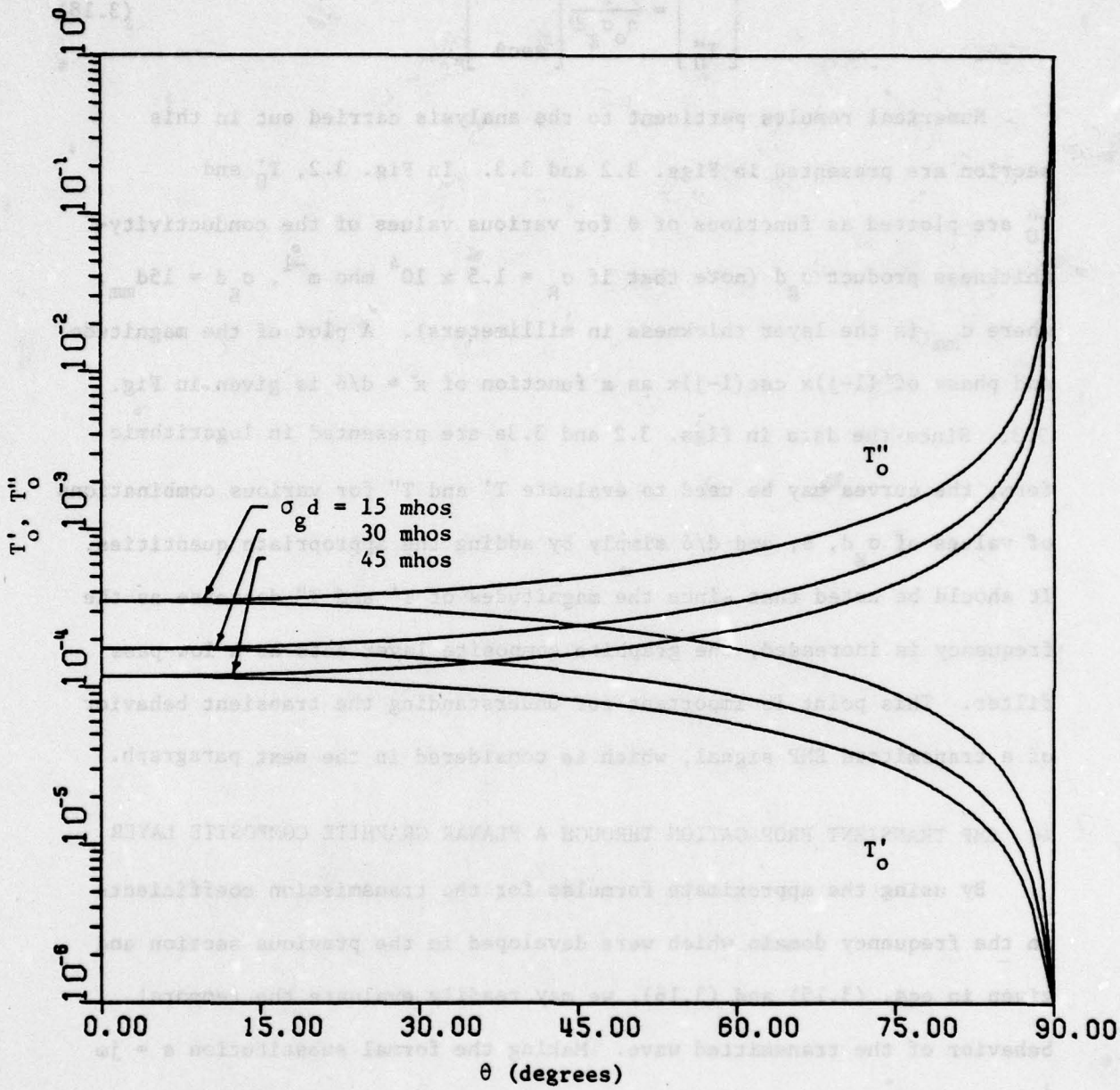
$$\begin{bmatrix} T'_0 \\ T''_0 \end{bmatrix} = \frac{2}{\eta_0 \sigma_g d} \begin{bmatrix} \cos \theta \\ \sec \theta \end{bmatrix} \quad (3.18)$$

Numerical results pertinent to the analysis carried out in this section are presented in Figs. 3.2 and 3.3. In Fig. 3.2, T'_0 and T''_0 are plotted as functions of θ for various values of the conductivity-thickness product $\sigma_g d$ (note that if $\sigma_g = 1.5 \times 10^4$ mho m^{-1} , $\sigma_g d = 15d_{mm}$, where d_{mm} is the layer thickness in millimeters). A plot of the magnitude and phase of $(1-j)x \csc(1-j)x$ as a function of $x = d/\delta$ is given in Fig. 3.3. Since the data in Figs. 3.2 and 3.3a are presented in logarithmic form, the curves may be used to evaluate T' and T'' for various combinations of values of $\sigma_g d$, θ , and d/δ simply by adding the appropriate quantities. It should be noted that since the magnitudes of T' and T'' decrease as the frequency is increased, the graphite composite layer acts as a low-pass filter. This point is important for understanding the transient behavior of a transmitted EMP signal, which is considered in the next paragraph.

4. EMP TRANSIENT PROPAGATION THROUGH A PLANAR GRAPHITE COMPOSITE LAYER

By using the approximate formulas for the transmission coefficients in the frequency domain which were developed in the previous section and given in eqs. (3.15) and (3.16), we may readily evaluate the temporal behavior of the transmitted wave. Making the formal substitution $s = j\omega$ in T' and T'' , we construct a Laplace integral for the transmitted field as follows:

$$E_{trans}(\tau) = \frac{1}{2\pi j} \int_{\Gamma_B} E_0(s) \frac{2}{\eta_0 \sigma_g d} \begin{bmatrix} \cos \theta \\ \sec \theta \end{bmatrix} \frac{\sqrt{s\tau_d}}{\sinh \sqrt{s\tau_d}} e^{s\tau} ds \quad (3.19)$$

Figure 3.2. T'_o and T''_o vs. θ

341-40

EMP 3-38

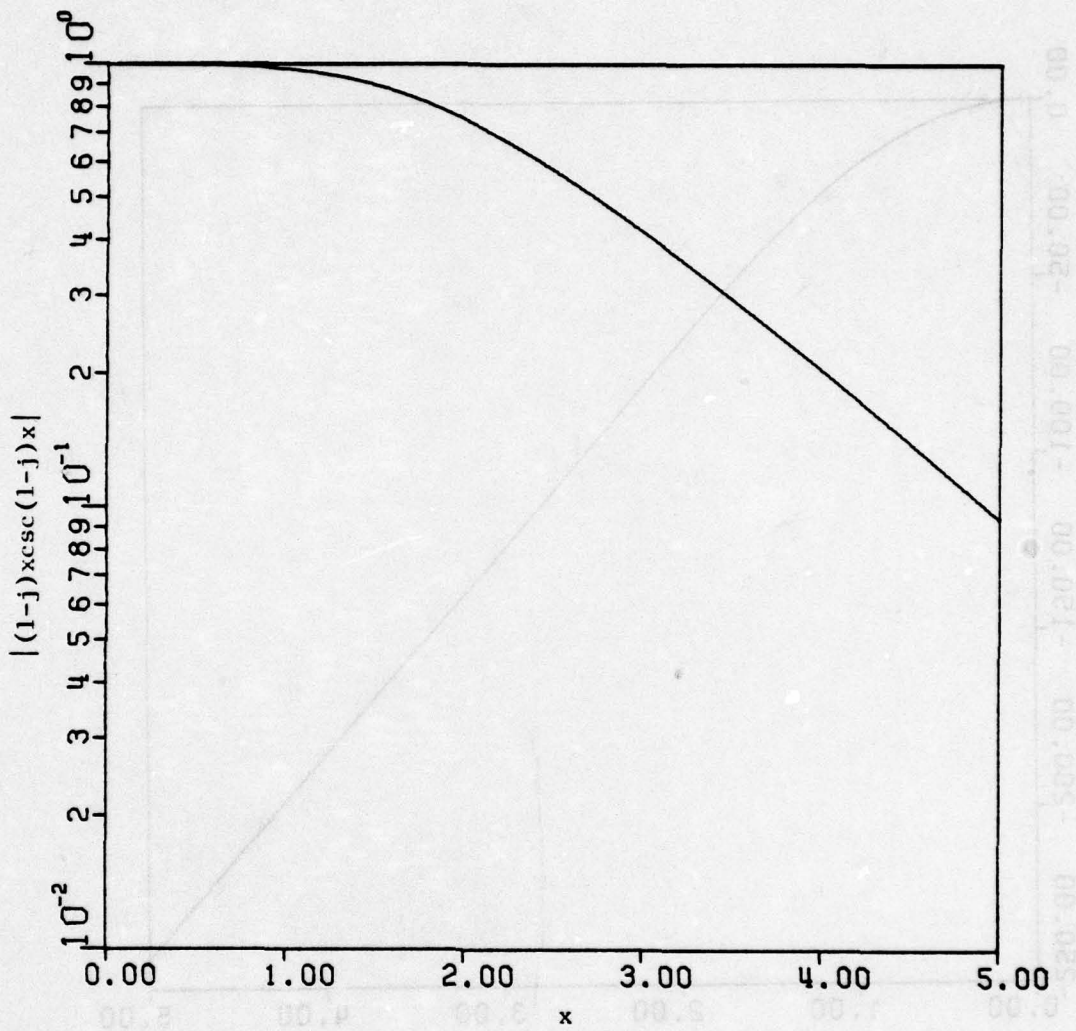


Figure 3.3a. Magnitude of $(1-j)xcsc(1-j)x$ vs. x

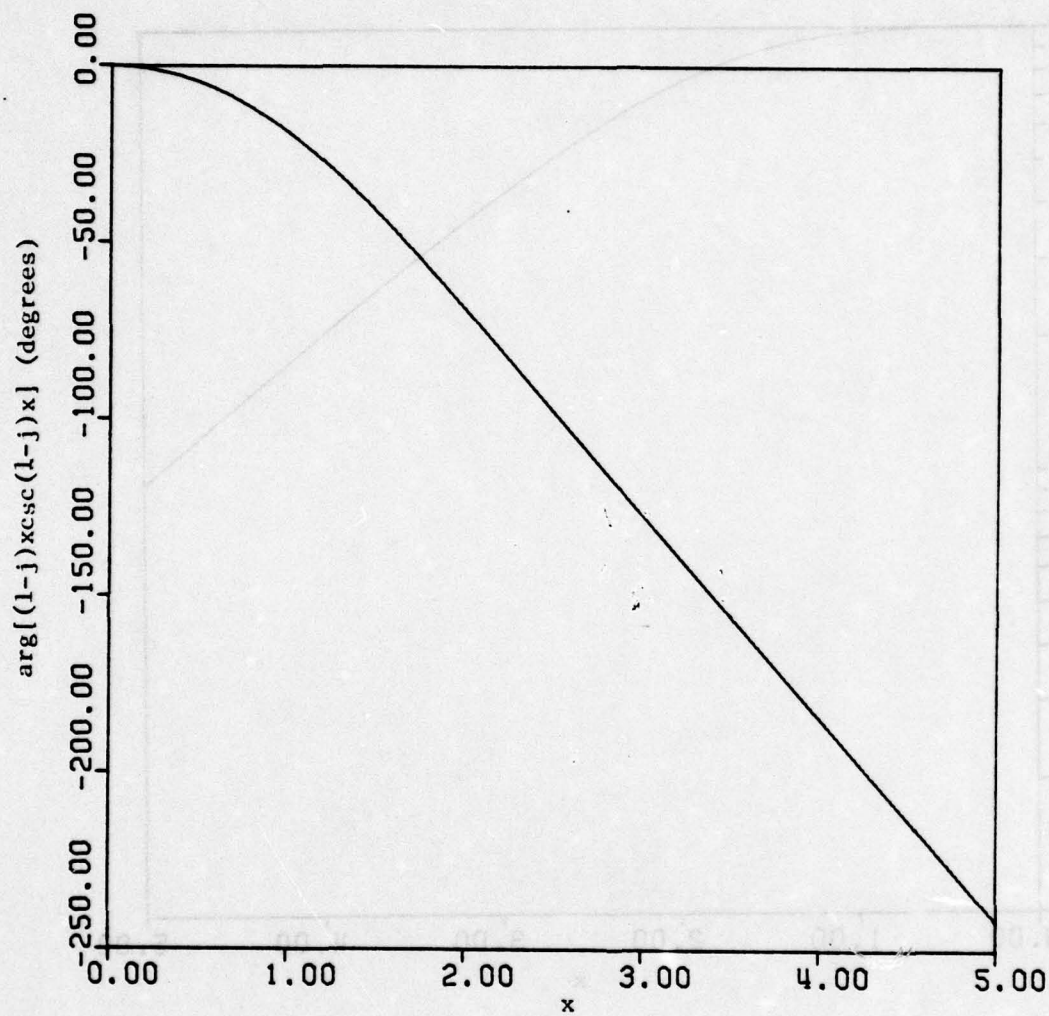


Figure 3.3b. Phase of $(1-j)xcsc(1-j)x$ vs. x

in which Γ_B denotes the usual Bromwich contour, τ_d is the shield diffusion time, defined by

$$\tau_d = \frac{\mu_0 \sigma}{g} d^2 \quad (3.20)$$

and

$$\tau = t - \frac{1}{c} [x \sin \theta + (z-d) \cos \theta] \quad (3.21)$$

$c = 1/\sqrt{\mu_0 \epsilon_0}$, the vacuum speed of light. In eq. (3.19), "cosθ" is to be used when the incident wave is polarized perpendicular to the plane of incidence, and "secθ" is to be used for parallel polarization. $E_o(s)$ denotes the Laplace transform of the EMP signal discussed in Section I; it is

$$E_o(s) = A \left[\frac{1}{s+\alpha} - \frac{1}{s+\beta} \right] \quad (3.22)$$

in which

$$A = (e^{-\alpha t_o} - e^{-\beta t_o})^{-1} = 1.1373\dots \quad (3.23a)$$

$$t_o = \frac{1}{\beta-\alpha} \ln \frac{\beta}{\alpha} \quad (3.23b)$$

$$\alpha = 4.80 \times 10^7 \quad (3.23c)$$

$$\beta = 1.76 \times 10^9 \quad (3.23d)$$

The integral in eq. (3.19) is readily evaluated using the Cauchy residue theorem. The poles of the integrand occur at $s = -\alpha$, $s = -\beta$, and

$$s = s_n = -\frac{n^2 \pi^2}{\tau_d^2} \quad (n \geq 1) \quad (3.24)$$

Furthermore, it is easy to show that Γ_B may be closed at infinity in the right half plane for $\tau < 0$, yielding a null result for $E(\tau)$, in accordance with causality; and for $\tau > 0$, Γ_B may be closed in the left half plane at infinity to yield for $E(\tau)$:

$$\begin{aligned}
 E(\tau) = & \frac{2A}{\eta_0 \sigma g d} \left[\frac{\cos \theta}{\sec \theta} \right] U(\tau) \left\{ \sqrt{\alpha \tau_d} \csc \sqrt{\alpha \tau_d} e^{-\alpha \tau} \right. \\
 & \left. - \sqrt{\beta \tau_d} \csc \sqrt{\beta \tau_d} e^{-\beta \tau} \right\} \\
 & + 2 \sum_{n=1}^{\infty} \frac{(-1)^n (n\pi)^2 (\alpha \tau_d - \beta \tau_d)}{(n^2 \pi^2 - \alpha \tau_d)(n^2 \pi^2 - \beta \tau_d)} e^{-n^2 \pi^2 \tau / \tau_d} \quad (3.25)
 \end{aligned}$$

$U(\tau)$ is the unit step function. The result in eq. (3.25) is based upon the assumption that all the poles of the integrand in eq. (3.19) are simple, i.e., that

$$(\alpha \tau_d \text{ or } \beta \tau_d) \neq n^2 \pi^2 \quad (3.26)$$

for any $n \neq 0$. If this condition is violated, the appropriate limit of eq. (3.25) can be taken to yield the correct result.

Plots of $E(\tau)$ vs. τ , normalized by $(2/\eta_0 \sigma g d)$, are given for the case $\theta = 0^\circ$ in Fig. 3.4, for three values of τ_d . The values chosen correspond if μ_g is chosen equal to the free-space value $4\pi \times 10^{-7}$ henry m^{-1} and $\sigma_g = 1.5 \times 10^4$ mho m^{-1} , to thicknesses d of 1, 2, and 3 mm. A non-normalized curve of the incident EMP signal is included for comparison. One will note the increasing attenuation of the peak value of the transmitted signal, the increasing time delay before the main buildup of the transmitted signal, and the increasing pulse width of the transmitted signal as d is increased. All these features are in keeping with the low-pass filter characteristic of the graphite composite layer which has been mentioned previously.

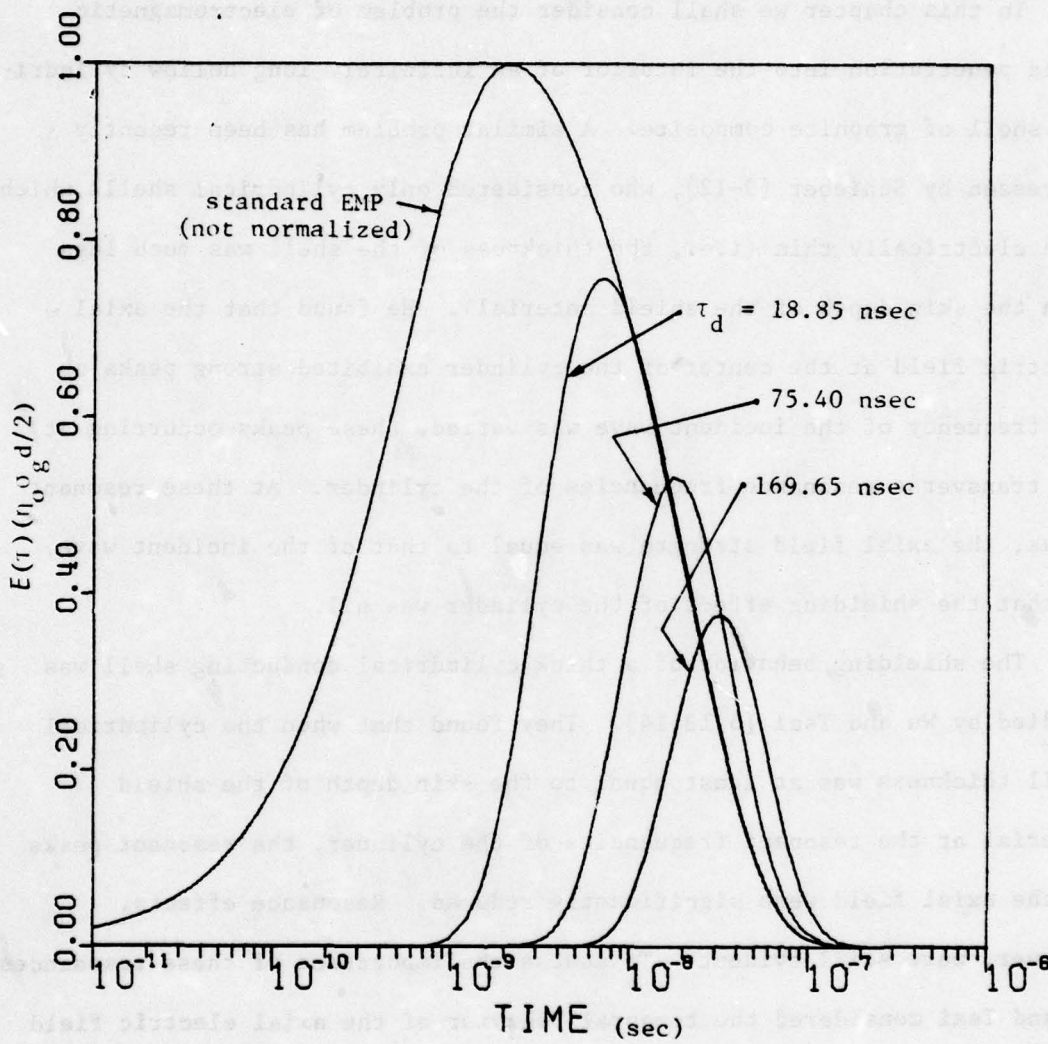


Figure 3.4. Normalized transmitted EMP waveforms: air to rovand graphite slab, normal incidence

SECTION IV

CYLINDRICAL GRAPHITE COMPOSITE SHIELDS

1. INTRODUCTION

In this chapter we shall consider the problem of electromagnetic field penetration into the interior of an infinitely long hollow cylindrical shell of graphite composite. A similar problem has been recently addressed by Schieber [9-12], who considered only cylindrical shells which were electrically thin (i.e., the thickness of the shell was much less than the skin depth of the shield material). He found that the axial electric field at the center of the cylinder exhibited strong peaks as the frequency of the incident wave was varied, these peaks occurring at the transverse resonance frequencies of the cylinder. At these resonant peaks, the axial field strength was equal to that of the incident wave, so that the shielding effect of the cylinder was nil.

The shielding behavior of a thick cylindrical conducting shell was studied by Wu and Tsai [5,13,14]. They found that when the cylindrical shell thickness was at least equal to the skin depth of the shield material at the resonant frequencies of the cylinder, the resonant peaks in the axial field were significantly reduced. Resonance effects, however, were still evident. To assess the importance of these resonances, Wu and Tsai considered the temporal behavior of the axial electric field when the cylindrical shell was illuminated by a normally incident TM_z -polarized plane wave whose time dependence was that of the standard EMP signal which has already been discussed. They found that the temporal behavior of the axial field was only slightly affected by the cylindrical resonances in a "worst case" analysis. In their example, the radius of the cylinder was 10 m and the product of the conductivity and shell

thickness was 0.1 mho. The reason for this behavior is, of course, that for cylinders of this size the lowest-order resonances occur for frequencies far out in the "tail" of the EMP spectrum, and so are only weakly excited. As the radius of the cylinder is decreased, the resonant frequencies are increased and their excitation becomes even weaker.

The cylindrical shells to be considered in this section have radii of 2 m or less (typical aircraft-fuselage sizes) and conductivity-thickness products of the order of 30 mhos. We therefore expect the resonance effects on the transient behavior of the internal fields induced by an EMP signal to be negligible. We introduce a new frequency-domain measure of shielding effectiveness for hollow bodies of resonant size or less which takes the entire internal field into account. This measure, based on a ratio of stored energies in the interior of the body, represents the space averages of the internal fields.

In the next paragraph, the problem of plane-wave scattering from a cylindrical shell of graphite composite is formulated in the frequency domain, using the ECS developed in the previous chapter for this material. We present results illustrating the energy shielding ratio as a function of frequency for several representative cases. Some time-domain considerations are discussed in paragraph 3 of this section.

2. FORMULATION OF THE PROBLEM: FREQUENCY-DOMAIN RESULTS

The geometry of the problem is shown in Fig. 4.1. An infinitely long cylindrical shell of graphite composite, whose inner and outer radii are a and b , respectively, is illuminated by a plane electromagnetic wave. The shell thickness $d = b-a$ is small in comparison to the mean

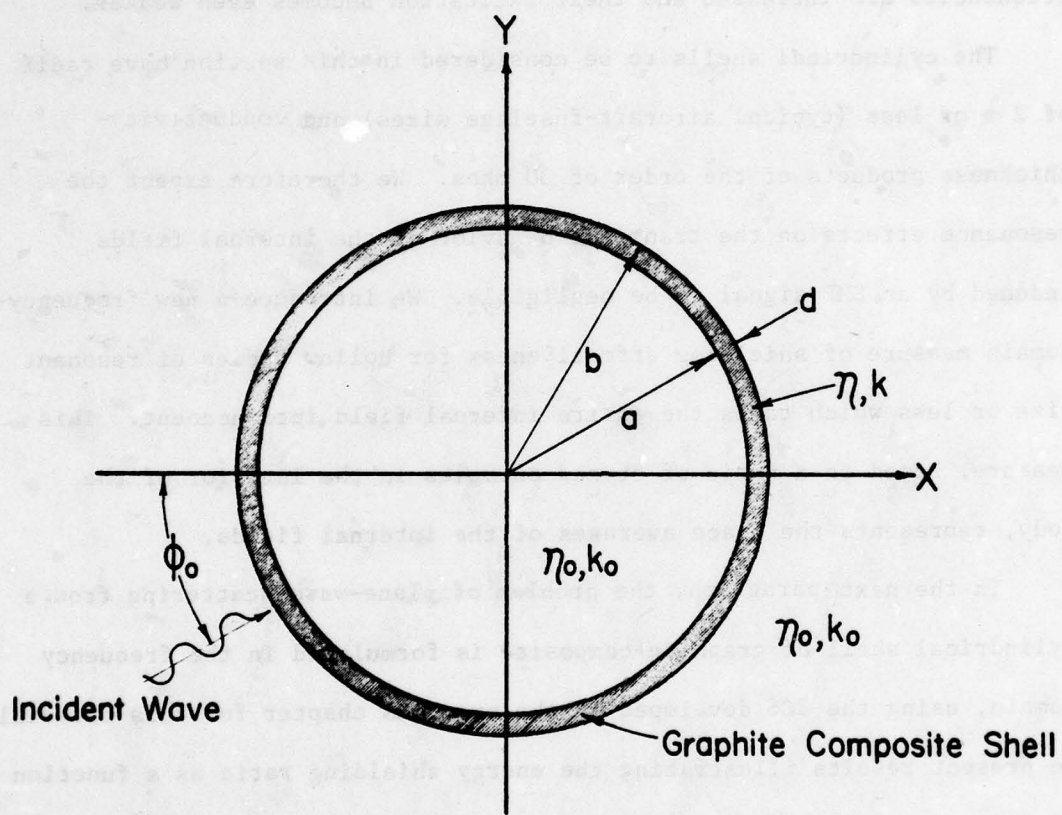


Figure 4.1. Plane-wave penetration of, and scattering by, a cylindrical shell of graphite composite: geometry of the problem

radius $\rho_0 = \sqrt{ab}$. The medium outside and inside the shell is free space.

For simplicity we consider only the case in which the propagation vector of the incident wave has no axial component and we shall investigate the two possible wave polarizations separately. The total fields may then be obtained by superposition.

Consider first the case in which the incident wave is polarized TM with respect to z. The field components present are E_z , H_ϕ , and H_ρ , where

$$E_z = -j\omega\mu_0 \Psi \quad (4.1a)$$

$$H_\phi = -\frac{\partial\Psi}{\partial\rho} \quad (4.1b)$$

$$H_\rho = \frac{1}{\rho} \frac{\partial\Psi}{\partial\phi} \quad (4.1c)$$

and

$$\frac{1}{\rho} \frac{\partial}{\partial\rho} \left(\rho \frac{\partial\Psi}{\partial\rho} \right) + \frac{1}{\rho^2} \frac{\partial^2\Psi}{\partial\phi^2} + k_o^2 \Psi = 0 \quad (4.2)$$

in the free-space regions. In the interior and exterior regions of the problem, appropriate expressions for Ψ are

$$0 \leq \rho < a: \quad \Psi = \frac{-E_o}{j\omega\mu_0} \sum_{n=-\infty}^{\infty} A_n J_n(k_o \rho) e^{jn(\phi-\phi')} \quad (4.3a)$$

$$b < \rho \leq \infty: \quad \Psi = \frac{-E_o}{j\omega\mu_0} \sum_{n=-\infty}^{\infty} [J_n(k_o \rho) + B_n H_n^{(2)}(k_o \rho)] e^{jn(\phi-\phi')} \quad (4.3b)$$

where A_n and B_n are to be determined, E_o is the amplitude of the incident electric field, and

$$\phi' = \phi_o + \pi/2 \quad (4.4)$$

ϕ_o is the angle of incidence shown in Fig. 4.1.

In order to evaluate the coefficients A_n and B_n , the tangential field components are connected across the graphite composite shell using the appropriate connection supermatrix, which is that given in eq. (3.3), modified for the change in the coordinate system (\bar{a}_z is replaced by \bar{a}_ϕ):

$$\bar{\bar{M}}_t = \begin{bmatrix} \bar{I} \cos(1-j)d/\delta & -j \frac{n}{n_o} \bar{a}_\phi \times \bar{I} \sin(1-j)d/\delta \\ j \frac{n_o}{n} \bar{a}_\phi \times \bar{I} \sin(1-j)d/\delta & \bar{I} \cos(1-j)d/\delta \end{bmatrix} \quad (4.5)$$

The spectra of the tangential field components at $\rho=a$ and $\rho=b$ are

$$\tilde{\tilde{E}}_t(\rho=a) = E_o A_n J_n(k_o a) e^{-jn\phi'} \bar{a}_z \quad (4.6a)$$

$$n_o \tilde{\tilde{H}}_t(\rho=a) = -j E_o A_n J'_n(k_o a) e^{-jn\phi'} \bar{a}_\phi \quad (4.6b)$$

$$\tilde{\tilde{E}}_t(\rho=b) = E_o [J_n(k_o b) + B_n H_n^{(2)}(k_o b)] e^{-jn\phi'} \bar{a}_z \quad (4.6c)$$

$$n_o \tilde{\tilde{H}}_t(\rho=b) = -j E_o [J'_n(k_o b) + B_n H_n^{(2)'}(k_o b)] e^{-jn\phi'} \bar{a}_\phi \quad (4.6d)$$

in which the primes ('') denote differentiation with respect to the argument.

For this problem, the spectral variable $\bar{k}_t = (n/\rho)\bar{a}_\phi$. Connecting these spectral components using $\bar{\bar{M}}_t$ as given in eq. (4.5) yields a pair of equations for A_n and B_n :

$$\begin{bmatrix} J_n(k_o a)C + \frac{n}{n_o} J'_n(k_o a)S & -H_n^{(2)}(k_o b) \\ J'_n(k_o a)C - \frac{n_o}{n} J_n(k_o a)S & -H_n^{(2)'}(k_o b) \end{bmatrix} \begin{bmatrix} A_n \\ B_n \end{bmatrix} = \begin{bmatrix} J_n(k_o b) \\ J'_n(k_o b) \end{bmatrix} \quad (4.7)$$

Solving eq. (4.7) for A_n and B_n , we obtain

$$A_n = \frac{1}{D_n} \left(\frac{2j}{\pi k_o b} \right) \quad (4.8a)$$

$$B_n = \frac{1}{D_n} \left\{ C [J_n(k_o a) J'_n(k_o b) - J'_n(k_o a) J_n(k_o b)] + S \left[\frac{n}{n_o} J'_n(k_o a) J'_n(k_o b) + \frac{n_o}{n} J_n(k_o a) J_n(k_o b) \right] \right\} \quad (4.8b)$$

where

$$D_n = C [J'_n(k_o a) H_n^{(2)}(k_o b) - J_n(k_o a) H_n^{(2)'}(k_o b)] - S \left[\frac{n}{n_o} J'_n(k_o a) H_n^{(2)'}(k_o b) + \frac{n_o}{n} J_n(k_o a) H_n^{(2)}(k_o b) \right] \quad (4.9)$$

C and S denote $\cos(l-j)d/\delta$ and $\sin(l-j)d/\delta$ respectively. A_n and B_n may be simplified if we assume that $k_o d \ll 1$ and $|n/n_o|^2 \ll 1$. These conditions hold throughout the EMP spectrum in the cases we consider; so we obtain

$$A_n \approx [C + \frac{n_o \sigma g d}{2} (\pi k_o \rho_o) J_n(k_o \rho_o) H_n^{(2)}(k_o \rho_o) \frac{S}{(l-j)d/\delta}]^{-1} \quad (4.10a)$$

$$B_n \approx -A_n \frac{n_o \sigma g d}{2} (\pi k_o \rho_o) J_n^2(k_o \rho_o) \frac{S}{(l-j)d/\delta} \quad (4.10b)$$

A useful frequency-domain measure of the shielding effectiveness of the graphite shell is the ratio of the time-average stored energy per unit length inside the shell ($0 < \rho < a$) to the time-average stored energy per unit length in the same region with the shell removed. Since this ratio is obtained by integrating the stored energy density throughout the cylindrical volume, it represents an "averaged" shielding effect, and so may be more useful than, say, the axial field strength, as a shielding effectiveness measure for a closed surface. It is easy to show that the time-average stored energy per unit length inside the cylinder is

$$W = \frac{\pi \epsilon_0 E_0^2}{2} \sum_{n=-\infty}^{\infty} |A_n|^2 \int_0^a [J_n^2(k_0 \rho) \left(1 + \frac{n^2}{k_0^2 a^2}\right) + J'_n(k_0 \rho)^2] \rho d\rho \quad (4.11)$$

In the absence of the cylinder, the time-average stored energy in the same volume is simply $\epsilon_0 \pi a^2 E_0^2 / 2$; so performing the integrations in eq. (4.11) and normalizing the result yields the "energy shielding ratio" r_w :

$$r_w = \sum_{n=-\infty}^{\infty} |A_n|^2 [J'_n(k_0 a)^2 + J_n(k_0 a)^2 \left(1 - \frac{n^2}{k_0^2 a^2}\right) + \frac{1}{k_0 a} J_n(k_0 a) J'_n(k_0 a)] \quad (4.12)$$

When $k_0 a \ll 1$, $r_w \approx \frac{1}{2} (|A_0|^2 + |A_1|^2)$, and we obtain an approximate low-frequency expression for r_w as follows:

$$\begin{aligned} r_w \Big|_{k_0 a \ll 1} &\approx \frac{1}{2} \left\{ |C - j \eta_0 \sigma_g d k_0 \rho_0 \frac{s}{(1-j)d/\delta} \ln k_0 \rho_0|^{-2} \right. \\ &\quad \left. + |C + j \frac{\eta_0 \sigma_g d}{2} k_0 \rho_0 \frac{s}{(1-j)d/\delta}|^{-2} \right\} \end{aligned} \quad (4.13)$$

Curves of r_w as a function of frequency are given in Figs. 4.2-4.4 for various values of ρ_0 , d , and σ_g . The values of ρ_0 chosen correspond to typical aircraft; $d = 1, 2, \text{ and } 3 \text{ mm}$; and σ_g varies around the base value $1.5 \times 10^4 \text{ mho m}^{-1}$.

The analysis for the case in which the incident wave is polarized TE to z is similarly carried out. The field components present are H_z , E_ϕ , and E_ρ , where

$$H_z = j \omega \epsilon_0 \phi \quad (4.14a)$$

$$E_\phi = - \frac{\partial \phi}{\partial \rho} \quad (4.14b)$$

$$E_\rho = \frac{1}{\rho} \frac{\partial \phi}{\partial \phi} \quad (4.14c)$$

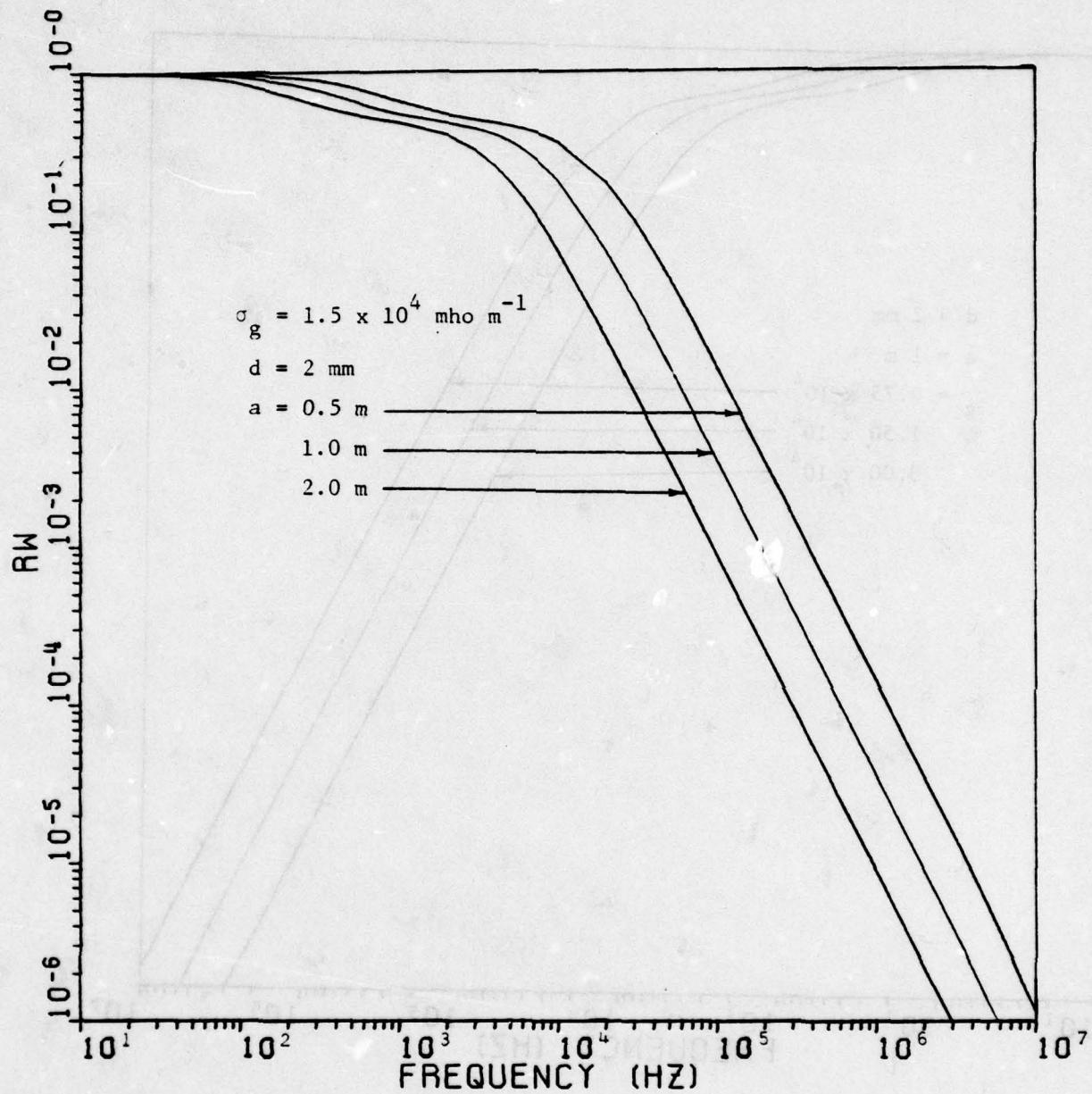


Figure 4.2. Energy shielding ratio r_w vs. frequency with a as parameter; $d = 2 \text{ mm}$, $\sigma_g = 1.5 \times 10^4 \text{ mho m}^{-1}$

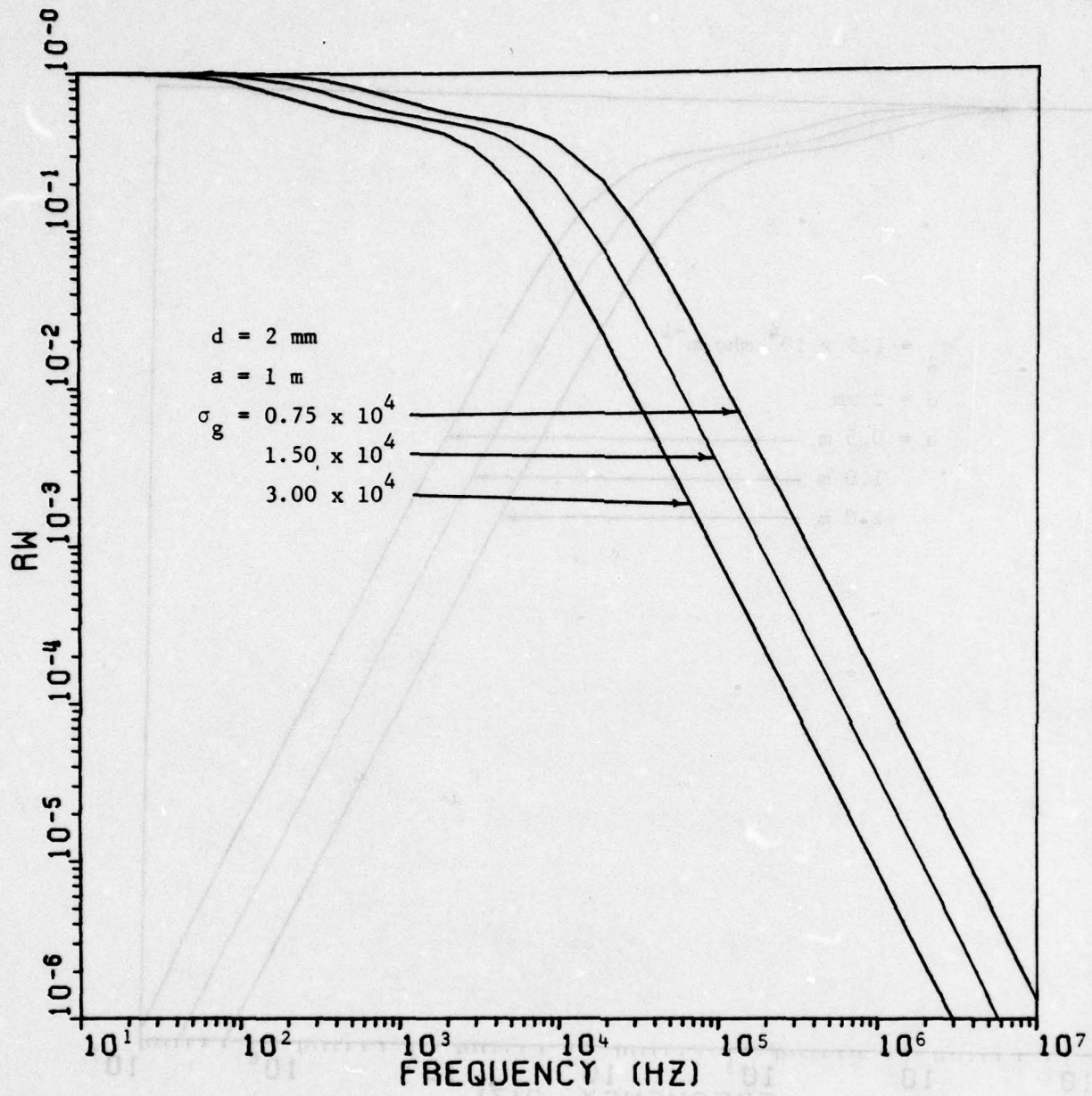


Figure 4.3. Energy shielding ratio r_w vs. frequency with σ_g as parameter; $d = 2 \text{ mm}$, $a = 1 \text{ m}$

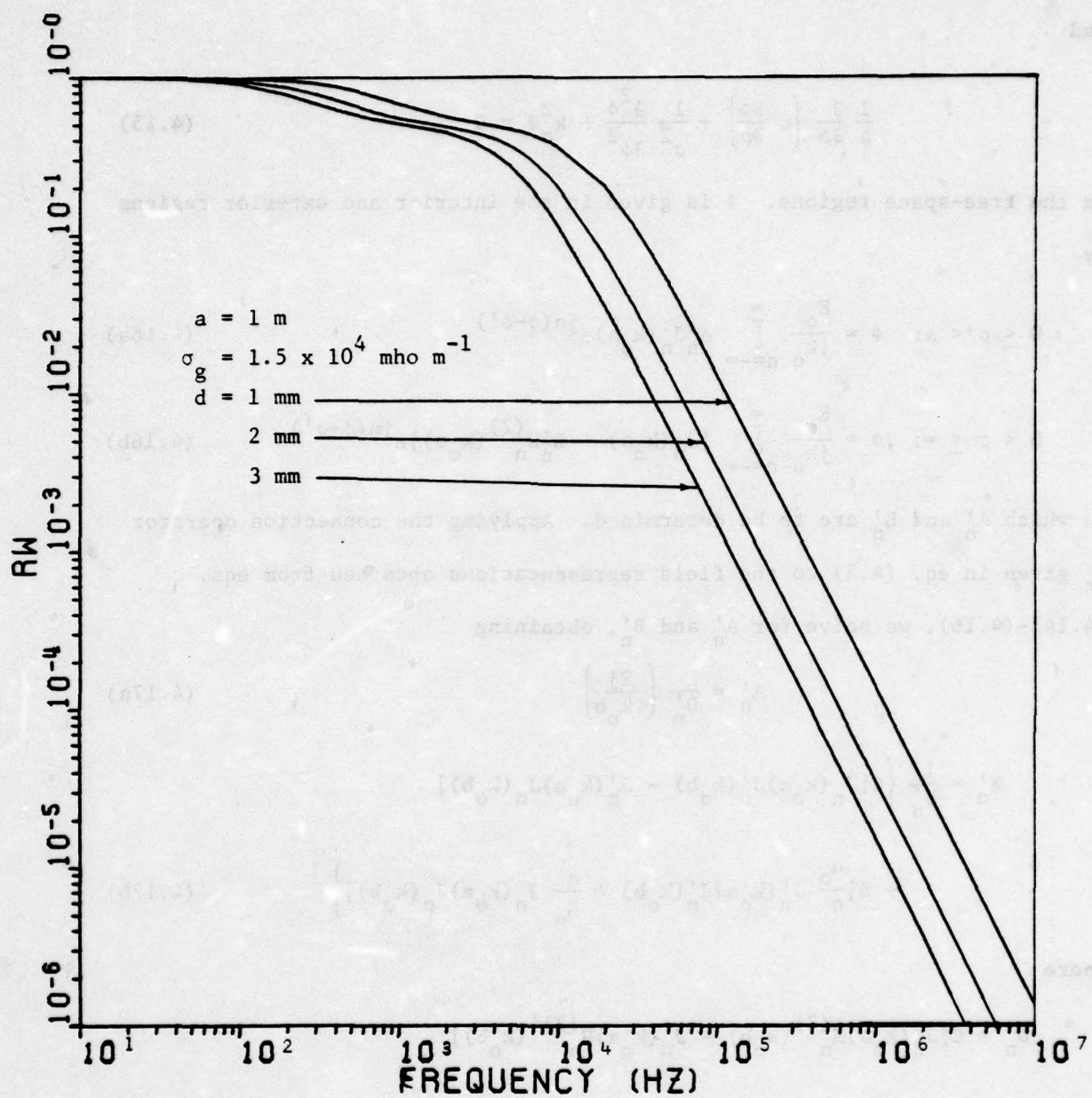


Figure 4.4. Energy shielding ratio r_w vs. frequency with d as parameter; $a = 1 \text{ m}$, $\sigma_g = 1.5 \times 10^4 \text{ mho m}^{-1}$

and

$$\frac{1}{\rho} \frac{\partial}{\partial \rho} \left(\rho \frac{\partial \Phi}{\partial \rho} \right) + \frac{1}{\rho^2} \frac{\partial^2 \Phi}{\partial \phi^2} + k_o^2 \Phi = 0 \quad (4.15)$$

in the free-space regions. Φ is given in the interior and exterior regions by

$$0 \leq \rho < a: \quad \Phi = \frac{E_o}{jk_o} \sum_{n=-\infty}^{\infty} A'_n J_n(k_o \rho) e^{jn(\phi-\phi')} \quad (4.16a)$$

$$b < \rho \leq \infty: \quad \Phi = \frac{E_o}{jk_o} \sum_{n=-\infty}^{\infty} [J_n(k_o \rho) + B'_n H_n^{(2)}(k_o \rho)] e^{jn(\phi-\phi')} \quad (4.16b)$$

in which A'_n and B'_n are to be determined. Applying the connection operator \bar{M}_t given in eq. (4.5) to the field representations obtained from eqs.

(4.14)-(4.16), we solve for A'_n and B'_n , obtaining

$$A'_n = \frac{1}{D'_n} \left(\frac{2j}{\pi k_o b} \right) \quad (4.17a)$$

$$B'_n = \frac{1}{D'_n} \left\{ C [J_n(k_o a) J'_n(k_o b) - J'_n(k_o a) J_n(k_o b)] \right. \\ \left. + S \left[\frac{n_o}{n} J'_n(k_o a) J'_n(k_o b) + \frac{n}{n_o} J_n(k_o a) J_n(k_o b) \right] \right\} \quad (4.17b)$$

where

$$D'_n = C [J'_n(k_o a) H_n^{(2)}(k_o b) - J_n(k_o a) H_n^{(2)'}(k_o b)] \\ - S \left[\frac{n_o}{n} J'_n(k_o a) H_n^{(2)'}(k_o b) + \frac{n}{n_o} J_n(k_o a) H_n^{(2)}(k_o b) \right] \quad (4.18)$$

Approximate expressions for A'_n and B'_n , valid if $k_o d \ll 1$ and $|n/n_o|^2 \ll 1$

as we assume, are

$$A'_n = [C + \frac{\eta_0 \sigma g d}{2} (\pi k_o \rho_o) J'_n(k_o \rho_o) H_n^{(2)}(k_o \rho_o) \frac{s}{(1-j)d/\delta}]^{-1} \quad (4.19a)$$

$$B'_n = -A'_n \frac{\eta_0 \sigma g d}{2} (\pi k_o \rho_o) J'_n(k_o \rho_o)^2 \frac{s}{(1-j)d/\delta} \quad (4.19b)$$

The energy shielding ratio for this polarization, r'_w , is given by

$$\begin{aligned} r'_w &= \sum_{n=-\infty}^{\infty} |A'_n|^2 [J'_n(k_o a)^2 + J_n(k_o a)^2 \left(1 - \frac{n^2}{k_o^2 a^2}\right) \\ &\quad + \frac{1}{k_o a} J_n(k_o a) J'_n(k_o a)] \end{aligned} \quad (4.20)$$

In the case $k_o a \ll 1$, $r'_w \approx \frac{1}{2} (|A'_0|^2 + |A'_1|^2)$, and we obtain an approximate low-frequency expression for r'_w as

$$\begin{aligned} r'_w \Big|_{k_o a \ll 1} &\approx \frac{1}{2} \left\{ \left| C + j \frac{\eta_0 \sigma g d}{2} k_o \rho_o \frac{s}{(1-j)d/\delta} \right|^{-2} \right. \\ &\quad \left. + \left| C - j \frac{\eta_0 \sigma g d}{2k_o \rho_o} \frac{s}{(1-j)d/\delta} \right|^{-2} \right\} \end{aligned} \quad (4.21)$$

Curves of r'_w as a function of frequency are given in Figs. 4.5-4.7 for the same values of a , d , and σ_g used in the curves for r_w calculated previously.

It will be noted that when $d/\delta \ll 1$, $r_w \rightarrow 1$ as $k_o \rho_o \rightarrow 0$ but $r'_w \rightarrow \frac{1}{2}$ as $k_o \rho_o \rightarrow 0$. This is so because the TE electric field (which is normal to the cylinder axis) terminates on surface charges on the cylinder surface. Thus r'_w contains only a contribution from the internal magnetic field, while both electric and magnetic fields contribute to r_w . One will also note from eqs. (4.13) and (4.21) and Figs. 4.2-4.7 that the principal "break frequency" for both r_w and r'_w is approximately $1/\pi \mu_0 \rho_o \sigma g d$.

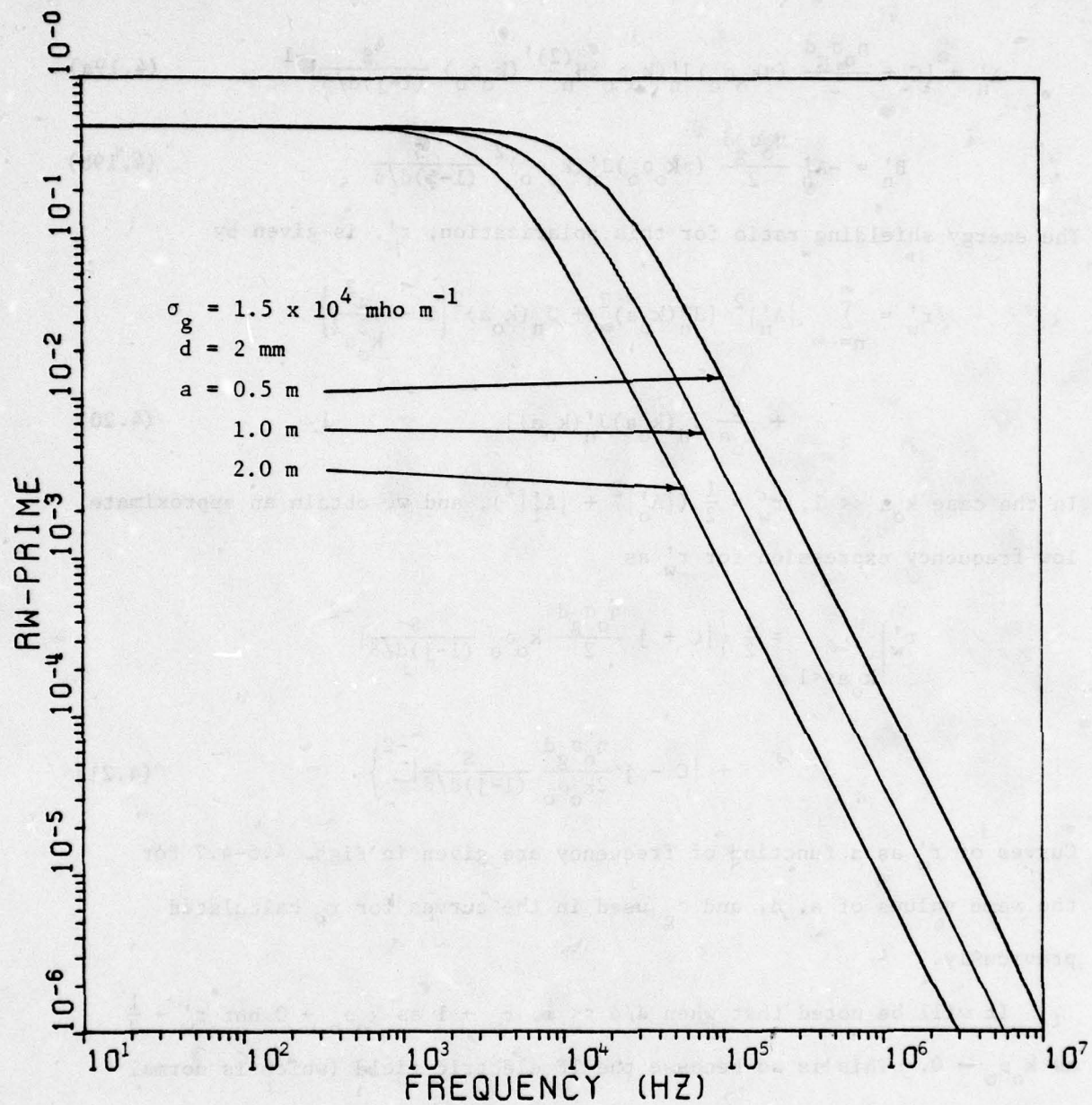


Figure 4.5. Energy shielding ratio r'_W vs. frequency with a as parameter;
 $d = 2 \text{ mm}$, $\sigma_g = 1.5 \times 10^4 \text{ mho m}^{-1}$

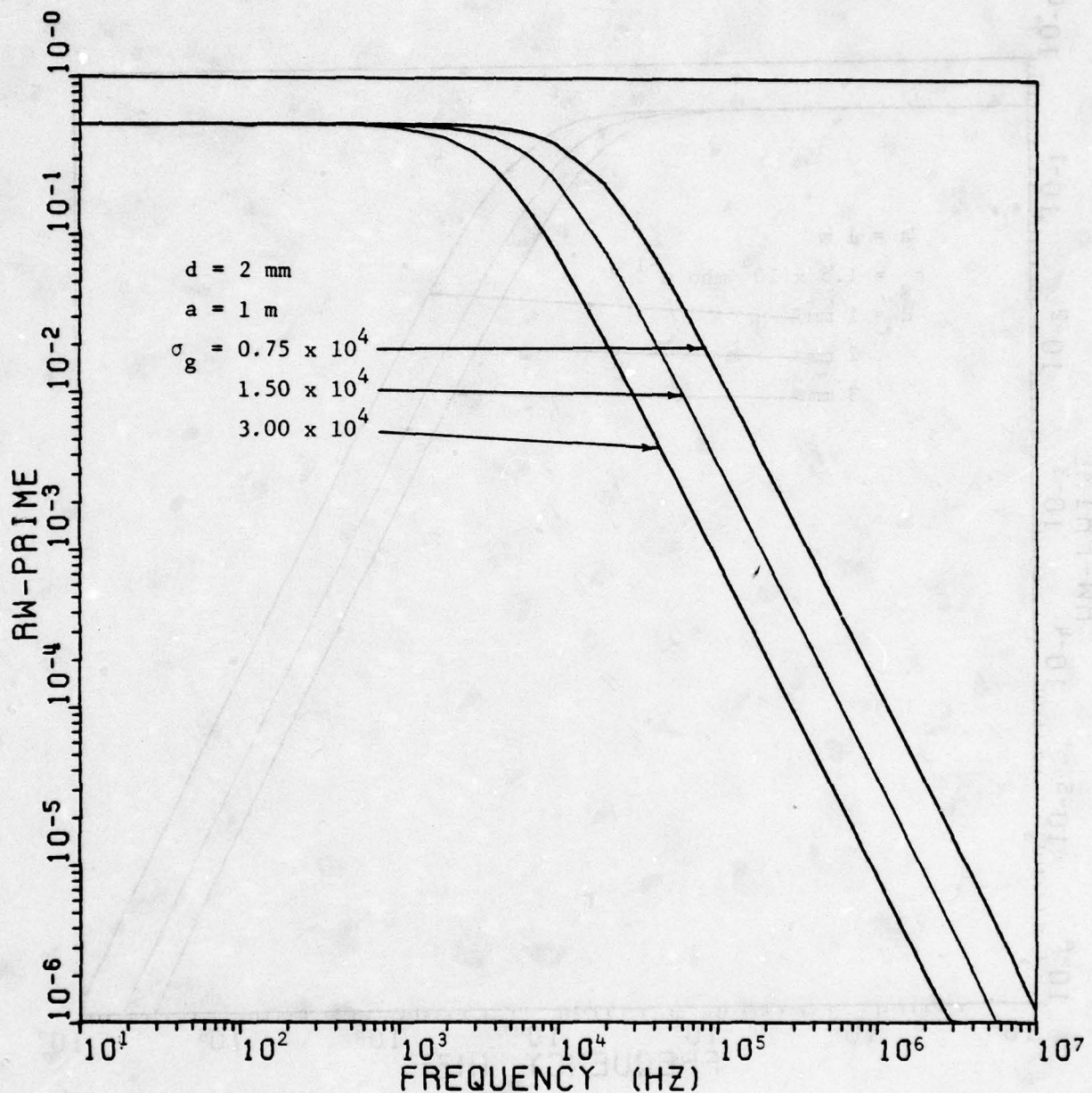


Figure 4.6. Energy shielding ratio r'_w vs. frequency with σ_g as parameter; $d = 2$ mm, $a = 1$ m

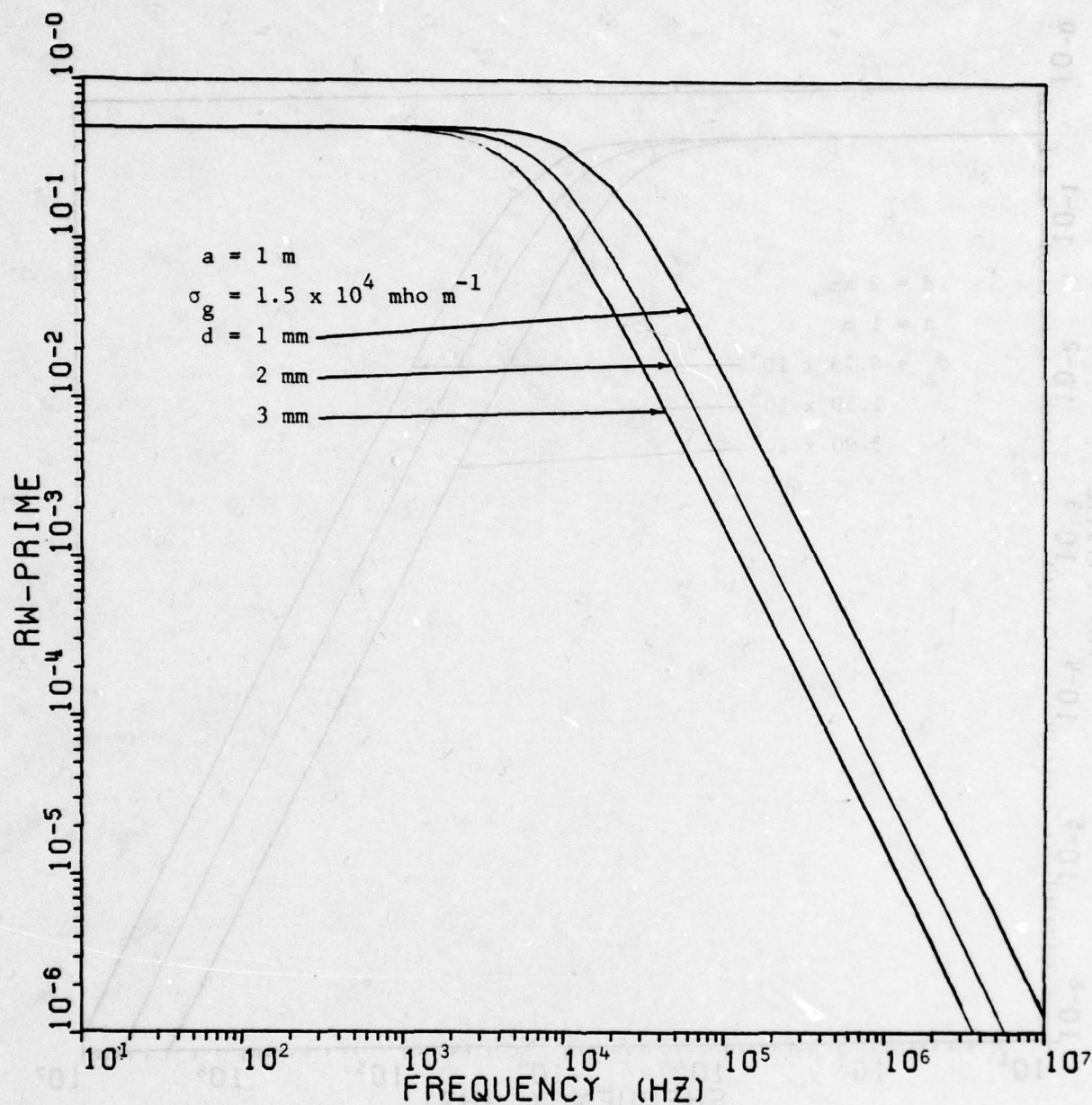


Figure 4.7. Energy shielding ratio r'_w vs. frequency with d as parameter;
 $a = 1 \text{ m}$, $\sigma_g = 1.5 \times 10^4 \text{ mho m}^{-1}$

3. TIME-DOMAIN SHIELDING

In the frequency domain the ratio of the internal magnetic field H_{int} to the incident magnetic field H_{inc} is readily shown at low frequencies to be

$$\frac{H_{int}}{H_{inc}} = [C + j \frac{\eta_0 \sigma d}{2} k_0 \rho_0 \frac{s}{(1-j)d/\delta}]^{-1} \quad (4.22)$$

for either polarization. We now construct a Laplace integral for the internal field as follows (the incident waveform is the standard EMP double exponential):

$$H_{int}(t) = \frac{2dA}{\eta_0 \rho_0} \frac{1}{2\pi j} \int_{\Gamma_B} \left(\frac{1}{s+\alpha} - \frac{1}{s+\beta} \right) \frac{e^{st}}{\sqrt{s\tau_d} \sinh \sqrt{s\tau_d} + \frac{2d}{\rho_0} \cosh \sqrt{s\tau_d}} ds \quad (4.23)$$

in which all quantities have been previously defined. Now $2d/\rho_0 \ll 1$ in the cases which we consider, so that the poles of the integrand, in addition to those at $s = -\alpha$ and $s = -\beta$, are approximately located at $s = -2d/\rho_0 \tau_d$ and $-n^2 \pi^2 / \tau_d$ ($n \geq 1$). Thus we obtain for the internal magnetic field the approximate expression

$$\begin{aligned} H_{int}(t) &\approx \frac{2dA}{\rho_0 \eta_0} \left[\frac{e^{-\beta t}}{\sqrt{\beta \tau_d} \sin \sqrt{\beta \tau_d}} - \frac{e^{-\alpha t}}{\sqrt{\alpha \tau_d} \sin \sqrt{\alpha \tau_d}} \right] \\ &+ 2(\beta-\alpha)\tau_d \sum_{n=1}^{\infty} \frac{(-1)^n e^{-n^2 \pi^2 t / \tau_d}}{(\alpha \tau_d - n^2 \pi^2)(\beta \tau_d - n^2 \pi^2)} \\ &+ \left[\frac{1}{\alpha \tau_d} - \frac{1}{\beta \tau_d} \right] e^{-(2d/\rho_0 \tau_d)t} U(t) \end{aligned} \quad (4.24)$$

in which we have made use of the assumption $\alpha \tau_d \gg 2d/\rho_0$. This assumption is easily satisfied in the cases we consider.

For late times, the dominant contribution to $H_{int}(t)$ is the last term in (4.24) (cf. ref. [15]):

$$H_{int}(t) \rightarrow \frac{2Ad}{\eta_0 \rho_0} \left(\frac{1}{\alpha \tau_d} - \frac{1}{\beta \tau_d} \right) e^{-(2d/\rho_0 \tau_d)t} \quad (4.25)$$

A plot of $\eta_0 H_{int}(t)$ vs. t for three values of τ_d is shown in Fig. 4.8⁺.

The three values of τ_d chosen correspond to thicknesses d of 1, 2, and 3 mm if $\sigma_g = 1.5 \times 10^4$ mho m^{-1} and $\mu_g = \mu_0$. The radius ρ_0 is taken to be 1 m in each case. The contribution of the expression in (4.25) at late times is readily apparent.

Comparing Fig. 4.8 with Fig. 3.4, one will observe the "integrating" or "low-pass" character of the cylindrical geometry itself. Thus an incident signal is, in a sense, doubly low-pass filtered in passing into the interior of a cylindrical region shielded by a conducting shell. Contrasting behavior is evidenced by screened composite structures, which we shall consider in the next two sections.

⁺The reader is reminded that in Cal Comp plots such as Fig. 4.8, the axis labeling is such that the exponential factor (in this case 10^{-2}) is to be associated with the ordinate values, not with the axis label. Thus the maximum ordinate in Fig. 4.8 is 0.0025.

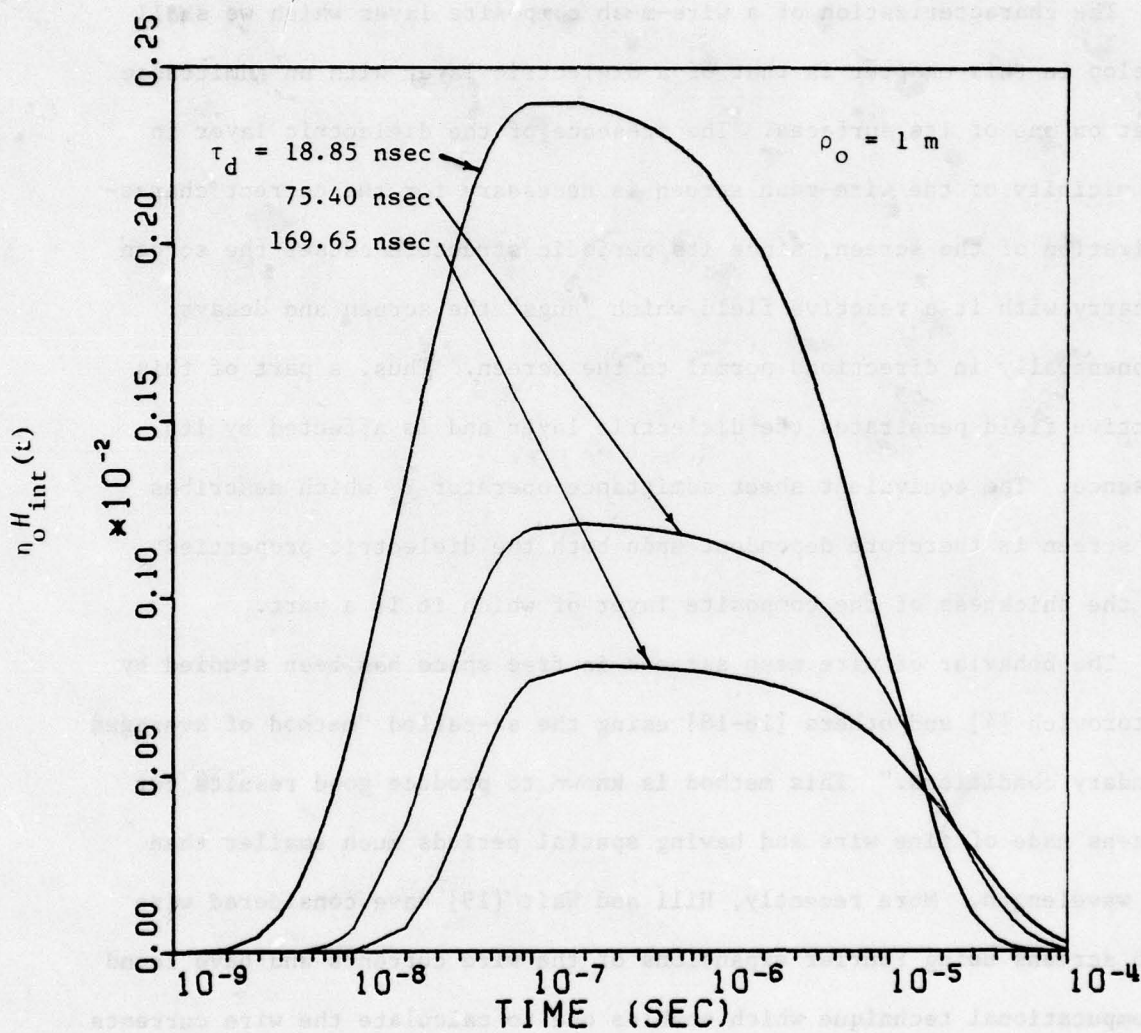


Figure 4.8. (n_o) times internal magnetic field for graphite cylindrical shell vs. t ; $\rho_o = 1 \text{ m}$

SECTION V

PLANAR WIRE-MESH COMPOSITE SHIELDS

1. INTRODUCTION

The characterization of a wire-mesh composite layer which we shall develop in this chapter is that of a dielectric layer with an admittance sheet on one of its surfaces. The presence of the dielectric layer in the vicinity of the wire-mesh screen is necessary for the correct characterization of the screen, since its periodic structure causes the screen to carry with it a reactive field which "hugs" the screen and decays exponentially in directions normal to the screen. Thus, a part of this reactive field penetrates the dielectric layer and is affected by its presence. The equivalent sheet admittance operator \tilde{Y}_s which describes the screen is therefore dependent upon both the dielectric properties and the thickness of the composite layer of which it is a part.

The behavior of wire mesh screens in free space has been studied by Kontorovich [4] and others [16-18] using the so-called "method of averaged boundary conditions." This method is known to produce good results for screens made of fine wire and having spatial periods much smaller than the wavelength. More recently, Hill and Wait [19] have considered wire mesh screens using Fourier expansions of the wire currents and have found a computational technique which enables one to calculate the wire currents relatively rapidly when the mesh size is small with respect to the wavelength. We shall employ a method similar to, but an extension of, that used by Hill and Wait to speed the convergence of the numerical solution for the wire currents.

The screens which have been used to shield boron-epoxy composites are not generally fine enough to allow the unconcerned use of the thin-wire approximation which is basic to the present theory of wire-mesh screens. We shall, therefore, compare the results of our main analysis (which is based upon the thin-wire approximation) with the results obtained by considering the limit in which the screen is replaced by a conductor with a periodic distribution of small rectangular apertures in it. Using this comparison procedure, we can then establish bounds on the behavior of "thick-wire" mesh screens.

In paragraphs 2 and 3 of this section, we formulate the problem of plane-wave scattering by a fine wire-mesh screen in the surface of a dielectric layer of finite thickness. An equivalent sheet impedance for the screen is derived in paragraph 4, and the fields transmitted through the wire-mesh composite layer are considered in paragraph 5. The "perforated screen" model is discussed in paragraph 6 and comparisons drawn between the two models.

2. FORMULATION OF THE PROBLEM

The geometry of the problem is shown in Fig. 5.1. A dielectric layer of relative permittivity ϵ_r (which may be complex) and relative permeability μ is located in the region $0 \leq z \leq d$. A rectangular grid of conducting wires is embedded in the upper ($z=0$) surface of the layer: wires parallel to the y -axis are located at $x=pa$ ($p = 0, \pm 1, \dots$) and wires parallel to the x -axis are located at $y = qb$ ($q = 0, \pm 1, \dots$). The wire junctions are assumed to be bonded. The wire radius r is assumed to be small in comparison to the spacings a and b and to the wavelengths in

collected evidence and findings of their need and nature, location and
methods used to test telecommunications equipment or devices and influences on them
described to provide information for choice of either normalization or
calibration when due to situation and circumstances, there are no specific
instructions given in the instructions given in the reference material at hand.

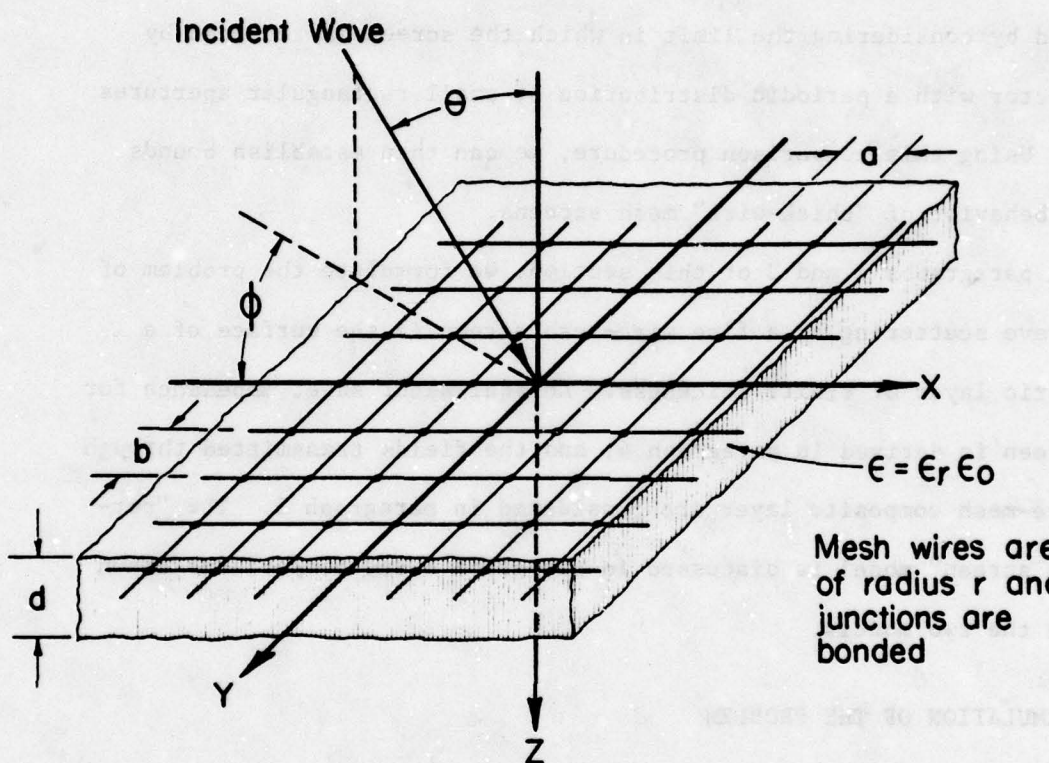


Figure 5.1. Reflection and transmission of a plane wave by a dielectric layer with embedded wire-mesh screen: geometry of the problem

free space and in the layer material; thus the wire currents are purely axial and the thin-wire approximations are valid. The wire impedance per unit length is given by

$$Z_w = \frac{n_w}{2\pi r} \frac{I_o(\tau_w r)}{I_1(\tau_w r)} \quad (5.1)$$

in which

$$n_w = (j\omega\mu_w/\sigma_w)^{1/2} \quad (5.2a)$$

$$\tau_w = (j\omega\mu_w\sigma_w)^{1/2} \quad (5.2b)$$

μ_w and σ_w denote respectively the wire permeability and conductivity, and $I_n(\cdot)$ denotes the modified Bessel function of the first kind. The time dependence is assumed to be $\exp(j\omega t)$.

The region outside the layer is free space. A plane electromagnetic wave is incident upon the layer from the region $z < 0$. The incident electric field is given by

$$\bar{E}_{inc} = \bar{E}_o e^{-jk_o \cdot \bar{r}} \quad (5.3)$$

in which \bar{r} is the position vector, and

$$\bar{k}_o = k_o (\bar{a}_x \sin\theta \cos\phi + \bar{a}_y \sin\theta \sin\phi + \bar{a}_z \cos\theta) \quad (5.4)$$

$$\begin{aligned} \bar{E}_o = E_{o\theta} (\bar{a}_x \cos\theta \cos\phi + \bar{a}_y \cos\theta \sin\phi - \bar{a}_z \sin\theta) \\ + E_{o\phi} (-\bar{a}_x \sin\phi + \bar{a}_y \cos\phi) \end{aligned} \quad (5.5)$$

$E_{o\theta}$ and $E_{o\phi}$ denote respectively the amplitudes of the θ -polarized and ϕ -polarized components of the incident electric field, θ and ϕ are the incidence angles in spherical coordinates, and $k_o = \omega\sqrt{\mu_o\epsilon_o}$.

The wire currents I_x and I_y are expressed in terms of space-harmonic series as follows:

$$I_x(y = qb) = e^{-jk_{x0}qb} \sum_{m=-\infty}^{\infty} \tilde{I}_{xm} e^{-jk_{xm}x} \quad (5.6a)$$

$$I_y(x = pa) = e^{-jk_{y0}pa} \sum_{n=-\infty}^{\infty} \tilde{I}_{yn} e^{-jk_{yn}y} \quad (5.6b)$$

\tilde{I}_{xm} and \tilde{I}_{yn} denote the space-harmonic components of the currents I_x and I_y respectively, and

$$k_{xm} = k_0 \sin\theta \cos\phi + 2\pi m/a \quad (5.7a)$$

$$k_{yn} = k_0 \sin\theta \sin\phi + 2\pi n/b \quad (5.7b)$$

The electromagnetic field is expressed in terms of a vector function $\bar{\Psi}$ as follows:

$$\bar{H} = \nabla \times \bar{\Psi} \quad (5.8a)$$

$$\bar{E} = \frac{1}{j\omega\epsilon} [\nabla\nabla + k^2 \bar{I}] \cdot \bar{\Psi} \quad (5.8b)$$

where $\bar{\Psi} = \psi_x \bar{a}_x + \psi_y \bar{a}_y$ and

$$\nabla^2 \bar{\Psi} + k^2 \bar{\Psi} = 0 \quad (5.9)$$

with $k^2 = k_0^2 \epsilon_r$ and $\epsilon = \epsilon_0 \epsilon_r$ for $0 \leq z \leq d$; and $k^2 = k_0^2$, $\epsilon = \epsilon_0$ elsewhere.

The periodic nature of the wire grid indicates that the various field quantities will be most conveniently expressed in terms of two-dimensional space harmonic series as

$$F(x, y, z) = \sum_{m=-\infty}^{\infty} \sum_{n=-\infty}^{\infty} \tilde{F}_{mn}(z) e^{-jk_{xm}x} e^{-jk_{yn}y} \quad (5.10)$$

We thus obtain for the tangential (x and y) space-harmonic components of \bar{E} and \bar{H} the following expressions:

$$\tilde{\tilde{E}}_{tmn} = \frac{1}{j\omega\epsilon} \bar{\bar{P}}_{mn} \cdot \tilde{\tilde{\Psi}}_{mn} \quad (5.11a)$$

$$\tilde{\tilde{H}}_{tmn} = \frac{d}{dz} (\bar{a}_z \times \tilde{\tilde{\Psi}}_{mn}) \quad (5.11b)$$

in which

$$\bar{\bar{P}}_{mn} = \begin{bmatrix} k^2 - k_{xm}^2 & -k_{xm} k_{yn} \\ -k_{xm} k_{yn} & k^2 - k_{yn}^2 \end{bmatrix} \quad (5.12)$$

In the dielectric layer, $\bar{\bar{P}}_{mn} = \bar{\bar{P}}_{dmn}$, $k^2 = k_o^2 \epsilon_r$, and $\epsilon = \epsilon_o \epsilon_r$; elsewhere $\bar{\bar{P}}_{mn} = \bar{\bar{P}}_{omn}$, $k^2 = k_o^2$, and $\epsilon = \epsilon_o$. The space-harmonic components of the surface current density due to the currents in the grid wires are

$$\tilde{\tilde{J}}_{smn} = \frac{\tilde{I}_{xm}}{b} \bar{a}_x + \frac{\tilde{I}_{yn}}{a} \bar{a}_y \quad (5.13)$$

We now construct appropriate solutions for $\tilde{\tilde{\Psi}}_{mn}$ in each of the three regions of the problem. We have

$$-\infty < z < 0: \quad \tilde{\tilde{\Psi}}_{mn} = \bar{A}_{mn} e^{jk_{zomn} z} + \bar{\pi}_{mn} e^{-jk_{zomn} z} \quad (5.14a)$$

$$0 < z < d: \quad \tilde{\tilde{\Psi}}_{mn} = \bar{B}_{mn} \cos k_{zdmn} z + \bar{C}_{mn} \sin k_{zdmn} z \quad (5.14b)$$

$$d < z < \infty: \quad \tilde{\tilde{\Psi}}_{mn} = \bar{D}_{mn} e^{-jk_{zomn}(z-d)} \quad (5.14c)$$

where $k_{zomn}^2 = k_o^2 - k_{xm}^2 - k_{yn}^2$ and $k_{zdmn}^2 = k_o^2 \epsilon_r - k_{xm}^2 - k_{yn}^2$; \bar{A}_{mn} - \bar{D}_{mn} are vector functions of m and n to be determined; and $\bar{\pi}_{mn}$ represents the incident wave:

$$\bar{\pi}_{mn} = j\omega\epsilon_o \delta_m \delta_n \bar{\bar{P}}_{omn}^{-1} \cdot \bar{E}_{ot} \quad (5.15)$$

δ_k denotes the Kronecker delta-function and $\bar{E}_{ot} = (\bar{I} - \bar{a}_z \bar{a}_z) \cdot \bar{E}_o$ [cf. eq. (5.5)].

We are now in a position to construct the boundary-condition equations from which the unknowns $\bar{A}_{mn} - \bar{D}_{mn}$ may be determined in terms of $\bar{\pi}_{mn}$ and $\tilde{\bar{J}}_{smn}$. By ensuring continuity of tangential \bar{E} at $z = 0$ and $z = d$, continuity of tangential \bar{H} at $z = d$, and the appropriate discontinuity of tangential \bar{H} at $z = 0$, we obtain the following system of equations:

$$\bar{P}_o \cdot \bar{A} - \frac{1}{\epsilon_r} \bar{P}_d \cdot \bar{B} = -\bar{P}_o \cdot \bar{\pi} \quad (5.16a)$$

$$\bar{A} - \frac{k_{zd}}{jk_{zo}} \bar{C} = \bar{\pi} + \frac{1}{jk_{zo}} \tilde{\bar{J}}_s \quad (5.16b)$$

$$\frac{1}{\epsilon_r} \cos k_{zd}d \bar{P}_d \cdot \bar{B} + \frac{1}{\epsilon_r} \sin k_{zd}d \bar{P}_d \cdot \bar{C} - \bar{P}_o \cdot \bar{D} = 0 \quad (5.16c)$$

$$k_{zd} \sin k_{zd}d \bar{B} - k_{zd} \cos k_{zd}d \bar{C} - jk_{zo} \bar{D} = 0 \quad (5.16d)$$

We have dropped the (m,n) subscripts in eq. (5.16) and in the following, for simplicity of notation. They will be reinserted where necessary for clarity.

It is sufficient for our purposes to solve eq. (5.16) for \bar{A} and \bar{D} .

We obtain, after some tedious but straightforward manipulations,

$$\bar{A} = \bar{F} \cdot (\bar{\Lambda} \cdot \bar{\pi} + \frac{1}{2jk_{zo}} \bar{\Gamma} \cdot \tilde{\bar{J}}_s) \quad (5.17a)$$

$$\bar{D} = \bar{F} \cdot (\bar{\pi} + \frac{1}{2jk_{zo}} \tilde{\bar{J}}_s) \sec k_{zd}d \quad (5.17b)$$

in which

$$\bar{F} = [\bar{\Gamma} + \frac{\xi}{2} \left(\frac{k_{zo}}{\epsilon_r} \bar{P}_o^{-1} \cdot \bar{P}_d + k_{zd}^2 \epsilon_r \bar{P}_d^{-1} \cdot \bar{P}_o \right)]^{-1} \quad (5.18a)$$

$$\bar{\Lambda} = \frac{\xi}{2} \left(\frac{k_{zo}}{\epsilon_r} \bar{P}_o^{-1} \cdot \bar{P}_d - k_{zd}^2 \epsilon_r \bar{P}_d^{-1} \cdot \bar{P}_o \right) \quad (5.18b)$$

$$\bar{\Gamma} = \bar{I} + \xi \frac{k_{zo}^2}{\epsilon_r} \bar{P}_o^{-1} \cdot \bar{P}_d \quad (5.18c)$$

and

$$\xi = \frac{j \tan k_{zd} d}{k_{zo} k_{zd}} \quad (5.19)$$

\bar{F} , $\bar{\Lambda}$, and $\bar{\Gamma}$ may also be expressed as follows:

$$\bar{F} = a_f \bar{I} + b_f \bar{K}_y \quad (5.20a)$$

$$\bar{\Lambda} = a_\lambda \bar{I} + b_\lambda \bar{K}_x \quad (5.20b)$$

$$\bar{\Gamma} = a_\gamma \bar{I} + b_\gamma \bar{K}_x \quad (5.20c)$$

in which

$$\bar{K}_x = \begin{bmatrix} k_x^2 & k_x k_y \\ k_x k_y & k_y^2 \end{bmatrix} \quad (5.21a)$$

$$\bar{K}_y = \begin{bmatrix} k_y^2 & -k_x k_y \\ -k_x k_y & k_x^2 \end{bmatrix} \quad (5.21b)$$

and

$$a_f = [1 + \frac{\xi}{2} \left(k_{zo}^2 \epsilon_r + \frac{k_{zd}^2}{\epsilon_r} \right)]^{-1} \quad (5.22a)$$

$$b_f = \frac{-\xi}{2\epsilon_r} (\epsilon_r - 1)^2 a_f [1 + \frac{\xi}{2} (k_{zo}^2 + k_{zd}^2)]^{-1} \quad (5.22b)$$

$$a_\lambda = -\frac{\xi}{2} k_o^2 (\epsilon_r - 1) \quad (5.22c)$$

$$b_\lambda = \frac{\xi}{2\epsilon_r} (\epsilon_r^2 - 1) \quad (5.22d)$$

$$a_\gamma = 1 + \xi k_{zo}^2 \quad (5.22e)$$

$$b_\gamma = \frac{\xi}{\epsilon_r} (\epsilon_r - 1) \quad (5.22f)$$

In order to determine the still unknown wire currents and thereby complete the solution to the problem, we apply the boundary condition at the wire surfaces that the component of \bar{E} parallel to a wire axis is equal to the wire current times its impedance per unit length. Since the wires have been assumed to be thin, it suffices to apply this condition at the tops of the wires, i.e.,

$$E_x(x, qb, -r) = Z_w I_x(y = qb) \quad (q = 0, \pm 1, \dots) \quad (5.23a)$$

$$E_y(p_a, y, -r) = Z_w I_y(x = p_a) \quad (p = 0, \pm 1, \dots) \quad (5.23b)$$

The conditions (5.23) lead directly to the following coupled set of equations:

$$\begin{aligned} \frac{1}{j\omega\epsilon_0} \sum_{n=-\infty}^{\infty} \frac{e^{-jk_{zomn}r}}{2jk_{zomn}} \bar{a}_x \cdot \bar{a}_{mn} \cdot \bar{j}_{smn} - Z_w \bar{I}_{xm} \\ = -\bar{a}_x \cdot \bar{b} \cdot \bar{E}_{ot} \delta_m \quad (m = 0, \pm 1, \dots) \end{aligned} \quad (5.24a)$$

$$\begin{aligned} \frac{1}{j\omega\epsilon_0} \sum_{m=-\infty}^{\infty} \frac{e^{-jk_{zomn}r}}{2jk_{zomn}} \bar{a}_y \cdot \bar{a}_{mn} \cdot \bar{j}_{smn} - Z_w \bar{I}_{yn} \\ = -\bar{a}_y \cdot \bar{b} \cdot \bar{E}_{ot} \delta_n \quad (n = 0, \pm 1, \dots) \end{aligned} \quad (5.24b)$$

in which

$$\bar{a}_{mn} = \bar{P}_{omn} \cdot \bar{F}_{mn} \cdot \bar{\Gamma}_{mn} \quad (5.25a)$$

$$\bar{\bar{b}} = \bar{\bar{P}}_{ooo} \cdot (\bar{\bar{F}}_{oo} \cdot \bar{\bar{A}}_{oo} e^{-jk_{zooo}r} + \bar{\bar{I}} e^{jk_{zooo}r}) \cdot \bar{\bar{P}}_{ooo}^{-1} \quad (5.25b)$$

Since $k_{zooo}r = k_o r \cos\theta \leq k_o r \ll 1$, we have

$$\bar{\bar{b}} \approx \bar{\bar{P}}_{ooo} \cdot (\bar{\bar{F}}_{oo} \cdot \bar{\bar{A}}_{oo} + \bar{\bar{I}}) \cdot \bar{\bar{P}}_{ooo}^{-1} \quad (5.26)$$

Equations (5.24) can now be solved for the wire currents, and the solution to the problem is formally complete. We address the problem of solving eq. (5.24) in the next paragraph.

3. GRID CURRENTS

Equations (5.24) may be rewritten as follows:

$$U_m \bar{I}_{xm} + \sum_{n=-\infty}^{\infty} V_{mn} \bar{I}_{yn} = R_o \delta_m \quad (m = 0, \pm 1, \dots) \quad (5.27a)$$

$$W_n \bar{I}_{yn} + \sum_{m=-\infty}^{\infty} X_{mn} \bar{I}_{xm} = S_o \delta_n \quad (n = 0, \pm 1, \dots) \quad (5.27b)$$

in which

$$U_m = Z_w - \frac{1}{j\omega\epsilon_o} \sum_{n=-\infty}^{\infty} a_{mn}^{(1,1)} \frac{e^{-jk_{zomn}r}}{2jk_{zomn}b} \quad (5.28a)$$

$$V_{mn} = -\frac{1}{j\omega\epsilon_o} a_{mn}^{(1,2)} \frac{e^{-jk_{zomn}r}}{2jk_{zomn}a} \quad (5.28b)$$

$$W_n = Z_w - \frac{1}{j\omega\epsilon_o} \sum_{m=-\infty}^{\infty} a_{mn}^{(2,2)} \frac{e^{-jk_{zomn}r}}{2jk_{zomn}a} \quad (5.28c)$$

$$X_{mn} = -\frac{1}{j\omega\epsilon_o} a_{mn}^{(2,1)} \frac{e^{-jk_{zomn}r}}{2jk_{zomn}b} \quad (5.28d)$$

$$\begin{aligned} R_o &= E_{o\theta} (b^{(1,1)} \cos\theta \cos\phi + b^{(1,2)} \cos\theta \sin\phi) \\ &\quad + E_{o\phi} (-b^{(1,1)} \sin\phi + b^{(1,2)} \cos\phi) \end{aligned} \quad (5.28e)$$

$$\begin{aligned} S_o &= E_{o\theta} (b^{(2,1)} \cos\theta \cos\phi + b^{(2,2)} \cos\theta \sin\phi) \\ &\quad + E_{o\phi} (-b^{(2,1)} \sin\phi + b^{(2,2)} \cos\phi) \end{aligned} \quad (5.28f)$$

$$\begin{aligned} a_{mn}^{(1,1)} &= a_{fmn} [k_o^2 (1 + \xi_{mn} k_{zomn}^2) - k_{xm}^2 (1 + \xi_{mn} \frac{k_{zomn}^2}{\epsilon_r})] \\ &\quad + b_{fmn} k_o^2 k_{yn}^2 (1 + \xi_{mn} k_{zomn}^2) \end{aligned} \quad (5.29a)$$

$$\begin{aligned} a_{mn}^{(1,2)} &= a_{mn}^{(2,1)} = -a_{fmn} k_{xm} k_{yn} (1 + \xi_{mn} \frac{k_{zomn}^2}{\epsilon_r}) \\ &\quad - b_{fmn} k_o^2 k_{xm} k_{yn} (1 + \xi_{mn} k_{zomn}^2) \end{aligned} \quad (5.29b)$$

$$\begin{aligned} a_{mn}^{(2,2)} &= a_{fmn} [k_o^2 (1 + \xi_{mn} k_{zomn}^2) - k_{yn}^2 (1 + \xi_{mn} \frac{k_{zomn}^2}{\epsilon_r})] \\ &\quad + b_{fmn} k_o^2 k_{xm}^2 (1 + \xi_{mn} k_{zomn}^2) \end{aligned} \quad (5.29c)$$

$$b^{(1,1)} = 1 + a_{\lambda oo} a_{foo} + a_{foo} b_{\lambda oo} k_{xo}^2 + a_{\lambda oo} b_{foo} k_{yo}^2 \quad (5.29d)$$

$$b^{(1,2)} = b^{(2,1)} = k_{xo} k_{yo} (a_{foo} b_{\lambda oo} + a_{\lambda oo} b_{foo}) \quad (5.29e)$$

$$b^{(2,2)} = 1 + a_{\lambda oo} a_{foo} + a_{\lambda oo} b_{foo} k_{xo}^2 + a_{foo} b_{\lambda oo} k_{yo}^2 \quad (5.29f)$$

Equations (5.24) can be solved numerically for \tilde{I}_{xm} and \tilde{I}_{yn} ; however,

Hill and Wait [19] have shown that in the case where the dielectric layer is absent (i.e., the wire grid is in free space), convergence of these equations can be extremely slow. They found that by incorporating a Kirchhoff's-law junction condition into the solution, the convergence

was radically improved. Anticipating a similar difficulty in the present situation, we shall modify eq. (5.24) by incorporating junction conditions which should speed the solution.

Consider the functions[†]

$$f_a(x) = \frac{-1}{2\pi j} \sum_{n=-\infty}^{\infty} \frac{1}{n} e^{-2jn\pi x/a} \quad (5.30a)$$

$$g_a(x) = \frac{-a}{(2\pi)^2} \sum_{n=-\infty}^{\infty} \frac{1}{n^2} e^{-2jn\pi x/a} \quad (5.30b)$$

which are shown in Fig. 5.2. $f_a(x)$ has a unit jump discontinuity at $x=0, \pm a, \dots$; $g_a(x)$ has a unit discontinuity in slope at $x=0, \pm a, \dots$. Let us write for $I_x(x, y = qb)$ and $I_y(x = pa, y)$:

$$\begin{aligned} I_x(x, y = qb) &= e^{-jk_y o qb} e^{-jk_x o x} [\Delta f_a(x) + s_x g_a(x) \\ &\quad + \sum_{m=-\infty}^{\infty} \tilde{I}'_{xm} e^{-2jm\pi x/a}] \end{aligned} \quad (5.31a)$$

$$\begin{aligned} I_y(x = pa, y) &= e^{-jk_x o pa} e^{-jk_y o y} [-\Delta f_b(y) + s_y g_b(y) \\ &\quad + \sum_{n=-\infty}^{\infty} \tilde{I}'_{yn} e^{-2\pi jny/b}] \end{aligned} \quad (5.31b)$$

The parameters Δ , s_x , and s_y are still to be determined; it will be noted, however, that Kirchhoff's current law is automatically satisfied at the wire junctions. The expressions given in eq. (5.31) are equivalent to

$$\tilde{I}_{xm} = \tilde{I}'_{xm} - \left[\frac{\Delta}{2\pi jm} + \frac{as_x}{(2\pi m)^2} \right] (1 - \delta_m) \quad (5.32a)$$

[†]The primes on the summation signs in eq. (5.30) and elsewhere indicate that the term $n=0$ is deleted.

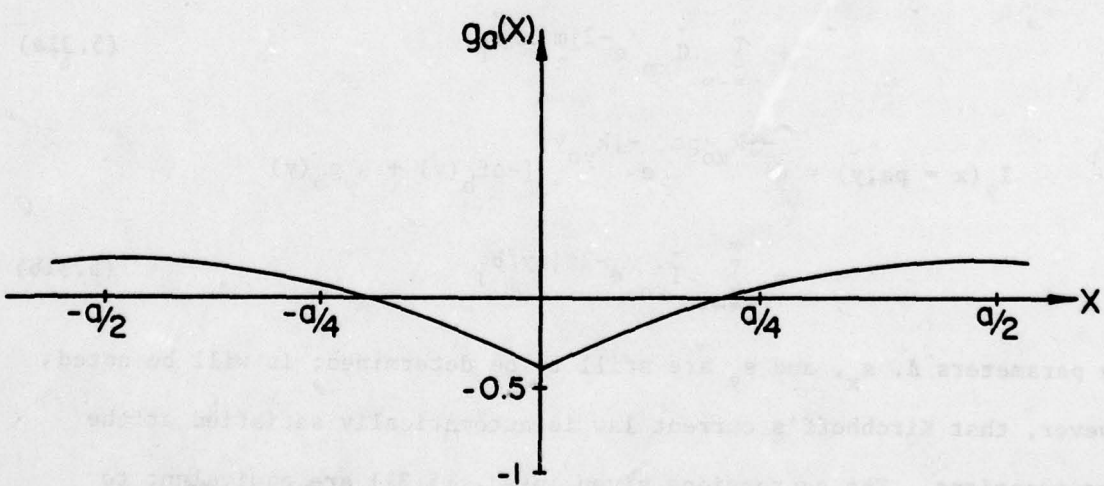
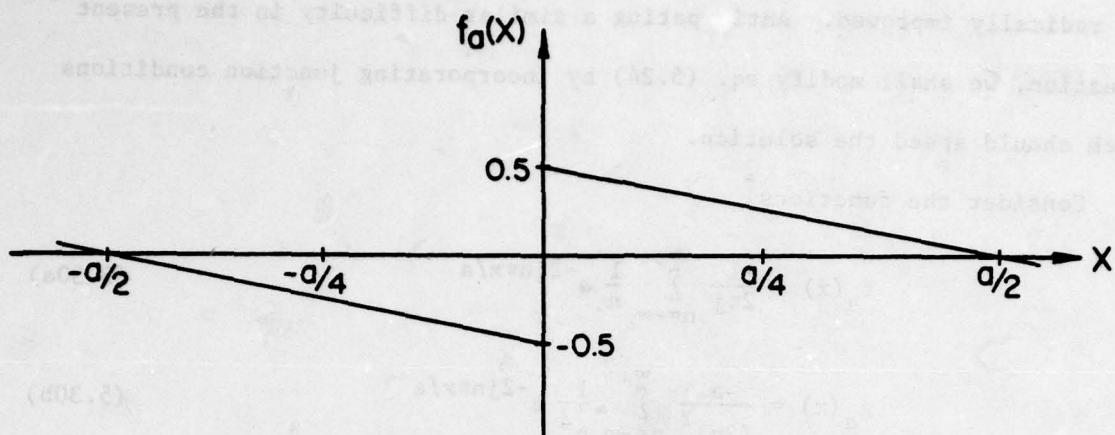


Figure 5.2. Functions $f_a(x)$ and $g_a(x)$ vs. x

$$\tilde{I}_{yn} = \tilde{I}'_{yn} + \left[\frac{\Delta}{2\pi j n} - \frac{bs_y}{(2\pi n)^2} \right] (1 - \delta_n) \quad (5.32b)$$

It is now required that the charge density on each wire be continuous at the junctions, i.e.,

$$\frac{\partial I_x}{\partial x} \Big|_{x=pa^-} = \frac{\partial I_x}{\partial x} \Big|_{x=pa^+} \quad (5.33a)$$

$$\frac{\partial I_y}{\partial y} \Big|_{y=qb^-} = \frac{\partial I_y}{\partial y} \Big|_{y=qb^+} \quad (5.33b)$$

for all p,q. The conditions of (5.33) are obtained from the continuity equation. Imposing these conditions yields expressions for s_x and s_y in terms of Δ :

$$s_x = jk_{xo} \Delta \quad (5.34a)$$

$$s_y = -jk_{yo} \Delta \quad (5.34b)$$

If these expressions are introduced into eq. (5.32), we obtain

$$\tilde{I}_{xm} = \tilde{I}'_{xm} - \Delta(1-\delta_m) \left[\frac{1}{2\pi j m} + \frac{jk_{xo} a}{(2\pi m)^2} \right] \quad (5.35a)$$

$$\tilde{I}_{yn} = \tilde{I}'_{yn} + \Delta(1-\delta_n) \left[\frac{1}{2\pi j n} + \frac{jk_{yo} b}{(2\pi n)^2} \right] \quad (5.35b)$$

The final condition to be imposed is that the charge density on the "x-wires" be equal to that on the "y-wires" at the junctions. This requirement leads to the condition

$$\frac{\partial I_x}{\partial x} \Big|_{\substack{x=pa \\ y=qb}} = \frac{\partial I_y}{\partial y} \Big|_{\substack{x=pa \\ y=qb}} \quad (5.36)$$

which yields the equation for Δ :

$$\Delta = \left[\frac{1}{b} \left(1 + \frac{k_{yo}^2 b^2}{12} \right) + \frac{1}{a} \left(1 + \frac{k_{xo}^2 a^2}{12} \right) \right]^{-1}$$

$$j \left[\sum_{n=-\infty}^{\infty} k_{yn} \tilde{I}'_{yn} - \sum_{m=-\infty}^{\infty} k_{xm} \tilde{I}'_{xm} \right] \quad (5.37)$$

This last condition may be interpreted physically by noting that it implies no potential difference between the wires at a junction. Kontorovich [4] used a more general condition than (5.36) to include the effect of a finite junction impedance. Inclusion of this effect in our analysis can be shown to modify eq. (5.37) by an additive term ζ in the first square brackets; and

$$\zeta = j\omega K Z_j \quad (5.38)$$

where Z_j is the junction impedance and K is a proportionality constant given by

$$K = \frac{1}{V_{pq}} \left[q_x(x=pa, y=qb) - q_y(x=pa, y=qb) \right] \quad (5.39)$$

V_{pq} is the junction potential difference and q_x and q_y denote respectively the linear charge densities on the "x-wires" and the "y-wires." It is tempting to proceed with incorporating this junction condition in our present analysis. However, we recognize that by initially formulating our problem with the x-wires and y-wires coplanar, the solution for the currents will converge to the result for which $\zeta=0$, no matter what value of ζ is initially assigned. Therefore, we shall consider only the bonded-junction limit in the present work, and reserve the case of finite junction impedance for further study.

Incorporating eqs. (5.35) into eq. (5.27) and simplifying, we obtain a new set of coupled equations for the "modified" space harmonics \tilde{I}'_{xm} and \tilde{I}'_{yn} as follows: together with eq. (5.37), we have

$$U_m \tilde{I}'_{xm} + \sum_{n=-\infty}^{\infty} V_{mn} \tilde{I}'_{yn} - P_m \Delta = R_o \delta_m \quad (m = 0, \pm 1, \dots) \quad (5.40a)$$

$$W_n \tilde{I}'_{yn} + \sum_{m=-\infty}^{\infty} X_{mn} \tilde{I}'_{xm} + Q_n \Delta = S_o \delta_n \quad (n = 0, \pm 1, \dots) \quad (5.40b)$$

in which

$$\begin{aligned} P_m &= U_m \left[\frac{1}{2\pi j m} + \frac{j k_{xo} a}{(2m\pi)^2} \right] (1 - \delta_m) \\ &\quad - \sum_{n=-\infty}^{\infty} V_{mn} \left[\frac{1}{2\pi j n} + \frac{j k_{yo} b}{(2n\pi)^2} \right] \end{aligned} \quad (5.41a)$$

$$\begin{aligned} Q_n &= W_n \left[\frac{1}{2\pi j n} + \frac{j k_{yo} b}{(2n\pi)^2} \right] (1 - \delta_n) \\ &\quad - \sum_{m=-\infty}^{\infty} X_{mn} \left[\frac{1}{2\pi j m} + \frac{j k_{xo} a}{(2m\pi)^2} \right] \end{aligned} \quad (5.41b)$$

The various summations required in the evaluation of the currents can be put into rapidly convergent form by adding to and subtracting from each summand its dominant behavior for large values of the summation index, and then performing the sum over the added dominant terms in closed form. We readily obtain

$$\begin{aligned} U_m &= Z_w - \frac{q_m}{2\pi j \omega \epsilon_o} \ln(1 - e^{-2\pi r/b})^{-1} - \frac{a_{mo}^{(1,1)}}{j \omega \epsilon_o} \frac{-jk_{zomo} r}{2jk_{zomo} b} \\ &\quad - \frac{1}{j \omega \epsilon_o} \sum_{n=-\infty}^{\infty} \left[a_{mn}^{(1,1)} \frac{-jk_{zomn} r}{2jk_{zomn} b} - \frac{q_m}{4|n|\pi} e^{-2|n|\pi r/b} \right] \end{aligned} \quad (5.42a)$$

$$w_n = z_w - \frac{r_n}{2\pi j\omega\epsilon_0} \ln(1 - e^{-2\pi r/a})^{-1} - \frac{a_{on}^{(2,2)}}{j\omega\epsilon_0} \frac{e^{-jk_{zoon}r}}{2jk_{zoon}a} \\ - \frac{1}{j\omega\epsilon_0} \sum_{m=-\infty}^{\infty} \left[a_{mn}^{(2,2)} \frac{e^{-jk_{zomn}r}}{2jk_{zomn}a} - \frac{r_n}{4|m|\pi} e^{-2|m|\pi r/a} \right] \quad (5.42b)$$

$$\sum_{n=-\infty}^{\infty} \frac{v_{mn}}{n} = - \frac{s_m}{2\pi j\omega\epsilon_0} \ln(1 - e^{-2\pi r/b})^{-1} \\ - \frac{1}{j\omega\epsilon_0} \sum_{n=-\infty}^{\infty} \left[a_{mn}^{(1,2)} \frac{e^{-jk_{zomn}r}}{2njk_{zomn}b} - \frac{s_m}{4|n|\pi} e^{-2|n|\pi r/b} \right] \quad (5.42c)$$

$$\sum_{m=-\infty}^{\infty} \frac{x_{mn}}{m} = - \frac{t_n}{2\pi j\omega\epsilon_0} \ln(1 - e^{-2\pi r/a})^{-1} \\ - \frac{1}{j\omega\epsilon_0} \sum_{m=-\infty}^{\infty} \left[a_{mn}^{(2,1)} \frac{e^{-jk_{zomn}r}}{2mjka_{zomn}b} - \frac{t_n}{4|m|\pi} e^{-2|m|\pi r/a} \right] \quad (5.42d)$$

in which

$$q_m = \lim_{|n| \rightarrow \infty} a_{mn}^{(1,1)} = k_o^2 - \frac{2k_x^2}{1 + \epsilon_r} \quad (5.43a)$$

$$r_n = \lim_{|m| \rightarrow \infty} a_{mn}^{(2,2)} = k_o^2 - \frac{2k_y^2}{1 + \epsilon_r} \quad (5.43b)$$

$$s_m = \lim_{|n| \rightarrow \infty} a_{mn}^{(1,2)} \frac{b}{na} = \frac{-4\pi k_x m}{a(\epsilon_r + 1)} \quad (5.43c)$$

$$t_n = \lim_{|m| \rightarrow \infty} a_{mn}^{(2,1)} \frac{a}{mb} = \frac{-4\pi k_y n}{b(\epsilon_r + 1)} \quad (5.43d)$$

The above results hold when $d > 0$. (If $d = 0$, the correct results are obtained by setting $\epsilon_r = 1$).

We are now in a position to calculate the wire currents in a relatively efficient manner, and from the currents to construct all the field quantities of interest in the problem. Our principal interest, however, is in developing a relatively simple characterization of the screen embedded in the surface of the composite, in the form of an equivalent sheet impedance. This problem is addressed in the next paragraph.

4. EQUIVALENT SHEET IMPEDANCE OF THE GRID

In this paragraph we derive an equivalent sheet impedance for the wire grid embedded in the surface of the dielectric layer. The relation which we seek is

$$\tilde{\tilde{E}}_{too} = \bar{\bar{Z}}_s \cdot \tilde{\tilde{J}}_{soo} = \bar{\bar{Y}}_s^{-1} \cdot \tilde{\tilde{J}}_{soo} \quad (5.44)$$

which relates the space-averaged tangential electric field at the grid to the space-averaged surface current density [cf. eq. (2.16)].

From eqs. (5.11a), (5.14a), and (5.17a) we obtain

$$\begin{aligned} \tilde{\tilde{E}}_{too}(z=0) &= \frac{1}{j\omega\epsilon_0} \bar{\bar{P}}_{ooo} \cdot (\bar{\bar{A}}_{oo} + \bar{\bar{\pi}}_{oo}) \\ &= \frac{1}{j\omega\epsilon_0} (\bar{\bar{P}}_{ooo} \cdot \bar{\bar{F}}_{oo} \cdot \bar{\bar{\Lambda}}_{oo} + \bar{\bar{P}}_{ooo}) \cdot \bar{\bar{\pi}}_{oo} \\ &\quad - \frac{n_o}{2k_o^2} \sec\theta \bar{\bar{P}}_{ooo} \cdot \bar{\bar{F}}_{oo} \cdot \bar{\bar{\Gamma}}_{oo} \cdot \tilde{\tilde{J}}_{soo} \end{aligned} \quad (5.45)$$

and using eqs. (5.15) and (5.25),

$$\tilde{\tilde{E}}_{too}(z=0) = \bar{\bar{b}} \cdot \bar{\bar{E}}_{ot} - \frac{n_o}{2k_o^2} \sec\theta \bar{\bar{a}}_{oo} \cdot \tilde{\tilde{J}}_{soo} \quad (5.46)$$

Now substituting eq. (5.44) in (5.46), we have

$$\bar{\bar{z}}_s \cdot \tilde{j}_{soo} = \bar{b} \cdot \bar{E}_{ot} - \frac{n_o}{2k_o^2} \sec\theta \bar{a}_{oo} \cdot \tilde{j}_{soo} \quad (5.47)$$

The system of eqs. (5.27), or (5.37) and (5.40), can, in principle at least, be reduced to a system of the form

$$\tilde{U}\tilde{I}_{xo} + \tilde{V}\tilde{I}_{yo} = R_o \quad (5.48a)$$

$$\tilde{X}\tilde{I}_{xo} + \tilde{W}\tilde{I}_{yo} = S_o \quad (5.48b)$$

or, equivalently,

$$\begin{bmatrix} \tilde{bU} & \tilde{aV} \\ \tilde{bX} & \tilde{aW} \end{bmatrix} \begin{bmatrix} \tilde{I}_{xo}/b \\ \tilde{I}_{yo}/a \end{bmatrix} = \begin{bmatrix} R_o \\ S_o \end{bmatrix} \quad (5.49)$$

Now,

$$\begin{bmatrix} R_o \\ S_o \end{bmatrix} = \bar{b} \cdot \bar{E}_{ot} \quad (5.50)$$

and defining

$$\bar{\bar{z}}_g = \begin{bmatrix} \tilde{bU} & \tilde{aV} \\ \tilde{bX} & \tilde{aW} \end{bmatrix} \quad (5.51)$$

we obtain

$$\bar{\bar{z}}_g \cdot \tilde{j}_{soo} = \bar{b} \cdot \bar{E}_{ot} \quad (5.52)$$

Substituting eq. (5.52) into eq. (5.47) yields

$$\bar{\bar{z}}_s = \bar{\bar{z}}_g - \frac{n_o}{2k_o^2} \sec\theta \bar{a}_{oo} \quad (5.53)$$

which is the relation required. It is evident that the problem of finding the equivalent transfer impedance \bar{Z}_s has been reduced to determining the impedance \bar{Z}_g . This can always be done numerically, of course: calculating the currents \tilde{I}_{xo} and \tilde{I}_{yo} from (5.37) and (5.40) for given $E_{o\theta}$ and $E_{o\phi}$ permits the evaluation of \tilde{U} , \tilde{V} , \tilde{W} , and \tilde{X} ; however, we recognize that in the applications we have intended to consider, the mesh dimensions will always be much smaller than the wavelengths involved. As a consequence, an approximate analytic solution can be obtained.

The approximate solution is based on the fact that in the low-frequency limit, the system of equations (5.40) together with the auxiliary condition (5.37) has proven to converge using only one modified space-harmonic in I_x and I_y (discussion of the appropriate numerical results is deferred to paragraph 7 of this section). Therefore, in this limit, we have

$$\tilde{U} = U_o + k_{xo} f P_o \quad (5.54a)$$

$$\tilde{V} = V_{oo} - k_{yo} f P_o \quad (5.54b)$$

$$\tilde{X} = X_{oo} - k_{xo} f Q_o \quad (5.54c)$$

$$\tilde{W} = W_o + k_{yo} f Q_o \quad (5.54d)$$

in which

$$f = j \left[\frac{1}{b} \left(1 + \frac{k_{yo}^2 b^2}{12} \right) + \frac{1}{a} \left(1 + \frac{k_{xo}^2 a^2}{12} \right) \right]^{-1} \quad (5.55)$$

Thus, if

$$\bar{Z}_s = \begin{bmatrix} z_{sxx} & z_{sxy} \\ z_{syx} & z_{syy} \end{bmatrix} \quad (5.56)$$

then

$$Z_{sxx} = Z_w b - \frac{1}{j\omega\epsilon_0} \sum_{n=-\infty}^{\infty} \frac{e^{-jk_z oon r}}{2jk_z oon} \left\{ a_{on}^{(1,1)} - k_{xo} \frac{b}{a} f \left[\frac{1}{2\pi j n} + \frac{jk_yo b}{(2\pi n)^2} \right] a_{on}^{(1,2)} \right\} \quad (5.57a)$$

$$Z_{sxy} = \frac{-fk_yo}{j\omega\epsilon_0} \sum_{n=-\infty}^{\infty} a_{on}^{(1,2)} \frac{e^{-jk_z oon r}}{2jk_z oon} \left[\frac{1}{2\pi j n} + \frac{jk_yo b}{(2\pi n)^2} \right] \quad (5.57b)$$

$$Z_{syx} = \frac{-fk_{xo}}{j\omega\epsilon_0} \sum_{m=-\infty}^{\infty} a_{mo}^{(2,1)} \frac{e^{-jk_z omo r}}{2jk_z omo} \left[\frac{1}{2\pi j m} + \frac{jk_{xo} a}{(2\pi m)^2} \right] \quad (5.57c)$$

$$Z_{syy} = Z_w a - \frac{1}{j\omega\epsilon_0} \sum_{m=-\infty}^{\infty} \frac{e^{-jk_z omo r}}{2jk_z omo} \left\{ a_{mo}^{(2,2)} - k_{yo} \frac{a}{b} f \left[\frac{1}{2\pi j m} + \frac{jk_{xo} a}{(2\pi m)^2} \right] a_{mo}^{(2,1)} \right\} \quad (5.57d)$$

In obtaining the above results we have used the approximation

$\exp(jk_o r \cos\theta) \approx 1$. In order to simplify the results of eq. (5.56)

further, we take the limit as $k_o a$, $k_o b$, $k_d a$, $k_d b$, $k_{xo} a$, and $k_{yo} b$ all approach zero, retaining only terms of first order in the final results.

We obtain, after some tedious manipulation,

$$Z_{sxx} \approx Z_w b + j\eta_o \frac{k_o b}{2\pi} L_{1b} - j\eta_o \frac{k_o b}{2\pi} \frac{k_{xo}^2}{k_o^2} (1 + \frac{if}{a}) L_{2b} \quad (5.58a)$$

$$Z_{sxy} \approx - \frac{\eta_o f k_{xo} k_{yo}}{2\pi k_o} L_{2b} \quad (5.58b)$$

$$Z_{syx} \approx - \frac{\eta_o f k_{xo} k_{yo}}{2\pi k_o} L_{2a} \quad (5.58c)$$

$$Z_{syy} = Z_w a + j\eta_o \frac{k_o a}{2\pi} L_{1a} - j\eta_o \frac{k_o a}{2\pi} \frac{k^2_{yo}}{k_o^2} (1 + \frac{jf}{b}) L_{2a} \quad (5.58d)$$

in which

$$L_{1q} = \sum_{n=1}^{\infty} \frac{e^{-2n\pi r/q}}{n} = \ln(1 - e^{-2\pi r/q})^{-1} \quad (5.59a)$$

$$L_{2q} = \sum_{n=1}^{\infty} \frac{e^{-2n\pi r/q}}{n} \left[\frac{1 + t_{nq}/\epsilon_r}{1 + \frac{1}{2} t_{nq} (\epsilon_r + \frac{1}{\epsilon_r})} \right] \quad (5.59b)$$

$$t_{nq} = \tanh \left(\frac{2n\pi d}{q} \right) \quad (5.59c)$$

where $q = a$ or b .

Let us now consider the eigenvalues of the impedance matrix \bar{Z}_s for the case of a square mesh, $a=b$. It is easy to show that the two eigenvalues Z_{s1} and Z_{s2} are given by

$$Z_{s1} = Z_w a + j\eta_o \left(\frac{k_o a}{2\pi} \right) \ln(1 - e^{-2\pi r/a})^{-1} \quad (5.60a)$$

$$Z_{s2} = Z_{s1} - j\eta_o \left(\frac{k_o a}{2\pi} \right) \frac{k_{to}^2}{2k_o^2} L_{2a} \quad (5.60b)$$

where $k_{to}^2 = k_{xo}^2 + k_{yo}^2 = k_o^2 \sin^2 \theta$. Consideration of the eigenvalue equation

$$(\bar{Z}_s - Z_{si} \bar{I}) \cdot \tilde{J}_{soo} = 0 \quad (5.61)$$

for $i = 1, 2$ reveals that

$$\text{for } Z_s = Z_{s1}: \quad \bar{k}_{to} \cdot \tilde{J}_{soo} = 0 \quad (5.62a)$$

$$\text{for } Z_s = Z_{s2}: \quad \bar{k}_{to} \times \tilde{J}_{soo} = 0 \quad (5.62b)$$

where $\bar{k}_{to} = k_{xo} \bar{a}_x + k_{yo} \bar{a}_y$. The conditions of eq. (5.62) are immediately

recognized as those corresponding to perpendicular and parallel polarization respectively; therefore

$$Z_{s1} = Z'_s = 1/Y'_s \quad (5.63)$$

is the equivalent sheet impedance for a perpendicular-polarized field, and

$$Z_{s2} = Z''_s = 1/Y''_s \quad (5.64)$$

is the equivalent sheet impedance for a parallel-polarized field.

Several features of these results are worthy of some discussion.

These are:

- (a) Z'_s and Z''_s (or Y'_s and Y''_s) are isotropic, i.e., they do not depend upon the angle ϕ . This result is not surprising, since a bonded wire mesh in free space is known to behave isotropically [4,19] at low frequencies.
- (b) Z'_s and Z''_s are not equal except when $\bar{k}_{to} = \bar{0}$; thus the wire mesh is fundamentally different from a simple surface admittance layer in this respect.
- (c) Z''_s is dependent upon k_{to}^2 , so the wire mesh is spatially dispersive. This result also agrees with the known results for the wire mesh in free space.
- (d) Z''_s depends upon ϵ_r and d . Physically, this occurs because for parallel polarization a normal component of electric field is present which penetrates the dielectric layer. The real importance of this result is that the behavior of the grid depends upon its surroundings. As a consequence, the total behavior of the grid and the dielectric layer cannot be found by considering these components separately.

(e) The function L_{2a} is bounded as follows:

$$\ln(1 - e^{-2\pi r/a})^{-1} \geq L_{2a} \geq \frac{2}{1 + \epsilon_r} \ln(1 - e^{-2\pi r/a})^{-1}$$

The upper bound follows from setting $\epsilon_r = 1$ and/or $d = 0$ in (5.59b); the lower bound follows from letting d/a become large in that equation.

(f) With regard to the observation made in 5 above, it must be emphasized that $|\epsilon_r|$ cannot be too large, since the condition $(k_d a / 2\pi) \ll 1$ must hold in order for our approximate analysis to be valid.

The thickness of the dielectric layer can be simply accounted for by defining an equivalent relative permittivity ϵ_{eqr} as follows:

$$\epsilon_{eqr} = \frac{2}{L_{2a}} \ln(1 - e^{-2\pi r/a})^{-1} - 1 \quad (5.65)$$

ϵ_{eqr} will depend upon d/a , ϵ_r , and (weakly) upon r/a ; and

$$Z_s'' = Z_w a + j n_0 \left(\frac{k_a}{2\pi} \right) \left[1 - \frac{k_{to}^2}{k_o^2 (1 + \epsilon_{eqr})} \right] \ln(1 - e^{-2\pi r/a})^{-1} \quad (5.66)$$

where $1 \leq \epsilon_{eqr} \leq \epsilon_r$. We have calculated curves of ϵ_{eqr} vs. d/a for various values of ϵ_r and r/a ; the results are shown in Fig. 5.3. It is evident from these numerical results that when d/a is greater than unity, $\epsilon_{eqr} \approx \epsilon_r$; and since this is the situation which normally prevails in wire-mesh composite applications, we shall set $\epsilon_{eqr} = \epsilon_r$ in the remainder of this Note.

A generalization of this result is obvious: if a wire grid is embedded between two dielectric layers of relative permittivity ϵ_{r1} and ϵ_{r2} and the thicknesses of both of the layers exceeds a , then the equivalent surface transfer impedances of the grid will be simply

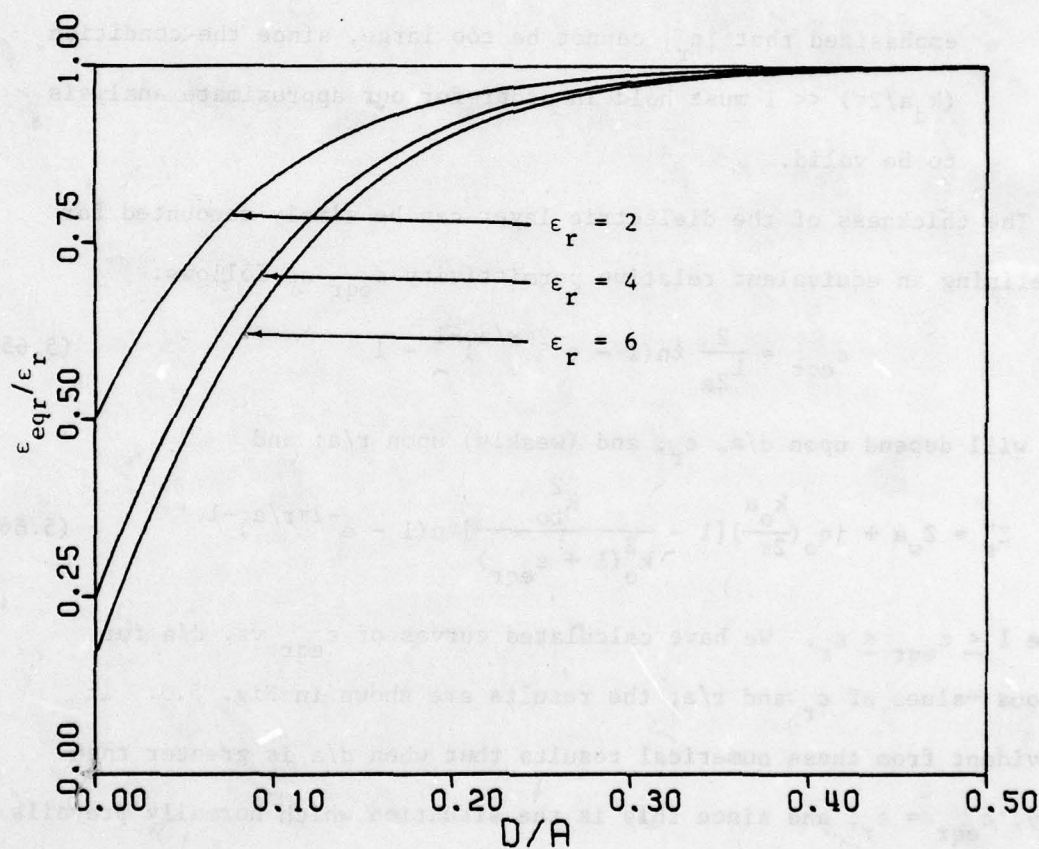


Figure 5.3a. ϵ_{eqr} vs. d/a for $\epsilon_r = 2, 4, 6$; $r/a = 0.25$

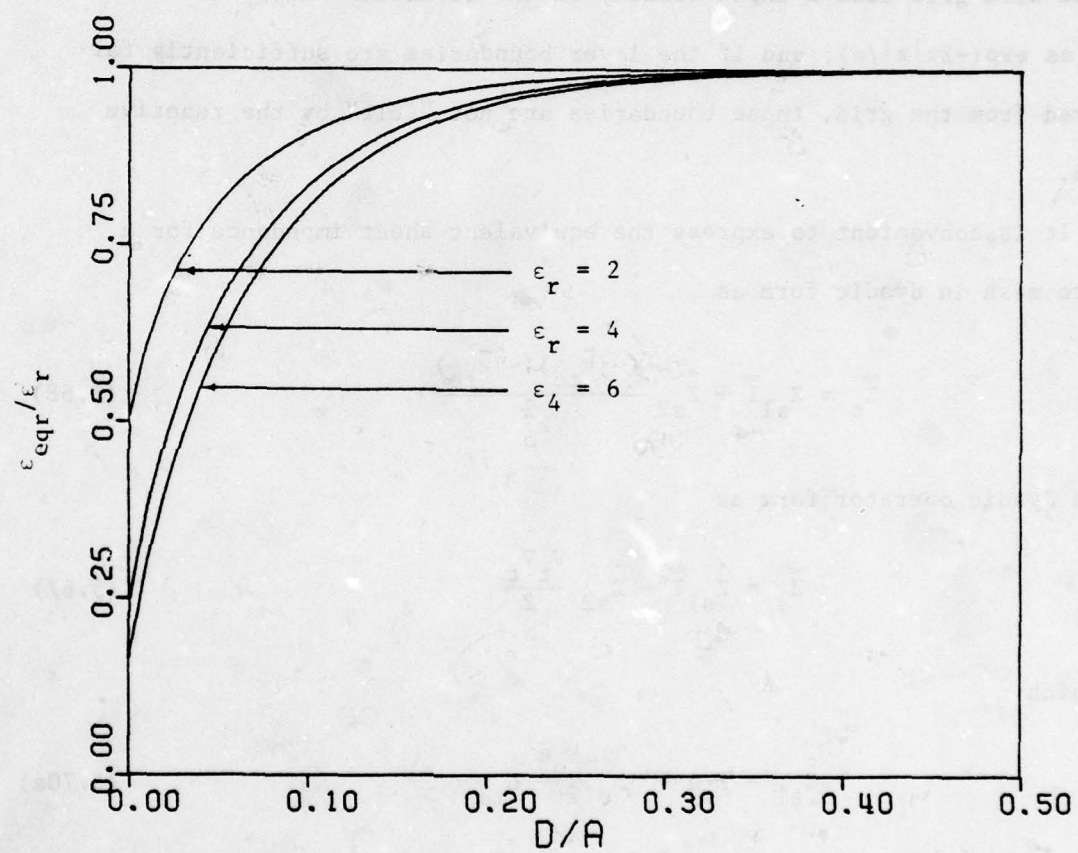


Figure 5.3b. ϵ_{eqr} vs. d/a for $\epsilon_r = 2, 4, 6$; $r/a = 0.025$

AD-A073 770

AIR FORCE WEAPONS LAB KIRTLAND AFB NM
ELECTROMAGNETIC PULSE INTERACTION NOTES -- EMP 3-38. (U)
MAY 79 C E BAUM

F/G 20/14

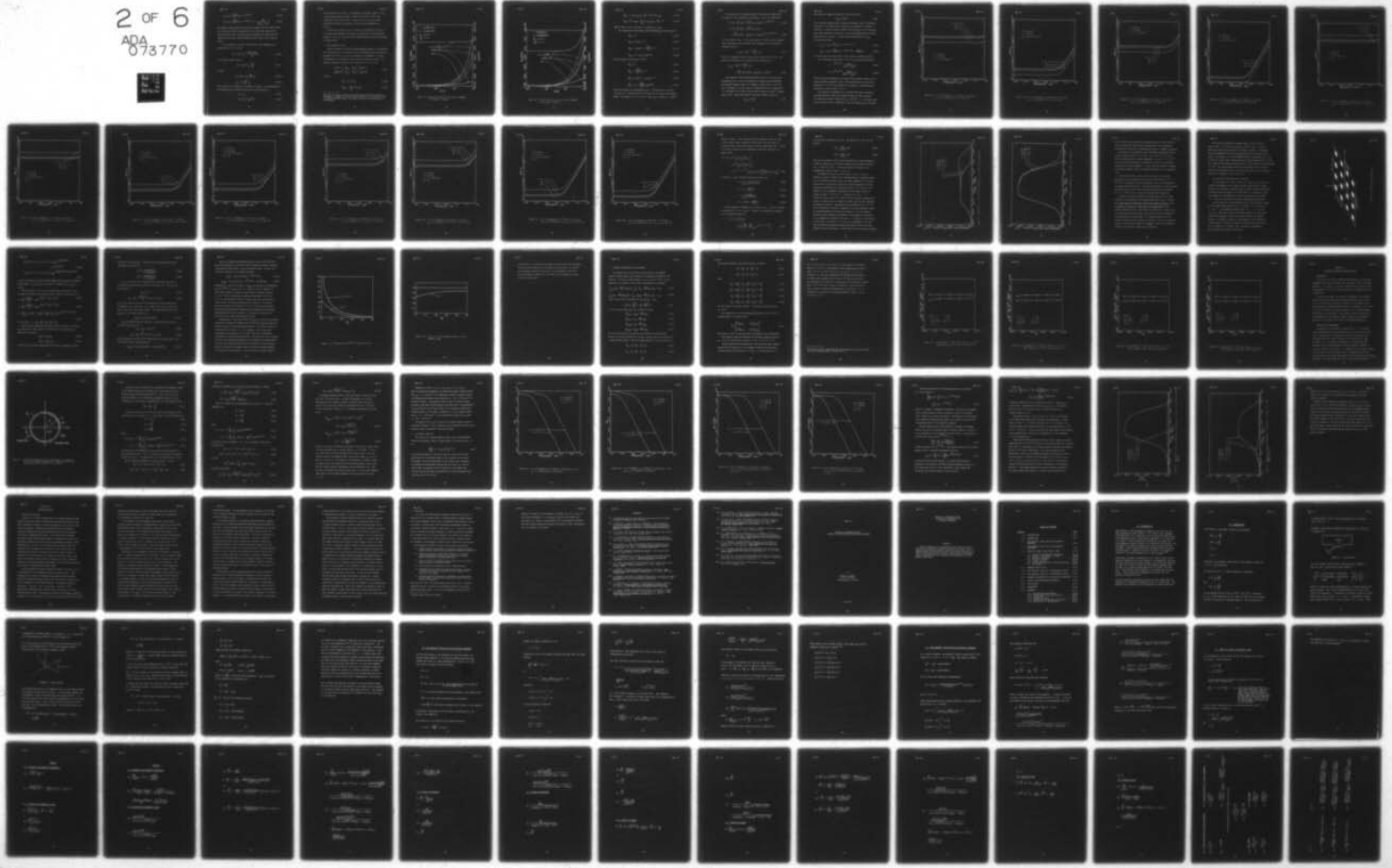
UNCLASSIFIED

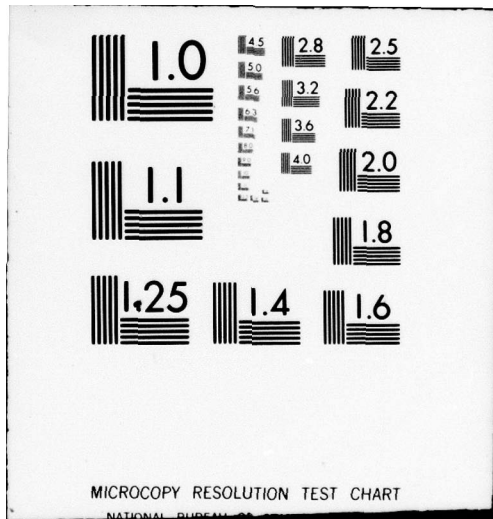
AFWL-TR-79-401

SBIE -AD-E200 329

NL

2 OF 6
ADA
073770





$$Z'_s = Z_w a + \frac{j\omega\mu_0 a}{2\pi} \ln(1 - e^{-2\pi r/a})^{-1} \quad (5.67a)$$

$$Z''_s = Z_w a + \frac{j\omega\mu_0 a}{2\pi} \ln(1 - e^{-2\pi r/a})^{-1} [1 - \frac{k_{to}^2}{k_o^2(\epsilon_{r1} + \epsilon_{r2})}] \quad (5.67b)$$

The physical reason behind these results is simply that the reactive field of the wire grid decays exponentially in the directions normal to the grid as $\exp(-2\pi|z|/a)$; and if the layer boundaries are sufficiently far removed from the grid, these boundaries are not "felt" by the reactive field.

It is convenient to express the equivalent sheet impedance for a square mesh in dyadic form as

$$\bar{Z}_s = \hat{Z}_{s1} \bar{I} + \hat{Z}_{s2} \frac{(-j\bar{k}_{to})(-j\bar{k}_{to})}{k_o^2} \quad (5.68)$$

or in dyadic operator form as

$$\bar{Z}_s = \hat{Z}_{s1} \bar{I} + \hat{Z}_{s2} \frac{\nabla_t \nabla_t}{k_o^2} \quad (5.67)$$

in which

$$\hat{Z}_{s1} = Z_w a + jn_o \frac{k_o a}{2\pi} L_{1a} \quad (5.70a)$$

$$\hat{Z}_{s2} = jn_o \frac{k_o a}{4\pi} L_{2a} \quad (5.70b)$$

and ∇_t denotes the transverse or surface del operator. The eigenoperators for perpendicular and parallel polarization are then given by

$$Z'_s = \hat{Z}_{s1} \quad (5.71a)$$

$$Z''_s = \hat{Z}_{s1} + \hat{Z}_{s2} \nabla_t^2 / k_o^2 \quad (5.71b)$$

We have used the fact that ∇_t is equivalent in the space domain to $-jk_z$ to in the Fourier spectral domain to construct the result (5.69) from (5.68) and (5.71b) from (5.67b). Curves of $Z'_s = R_s + jX_s$ are shown plotted as functions of frequency for typical screen parameters in Fig. 5.4.

In the next paragraph we shall consider the problem of transmission of a plane electromagnetic wave through a planar layer of the wire-mesh composite, using the equivalent sheet impedance \bar{Z}_s which has been developed in this paragraph.

5. THE TRANSMITTED FIELD

Having developed an equivalent sheet impedance operator to characterize the wire-mesh screen, we may make use of the boundary-connection formalism developed in Section II to solve the problem of transmission of a plane electromagnetic wave through a planar wire-mesh composite shield[†]. The boundary connection relation for our problem is (cf. eq. (2.19))

$$\begin{bmatrix} \tilde{\mathbf{E}}_t(0-) \\ n_o \tilde{\mathbf{H}}_t(0-) \end{bmatrix} = \begin{bmatrix} \bar{M}_{t11} & \bar{M}_{t12} \\ \bar{M}_{t21} & \bar{M}_{t22} \end{bmatrix} \cdot \begin{bmatrix} \tilde{\mathbf{E}}_t(d+) \\ n_o \tilde{\mathbf{H}}_t(d+) \end{bmatrix} \quad (5.72)$$

in which

$$\bar{M}_{t11} = \bar{I} \cos k_{zd} d \quad (5.73a)$$

$$\bar{M}_{t12} = -\frac{1}{\sqrt{\epsilon_r}} \bar{U} \sin k_{zd} d \quad (5.73b)$$

[†]We could, of course, calculate the transmitted field directly from the analysis in paragraph 2 of this section. However, in the frequency range of interest for EMP studies, the approach based on the equivalent \bar{Z}_s is much simpler.

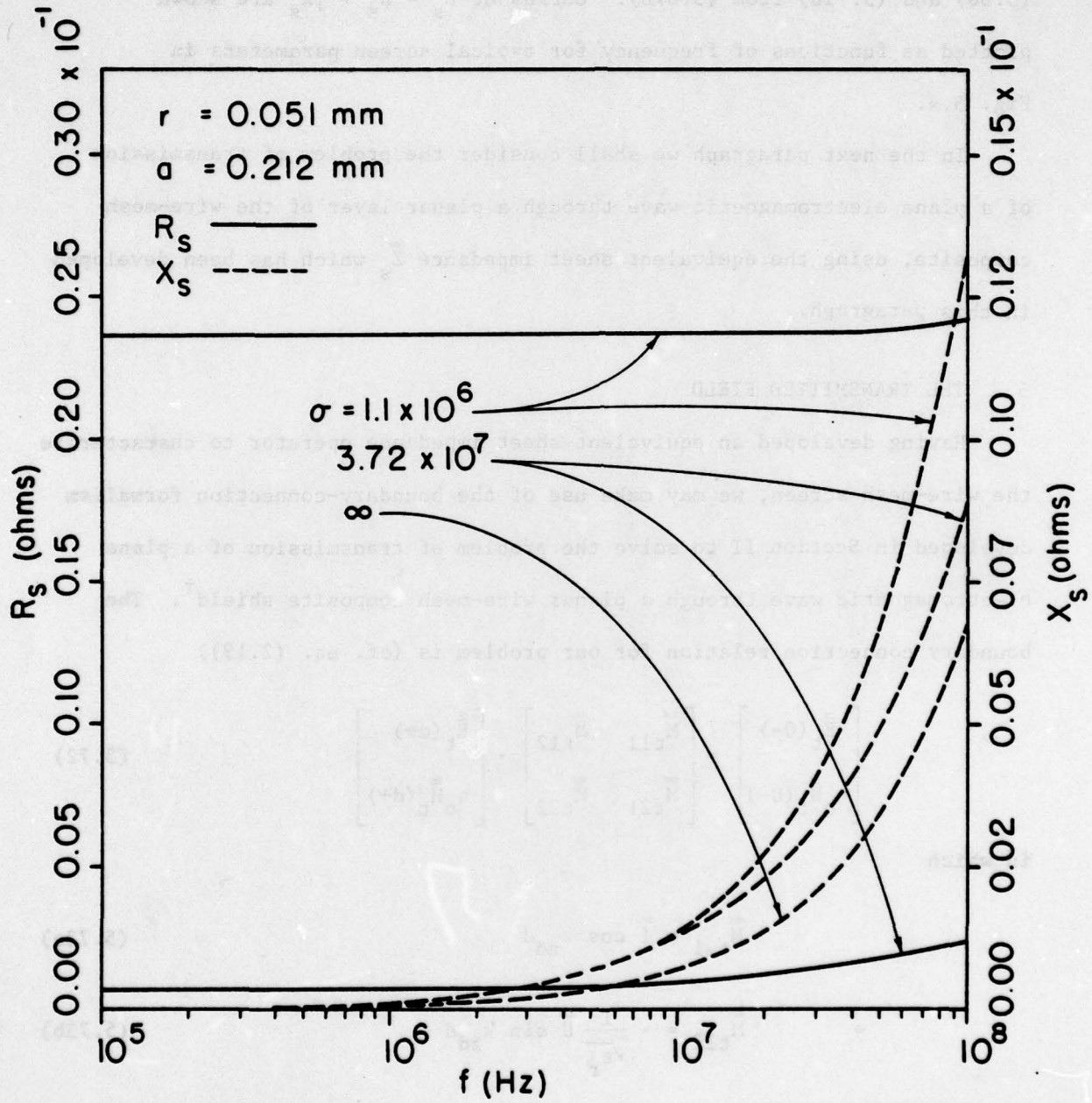


Figure 5.4a. Curves of R_s and X_s ($Z' = R_s + jX_s$) vs. frequency;
 $r = 0.051 \text{ mm}$, $a = 0.212 \text{ mm}$

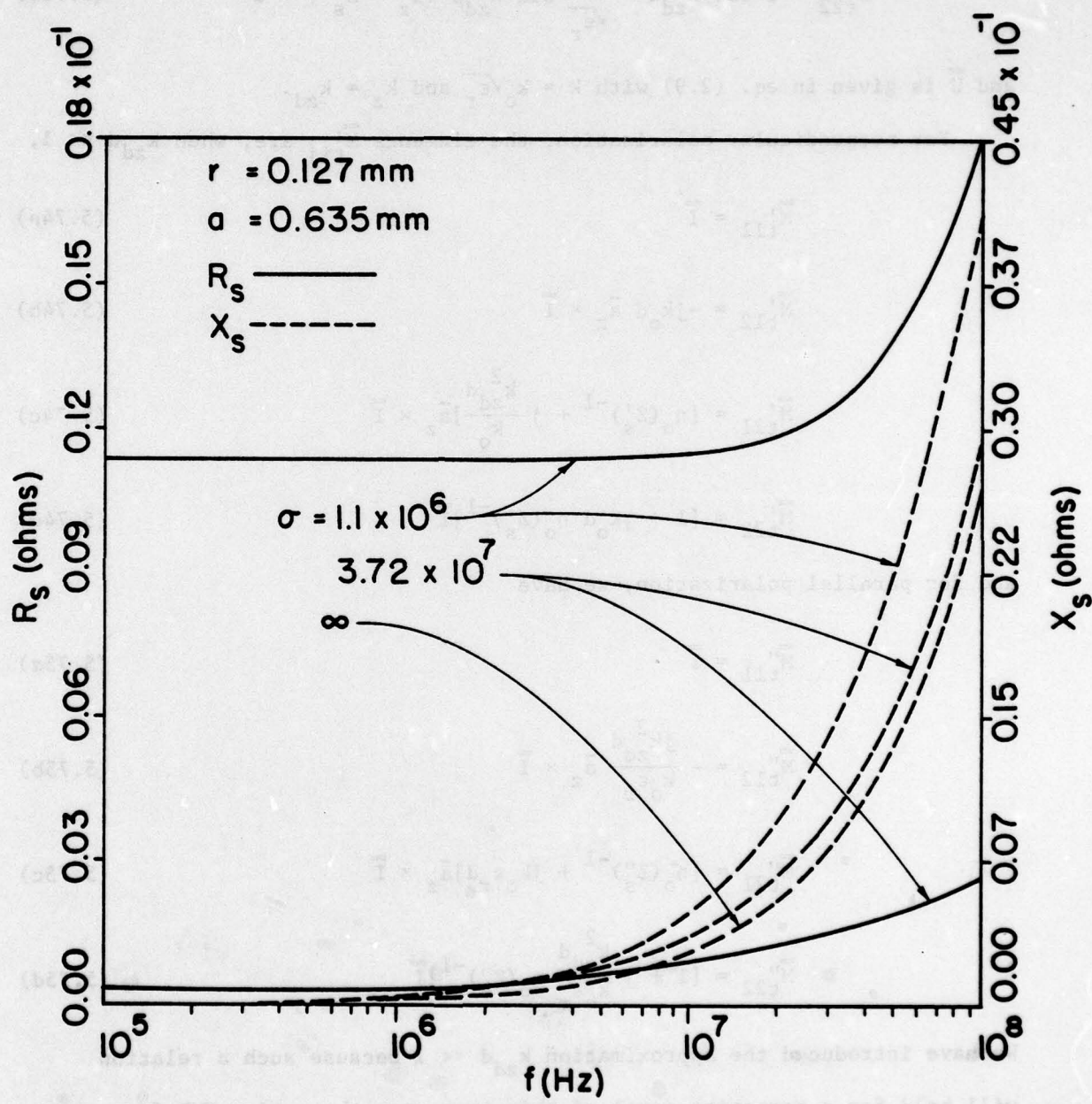


Figure 5.4b. Curves of R_s and X_s ($Z'_s = R_s + jX_s$) vs. frequency;
 $r = 0.127 \text{ mm}$, $a = 0.635 \text{ mm}$

$$\bar{M}_{t21} = \eta_0 \cos k_{zd} d \bar{a}_z \times \bar{Z}_s^{-1} + \sqrt{\epsilon_r} \bar{U} \sin k_{zd} d \quad (5.73c)$$

$$\bar{M}_{t22} = \bar{I} \cos k_{zd} d - \frac{\eta_0}{\sqrt{\epsilon_r}} \sin k_{zd} d (\bar{a}_z \times \bar{Z}_s^{-1}) \cdot \bar{U} \quad (5.73d)$$

and \bar{U} is given in eq. (2.9) with $k = k_0 \sqrt{\epsilon_r}$ and $k_z = k_{zd}$.

For perpendicular polarization, the elements \bar{M}'_{tij} are, when $k_{zd} d \ll 1$,

$$\bar{M}'_{t11} = \bar{I} \quad (5.74a)$$

$$\bar{M}'_{t12} = -jk_0 d \bar{a}_z \times \bar{I} \quad (5.74b)$$

$$\bar{M}'_{t21} = [\eta_0 (Z'_s)^{-1} + j \frac{k_{zd}^2 d}{k_0}] \bar{a}_z \times \bar{I} \quad (5.74c)$$

$$\bar{M}'_{t22} = [1 + jk_0 d \eta_0 (Z'_s)^{-1}] \bar{I} \quad (5.74d)$$

and for parallel polarization, we have

$$\bar{M}''_{t11} = \bar{I} \quad (5.75a)$$

$$\bar{M}''_{t12} = -\frac{jk_{zd}^2 d}{k_0 \epsilon_r} \bar{a}_z \times \bar{I} \quad (5.75b)$$

$$\bar{M}''_{t21} = [\eta_0 (Z''_s)^{-1} + jk_0 \epsilon_r d] \bar{a}_z \times \bar{I} \quad (5.75c)$$

$$\bar{M}''_{t22} = [1 + j \frac{k_{zd}^2 d}{k_0 \epsilon_r} \eta_0 (Z''_s)^{-1}] \bar{I} \quad (5.75d)$$

We have introduced the approximation $k_{zd} d \ll 1$ because such a relation will hold for a composite panel of this type over the entire EMP frequency range: for example, if $\epsilon_r = 4.0$ and $d = 2\text{mm}$, $k_{zd} d \leq 0.0084$ at $f = 10^8 \text{ Hz}$.

Now carrying out an analysis similar to that done in Chapter III, we obtain for the transmission coefficients T' and T'' the expressions

$$T' = \left\{ 1 + \left[\frac{\eta_0}{2} (Z'_s)^{-1} + \frac{jk_0 d}{2} (\epsilon_r - 1) \right] \sec \theta \right\}^{-1} e^{-jk_0 d \cos \theta} \quad (5.76a)$$

$$T'' = \left\{ 1 + \left[\frac{\eta_0}{2} (Z''_s)^{-1} + \frac{jk_0 d}{2} (\epsilon_r - 1) \right] \cos \theta + \frac{jk_0 d}{2} \sin^2 \theta \left(1 - \frac{1}{\epsilon_r} \right) [\sec \theta + \eta_0 (Z''_s)^{-1}] \right\}^{-1} e^{-jk_0 d \cos \theta} \quad (5.76b)$$

to first order in $(k_0 d)$. It is clear from eq. (5.76a) that for perpendicular polarization, the equivalent sheet admittance for the wire-mesh composite layer is

$$Y'_{s,eq} = (Z'_s)^{-1} + \frac{jk_0 d}{\eta_0} (\epsilon_r - 1) \quad (5.77)$$

which is in agreement with the result given earlier in eq. (2.31). For parallel polarization the "equivalent" sheet admittance is

$$Y''_{s,eq} = (Z''_s)^{-1} + \frac{jk_0 d}{\eta_0} (\epsilon_r - 1) + \frac{jk_0 d}{\eta_0} \sin^2 \theta \sec \theta \left(1 - \frac{1}{\epsilon_r} \right) [\sec \theta + \eta_0 (Z''_s)^{-1}] \quad (5.78)$$

The equivalent sheet admittances given above can be substantially simplified if we restrict our attention to realistic screen parameters and the EMP frequency range. For example, a screen with $a = 0.635$ mm (40×40 meshes to the inch) made of stainless-steel wire (conductivity 1.1×10^6 mho m^{-1}) of radius 0.05 mm yields a value of $|\eta_0 (Z'_s)^{-1}|$ greater than 3×10^3 . Thus we may neglect terms proportional to $k_0 d$; and

$$Y'_{s,eq} \approx (Z'_s)^{-1} \quad (5.79)$$

and, except for angles of incidence θ very close to 90° ,

$$Y''_{s,eq} = (Z''_s)^{-1} \quad (5.80)$$

It is therefore apparent that the screened composite layer is essentially equivalent to the screen alone, insofar as its behavior as a shield is concerned. It should be noted, however, that the effect of the dielectric layer does indeed enter the results, in that Z''_s depends upon the relative permittivity of the layer. We give explicit expressions for $Y'_{s,eq}$ and $Y''_{s,eq}$ for plane waves below:

$$Y'_{s,eq} \approx [Z_w a + \frac{j\omega\mu_o a}{2\pi} \ln(1 - e^{-2\pi r/a})]^{-1} \quad (5.81a)$$

$$Y''_{s,eq} \approx [Z_w a + \frac{j\omega\mu_o a}{2\pi} \ln(1 - e^{-2\pi r/a})]^{-1} (1 - \frac{\sin^2\theta}{1 + \epsilon_r})^{-1} \quad (5.81b)$$

For fields other than plane waves, $\sin^2\theta$ should be replaced by k_{to}^2/k_o^2 .

The transmission coefficients T' and T'' are given approximately by

$$T' \approx e^{-jk_o d \cos\theta} \frac{2\cos\theta}{2\cos\theta + \eta_o (Z'_s)^{-1}} \quad (5.82a)$$

$$T'' \approx e^{-jk_o d \cos\theta} \frac{2\sec\theta}{2\sec\theta + \eta_o (Z''_s)^{-1}} \quad (5.82b)$$

These very simple expressions will quickly yield numerical values for the frequency-domain transmitted field. Some representative curves of the magnitudes of T' and T'' as functions of frequency for various angles of incidence are shown in Figs. 5.5-5.8.

The problem of transmission of a transient EMP signal through the wire-mesh composite layer is of interest and may be easily attacked.

For simplicity, we shall assume that $Z_w = (\pi r^2 \sigma_w)^{-1}$, i.e., that the screen wires have radii small in comparison to the skin depth over the frequency

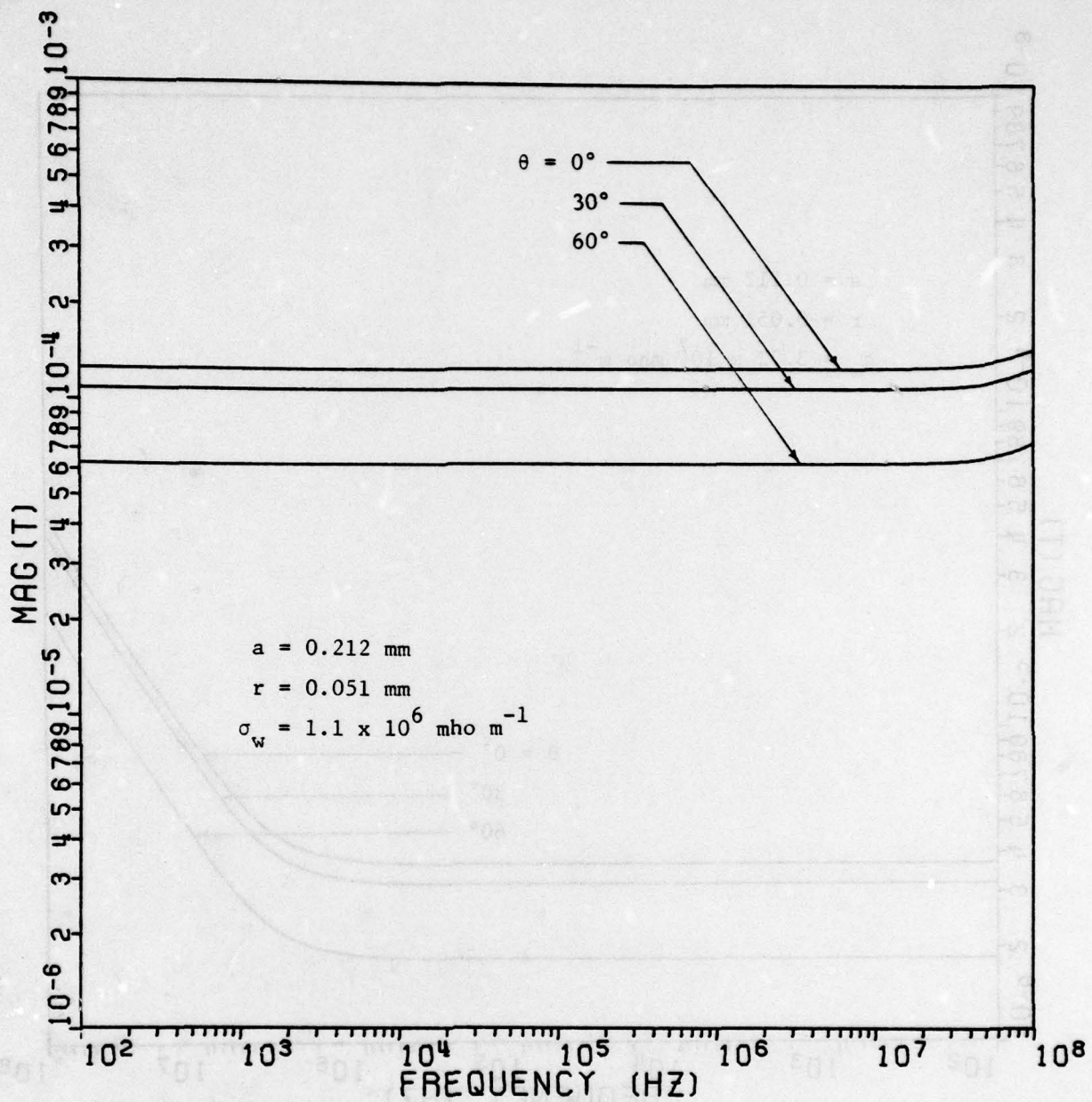


Figure 5.5a. $|T'|$ vs. frequency; $a = 0.212 \text{ mm}$, $r = 0.051 \text{ mm}$,
 $\sigma_w = 1.1 \times 10^6 \text{ mho m}^{-1}$; $\theta = 0^\circ$, 30° , 60°

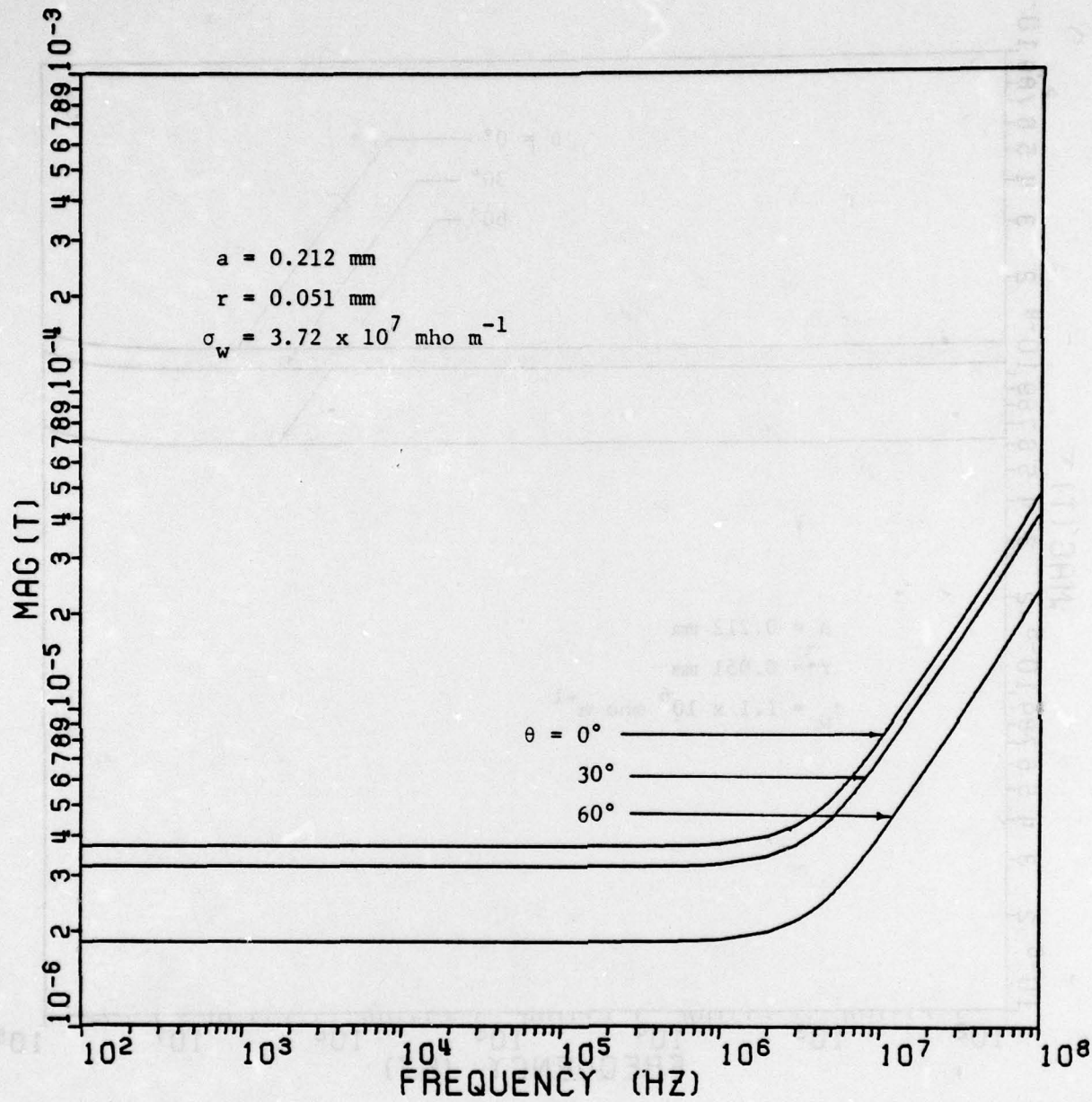


Figure 5.5b. $|T'|$ vs. frequency; $a = 0.212 \text{ mm}$, $r = 0.051 \text{ mm}$,
 $\sigma_w = 3.72 \times 10^7 \text{ mho m}^{-1}$; $\theta = 0^\circ, 30^\circ, 60^\circ$

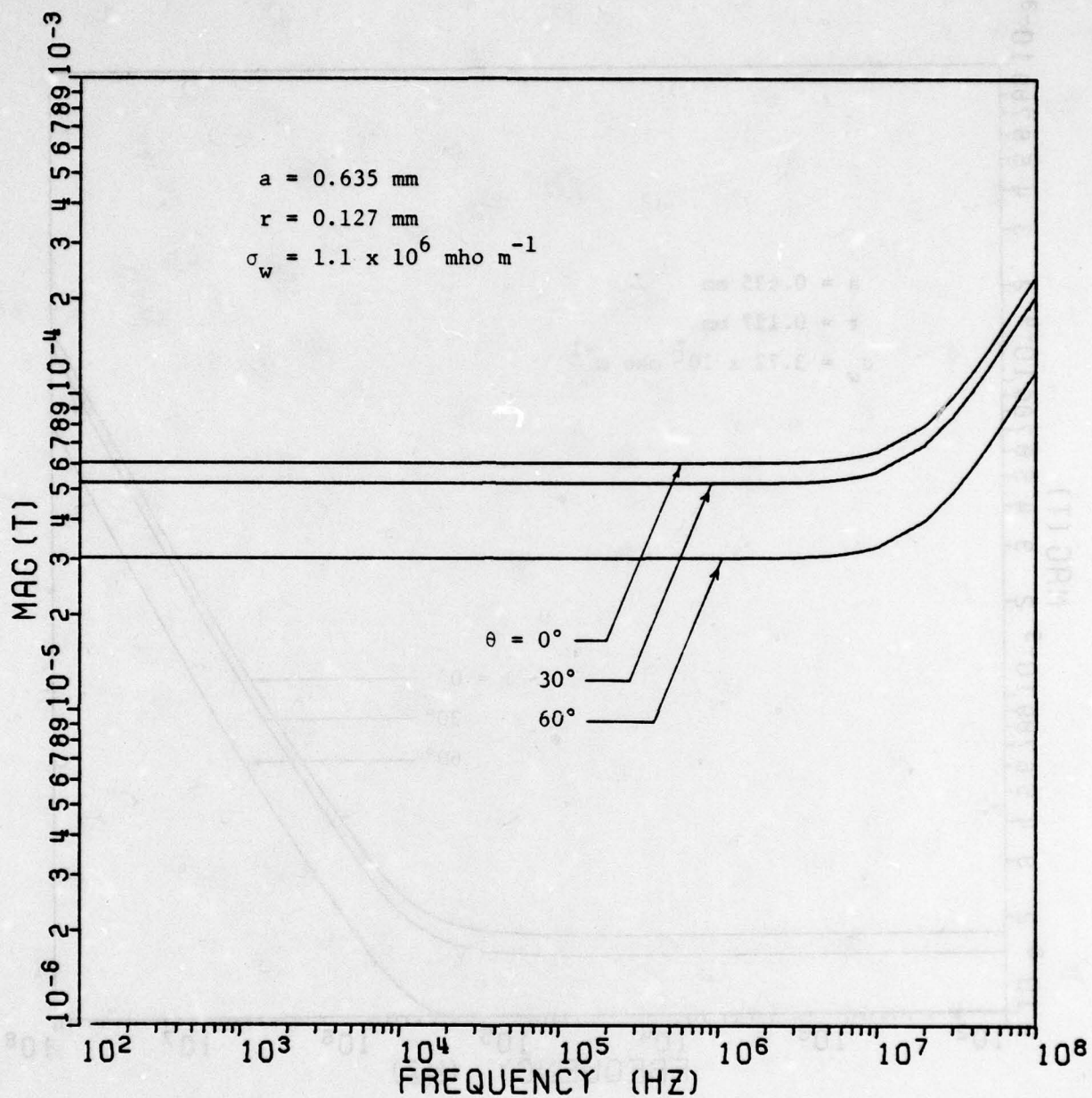


Figure 5.6a. $|T'|$ vs. frequency; $a = 0.625 \text{ mm}$, $r = 0.127 \text{ mm}$,
 $\sigma_w = 1.1 \times 10^6 \text{ mho m}^{-1}$; $\theta = 0^\circ, 30^\circ, 60^\circ$

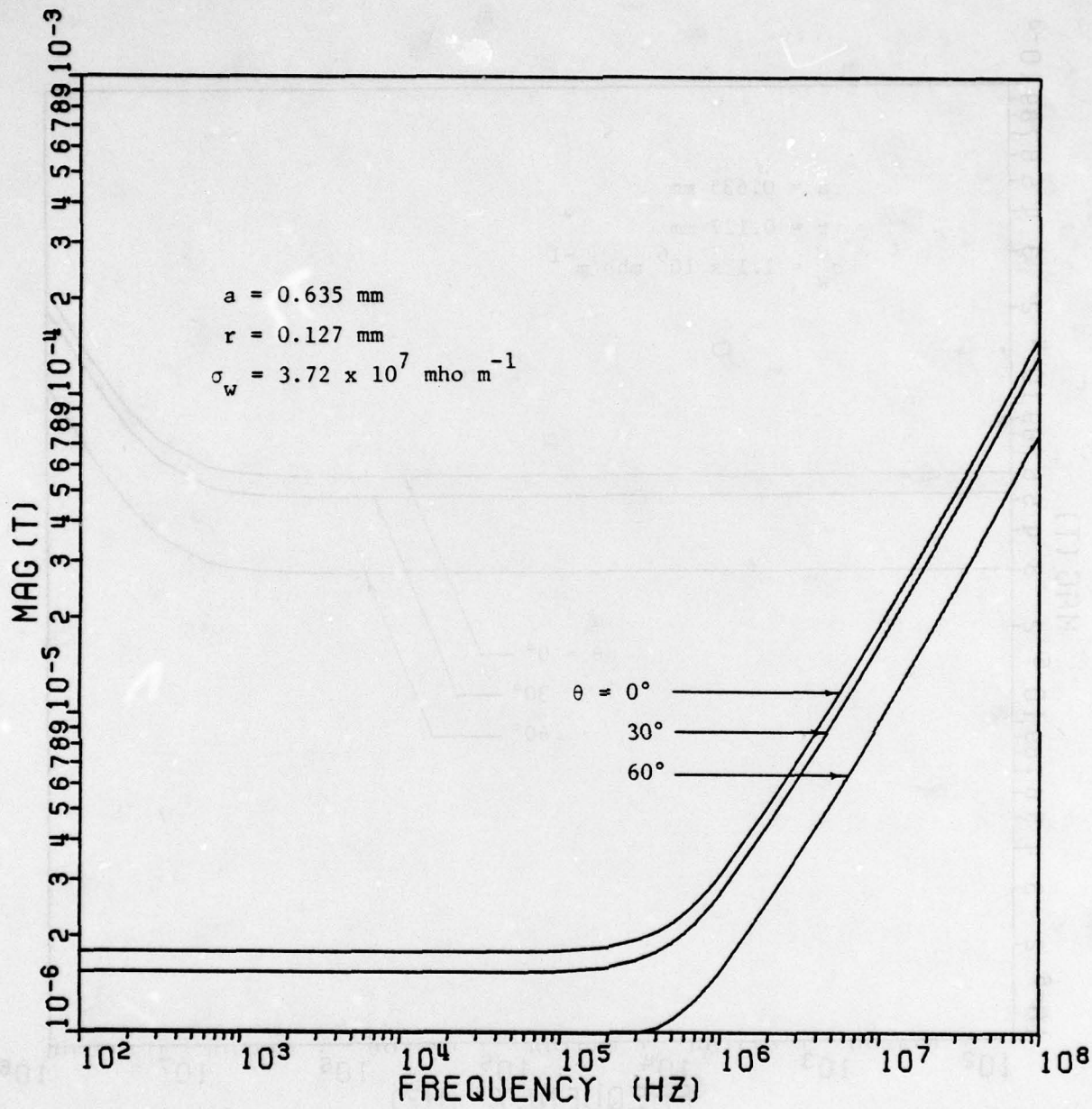


Figure 5.6b. $|T'|$ vs. frequency; $a = 0.625 \text{ mm}$, $r = 0.127 \text{ mm}$,
 $\sigma_w = 3.72 \times 10^7 \text{ mho m}^{-1}$; $\theta = 0^\circ$, 30° , 60°

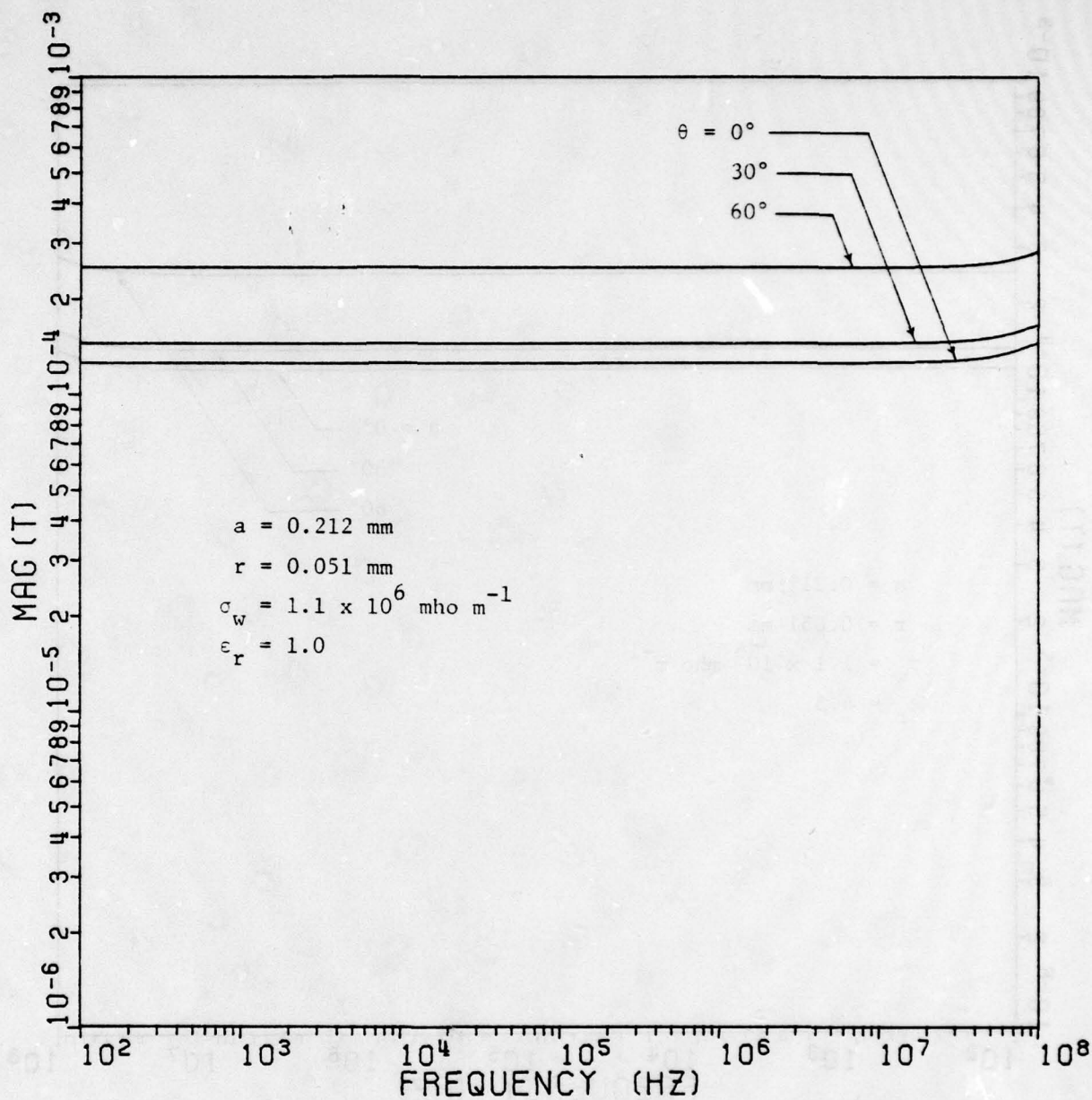


Figure 5.7a. $|T''|$ vs. frequency; $a = 0.212 \text{ mm}$, $r = 0.051 \text{ mm}$,
 $\sigma_w = 1.1 \times 10^6 \text{ mho m}^{-1}$, $\epsilon_r = 1.0$; $\theta = 0^\circ, 30^\circ, 60^\circ$

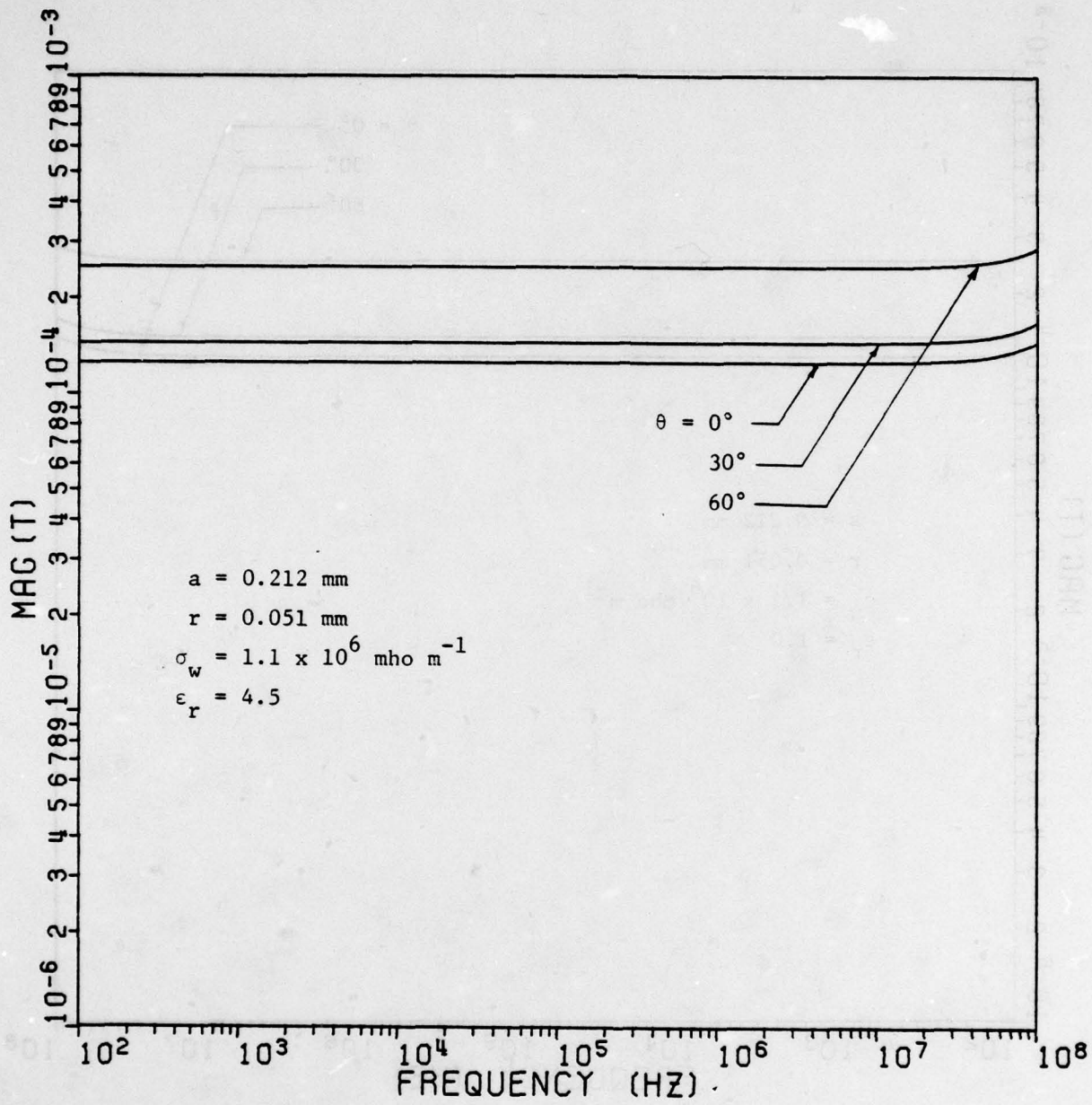


Figure 5.7b. $|T''|$ vs. frequency; $a = 0.212 \text{ mm}$, $r = 0.051 \text{ mm}$,
 $\sigma_w = 1.1 \times 10^6 \text{ mho m}^{-1}$, $\epsilon_r = 4.5$; $\theta = 0^\circ, 30^\circ, 60^\circ$

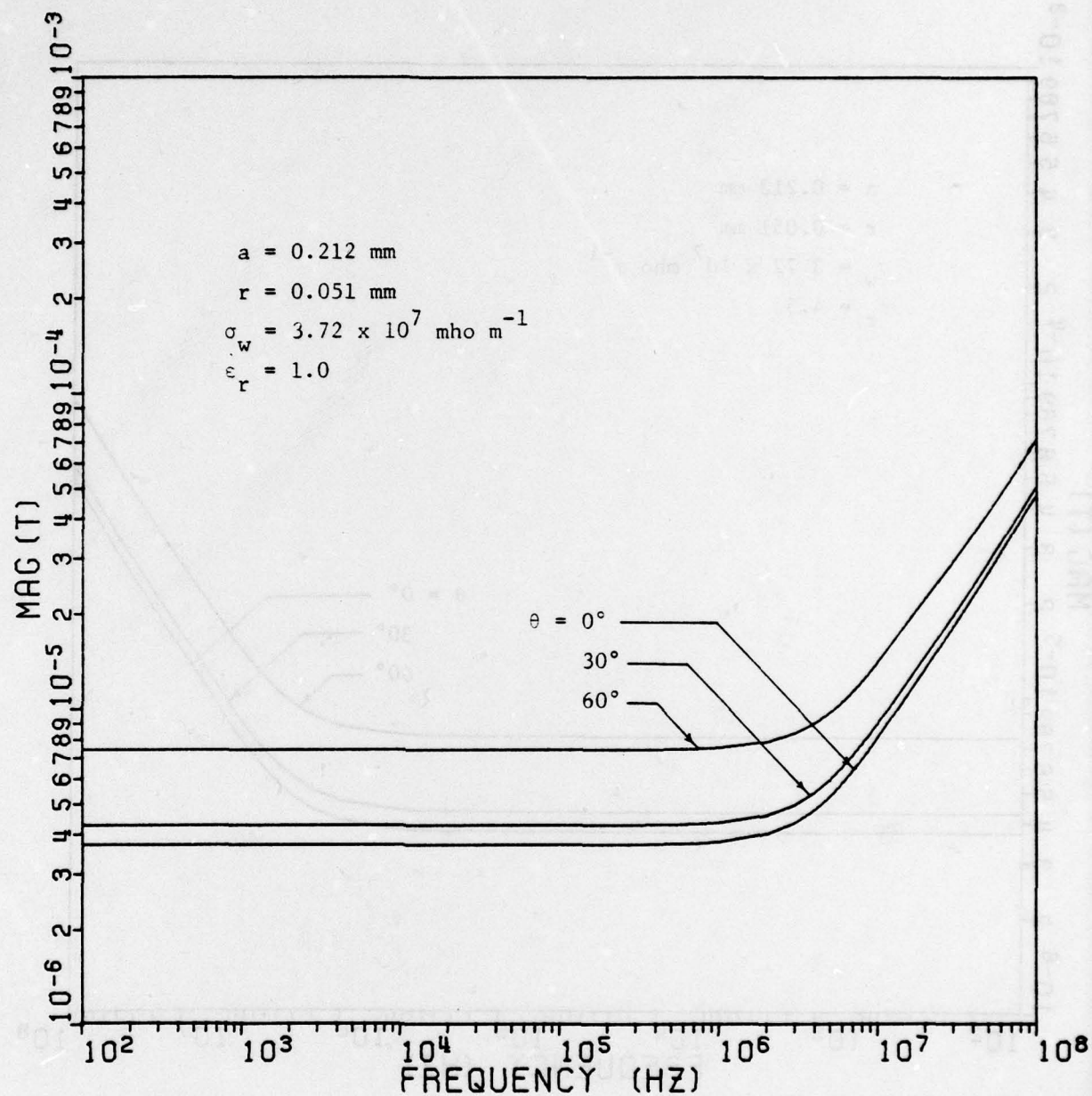


Figure 5.7c. $|T''|$ vs. frequency; $a = 0.212 \text{ mm}$, $r = 0.051 \text{ mm}$,
 $\sigma_w = 3.72 \times 10^7 \text{ mho m}^{-1}$, $\epsilon_r = 1.0$; $\theta = 0^\circ$, 30° , 60°

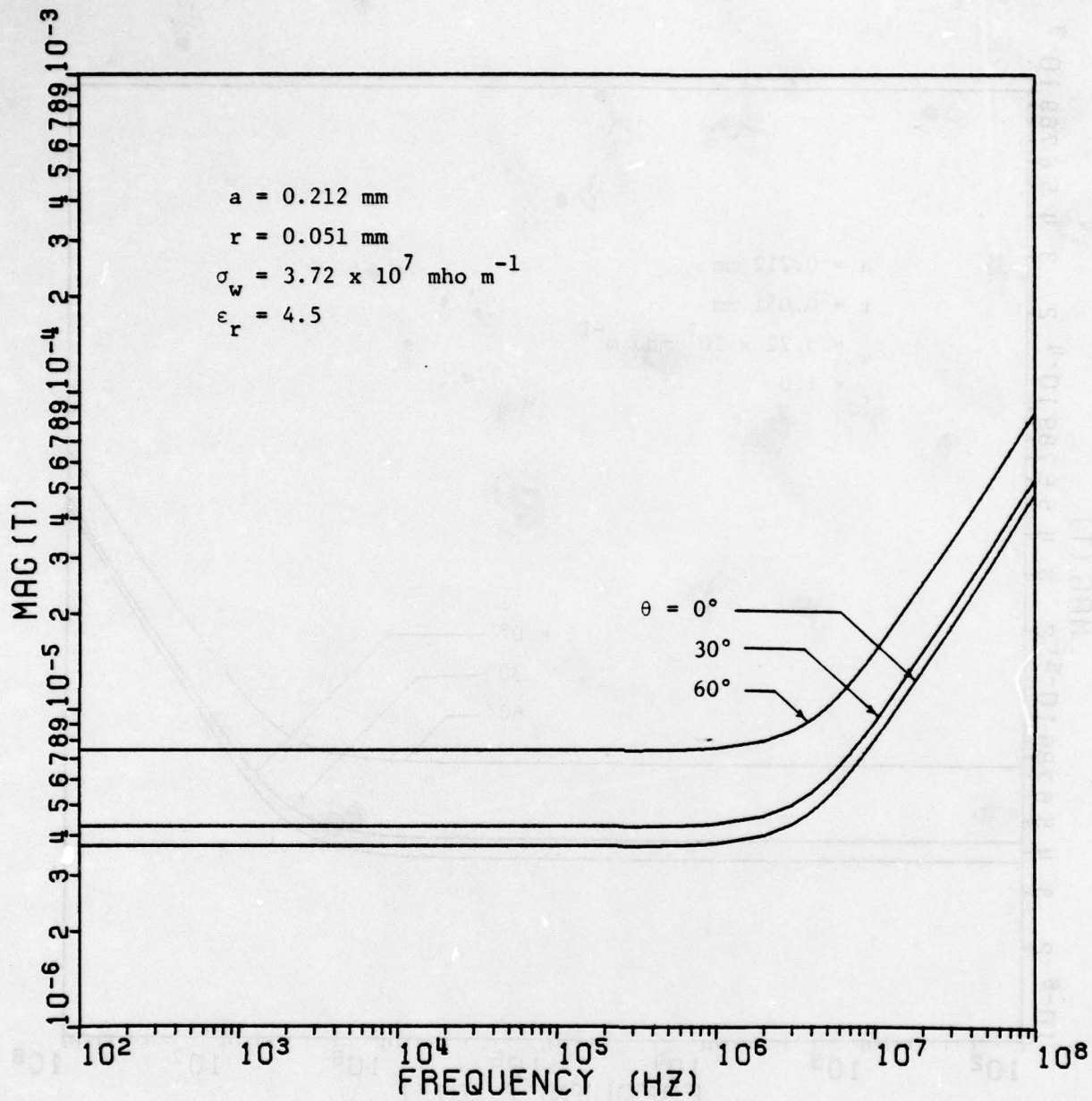


Figure 5.7d. $|T''|$ vs. frequency; $a = 0.212 \text{ mm}$, $r = 0.051 \text{ mm}$,
 $\sigma_w = 3.72 \times 10^7 \text{ mho m}^{-1}$, $\epsilon_r = 4.5$; $\theta = 0^\circ$, 30° , 60°

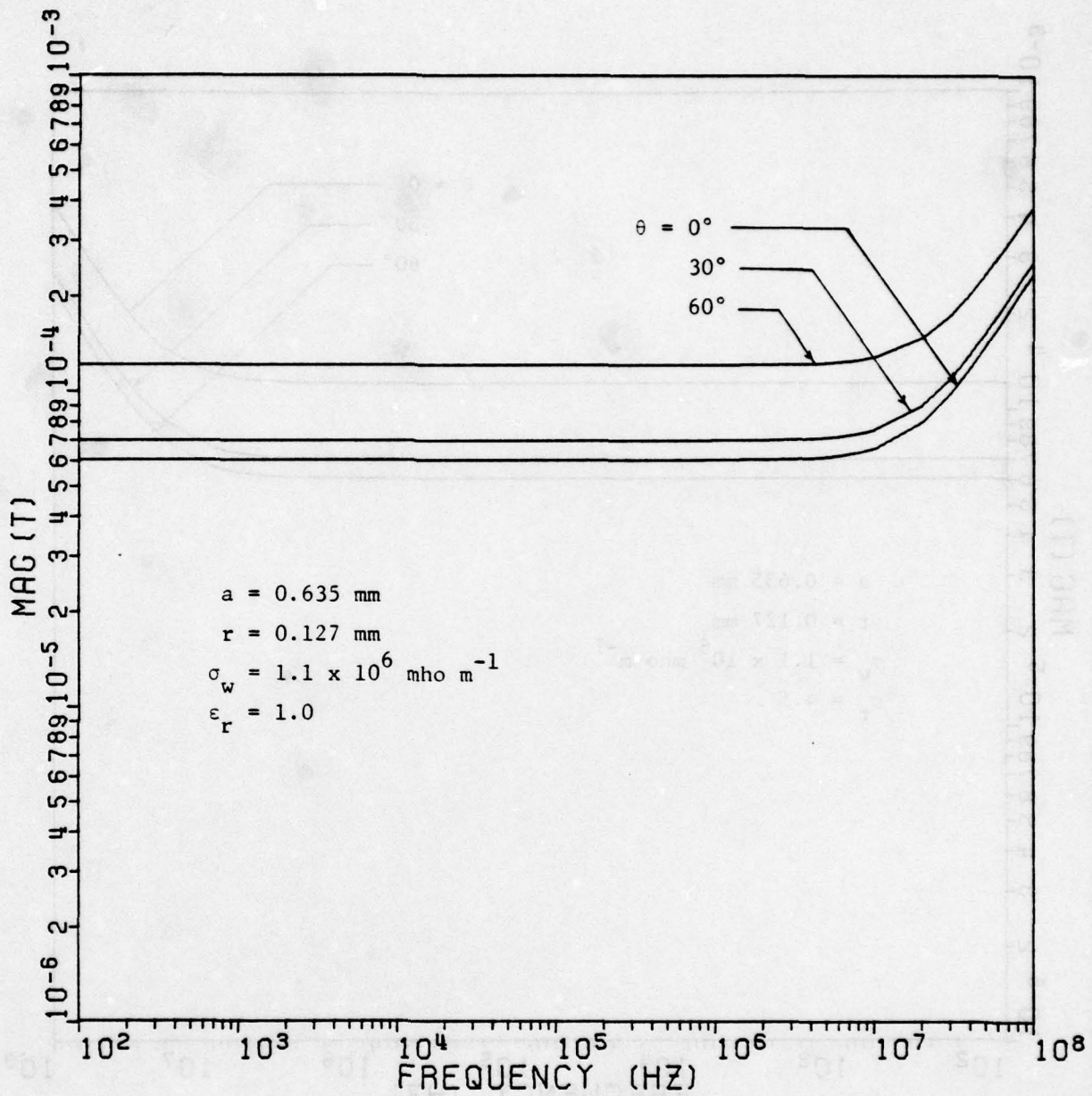


Figure 5.8a. $|T''|$ vs. frequency; $a = 0.635 \text{ mm}$, $r = 0.127 \text{ mm}$,
 $\sigma_w = 1.1 \times 10^6 \text{ mho m}^{-1}$, $\epsilon_r = 1.0$; $\theta = 0^\circ$, 30° , 60°

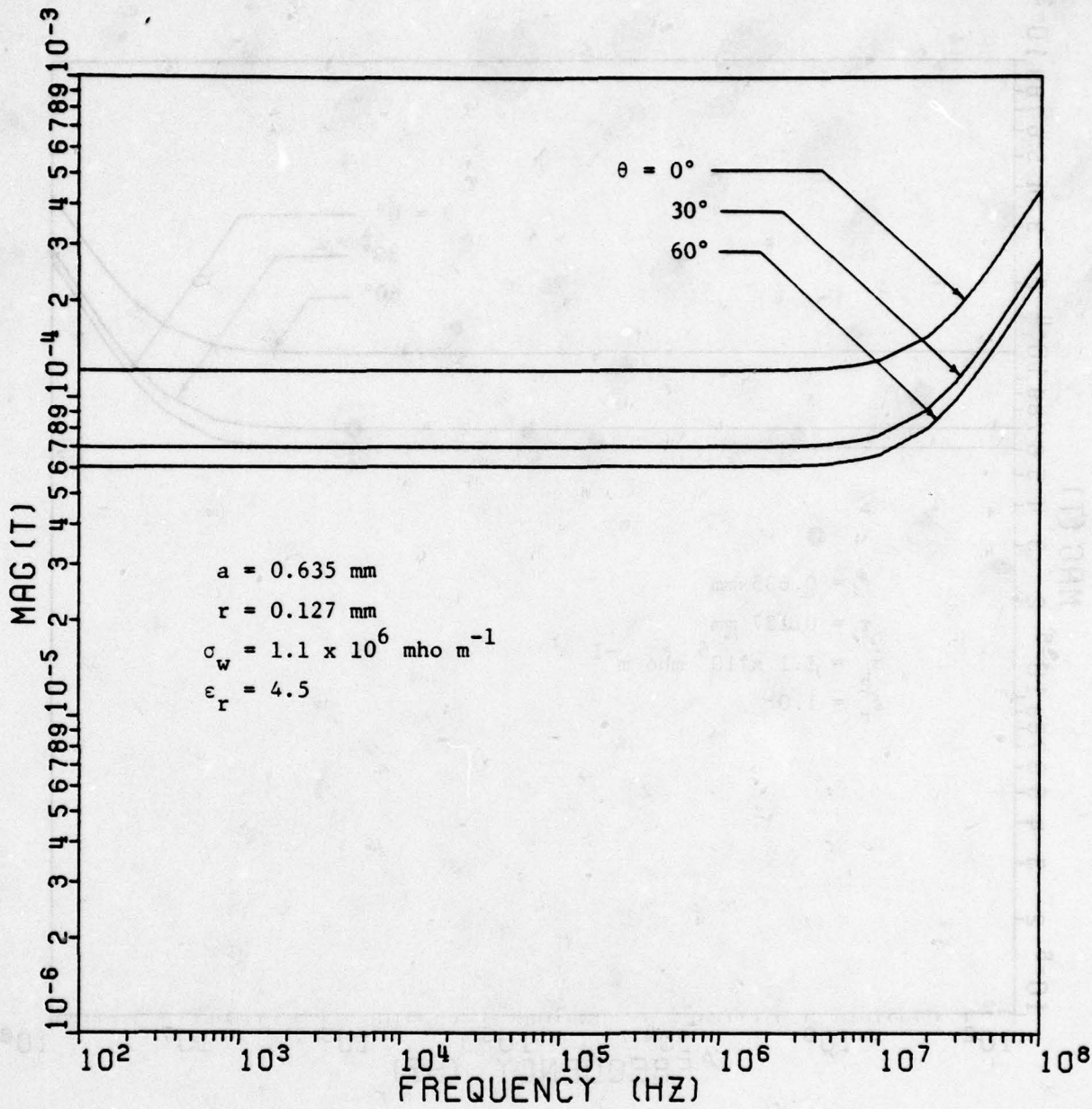


Figure 5.8b. $|T''|$ vs. frequency; $a = 0.635 \text{ mm}$, $r = 0.127 \text{ mm}$,
 $\sigma_w = 1.1 \times 10^6 \text{ mho m}^{-1}$, $\epsilon_r = 4.5$; $\theta = 0^\circ, 30^\circ, 60^\circ$

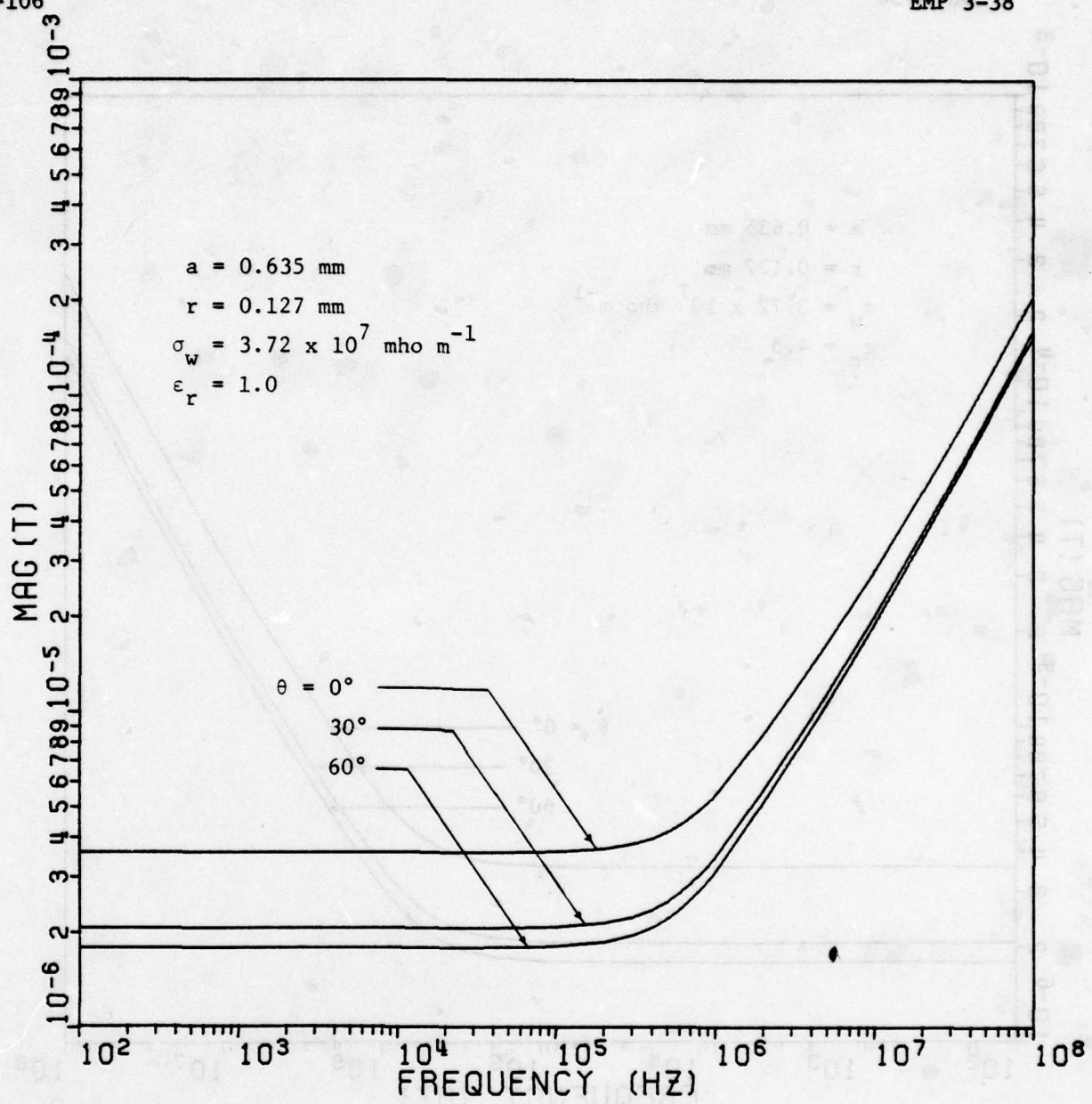


Figure 5.8c. $|T''|$ vs. frequency; $a = 0.635 \text{ mm}$, $r = 0.127 \text{ mm}$,
 $\sigma_w = 3.72 \times 10^7 \text{ mho m}^{-1}$, $\epsilon_r = 1.0$; $\theta = 0^\circ$, 30° , 60°

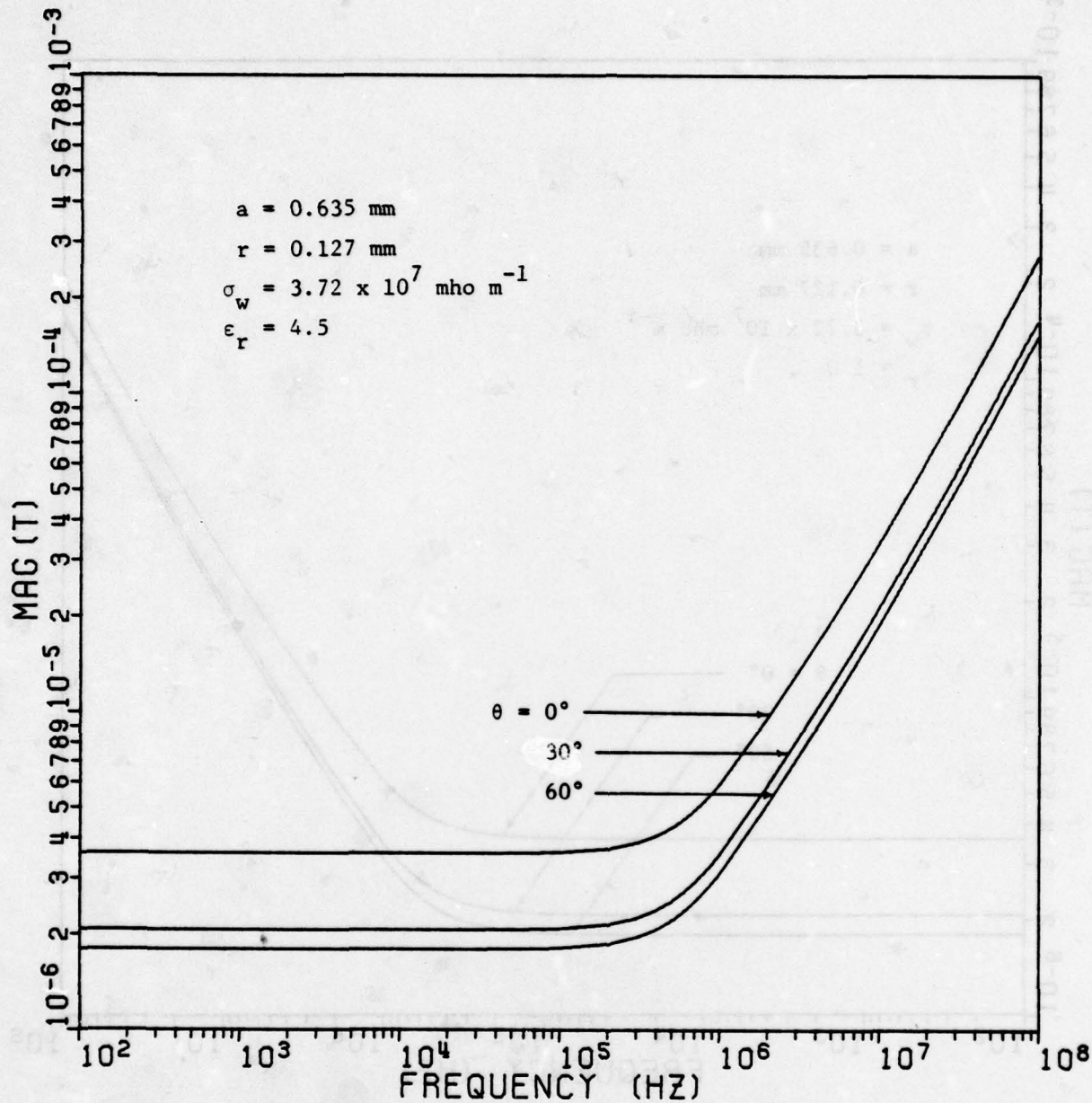


Figure 5.8d. $|T''|$ vs. frequency; $a = 0.635 \text{ mm}$, $r = 0.127 \text{ mm}$,
 $\sigma_w = 3.72 \times 10^7 \text{ mho m}^{-1}$, $\epsilon_r = 4.5$; $\theta = 0^\circ$, 30° , 60°

range of interest. This assumption will be reasonably valid over most of the frequency range occupied by an EMP signal, and will lead to a relatively simple analytical expression for the transmitted field. Setting up a Laplace integral for the transmitted fields $E_t'(\tau)$ and $E_t''(\tau)$, we easily obtain

$$\begin{aligned} E_t',''(\tau) &= Ae^{-\alpha\tau} \left[\frac{\gamma','' - \alpha}{\delta','' + \gamma','' - \alpha} \right] \\ &- Ae^{-\beta\tau} \left[\frac{\gamma','' - \beta}{\delta','' + \gamma','' - \beta} \right] \\ &- Ae^{-(\delta','' + \gamma','')\tau} \left[\frac{\delta',''(\beta - \alpha)}{(\delta','' + \gamma','' - \alpha)(\delta','' + \gamma','' - \beta)} \right] \end{aligned} \quad (5.83)$$

in which A, α , and β have been previously defined, and

$$\gamma' = \frac{2}{\mu_0 r^2 \sigma_w \ln(1 - e^{-2\pi r/a}) - 1} \quad (5.84a)$$

$$\gamma'' = \gamma'(1 - \frac{\sin^2 \theta}{1 + \epsilon_r})^{-1} \quad (5.84b)$$

$$\delta' = \frac{\pi c \sec \theta}{a \ln(1 - e^{-2\pi r/a}) - 1} \quad (5.84c)$$

$$\delta'' = \delta' \cos^2 \theta (1 - \frac{\sin^2 \theta}{1 + \epsilon_r})^{-1} \quad (5.84d)$$

Now for angles of incidence not too close to 90° , δ' and δ'' are large in comparison to α , β , γ' , and γ'' . Therefore, an approximate expression for the transmitted field is

$$\begin{aligned} E_t',''(\tau) &= \frac{\gamma',''}{\delta',''} E_o(\tau) \\ &+ \frac{1}{\delta',''} \left[\frac{dE_o}{d\tau} - \frac{dE_o}{d\tau} \Big|_{\tau=0} e^{-(\delta','' + \gamma','')\tau} \right] \end{aligned} \quad (5.85)$$

in which $E_o(\tau)$ is given in eq. (1.1). The factors γ'/δ' and γ''/δ'' are given by

$$\frac{\gamma'}{\delta'} = \frac{2a}{\pi n_o r^2 \sigma_w} \cos\theta \quad (5.86a)$$

$$\frac{\gamma''}{\delta''} = \frac{2a}{\pi n_o r^2 \sigma_w} \sec\theta \quad (5.86b)$$

Note that the quantity $\pi r^2 \sigma_w/a$ plays the same role in these expressions as does the quantity $\sigma_g d$ in related formulas for the graphite composite case. Curves of $E_t(\tau)$ vs. τ at normal incidence are shown for two representative cases in Figs. 5.9 and 5.10.

The shapes of the $E_t(\tau)$ curves of Figs. 5.9 and 5.10 can be understood readily in terms of the "differentiating" or high-pass character of the bonded wire-mesh screen. The sheet impedance of the screen comprises both resistive and inductively reactive components, and thus increases in magnitude with increasing frequency. The effect of this behavior on the transmission coefficient in the frequency domain is evident in Figs. 5.5 through 5.8: configurations with $\sigma_w = 1.1 \times 10^6$ mho m^{-1} yield values of $|T'|$ and $|T''|$ which are nearly constant with respect to frequency over the range of interest, and the sheet impedance is primarily resistive. Increasing the wire conductivity to 3.72×10^7 mho m^{-1} decreases the resistive component of the sheet impedance, making the reactive component relatively more important. For the two mesh size/wire radius combinations considered, the transmission coefficient at low frequencies is higher for the case $a = 0.212$ mm, $r = 0.051$ mm than for the case $a = 0.635$ mm, $r = 0.127$ mm, as a consequence of the fact that the second configuration contains more metal per unit area, even though the mesh size is larger. On the other hand, the inductive reactance

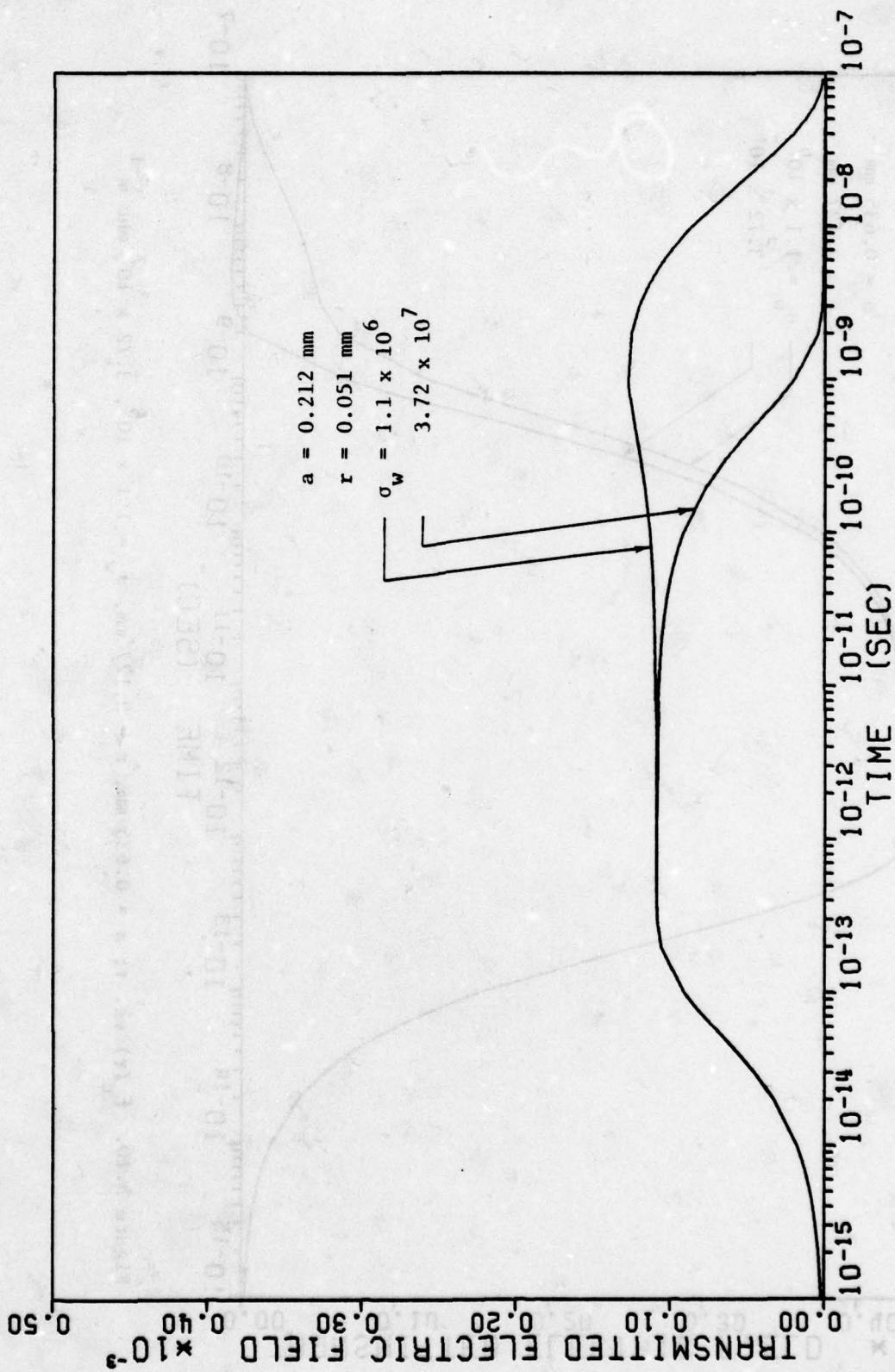


Figure 5.9. $E_t(\tau)$ vs. τ ; $a = 0.212 \text{ mm}$, $r = 0.051 \text{ mm}$, $\sigma_w = 1.1 \times 10^6$, $3.72 \times 10^7 \text{ mho m}^{-1}$

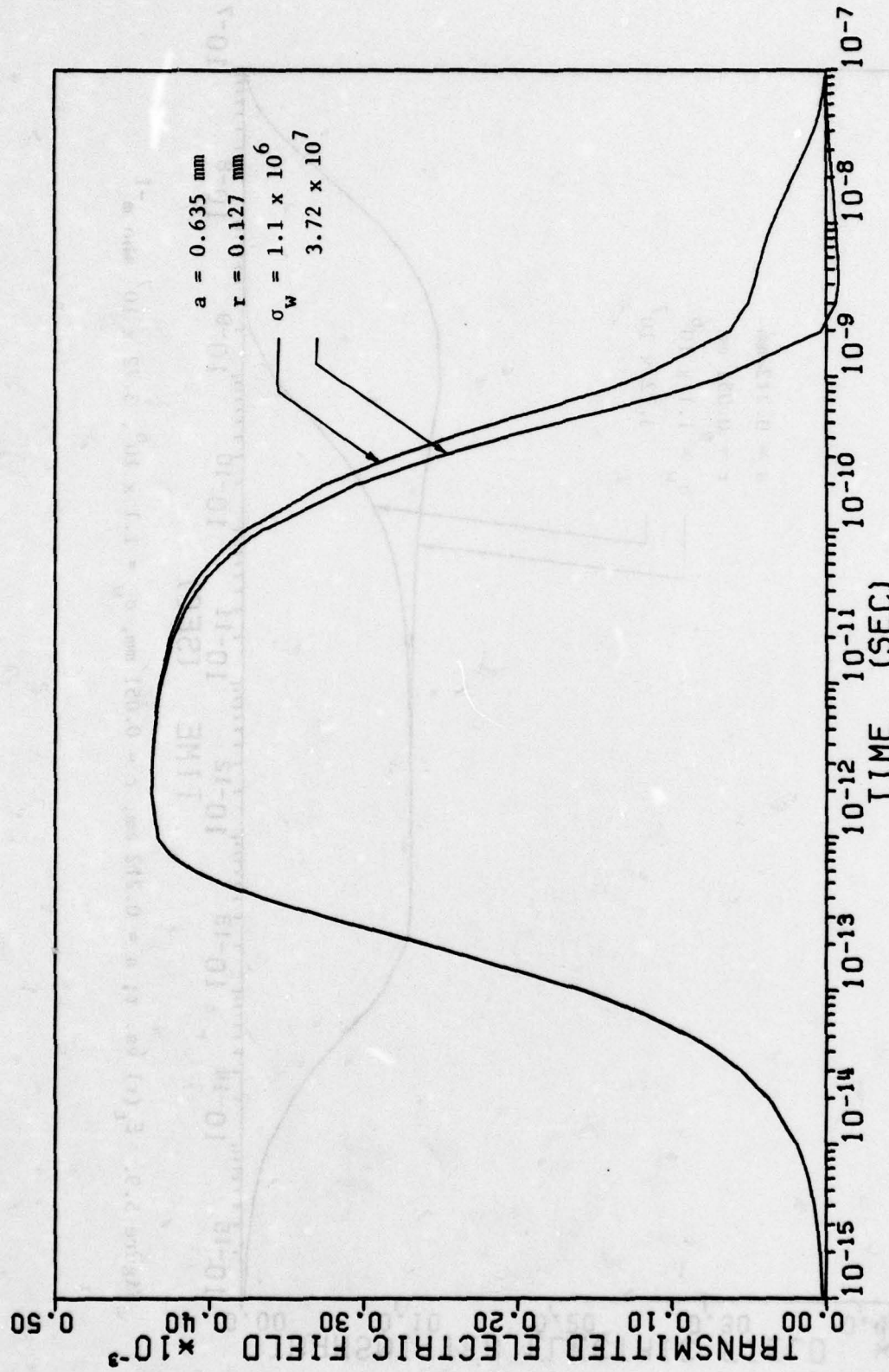


Figure 5.10. $E_t(\tau)$ vs. τ ; $a = 0.635\ mm$, $r = 0.127\ mm$, $\sigma_w = 1.1 \times 10^6$, $3.72 \times 10^7\ mho\ m^{-1}$

of the 0.635/0.127 configuration is larger than that of the 0.212/0.051 mesh, for equal wire conductivity; the magnitude of the transmission coefficient for this case is correspondingly greater at higher frequencies.

The effect of this behavior on the time-domain transmitted electric field is evident in Figs. 5.9 and 5.10. The 0.212/0.051 mesh yields an $E_t(\tau)$ response which is nearly independent of σ_w up to $\tau = 5 \times 10^{-12}$ sec; this early-time behavior is principally a result of the inductive reactance of the sheet impedance. At later times the resistive component of the sheet impedance exerts the dominating influence on the transmitted field.

The 0.635/0.127 mesh, on the other hand, yields a much higher amplitude for the transmitted field at early times (again, up to $\tau = 5 \times 10^{-12}$ sec, the response is nearly independent of σ_w) as a consequence of its larger inductive reactance. The late-time amplitude is again dominated by the resistance of the screen, although some undershoot is apparent for $\tau > 2 \times 10^{-9}$ sec for the case of the larger wire conductivity.

The most interesting comparison to be made among the four curves presented is that between the two higher-conductivity cases. The finer mesh, even though its equivalent conductivity-thickness product $\pi r^2 \sigma_w / a$ is smaller by a factor of 2 than that of the larger mesh, yields a smaller transmitted field. This observation leads one to conclude that the conductivity-thickness product alone cannot be used as a measure of the effectiveness of mesh shields. The time-domain behavior of the incident fields must also be taken into account; in fact, an interesting problem for further study would be to design a screen to yield minimum transmitted field under a given set of constraints.

One should also compare the curves in Figs. 5.9 and 5.10 with those in Fig. 5.4 for the planar graphite composite layer. The pulse shapes have already been discussed. Of interest, however, is comparing the peak transmitted electric field amplitudes for the two types of composite. For example, a 2 mm thick graphite panel of conductivity $\sigma_g = 1.5 \times 10^4$ mho m^{-1} yields a peak transmitted electric field amplitude of 9.7×10^{-5} ; the 0.635/0.127 mesh yields a peak value of 45×10^{-5} ; and the 0.212/0.051 mesh, 15×10^{-5} . The screened panel would thus seem generally to be a poorer shield than the graphite panel, at least at early times. We will return to this type of comparison in the next section.

6. THE PERFORATED SCREEN MODEL FOR A WIRE MESH

In this paragraph we briefly consider the problem of transmission of a plane electromagnetic wave through a periodic square array of square apertures in a perfectly conducting plane, in order to compare the results to those previously obtained for the wire mesh. Our purpose is to gain some insight into the behavior of the mesh screen when the assumption $r/a \ll 1$ does not apply and the thin-wire approximation breaks down.

Let the screen be in the surface $z=0$ and let the apertures be square of side length h and centered at $(x = (m + 1/2)a, y = (n + 1/2)a)$ for $-\infty < m, n < \infty$. The geometry is shown in Fig. 5.11. It is well known (cf., e.g., [20]) that an electrically small aperture in a conducting screen can be modeled in terms of equivalent electric and magnetic dipoles. We therefore consider the electromagnetic field radiated by a planar array of electric and magnetic dipoles in free space located at $(x = (m+1/2)a, y = (n+1/2)a, z=0)$. The electric and magnetic dipole moments are assumed to be given by

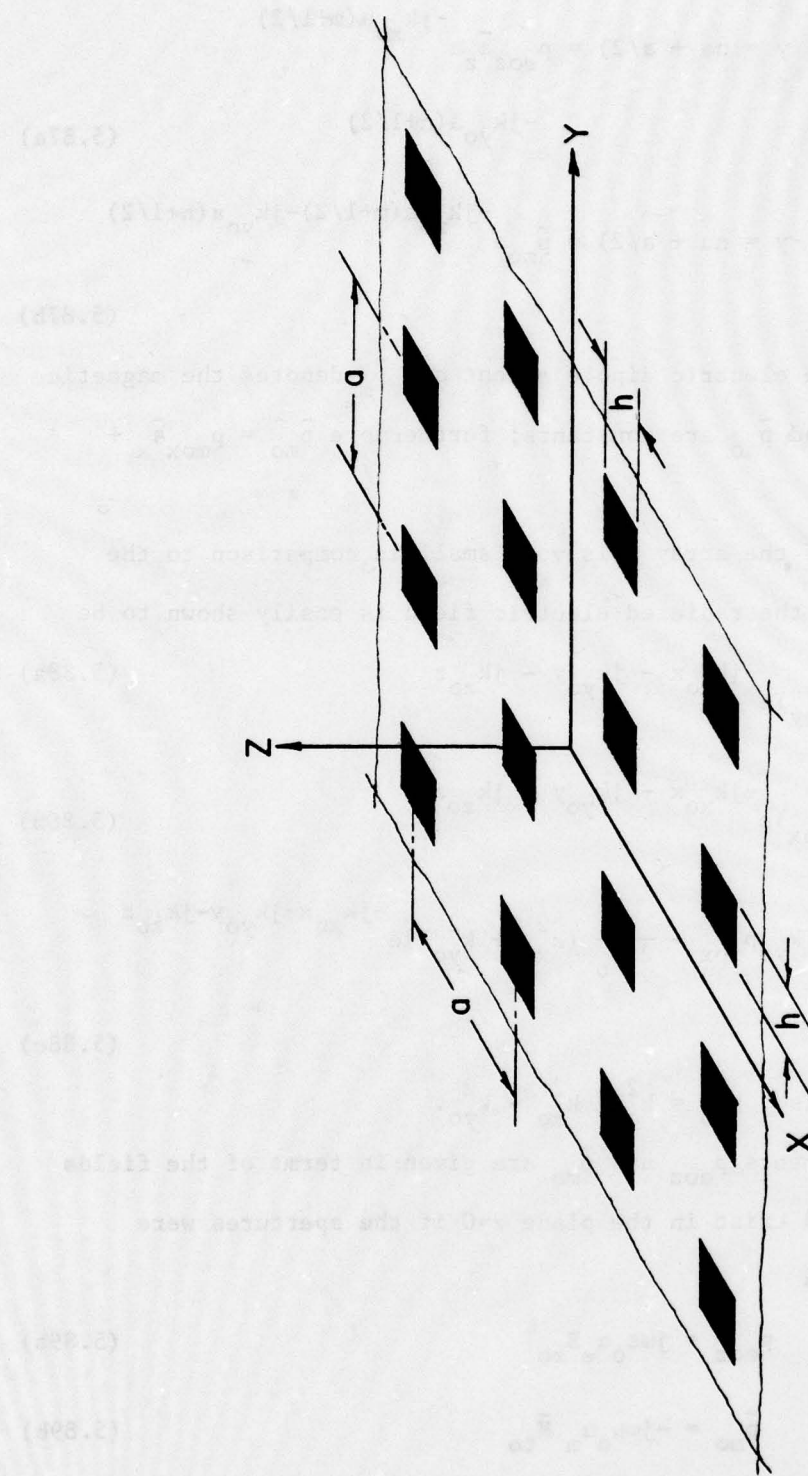


Figure 5.11. Perforated screen geometry

$$\bar{p}_e(x = ma + a/2, y = na + a/2) = p_{eo} \bar{a}_z e^{-jk_{xo} a(m+1/2)} \\ \cdot e^{-jk_{yo} a(n+1/2)} \quad (5.87a)$$

$$\bar{p}_m(x = ma + a/2, y = na + a/2) = \bar{p}_{mo} e^{-jk_{xo} a(m+1/2)-jk_{yo} a(n+1/2)} \\ \quad (5.87b)$$

in which \bar{p}_e denotes the electric dipole moment and \bar{p}_m denotes the magnetic dipole moment. p_{eo} and \bar{p}_{mo} are constants; furthermore $\bar{p}_{mo} = p_{mox} \bar{a}_x + p_{moy} \bar{a}_y$.

When the period of the array a is very small in comparison to the free-space wavelength, the radiated electric field is easily shown to be

$$E_x = \frac{1}{2a^2} \left(\frac{k_{xo} p_{eo}}{\omega \epsilon_0} - p_{moy} \right) e^{-jk_{xo} x - jk_{yo} y - jk_{zo} z} \quad (5.88a)$$

$$E_y = \frac{1}{2a^2} \left(\frac{k_{yo} p_{eo}}{\omega \epsilon_0} + p_{mox} \right) e^{-jk_{xo} x - jk_{yo} y - jk_{zo} z} \quad (5.88b)$$

$$E_z = \frac{1}{2a^2 k_{zo}} [k_{xo} p_{moy} - k_{yo} p_{mox} - \frac{1}{2\omega \epsilon_0} (k_{xo}^2 + k_{yo}^2)] e^{-jk_{xo} x - jk_{yo} y - jk_{zo} z} \\ \quad (5.88c)$$

in the region $z > 0$; also, $k_{zo}^2 = k_o^2 - k_{xo}^2 - k_{yo}^2$.

Now the dipole moments p_{eo} and \bar{p}_{mo} are given in terms of the fields E_{zo} and \bar{H}_{to} which would exist in the plane $z=0$ if the apertures were closed by the relations

$$p_{eo} = j\omega \epsilon_0 \alpha_e E_{zo} \quad (5.89a)$$

$$\bar{p}_{mo} = -j\omega \mu_0 \alpha_m \bar{H}_{to} \quad (5.89b)$$

in which α_e and α_m denote respectively the electric and magnetic polariz-

abilities of the apertures. Latham [20] has calculated these polarizabilities; his results are

$$\alpha_e/a^3 = \frac{0.114 (h/a)^3}{1 + 0.104(h/a)^3} \quad (5.90a)$$

$$\alpha_m/a^3 = \frac{0.260 (h/a)^3}{1 - 0.185(h/a)^3} \quad (5.90b)$$

Let us now assume that a perpendicularly polarized plane wave is incident upon the perforated screen from the region $z < 0$. Then E_{zo} and \bar{H}_{to} are given by

$$E_{zo} = E'_{zo} = 0 \quad (5.91a)$$

$$\bar{H}_{to} = \bar{H}'_{to} = \frac{-2E'_o \cos\theta}{n_o} (\bar{a}_x \cos\phi + \bar{a}_y \sin\phi) \quad (5.91b)$$

in which E'_o denotes the electric field amplitude in the incident wave; furthermore, $k_{xo} = k_o \sin\theta \cos\phi$, $k_{yo} = k_o \sin\theta \sin\phi$, and $k_{zo} = k_o \cos\theta$, in which θ and ϕ are the incidence angles. The transmitted electric field amplitude is now easily shown to be

$$E'_{trans} = jk_o a \cos\theta (\alpha_m/a^3) E'_o \quad (5.92)$$

When a parallel-polarized plane wave is incident upon the screen, the fields E_{zo} and \bar{H}_{to} are

$$E_{zo} = E''_{zo} = -2E''_o \sin\theta \quad (5.93a)$$

$$\bar{H}_{to} = \bar{H}''_{to} = \frac{2E''_o}{n} (-\bar{a}_x \sin\phi + \bar{a}_y \cos\phi) \quad (5.93b)$$

where E''_o denotes the electric field amplitude in the incident wave. The transmitted electric field amplitude is

$$E''_{trans} = jk_o a \sec\theta (\alpha_m/a^3) [1 - (\alpha_e/\alpha_m) \sin^2\theta] E''_o \quad (5.94)$$

Now let us compare the expressions given in eqs. (5.92) and (5.94) with those obtained for the electric field transmitted through a perfectly conducting wire mesh screen, in the low-frequency limit. We have, from the results obtained in the previous paragraph,

$$E'_{\text{trans}} \approx jk_o a \cos\theta \frac{1}{\pi} \ln(1 - e^{-2\pi r/a})^{-1} E'_o \quad (5.95a)$$

$$E''_{\text{trans}} \approx jk_o a \sec\theta \frac{1}{\pi} \ln(1 - e^{-2\pi r/a})^{-1} (1 - \frac{1}{2} \sin^2\theta) E''_o \quad (5.95b)$$

Examining eqs. (5.92) and (5.95a) for E'_{trans} , we see that the expressions $\frac{1}{\pi} \ln(1 - e^{-2\pi r/a})^{-1}$ and a_m/a^3 (cf. eq. (5.90b)) are to be compared. We shall compare them on the basis of equal optical coverage by letting $h = a - 2r$. The two expressions are shown as functions of r/a in Fig. 5.12. The wire-mesh model factor is always larger than the perforated-screen factor; the former is accurate in the limit $r/a \rightarrow 0$, and the latter is accurate in the limit $r/a \rightarrow 0.5$. It is clear that the wire mesh model overestimates the transmitted field amplitude, and therefore underestimates the induced currents on the screen, for values of r/a which are not very small in comparison to unity.

Examining eqs. (5.94) and (5.95b) for E''_{trans} , we see that the relevant comparison is between the constant factor 0.5 for the wire-mesh model and the ratio a_e/a_m for the perforated-screen model. This ratio is shown as a function of r/a in Fig. 5.13. It is apparent that the mesh model overestimates the importance of the " $\sin^2\theta$ " term in the transmission coefficient for parallel-polarized fields. The reason for this is probably the use of the thin-wire approximation in the analysis of the mesh model. In effect, the equivalent permittivity of the mesh for electric fields normal to the plane of the mesh, caused by induced line dipole moments on the wires, has been ignored. It is clear from our earlier analysis

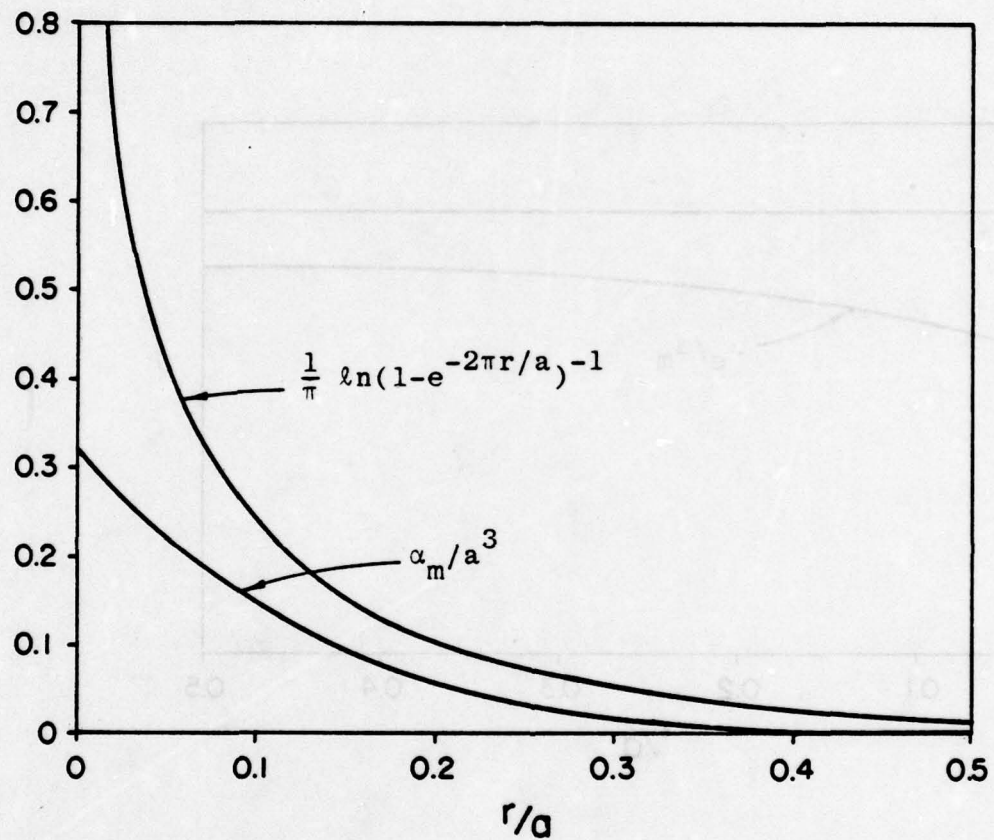


Figure 5.12. Functions $\frac{1}{\pi} \ln(1-e^{-2\pi r/a})^{-1}$ and α_m/a^3 vs. r/a

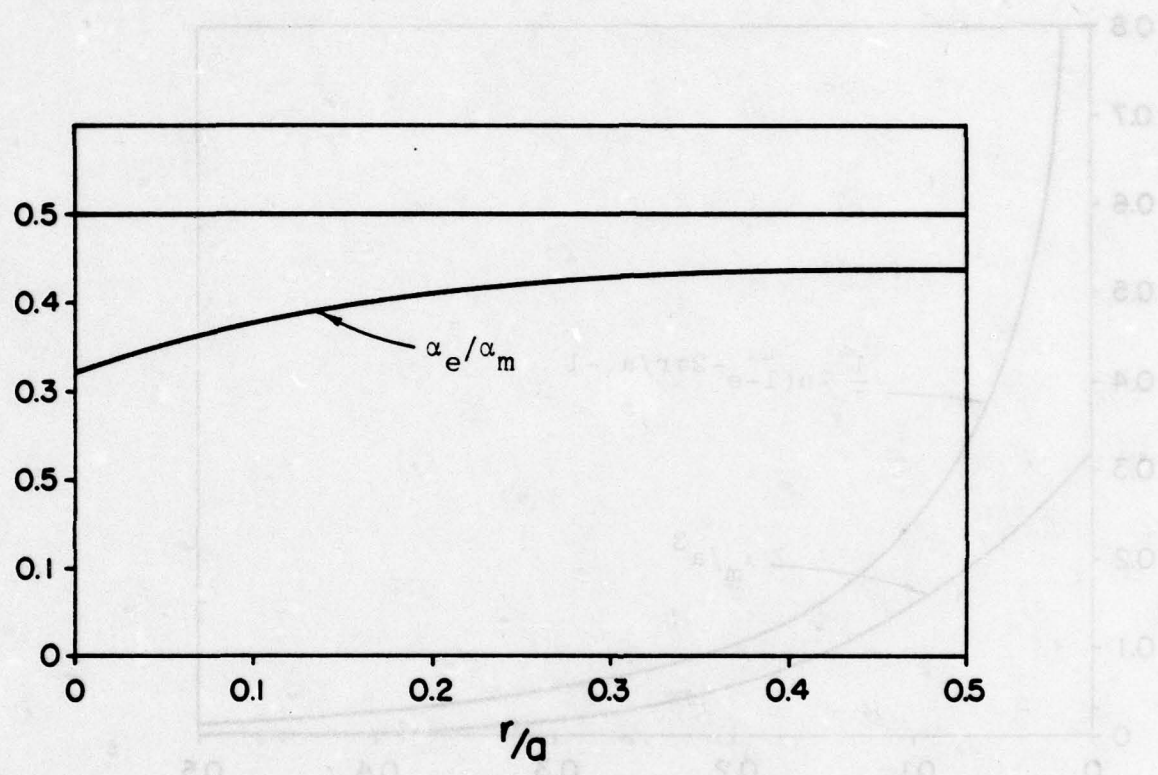


Figure 5.13. α_e/α_m vs. r/a ; the constant value 0.5 is also explicitly shown

of the effect of a dielectric environment on the wire mesh that including these line dipole moments would decrease the coefficient of the " $\sin^2\theta$ " term and thereby improve the accuracy of our approximate solution for the sheet impedance operator \bar{Z}_s . This aspect of the problem would seem worthy of further study.

7. NUMERICAL COMPUTATION OF GRID CURRENTS

The equations (5.37) and (5.40) can be solved for the modified current harmonics \tilde{I}'_{xn} and \tilde{I}'_{yn} by means of the procedure outlined in this paragraph. We begin by substituting eq. (5.37) into eq. (5.40), thereby eliminating the variable Δ from further consideration and yielding

$$\sum_{n=-\infty}^{\infty} (U_m \delta_{mn} + \frac{jqa}{2} P_m k_{xn}) \tilde{I}'_{xn} + \sum_{n=-\infty}^{\infty} (V_{mn} - \frac{jqa}{2} P_m k_{yn}) \tilde{I}'_{yn} = R_o \delta_m \quad (5.95a)$$

$$\sum_{n=-\infty}^{\infty} (X_{nm} - \frac{jqa}{2} Q_m k_{xn}) \tilde{I}'_{xn} + \sum_{n=-\infty}^{\infty} (W_m \delta_{mn} + \frac{jqa}{2} Q_m k_{yn}) \tilde{I}'_{yn} = S_o \delta_m \quad (5.95b)$$

as the coupled sets of equations for \tilde{I}'_{xn} and \tilde{I}'_{yn} . Also,

$$q = [\frac{a}{b} (\frac{1}{2} + \frac{k^2 b^2}{24}) + (\frac{1}{2} + \frac{k^2 x_0 a^2}{24})]^{-1} \quad (5.96)$$

Now define matrices \bar{M}_{xx} , \bar{M}_{xy} , \bar{M}_{yx} , and \bar{M}_{yy} such that

$$(\bar{M}_{xx})_{mn} = U_m \delta_{mn} + \frac{jqa}{2} P_m k_{xn} \quad (5.97a)$$

$$(\bar{M}_{xy})_{mn} = V_{mn} - \frac{jqa}{2} P_m k_{yn} \quad (5.97b)$$

$$(\bar{M}_{yx})_{mn} = X_{nm} - \frac{jqa}{2} Q_m k_{xn} \quad (5.97c)$$

$$(\bar{M}_{yy})_{mn} = W_m \delta_{mn} + \frac{jqa}{2} Q_m k_{yn} \quad (5.97d)$$

and let $\tilde{\bar{I}}'_x$ and $\tilde{\bar{I}}'_y$ denote the modified space harmonic current vectors.

Finally, let \bar{R}_o and \bar{S}_o denote the "driving" vectors; these each possess only a single nonzero element. Then the coupled equations (5.95) may be written

$$\bar{M}_{xx} \cdot \tilde{\bar{I}}'_x + \bar{M}_{xy} \cdot \tilde{\bar{I}}'_y = \bar{R}_o \quad (5.98a)$$

$$\bar{M}_{yx} \cdot \tilde{\bar{I}}'_x + \bar{M}_{yy} \cdot \tilde{\bar{I}}'_y = \bar{S}_o \quad (5.98b)$$

This system is readily solved for \tilde{I}'_x and \tilde{I}'_y . We obtain

$$\tilde{I}'_x = \bar{\bar{N}}_{xr} \cdot \bar{R}_o - \bar{\bar{N}}_{xs} \cdot \bar{s}_o \quad (5.99a)$$

$$\tilde{I}'_y = \bar{\bar{N}}_{yr} \cdot \bar{R}_o - \bar{\bar{N}}_{ys} \cdot \bar{s}_o \quad (5.99b)$$

where

$$\bar{\bar{N}}_{xr} = (\bar{M}_{xy}^{-1} \cdot \bar{M}_{xx} - \bar{M}_{yy}^{-1} \cdot \bar{M}_{yx})^{-1} \cdot \bar{M}_{xy}^{-1} \quad (5.100a)$$

$$\bar{\bar{N}}_{xs} = (\bar{M}_{xy}^{-1} \cdot \bar{M}_{xx} - \bar{M}_{yy}^{-1} \cdot \bar{M}_{yx})^{-1} \cdot \bar{M}_{yy}^{-1} \quad (5.100b)$$

$$\bar{\bar{N}}_{yr} = (\bar{M}_{xx}^{-1} \cdot \bar{M}_{xy} - \bar{M}_{yx}^{-1} \cdot \bar{M}_{yy})^{-1} \cdot \bar{M}_{xx}^{-1} \quad (5.100c)$$

$$\bar{\bar{N}}_{ys} = (\bar{M}_{xx}^{-1} \cdot \bar{M}_{xy} - \bar{M}_{yx}^{-1} \cdot \bar{M}_{yy})^{-1} \cdot \bar{M}_{yx}^{-1} \quad (5.100d)$$

and the solution is formally complete. Δ can now be calculated using eq. (5.37).

The calculation of the grid impedance \bar{Z}_g defined in eq. (5.52) is straightforward. We readily obtain

$$\bar{Z}_g = \begin{bmatrix} \frac{1}{b} (\bar{\bar{N}}_{xr})_{oo} & -\frac{1}{b} (\bar{\bar{N}}_{xs})_{oo} \\ \frac{1}{a} (\bar{\bar{N}}_{yr})_{oo} & -\frac{1}{a} (\bar{\bar{N}}_{ys})_{oo} \end{bmatrix}^{-1} \quad (5.101)$$

Now using eq. (5.53), we may calculate the equivalent sheet impedance \bar{Z}_s .

The efficient numerical evaluation of the matrix elements defined in eq. (5.97) has already been discussed (cf. eqs. (5.42) and (5.43)).

We have calculated the eigenvalues of the equivalent sheet impedance operator \bar{Z}_s as a function of N , the number of modified space harmonics included in \tilde{I}'_x and \tilde{I}'_y (note that $N = 1, 3, 5, \dots$), for the case $d/a = 1$,

$b/a = 1$, $r/a = 0.01$, $\epsilon_r = 4.5$, $\sigma_w = \infty$, $\theta = 60^\circ$, where $\phi = 0^\circ$ and 45° and $k_o a = 1.0$ and 0.1 . The results of these computations are shown in Figs. 5.14-5.17, in which values of X'_s and X''_s ($Z_s' = jX_s'$, $Z_s'' = jX_s''$) are plotted vs. N . The rapid convergence of X'_s and X''_s with increasing N is evident (note, however, that in the $\phi = 45^\circ$ cases this is not at all surprising, since there is no discontinuity in the junction currents when $\phi = 45^\circ$, 135° , 225° , or 315° , by symmetry). The use of the $N=1$ case to derive an analytical approximation for \bar{Z}_s when $k_o a \ll 1$ is justified by the rapidity of convergence apparent in Figs. 5.16 and 5.17 for $k_o a = 0.1^+$.

[†]Note that for typical mesh dimensions the maximum value of $k_o a$ occurring in the EMP frequency range is of order 10^{-3} .

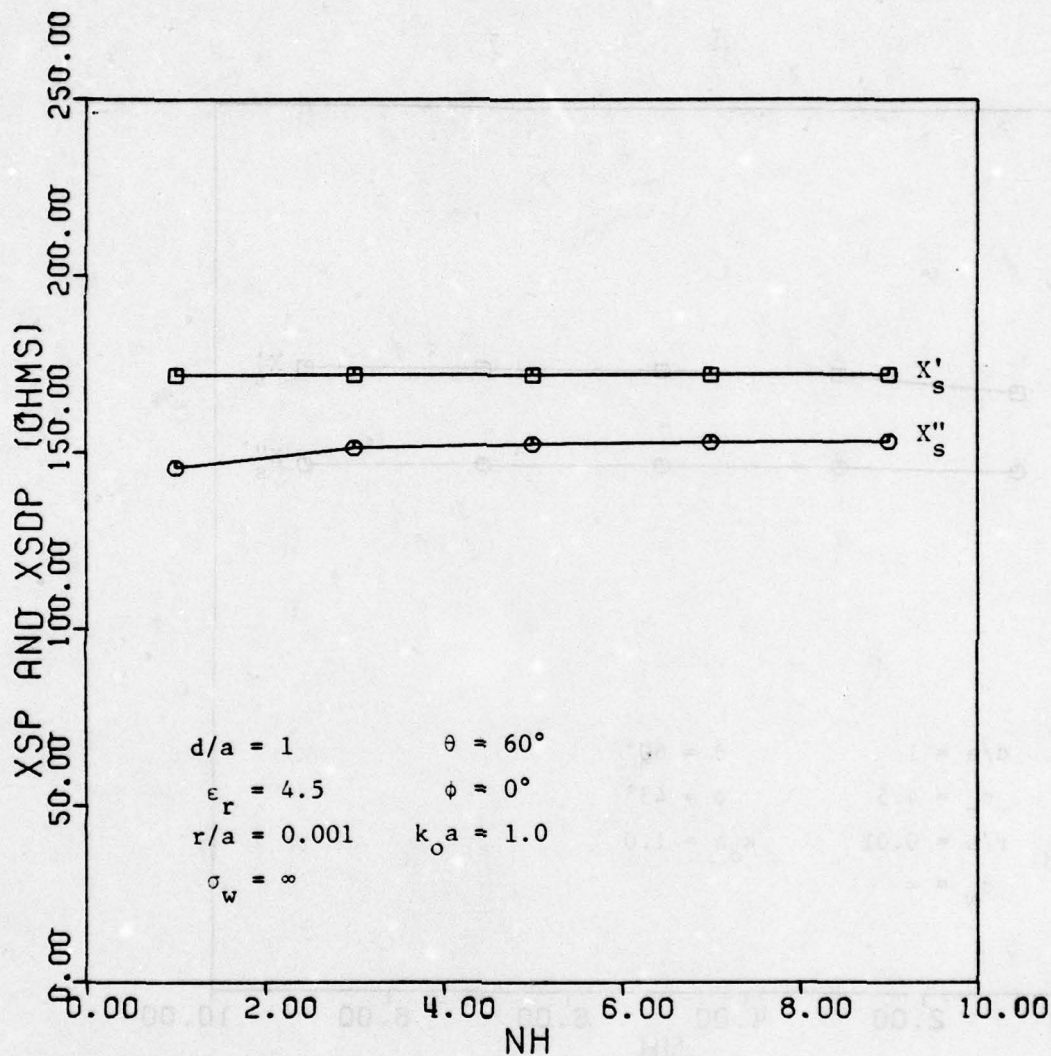


Figure 5.14. X'_s and X''_s ($Z'_s, ''_s = jX'_s, ''_s$) vs. N; $d/a = 1$, $\epsilon_r = 4.5$, $r/a = 0.01$, $\sigma_w = \infty$, $\theta = 60^\circ$, $\phi = 0^\circ$, $k_o a = 1.0$

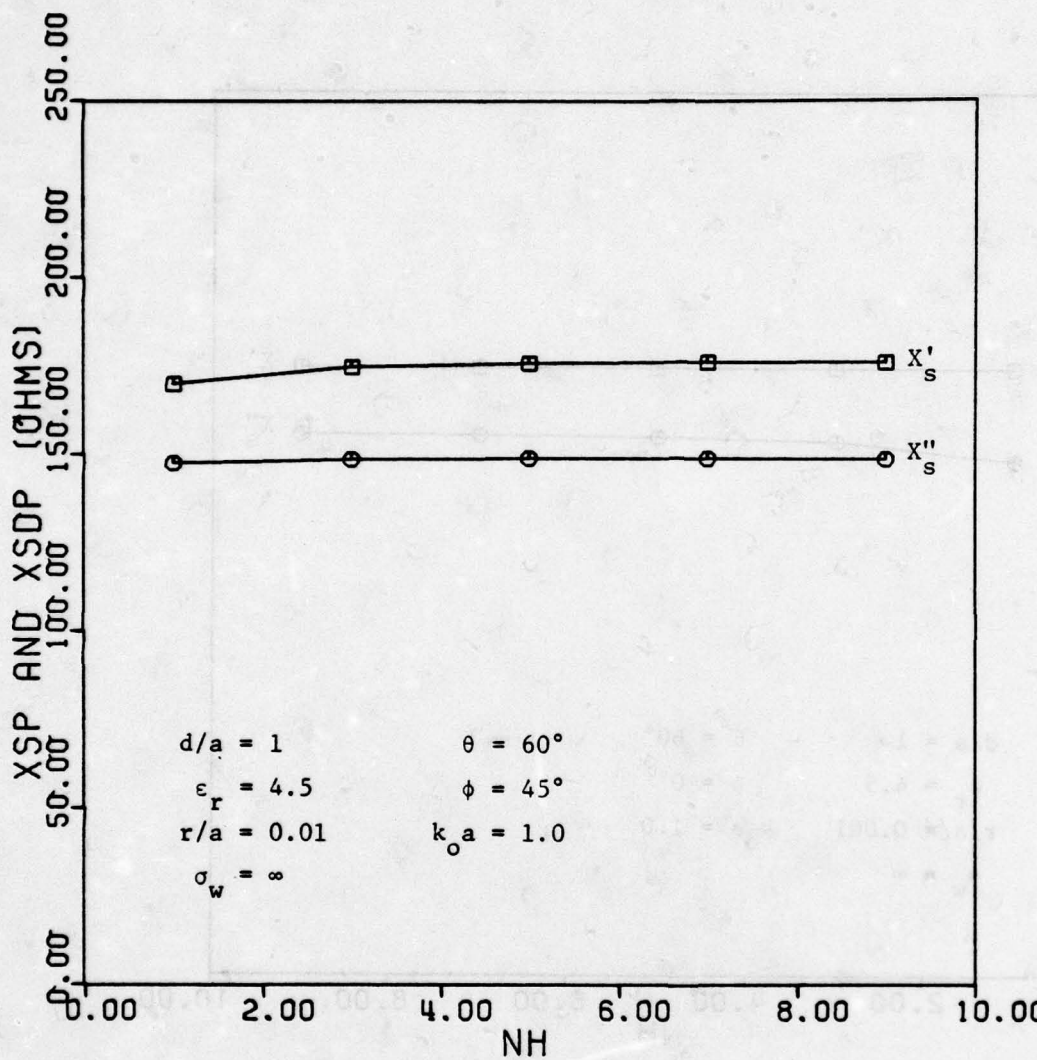


Figure 5.15. X'_s and X''_s ($Z_s' = jX_s''$) vs. N; $d/a = 1$, $\epsilon_r = 4.5$, $r/a = 0.01$, $\sigma_w = \infty$, $\theta = 60^\circ$, $\phi = 45^\circ$, $k_o a = 1.0$

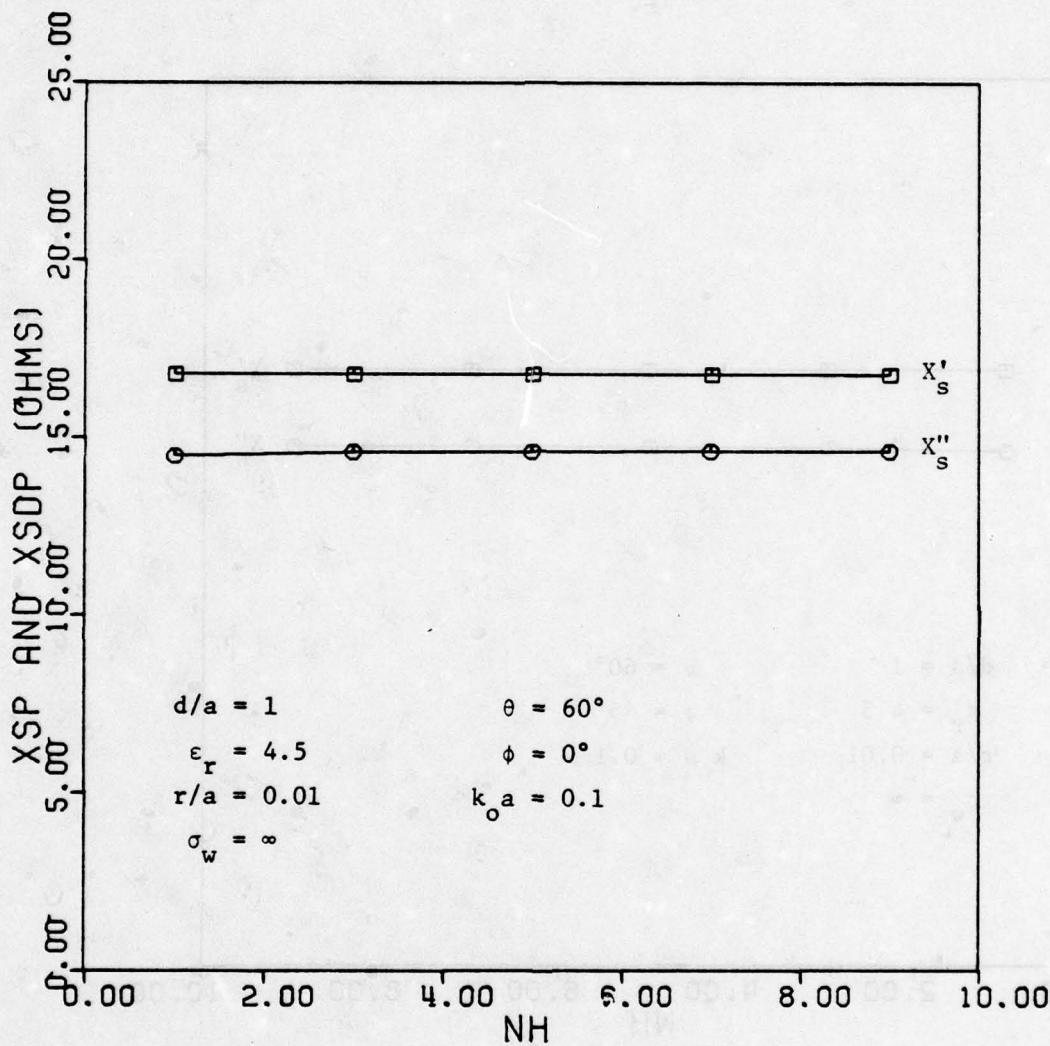


Figure 5.16. X'_s and X''_s ($Z_s' = jX_s'$, $Z_s'' = jX_s''$) vs. N; $d/a = 1$, $\epsilon_r = 4.5$,
 $r/a = 0.01$, $\sigma_w = \infty$, $\theta = 60^\circ$, $\phi = 0^\circ$, $k_o a = 0.1$

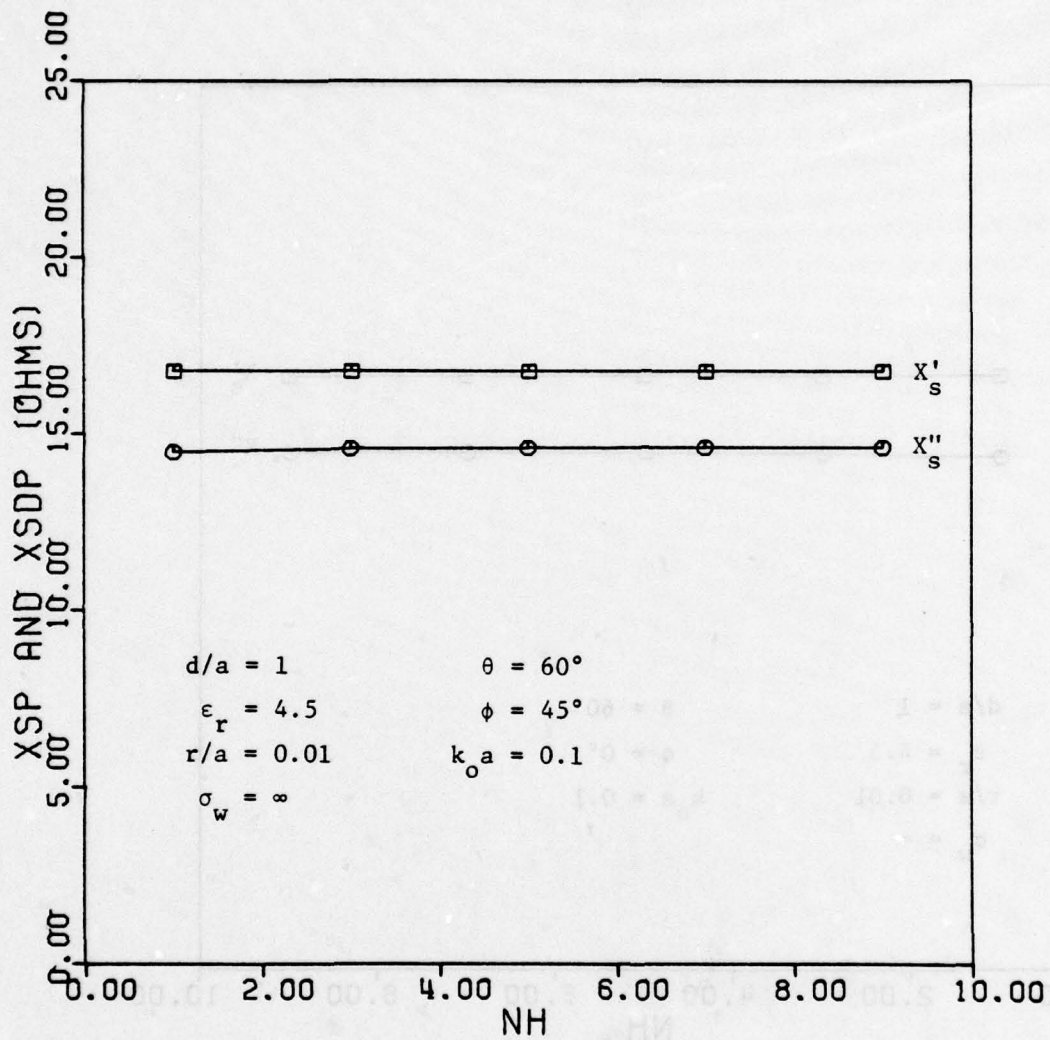


Figure 5.17. X'_s and X''_s ($Z_s' = jX_s'$, $Z_s'' = jX_s''$) vs. N; $d/a = 1$, $\epsilon_r = 4.5$, $r/a = 0.01$, $\sigma_w = \infty$, $\theta = 60^\circ$, $\phi = 45^\circ$, $k_o a = 0.1$

SECTION VI

CYLINDRICAL WIRE-MESH COMPOSITE SHIELDS

1. INTRODUCTION

In this section we shall consider the interaction of a plane electromagnetic wave with an infinitely long cylindrical shell of wire-mesh composite. As in Section IV, we shall consider only the cases in which the propagation vector of the incident wave has no component along the cylinder axis.

In the next paragraph, the problem is formulated in the frequency domain using the equivalent sheet impedance developed in the previous section to describe the screen in the surface of the composite shell. Some representative frequency-domain results are presented. In paragraph 3, we briefly consider the transient behavior of the internal magnetic field when the circumference of the cylinder is small in comparison to the wavelength over the frequency range of interest and the temporal behavior of the incident wave is that of the standard EMP signal.

2. FORMULATION OF THE PROBLEM

The geometry of the problem is shown in Fig. 6.1. An infinitely long cylindrical shell of wire-mesh composite of inner and outer radii a and b respectively is illuminated by a plane electromagnetic wave. The medium inside and outside the shell is free space and the shell thickness $d = b - a$ is small in comparison to the mean radius \sqrt{ab} . The side of the wire-mesh composite in which the grid is embedded is the outer surface of the cylinder. For simplicity we shall again consider only the case in which the incident wave's propagation vector has no axial component, and we shall investigate the two possible wave polarizations separately. The total fields may then be obtained by superposition.

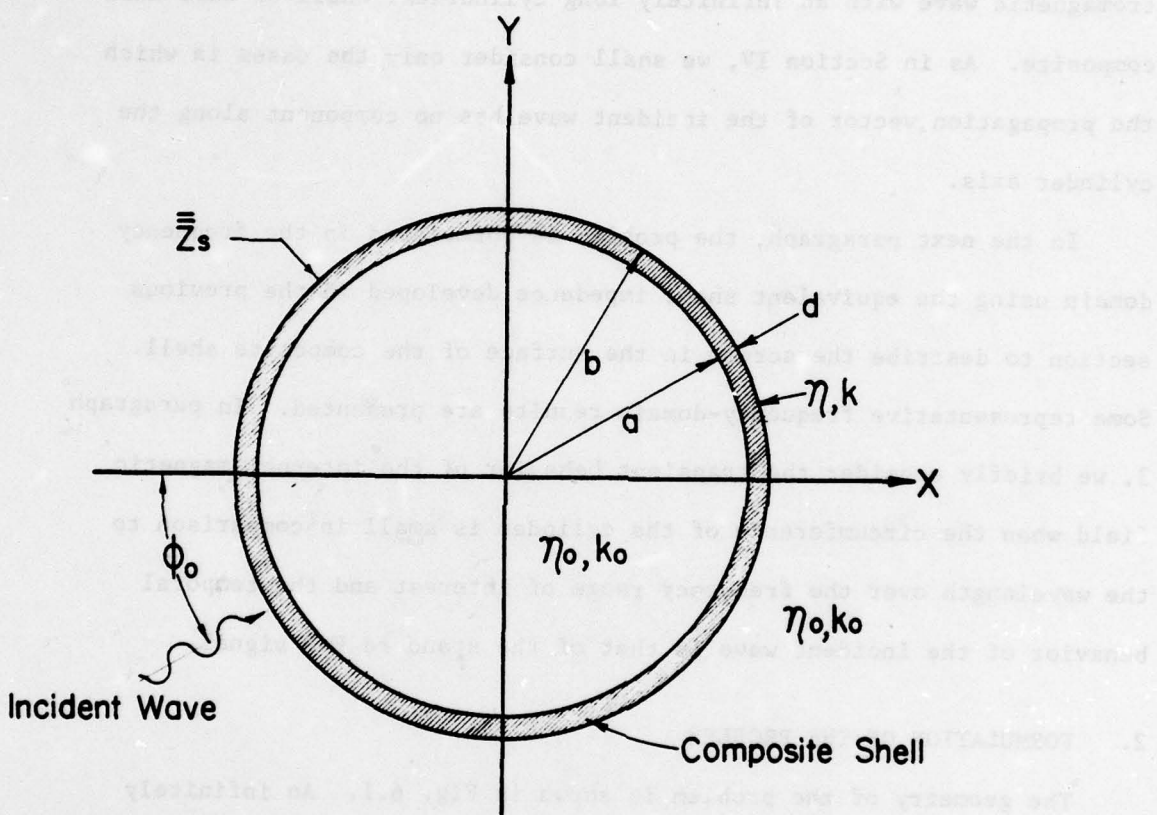


Figure 6.1. Plane wave penetration of, and scattering by, a cylindrical shell of boron-epoxy composite with a bonded wire-mesh screen in the outer surface: geometry of the problem

The shell itself is modeled as an equivalent sheet impedance, based on the results obtained for the planar case in the previous section. We shall denote the mean shell radius by ρ_o . Z_s'' , which, as will be recalled, depends upon the transverse propagation constant, will be denoted $Z_{s,n}''$ for each angular eigenfunction in the field expansion, and

$$k_{to}^2 = k_{ton}^2 = \frac{n^2}{\rho_o^2} \quad (6.1)$$

Consider first the case in which the incident electromagnetic wave is polarized TM with respect to z . In this case, the field components are

$$E_z = -j\omega\mu_0\Psi \quad (6.2a)$$

$$H_\phi = -\frac{\partial\Psi}{\partial\rho} \quad (6.2b)$$

$$H_\rho = \frac{1}{\rho}\frac{\partial\Psi}{\partial\phi} \quad (6.2c)$$

where

$$0 \leq \rho \leq \rho_o : \quad \Psi = \frac{-E_o}{j\omega\mu_o} \sum_{n=-\infty}^{\infty} A_n J_n(k_o\rho) e^{jn(\phi-\phi')} \quad (6.3a)$$

$$\rho \geq \rho_o : \quad \Psi = \frac{-E_o}{j\omega\mu_o} \sum_{n=-\infty}^{\infty} [J_n(k_o\rho) + B_n H_n^{(2)}(k_o\rho)] e^{jn(\phi-\phi')} \quad (6.3b)$$

A_n and B_n are to be determined, E_o is the electric field amplitude of the incident wave, and $\phi' = \phi_o + \pi/2$, where ϕ_o is the angle of incidence as shown in Fig. 6.1. The appropriate Z_s for this polarization is Z_s' .

Now the boundary conditions at $\rho=\rho_o$ are applied. We have

$$E_z(\rho = \rho_o^-) = E_z(\rho = \rho_o^+) = E_z(\rho = \rho_o) \quad (6.4a)$$

$$H_\phi(\rho = \rho_o^+) - H_\phi(\rho = \rho_o^-) = (Z_s')^{-1} E_z(\rho = \rho_o) \quad (6.4b)$$

from which expressions for A_n and B_n are readily obtained. We find

$$A_n = \left[1 + \pi k_o \rho_o \frac{\eta_o (z_s')^{-1}}{2} J_n(k_o \rho_o) H_n^{(2)}(k_o \rho_o) \right]^{-1} \quad (6.5a)$$

$$B_n = -\pi k_o \rho_o \frac{\eta_o (z_s')^{-1}}{2} J_n^2(k_o \rho_o) A_n \quad (6.5b)$$

When the incident wave is polarized TE with respect to z , the field components are

$$H_z = j\omega \epsilon_o \Phi \quad (6.6a)$$

$$E_\phi = -\frac{\partial \Phi}{\partial \rho} \quad (6.6b)$$

$$E_\rho = \frac{1}{\rho} \frac{\partial \Phi}{\partial \phi} \quad (6.6c)$$

where

$$0 \leq \rho \leq \rho_o : \Phi = \frac{E_o}{jk_o} \sum_{n=-\infty}^{\infty} A'_n J_n(k_o \rho) e^{jn(\phi-\phi')} \quad (6.7a)$$

$$\rho > \rho_o : \Phi = \frac{E_o}{jk_o} \sum_{n=-\infty}^{\infty} [J_n(k_o \rho) + B'_n H_n^{(2)}(k_o \rho)] e^{jn(\phi-\phi')} \quad (6.7b)$$

A'_n and B'_n are to be determined. At $\rho = \rho_o$, the boundary conditions to be applied are

$$E_\phi(\rho = \rho_o^-) = E_\phi(\rho = \rho_o^+) = E_\phi(\rho = \rho_o) \quad (6.8a)$$

$$H_z(\rho = \rho_o^+) - H_z(\rho = \rho_o^-) = -(z_s'')^{-1} E_\phi(\rho = \rho_o) \quad (6.8b)$$

in which

$$(z_s'')^{-1} E_\phi(\rho_o) \equiv \sum_{n=-\infty}^{\infty} (z_{s,n}'')^{-1} E_{\phi n}(\rho_o) \quad (6.9)$$

We find for A'_n and B'_n

$$A'_n = \left[1 + \pi k_o \rho_o \frac{\eta_o (z_{s,n}'')^{-1}}{2} J'_n(k_o \rho_o) H_n^{(2)'}(k_o \rho_o) \right]^{-1} \quad (6.10a)$$

$$B'_n = -\pi k_o \rho_o \frac{n_o(z''_{s,n})^{-1}}{2} [J'_n(k_o \rho_o)]^2 A'_n \quad (6.10b)$$

The energy shielding ratios r_w and r'_w are given in terms of A_n and A'_n in eqs. (4.12) and (4.20). To obtain expressions for r_w and r'_w appropriate for the screened composite cylindrical shell, A_n and A'_n given in eqs. (6.5a) and (6.10a) are substituted into eqs. (4.12) and (4.20) respectively. When $k_o a \ll 1$, approximate expressions for r_w and r'_w are

$$\begin{aligned} r_w \Big|_{k_o a \ll 1} &= \frac{1}{2} \left\{ \left| 1 - j k_o \rho_o n_o(z')^{-1} \ln k_o \rho_o \right|^{-2} \right. \\ &\quad \left. + \left| 1 + j k_o \rho_o \frac{n_o(z')^{-1}}{2} \right|^{-2} \right\} \end{aligned} \quad (6.11a)$$

$$\begin{aligned} r'_w \Big|_{k_o a \ll 1} &= \frac{1}{2} \left\{ \left| 1 + j k_o \rho_o \frac{n_o(z''_{s,0})^{-1}}{2} \right|^{-2} \right. \\ &\quad \left. + \left| 1 - j n_o \frac{(z''_{s,1})^{-1}}{2 k_o \rho_o} \right|^{-2} \right\} \end{aligned} \quad (6.11b)$$

Curves of r_w and r'_w as functions of frequency are given for various values of screen parameters and a cylinder radius $\rho_o = 1$ m in Figs. 6.2 and 6.3. (a_m , rather than a , denotes the mesh size in this section). As in the related curves for the graphite shell, we note that unless $\sigma_w = \infty$, $r_w \rightarrow 1$ and $r'_w \rightarrow 0.5$ as $f \rightarrow 0$. The reason for this behavior, as before, is that r'_w contains only a contribution from the internal magnetic field, while both the internal electric and magnetic fields contribute to r_w . Also, we have not included curves for r'_w in the case $\epsilon_r = 1$; over the frequency range shown, they are indistinguishable from the curves for the case $\epsilon_r = 4.5$.

Comparison of Figs. 6.2 and 6.3 with Figs. 4.2-4.7 reveals that for cylindrical geometries the screened boron-epoxy composite shells with $\sigma_w = 1.1 \times 10^6 \text{ mho m}^{-1}$ are comparable to graphite composite shells in shielding effectiveness, while those with $\sigma_w = 3.72 \times 10^7 \text{ mho m}^{-1}$ are decidedly superior. The reason for this is that the principal break frequency, below which the shielding is relatively poor, is approximately $1/(\pi\mu_0\rho_0(\pi r^2\sigma_w/a))$; and $\pi r^2\sigma_w/a$, which is the equivalent conductivity-thickness product for the mesh is comparable to $\sigma_g d$ for graphite shells when $\sigma_w = 1.1 \times 10^6 \text{ mho m}^{-1}$, but is significantly larger than $\sigma_g d$ when $\sigma_w = 3.72 \times 10^7 \text{ mho m}^{-1}$.

Not shown in the r_w and r'_w curves is the higher-frequency effect of the screen inductance. This is apparent in the time-domain internal field response, which is discussed in the next paragraph.

3. TIME-DOMAIN SHIELDING

The ratio of the internal magnetic field to the incident magnetic field in the frequency domain is readily shown to be given when $k_0\rho_0 \ll 1$ by

$$\frac{H_{int}}{H_{inc}} = [1 + jk_0\rho_0 \frac{n_0}{2} (Z'_s)^{-1}]^{-1} \quad (6.12)$$

for either polarization. This result does not involve the relative permittivity of the composite shell at all, since the case in which the magnetic field is perpendicular to the cylinder axis corresponds to perpendicular polarization (and Z'_s does not involve ϵ_r), and the case in which the magnetic field is parallel to the cylinder axis utilizes only the $n=0$ angular eigenfunction in the low-frequency limit (and $Z''_{s,0}$ does not involve ϵ_r).

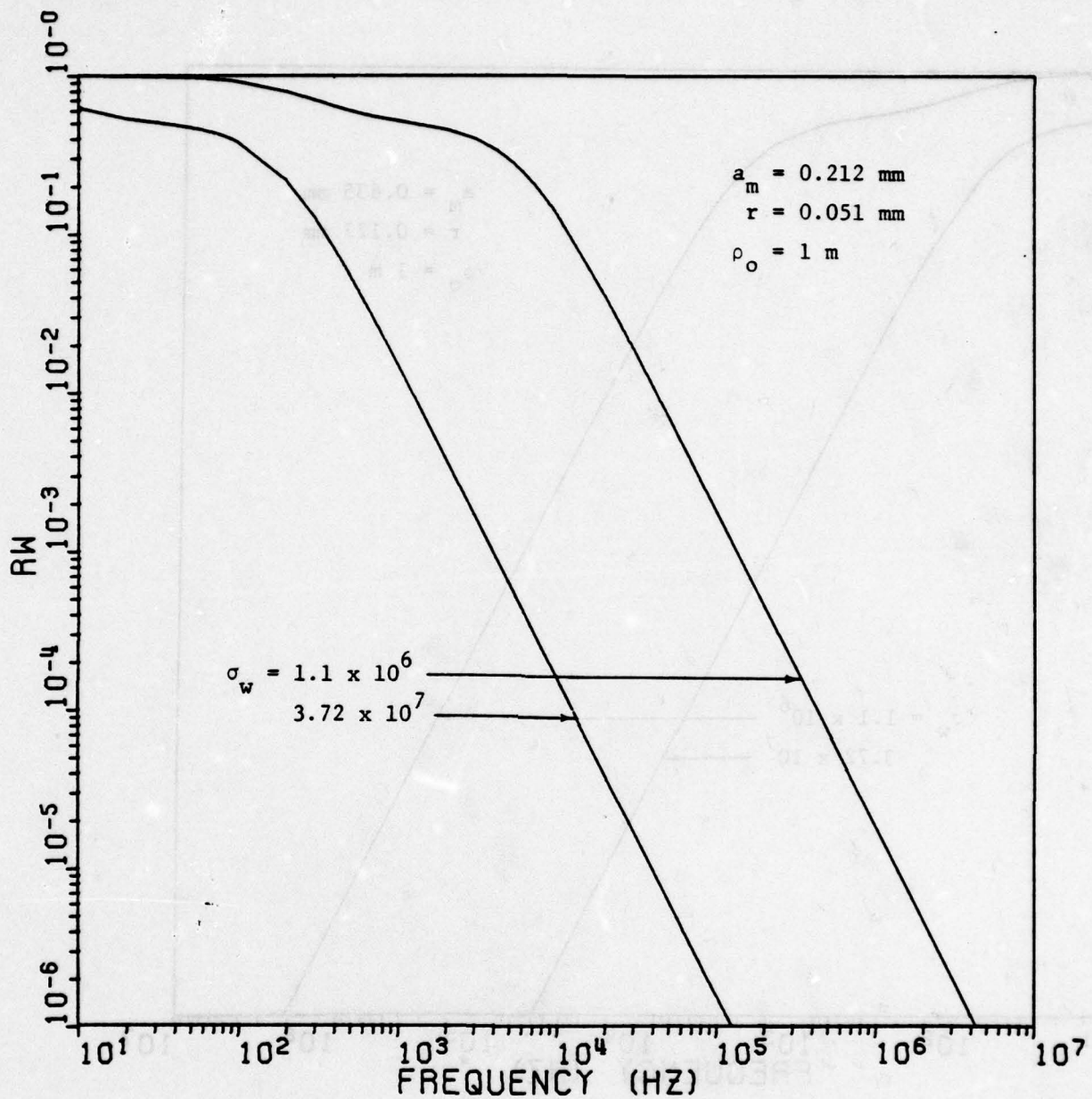


Figure 6.2a. r_w vs. frequency; $a_m = 0.212$ mm, $r = 0.051$ mm, $\rho_o = 1$ m;
 $\sigma_w = 1.1 \times 10^6$ and 3.72×10^7 mho m⁻¹

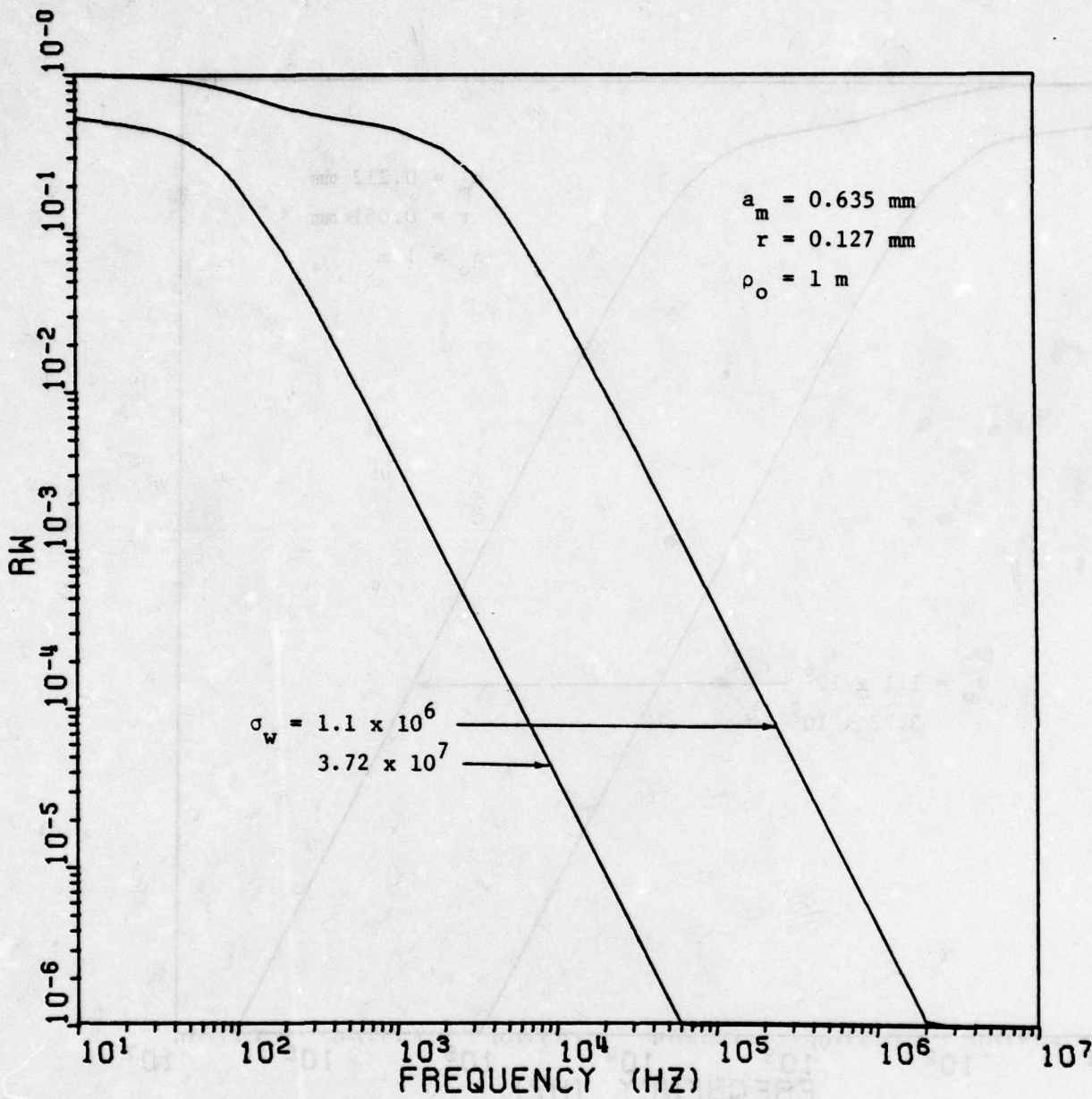


Figure 6.2b. r_w vs. frequency; $a_m = 0.635$ mm, $r = 0.127$ mm, $\rho = 1$ m;
 $\sigma_w = 1.1 \times 10^6$ and 3.72×10^7 mho m^{-1}

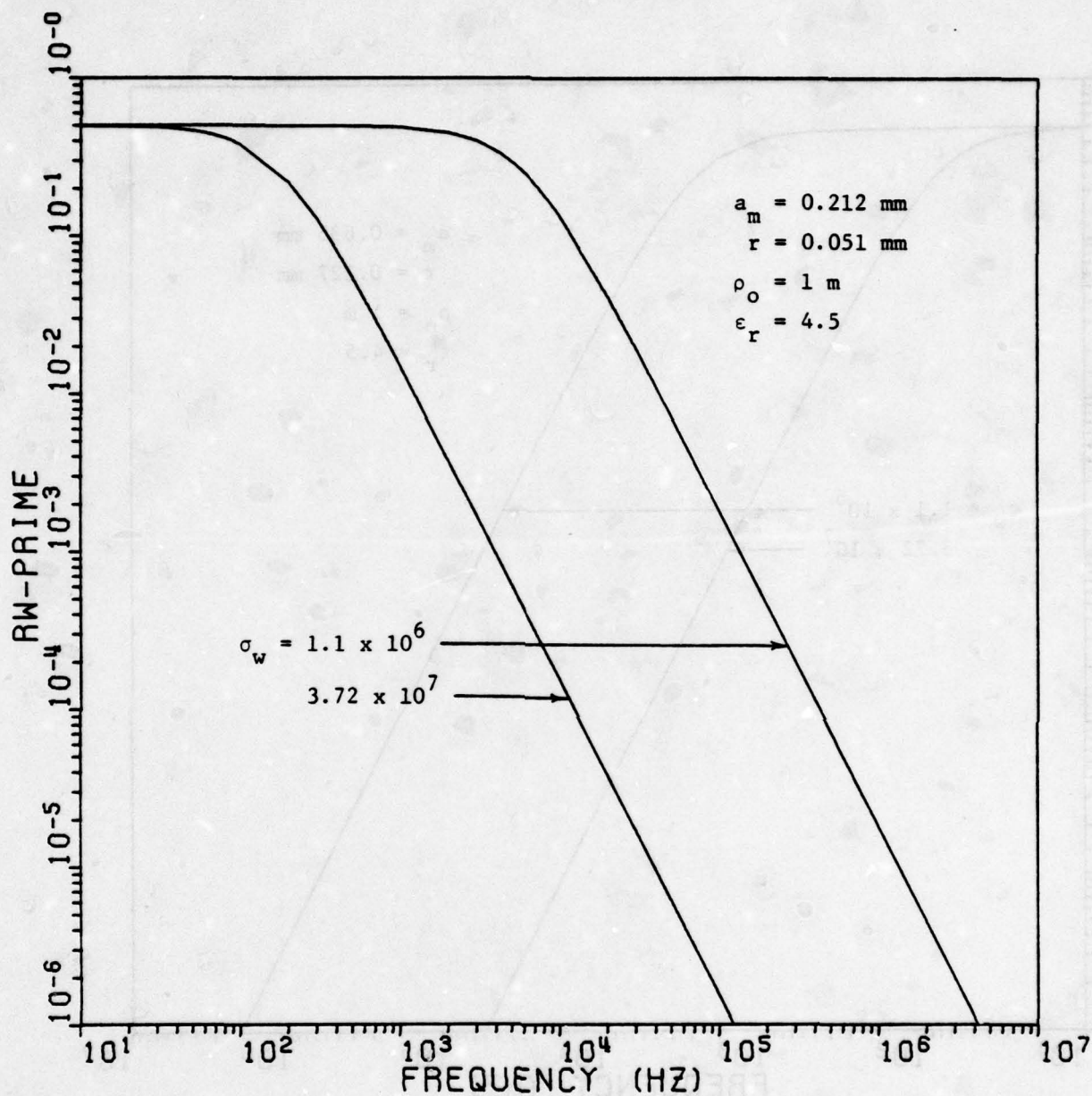


Figure 6.3a. r'_w vs. frequency; $a_m = 0.212 \text{ mm}$, $r = 0.051 \text{ mm}$,
 $\rho_o = 1 \text{ m}$; $\sigma_w = 1.1 \times 10^6$ and $3.72 \times 10^7 \text{ mho m}^{-1}$;
 $\epsilon_r = 4.5$

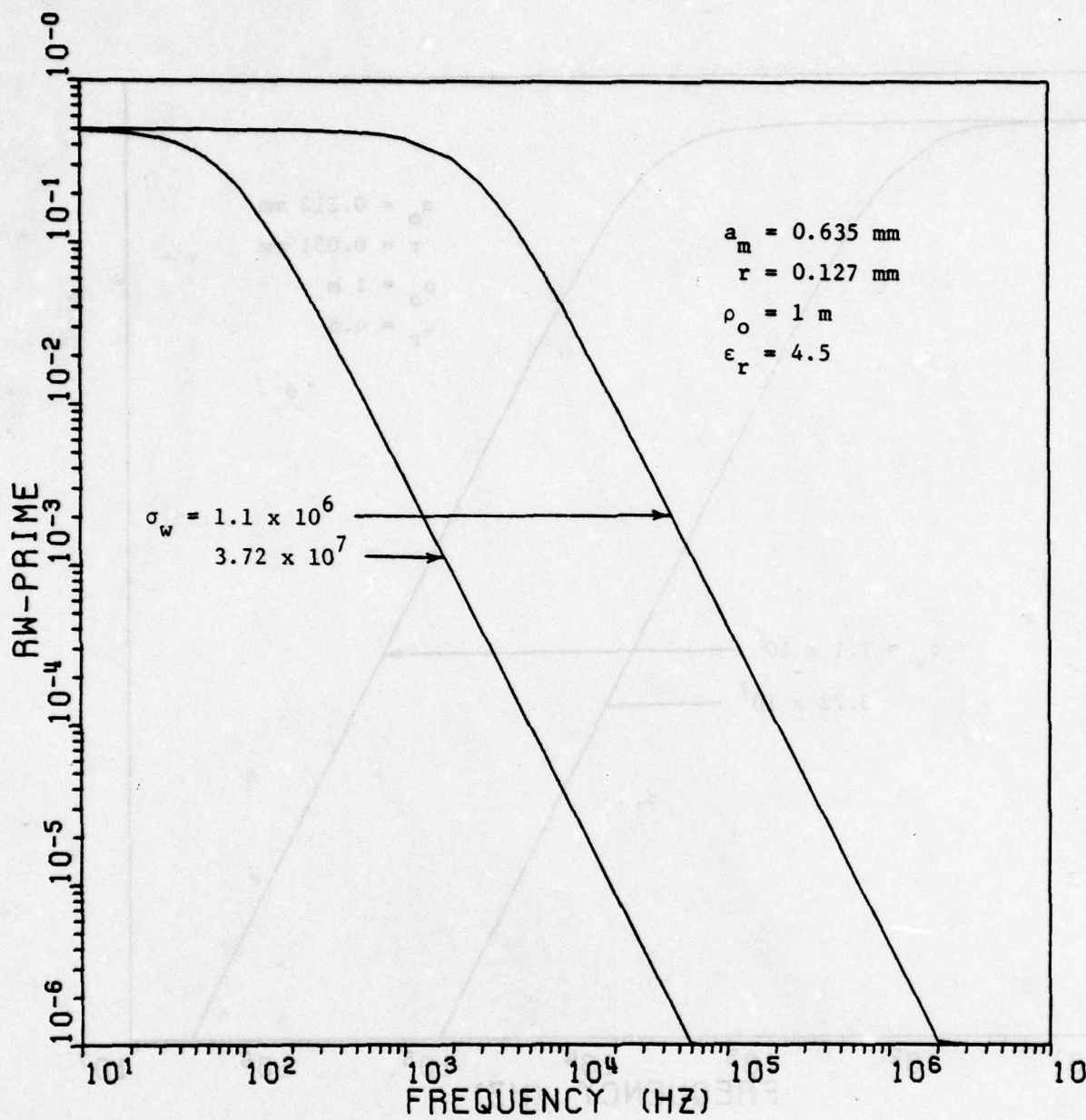


Figure 6.3b. r'_w vs. frequency; $a_m = 0.635 \text{ mm}$, $r = 0.127 \text{ mm}$,
 $\rho_0 = 1 \text{ m}$; $\sigma_w = 1.1 \times 10^6$ and $3.72 \times 10^7 \text{ mho m}^{-1}$;
 $\epsilon_r = 4.5$.

When the screen wires are perfectly conducting, the result in eq. (6.12) reduces to

$$\begin{aligned} \frac{H_{int}}{H_{inc}} &= \left\{ 1 + \frac{\pi \rho_0}{a_m} \ln^{-1}(1 - e^{-2\pi r/a_m})^{-1} \right\}^{-1} \\ &\approx \frac{a_m}{\pi \rho_0} \ln(1 - e^{-2\pi r/a_m})^{-1} \end{aligned} \quad (6.13)$$

which is a constant, independent of frequency. Thus the time dependence of the internal magnetic field is identical to that of the incident field, except for a constant attenuation. This behavior is attributable to the combined "differentiating" effect of the perfect screen and the "integrating" effect of the cylindrical geometry.

Another simple result of some interest is obtained if we assume that $Z_w = R_w$ over the frequency range of interest, where $R_w = (\pi r^2 \sigma_w)^{-1}$ is the resistance per unit length of the screen wires. In this case, we find that when $(a_m / \pi \rho_0) \ln(1 - e^{-2\pi r/a_m})^{-1} \ll 1$,

$$\frac{H_{int}}{H_{inc}} \approx \frac{a_m L}{\pi \rho_0} \frac{j\omega + 2\pi R_w / \mu_0 L}{j\omega + 2R_w a_m / \mu_0 \rho_0} \quad (6.14)$$

in which L denotes $\ln(1 - e^{-2\pi r/a_m})^{-1}$. The impulse response of the internal magnetic field is therefore approximately given by

$$H_{int}(t) \approx \frac{a_m L}{\pi \rho_0} \delta(t) + \frac{2R_w a_m}{\mu_0 \rho_0} e^{-(2R_w a_m / \mu_0 \rho_0)t} \quad (6.15)$$

so that the internal field response to a standard EMP waveform is dominated at late times by the slowly decaying exponential function in the second term in (6.15). More specifically, under standard EMP excitation, the internal magnetic field is given by

$$\begin{aligned} n_o H_{int}(t) \approx & \frac{a_m L}{\pi \rho_o} A [e^{-\alpha t} - e^{-\beta t}] + A \left(\frac{2R_w a_m}{\mu_o \rho_o} \right) \left[\frac{1}{\beta} e^{-\beta t} - \frac{1}{\alpha} e^{-\alpha t} \right] \\ & + A \left(\frac{1}{\alpha} - \frac{1}{\beta} \right) \left(\frac{2R_w a_m}{\mu_o \rho_o} \right) e^{-(2R_w a_m / \mu_o \rho_o)t} \end{aligned} \quad (6.16)$$

in which we have made use of the fact that $(\beta$ and $\alpha) \gg 2R_w a_m / \mu_o \rho_o$ in typical cases. Representative curves of $n_o H_{int}(t)$ vs. t are shown in Figs. 6.4 and 6.5 for various values of screen parameters and a cylinder radius, $\rho_o = 1$ m.

The curves in Figs. 6.4 and 6.5 show very clearly the enhancement in shielding effectiveness with increasing wire conductivity. In the curves of Fig. 6.4, for example, the peak value of the internal field drops from about 0.09 to about 0.005 when σ_w is increased from 1.1×10^6 to 3.72×10^7 mho m⁻¹. One will also note the long "tails" of the internal field waveforms due to the term in the expression in (6.16) depending on t as $\exp(-2R_w a_m t / \mu_o \rho_o)$.

Comparing the lower-conductivity curves in the two figures, one notes immediately that the 0.635/0.127 mesh is a better shield than the 0.212/0.051 mesh; this is a consequence of the larger equivalent conductivity-thickness product of the former configuration. It is also apparent that the "integrating" effect of the cylindrical geometry has delayed the onset of the peak signal, in comparison with the planar case (cf. Figs. 5.9 and 5.10). Thus the wire conductivity (or, more precisely, the equivalent conductivity-thickness product) controls the behavior of the internal waveform. In the higher-conductivity cases the inductive reactance of the screen becomes more important: one will notice the peak in the

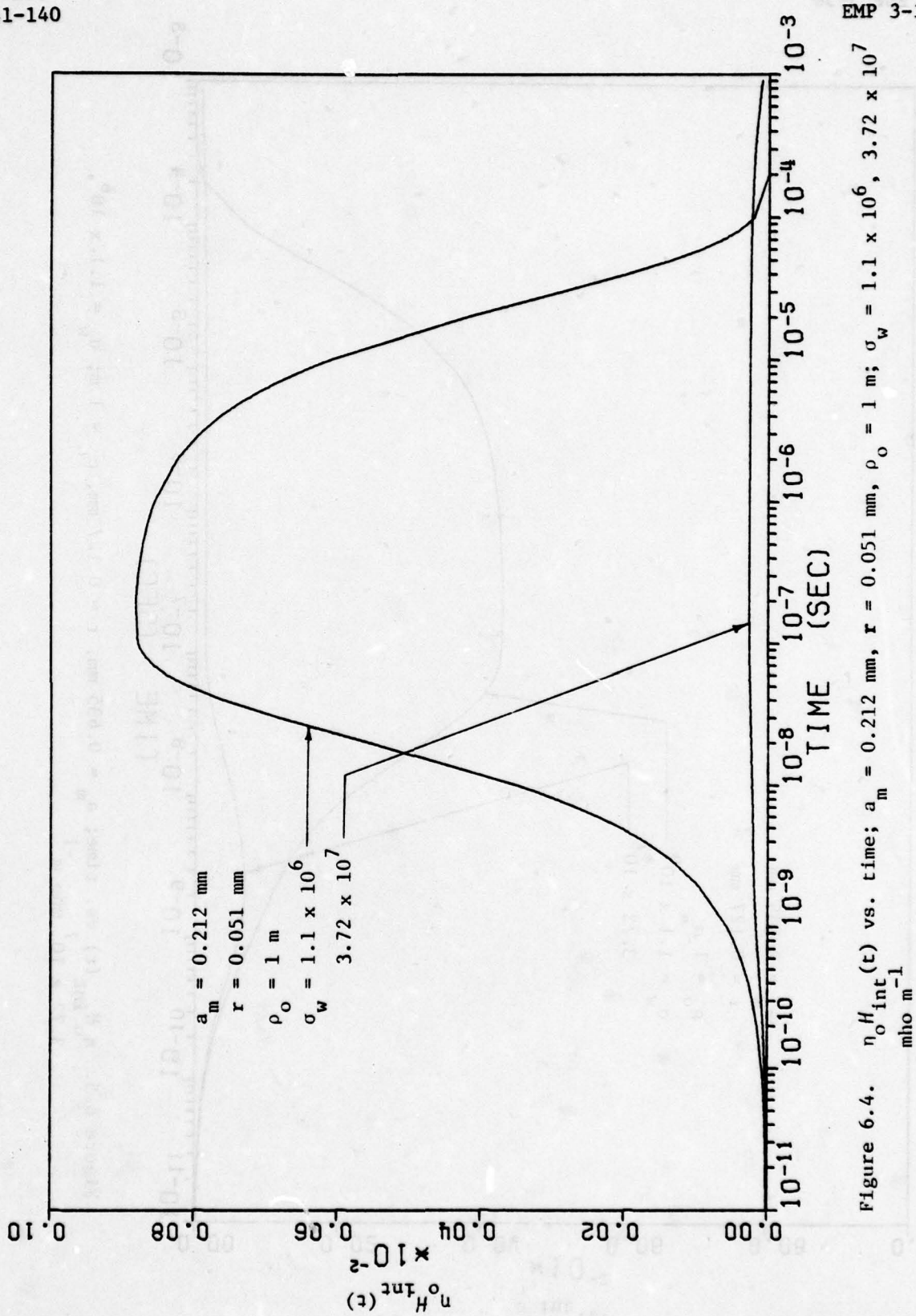


Figure 6.4. $\eta_0 H_{int}(t)$ vs. time; $a_m = 0.212 \text{ mm}$, $r = 0.051 \text{ mm}$, $\rho_o = 1 \text{ m}$; $\sigma_w = 1.1 \times 10^6$, $3.72 \times 10^7 \text{ mho m}^{-1}$

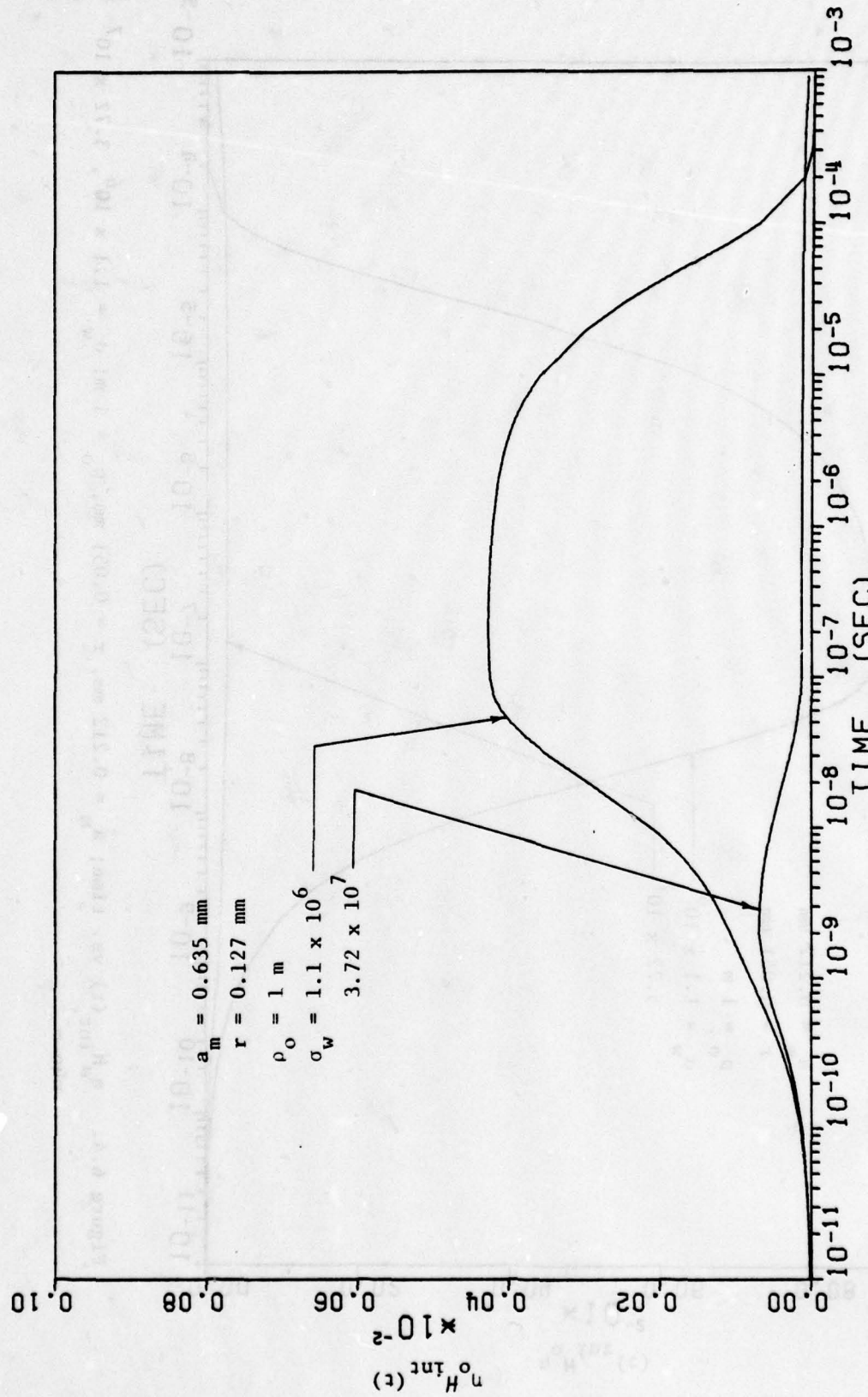


Figure 6.5. $n_0 H_{int}(t)$ vs. time; $a_m = 0.635 \text{ mm}$, $r = 0.127 \text{ mm}$, $\rho_o = 1 \text{ m}$; $\sigma_w = 1.1 \times 10^6$,
 $3.72 \times 10^7 \text{ mho m}^{-1}$

response for the 0.635/0.127 mesh near $t = 2 \times 10^{-9}$ sec. This peak is absent in the response of the 0.212/0.051 mesh because of its lower inductive reactance.

Finally, if one compares the responses in Figs. 6.4 and 6.5 with those in Fig. 4.8 for the graphite composite cylindrical shells' internal field, one notes that the peak internal field for the thickest graphite composite shell is about the same as that for the "worst-case" screened boron-epoxy composite shell; furthermore, the "best-case" screened boron-epoxy shell response is lower than that of the thickest graphite shell by a factor of roughly 20. One could conclude from these results that a fine mesh screen made of highly conducting (Al or Cu) wire would be a much better shield for cylindrical geometries and EMP waveforms than even a thick graphite laminate.

SECTION VII

CONCLUDING REMARKS

1. SUMMARY AND DISCUSSION

In this Note we have considered both the frequency-domain and time-domain shielding provided by graphite-epoxy and screened boron-epoxy composite laminates in planar or cylindrical geometries, with respect to EMP signals and spectra. Graphite-epoxy composites have been modeled as isotropic, homogeneous conducting materials and boron-epoxy composites as isotropic, homogeneous dielectrics. The screen used in screened boron-epoxy panels has been modeled under the assumptions that the wire junctions are bonded and that the thin-wire approximation applies. These assumptions may, in fact, not be well-satisfied in practice (the wire junctions may be imperfect due to oxidation at the junction points of overlapping wires and the condition that the wire radius is small in comparison to the mesh period is not generally well met); however, they provide a reasonable starting point for analysis and yield conservative estimates of the mesh shielding effectiveness, since the thin-wire approximation tends to underestimate the mesh current.

We have developed a boundary connection supermatrix formalism which is a generalization of the transmission matrix of network theory. Such a formalism will be useful in dealing with shielding problems involving bodies of non-separable shape as long as the local radii of curvature are small in comparison to the shield thickness. The boundary connection supermatrix possesses many intersecting properties which have not been touched on here but which will be the subject of a forthcoming Interaction Note. The principal utilities of the boundary connection supermatrix are its generality (in that general multilayer shields with sheet

immittances between layers are easily described) and the fact that its use effectively reduces the number of regions which must be considered in a shielding calculation by at least one.

The transmission of electromagnetic plane waves through planar graphite composite laminates is straightforward to analyze, and some useful approximate formulas for the transmission coefficients of such a structure have been given. The transmitted time-domain field behaves in a manner easily understood on the basis of the low-pass filter characteristic of conducting materials. We have calculated some time-domain curves for typical cases and have found, for example, that the peak value of the electric field transmitted through a 2 mm thick graphite composite panel is approximately 10^{-4} of the peak value of the incident field.

Penetration of electromagnetic fields into the interior of cylindrical shells of graphite composite has been considered. Over the frequency range which has been of principal interest to us, and for cylinder radii on the order of 2 m or less, resonance effects are of little importance. Consequently, low-frequency approximations are useful. We have suggested a new frequency-domain measure of the shielding effectiveness of closed surfaces in terms of the time-average electromagnetic energy stored in the interior of the region, and have given simple formulas for this quantity for cylindrical bodies. We have also presented representative curves to illustrate the dependence of this shielding parameter on frequency for several typical graphite-composite cylinders, and have pointed out that the principal "break frequency" below which the shielding is poor is given approximately by $1/\pi\mu_0\sigma g d\rho_0$. The time-domain internal magnetic field resulting from an incident EMP signal has been calculated for some

representative cases. Its time dependence can be understood on the basis of the "low-pass" character of both the composite shell material and the cylindrical geometry itself.

The principal difficulty in treating screened boron-epoxy composite laminates lies in finding an appropriate sheet-immittance description for the screen. We have developed such a description appropriate for the case where the mesh dimensions are electrically small, and which takes the presence of the composite panel into account. Our result constitutes an extension of the classic work of Kontorovich. Using this method of characterizing the mesh we have addressed the problems of plane-wave transmission through a planar screened boron-epoxy composite layer and penetration into the interior of a cylindrical shell of screened composite material. We have found that the composite layer itself, except for its effect on the sheet impedance of the screen, is relatively unimportant insofar as the shielding behavior of the screened laminate is concerned. Thus one needs to consider only the sheet impedance, properly modified to take into account the presence of the composite layer, in the analysis of shielding problems.

The principal difference between graphite and screened boron-epoxy composites from a signal-transmission standpoint is that the graphite composite tends to act as a low-pass or integrating filter, while the screened boron-epoxy composite behaves as a high-pass or differentiating filter. Thus the time-domain field transmitted through a planar layer of screened composite contains a contribution proportional to the derivative of the input waveform, as a result of the inductive component of the screen impedance. For standard EMP incident signals, this leads to an early-time

response dominated by this derivative term, while the later-time response is influenced most strongly by the wire conductivity in the mesh.

The cylindrical screened-composite shell is of particular interest from an analytical standpoint because the integrating effect of the cylindrical geometry tends to cancel the differentiating effect of the wire-mesh screen. In fact, for an ideal screen with perfectly conducting wires the internal magnetic field waveform is identical, except for a reduction in amplitude, to the incident waveshape. For the screen parameters which have been considered in this report, it has been shown that the energy shielding ratio principal break frequency tends to be lower than that of a comparable graphite composite shell, especially when the screen wires are highly conductive. Thus the screened boron-epoxy composite shell can be a much better shield than a graphite composite shell as a consequence of its larger equivalent conductivity-thickness product. However, we have also noted that the equivalent conductivity-thickness product alone is not a completely valid descriptor of screened composite panels; it is only useful at low frequencies, or, equivalently, at late times. At early times the mesh size is the critical parameter, since it determines the inductance of the sheet. In fact, we have presented numerical data which indicate that overall, a screen with a smaller equivalent conductivity-thickness product can be a better shield than another with a larger product, at least with respect to the incident-field waveforms considered here. This result suggests the possibility that one might even design a screen, whose wires have a given conductivity and which possesses a given amount of metal per unit area, for optimum shielding performance against a given incident waveshape.

2. CONCLUSION

It is clear that while advanced composite laminates are not yet as effective as, say, aluminum panels in shielding against unwanted penetration of electromagnetic fields, they are nonetheless good enough to be used as aircraft or missile skins without placing an unreasonable burden on the internal shielding (conduit, cable braids, etc.). This fact, coupled with the strength and weight advantages of advanced composites, guarantees the increased future use of these materials, and points up the importance of continued study both of their intrinsic electrical properties and of the fundamental electromagnetic boundary-value problems which involve them.

Some suggested problems for future study include the following:

- (a) Integral-equation formulation of scattering problems involving hollow composite shells, using the boundary connection supermatrix[†].
- (b) Singularity Expansion Method (SEM) solutions of transient scattering/penetration problems involving hollow composite shells of separable or non-separable shape
- (c) Study of effects of imperfect panel-to-panel joints and joints between metallic and composite panels
- (d) Field penetration through apertures in composite panels
- (e) Continued study of bonded and unbonded wire meshes, including the effects of linear and nonlinear junction impedance and dielectric environments
- (f) Canonical problems involving the propagation of surface waves on wire meshes, including interactions with nearby conductors; composite waveguides.

These are only a few of the many problems which come to mind. Advanced composites provide solutions to many problems because of their great strength and light weight; but to the electromagnetic theorist and the

[†]Currently under study by the author.

engineer concerned with electromagnetic shielding, they are a source of many future challenges. It is sincerely hoped that this report will contribute to an improved understanding of the electromagnetic shielding behavior of these materials and excite the interest of other investigators who will continue to study them.

REFERENCES

- [1] "A Technology Plan for Electromagnetic Characteristics of Advanced Composites," RADC-TR-76-206, July 1976.
- [2] L. Allen, W. F. Walker, and K. R. Siarkiewicz, "An Investigation of the Electromagnetic Properties of Advanced Composite Materials," IEEE 1976 International Symposium on Electromagnetic Compatibility Record, pp. 174-179.
- [3] K. F. Casey, "EMP Penetration through Advanced Composite Skin Panels," Interaction Notes, Note 315, December 1976.
- [4] M. I. Kontorovich, "Averaged Boundary Conditions at the Surface of a Grating with Square Mesh," Radio Engineering and Electronic Physics, Vol. 8, pp. 1446-1454, 1963.
- [5] T.-K. Wu and L. L. Tsai, "Time Domain Shielding Properties of Conducting Cylindrical Shells," IEEE Transactions on Electromagnetic Compatibility, Vol. EMC-17, pp. 191-193, August 1975.
- [6] G. L. Ragan, Microwave Transmission Circuits: Dover Publications, New York, 1965, Ch. 9.
- [7] R. F. Harrington and J. R. Mautz, "An Impedance Sheet Approximation for Thin Dielectric Shells," IEEE Transactions on Antennas and Propagation, Vol. AP-23, pp. 531-534, July 1975.
- [8] J. R. Wait, "Propagation of Electromagnetic Waves along a Thin Plasma Sheet," Canadian Journal of Physics, Vol. 28, pp. 1586-1594, December 1960.
- [9] D. Schieber, "Shielding Performance of Metallic Cylinders," IEEE Transactions on Electromagnetic Compatibility, Vol. EMC-15, pp. 12-15, February 1973.
- [10] D. Schieber, "Correction to 'Shielding Performance of Metallic Cylinders'," IEEE Transactions on Electromagnetic Compatibility, Vol. EMC-15, p. 88, May 1973.
- [11] C. W. Harrison, Jr., "Comments on 'Shielding Performance of Metallic Cylinders'," IEEE Transactions on Electromagnetic Compatibility, Vol. EMC-15, p. 150, August 1973, and Author's Reply, same issue.
- [12] J. R. Wait, "Comments on 'Shielding Performance of Metallic Cylinders' and Comments by C. W. Harrison, Jr. and Reply by D. Schieber," IEEE Transactions on Electromagnetic Compatibility, Vol. EMC-16, p. 52, February 1974.

- [13] T.-K. Wu and L. L. Tsai, "Shielding Properties of Thick Conducting Cylindrical Shells," IEEE Transactions on Electromagnetic Compatibility, Vol. EMC-16, pp. 201-204, November 1974.
- [14] T.-K. Wu and L. L. Tsai, "Shielding Properties of Thick Conducting Cylindrical Shells with an Obliquely Incident Plane Wave," IEEE Transactions on Electromagnetic Compatibility, Vol. EMC-17, pp. 189-191, August 1975.
- [15] R. W. Latham and K. S. H. Lee, "Theory of Inductive Shielding," Canadian Journal of Physics, Vol. 46, pp. 1745-1752, 1968.
- [16] M. I. Kontorovich, V. Yu. Petrun'kin, N. A. Yesepkina, and M. I. Astrakhan, "The Coefficient of Reflection of a Plane Electromagnetic Wave from a Plane Wire Mesh," Radio Engineering and Electronic Physics, Vol. 7, pp. 222-231, February 1962.
- [17] M. I. Astrakhan, "Averaged Boundary Conditions on the Surface of a Lattice with Rectangular Cells," Radio Engineering and Electronic Physics, Vol. 9, pp. 1239-1241, August 1964.
- [18] M. I. Astrakhan, "Reflecting and Screening Properties of Plane Wire Grids," Telecommunications and Radio Engineering, Vol. 23, pp. 76-83, January 1968.
- [19] D. A. Hill and J. R. Wait, "Electromagnetic Scattering of an Arbitrary Plane Wave by a Wire Mesh with Bonded Junctions," Sensor and Simulation Notes, Note 231, Section II, 10 June 1977.
- [20] R. W. Latham, "Small Holes in Cable Shields," Interaction Notes, Note IN 118, September 1972.

NOTE 342

**FIELDS IN A RECTANGULAR CAVITY
EXCITED BY A PLANE WAVE ON AN ELLIPTICAL APERTURE**

by

**Harvey J. Fletcher
Alan K. Harrison**

Eyring Research Institute

June 1978

FIELDS IN A RECTANGULAR CAVITY
EXCITED BY A PLANE WAVE ON AN
ELLIPTICAL APERTURE

ABSTRACT

Explicit expressions are developed for the fields in a rectangular cavity produced by a plane wave incident on an arbitrarily oriented and positioned elliptical aperture of the cavity. Only low frequency waves are considered so that a quasi-static approach can be used. Cavity excitation at frequencies near resonance is examined. Fourier techniques are used to generalize these results to electromagnetic pulse input.

TABLE OF CONTENTS

<u>Section</u>		<u>Page</u>
1.0	INTRODUCTION	342-3
2.0	ASSUMPTIONS	342-4
3.0	THE ELECTRIC FIELD DUE TO AN ELLIPTIC APERTURE	342-10
4.0	THE MAGNETIC FIELD DUE TO AN ELLIPTIC APERTURE	342-15
5.0	TABLE OF FIELDS FOR SPECIAL CASES	342-18
5.1	Electric and Magnetic Potentials	342-20
5.2	Electric and Magnetic Fields	342-20
5.3	Fields on Aperture	342-25
5.4	Fields on Screen	342-26
5.5	Fields on Axis	342-31
5.6	Dipole Equivalents at Large Distances	342-32
5.7	Far Fields	342-32
6.0	GENERAL SHAPE CAVITY	342-34
7.0	THE ELECTRIC FIELD OF A RECTANGULAR CAVITY	342-36
8.0	THE MAGNETIC FIELD OF A RECTANGULAR CAVITY	342-44
9.0	GENERAL ORIENTATION OF AN ELLIPTIC APERATURE	342-48
10.0	CAVITY EXCITATION NEAR RESONANCE	342-54
11.0	PULSE INPUT	342-62
12.0	REFERENCES	342-68
13.0	APPENDIX	342-69
13.1	Ellipsoidal Coordinates	342-69
13.2	Oblate Spheroidal Coordinates	342-74
13.3	Integrals	342-75
13.4	Laplace Equation	342-77
13.5	Derivation of Boundary Conditions	342-80
13.6	Derivation of Coefficients	342-81

1.0 INTRODUCTION

The problem of electromagnetic penetration of cavities has been discussed by many authors. L-W. Chen⁽¹⁾ has discussed the penetration of a rectangular cavity through a small elliptical aperture using a quasi-static approach. D.K. Cheng and C.A. Chen⁽¹¹⁾ have treated this problem for the case of an electromagnetic pulse incident on an aperture of arbitrary size and shape, but explicit expressions for the fields were not obtained. Other investigators have examined various kinds of nonrectangular or general cavities, for which the reader is referred to the bibliography of C.M. Butler et al.⁽¹²⁾

This paper includes an extension of L-W. Chen's work to give explicit expressions for the fields in a rectangular cavity as infinite series of the natural modes. The elliptical aperture is taken to be small so that the quasi-static approach may be used, but a dipole approximation is not used at the aperture. The position and orientation of the aperture are arbitrary. These results are extended to cavities with non-perfectly-conducting walls.

Fourier transform techniques are used to find explicitly the response of a perfectly conducting cavity to a plane EMP. The position and orientation of the aperture are again arbitrary.

2.0 ASSUMPTIONS

The fields in free space satisfy the relations

$$\nabla \times \vec{E} = -\mu_0 \frac{\partial \vec{H}}{\partial t}$$

$$\nabla \times \vec{H} = \epsilon_0 \frac{\partial \vec{E}}{\partial t}$$

$$\nabla \cdot \vec{E} = 0$$

$$\nabla \cdot \vec{H} = 0$$

where \vec{E} is the electric field and \vec{H} is the magnetic field and ϵ_0 and μ_0 are constants.

By taking the curl of these equations, one obtains

$$\nabla^2 \vec{E} = \frac{1}{c^2} \frac{\partial^2 \vec{E}}{\partial t^2}$$

and

$$\nabla^2 \vec{H} = \frac{1}{c^2} \frac{\partial^2 \vec{H}}{\partial t^2}$$

If one assumes that $\vec{E} = \vec{E}_0(x, y, z)e^{j\omega t}$, then $\nabla^2 \vec{E} = -k^2 \vec{E}$ where $k = \frac{\omega}{c}$. If the frequency is low, then the $k^2 \vec{E}$ term can be neglected and \vec{E} satisfies the Laplace Equation. This is equivalent

to saying $\nabla \times \vec{E} = 0$ or $\vec{E} = -\nabla \phi$ and similarly $\vec{H} = -\nabla \phi^*$ where $\nabla^2 \phi = \nabla^2 \phi^* = 0$.

Consider a plane wave incident on an aperture of a cavity as in Figure 2.1.

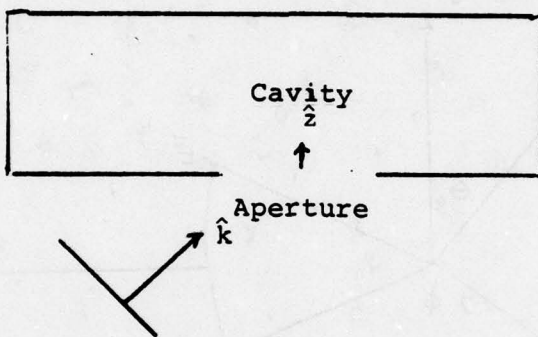


FIGURE 2.1 Incident Wave

Let the incident wave have the orientation with respect to the x, y , and z axes given by Euler angles⁽⁵⁾

$$\begin{pmatrix} \hat{E}^i \\ \hat{H}^i \\ \hat{k} \end{pmatrix} = \begin{pmatrix} C\psi C\phi - C\theta S\phi S\psi & C\psi S\phi + C\theta C\phi S\psi & S\psi S\theta \\ -S\psi C\phi - C\theta S\phi C\psi & -S\psi S\phi + C\theta C\phi C\psi & C\psi S\theta \\ S\theta S\psi & -S\theta C\psi & C\theta \end{pmatrix} \begin{pmatrix} \hat{x} \\ \hat{y} \\ \hat{z} \end{pmatrix}$$

where \hat{z} is the unit vector perpendicular to a planar aperture of zero thickness. Let \hat{x} and \hat{y} be perpendicular to \hat{z} and in the plane of the aperture. ϕ represents a rotation of the x, y, z axes about the z axis to form x', y', z axis. θ represents a subsequent rotation about the x' axis to form x'', y'', z' axes. Then,

ψ represents a rotation about z' to obtain x'', y'', z' axes which are in the direction of \hat{E}^i , \hat{H}^i , \hat{k} as in Figure 2.2.

\hat{k} is a unit vector in the direction of the Poynting vector and must not be confused with \hat{z} . \hat{E}^i is the incident electric vector and \hat{H}^i is the incident magnetic vector.

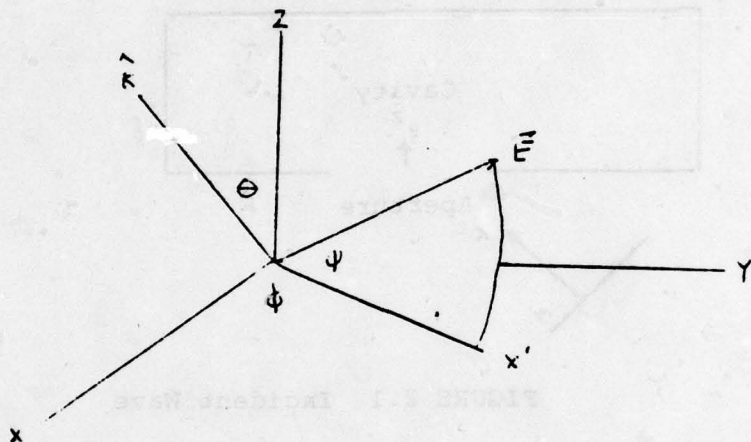


FIGURE 2.2 Euler Angles

From these definitions it is apparent that θ is the angle between the Poynting vector and the z axis. ψ is the angle between the intersection of the wave plane with the xy plane and \hat{E} . ϕ is the angle between the x axis and the intersection of the xy plane with the wave plane. Thus, θ and ϕ give the direction of the wave and ψ is the polarization angle. The incident fields can be expressed as

$$\hat{E}^i = E_0^i [\hat{x} (C\psi C\theta - C\theta S\phi S\psi) + \hat{y} (C\psi S\phi + C\theta C\phi S\psi) + \hat{z} S\psi S\theta]$$

$$f(t - \frac{\hat{k} \cdot \vec{r}}{c_0})$$

$$\hat{H}^i = H_0^i [\hat{x}(-S\psi C\phi - C\theta S\phi C\psi) + \hat{y}(-S\psi S\phi + C\theta C\phi C\psi) + \hat{z} C\psi S\theta]$$

$$f(t - \frac{\vec{k} \cdot \vec{r}}{c_0})$$

Where S, C stand for sine and cosine and c_0 is the velocity of light ($c_0 = \frac{1}{\sqrt{\epsilon_0 \mu_0}}$). A pulse (EMP) would be a special case of the time factor $f(t)$.

If we first solve the problem with $f(t) = e^{j\omega t}$, we can find the general result of EMP by taking the Fourier Transform.

If \hat{k} , the unit vector in the direction of the incident wave, is equal to $k_1 \hat{x} + k_2 \hat{y} + k_3 \hat{z}$, then the unit vector in the direction of the reflected wave must be $k_1 \hat{x} + k_2 \hat{y} - k_3 \hat{z}$.

In order that the total wave have the proper boundary conditions at a conducting surface, the reflecting electric field must be of the form

$$\hat{E}^r = E_0^i [-\hat{x}(C\psi C\theta - C\theta S\phi S\psi) - \hat{y}(C\psi S\phi + C\theta C\phi S\psi) + \hat{z} S\psi S\theta]$$

$$f(t - k_1 x - k_2 y + k_3 z)$$

where $k_1 = S\theta S\phi$, $k_2 = -S\theta C\psi$, and $k_3 = C\theta$

$$\vec{E}^0 = \vec{E}^i + \vec{E}^r$$

$$\vec{H}^0 = \vec{H}^i + \vec{H}^r$$

These satisfy the boundary conditions

$$\hat{z} \times \vec{E}^0 = 0, \frac{\partial}{\partial z} \hat{z} \cdot \vec{E}^0 = 0, \hat{z} \cdot \vec{H}^0 = 0, \hat{z} \cdot \vec{E}^0 = 2\hat{z} \cdot \vec{E}^i \text{ at } z=0$$

where

$$\vec{H}^i = \frac{1}{Z_0} \hat{x} \times \vec{E}^i \quad \text{and} \quad \vec{H}^r = \frac{1}{Z_0} \hat{k}^r \times \vec{E}^r$$

$$\vec{E}^i = -Z_0 \hat{k}^i \times \vec{H}^i \quad \text{and} \quad \vec{E}^r = -Z_0 \hat{k}^r \times \vec{H}^r$$

where $Z_0 = \sqrt{\frac{\mu_0}{\epsilon_0}}$ is the free wave impedance. Thus, the fields in the absence of an aperture are

$$\vec{E}^0 = \hat{z} E_z^0$$

$$\vec{H}^0 = \hat{x} H_x^0 + \hat{y} H_y^0$$

E_z^0 , H_x^0 , and H_y^0 are constants given by

$$E_z^0 = 2E_0^i S\psi C\theta$$

$$H_x^0 = 2H_0^i (-S\psi C\phi - C\theta S\phi C\psi)$$

$$H_y^0 = 2H_0^i (-S\psi S\phi + C\theta C\phi C\psi)$$

In these and all subsequent equations up to and including Section 10.0, the time dependence $e^{j\omega t}$ is implicitly understood. Let us seek a solution for a sinusoidal input which has a wavelength which is large compared to the diameter of the aperture. This can be approximated by letting $f(t) = 1$. In other words, the incident wave would produce a constant field across the aperture. We neglect also the departure from a plane wave due to the front face of the cavity being non-infinite. We also have assumed that the outside surface of the cavity is a perfect conductor. We cannot assume the inside is a perfect conductor or there would be infinite resonances when the incoming wave had a frequency equal to one of the natural frequencies of the cavity.

Let us assume the aperture thickness is infinitesimally small and that the field at the aperture is the same as that produced in an infinite sheet with the same shape aperture. The presence of a large cavity is assumed not to affect the field very much at the aperture.

3.2 THE ELECTRIC FIELD DUE TO AN ELLIPTIC APERTURE

3.0 THE ELECTRIC FIELD DUE TO AN ELLIPTIC APERTURE

To find the fields in the aperture we find the fields in a similar shape aperture in an infinite conducting screen and assume that this is a good approximation. We can thus find the electric potential which satisfies

$\nabla^2 \phi = 0$ indicates that ϕ is a scalar function.

$$\vec{E} = -\nabla \phi$$

$\vec{E} = \vec{E}_0 = 2E_0^i S\psi S\theta \hat{z}$ at large distances from the aperture
on the incident side

$\vec{E} = 0$ at large distances from the aperture on the shadow side

$\hat{n} \times \vec{E} = 0$ on the inside and outside of the screen

\hat{E} and $\frac{\partial \hat{E}}{\partial Z}$ are continuous everywhere particularly at the aperture

Ellipsoidal coordinates are the natural coordinates for this problem (see appendix).

The potential if no aperture were present would be

$$\phi_0 \equiv -E^0 z = -\frac{\sqrt{\xi n \zeta}}{ab} E_z^0 \operatorname{sign} z$$

Assume the general potential to be

$$\phi = \phi_0 F(\xi)$$

Substituting this into Laplace Equation one gets that $F(\xi)$ must satisfy

$$\frac{d^2 F}{d\xi^2} + \frac{dF}{d\xi} \ln (\xi R_\xi) = 0$$

or

$$F(\xi) = A \int_{\xi}^{\infty} \frac{d\xi}{\xi^{3/2} (\xi+a^2)^{1/2} (\xi+b^2)^{1/2}} + B$$

Therefore

$$\phi_1 (z < 0) = \phi_0^- [A \int_{\xi}^{\infty} + B]$$

$$\phi_2 (z > 0) = \phi_0^+ [C \int_{\xi}^{\infty} + D]$$

with the boundary conditions

$$\phi_1 (\xi = \infty) = \phi_0^-$$

$$\phi_2 (\xi = \infty) = 0$$

$$\lim_{\xi \rightarrow 0} \phi_1 = \lim_{\xi \rightarrow 0} \phi_2$$

$$\lim_{\xi \rightarrow 0} \frac{\partial \phi_1}{\partial z} = \lim_{\xi \rightarrow 0} \frac{\partial \phi_2}{\partial z}$$

The condition that tangential \vec{E} is zero on the screen is automatically satisfied.

The other boundary conditions are satisfied if $D=0$, $B=1$

$$A = -C = \frac{1}{2 \lim_{\xi \rightarrow 0} \frac{(2z^2(\xi+a^2)^{1/2}(\xi+b^2)^{1/2}}{(\xi-a)(\xi-z) \xi^{3/2}} - \frac{2(\xi+b^2)^{1/2}}{\xi^{1/2} b^2 (\xi+a^2)^{1/2}}}$$

$$+ \frac{2E(a, e)}{ab^2}$$

$$a = \cot^{-1} \frac{\xi^{1/2}}{a}$$

$$e = \sqrt{1 - b^2/a^2}$$

E is the elliptic integral of the first kind. (See appendix for integrals.) Care must be taken since this is an indeterminate form. After taking the limit, we obtain

$$A = \frac{ab^2}{4E(\frac{\pi}{2}, e)}$$

$$\phi_2 = \frac{ab^2 E_z^0 z}{4E(\frac{\pi}{2}, e)} \int_{\xi}^{\infty} \frac{d\xi}{\xi^{3/2} (\xi+a^2)^{1/2} (\xi+b^2)^{1/2}}$$

$$= \frac{ab^2 E_z^0 z}{2E(\frac{\pi}{2}, e)} \left[-\frac{E(\alpha, e)}{ab^2} + \frac{(\xi+b^2)^{1/2}}{b^2 \xi^{1/2} (\xi+a^2)^{1/2}} \right]$$

The electric fields on the shadow side can be found from

$$\vec{E} = -\nabla\phi_2$$

If rectangular coordinates are used for the ∇ operator, then ξ can be thought of as an implicit function of x, y , and z . $\xi_x \equiv \frac{\partial \xi}{\partial x}$, $\xi_y \equiv \frac{\partial \xi}{\partial y}$, $\xi_z \equiv \frac{\partial \xi}{\partial z}$ can be found in the appendix.

These are obtained by implicit differentiation of the expressions $x = x(\xi, \eta, \zeta)$, $y = y(\xi, \eta, \zeta)$, and $z = z(\xi, \eta, \zeta)$. These give for \vec{E}

$$E_x = \frac{2E_z^0 A x z (\xi+b^2)^{1/2}}{\xi^{1/2} (\xi+a^2)^{1/2} (\xi-\zeta) (\xi-\eta)}$$

$$E_y = \frac{2E_z^0 A y z (\xi+a^2)^{1/2}}{\xi^{1/2} (\xi+b^2)^{1/2} (\xi-\zeta) (\xi-\eta)}$$

$$E_z = \frac{2E_z^0 A}{a^2 b^2} \left[a E(\alpha, e) - \frac{\xi^{1/2} (\xi+b^2)^{1/2} (a^2 \xi - a^2 \eta - a^2 \zeta - \eta \zeta)}{(\xi-\eta) (\xi-\zeta) (\xi+a^2)^{1/2}} \right]$$

where

$$A = \frac{ab^2}{4E(\frac{\pi}{2}, e)}, \quad e = \sqrt{1 - \frac{b^2}{a^2}}, \quad \alpha = \cot^{-1} \frac{\xi^{1/2}}{a}$$

Special values of these fields are given in Section 5.0.

The fields on the incident side of the screen are given by symmetry conditions of Bethe: (10)

$$E_x(x, y, z) = E_x^0(x, y, z)$$

$$E_y(x, y, -z) = E_y^0(x, y, z)$$

$$E_z(x, y, -z) = E_z^0 - H_z(x, y, z)$$

$$H_x(x, y, -z) = H_x^0 - H_x(x, y, z)$$

$$H_y(x, y, -z) = H_y^0 - H_y(x, y, z)$$

$$H_z(x, y, -z) = H_z^0(x, y, z)$$

4.0 THE MAGNETIC FIELD DUE TO AN ELLIPTIC APERTURE

In a similar fashion, the magnetic field is given by $\vec{H} = -\nabla\phi^*$
 where $\nabla^2\phi^* = 0$. As $z \rightarrow -\infty$, $\phi^* \rightarrow -H_x^0 x - H_y^0 y$ where as before,

$$H_x^0 = 2H_0^i (-S\psi C\phi - C\theta S\phi C\psi)$$

$$H_y^0 = 2H_0^i (-S\psi S\phi + C\theta C\phi C\psi)$$

Let us treat each component independently.

$$\phi_0^* = -H_x^0 x = -\left[\frac{(\xi+a^2)(\eta+a^2)(\zeta+a^2)}{a^2(a^2-b^2)}\right]^{1/2} H_x^0 \text{ Sign } x$$

$$\text{Let } \phi_0^* = \phi_0^* F(\xi)$$

After substituting this in Laplace Equation (see appendix) and solving for $F(\xi)$, we obtain

$$F(\xi) = A \int_{\xi}^{\infty} \frac{d\xi}{\xi^{1/2} (\xi+a^2)^{3/2} (\xi+b^2)^{1/2}} + B$$

$$\phi_1^*(z \leq 0) = (A \int_{\xi}^{\infty} + B) \phi_0^*$$

$$\phi_2^*(z \geq 0) = (C \int_{\xi}^{\infty} + D) \phi_0^*$$

The boundary conditions are

$$\phi_1^*(\xi=\infty) = \phi_0^*$$

$$\phi_2^*(\xi=\infty) = 0$$

$$\phi_1^* = \phi_2^* \quad \text{at } \xi=0$$

$$\lim_{z \rightarrow 0^-} \frac{\partial \phi_1^*}{\partial z} = \lim_{z \rightarrow 0^+} \frac{\partial \phi_2^*}{\partial z} \quad \text{at } \xi=0$$

These equations determine the constants

$$B=1, D=0, -A=C = \frac{1}{2 \int_0^\infty \frac{d\xi}{\xi^{1/2} (\xi+a^2)^{3/2} (\xi+b^2)^{1/2}}}$$

These integrals are given in the appendix. A similar procedure is used to determine the components of \vec{H} due to H_y^0 . If we add the fields to H_x^0 and H_y^0 , we get the total magnetic field as

$$H_x^0 = \frac{H_x^0}{2} [F(\frac{\pi}{2}, e) - E(\frac{\pi}{2}, e)]^{-1} [F(a, e) - E(a, e)]$$

$$- \frac{\xi^{1/2} (\xi+b^2)^{1/2} (\eta+a^2)^{1/2} (\zeta+a^2)^{1/2}}{a(\xi-\zeta)(\xi-\eta)(\xi+a^2)^{1/2}}$$

$$- \frac{H_y^0 ab^2 (a^2-b^2) xy \xi^{1/2}}{2(\xi-\zeta)(\xi-\eta)(\xi+a^2)^{1/2} (\xi+b^2)^{1/2} [a^2 E(\frac{\pi}{2}, e) - b^2 F(\frac{\pi}{2}, e)]}$$

$$H_y = \frac{-H_x^0 a^3 e^2 xy \xi^{1/2}}{2(\xi-\eta)(\xi-\zeta) [F(\frac{\pi}{2}, e) - E(\frac{\pi}{2}, e)] (\xi+a^2)^{1/2} (\xi+b^2)^{1/2}}$$

$$- \frac{H_y^0 ab^2(a^2-b^2) y^2 \xi^{1/2} (\xi+a^2)^{1/2}}{2(\xi-\zeta)(\xi-\eta)(\xi+b^2)^{3/2} [a^2 E(\frac{\pi}{2}, e) - b^2 F(\frac{\pi}{2}, e)]}$$

$$+ \frac{H_y^0}{2} \frac{[a^2 E(\alpha, e) - b^2 F(\alpha, e) - \frac{a \xi^{1/2} (a^2-b^2)}{(\xi+a^2)^{1/2} (\xi+b^2)^{1/2}}]}{[a^2 E(\frac{\pi}{2}, e) - b^2 F(\frac{\pi}{2}, e)]}$$

$$H_z = \frac{-H_x^0 a^3 e^2 xz (\xi+b^2)^{1/2}}{2\xi^{1/2} (\xi-\eta)(\xi-\zeta) (\xi+a^2)^{1/2} [F(\frac{\pi}{2}, e) - E(\frac{\pi}{2}, e)]}$$

$$- \frac{H_y^0 ab^2(a^2-b^2) yz (\xi+a^2)^{1/2}}{2\xi^{1/2} (\xi-\eta)(\xi-\zeta)(\xi+b^2)^{1/2} [a^2 E(\frac{\pi}{2}, e) - b^2 F(\frac{\pi}{2}, e)]}$$

where $\alpha = \cot^{-1} \frac{\xi^{1/2}}{a}$, $e = \sqrt{1 - b^2/a^2}$ and F and E are elliptical integrals of the first and second kind.

5.0 TABLE OF FIELDS FOR SPECIAL CASES

All expressions in this table are for the shadow ($z \geq 0$) side of the screen. Definitions are:

$$\alpha = \cot^{-1} \frac{\sqrt{\xi}}{a}$$

$$e = \sqrt{1 - b^2/a^2}$$

$F(\phi, k)$ and $E(\phi, k)$ are elliptic integrals of the first and second kind, respectively

$\lim_{b \rightarrow a} \xi = \xi_{ob}$ and $\lim_{b \rightarrow a} \eta = \eta_{ob}$, where the subscripts refer to the oblate spheroidal coordinates used with a circular aperture. Thus, we may consider these two oblate spheroidal coordinates as special cases of the corresponding ellipsoidal coordinates when $b=a$. For this reason, no distinction is made between ξ and ξ_{ob} , η and η_{ob} in the table.

In the circular aperture case, it has sometimes been useful to express formulas in terms of

$$\hat{\rho} = \hat{x}\hat{x} + \hat{y}\hat{y}$$

$$\rho = \sqrt{x^2 + y^2} = \sqrt{\frac{(\xi + a^2)(\eta + a^2)}{a^2}}$$

and

$$\hat{\rho} = \frac{\hat{\rho}}{\rho}$$

342-19

EMP 3-38

See appendix for values of ξ , η and ζ on the aperture, screen
and axis and at large distances.

CIRCLE5.1 ELECTRIC AND MAGNETIC POTENTIALS

$$\Phi_E = - \frac{E_z^0 \sqrt{-\eta}}{\pi} \left(\frac{a\sqrt{\xi}}{a} - 1 \right)$$

$$\Phi_M = \frac{\sqrt{(\xi+a^2)(\eta+a^2)}}{\pi a} \left(\alpha - \frac{a\sqrt{\xi}}{\xi+a^2} \right) (H_x^0 \cos \phi + H_y^0 \sin \phi)$$

5.2 ELECTRIC AND MAGNETIC FIELDS

$$\vec{E} = \frac{E_z^0 a^2 \sqrt{-\eta} \hat{p}}{\pi (\xi-\eta) (\xi+a^2)} + \frac{\vec{E}^0}{\pi} \left(\alpha - \frac{a\sqrt{\xi}}{\xi-\eta} \right)$$

or

$$E_x = \frac{E_z^0 a^2 \sqrt{-\eta} x}{\pi (\xi-\eta) (\xi+a^2)}$$

$$E_y = \frac{E_z^0 a^2 \sqrt{-\eta} y}{\pi (\xi-\eta) (\xi+a^2)}$$

ELLIPSE5.1 ELECTRIC AND MAGNETIC POTENTIALS

$$\phi_E = \frac{E_z^0}{2E(\frac{\pi}{2}, e)} [-E(\alpha, e) + \frac{a\sqrt{\xi+b^2}}{\sqrt{\xi(\xi+a^2)}}]$$

$$\phi_M = \frac{xH_x^0}{2} \frac{F(\alpha, e) - E(\alpha, e)}{F(\frac{\pi}{2}, e) - E(\frac{\pi}{2}, e)} - \frac{H_y^0 a^3 e^2 y}{2[a^2 E(\frac{\pi}{2}, e) - b^2 F(\frac{\pi}{2}, e)]}$$

$$\cdot \frac{[a^2 E(\alpha, e) - b^2 F(\alpha, e)]}{a^3 e^2} - \frac{\sqrt{\frac{\xi}{(\xi+a^2)(\xi+b^2)}}}{}$$

5.2 ELECTRIC AND MAGNETIC FIELDS

$$E_x = \frac{E_z^0 ab^2 xz \sqrt{\xi+b^2}}{2(\xi-\eta)(\xi-\zeta)\sqrt{\xi(\xi+a^2)} E(\frac{\pi}{2}, e)}$$

$$E_y = \frac{E_z^0 ab^2 yz \sqrt{\xi+a^2}}{2(\xi-\eta)(\xi-\zeta)\sqrt{\xi(\xi+b^2)} E(\frac{\pi}{2}, e)}$$

$$E_z = \frac{E^0}{\pi} z \left(\alpha - \frac{a\sqrt{\xi}}{\xi-\eta} \right)$$

$$\vec{H} = \frac{\vec{H}^0}{\pi} \left(\alpha - \frac{a\sqrt{\xi}}{\xi+a^2} \right) - \frac{2a^2 \vec{H}^0 \cdot \vec{p} [a\sqrt{\xi} \vec{p} + (\xi+a^2)\sqrt{-\eta} \hat{z}]}{\pi (\xi+a^2)^2 (\xi-\eta)}$$

or

$$H_x = \frac{H_x^0}{\pi} \left(\alpha - \frac{a\sqrt{\xi}}{\xi+a^2} \right) - \frac{2a(\eta+a^2)\sqrt{\xi} \cos \phi}{\pi (\xi+a^2)(\xi-\eta)} (H_x^0 \cos \phi + H_y^0 \sin \phi)$$

$$H_y = \frac{H_y^0}{\pi} \left(\alpha - \frac{a\sqrt{\xi}}{\xi+a^2} \right) - \frac{2a\sqrt{\xi}(\eta+a^2) \sin \phi}{\pi (\xi+a^2)(\xi-\eta)} (H_x^0 \cos \phi + H_y^0 \sin \phi)$$

$$E_z = \frac{E_z^0}{2E(\frac{\pi}{2}, e)} [E(\alpha, e) - \frac{(a^2\xi - a^2\eta - a^2\zeta - \eta\zeta\sqrt{\xi(\xi+b^2)}}{a(\xi-\eta)(\xi-\zeta)\sqrt{\xi+a^2}}]$$

$$H_x = \frac{H_x^0}{2} [F(\frac{\pi}{2}, e) - E(\frac{\pi}{2}, e)]^{-1} [F(\alpha, e) - E(\alpha, e) - \frac{(\eta+a^2)(\xi+a^2)\sqrt{\xi(\xi+b^2)}}{a(\xi-\eta)(\xi-\zeta)\sqrt{\xi+a^2}}]$$

$$- \frac{H_y^0 a^3 b^2 e^2 xy\sqrt{\xi}}{2(\xi-\eta)(\xi-\zeta)\sqrt{(\xi+a^2)(\xi+b^2)}[a^2 E(\frac{\pi}{2}, e) - b^2 F(\frac{\pi}{2}, e)]}$$

$$H_y = - \frac{H_x^0 a^3 e^2 xy\sqrt{\xi}}{2(\xi-\eta)(\xi-\zeta)\sqrt{(\xi+a^2)(\xi+b^2)}[F(\frac{\pi}{2}, e) - E(\frac{\pi}{2}, e)]}$$

$$- \frac{H_y^0 a^3 b^2 e^2 y^2 \sqrt{\xi(\xi+a^2)}}{2(\xi-\eta)(\xi-\zeta)\sqrt{(\xi+b^2)}^3 [a^2 E(\frac{\pi}{2}, e) - b^2 F(\frac{\pi}{2}, e)]}$$

$$+ \frac{H_y^0}{2} [a^2 E(\frac{\pi}{2}, e) - b^2 F(\frac{\pi}{2}, e)]^{-1} [a^2 E(\alpha, e) - b^2 F(\alpha, e)]$$

$$- \frac{a^3 e^2 \sqrt{\xi}}{\sqrt{(\xi+a^2)(\xi+b^2)}}$$

$$H_z = - \frac{2a^2 \sqrt{-\eta} (xH_x^0 + yH_y^0)}{\pi(\xi+a^2)(\xi-\eta)}$$

5.3 FIELDS ON APERTURE

$$\vec{E} = \frac{\vec{E}^0}{2} + \frac{\vec{E}_z^0}{\pi\sqrt{a^2-p^2}}$$

or

$$E_x = \frac{x E_z^0}{\pi\sqrt{a^2-x^2-y^2}}$$

$$E_y = \frac{y E_z^0}{\pi\sqrt{a^2-x^2-y^2}}$$

$$E_z = \frac{E_z^0}{2}$$

$$H_z = - \frac{H_x^0 a^3 e^2 x z \sqrt{\xi + b^2}}{2(\xi - \eta)(\xi - \zeta) \sqrt{\xi(\xi + a^2)} [F(\frac{\pi}{2}, e) - E(\frac{\pi}{2}, e)]}$$

$$- \frac{H_y^0 a^3 b^2 e^2 y z \sqrt{\xi + a^2}}{2(\xi - \eta)(\xi - \zeta) \sqrt{\xi(\xi + b^2)} [a^2 E(\frac{\pi}{2}, e) - b^2 F(\frac{\pi}{2}, e)]}$$

5.3 FIELDS ON APERTURE

$$E_x = \frac{E_z^0 b x}{2a^2 E(\frac{\pi}{2}, e) \sqrt{1 - x^2/a^2 - y^2/b^2}}$$

$$E_y = \frac{E_z^0 y}{2b E(\frac{\pi}{2}, e) \sqrt{1 - x^2/a^2 - y^2/b^2}}$$

$$E_z = \frac{E_z^0}{2}$$

$$\vec{H} = \frac{\vec{H}^0}{2} - \frac{2(\vec{H}^0 \cdot \hat{r})}{\pi\sqrt{a^2 - r^2}} \hat{z}$$

or

$$H_x = \frac{H_x^0}{2}$$

$$H_y = \frac{H_y^0}{2}$$

$$H_z = - \frac{2(xH_x^0 + yH_y^0)}{\pi\sqrt{a^2 - x^2 - y^2}}$$

5.4 FIELDS ON SCREEN

$$\vec{E} = \frac{\vec{E}^0}{\pi} (\cot^{-1} \sqrt{\rho^2/a^2 - 1}) - \frac{1}{\rho^2/a^2 - 1} = \frac{\vec{E}^0}{\pi} \left(\alpha - \frac{a}{\sqrt{\xi}} \right)$$

$$H_x = \frac{H_x^0}{2}$$

$$H_y = \frac{H_y^0}{2}$$

$$H_z = - \frac{H_x^0 e^2 x}{2b[F(\frac{\pi}{2}, e) - E(\frac{\pi}{2}, e)]\sqrt{1 - x^2/a^2 - y^2/b^2}}$$

$$- \frac{H_y^0 e^2 ya^2}{2b[a^2 E(\frac{\pi}{2}, e) - b^2 F(\frac{\pi}{2}, e)]\sqrt{1 - x^2/a^2 - y^2/b^2}}$$

5.4 FIELDS ON SCREEN

$$\bar{E} = \frac{\bar{E}^0}{2E(\frac{\pi}{2}, e)} [E(\alpha, e) - \frac{a\sqrt{\xi+b^2}}{\sqrt{\xi(\xi+a^2)}}]$$

$$\hat{H} = \frac{\hat{H}^0}{\pi} \left(\cot^{-1} \sqrt{\rho^2/a^2 - 1} - \frac{\sqrt{\rho^2/a^2 - 1}}{\rho^2/a^2} \right) - \frac{2(\hat{H}^0 \cdot \hat{\rho}) \hat{\rho}}{\pi (\rho^2/a^2) \sqrt{\rho^2/a^2 - 1}}$$

$$= \frac{\hat{H}^0}{\pi} \left(\alpha - \frac{a\sqrt{\xi}}{\xi+a^2} \right) - \frac{2a^3 (\hat{H}^0 \cdot \hat{\rho}) \hat{\rho}}{\pi (\xi+a^2) \sqrt{\xi}}$$

or

$$H_x = \frac{H_x^0}{\pi} \left(\alpha - \frac{a\sqrt{\xi}}{\xi+a^2} \right) - \frac{2a^3 x (x H_x^0 + y H_y^0)}{\pi (\xi+a^2)^2 \sqrt{\xi}}$$

$$H_y = \frac{H_y^0}{\pi} \left(\alpha - \frac{a\sqrt{\xi}}{\xi+a^2} \right) - \frac{2a^3 y (x H_x^0 + y H_y^0)}{\pi (\xi+a^2)^2 \sqrt{\xi}}$$

$$H_x = \frac{H_x^0}{2} [F(\frac{\pi}{2}, e) - E(\frac{\pi}{2}, e)]^{-1} [F(\alpha, e) - E(\alpha, e) - \frac{a(\xi+a^2)\sqrt{\xi+b^2}}{(\xi-\zeta)\sqrt{\xi(\xi+a^2)}}]$$

$$- \frac{H_y^0 a^3 b^2 e^2 xy}{4(\xi-\zeta)\sqrt{\xi(\xi+a^2)(\xi+b^2)} [a^2 E(\frac{\pi}{2}, e) - b^2 F(\frac{\pi}{2}, e)]}$$

$$H_y = - \frac{H_x^0 a^3 e^2 xy}{2(\xi-\zeta)\sqrt{\xi(\xi+a^2)(\xi+b^2)} [F(\frac{\pi}{2}, e) - E(\frac{\pi}{2}, e)]}$$

$$- \frac{H_y^0 a^3 b^2 e^2 y^2 \sqrt{\xi+a^2}}{2(\xi-\zeta)\sqrt{\xi(\xi+b^2)^3} [a^2 E(\frac{\pi}{2}, e) - b^2 F(\frac{\pi}{2}, e)]}$$

$$+ \frac{H_y^0}{2} [a^2 E(\frac{\pi}{2}, e) - b^2 F(\frac{\pi}{2}, e)]^{-1} [a^2 E(\alpha, e) - b^2 F(\alpha, e)]$$

$$- \frac{a^3 e^2 \sqrt{\xi}}{\sqrt{(\xi+a^2)(\xi+b^2)}}]$$

$$H_z = 0$$

5.5 FIELDS ON AXIS

$$\vec{E} = \frac{\vec{E}^0}{\pi} \left(\cot^{-1} \frac{z}{a} - \frac{az}{a^2 + z^2} \right) = \frac{\vec{E}^0}{\pi} \left(\alpha - \frac{az}{\xi + a^2} \right)$$

$$\vec{H} = \frac{\vec{H}^0}{\pi} \left(\cot^{-1} \frac{z}{a} - \frac{az}{a^2 + z^2} \right) = \frac{\vec{H}^0}{\pi} \left(\alpha - \frac{az}{\xi + a^2} \right)$$

$$H_z = 0$$

5.5 FIELDS ON AXIS

$$\vec{E} = \frac{\vec{E}^0}{2E(\frac{\pi}{2}, e)} [E(\alpha, e) - \frac{az}{\sqrt{(z^2+a^2)(z^2+b^2)}}$$

$$H_x = \frac{H_x^0}{2} \frac{F(\alpha, e) - E(\alpha, e)}{F(\frac{\pi}{2}, e) - E(\frac{\pi}{2}, e)}$$

$$H_y = \frac{H_x^0}{2} [a^2 E(\frac{\pi}{2}, e) - b^2 F(\frac{\pi}{2}, e)]^{-1} [a^2 E(\alpha, e) - b^2 F(\alpha, e)$$

$$- \frac{a^3 e^2 z}{\sqrt{(z^2+a^2)(z^2+b^2)}}]$$

$$H_z = 0$$

5.6 DIPOLE EQUIVALENTS AT LARGE DISTANCES

$$\hat{P}_E = \frac{4}{3}\epsilon_0 a^3 \hat{E}^0$$

$$\hat{P}_M = -\frac{8}{3}a^3 \hat{H}^0$$

$$\hat{P}_M = -\frac{2\pi\epsilon_0 ab^2 E^0}{3E(\frac{\pi}{2}, e)}$$

$$\hat{P}_M = -\frac{2\pi H_x^0 a^3 e^2}{3[F(\frac{\pi}{2}, e) - E(\frac{\pi}{2}, e)]}$$

$$\hat{H} = -\frac{2\pi H_y^0 a^3 b^2 e^2}{3[a^2 E(\frac{\pi}{2}, e) - b^2 F(\frac{\pi}{2}, e)]}$$

For either aperture the far fields are given by:

$$\hat{E} = \frac{\hat{3r}(\hat{r} \cdot \hat{P}_E) - \hat{P}_E}{4\pi\epsilon_0 r^3}$$

$$\hat{H} = \frac{\hat{3r}(\hat{r} \cdot \hat{P}_M) - \hat{P}_M}{4\pi r^3}$$

5.7 FAR FIELDS

$$E_r = \frac{2a^3 E_z^0 \cos \theta}{3\pi r^3}$$

$$E_\theta = \frac{a^3 E_z^0 \sin \theta}{3\pi r^3}$$

$$E_r = \frac{ab^2 E_z^0 \cos \theta}{3r^3 E(\frac{\pi}{2}, e)}$$

$$E_\theta = \frac{ab^2 E_z^0 \sin \theta}{6r^3 E(\frac{\pi}{2}, e)}$$

$$E_\phi = 0$$

$$E_\Phi = 0$$

$$H_r = - \frac{4a^3 \sin \theta}{3\pi r^3} (H_x^0 \cos \phi + H_y^0 \sin \phi) \quad H_r = - \frac{H_x^0 a e^2 \sin \theta \cos \phi}{3r^3 [F(\frac{\pi}{2}, e) - E(\frac{\pi}{2}, e)]} - \frac{H_z^0 a b^2 e^2 \sin \theta \sin \phi}{3r^3 [a^2 E(\frac{\pi}{2}, e) - b^2 F(\frac{\pi}{2}, e)]}$$

$$H_\theta = \frac{2a^3 \cos \theta}{3\pi r^3} (H_x^0 \cos \theta + H_y^0 \sin \phi) \quad H_\theta = \frac{H_x^0 a e^2 \cos \theta \cos \phi}{6r^3 [F(\frac{\pi}{2}, e) - E(\frac{\pi}{2}, e)]} + \frac{H_y^0 a b^2 e^2 \cos \theta \sin \phi}{6r^3 [a^2 E(\frac{\pi}{2}, e) - b^2 F(\frac{\pi}{2}, e)]}$$

$$H_\phi = \frac{2a^3}{3\pi r^3} (-H_x^0 \sin \phi + H_y^0 \cos \phi) \quad H_\phi = - \frac{H_x^0 a e^2 \sin \phi}{6r^3 [F(\frac{\pi}{2}, e) - E(\frac{\pi}{2}, e)]} + \frac{H_y^0 a b^2 e^2 \cos \phi}{6r^3 [a^2 E(\frac{\pi}{2}, e) - b^2 F(\frac{\pi}{2}, e)]}$$

AD-A073 770

AIR FORCE WEAPONS LAB KIRTLAND AFB NM
ELECTROMAGNETIC PULSE INTERACTION NOTES -- EMP 3-38. (U)

F/G 20/14

MAY 79 C E BAUM

AFWL-TR-79-401

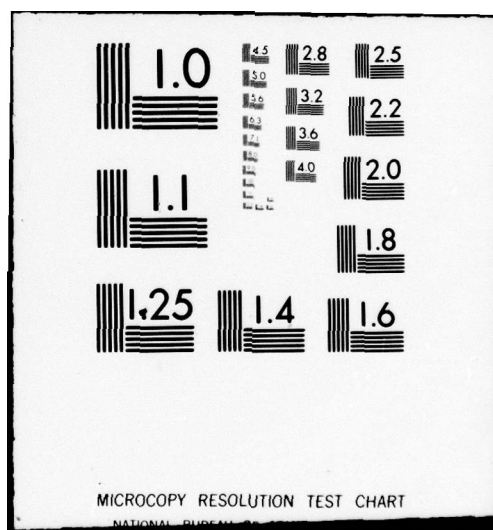
SBIE -AD-E200 329

NL

UNCLASSIFIED

3 OF 6
ADA
073770





6.0 GENERAL SHAPE CAVITY

Jones⁽⁶⁾ gives the field in a cavity produced by an aperture field as

$$\vec{E} = \sum A_M \vec{E}_M$$

$$\vec{H} = \nabla\phi + j\omega_0\epsilon_0 \sum \frac{A_M}{k_M^2} \nabla \times \vec{E}_M$$

where

$$A_M = (k_0^2 - k_M^2)^{-1} \int_S (\nabla \times \vec{E}) \cdot (\nabla \times \vec{E}_M) dS$$

and \vec{E}_M are the natural modes of the cavity normalized such that

$$\int_V |\vec{E}_M|^2 dV = 1$$

V is the volume of the cavity. S is the surface of the cavity.

$$k_M^2 = \omega_M^2/c_0^2, \quad k_0^2 = \frac{\omega_0^2}{c_0^2}$$

$$\omega_M = 2\pi f_M, \quad \omega_0 = 2\pi f_0$$

f_M = a natural frequency, f_0 = frequency of the impressed aperture field

corresponding to the field \vec{E}_M

c_0 = the speed of light

$$\phi = \int_{S_a} \hat{n} \cdot \vec{H} G(\vec{r}, \vec{r}') dS$$

(not the same ϕ as in previous sections)

$$\text{where } \nabla^2 G = -\delta(\vec{r}-\vec{r}')$$

$$\frac{\partial G}{\partial n}|_S = 0$$

G = Green's function

S_a = aperture

For a perfectly conducting cavity $\hat{n} \times \vec{E} = 0$ so that

$$A_M = [k_0^2 - k_M^2]^{-1} \int_{S_a} \hat{n} \times \vec{E} \cdot \nabla \times \vec{E}_M dS$$

\hat{n} is the unit normal outward from the cavity.

If we used Stokes' differentiation, we could obtain

\vec{H} by $\vec{H} = -\nabla \times \vec{E}/j\omega\mu_0$. The introduction of ϕ circumvents the need to differentiate an infinite series. It can be seen from these equations that after the natural modes and the Green's function have been determined, the field in the cavity is determined by the normal \vec{H} and the tangential \vec{E} at the aperture.

7.0 THE ELECTRIC FIELD OF A RECTANGULAR CAVITY

The electric field is given in Section 6.0 where $\hbar = -2$. The normal modes \vec{E}_M of a rectangular cavity are found by solving the wave equation in rectangular coordinates subject to the constraints that $\partial E_n / \partial n$ and tangential \vec{E} are both zero on the boundary of the shorted cavity. They are given by Chen⁽¹⁾ and Waldron⁽⁸⁾ as:

$$\text{TE modes: } \vec{E}_M^{(1)} = \frac{k_2 N^{1/2} x}{k_c} \cos k_1 x' \sin k_2 y' \sin k_3 z'$$

$$- \frac{k_1 N^{1/2} y}{k_c} \sin k_1 x' \cos k_2 y' \sin k_3 z'$$

$$m=0,1,2,\dots; n=0,1,2,\dots; p=1,2,3,\dots; m^2+n^2 \neq 0$$

$$\text{TM Modes: } \vec{E}_M^{(2)} = \frac{-k_1 k_3 N^{1/2} x}{k_M k_c} \cos k_1 x' \sin k_2 y' \sin k_3 z'$$

$$- \frac{k_2 k_3 N^{1/2} y}{k_M k_c} \sin k_1 x' \cos k_2 y' \sin k_3 z'$$

$$+ \frac{k_c N^{1/2} z}{k_M} \sin k_1 x' \sin k_2 y' \cos k_3 z'$$

$$m=1,2,\dots; n=1,2,\dots; p=0,1,2,\dots$$

most cases the two sets of modes are orthogonal. In addition, the two sets of modes have certain useful properties which are summarized below.

TE Modes: $\hat{H}_M^{(1)} = \frac{-k_1 k_3 N^{1/2} \hat{x}}{j\omega_M \mu_0 k_c} \sin k_1 x' \cos k_2 y' \cos k_3 z'$
 $- \frac{k_2 k_3 N^{1/2} \hat{y}}{j\omega_M \mu_0 k_c} \cos k_1 x' \sin k_2 y' \cos k_3 z'$

$+ \frac{k_c N^{1/2} \hat{z}}{j\omega_M \mu_0} \cos k_1 x' \cos k_2 y' \sin k_3 z'$

$m=0, 1, 2, \dots; n=0, 1, 2, \dots; p=1, 2, \dots; m^2+n^2 \neq 0$

TM Modes: $\hat{H}_M^{(2)} = \frac{j k_2 N^{1/2} \hat{x}}{z_o k_c} \sin k_1 x' \cos k_2 y' \cos k_3 z'$
 $- \frac{j k_1 N^{1/2} \hat{y}}{z_o k_c} \cos k_1 x' \sin k_2 y' \cos k_3 z'$

$m=1, 2, \dots; n=1, 2, \dots; p=0, 1, 2, \dots$

where the index M corresponds to the triplet (m, n, p), and

$$k_1 = \frac{m\pi}{a_0}, \quad k_2 = \frac{n\pi}{b_0}, \quad k_3 = \frac{p\pi}{h_0}, \quad k_c = (k_1^2 + k_2^2)^{1/2}, \quad k_M = (k_c^2 + k_3^2)^{1/2}$$

a_0 , b_0 , and h_0 are the dimensions of the cavity, and x' , y' and z' are measured from the walls of the cavity.

$$N = \frac{8}{a_0 b_0 h_0} \epsilon_m \epsilon_n \epsilon_p$$

where

$$\epsilon_\ell = 1 \text{ if } \ell \neq 0$$

$$\epsilon_\ell = 1/2 \text{ if } \ell = 0$$

For an elliptical aperture in the $z'=0$ face of the cavity, let the center of the ellipse be at x_0, y_0 from the corner of the box.

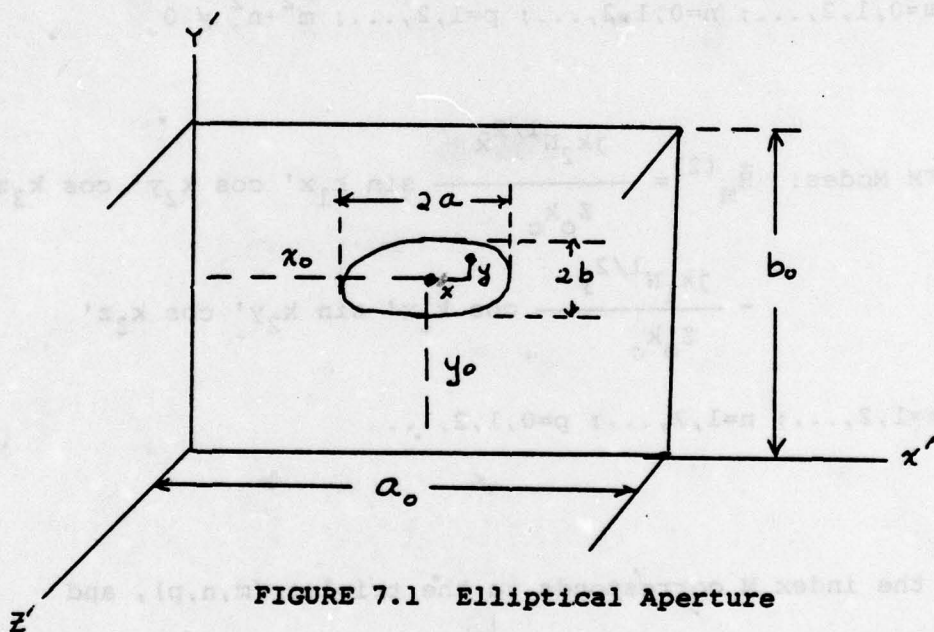


FIGURE 7.1 Elliptical Aperture

Since the values of x and y used in the expressions for the aperture fields are measured from the center of the aperture, we have:

$$x' = x_0 + x$$

$$y' = y_0 + y$$

$$z' = z = 0$$

The expression for A_M becomes

$$A_M^{(i)} = R_M^{-1} \int_{S_a} \hat{f}x \cdot \nabla \times \vec{E}_M^{(i)} ds$$

$$= -j\omega_M \mu_0 R_M^{-1} \int_{S_a} (E_y H_{Mx}^{(i)} - E_x H_{My}^{(i)}) ds \quad i=1,2$$

where

$$R_M = k_o^2 - k_M^2$$

and now

$$\vec{E} = \sum_{i=1}^2 \sum_M A_M^{(i)} \vec{E}_M^{(i)}$$

and E_x and E_y are the fields for an aperture of an infinite conducting screen.

For a general aperture and general fields at the aperture, the electric field in a rectangular cavity is given by:

$$E_x = \sum_M \frac{-k_3 N \cos k_1 x' \sin k_2 y' \sin k_3 z'}{k^2 - k_M^2} \int_A x \cos k_1 x' \sin k_1 y' ds$$

$$E_y = \sum_M \frac{-k_3 N \sin k_1 x' \cos k_2 y' \sin k_3 z'}{k^2 - k_M^2} \int_A y \sin k_1 x' \cos k_2 y' ds$$

$$E_z = \sum_M \frac{N \sin k_1 x' \sin k_2 y' \cos k_3 z'}{k^2 - k_M^2} \int_A (k_1 E_x \cos k_1 x' \sin k_1 y' + k_2 E_y \sin k_1 x' \cos k_1 y') ds$$

For an elliptical aperture, the aperture electric field (assuming no reflections from the cavity) is given by:

$$E_x = \frac{E_z^0 bx}{2a^2 E(\frac{\pi}{2}, e) \sqrt{1-x^2/a^2 - y^2/b^2}}$$

$$E_y = \frac{E_z^0 y}{2b E(\frac{\pi}{2}, e) \sqrt{1-x^2/a^2 - y^2/b^2}}$$

$$H_{Mx}^{(1)} = \frac{-k_1 k_3 N^{1/2}}{j\omega_M \mu_0 k_c} \sin k_1 x' \cos k_2 y'$$

$$H_{Mx}^{(2)} = \frac{j\omega_M \epsilon_0 k_2 N^{1/2}}{k_M k_c} \sin k_1 x' \cos k_2 y'$$

$$H_{My}^{(1)} = \frac{-k_2 k_3 N^{1/2}}{j\omega_M \mu_0 k_c} \cos k_1 x' \sin k_2 y'$$

$$H_{My}^{(2)} = \frac{-j\omega_M \epsilon_0 k_1 N^{1/2}}{k_M k_c} \cos k_1 x' \sin k_2 y'$$

$$A_M^{(1)} = \frac{-k_3 N^{1/2} E_z^0}{2k_c R_M a^2 b E(\frac{\pi}{2}, \epsilon)} [k_2 b^2 \int_{S_a} \frac{x \cos k_1 x' \sin k_2 y' ds}{(1-x'^2/a^2 - y'^2/b^2)^{1/2}}$$

$$- k_1 a^2 \int_{S_a} \frac{y \sin k_1 x' \cos k_2 y' ds}{(1-x'^2/a^2 - y'^2/b^2)^{1/2}]}$$

$$A_M^{(2)} = \frac{k_M N^{1/2} E_z^0}{2k_c R_M a^2 b E(\frac{\pi}{2}, \epsilon)} [k_1 b^2 \int_{S_a} \frac{x \cos k_1 x' \sin k_2 y' ds}{(1-x'^2/a^2 - y'^2/b^2)^{1/2}}$$

$$+ k_2 a^2 \int_{S_a} \frac{y \sin k_1 x' \cos k_2 y' ds}{(1-x'^2/a^2 - y'^2/b^2)^{1/2}]}$$

These integrals can be integrated in terms of elementary functions

$$I_1 = \int_{S_a} \frac{x \cos k_1 x' \sin k_2 y' ds}{\sqrt{1-x'^2/a^2 - y'^2/b^2}}$$

$$= \int_{-a}^a \int_{-b/\sqrt{1-x^2/a^2}}^{b/\sqrt{1-x^2/a^2}} \frac{x \cos[\frac{m\pi}{a} (x_0+x)] \sin[\frac{n\pi}{b} (y_0+y)] dy dx}{\sqrt{1-x^2/a^2 - y^2/b^2}}$$

$$= -4 \sin \frac{m\pi x_0}{a} \sin \frac{n\pi y_0}{b} \int_0^a \int_0^{b/\sqrt{1-x^2/a^2}} \frac{x \cos \frac{n\pi y}{b} \sin \frac{m\pi x}{a} dy dx}{\sqrt{1-x^2/a^2 - y^2/b^2}}$$

$$= -2 \sin k_1 x_0 \sin k_2 y_0 \int_0^a x \sin \frac{m\pi x}{a} J_0 \left(\frac{n\pi b}{b_0} \sqrt{1-x^2/a^2} \right) dx$$

(See appendix.) Let $v = \frac{n\pi b}{b_0} \sqrt{1-x^2/a^2}$; $a = \frac{n\pi b}{b_0}$; and $\beta = \frac{mb_0 a}{na_0 b}$

$$I_1 = \frac{-2a^2 b_0^2 \sin k_1 x_0 \sin k_2 y_0}{n^2 \pi b} \int_0^a v J_0(v) \sin \beta \sqrt{a^2 - v^2} dv$$

$$I_1 = -\pi \sqrt{2\pi} a^3 b k_1 \sin k_1 x_0 \sin k_2 y_0 J_{3/2}(s)/s^{3/2}$$

$$\text{where } s = [(k_1 a)^2 + (k_2 b)^2]^{1/2} \quad (\text{see appendix})$$

Similarly:

$$I_2 = \int_{-a}^a \frac{y \sin k_1 x' \cos k_2 y'}{\sqrt{1-x'^2/a^2-y'^2/b^2}} ds$$

$$I_2 = -\pi \sqrt{2\pi} ab^3 k_2 \sin k_1 x_0 \sin k_2 y_0 J_{3/2}(s)/s^{3/2}$$

After substituting these expressions, one obtains:

$$A_M^{(1)} = 0$$

$$A_M^{(2)} = \frac{-\pi ab^2 k_C k_M E_z^0 \sin \frac{m\pi x_0}{a_0} \sin \frac{n\pi y_0}{b_0} N^{1/2} (\sin s - s \cos s)}{E(\frac{\pi}{2}, e) s^3 R_M}$$

$$\hat{E} = \frac{8\pi ab^2 E_z^0}{a_0 b_0 h_0 E(\frac{\pi}{2}, e)} \sum_m \sum_n \sum_p \frac{\epsilon_p \sin \frac{m\pi x_0}{a_0} \sin \frac{n\pi y_0}{b_0}}{[k_o^2 - k_M^2] s^3}$$

$$[k_1 k_3 \cos \frac{m\pi x'}{a_0} \sin \frac{n\pi y'}{b_0} \sin \frac{p\pi z'}{h_0}] \times$$

$$+ k_2 k_3 \sin \frac{m\pi x'}{a_0} \cos \frac{n\pi y'}{b_0} \sin \frac{p\pi z'}{h_0} \hat{y}$$

$$- k_c^2 \sin \frac{m\pi x'}{a_0} \sin \frac{n\pi y'}{b_0} \cos \frac{p\pi z'}{h_0} 2] (\sin s - s \cos s)$$

For a circular aperture $s = k_a$ and the factor in front of the summation sign becomes $16 a^3 E_z^0 / a_0 b_0 h_0$ where a is the radius of the aperture.

8.0 THE MAGNETIC FIELD OF A RECTANGULAR CAVITY

If we could find \vec{E} as a power series in k_o (i.e., ω_o/c_o) as
 $\vec{E} = \vec{E}^{(0)} + k_o \vec{E}^{(1)} + k_o^2 \vec{E}^{(2)} + \dots$; then \vec{H} could be calculated from

$$\vec{H} = \frac{\nabla \times \vec{E}}{-j\omega_o \mu_o} = \frac{\nabla \times \vec{E}^{(1)}}{-jz_o} + 0(k_o) = \vec{H}^{(0)} + k_o \vec{H}^{(1)} + \dots$$

$$\vec{H}^{(0)} = j \frac{\nabla \times \vec{E}^{(1)}}{z_o}$$

In deriving the aperture field, we assumed a low frequency incoming wave so that $\nabla^2 \phi = 0$ and first order terms in k_o were neglected. This was equivalent to finding $\vec{E}^{(0)}$ and not $\vec{E}^{(1)}$. Hence, $\vec{H}^{(0)}$ cannot be calculated from the \vec{E} that was given in the previous chapter by using

$$\vec{H} = \frac{\nabla \times \vec{E}}{-j\omega_o \mu_o}$$

Instead, let us use the method of Jones⁽⁶⁾. He gives

$$\vec{H} = \nabla \phi + k_o \sum_M \frac{A_M \vec{H}_M}{k_M} = \nabla \phi + k_o \sum_{i=1}^2 \sum_M \frac{A_M^{(i)} \vec{H}_M^{(i)}}{k_M}$$

where

$$\phi(\vec{r}') = \int_{S_a} \hat{n} \cdot \vec{H} G(\vec{r}, \vec{r}') ds$$

where \vec{r} is the variable of integration, measured from the corner of the cavity; and G , the Green's function, is a solution of the boundary value problem

$$\nabla^2 G = -\delta(\vec{r} - \vec{r}')$$

$$\frac{\partial G}{\partial n} \Big|_{S_a} = 0$$

Using finite transforms it can be shown that

$$G(\vec{r}, \vec{r}') = \sum_{mnp} \frac{N}{k_M} \cos k_1 x' \cos k_2 y' \cos k_3 z' \cos k_1 \bar{x} \cos k_2 \bar{y} \cos k_3 \bar{z}$$

where $\bar{x} = x_o + x$, $\bar{y} = y_o + y$, $\bar{z} = z = 0$ on the aperture. $m^2 + n^2 + p^2 \neq 0$ and $\hat{n} \cdot \vec{H} = -H_z$ at $z=0$ and all sums go from 0 to ∞ and $N = 8 \epsilon_m \epsilon_n \epsilon_p / a_o h_o b_o$

On an elliptical aperture, we have found that to the zero order

$$H_z = \frac{-H_x^0 e^2 x}{2b[F(\frac{\pi}{2}, e) - E(\frac{\pi}{2}, e)] \sqrt{1-x^2/a^2 - y^2/b^2}}$$

$$- \frac{H_y^0 e^2 y a^2}{2b[a^2 E(\frac{\pi}{2}, e) - b^2 F(\frac{\pi}{2}, e)] \sqrt{1-x^2/a^2 - y^2/b^2}}$$

The integrals can be determined from the table in the appendix.

The expression for \hat{H} is

$$\hat{H}(x', y', z') = \frac{8\pi a^3 e^2}{a_0 b_0 h_0} \sum_{m=0}^{\infty} \sum_{n=0}^{\infty} \sum_{p=0}^{\infty} \epsilon_m \epsilon_n \frac{\epsilon_p}{k_M^2 s^3} (\sin s - s \cos s)$$

$$(k_1 \hat{x} \sin k_1 x' \cos k_2 y' \cos k_3 z' + k_2 \hat{y} \cos k_1 x' \sin k_2 y' \cos k_3 z')$$

$$+ k_3 \hat{z} \cos k_1 x' \cos k_2 y' \sin k_3 z')$$

$$\left[\frac{H_x^0 k_1 \sin k_1 x_0 \cos k_2 y_0}{F(\frac{\pi}{2}, e) - E(\frac{\pi}{2}, e)} + \frac{b^2 H_y^0 k_2 \cos k_1 x_0 \sin k_2 y_0}{a^2 E(\frac{\pi}{2}, e) - b^2 F(\frac{\pi}{2}, e)} \right]$$

$$- \frac{8j a b^2 k_0 E_x^0}{a_0 b_0 h_0 Z_0 E(\frac{\pi}{2}, e)} \sum_{m=1}^{\infty} \sum_{n=1}^{\infty} \sum_{p=0}^{\infty} \frac{\epsilon_p \sin k_1 x_0 \sin k_2 y_0}{s^3 R_M}$$

$$(\sin s - s \cos s) (k_2 \hat{x} \sin k_1 x' \cos k_2 y' \cos k_3 z' - k_1 \hat{y} \cos k_1 x'$$

$$\sin k_2 y' \cos k_3 z')$$

where $m^2 + n^2 \neq 0$ in the first triple summation and, as before,

$$\epsilon_p = 1 \text{ if } p \neq 0 \text{ and } \epsilon_p = \frac{1}{2} \text{ if } p = 0$$

$$s = (a^2 k_1^2 + b^2 k_2^2)^{1/2}, \quad k_1 = \frac{m\pi}{a_0}, \quad k_2 = \frac{n\pi}{b_0}, \quad k_3 = \frac{p\pi}{h_0}, \quad k_c = (k_1^2 + k_2^2)^{1/2}$$

$$k_M = (k_c^2 + k_3^2)^{1/2}, \quad k_0 = \frac{\omega_0}{c}, \quad \omega_0 = 2\pi f_0, \quad e = (1 - b^2/a^2)^{1/2},$$

$$F\left(\frac{\pi}{2}, e\right) = \int_0^{\pi/2} (1 - e^2 \sin^2 \phi)^{1/2} d\phi, \quad E\left(\frac{\pi}{2}, e\right) = \int_0^{\pi/2} (1 - e^2 \sin^2 \phi)^{-1/2} d\phi$$

$$R_M = k_0^2 - k_m^2$$

$$E_z^0 = 2E_0^i \sin \psi \sin \theta, \quad H_x^0 = -2H_0^i (\sin \psi \cos \theta + \cos \theta \sin \phi \cos \psi)$$

$$H_y^0 = -2H_0^i (\sin \phi \sin \psi - \cos \theta \cos \phi \cos \psi), \quad z_0 = \sqrt{\frac{\mu_0}{\epsilon_0}}, \quad H_0^i = \frac{E_0^i}{z_0}$$

The input variables are $\theta, \phi, \psi, E_0^i, f_0, a, b, x_0, y_0, a_0, b_0, h_0, x', y', z'$.

Note that the k_0 terms were not included in the aperture fields since $k_0 a \ll 1$ but are included in the cavity fields since k_0 is of the same order as k_M .

9.0 GENERAL ORIENTATION OF AN ELLIPTIC APERTURE

Let us generalize the case of an elliptical aperture in a rectangular cavity, by rotating the axes of the ellipse an angle θ_0 .

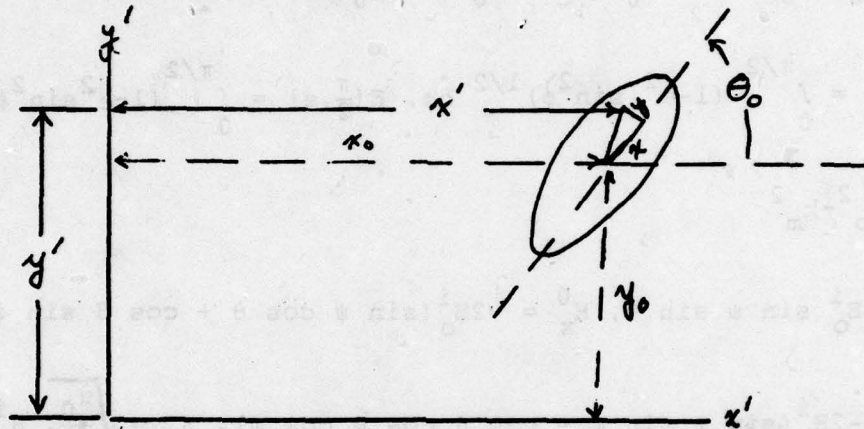


Figure 1

GENERAL ORIENTATION OF ELLIPTICAL APERTURE

From the geometry it follows that

$$\left\{ \begin{array}{l} x' = x_0 + \rho \cos(\theta + \theta_0) = x_0 + \rho (\cos \theta \cos \theta_0 - \sin \theta \sin \theta_0) \\ \quad = x_0 + x \cos \theta_0 - y \sin \theta_0 \\ \\ y' = y_0 + \rho \sin(\theta + \theta_0) = y_0 + \rho (\sin \theta \cos \theta_0 + \sin \theta_0 \cos \theta) \\ \quad = y_0 + y \cos \theta_0 + x \sin \theta_0 \end{array} \right.$$

The expansion coefficients are given by

$$A_M^{(1)} = \frac{k_3 N^{1/2} E_z^0 (-k_2 b^2 I_1 + k_1 a^2 I_2)}{2k_c R_M a^2 b E(\frac{\pi}{2}, e)}$$

$$A_M^{(2)} = \frac{k_M N^{1/2} E_z^0 (k_1 b^2 I_1 + k_2 a^2 I_2)}{2k_c R_M a^2 b E(\frac{\pi}{2}, e)}$$

where

$$I_1 = \int_{S_a} \frac{x \cos k_1 x' \sin k_2 y' ds}{\sqrt{1-x'^2/a^2-y'^2/b^2}}$$

$$I_2 = \int_{S_a} \frac{y \sin k_1 x' \cos k_2 y' ds}{\sqrt{1-x'^2/a^2-y'^2/b^2}}$$

The trigonometric factors are

$$\cos k_1 x' = \cos k_1 x_o [\cos(k_1 x \cos \theta_o) \cos(k_1 y \sin \theta_o)]$$

$$+ \sin(k_1 x \cos \theta_o) \sin(k_1 y \sin \theta_o)]$$

$$- \sin k_1 x_o [\sin(k_1 x \cos \theta_o) \cos(k_1 y \sin \theta_o)]$$

$$- \sin(k_1 y \sin \theta_o) \cos(k_1 x \cos \theta_o)]$$

$$\sin k_1 x' = \sin k_1 x_o [\cos(k_1 x \cos \theta_o) \cos(k_1 y \sin \theta_o)$$

$$+ \sin(k_1 x \cos \theta_o) \sin(k_1 y \sin \theta_o)]$$

$$+ \cos k_1 x_o [\sin(k_1 x \cos \theta_o) \cos(k_1 y \sin \theta_o)$$

$$- \sin(k_1 y \sin \theta_o) \cos(k_1 x \cos \theta_o)]$$

$$\cos k_2 y' = \cos k_2 y_o [\cos(k_2 x \sin \theta_o) \cos(k_2 y \cos \theta_o)$$

$$- \sin(k_2 x \sin \theta_o) \sin(k_2 y \cos \theta_o)]$$

$$- \sin k_2 y_o [\sin(k_2 x \sin \theta_o) \cos(k_2 y \cos \theta_o)$$

$$+ \cos(k_2 x \sin \theta_o) \sin(k_2 y \cos \theta_o)]$$

$$\sin k_2 y' = \sin k_2 y_o [\cos(k_2 x \sin \theta_o) \cos(k_2 y \cos \theta_o)$$

$$- \sin(k_2 x \sin \theta_o) \sin(k_2 y \cos \theta_o)]$$

$$+ \cos k_2 y_o [\sin(k_2 x \sin \theta_o) \cos(k_2 y \cos \theta_o)$$

$$+ \cos(k_2 x \sin \theta_o) \sin(k_2 y \cos \theta_o)]$$

Each of the above integrals involves 16 terms. However, because of symmetry, all but four are zero. With the use of trigonometric identities, these can be evaluated.

$$A_M^{(1)} = \frac{\pi k_3 k_c N^{1/2} E_z^0 ab^2 \sin \theta_o}{2 R_M E(\frac{\pi}{2}, e)} [\cos(k_1 x_o + k_2 y_o) (s_1 \cos s_1 - \sin s_1)/s_1^3$$

$$+ \cos(k_1 x_o - k_2 y_o) (s_2 \cos s_2 - \sin s_2)/s_2^3]$$

$$A_M^{(2)} = \frac{\pi k_M k_c N^{1/2} E_z^0 ab^2 \cos \theta_o}{2 R_M E(\frac{\pi}{2}, e)} [\cos(k_1 x_o - k_2 y_o) (s_2 \cos s_2 - \sin s_2)/s_2^3$$

$$- \cos(k_1 x_o + k_2 y_o) (s_1 \cos s_1)/s_1^3]$$

where

$$s_1 = [a^2 (k_1 \cos \theta_o + k_2 \sin \theta_o)^2 + b^2 (k_1 \sin \theta_o - k_2 \cos \theta_o)^2]^{1/2}$$

$$s_2 = [a^2 (-k_1 \cos \theta_o + k_2 \sin \theta_o)^2 + b^2 (k_1 \sin \theta_o + k_2 \cos \theta_o)^2]^{1/2}$$

As $\theta_o \rightarrow 0$, $A_M^{(1)}$ goes to zero and $A_M^{(2)}$ goes to the value previously calculated. As $\theta_o \rightarrow \frac{\pi}{2}$, $A_M^{(2)}$ goes to zero and

$$A_M^{(1)} \rightarrow \frac{\pi k_3 k_c N^{1/2} E_z^0 ab^2}{s_1^3 R_M E(\frac{\pi}{2}, e)} (s' \cos s' - \sin s') \cos k_1 y_o \cos k_2 y_o$$

$$\text{where } s' = (a^2 k_2^2 + b^2 k_1^2)^{1/2}$$

In any case, the electric field is

$$\vec{E} = \sum_M (A_M^{(1)} \vec{E}_M^{(1)} + A_M^{(2)} \vec{E}_M^{(2)})$$

In order to find \vec{H} , $\nabla\phi$ can be determined from the same relations used previously.

$$\nabla\phi = \frac{4\pi a^3 e^2}{a_o b_o h_o} \sum_{m=0}^{\infty} \sum_{n=0}^{\infty} \sum_{p=0}^{\infty} \frac{\epsilon_m \epsilon_n \epsilon_p}{k_M^2} (k_1 \hat{x} \sin k_1 x' \cos k_2 y' \cos k_3 z'$$

$$+ k_2 \hat{y} \cos k_1 x' \sin k_2 y' \cos k_3 z' + k_3 \hat{z} \cos k_1 x' \cos k_2 y' \sin k_3 z').$$

$$\left\{ s_1^{-3} (\sin s_1 - s_1 \cos s_1) \sin(k_1 x_o + k_2 y_o) \cdot \right.$$

$$\left[\frac{H_x^o (k_1 \cos \theta_o + k_2 \sin \theta_o)}{F(\frac{\pi}{2}, e) - E(\frac{\pi}{2}, e)} - \frac{H_y^o b^2 (k_1 \sin \theta_o - k_2 \cos \theta_o)}{a^2 E(\frac{\pi}{2}, e) - b^2 F(\frac{\pi}{2}, e)} \right]$$

$$+ s_2^{-3} (\sin s_2 - s_2 \cos s_2) \sin(k_1 x_o - k_2 y_o) \cdot$$

$$\left[\frac{H_x^o (k_1 \cos \theta_o - k_2 \sin \theta_o)}{F(\frac{\pi}{2}, e) - E(\frac{\pi}{2}, e)} - \frac{H_y^o b^2 (k_1 \sin \theta_o + k_2 \cos \theta_o)}{a^2 E(\frac{\pi}{2}, e) - b^2 F(\frac{\pi}{2}, e)} \right] \}$$

When $\theta_o = 0$ this reduces to the result derived earlier, which is the first half of the expression on page (8-3). When $\theta_o = \frac{\pi}{2}$,

$$\nabla\phi = \frac{8\pi a^3 e^2}{a_o b_o h_o} \sum_{m=0}^{\infty} \sum_{n=0}^{\infty} \sum_{p=0}^{\infty} \frac{\epsilon_m \epsilon_n \epsilon_p}{k_M^2} (k_1 \hat{x} \sin k_1 x' \cos k_2 y' \cos k_3 z' +$$

$$k_2 \hat{y} \cos k_1 x' \sin k_2 y' \cos k_3 z' + k_3 \hat{z} \cos k_1 x' \cos k_2 y' \sin k_3 z')$$

$$(\sin s' - s' \cos s')/s'^3$$

$$\cdot \left[\frac{H_x^o k_2 \cos k_1 x_o \sin k_2 y_o}{F(\frac{\pi}{2}, e) - E(\frac{\pi}{2}, e)} - \frac{H_y^o b^2 k_1 \sin k_1 x_o \cos k_2 y_o}{a^2 E(\frac{\pi}{2}, e) - b^2 F(\frac{\pi}{2}, e)} \right]$$

where

$$s' = \sqrt{k_1^2 a^2 + k_2^2 b^2}$$

СКОРОСТЬ ЯЗЫК ПОЛАТИЧЕСКАЯ 0.61

ищется вспомогательное значение s' для определения времени полета
и времени, необходимого для пролета расстояния s .

$$\frac{d(s')}{dt} = \frac{ds'}{dt} = \frac{ds}{dt}$$

ищется значение s' из уравнения для s' , т.е. сопоставляются значения s' и $\frac{ds'}{dt}$.
Абсолютные идентификации идентифицируются из условия равенства s' и $\frac{ds'}{dt}$.
При этом $s' = 0 = \frac{ds'}{dt}$ и это означает, что значение s' определяется из уравнения

$$(1) \frac{d(s')}{dt} = \frac{ds'}{dt} = \frac{s}{t}$$

или $s' = s t$ (абсолютное значение)

$$s' = \frac{1}{\frac{1}{s} - \frac{1}{t}} = \frac{st}{t-s}$$

$$s' = \frac{1}{\frac{1}{s} - \frac{1}{t}} = \frac{st}{t-s}$$

$$s' = \frac{st}{t-s}$$

ищется значение s' из уравнения (1), т.е. $s' = s t$ и это означает, что значение s' определяется из уравнения

10.0 CAVITY EXCITATION NEAR RESONANCE

The boundary condition for a metal which is not perfectly conducting is derived in the appendix as

$$\hat{n} \times \vec{E} = \sqrt{\omega \mu_0 / 2\sigma} (1+j) \vec{H}$$

(see also Reference 9). If the resonance is to be damped, we must use the above formula in evaluating the coefficients A_M . $\nabla \phi$ is unchanged because $\hat{n} \cdot \vec{H} \approx \hat{n} \cdot \hat{n} \times \vec{E} = 0$ on the metal.

Following the method of Chen,⁽³⁾ we obtain

$$\vec{E} = \sum_{M,i} A_M^{(i)} \vec{E}_M^{(i)}$$

(see appendix). Where

$$\begin{aligned} A_M^{(i)} &= \frac{1}{k_o^2 - k_M^2} \int_S \hat{n} \times \vec{E} \cdot \nabla \times \vec{E}_M^{(i)} dS \\ &= \frac{1}{k_o^2 - k_M^2} \left[\int_{S_a} \hat{n} \times \vec{E} \cdot \nabla \times \vec{E}_M^{(i)} dS + \int_{S_1} \hat{n} \times \vec{E} \cdot \nabla \times \vec{E}_M^{(i)} dS \right] \\ &= \frac{1}{k_o^2 - k_M^2} \left[\int_{S_a} \hat{n} \times \vec{E} \cdot \nabla \times \vec{E}_M^{(i)} dS + \sqrt{\omega \mu_0 / 2\sigma} (1+j) \int_{S_1} \vec{H} \cdot \nabla \times \vec{E}_M^{(i)} dS \right] \end{aligned}$$

At this point, we should note that the series for \vec{E} is not uniformly convergent since $\hat{n} \times \vec{E}_M^{(i)}$ is zero on the boundary

whereas $\hat{n} \times \vec{E}$ is not. Hence, we will use the expression for \vec{H} which has a uniformly convergent series

$$\vec{H} = \nabla\phi + k_o \sum_{M,i} \frac{A_M^{(i)} H_M^{(i)}}{k_M}$$

Substituting this in the above surface integral, we obtain

$$(k_o^2 - k_M^2) A_M^{(i)} = \int_{S_a} \hat{n} \times \vec{E} \cdot \nabla \times \vec{E}_M^{(i)} dS + \sqrt{\omega\mu/2\sigma} (1+j)$$

$$\begin{aligned} & \cdot \left[\int_{S_1} \nabla\phi \cdot \nabla \times \vec{E}_M^{(i)} dS + k_o \sum_{M,\ell} \frac{A_M^{(\ell)} H_M^{(\ell)}}{k_M} \int_{S_1} \vec{H}_M^{(\ell)} \cdot \nabla \times \vec{E}_M^{(i)} dS \right] \\ & = I_M^{(i)} + \sqrt{\omega\mu/2\sigma} (1+j) [J_M^{(i)} - j k_o z_o k_M \sum_{M,\ell} \frac{A_M^{(\ell)} K_{MM}^{(i\ell)}}{k_M}] \end{aligned}$$

These integrals can be evaluated for particular apertures.

Let us consider a rotated elliptic aperture.

$$\begin{aligned} \nabla\phi = \sum_M \frac{\bar{N}}{k_M^2} [-2\bar{k}_1 \sin \bar{k}_1 x' \cos \bar{k}_2 y' \cos \bar{k}_3 z' - \hat{y}\bar{k}_2 \cos \bar{k}_1 x' \\ \sin \bar{k}_2 y' \cos \bar{k}_3 z' - 2\bar{k}_3 \cos \bar{k}_1 x' \cos \bar{k}_2 y' \sin \bar{k}_3 z'] P_M^- \end{aligned}$$

$$\text{where } P_M = \int_{S_a} \hat{n} \cdot \vec{H} \cos k_1 \bar{x} \cos k_2 \bar{y} dS$$

$$I_M^{(i)} = \int_{S_a} \hat{n} \times \vec{E} \cdot \vec{H}_M^{(i)} dS (-j k_M z_o)$$

$$K_{MM}^{(i\ell)} = \int_{S_1} \vec{H}_M^{(\ell)} \cdot \vec{H}_M^{(i)} dS$$

$$\begin{aligned}
 J_M^{(i)} &= \int_{S_1} \nabla \phi \cdot \nabla x E_M^{(i)} ds = -jk_M z_o \int_{S_1} \nabla \phi \cdot \vec{H}_M^{(i)} ds \\
 &= -jk_M z_o \sum_{\vec{k}_M} \frac{\bar{N}P_M}{k_M^2} \int_{S_1} \vec{H}_M^{(i)} \cdot [-\bar{k}_1 x' \sin \bar{k}_1 x' \cos \bar{k}_2 y' \cos \bar{k}_3 z' \\
 &\quad -\bar{k}_2 y' \cos \bar{k}_1 x' \sin \bar{k}_2 y' \cos \bar{k}_3 z' \\
 &\quad -\bar{k}_3 z' \cos \bar{k}_1 x' \cos \bar{k}_2 y' \sin \bar{k}_3 z'] ds
 \end{aligned}$$

$$\begin{aligned}
 P_M &= \frac{-\pi e^2 a^3}{2} \left\{ \frac{H_x^o}{F(\frac{\pi}{2}, e) - E(\frac{\pi}{2}, e)} [\sin(k_1 x_o + k_2 y_o) C_1 (\sin s_1 - s_1 \cos s_1) / s_1^3 \right. \\
 &\quad \left. - \sin(k_1 x_o - k_2 y_o) C_2 (\sin s_2 - s_2 \cos s_2) / s_1^3] \right. \\
 &\quad \left. + \frac{H_y^o b^2}{b^2 F(\frac{\pi}{2}, e) - a^2 E(\frac{\pi}{2}, e)} [\sin(k_1 x_o - k_2 y_o) C_3 (\sin s_2 - s_2 \cos s_2) / s_2^3 \right. \\
 &\quad \left. - \sin(k_1 x_o + k_2 y_o) C_4 (\sin s_1 - s_1 \cos s_1) / s_1^3] \right.
 \end{aligned}$$

where

$$C_1 = k_1 \cos \theta_o + k_2 \sin \theta_o$$

$$C_2 = -k_1 \cos \theta_o + k_2 \sin \theta_o$$

$$C_3 = k_1 \sin \theta_o + k_2 \cos \theta_o$$

$$C_4 = -k_1 \sin \theta_o + k_2 \cos \theta_o$$

$$s_1 = (a^2 c_1^2 + b^2 c_4^2)^{1/2}$$

$$s_2 = (a^2 c_2^2 + b^2 c_3^2)^{1/2}$$

$$K_{MM}^{(11)} = \frac{-2}{k_M k_{\bar{M}} z_o^2 k_c \bar{k}_c} \left\{ \frac{(\epsilon_1 \bar{\epsilon}_1)^{1/2}}{a_o} \delta_n^{\bar{n}} \delta_p^{\bar{p}} [1 + (-1)^{m+n}] \right.$$

$$(k_2^2 k_3^2 + k_c^2 \bar{k}_c^2) + \frac{(\epsilon_2 \bar{\epsilon}_2)^{1/2}}{b_o} \delta_m^{\bar{m}} \delta_p^{\bar{p}} [1 + (-1)^{n+\bar{n}}]$$

$$(k_1^2 k_3^2 + k_c^2 \bar{k}_c^2) + \frac{1}{h_o} \delta_m^{\bar{m}} \delta_n^{\bar{n}} [1 + (-1)^{p+\bar{p}}] k_2^2 k_3 \bar{k}_3 \}$$

$$K_{MM}^{(12)} = \frac{2k_3}{k_M k_c \bar{k}_c z_o^2} \left\{ \frac{-\epsilon_2^{1/2} k_1 \bar{k}_2}{b_o} \delta_m^{\bar{m}} \delta_p^{\bar{p}} [1 + (-1)^{n+\bar{n}}] \right.$$

$$\left. + \frac{\epsilon_1^{1/2} \bar{k}_1 k_2}{a_o} \delta_n^{\bar{n}} \delta_p^{\bar{p}} [1 + (-1)^{m+\bar{m}}] \right\}$$

$$K_{MM}^{(21)} = \frac{2k_3}{k_{\bar{M}} k_c \bar{k}_c z_o^2} \left\{ - \frac{\bar{\epsilon}_2^{1/2} k_1 k_2}{b_o} \delta_m^{\bar{m}} \delta_p^{\bar{p}} [1 + (-1)^{n+\bar{n}}] \right.$$

$$\left. + \frac{\bar{\epsilon}_1^{1/2} k_1 \bar{k}_2}{a_o} \delta_n^{\bar{n}} \delta_p^{\bar{p}} [1 + (-1)^{m+\bar{m}}] \right\}$$

$$K_{MM}^{(22)} = -\frac{2k_1 \bar{k}_1 \delta^{\bar{n}} \bar{p}}{a_o k_c \bar{k}_c z_o^2} [1+(-1)^{m+\bar{m}}] - \frac{2k_2 \bar{k}_2 \delta^{\bar{m}} \bar{p}}{b_o k_c \bar{k}_c z_o^2} [1+(-1)^{m+\bar{m}}]$$

$$-\frac{2(\epsilon_3 \bar{\epsilon}_3)^{1/2} \delta^{\bar{m}} \delta^{\bar{n}}}{h_o z_o^2} [1+(-1)^{p+\bar{p}}]$$

$$J_M^{(1)} = -jk_3 \sqrt{2} \left\{ \frac{k_2^2}{\sqrt{a_o}} \sum_n \frac{[1+(-1)^{n+\bar{n}}] \cdot b_{mnp}}{k_{mnp}^2} \right.$$

$$\left. - \frac{k_1^2}{\sqrt{b_o}} \sum_m \frac{[1+(-1)^{m+\bar{m}}] p_{mnp}}{k_{mnp}^2} + \frac{k_c^2}{\sqrt{h_o}} \sum_p \frac{[1+(-1)^{p+\bar{p}}] p_{mnp}}{k_{mnp}^2} \right\}$$

$$J_M^{(2)} = -\frac{k_1 k_2 k_M \sqrt{2}}{k_c} \left\{ -\frac{1}{\sqrt{b_o}} \sum_n \frac{[1+(-1)^{n+\bar{n}}] p_{mnp}}{k_{mnp}^2} \right.$$

$$\left. + \frac{1}{\sqrt{a_o}} \sum_m \frac{[1+(-1)^{m+\bar{m}}] p_{mnp}}{k_{mnp}^2} \right\}$$

$$I_M^{(1)} = \frac{\pi k_3 k_c N^{1/2} E_z^o ab^2 \sin \theta_o}{2E(\frac{\pi}{2}, e)} [\cos(k_1 x_o + k_2 y_o) (s_1 \cos s_1 - \sin s_1)/s_1^3$$

$$+ \cos(k_1 x_o - k_2 y_o) (s_2 \cos s_2 - \sin s_2)/s_2^3]$$

$$I_M^{(2)} = \frac{\pi k_M k_c N^{1/2} E_z^o ab^2 \cos \theta_o}{2E(\frac{\pi}{2}, e)} [\cos(k_1 x_o - k_2 y_o) (s_2 \cos s_2 - \sin s_2)/s_2^3$$

$$- \cos(k_1 x_o + k_2 y_o) (s_1 \cos s_1 - \sin s_1)/s_1^3]$$

To solve the doubly infinite set of equations for A_M , separate out the diagonal terms.

$$[k_o^2 - k_M^2 + j k_o z_o K_{MM}^{(11)} \sqrt{\omega \mu_o / 2\sigma} (1+j), A_M^{(1)}$$

$$+ j k_o z_o \sqrt{\omega \mu_o / 2\sigma} (1+j) K_{MM}^{(12)} A_M^{(2)}$$

$$= I_M^{(1)} + \sqrt{\omega \mu_o / 2\sigma} (1+j) [J_M^{(1)} - j k_o z_o k_M \cdot \sum_{M \neq M, \ell} \frac{A_M^{(\ell)} K_{MM}^{(1\ell)}}{k_M}]$$

$$[k_o^2 - k_M^2 + j k_o z_o K_{MM}^{(22)} \sqrt{\omega \mu_o / 2\sigma} (1+j)] A_M^{(2)} + j k_o z_o \sqrt{\omega \mu_o / 2\sigma} (1+j)$$

$$A_M^{(1)} K_{MM}^{(21)} = I_M^{(2)} + \sqrt{\omega \mu_o / 2\sigma} (1+j) [J_M^{(2)} - j k_o k_M z_o \sum_{M \neq M, \ell} \frac{A_M^{(\ell)} K_{MM}^{(2\ell)}}{k_M}]$$

If k_o is close to some k_M , say k_N , then the above equations are approximately

$$A_M^{(1)} = \frac{I_M^{(1)}}{k_o^2 - k_M^2} \quad M \neq N$$

$$A_M^{(2)} = \frac{I_M^{(2)}}{k_o^2 - k_M^2} \quad M \neq N$$

where the terms involving $1/\sqrt{\sigma}$ have been neglected. These can be substituted into the resonant equation to obtain

$$[k_o^2 - k_N^2 - z_o k_o K_{NN}^{(11)} \sqrt{\omega \mu_o / 2\sigma} (1-j)] A_N^{(1)} - k_o z_o k_N K_{NN}^{(12)} A_N^{(2)} (1-j)$$

$$\sqrt{\omega \mu_o / 2\sigma} = I_N^{(1)} + \sqrt{\omega \mu_o / 2\sigma} (1+j) J_N^{(1)} + k_o z_o k_N \sqrt{\omega \mu_o / 2\sigma} (1-j)$$

$$\sum_{M \neq N} \frac{k_{NM}^{(11)} I_M^{(1)} + k_{NM}^{(12)} I_M^{(2)}}{k_M (k_o^2 - k_M^2)} = F_1$$

$$[k_o^2 - k_N^2 - z_o k_o K_{NN}^{(22)} \sqrt{\omega \mu_o / 2\sigma} (1-j)] A_N^{(2)} - k_o z_o k_N K_{NN}^{(21)} A_N^{(1)}$$

$$\sqrt{\omega \mu_o / 2\sigma} (1-j) = I_N^{(2)} + \sqrt{\omega \mu_o / 2\sigma} (1+j) J_N^{(2)} + k_o z_o k_N \sqrt{\omega \mu_o / 2\sigma} (1-j)$$

$$\sum_{M \neq N} \frac{k_{NM}^{(21)} I_M^{(1)} + k_{NM}^{(22)} I_M^{(2)}}{k_M (k_o^2 - k_M^2)} = F_2$$

This set of two equations and two unknowns can be solved for
 $A_N^{(1)}$ and $A_N^{(2)}$

$$A_N^{(1)} = \frac{1}{\Delta} (F_1 D - F_2 B)$$

$$A_N^{(2)} = \frac{1}{\Delta} (F_2 A - F_1 C)$$

where $\Delta = AD - BC$

$$A = k_o^2 - k_N^2 - z_o k_o K_{NN}^{(11)} \sqrt{\omega \mu_o / 2\sigma} (1-j)$$

$$B = -z_o k_o K_{NN}^{(12)} \sqrt{\omega \mu_o / 2\sigma} (1-j)$$

$$C = -z_o k_o K_{NN}^{(21)} \sqrt{\omega \mu_o / 2\sigma} (1-j)$$

$$D = k_o^2 - k_N^2 - z_o k_o K_{NN}^{(2)} \sqrt{\omega \mu_o / 2\sigma} (1-j)$$

If k_o is close to more than one k_M , say $k_{N_1}, k_{N_2}, \dots, k_{N_e}$, then we still have

$$A_M^{(i)} = \frac{I_M^{(i)}}{k_o^2 - k_M^2} \quad M \neq N_1, N_2, \dots, N_e$$

and we can proceed as above to find $A_{N_1}^{(i)}, A_{N_2}^{(i)}, \dots, A_{N_e}^{(i)}$ by solving $2e$ equations in $2e$ unknowns.

If this approximation is not made, then the equation for $A_M^{(i)}$ must be solved by numerical techniques. If $m, n, p < 10$, this leads to eight independent sets of equations with a maximum of 250 equations in each set. There would be 1701 unknowns which would be a laborious calculation.

It is important to note that $A_N^{(i)}$ does not go to infinity as $\omega \rightarrow \omega_N$.

11.0 PULSE INPUT

Let an incoming wave incident on the aperture be an electro-magnetic pulse (EMP) instead of a sinusoidal wave. The Fourier transform of Maxwell's Equations are of the same form as if we had assumed a sinusoidal input. If the incoming field is of the form $\vec{E}^i = \int_0^\infty e^{-j\omega t} f(t) dt$ then the Fourier transform is $\vec{E}^i = \vec{E}^i F(\omega)$.

$$\text{Where } F(\omega) = \int_{-\infty}^{\infty} e^{-j\omega t} f(t) dt$$

The inverse transform is

$$f(t) = \frac{1}{2\pi} \int_{-\infty}^{\infty} e^{j\omega t} F(\omega) d\omega$$

To find the response of a cavity to EMP we must multiply the result of a sinusoidal input by $F(\omega)$ and then take the inverse transform of the result. As an example consider the function illustrated in Figure 3.

$$f(t) = (e^{-\alpha t} - e^{-\beta t}) u(t) \text{ where } 0 < \alpha < \beta$$

and $u(t)$ is the unit step function.

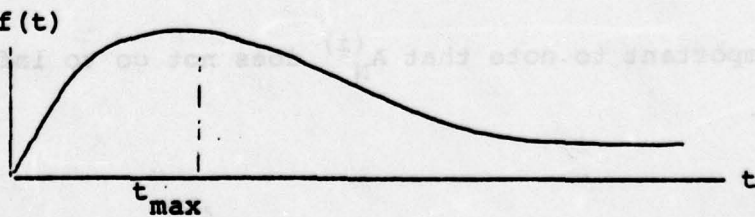


Figure 3. EMP

The maximum occurs at $t_{\max} = \frac{1}{\beta-\alpha} \ln \beta/\alpha$

The transform of $f(t)$ is

$$F(\omega) = \frac{1}{\alpha+j\omega} - \frac{1}{\beta+j\omega}$$

The transformed field in a perfectly conducting cavity of arbitrary shape and arbitrary aperture is given by

$$\hat{\mathbf{E}} = c_0^2 \sum_M \hat{\mathbf{E}}_M^{(i)} \int_{S_a} \hat{\mathbf{n}} \times \hat{\mathbf{E}}_M^{(i)} ds$$

$$\frac{\omega^2 - \omega_M^2}{k^2 M}$$

Let $\hat{\mathbf{E}}$ on the aperture be $F(\omega)\hat{\mathbf{G}}(\mathbf{r})$. It follows that

$$\hat{\mathbf{E}}(\mathbf{r}, t) = \sum_M \frac{\hat{\mathbf{E}}_M}{k^2 M} \int_{S_a} \hat{\mathbf{n}} \times \hat{\mathbf{G}}(\mathbf{r}) \cdot \nabla \times \hat{\mathbf{E}}_M ds B_M(t)$$

where $B_M(t) = \text{inverse Fourier transform of } \frac{\omega_M^2 F(\omega)}{\omega^2 - \omega_M^2}$

$$= \frac{1}{2\pi} \int_{-\infty}^{\infty} \frac{\omega_M^2 e^{j\omega t}}{\omega^2 - \omega_M^2} \left(\frac{1}{\alpha+j\omega} - \frac{1}{\beta+j\omega} \right) d\omega$$

$B_M(t)$ gives the time dependence of each mode.

This integral has a singularity but the principal value exists.

It can be verified by direct integration that

$$\mathcal{F.T} \left[-\omega_M \sin \omega_M t e^{-\gamma t} u(t) \right] = \frac{-\omega_M^2}{(\gamma + j\omega)^2 + \omega_M^2} \quad (\gamma > 0)$$

As $\gamma \rightarrow 0+$ this is $\frac{\omega_M^2}{\omega^2 - \omega_M^2}$

Using the convolution theorem, the inverse Fourier Transform of the product $\mathcal{F}_1(\omega)\mathcal{F}_2(\omega)$ is given by

$$\int_{-\infty}^{\infty} f_1(t-\tau) f_2(\tau) d\tau. \quad \text{Let } \mathcal{F}_1(\omega) = \frac{-\omega_M^2}{(\gamma + j\omega)^2 + \omega_M^2}$$

and $\mathcal{F}_2(\omega) = \frac{1}{\alpha + j\omega} - \frac{1}{\beta + j\omega}$. It follows that

$$f_1(t) = -\omega_M \sin \omega_M t e^{-\gamma t} u(t)$$

$$f_2(t) = (e^{-\alpha t} - e^{-\beta t}) u(t)$$

$$B_M(t) = -\lim_{\gamma \rightarrow 0+} \int_{-\infty}^{\infty} \omega_M \sin \omega_M(t-\tau) e^{-\gamma(t-\tau)} u(t-\tau) (e^{-\alpha\tau} - e^{-\beta\tau}) u(\tau) d\tau$$

$$= -\lim_{\gamma \rightarrow 0+} u(t) \omega_M \int_0^t \sin \omega_M(t-\tau) (e^{-\gamma t+\gamma\tau-\alpha\tau} - e^{-\gamma t+\gamma\tau-\beta\tau}) d\tau$$

$$= -\lim_{\gamma \rightarrow 0+} \omega_M u(t) \left\{ \frac{\omega_M e^{-at} - e^{-\gamma t} [(\gamma-a) \sin \omega_M t + \omega_M \cos \omega_M t]}{(\gamma-a)^2 + \omega_M^2} \right. \\ \left. - \frac{\omega_M e^{-\beta t} - e^{-\gamma t} [(\gamma-\beta) \sin \omega_M t + \omega_M \cos \omega_M t]}{(\gamma-\beta)^2 + \omega_M^2} \right\}$$

$$\begin{aligned} B_M(t) &= -u(t) \omega_M \left\{ \frac{\omega_M e^{-at} + a \sin \omega_M t - \omega_M \cos \omega_M t}{a^2 + \omega_M^2} \right. \\ &\quad \left. - \frac{\omega_M e^{-\beta t} + \beta \sin \omega_M t - \omega_M \cos \omega_M t}{\beta^2 + \omega_M^2} \right\} \end{aligned}$$

This is made up of a distorted EMP

$$-u(t) \left[\frac{\omega_M^2 e^{-at}}{\omega_M^2 + a^2} - \frac{\omega_M^2 e^{-\beta t}}{\beta^2 + \omega_M^2} \right]$$

plus the undamped natural modes. The distortion goes to zero as $\omega_M \rightarrow \infty$. The maximum value of the distorted wave as well as the undamped wave both have an upper bound of one. The maximum of $B_M(t)$ has an upper bound of two. This can be obtained for intermediate ω , i.e., when $a \ll \omega_M \ll \beta$ so that

$$B_M(t) \approx -u(t) (1 - \cos \omega_M t)$$

$$t_{\max} = \frac{\pi}{\omega_M}$$

For large ω_M ($\alpha \ll \beta \ll \omega_M$), $B_M(t) = -u(t) (e^{-\alpha t} - e^{-\beta t})$ (EMP shape)

and for small ω_M ($\omega_M \ll \alpha \ll \beta$)

$$B_M(t) = -u(t) \frac{\omega_M}{\alpha} \sin \omega_M t \quad (\text{no EMP shape})$$

For the case of very large ω_M ,

$$\vec{E}(r,t) = -u(t) (e^{-\alpha t} - e^{-\beta t}) \sum_M \frac{\vec{E}_M}{k_M^2} \int_{S_a} \hat{n} \times \vec{G}(r) \cdot \nabla \times \vec{E}_M ds$$

$$= -f(t) \sum_M \frac{\vec{E}_M}{k_M^2} \int_{S_a} \hat{n} \times \vec{G}(r) \cdot \nabla \times \vec{E}_M ds$$

where the input on the aperture is $\vec{G}(r)f(t)$.

We note that the plane-wave expressions

$$\vec{E}(r,t) = f(t) \sum_M \vec{A}_M \vec{E}_M, \quad f(t) = e^{j\omega t}$$

$$\vec{A}_M = \int_{S_a} \hat{n} \times \vec{G}(r) \cdot \nabla \times \vec{E}_M ds$$

$$k_0^2 - k_M^2$$

yield the same expression when $\omega_M \gg \omega_0$.

The wave length of the natural modes of a rectangular cavity are

$$\lambda_M = \frac{2}{\sqrt{\frac{m^2}{a_0^2} + \frac{n^2}{b_0^2} + \frac{p^2}{h_0^2}}}$$

To satisfy the boundary conditions only one of m, n, p can be zero at one time.

If $a_0 < b_0 < h_0$ then the largest wave length occurs when $m=0$, $n=1$, $p=1$. Hence

$$\lambda_M \leq \frac{2}{\sqrt{\frac{1}{b_0^2} + \frac{1}{h_0^2}}} < 2b_0$$

The largest wave length is less than twice the intermediate dimension of the cavity.

If the rise time of EMP is 3.5 ns and the fall time is 275 ns, then

$$\alpha = \frac{1}{\text{fall time}} = 3.6 \text{ MHz}$$

$$\beta = \frac{1}{\text{rise time}} = 286 \text{ MHz}$$

If a cavity has an intermediate length of 3 meters, its lowest natural frequency is greater than 50 MHz. From the above analysis we see that this lowest mode could have twice the amplitude of the incoming EMP, and its peak would occur at 10 ns after the pulse hit the aperture.

12.0 REFERENCES

1. Leigh-Wei Chen, "On Cavity Excitation Through Small Apertures," IN 45, AFWL Interaction Notes.
2. I.S. Gradshteyn, Table of Integrals Series and Products, Academic Press, 1965.
3. Handbook of Mathematical Functions, Ed. by M. Abramowitz Dover, 1964.
4. Standard Mathematical Tables, Ed. by S.M. Selby, The Chemical Rubber Company, 1967.
5. H. Goldstein, Classical Mechanics, Addison-Wesley, 1950.
6. D.S. Jones, The Theory of Electromagnetism, Macmillan, 1964, pages 222-223.
7. N.J. Rudie, Principles and Techniques of Radiation Hardening, Volume 3.
8. R.A. Waldron, Theory of Guided Electromagnetic Waves, Van Nostrand, 1969.
9. J.D. Jackson, Classical Electrodynamics, John Wiley & Sons, New York, 1962.
10. H.A. Bethe, "Theory of Diffraction of Small Holes," The Physical Review, Vol. 66, #7,8, page 163, October 1, 1944.
11. D.K. Cheng, and C.A. Chen, "On Transient Electromagnetic Excitation of a Rectangular Cavity Through an Aperture," IN 237, AFWL Interaction Notes.
12. C.M. Butler, Y. Rahmat-Samii, and R. Mittra, "Electromagnetic Penetration Through Apertures in Conducting Surfaces," IEEE Transactions on Antennas and Propagation, Vol. AP-26, #1, January, 1978, p. 82.

13.0 APPENDIX13.1 ELLIPSOIDAL COORDINATES ξ, η, ζ

$$1. \quad x^2 = \frac{(\xi+a^2)(\eta+a^2)(\zeta+a^2)}{a^2(a^2-b^2)}, \quad y^2 = \frac{(\xi+b^2)(\eta+b^2)(\zeta+b^2)}{-b^2(a^2-b^2)},$$

$$z^2 = \frac{\xi\eta\zeta}{a^2b^2}$$

$$a > b, \quad 0 \leq \xi < \infty, \quad -b^2 \leq \eta \leq 0, \quad -a^2 \leq \zeta \leq -b^2$$

Let ϕ be defined as $\zeta = -a^2 + (a^2-b^2) \cos^2 \phi$

If $\xi \rightarrow \infty$, then $\xi/r^2 \rightarrow 1$

If $\eta \rightarrow -b^2$, then the surface of constant η is $y=0$ and $\frac{x^2}{a^2-b^2} - \frac{z^2}{b^2} \leq 1$

If $\zeta \rightarrow -b^2$, then the surface of constant ζ is $y=0$ and $\frac{x^2}{a^2-b^2} - \frac{z^2}{b^2} \geq 1$

If $\zeta \rightarrow -a^2$, then the surface of constant ζ is $x=0$

If $\eta = -b^2$ and $\zeta = -a^2$, the locus is the z axis

If $b > a$, then the coordinates ξ, η, ζ are related to the oblate coordinates $\xi_{ob}, \eta_{ob}, \phi_{ob}$ as $\phi = \phi_{ob}$, $\xi = \xi_{ob}$, and $\eta = \eta_{ob}$

If $\eta \rightarrow 0$, then the surface of constant η is $z=0$, $x^2/a^2 + y^2/b^2 \geq 1$

If $\xi \rightarrow 0$, then the surface of constant ξ is $z=0$, $x^2/a^2 + y^2/b^2 \leq 1$

$$2. \quad \frac{x^2}{a^2+\mu} + \frac{y^2}{b^2+\mu} + \frac{z^2}{\mu} = 1 \text{ where } \mu = \xi, \eta, \text{ or } \zeta$$

On the z -axis, $\eta = -b^2$, $\zeta = -a^2$, and $\xi = z^2$.

On the aperture, $\xi = 0$ and $\eta, \zeta = \frac{\rho^2 - a^2 - b^2}{2} \pm [(\frac{\rho^2 - a^2 - b^2}{2})^2 + a^2 b^2 (-1 + \frac{x^2}{a^2} + \frac{y^2}{b^2})]^{1/2}$

On the screen, $\eta = 0$ and $\xi, \zeta = \frac{\rho^2 - a^2 - b^2}{2} \pm [(\frac{\rho^2 - a^2 - b^2}{2})^2 + a^2 b^2 (-1 + \frac{x^2}{a^2} + \frac{y^2}{b^2})]^{1/2}$

For the far field, then $\xi/r^2 \rightarrow 1$ and $\eta, \zeta \rightarrow -\frac{1}{2r^2} [b^2 x^2 + a^2 y^2 + (a^2 + b^2) z^2] \pm \frac{1}{2r^2} \{[b^2 x^2 + a^2 y^2 + (a^2 + b^2) z^2]^2 - 4a^2 b^2 z^2 r^2\}^{1/2}$

If $\xi \gg a^2$ and $z=0$, then $\xi \approx \rho^2$, $\eta=0$ and $\zeta \approx -a^2 + (a^2 - b^2) \cos^2 \phi$
where $\cos \phi = x/\rho$

3. The inverse transformation involves the cubic equation

$$\mu^3 + \mu^2 [a^2 + b^2 - r^2] + \mu [-(a^2 + b^2) z^2 + a^2 b^2 (1 - x^2/a^2 - y^2/b^2)] - a^2 b^2 z^2 = 0$$

The solutions give ξ, η, ζ in terms of x, y, z as follows⁽⁴⁾:

$$\xi = -\frac{p}{3} + m \cos \theta_1$$

$$\eta = -\frac{p}{3} + m \cos (\theta_1 + \frac{4\pi}{3})$$

$$\zeta = -\frac{p}{3} + m \cos (\theta_1 + \frac{2\pi}{3})$$

where

$$\theta_1 \equiv \frac{1}{3} \cos^{-1} \frac{3b}{Am}$$

$$m \equiv 2\sqrt{-A}/3$$

$$A = Q - P^2/3$$

$$B = \frac{1}{27} (2P^3 - 9Q + 27R)$$

$$P = a^2 + b^2 - x^2 - y^2 - z^2$$

$$Q = a^2 b^2 - a^2 z^2 - b^2 z^2 - a^2 y^2 - b^2 x^2$$

$$R = -a^2 b^2 z^2$$

The following argument shows which solution of the cubic corresponds to each of the coordinates ξ, η, ζ . It is seen from the cubic equation written in the form

$$\frac{x^2}{a^2 + \mu} + \frac{y^2}{b^2 + \mu} + \frac{z^2}{\mu} = 1$$

that the surfaces of constant μ are

ellipsoids if $0 \leq \mu < +\infty$ ($\mu = \xi$)

hyperboloids of one sheet if $-b^2 \leq \mu \leq 0$ ($\mu = \eta$)

hyperboloids of two sheets if $-a^2 \leq \mu \leq -b^2$ ($\mu = \zeta$)

and that any point in space is on exactly one surface from each of these three families. Thus, the equation always has three real solutions for μ , one in each of the intervals just

cited. If the three roots are distinct,⁽⁴⁾ then

$$\frac{A^3}{27} + \frac{B^2}{4} < 0$$

Therefore, $A < 0$ and $m = 2\sqrt{-A/3}$ is real and positive. Also,

$$\frac{\frac{B^2}{4}}{-\frac{A^3}{27}} < 1$$

$$\frac{9B^2}{A^2 m^2} < 1$$

$|\frac{3B}{Am}| < 1$
so that $\theta_1 = 1/3 \cos^{-1} \frac{3B}{Am}$ is real.

$$0 \leq \theta_1 \leq \frac{\pi}{3}$$

$$\frac{1}{2} \leq \cos \theta_1 \leq 1$$

$$-1 \leq \cos (\theta_1 + \frac{2\pi}{3}) \leq -\frac{1}{2}$$

$$-\frac{1}{2} \leq \cos (\theta_1 + \frac{4\pi}{3}) \leq \frac{1}{2}$$

Thus,

$$\cos(\theta_1 + \frac{2\pi}{3}) \leq \cos(\theta_1 + \frac{4\pi}{3}) \leq \cos \theta_1$$

$$-\frac{P}{3} + m \cos(\theta_1 + \frac{2\pi}{3}) \leq -\frac{P}{3} + m \cos(\theta_1 + \frac{4\pi}{3}) \leq -\frac{P}{3} + m \cos \theta_1$$

Since these expressions are the solutions of the cubic equation, it is now apparent which corresponds to each of the ellipsoidal coordinates:

$$\xi = -\frac{P}{3} + \cos \theta_1$$

$$\eta = -\frac{P}{3} + \cos(\theta_1 + \frac{4\pi}{3})$$

$$\zeta = -\frac{P}{3} + \cos(\theta_1 + \frac{2\pi}{3})$$

There are two curves on which not all the roots are distinct: The ellipse $x^2/a^2 + y^2/b^2 = 1$, $z=0$, where $\xi=\eta=0$; and the hyperbola $x^2/a^2 - b^2 - z^2/b^2 = 1$, $y=0$, where $\eta=\zeta=-b^2$.

In both cases, it may be shown that $A < 0$ and $A^3/27 + B^2/4 = 0$, whence $m > 0$, $|3B/Am| = 1$, and θ_1 is real. Then the proof follows as before.

13.2 OBLATE SPHEROIDAL COORDINATES ξ, η, ϕ

(a=b)

$$\frac{x^2}{\mu+a^2} + \frac{y^2}{\mu+a^2} + \frac{z^2}{\mu} = 1 \quad \text{where } \mu = \xi \text{ or } \eta$$

$$\rho^2 = x^2 + y^2 = (\xi + a^2)(\eta + a^2)/a^2, z^2 = -\xi\eta/a^2$$

$$0 \leq \xi < \infty, -a^2 \leq \eta \leq 0$$

$$\xi, \eta = \frac{r^2 - a^2}{2} \pm [(\frac{r^2 - a^2}{2})^2 + a^2 z^2]^{1/2}$$

$$\phi = \tan^{-1} y/x$$

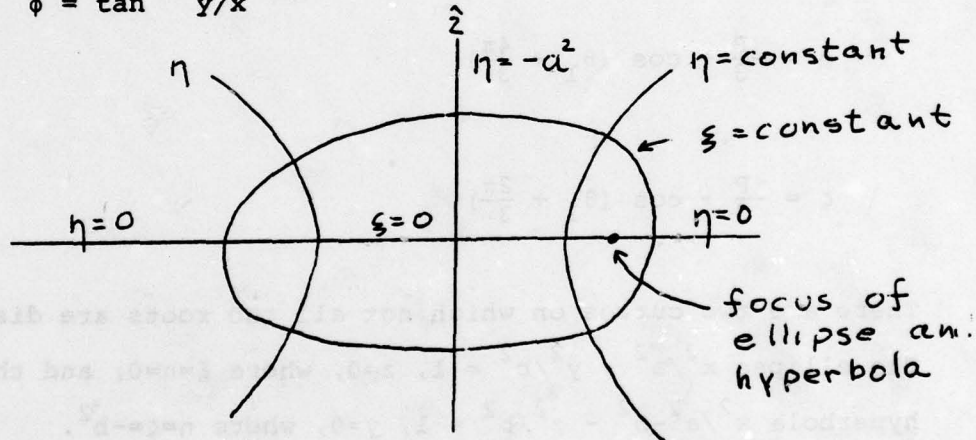


FIGURE 10.1 Oblate Spheroidal Coordinates

On the z axis, $\xi = z^2, \eta = -a^2$

On the aperture, $\xi = 0$ and $\eta = -a^2 + \rho^2$

On the screen, $\eta = 0$ and $\xi = -a^2 + \rho^2$

For the far field, $\xi/r^2 + 1$ and $\eta = \frac{-a^2 z^2}{r^2} = -a^2 \cos^2 \theta$ where θ is the angle between the z axis and \vec{r} .

13.3 INTEGRALS AND FORMULAE

$$\alpha = \cot^{-1}(\xi^{1/2}/a)$$

$$e = (1-b^2/a^2)^{1/2}$$

$$a > b$$

$$1. \int_{\xi}^{\infty} \frac{d\xi}{\xi^{1/2} (\xi+a^2)^{3/2} (\xi+b^2)^{1/2}} = \frac{2[F(\alpha, e) - E(\alpha, e)]}{a(a^2-b^2)} \quad (\text{grad } (2) \quad 222/18)$$

$$2. \int_{\xi}^{\infty} \frac{d\xi}{\xi^{1/2} (\xi+a^2)^{1/2} (\xi+b^2)^{3/2}} = \frac{2[a^2 E(\alpha, e) - b^2 F(\alpha, e)]}{ab^2 (a^2-b^2)}$$

$$- \frac{2\xi^{1/2}}{b^2 (\xi+a^2)^{1/2} (\xi+b^2)^{1/2}} \quad (\text{Grad } (2) \quad 222/12)$$

$$3. \int_{\xi}^{\infty} \frac{d\xi}{\xi^{3/2} (\xi+a^2)^{1/2} (\xi+b^2)^{1/2}} = \frac{2}{b^2 \xi^{1/2}} \frac{(\xi+b^2)^{1/2}}{(\xi+a^2)^{1/2}} - \frac{2}{ab^2} E(\alpha, e)$$

(Grad (2) 221/6)

$$4. \int_0^{\infty} \frac{d\xi}{\xi^{1/2} (\xi+a^2)^{3/2} (\xi+b^2)^{1/2}} = \frac{2}{a(a^2-b^2)} [F(\frac{\pi}{2}, e) - E(\frac{\pi}{2}, e)]$$

$$5. \int_0^{\infty} \frac{d\xi}{\xi^{1/2} (\xi+a^2)^{1/2} (\xi+b^2)^{3/2}} = \frac{2}{ab^2 (a^2-b^2)} [a^2 E(\frac{\pi}{2}, e) - b^2 F(\frac{\pi}{2}, e)]$$

$$6. \lim_{\epsilon \rightarrow 0} \epsilon^{1/2} \int_{\epsilon}^{\infty} \frac{d\xi}{\xi^{3/2} (\xi+a^2)^{1/2} (\xi+b^2)^{1/2}} = \frac{2}{ab}$$

$$7. E(a, e) = \int_0^a \sqrt{1-e^2 \sin^2 \phi} d\phi$$

$$8. F(a, e) = \int_0^a \frac{d\phi}{\sqrt{1-e^2 \sin^2 \phi}}$$

$$9. \lim_{b \rightarrow a} \frac{\xi + a^2}{F(\frac{\pi}{2}, e) - E(\frac{\pi}{2}, e)} = \frac{4a^2}{\pi} \cos^2 \phi$$

$$10. \lim_{b \rightarrow a} \frac{e^2}{F(\frac{\pi}{2}, e) - E(\frac{\pi}{2}, e)} = \frac{4}{\pi}$$

$$11. \lim_{b \rightarrow a} \frac{a^2 - b^2}{a^2 E(\frac{\pi}{2}, e) - b^2 F(\frac{\pi}{2}, e)} = \frac{4}{\pi}$$

$$12. \lim_{b \rightarrow a} \frac{F(a, e) - E(a, e)}{F(\frac{\pi}{2}, e) - E(\frac{\pi}{2}, e)} = \frac{2}{\pi} \left(a - \frac{a \xi^{1/2}}{\xi + a^2} \right)$$

$$13. \lim_{b \rightarrow a} \frac{a^2 E(a, e) - b^2 F(a, e)}{a^2 E(\frac{\pi}{2}, e) - b^2 F(\frac{\pi}{2}, e)} = \frac{2}{\pi} \left(a + \frac{a \xi^{1/2}}{\xi + a^2} \right)$$

$$14. \int_0^1 \frac{\cos ax dx}{\sqrt{1-x^2}} = \frac{\pi}{2} J_0(a) \quad (\text{grad } (2) \ 419/3.753/2)$$

$$15. \int_0^a x^{v+1} \sin(b\sqrt{a^2 - x^2}) J_v(x) dx = \sqrt{\pi/2} a^{v+3/2} b (1+b^2)^{-v/2-3/4}$$

$$J_{v+3/2}(a\sqrt{1+b^2}) \quad (\text{grad } (2) \ 761/1)$$

$$16. \quad j_n(z) = \sqrt{\pi/2z} J_{n+1/2}(z) \quad (\text{Abram } (3) \ 437/10.1.1)$$

$$17. \quad j_1(z) = \frac{\sin z}{z^2} - \frac{\cos z}{z} \quad (\text{Abram } (3) \ 438/10.1.11)$$

$$18. \quad E\left(\frac{\pi}{2}, e\right) = \frac{\pi}{2} \left[1 - \left(\frac{1}{2}\right)^2 \frac{e^2}{1} - \left(\frac{1 \cdot 3}{2 \cdot 4}\right)^2 \frac{e^4}{3} - \left(\frac{1 \cdot 3 \cdot 5}{2 \cdot 4 \cdot 6}\right)^2 \frac{e^6}{5} - \dots \right]$$

(Abram (3) 591/17.3.12)

$$19. \quad F\left(\frac{\pi}{2}, e\right) = \frac{\pi}{2} \left[1 + \left(\frac{1}{2}\right)^2 e^2 + \left(\frac{1 \cdot 3}{2 \cdot 4}\right)^2 e^4 + \left(\frac{1 \cdot 3 \cdot 5}{2 \cdot 4 \cdot 6}\right)^2 e^6 + \dots \right]$$

(Abram (3) 591/17.3.11)

13.4 LAPLACE EQUATION

$$1. \quad \nabla^2 s = \frac{1}{h_1 h_2 h_3} \left[\frac{\partial}{\partial \mu_1} \left(\frac{h_2 h_3}{h_1} \frac{\partial s}{\partial \mu_1} \right) + \frac{\partial}{\partial \mu_2} \left(\frac{h_1 h_3}{h_2} \frac{\partial s}{\partial \mu_2} \right) + \frac{\partial}{\partial \mu_3} \left(\frac{h_1 h_2}{h_3} \frac{\partial s}{\partial \mu_3} \right) \right]$$

where

$$h_j^2 = \sum_{i=1}^3 \left(\frac{\partial x_i}{\partial \mu_j} \right)^2$$

$$x_i = x_i(\mu_1, \mu_2, \mu_3) \quad (\mu_j \text{ is an orthogonal system}) \quad (\text{CRC } (4) \text{ p. 494})$$

$$2. \hat{e}_{H_i} = \frac{1}{h_i} \frac{\partial \vec{r}}{\partial \mu_i}$$

$$\text{where } \vec{r} = \sum_{i=1}^3 \hat{x}_i x_i = x\hat{x} + y\hat{y} + z\hat{z}$$

3. For ellipsoidal coordinates

$$h_1 = \frac{1}{2} \left[\frac{(\xi-\eta)(\xi-\zeta)}{(\xi+a^2)(\xi+b^2)\xi} \right]^{1/2}$$

$$h_2 = \frac{1}{2} \left[\frac{(\xi-\eta)(\zeta-\eta)}{(\eta+a^2)(\eta+b^2)\eta} \right]^{1/2}$$

$$h_3 = \frac{1}{2} \left[\frac{(\zeta-\xi)(\zeta-\eta)}{(\zeta+a^2)(\zeta+b^2)\zeta} \right]^{1/2}$$

$$\nabla^2 S = \frac{-4}{(\xi-\eta)(\xi-\zeta)(\eta-\zeta)} [(\eta-\zeta) R_\xi \frac{\partial}{\partial \xi} R_\xi \frac{\partial S}{\partial \xi}$$

$$+ (\xi-\zeta) R_\eta \frac{\partial}{\partial \eta} R_\eta \frac{\partial S}{\partial \eta} + (\xi-\eta) R_\zeta \frac{\partial}{\partial \zeta} R_\zeta \frac{\partial S}{\partial \zeta}]$$

$$\text{where } R_\xi = [\xi(\xi+a^2)(\xi+b^2)]^{1/2}$$

$$R_\eta = [-\eta(\eta+a^2)(\eta+b^2)]^{1/2}$$

$$R_\zeta = [\zeta(\zeta+a^2)(\zeta+b^2)]^{1/2}$$

$$x_\xi = \frac{(\eta+a^2)(\zeta+a^2)}{2xa^2(a^2-b^2)}, \quad y_\xi = \frac{(\eta+b^2)(\zeta+b^2)}{-2yb^2(a^2-b^2)}, \quad z_\xi = \frac{\eta\zeta}{2za^2b^2}$$

$$x_\eta = \frac{(\xi+a^2)(\zeta+a^2)}{2xa^2(a^2-b^2)}, \quad y_\eta = \frac{(\xi+b^2)(\zeta+b^2)}{-2yb^2(a^2-b^2)}, \quad z_\eta = \frac{\xi\zeta}{2za^2b^2}$$

$$x_\zeta = \frac{(\xi+a^2)(\eta+a^2)}{2xa^2(a^2-b^2)}, \quad y_\zeta = \frac{(\xi+b^2)(\eta+b^2)}{-2yb^2(a^2-b^2)}, \quad z_\zeta = \frac{\xi\eta}{2za^2b^2}$$

$$\hat{e}_\xi = \frac{1}{h_\xi} \frac{\partial \vec{r}}{\partial \xi} = \frac{1}{h_\xi} [\hat{x} x_\xi + \hat{y} y_\xi + \hat{z} z_\xi]$$

$$\hat{e}_\xi = \left[\frac{(\xi-\eta)(\xi-\zeta)}{\xi(\xi+a^2)(\xi+b^2)} \right]^{-1/2} [\hat{x} \frac{(\eta+a^2)(\zeta+a^2)}{xa^2(a^2-b^2)} - \hat{y} \frac{(\eta+b^2)(\zeta+b^2)}{yb^2(a^2-b^2)}$$

$$+ \frac{2\eta\zeta}{za^2b^2}]$$

$$\hat{e}_\eta = \left[\frac{\eta(\eta+a^2)(\eta+b^2)}{(\xi-\eta)(\zeta-\eta)} \right]^{1/2} [\hat{x} \frac{(\xi+a^2)(\zeta+a^2)}{xa^2(a^2-b^2)} - \hat{y} \frac{(\xi+b^2)(\zeta+b^2)}{yb^2(a^2-b^2)}$$

$$+ \frac{2\xi\zeta}{za^2b^2}]$$

$$\hat{e}_\zeta = \left[\frac{\zeta(\zeta+a^2)(\zeta+b^2)}{(\zeta-\xi)(\zeta-\eta)} \right]^{1/2} \left[x \frac{(\xi+a^2)(\eta+a^2)}{xa^2(a^2-b^2)} - y \frac{(\xi+b^2)(\eta+b^2)}{yb^2(a^2-b^2)} \right. \\ \left. + \frac{2\xi\eta}{za^2b^2} \right]$$

$$\xi_x = \frac{2x\xi(\xi+b^2)}{(\xi-\zeta)(\xi-\eta)}, \quad \xi_y = \frac{2y\xi(\xi+a^2)}{(\xi-\eta)(\xi-\zeta)}, \quad \xi_z = \frac{2z(\xi+a^2)(\xi+b^2)}{(\xi-\eta)(\xi-\zeta)}$$

$$\eta_x = \frac{2x\eta(\eta+b^2)}{(\eta-\xi)(\eta-\zeta)}, \quad \eta_y = \frac{2y\eta(\eta+a^2)}{(\eta-\xi)(\eta-\zeta)}, \quad \eta_z = \frac{2z(\eta+a^2)(\eta+b^2)}{(\eta-\xi)(\eta-\zeta)}$$

$$\zeta_x = \frac{2x\zeta(\zeta+b^2)}{(\zeta-\xi)(\zeta-\eta)}, \quad \zeta_y = \frac{2y\zeta(\zeta+a^2)}{(\zeta-\xi)(\zeta-\eta)}, \quad \zeta_z = \frac{2z(\zeta+a^2)(\zeta+b^2)}{(\zeta-\xi)(\zeta-\eta)}$$

$$\Delta = \begin{vmatrix} \xi_x & \eta_x & \zeta_x \\ \xi_y & \eta_y & \zeta_y \\ \xi_z & \eta_z & \zeta_z \end{vmatrix}^{-1} = \begin{vmatrix} x_\xi & x_\eta & x_\zeta \\ y_\xi & y_\eta & y_\zeta \\ z_\xi & z_\eta & z_\zeta \end{vmatrix} = \frac{(\xi-\eta)(\eta-\zeta)(\zeta-\xi)}{8a^2b^2(a^2-b^2)xyz}$$

13.5 DERIVATION OF BOUNDARY CONDITIONS

To get a boundary condition for an EMP plane wave, consider an incident wave which has a transform

$$\hat{\vec{E}}^i = \hat{\vec{E}}_o^i(\omega) \exp\left(-\frac{j\omega k_i}{c_o} \cdot \vec{r}\right)$$

If we neglect the reflected waves on the metal, then the transmitted wave will have fields related by

$$\hat{\vec{H}}^t = R_t \hat{x} \vec{E}^t \sqrt{\epsilon/\mu - j\sigma/\omega\mu} = \hat{k}_t \hat{x} \vec{E}^t \sqrt{-\frac{j\sigma}{\omega\mu}(1 + \frac{j\omega\epsilon}{\sigma})}$$

For EMP the highest "practical" frequency is 10^8 Hz. For copper $\omega\epsilon/\sigma = 2\pi(10^8)(10)(8.834 \times 10^{-12})/5.8 \times 10^7 = 10^{-9}$ so that the correction term can be neglected even for the highest frequency. Hence

$$R_t \hat{x} \vec{E}^t = \sqrt{\omega\mu/2\sigma} \hat{\vec{H}}^t (1+j)$$

At the boundary $\hat{n} \cdot \vec{H}$ is approximately zero so that $\hat{k}_t \hat{n} = \hat{n}$ = the normal into the metal. Since $\hat{n} \times \vec{E}^t$ is continuous across a boundary, then this must be the boundary condition inside the cavity, at the cavity wall. This is the boundary condition of Jackson. (2)

13.6 DERIVATION OF COEFFICIENTS

$$\nabla \times \vec{E} = -j\omega \mu_o \vec{H}$$

$$\nabla \times \vec{E}_M = -j\omega_M \mu_o \vec{H}_M$$

$$\nabla \times \vec{H} = j\omega \epsilon_o \vec{E}$$

$$\nabla \times \vec{H}_M = j\omega_M \epsilon_o \vec{E}_M$$

$$\begin{cases} \vec{E} = \sum A_M \vec{E}_M \\ \vec{H} = \nabla \phi + k_o \sum \frac{A_M \vec{H}_M}{k_M} \end{cases}$$

$$\phi = \int_S \hat{n} \cdot \vec{H} G(\vec{r}, \vec{r}') dS \quad \nabla^2 G = \delta(\vec{r}, \vec{r}')$$

$$\frac{\partial G}{\partial n} = 0 \text{ on } S$$

$$A_M = \int \vec{E} \cdot \vec{E}_M d\tau \quad \nabla \times \nabla \times E_M = +k_M^2 E_M$$

$$k_M^2 A_M = \int \vec{E} \cdot \nabla \times \nabla \times \vec{E}_M d\tau$$

$$k_o^2 A_M = \int \vec{E}_M \cdot \nabla \times \nabla \times \vec{E} d\tau$$

$$(k_o^2 - k_M^2) A_M = \int (\vec{E}_M \cdot \nabla \times \nabla \times \vec{E} - \vec{E} \cdot \nabla \times \nabla \times \vec{E}_M) d\tau$$

$$\nabla \cdot (\vec{E}_M \times \nabla \times \vec{E} - \vec{E} \times \nabla \times \vec{E}_M) = \nabla \times \vec{E} \cdot \nabla \times \vec{E}_M - \vec{E}_M \cdot \nabla \times \nabla \times \vec{E} - \nabla \times \vec{E}_M \cdot \nabla \times \vec{E} + \vec{E} \cdot \nabla \times \nabla \times \vec{E}_M$$

$$(k_o^2 - k_M^2) A_M = \int \nabla \cdot (\vec{E} \times \nabla \times \vec{E}_M - \vec{E}_M \times \nabla \times \vec{E}) d\tau$$

$$= \int_S \hat{n} \cdot (\vec{E} \times \nabla \times \vec{E}_M - \vec{E}_M \times \nabla \times \vec{E}) dS$$

$$= \int_S (\hat{n} \times \vec{E} \cdot \nabla \times \vec{E}_M - \hat{n} \times \vec{E}_M \cdot \nabla \times \vec{E}) dS$$

But $\hat{n} \times \vec{E}_M = 0$ on S

$$(k_o^2 - k_M^2) A_M = \int_S \hat{n} \cdot \vec{E} \times \nabla \times \vec{E}_M dS$$

NOTE 343

TRANSIENT ELECTROMAGNETIC CHARACTERIZATION OF ARBITRARY
CONDUCTING BODIES THROUGH AN APERTURE-PERFORATED CONDUCTING SCREEN

by

Korada R. Umashankar
Carl E. Baum

Air Force Weapons Laboratory

March 1978

TRANSIENT ELECTROMAGNETIC CHARACTERIZATION
OF ARBITRARY CONDUCTING BODIES THROUGH
AN APERTURE-PERFORATED CONDUCTING SCREEN

ABSTRACT

A general procedure for the systematic transient characterization of arbitrarily shaped conducting bodies placed behind an aperture-perforated conducting screen is discussed. Coupled integro-differential equations are derived for the complex coupled boundary value problem. A few specific examples of aperture-wire scatterer or antenna geometries are treated both analytically and numerically for transient electromagnetic characterization based on the singularity expansion method. Both the frequency and time domain results are given for the coupled problem.

TABLE OF CONTENTS

<u>Chapter</u>		<u>Page</u>
Introduction		343-8
I	General Formulation of the Aperture-Scatterer Integral Equation	343-10
II	Integral Equations for the Various Aperture and Slot Geometries	343-26
	A. Rectangular Aperture	343-26
	B. Narrow Slot	343-28
	C. Narrow Multiple Slots	343-30
	D. Infinitely Long Slots: TE and TM	343-32
	E. Numerical Results	343-36
	F. Aperture Dipole Moments and Penetrated Fields	343-46
III	Analysis of the Conducting Bodies in the Presence of Ground Screen	343-49
	A. Arbitrarily Oriented Thin Wire Configurations	343-49
	B. Numerical Examples of Wire Structures	343-56
	C. Two-Dimensional Conducting Scatterer Above a Ground Plane	343-56
	D. Numerical Results for Circular Cylinder	343-68
IV	Characterization of Bodies Behind Aperture-Perforated Screen	343-71
	A. Finite Wire Scatterer Behind a Rectangular Aperture	343-71
	B. Finite Wire Parallel to the Plane and Behind the Narrow Slot	343-75
	C. Numerical Results	343-76
	D. SEM Characterization	343-81
	E. Finite Wire Antenna Illuminating Narrow Slot Perforated Screen	343-106
	F. Equivalent Dipole Illuminating Narrow Slot in a Conducting Screen	343-112
References		343-126

ILLUSTRATIONS

<u>Figure</u>		<u>Page</u>
1.1	Conducting Scatterer Behind an Aperture Perforated Conducting Screen	343-11
1.2	Illuminated Half-Space Equivalences	343-12
1.3	Shadow Half-Space Equivalences	343-13
1.4	Antenna Behind an Aperture Perforated Conducting Screen	343-18
1.5	Illustration of the Closure of the Bromwich Contour in s-Plane	343-24
2.1	Narrow Slot in a Conducting Screen	343-27
2.2	Multiple Narrow Slots in a Conducting Screen	343-31
2.3	Infinite Slot in a Conducting Screen	343-33
2.4	TE Excited Infinite Slot	343-34
2.5	TM Excited Infinite Slot	343-34
2.6	TE Magnetic Current in 0.4-Wavelength Slot for Different ϵ_+	343-38
2.7	TE Magnetic Current in 0.5-Wavelength Slot for Different σ_+	343-39
2.8	TM Magnetic Current in 0.5-Wavelength Slot for Different ϵ_+	343-40
2.9	TM Magnetic Current in 0.5-Wavelength Slot for Different σ_+	343-41
2.10	Far Magnetic Field of TE Excited Slot for Different ϵ_+	343-42
2.11	Far Electric Field of TM Excited Slot for Different ϵ_+	343-43
2.12	Magnetic Current Distribution in a Square Aperture	343-44
2.13	Magnetic Current Distribution in a Narrow Rectangular Slot	343-45

ILLUSTRATIONS (Cont'd.)

<u>Figure</u>		<u>Page</u>
2.14	Electric Field Penetrated in the Region $z > 0$ for Square Aperture Compared with Magnetic Dipole Moment	343-47
2.15	Electric Field Penetrated in the Region $z > 0$ for Square Aperture Compared with Electric Dipole Moment	343-48
3.1	Arbitrarily Oriented Wires in Free Space	343-51
3.2	Coordinates of Two Coupled Wires	343-54
3.3	Testing Triangles on Two Coupled p and q Wires	343-55
3.4	Wire Biconical Antenna in Free Space	343-57
3.5	Currents I_1 and I_2 on Wire Biconical Antenna in Free Space	343-58
3.6	Far Field Pattern of Wire Biconical Antenna in Free Space, E_θ -Component	343-59
3.7	Wire Biconical Antenna Above and Perpendicular to Ground Plane	343-60
3.8	Currents I_1, I_2 and I_3, I_4 on Wire Biconical Antenna Above and Perpendicular to Ground Plane	343-61
3.9	Wire Biconical Antenna Above and Parallel to Ground Plane	343-62
3.10	Currents I_1 and I_2 on Wire Biconical Antenna Above and Parallel to Ground Plane	343-63
3.11	(a) Conducting Cylinder Above a Ground Plane (b) Ground Plane Replaced by a Cylinder Image	343-65
3.12	Geometry for the TM Scattering of an Infinite Cylinder and Its Image	343-66
3.13	Magnitude of the Current (TM) on Infinite Cylinder Above Ground Plane	343-69
3.14	Phase of the Current (TM) on Infinite Cylinder Above Ground Plane	343-70

ILLUSTRATIONS (Cont'd.)

<u>Figure</u>		<u>Page</u>
4.1	Finite Wire Scatterer Behind Narrow Slot Conducting Screen	343-72
4.2	Electric Current Distribution on Finite Wire Scatterer in the Presence of Slot, $L=0.5$, $a=0.001$, $\lambda=0.5$, $w=0.05$, $(x_c, y_c, z_c)=(0, 0, 0.5)$ at Frequency 300 MHz	343-77
4.3	Axial Magnetic Current Distribution in a Narrow Slot in the Presence of Wire, $L=0.5$, $a=0.001$, $\lambda=0.5$, $w=0.05$, $(x_c, y_c, z_c)=(0, 0, 0.5)$ at Frequency 300 MHz	343-78
4.4	Electric Current on Finite Wire at Its Center in the Presence of Slot as a Function of Frequency	343-79
4.5	Axial Magnetic Current in Narrow Slot at Its Center in the Presence of Wire as a Function of Frequency	343-80
4.6	Natural Resonance of Isolated Narrow Slot, $\lambda=2$, $w=0.1$	343-82
4.7	Trajectory of s_{11} as a Function of w/λ of Isolated Narrow Slot	343-83
4.8	Natural Resonance of Isolated Finite Wire, $L=2$, $a=0.01$	343-84
4.9	Geometry of Two Coupled Wires	343-86
4.10	Trajectory of the First Set of Poles s_{11} as a Function of v	343-88
4.11	Trajectory of the First Three Anti-Symmetry Poles s_{11} , s_{12} , and s_{13} as a Function of v	343-89
4.12	Natural Resonance of Finite Wire Placed Parallel Over a Perfect Electric Ground Plane	343-91
4.13	Trajectory of First Pole s_{11} as a Function of Distance Over the Ground Plane	343-92
4.14	Coupling Coefficient Corresponding to First Symmetric Pole s_{11} as a Function of v	343-93

ILLUSTRATIONS (Cont'd.)

<u>Figure</u>	<u>Page</u>
4.15 Coupling Coefficient Corresponding to First Anti-Symmetric Pole s_{11} as a Function of ν	343-94
4.16 Geometry of Finite Wire Over Ground Plane with No Slot Perforated	343-95
4.17 Time Domain Solution of Wire Over Ground Plane Based on SEM with Step Plane Wave Incident, $t=0$ at $z=0$	343-96
4.18 Natural Resonances of Finite Wire Behind a Narrow Slot Perforated Conducting Screen	343-99
4.19 Trajectory of the First Set of Poles s_{11} as a Function of $\cos\beta$	343-100
4.20 Trajectory of the Second Set of Poles s_{12} as a Function of $\cos\beta$	343-101
4.21 Time Domain Electric Current at the Center of Finite Wire in the Presence of Narrow Slot with Step Plane Wave Incident on Slot	343-102
4.22 Time Domain Magnetic Current at the Center of Narrow Slot in the Presence of Finite Wire with Step Plane Wave Incident on Slot	343-103
4.23 Time Domain Electric Current at the Center of Finite Wire in the Presence of Narrow Slot with EMP Incident on Slot	343-104
4.24 Time Domain Magnetic Current at the Center of Narrow Slot in the Presence of Finite Wire with EMP Incident on Slot	343-105
4.25 Finite Wire Antenna Behind Narrow Slot Conducting Screen	343-107
4.26 Electric Current on Finite Wire Antenna at Its Center in the Presence of Narrow Slot as a Function of Frequency	343-108
4.27 Axial Magnetic Current in Narrow Slot at Its Center in the Presence of Wire Antenna as a Function of Frequency	343-109

ILLUSTRATIONS (Cont'd.)

<u>Figure</u>		<u>Page</u>
4.28	Time Domain Electric Current at the Center of Finite Wire Antenna in the Presence of Narrow Slot, with Step Excitation Turned on at $t=0$	343-110
4.29	Time Domain Magnetic Current at the Center of Narrow Slot in the Presence of Wire Antenna, with Step Excitation Turned on at $t=0$	343-111
4.30	Equivalent Dipole Exciting Narrow Slot Perforated Conducting Screen	343-113
4.31	Real Part of the Electric Current on Equivalent Dipole in the Presence of Narrow Slot for $\cos\beta=1$	343-114
4.32	Imaginary Part of the Electric Current on Equivalent Dipole in the Presence of Narrow Slot for $\cos\beta=1$	343-115
4.33	Real Part of the Axial Magnetic Current in Slot in the Presence of Equivalent Dipole for $\cos\beta=1$	343-117
4.34	Imaginary Part of the Axial Magnetic Current in Slot in the Presence of Equivalent Dipole for $\cos\beta=1$	343-118
4.35	Real Part of Input Impedance of Equivalent Dipole in the Presence of Narrow Slot for $\cos\beta=1$	343-119
4.36	Imaginary Part of Input Impedance of Equivalent Dipole in the Presence of Narrow Slot for $\cos\beta=1$	343-120
4.37	Time Domain Electric Current on Equivalent Dipole at the Feed Point in the Presence of Narrow Slot, Turned on at $t=0$, for $(x_c, y_c)=(0.5, 0.5)$	343-121
4.38	Time Domain Axial Magnetic Current at the Center of Narrow Slot in the Presence of Equivalent Dipole, Turned on at $t=0$, for $(x_c, y_c)=(0.5, 0.5)$	343-122
4.39	Time Domain Electric Current on Equivalent Dipole at the Feed Point in the Presence of Narrow Slot, Turned on at $t=0$, for $(x_c, y_c)=(0.5, 1.0)$	343-123
4.40	Time Domain Axial Magnetic Current at the Center of Narrow Slot in the Presence of Equivalent Dipole, Turned on at $t=0$, for $(x_c, y_c)=(0.5, 1.0)$	343-124

INTRODUCTION

Electromagnetic transient excitation of arbitrarily shaped objects through an aperture-perforated conducting screen is a complex interaction problem. This has been given special attention recently, particularly in the broad area of EMP interaction and other related simulation applications. Also, a great deal of effort is being applied to assessing the electromagnetic effects on the protected objects behind screen in the event of external transient nuclear explosions.^{1,2} This problem of aperture coupling and penetration of electromagnetic energy has been studied by many investigators to characterize general complex aperture shapes in the form of holes, slits in a ground screen³⁻⁵ or in a scattering body itself,^{6,7} which are of practical importance in the electromagnetic pulse and in interference studies. But the transient analysis and the subsequent characteristic response prediction become a still further involved process if there are other scattering objects in the vicinity of apertures, wherein one has to take into account fully the mutual interaction between them.^{8,9}

As such diffraction by complex aperture shapes has been studied extensively by both analytical and numerical methods, basically in the frequency domain, based on the formulation of integral equations for the aperture-screen boundary value problem. A circular aperture,^{4,10} rectangular aperture,^{5,11-13} narrow finite slot and infinitely long slot¹⁴ in a conducting screen as canonical problems give a basic foundation to the treatment of general aperture shapes in a screen.

This paper reports the preliminary investigation of the interaction problem in terms of a set of coupled integro-differential equations for a general conducting scatterer placed behind an arbitrarily shaped aperture-perforated conducting screen. Basically this turns out to be a three-body scattering problem or a two-body scattering problem with a leaky ground plane due to the presence of the aperture. Further, the following specific hybrid

combinations are characterized from the integral equation formulations:

- i) narrow finite slot
- ii) array of narrow finite slots
- iii) single or multi-infinite slots
- iv) square and circular apertures

in the presence of simple objects in the form of

- i) finite straight wire
- ii) array of straight wires
- iii) infinitely long single and multiple wires
- iv) two-dimension plate surfaces

Both the frequency-domain and the time-domain characterization is discussed based on the extensive application of the Singularity Expansion Method.² Some numerical results are reported to explain various types of interaction.

CHAPTER I

General Formulation of the Aperture-Scatterer Integral Equation

The problem of electromagnetic coupling to a general conducting scatterer behind an aperture-perforated conducting screen is formulated in terms of a set of integro-differential equations. In figure 1.1 is shown the geometry of the interaction problem discussed, wherein S_a is an arbitrary shaped aperture in an infinite, perfectly conducting screen assumed to be in xy-plane, separating two half-space media. The left-hand space (medium 1) and the right-hand space (medium 2) respectively have permeability, permittivity and conductivity of $(\mu_-, \epsilon_-, \sigma_-)$ and $(\mu_+, \epsilon_+, \sigma_+)$ as their characteristics. The incident field $(\tilde{E}^i, \tilde{H}^i)$ is assumed to exist in left-hand space medium 1 and illuminates the aperture. The perfectly conducting general-shaped scatterer S_c is in the right-hand space (medium 2) (shadow side), which has direct electromagnetic coupling to the aperture S_a .

In the following a set of coupled integral equations are derived by treating the tangential aperture electric field \tilde{E}_{ta} or the equivalent magnetic current $\tilde{J}_{sm} = -\tilde{E}_{ta} \times \hat{I}_z$ and the equivalent induced electric current distribution \tilde{J}_s on the conducting scatterer as unknowns.

In figures 1.2 and 1.3 are indicated the step-by-step reduction of the original problem to an equivalent problem by invoking both image theory and field equivalence principle valid for only $z < 0$ and $z > 0$ respectively. Based on figure 1.2 the total magnetic field \tilde{H}_- and the total electric field \tilde{E}_- valid for $z < 0$, can be written^{14,15} in terms of the scattered field due to the equivalent magnetic current \tilde{J}_{sm} and the short-circuited fields $(\tilde{E}_{sc_}, \tilde{H}_{sc_})$,

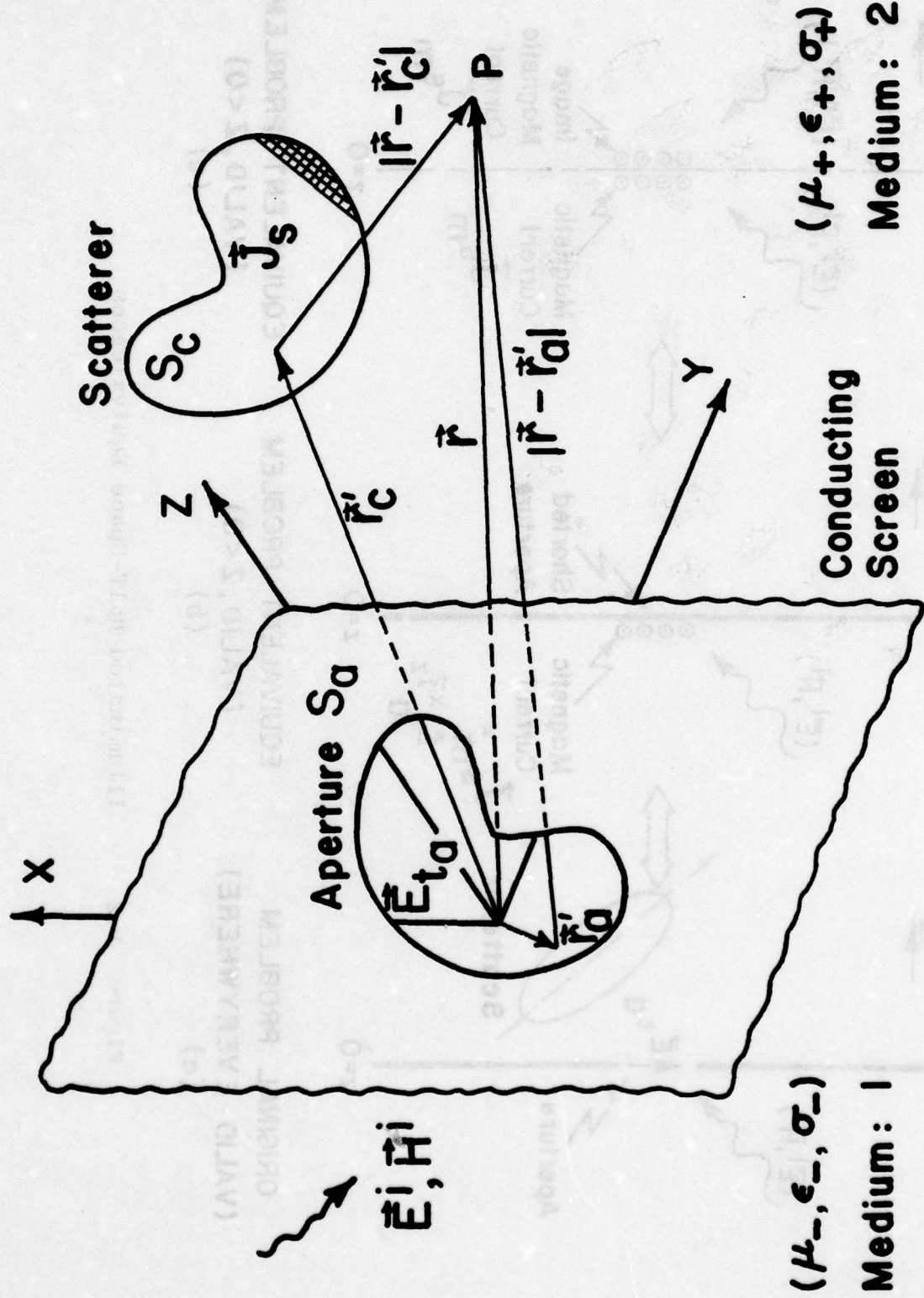


Figure 1.1

Conducting Scatterer Behind an Aperture
Perforated Conducting Screen

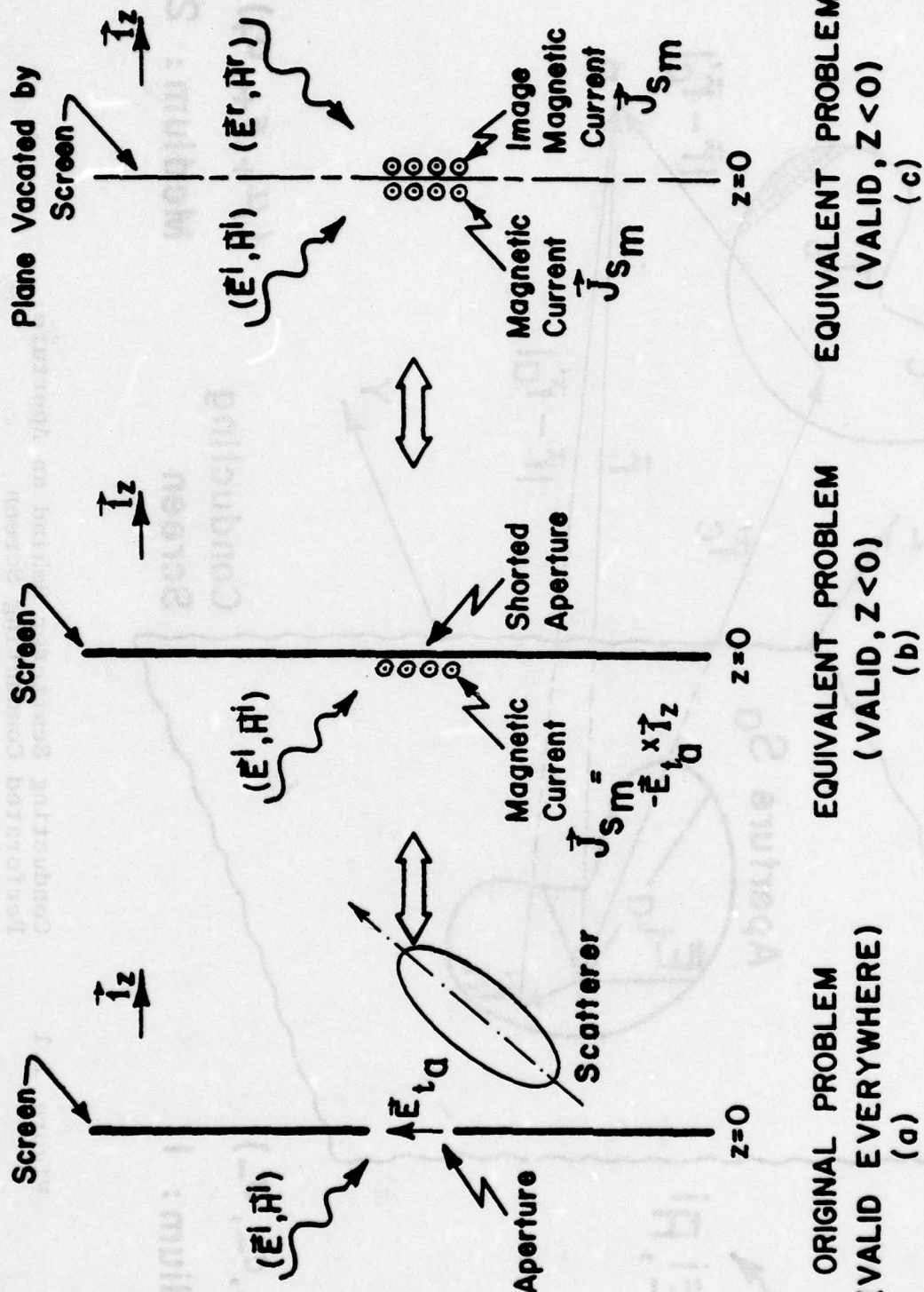


Figure 1.2 Illuminated Half-Space Equivalences

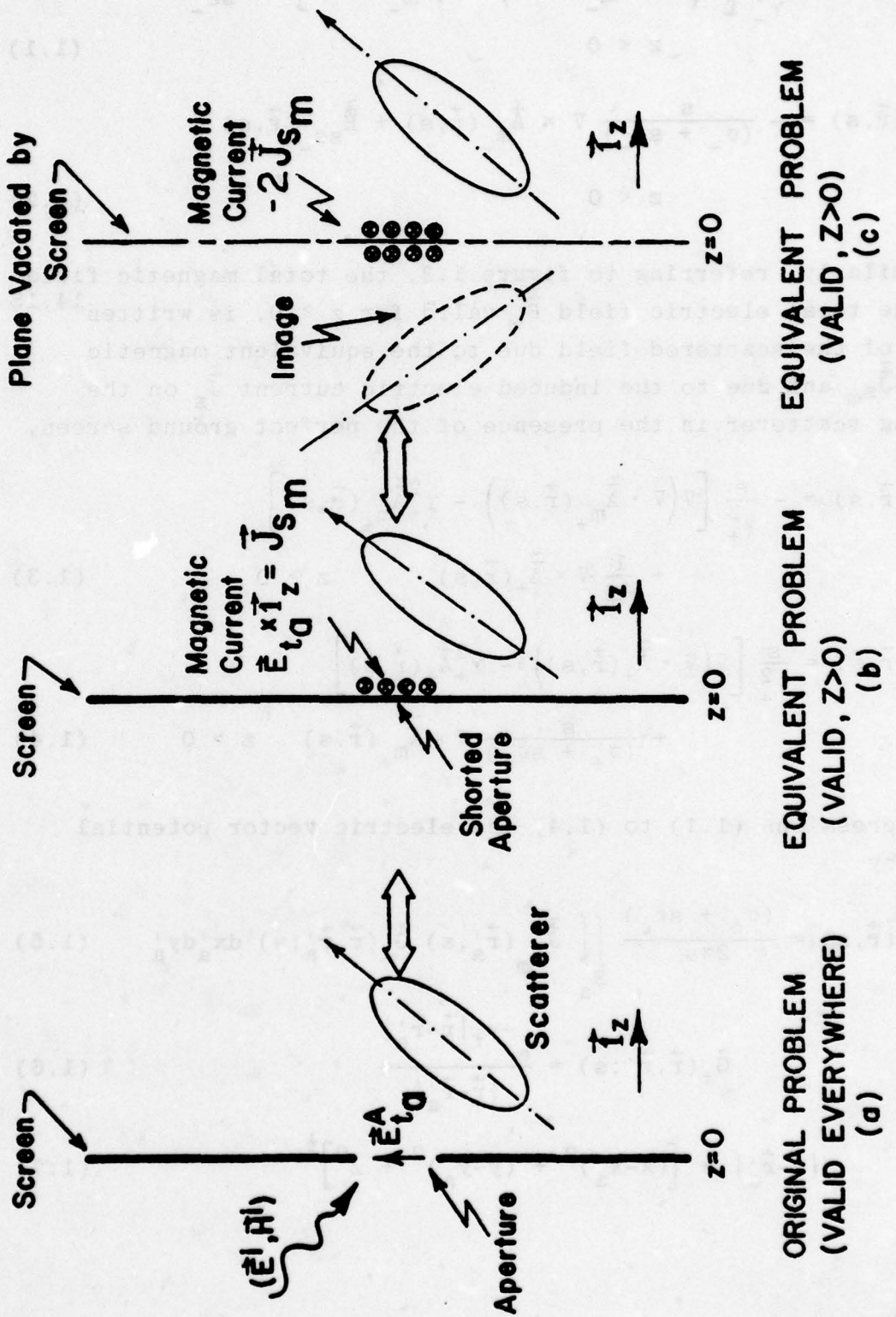


Figure 1.3

Shadow Half-Space Equivalences

$$\tilde{\vec{H}}_-(\vec{r}, s) = \frac{s}{\gamma_-^2} \left[\nabla \left(\nabla \cdot \tilde{\vec{A}}_{m_-}(\vec{r}, s) \right) - \gamma_-^2 \tilde{\vec{A}}_{m_-}(\vec{r}, s) \right] + \tilde{\vec{H}}_{sc_-}(\vec{r}, s) \quad z < 0 \quad (1.1)$$

$$\tilde{\vec{E}}_-(\vec{r}, s) = - \frac{s}{(\sigma_- + s\epsilon_-)} \nabla \times \tilde{\vec{A}}_{m_-}(\vec{r}, s) + \tilde{\vec{E}}_{sc_-}(\vec{r}, s) \quad z < 0 \quad (1.2)$$

Similarly, referring to figure 1.3, the total magnetic field $\tilde{\vec{H}}_+$ and the total electric field $\tilde{\vec{E}}_+$ valid for $z > 0$, is written^{14,15} in terms of the scattered field due to the equivalent magnetic current $-\tilde{\vec{J}}_{sm}$ and due to the induced electric current $\tilde{\vec{J}}_s$ on the conducting scatterer in the presence of the perfect ground screen,

$$\begin{aligned} \tilde{\vec{H}}_+(\vec{r}, s) = & - \frac{s}{\gamma_+^2} \left[\nabla \left(\nabla \cdot \tilde{\vec{A}}_{m_+}(\vec{r}, s) \right) - \gamma_+^2 \tilde{\vec{A}}_{m_+}(\vec{r}, s) \right] \\ & + \frac{1}{\mu_+} \nabla \times \tilde{\vec{A}}_+(\vec{r}, s) \quad z > 0 \end{aligned} \quad (1.3)$$

$$\begin{aligned} \tilde{\vec{E}}_+(\vec{r}, s) = & \frac{s}{\gamma_+^2} \left[\nabla \left(\nabla \cdot \tilde{\vec{A}}_+(\vec{r}, s) \right) - \gamma_+^2 \tilde{\vec{A}}_+(\vec{r}, s) \right] \\ & + \frac{s}{(\sigma_+ + s\epsilon_+)} \nabla \times \tilde{\vec{A}}_{m_+}(\vec{r}, s) \quad z > 0 \end{aligned} \quad (1.4)$$

In the expressions (1.1) to (1.4) the electric vector potential is given by

$$\tilde{\vec{A}}_{m_\pm}(\vec{r}, s) = \frac{(\sigma_\pm + s\epsilon_\pm)}{2\pi s} \iint_{S_a} \tilde{\vec{J}}_{sm}(\vec{r}'_a, s) \tilde{G}_\pm(\vec{r}, \vec{r}'_a; s) dx'_a dy'_a \quad (1.5)$$

$$\tilde{G}_\pm(\vec{r}, \vec{r}'; s) = \frac{e^{-\gamma_\pm |\vec{r}-\vec{r}'_a|}}{|\vec{r}-\vec{r}'_a|} \quad (1.6)$$

$$|\vec{r}-\vec{r}'_a| = \left[(x-x'_a)^2 + (y-y'_a)^2 + z^2 \right]^{\frac{1}{2}} \quad (1.7)$$

and the magnetic vector potential \tilde{A}_+ due to the conducting scatterer S_c and its image S_i is given by

$$\begin{aligned} \tilde{A}_+(\vec{r}, s) = & \frac{\mu_+}{4\pi} \left[\iint_{S_c} \tilde{J}_s(\vec{r}'_c, s) \tilde{g}(\vec{r}, \vec{r}'_c; s) d\vec{s}'_c \right. \\ & \left. + \iint_{S_i} \tilde{J}_{s_i}(\vec{r}'_i, s) \tilde{g}(\vec{r}, \vec{r}'_i; s) d\vec{s}'_i \right] \end{aligned} \quad (1.8)$$

$$\tilde{g}(\vec{r}, \vec{r}'_{c,i}; s) = \frac{e^{-\gamma_+ |\vec{r} - \vec{r}'_{c,i}|}}{|\vec{r} - \vec{r}'_{c,i}|} \quad (1.9)$$

and the propagation constant referred to each side of the medium

$$\gamma_\pm = [s\mu_\pm(\sigma_\pm + s\epsilon_\pm)]^{\frac{1}{2}} \quad (1.10)$$

in which s is the complex frequency with e^{st} field variations being assumed in the above field expressions. In fact s is the two-sided Laplace transform variable, and in deriving the above field expressions the following Laplace transform is applied to convert the field quantities from time domain to the complex frequency domain,²

$$\tilde{f}(s) \equiv \int_{-\infty}^{\infty} f(t) e^{-st} dt \quad (1.11)$$

whose inverse transform has the form

$$f(t) = \frac{1}{2\pi j} \int_{\Omega_o-j\infty}^{\Omega_o+j\infty} \tilde{f}(s) e^{st} ds \quad (1.12)$$

with $\Omega_1 < \text{Re}[s] < \Omega_2$ defining the strip of convergence and with the inversion contour in this strip ($\Omega_1 < \Omega_o < \Omega_2$).

A coupled set of integro-differential equations can now be formed using expressions (1.1) to (1.4) by enforcing the appropriate

boundary condition across the aperture and on the scatterer, that the transverse-to-z component of the magnetic field should be continuous across the aperture S_a and the tangential electric field should be zero on the conducting surface S_c of the scatterer,

$$\lim_{z \rightarrow (0-)} \tilde{H}_-(\vec{r}, s) = \lim_{z \rightarrow (0+)} \tilde{H}_+(\vec{r}, s) \quad (1.13)$$

and

$$\vec{i}_{S_c}(\vec{r}) \times \tilde{E}_+(\vec{r}, s) = \vec{0} \quad \vec{r} \in S_c \quad (1.14)$$

where \vec{i}_{S_c} is the outward-pointing unit vector on S_c . Hence, substituting the expressions (1.1) and (1.3) into the aperture boundary condition (1.13), we have,

$$\begin{aligned} & \frac{s}{\gamma_-^2} \left[\nabla \left(\nabla \cdot \tilde{A}_{m_-}(\vec{r}, s) \right) - \gamma_-^2 \tilde{A}_{m_-}(\vec{r}, s) \right] \times \vec{i}_z \\ & + \frac{s}{\gamma_+^2} \left[\nabla \left(\nabla \cdot \tilde{A}_{m_+}(\vec{r}, s) \right) - \gamma_+^2 \tilde{A}_{m_+}(\vec{r}, s) \right] \times \vec{i}_z \\ & - \frac{1}{\mu_+} \left[\nabla \times \tilde{A}_+(\vec{r}, s) \right] \times \vec{i}_z = - \tilde{H}_{sc_-}(\vec{r}, s) \times \vec{i}_z \\ & \vec{r} \in S_a \end{aligned} \quad (1.15)$$

Similarly, substituting the expression (1.4) into the conducting-scatterer boundary condition (1.14), we have

$$\begin{aligned} & \frac{s}{\gamma_+^2} \left[\nabla \left(\nabla \cdot \tilde{A}_+(\vec{r}, s) \right) - \gamma_+^2 \tilde{A}_+(\vec{r}, s) \right] \\ & + \frac{s}{(\sigma_+ + s\epsilon_+)} \nabla \times \tilde{A}_{m_+}(\vec{r}, s) = \vec{0} \quad \vec{r} \in S_c \end{aligned} \quad (1.16)$$

In principle, the expressions (1.15) and (1.16) are the exact set of coupled integral equations for the complex case of a scattering conducting body behind an aperture-perforated conducting

screen in terms of the unknown magnetic current distribution $\tilde{J}_{sm}(\vec{r}, s)$ in S_a and the induced electric current $\tilde{J}_s(\vec{r}, s)$ on S_c .

One may also note that the short-circuit magnetic field on the right-hand side of (1.15) is related to the incident magnetic field,

$$\tilde{H}_{sc-}(\vec{r}, s) = 2\tilde{H}^i(\vec{r}, s) \quad (1.17)$$

In many instances the left-hand side medium and the right-hand side medium will have same medium characteristics (μ , ϵ , σ); in such case the + and - subscripts in the expression (1.15) and (1.16) can be dropped and further the following coupled integral equations result:

$$\begin{aligned} & \left[\nabla \left(\nabla \cdot \tilde{A}_m(\vec{r}, s) \right) - \gamma^2 \tilde{A}_m(\vec{r}, s) \right] \times \vec{I}_z \\ & - \frac{(\sigma + s\epsilon)}{2} \left[\nabla \times \tilde{A}(\vec{r}, s) \right] \times \vec{I}_z = -\frac{\gamma^2}{s} \tilde{H}^i(\vec{r}, s) \times \vec{I}_z \\ & \vec{r} \in S_a \end{aligned} \quad (1.18)$$

and

$$\begin{aligned} & \left[\nabla \left(\nabla \cdot \tilde{A}(\vec{r}, s) \right) - \gamma^2 \tilde{A}(\vec{r}, s) \right] + s\mu \nabla \times \tilde{A}_m(\vec{r}, s) = \vec{0} \\ & \vec{r} \in S_c \end{aligned} \quad (1.19)$$

The electric vector potential \tilde{A}_m and the magnetic vector potential \tilde{A} introduced in the above expressions (1.18) and (1.19) are still given by the expressions (1.5) and (1.8) respectively after dropping the medium subscripts + and - in those definitions.

For analyzing the antenna problem, figure 1.4, one has to introduce slight modifications in the expressions (1.15) and (1.16). Since there is no incident field in the left-side medium 1, the right-hand side term in the expression (1.15) is equated to zero. Further, the boundary condition on the conducting surface S_c is that the tangential electric field is zero except at the antenna

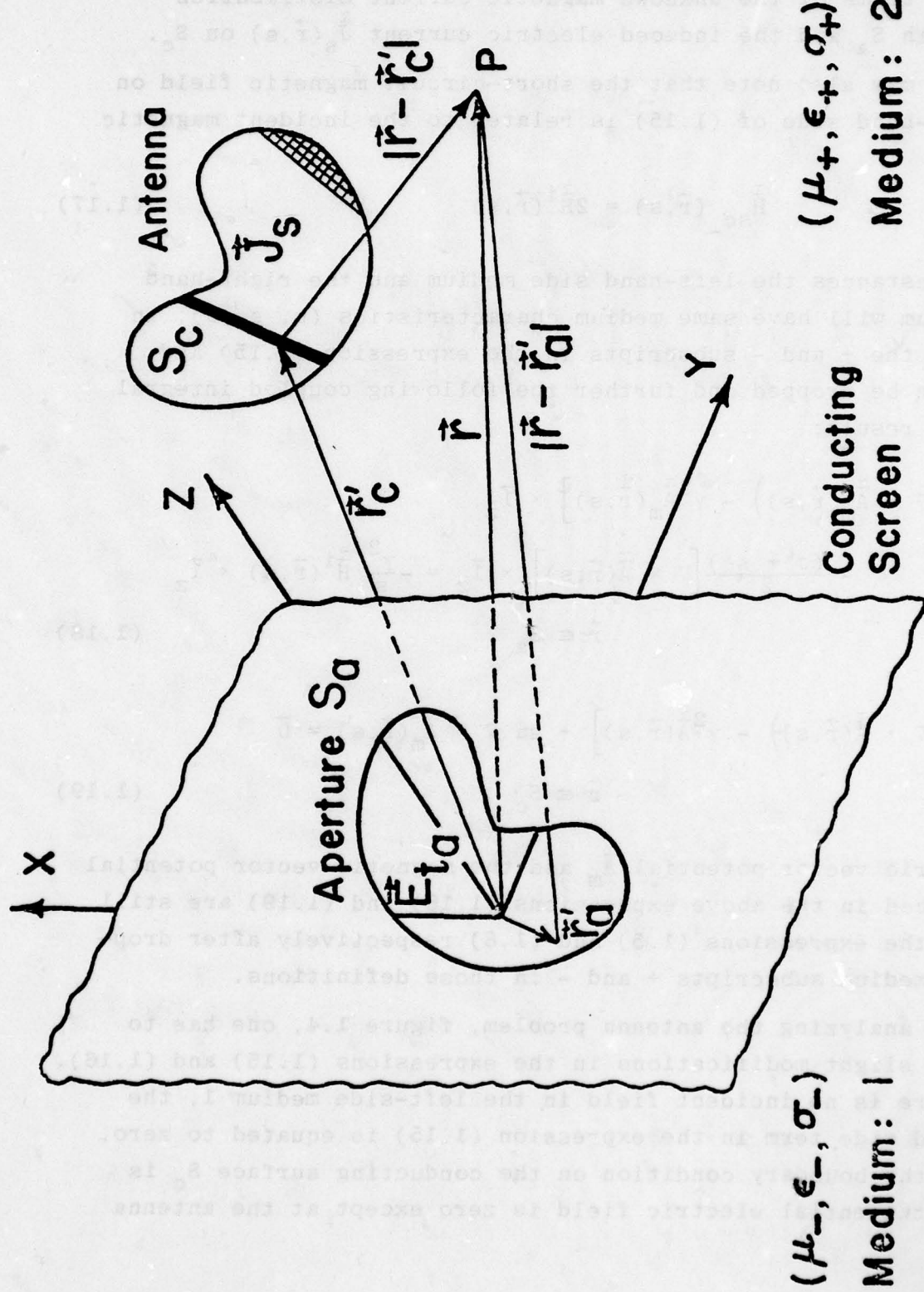


Figure 1.4 Antenna Behind an Aperture Perforated Conducting Screen

gaps across which excitation source generator is connected. Hence, the right-hand side of the expression (1.16) is replaced by $\tilde{\mathbf{E}}_s(\vec{r})(\vec{r} \in S_i)$ where $\tilde{\mathbf{E}}_s(\vec{r})$ is given appropriate source distribution on S_c . If both the incident field in the left-hand side medium and source generator at the structure are present simultaneously, one can invoke the superposition principle and analyze the problem in steps. The case when there exists incident excitation fields in both media 1 and 2, can be handled appropriately by introducing the difference of the two short-circuit fields ($\tilde{\mathbf{H}}_{sc_-}(\vec{r}, s) - \tilde{\mathbf{H}}_{sc_+}(\vec{r}, s)$) into the right-hand side of the expression (1.15) instead of the term $\tilde{\mathbf{H}}_{sc_-}(\vec{r}, s)$.

As stated earlier, the expressions (1.15) and (1.16) are the general set of coupled integro-differential equations derived in the complex frequency domain. For a specified geometry S_a of the aperture and S_c of the conducting scatterer, to obtain the current density responses the coupled integral equations are to be solved. If one is interested only with the time-harmonic solution, it is obtained by making the substitution $s = j\omega$, and similarly the time-domain responses can be obtained by taking the inverse transform, as defined by the expression (1.12), of the frequency domain solution. The expressions (1.15) and (1.16) can be written in a compact operator notation

$$\langle [\tilde{\Gamma}(\vec{r}, \vec{r}'; s)] ; [\tilde{\mathbf{J}}(\vec{r}', s)] \rangle = [\tilde{\mathbf{I}}(\vec{r}, s)] \quad (1.20)$$

where the symmetric product (similar to the inner product) between two vectors $\tilde{\mathbf{A}}(\vec{r}, \vec{r}')$ and $\tilde{\mathbf{B}}(\vec{r})$ is defined by

$$\langle \tilde{\mathbf{A}}(\vec{r}, \vec{r}') ; \tilde{\mathbf{B}}(\vec{r}) \rangle = \iint_S \tilde{\mathbf{A}}(\vec{r}, \vec{r}') \cdot \tilde{\mathbf{B}}(\vec{r}') dS \quad (1.21)$$

In the expression (1.20), the system Green's function $\tilde{\Gamma}(\vec{r}, \vec{r}'; s)$ is given by

$$\begin{bmatrix} \tilde{\Gamma}(\vec{r}, \vec{r}'; s) \\ \tilde{\Gamma}_c(\vec{r}, \vec{r}'; s) \end{bmatrix} = \begin{bmatrix} \tilde{\Gamma}_a(\vec{r}, \vec{r}_a'; s) & \tilde{\Gamma}_{ac}(\vec{r}, \vec{r}_a'; s) \\ \tilde{\Gamma}_{ca}(\vec{r}, \vec{r}_c'; s) & \tilde{\Gamma}_c(\vec{r}, \vec{r}_c'; s) \end{bmatrix}$$

where

$\tilde{\Gamma}_a(\vec{r}, \vec{r}_a'; s)$: aperture Green's function

$\tilde{\Gamma}_{ac}(\vec{r}, \vec{r}_a'; s)$: aperture-scatterer interaction Green's function

$\tilde{\Gamma}_{ca}(\vec{r}, \vec{r}_c'; s)$: scatterer-aperture interaction Green's function

$\tilde{\Gamma}_c(\vec{r}, \vec{r}_c'; s)$: scatterer Green's function

and the system current density response $\tilde{J}(\vec{r}', s)$ has two parts corresponding to the response of the aperture $\tilde{J}_{sm}(\vec{r}_a', s)$ and that of the conducting scatterer $\tilde{J}_s(\vec{r}_c', s)$,

$$\tilde{J}(\vec{r}', s) = \begin{bmatrix} \tilde{J}_{sm}(\vec{r}_a', s) \\ \tilde{J}_s(\vec{r}_c', s) \end{bmatrix} \quad (1.23)$$

and the right-hand side term $\tilde{F}(\vec{r}, s)$ in the expression (1.20) represents the forcing function related to the appropriate excitation.

Basically, there is no simple analytical approach to solve the operator integral equation (1.20). One of the most familiar techniques consists in reducing the integral-operator form of the equation to the corresponding matrix-operator form of the equation based on the method of moments.¹⁶ According to this method the unknown response $\tilde{J}(\vec{r}', s)$ is expanded in terms of N basis or expansion functions,¹⁶

$$\tilde{J}(\vec{r}', s) \approx \sum_{n=1}^N \tilde{J}_n(s) \tilde{F}(\vec{r}') \quad (1.24)$$

giving rise to a numerical response vector, and the equality of the equation on the objects is established by testing the operator integral equation (1.20) by certain weight functions¹⁶ $w_m(\vec{r}, s)$, $m = 1, 2, \dots, N$ and forming the inner product (1.21) within the domain of validity of the integral equation. In terms of the method of moments notation, the expression (1.20) reduces to the matrix equation

$$[\tilde{\Gamma}_{m,n}(s)] [\tilde{J}_n(s)] = [\tilde{I}_m(s)] \quad (1.25)$$

where

$[\tilde{\Gamma}_{m,n}(s)]$: generalized system matrix

$[\tilde{J}_n(s)]$: generalized response vector

$[\tilde{I}_m(s)]$: generalized excitation vector

The solution for the current response is obtained by numerically taking the inverse of the system matrix and post-multiplying by the excitation vector,

$$[\tilde{J}_n(s)] = [\tilde{\Gamma}_{m,n}(s)]^{-1} [\tilde{I}_m(s)] \quad (1.26)$$

Hence given a complex frequency of interest $s = \Omega + j\omega$, for given type of excitation, the current response of the aperture and the scatterer is obtained from the expression (1.20).

One of the direct and commonly adopted procedures to obtain the time-domain (transient) response of the scattering objects for a given type of excitation, is to solve the equation (1.26), with $s = j\omega$, for various values of the real-frequency ω corresponding to the specified frequency band of interest, and numerically obtain the inverse transform of the frequency domain data.^{2,17} Hence for the time-harmonic case,

$$[\tilde{J}_n(j\omega)] = [\tilde{\Gamma}_{m,n}(j\omega)]^{-1} [\tilde{I}_m(j\omega)] \quad (1.27)$$

and the transient or the time-domain solution is given by

$$[J_n(t)] = \frac{1}{2\pi} \int_{-\infty}^{+\infty} \left\{ [\tilde{r}_{m,n}(j\omega)]^{-1} \cdot [\tilde{I}_m(j\omega)] \right\} e^{j\omega t} d\omega \quad (1.28)$$

and the integration along the ω -axis is appropriately modified if one encounters any singularities either in the matrix inverse operator or in the excitation wave function.

An alternative approach recently developed for transient characterization and time-domain studies is the well-known singularity expansion method.^{2,17} This is based on the question of parameterization of the total transient response of an object. In the direct approach, expressions (1.27) and (1.28), the transient study is unavoidably laborious and costly from the amount of data to be processed if the response is to be studied at every point on the structure along with different types of excitation waveforms and polarizations. According to the SEM, it is possible to express the object response in terms of few number of parameters, and once this is done, one can freely study the responses both in the frequency domain and in the time domain.¹⁸⁻²⁰

The general formalism of the SEM began with the observations of the responses in the passive lumped circuit theory, and other experimental observations concerning the transient electromagnetic response of complex structures such as aircraft and missiles. It was observed, basically the time-domain response consists of damped sinusoids which correspond to the complex conjugate poles or the singularities in the Laplace complex frequency domain. In general one may encounter other forms of the singularities, such as multiple poles, branch points and branch cuts, essential singularities and even entire functions depending upon specific geometries under consideration. For most of the specific problems discussed in the context of this paper, only the first order pole singularities are important for the finite size conducting objects with the addition of branch cut type of singularities for the infinitely long scattering objects.

Rewriting the matrix operator equation (1.25) for the delta-function response, we have

$$\left[\tilde{r}_{m,n}(s) \right] \left[\tilde{U}_n(s) \right] = \left[\tilde{I}_m(s) \right] \quad (1.29)$$

Using the singularity expansion,² the current response of the object to a delta-function excitation is given by (in the class 2 form),

$$\left[\tilde{U}_n(s) \right] = \sum_{\alpha} \left\{ \beta_{\alpha} [\tilde{v}]_{\alpha} \cdot [\tilde{u}]_{\alpha} \right\} \frac{\left[\tilde{I}_m(s) \right]}{(s - s_{\alpha})} \quad (1.30)$$

where the complex natural frequencies s_{α} are obtained as the solution to the determinant equation,

$$\det \left[\tilde{r}_{m,n}(s) \right] = \vec{0} \quad (1.31)$$

the natural mode vector $[\tilde{v}]_{\alpha}$ and the coupling vector $[\tilde{u}]_{\alpha}$ are obtained as the solution to the homogeneous matrix equations,

$$\left[\tilde{r}_{m,n}(s_{\alpha}) \right] \left[\tilde{v} \right]_{\alpha} = \vec{0} \quad (1.32)$$

$$\left[\tilde{r}_{m,n}(s_{\alpha}) \right]^T \left[\tilde{u} \right]_{\alpha} = \vec{0} \quad (1.33)$$

and the normalization constant β_{α} is given by

$$\beta_{\alpha} = \frac{1}{[\tilde{u}]_{\alpha}^T \cdot \left\{ \frac{d}{ds} \left[\tilde{r}_{m,n}(s_{\alpha}) \right] \right\} \cdot [\tilde{v}]_{\alpha}} \quad (1.34)$$

Such a representation results in a compact form of the object response. For calculating the transient response, the Laplace inverse transform definition (1.12) is used by appropriately closing the Bromwich contour, figure 1.5, either to the right half or to the left half of the complex s plane. In the expression

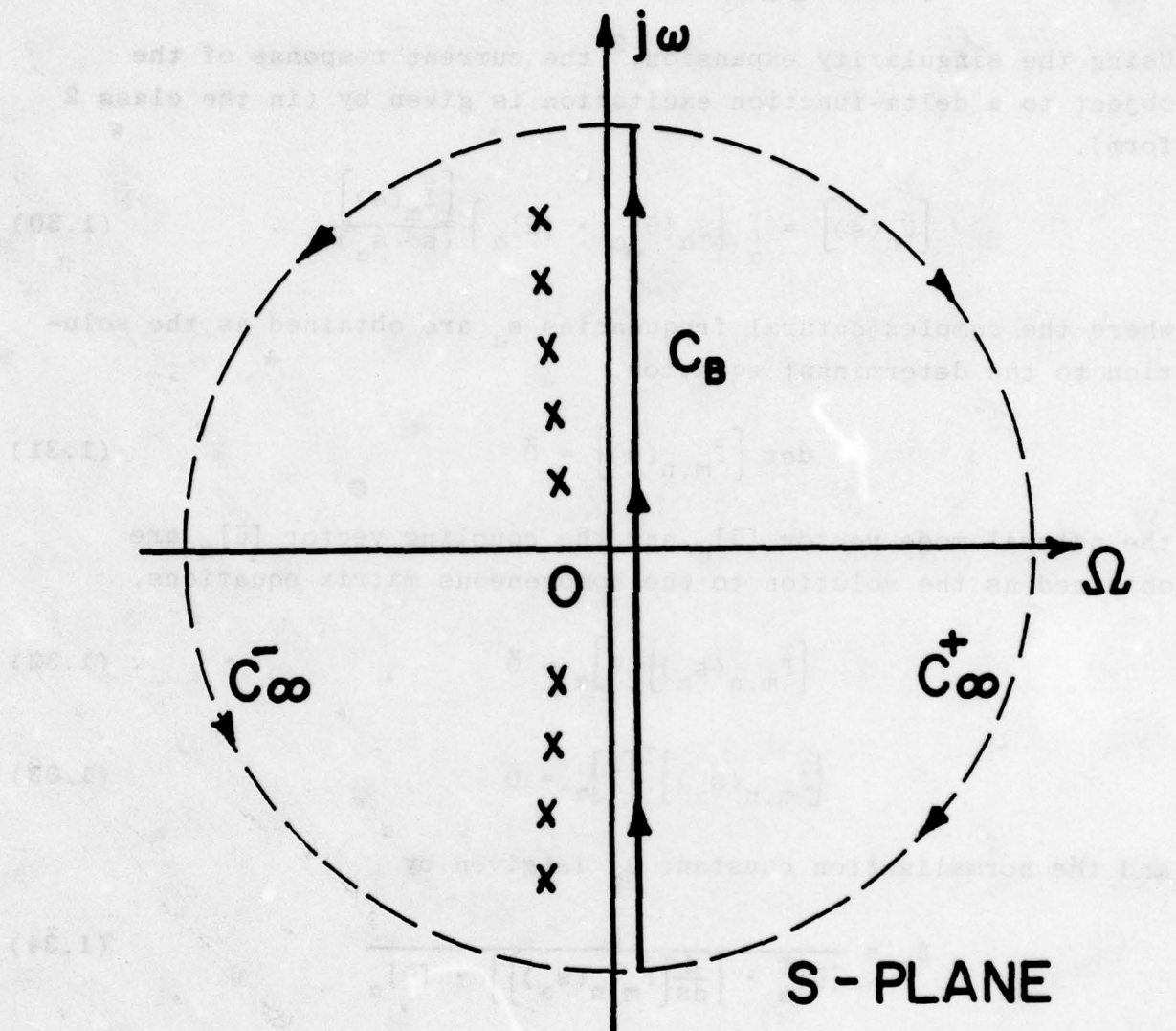


Figure 1.5 Illustration of the Closure of the Bromwich Contour in s-Plane

(1.30), the term $[\tilde{I}_m(s)]$ contains the incident excitation and it is to be modified if one wishes to incorporate other types of transient waveforms or convolute with the delta function response. Hence, we have the time domain solution,

$$[\tilde{U}_n(t)] = \sum_{\alpha} \tilde{\eta}_{\alpha} [\tilde{v}]_{\alpha} e^{s_{\alpha} t} u(t) \quad (1.35)$$

where $\tilde{\eta}_{\alpha}$ is the coupling coefficient defining the magnitude of the excitation coupling to a particular mode and $u(t)$ being a unit step function.²

CHAPTER II

Integral Equations for the Various
Aperture and Slot Geometries

The aperture-scatterer integral equations (1.15) and (1.16) reduce to a comparatively simple form for the case of diffraction by only an aperture in the planer conducting screen with no bodies placed behind it. In figure 2.1, if the conducting scatterer is removed, then the expression (1.15) becomes,

$$\begin{aligned} & \frac{s}{\gamma_-^2} \left[\nabla \left(\nabla \cdot \tilde{\tilde{A}}_m^- (\vec{r}, s) \right) - \gamma_-^2 \tilde{\tilde{A}}_m^- (\vec{r}, s) \right] \times \vec{I}_z \\ & + \frac{s}{\gamma_+^2} \left[\nabla \left(\nabla \cdot \tilde{\tilde{A}}_{m+} (\vec{r}, s) \right) - \gamma_+^2 \tilde{\tilde{A}}_{m+} (\vec{r}, s) \right] \times \vec{I}_z \\ & = -\tilde{\tilde{H}}_{sc-} (\vec{r}, s) \times \vec{I}_z \end{aligned} \quad (2.1)$$

$\vec{r} \in$ aperture S_a

and if both medium 1 and 2 separated by the screen have the same medium characteristics (μ , ϵ , σ), then the expression (2.1) further simplifies to

$$\left[\nabla \left(\nabla \cdot \tilde{\tilde{A}}_m (\vec{r}, s) \right) - \gamma^2 \tilde{\tilde{A}}_m (\vec{r}, s) \right] \times \vec{I}_z = -\frac{\gamma^2}{s} \tilde{\tilde{H}}^i (\vec{r}, s) \times \vec{I}_z \quad (2.2)$$

$\vec{r} \in$ aperture S_a

A. Rectangular Aperture

For the case of rectangular apertures, the electric vector potential $\tilde{\tilde{A}}_m$ can be resolved into its rectangular components,

$$\tilde{\tilde{A}}_m (\vec{r}, s) = \vec{I}_x \tilde{A}_{m_x} (\vec{r}, s) + \vec{I}_y \tilde{A}_{m_y} (\vec{r}, s) \quad (2.3)$$

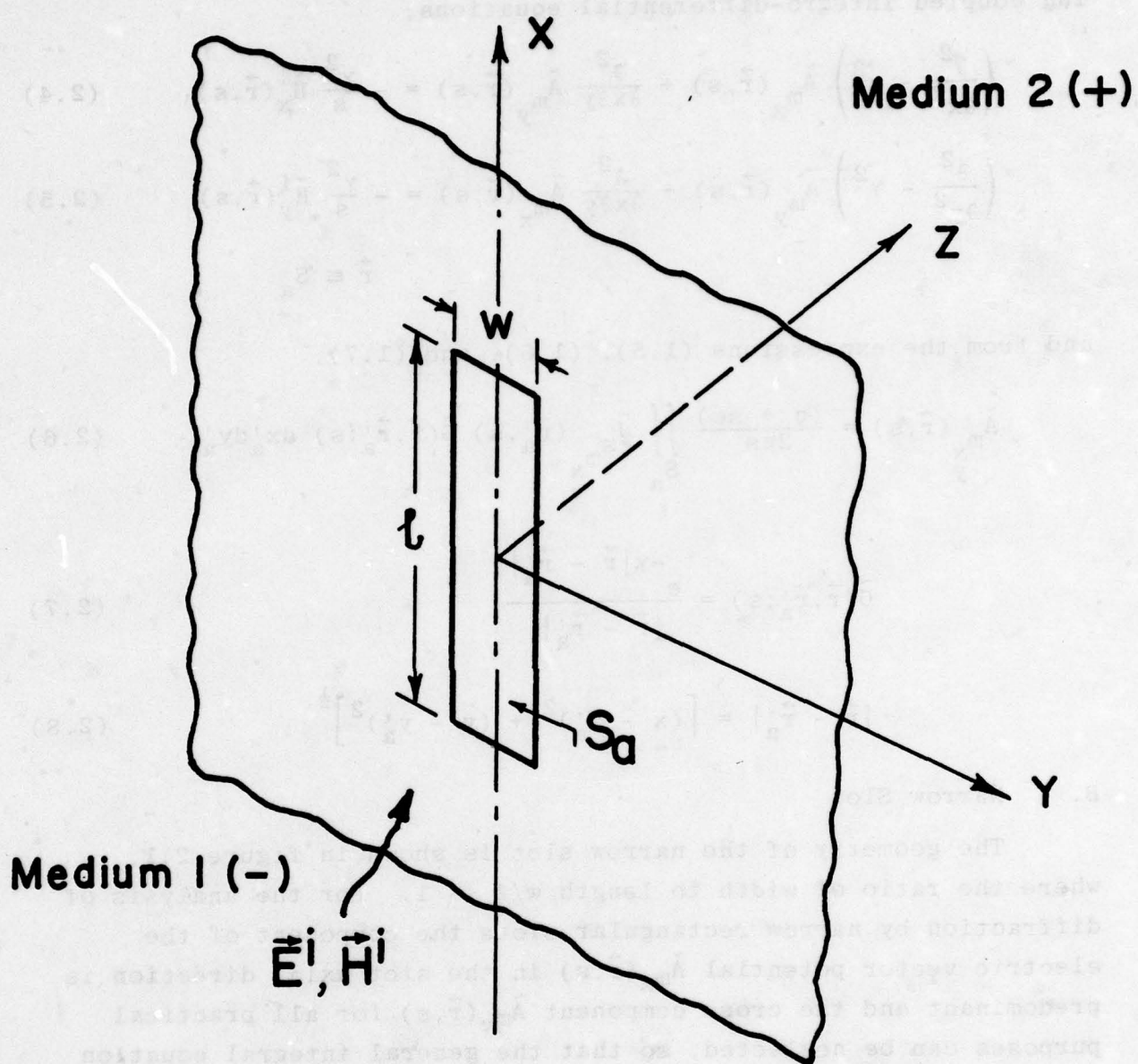


Figure 2.1 Narrow Slot in a Conducting Screen

and substituting (2.3) into the expression (2.2) yields the following coupled integro-differential equations,

$$\left(\frac{\partial^2}{\partial x^2} - \gamma^2 \right) \tilde{A}_{m_x}(\vec{r}, s) + \frac{\partial^2}{\partial x \partial y} \tilde{A}_{m_y}(\vec{r}, s) = - \frac{\gamma^2}{s} \tilde{H}_x^i(\vec{r}, s) \quad (2.4)$$

$$\left(\frac{\partial^2}{\partial y^2} - \gamma^2 \right) \tilde{A}_{m_y}(\vec{r}, s) + \frac{\partial^2}{\partial x \partial y} \tilde{A}_{m_x}(\vec{r}, s) = - \frac{\gamma^2}{s} \tilde{H}_y^i(\vec{r}, s) \quad (2.5)$$

$$\vec{r} \in S_a$$

and from the expressions (1.5), (1.6), and (1.7),

$$\tilde{A}_{m_x}(\vec{r}, s) = \frac{(\sigma + s\varepsilon)}{2\pi s} \iint_{S_a} \tilde{J}_{s_{m_x}}(\vec{r}'_a, s) \tilde{G}(\vec{r}, \vec{r}'_a; s) dx'_a dy'_a \quad (2.6)$$

$$\tilde{G}(\vec{r}, \vec{r}'_a; s) = \frac{e^{-\gamma |\vec{r} - \vec{r}'_a|}}{|\vec{r} - \vec{r}'_a|} \quad (2.7)$$

$$|\vec{r} - \vec{r}'_a| = \left[(x - x'_a)^2 + (y - y'_a)^2 \right]^{\frac{1}{2}} \quad (2.8)$$

B. Narrow Slot

The geometry of the narrow slot is shown in figure 2.1, where the ratio of width to length $w/\ell \ll 1$. For the analysis of diffraction by narrow rectangular slots the component of the electric vector potential $\tilde{A}_{m_x}(\vec{r}, s)$ in the slot axial direction is predominant and the cross component $\tilde{A}_{m_y}(\vec{r}, s)$ for all practical purposes can be neglected, so that the general integral equation for the narrow slot has the form,

$$\frac{s}{\gamma_-^2} \left(\frac{\partial^2}{\partial x^2} - \gamma_-^2 \right) \tilde{A}_{m_{x_-}}(\vec{r}, s) + \frac{s}{\gamma_+^2} \left(\frac{\partial^2}{\partial x^2} - \gamma_+^2 \right) \tilde{A}_{m_{x_+}}(\vec{r}, s) = - 2 \tilde{H}_x^i(\vec{r}, s) \quad (2.9)$$

\vec{r} in slot

and further specializing the expression (2.9), for the case of same medium characteristics (μ , ϵ , σ) on both sides, the integral equation (2.9) becomes,

$$\left(\frac{\partial^2}{\partial x^2} - \gamma^2 \right) \tilde{A}_{m_x}(\vec{r}, s) = - \frac{\gamma^2}{s} \tilde{H}_x^i(\vec{r}, s) \quad (2.10)$$

\vec{r} in slot

where

$$\tilde{A}_{m_x}(\vec{r}, s) = \frac{(\sigma + s\epsilon)}{2\pi s} \iint_{S_a} \tilde{J}_{s_{m_x}}(\vec{r}'_a, s) \tilde{G}(\vec{r}, \vec{r}'_a; s) dx'_a dy'_a \quad (2.11)$$

The magnetic current distribution $\tilde{J}_{s_{m_x}}(\vec{r}'_a, s)$ for a narrow slot can be written in terms of the axial distribution $m(x)$ and the transverse distribution $\zeta(y)$ which has the right type of singular distribution at the edges,²¹

$$J_{s_{m_x}}(x, y) = m(x) \zeta(y) \quad (2.12)$$

where

$$\zeta(y) = \frac{1}{\pi} \left[\left(\frac{w}{2} \right)^2 - y^2 \right]^{-\frac{1}{2}} \quad (2.13)$$

Substituting the narrow slot distribution (2.12) into the expression (2.11), we have for a narrow rectangular slot, the integro-differential equation,

$$\left(\frac{\partial^2}{\partial x^2} - \gamma^2 \right) \tilde{A}_{m_x}(x, s) = - \frac{\gamma^2}{s} \tilde{H}_x^i(x, s) , \quad (2.14)$$

$-\frac{\ell}{2} < x < \frac{\ell}{2}$

where

$$\tilde{A}_{m_x}(x, s) = \frac{(\sigma + s\epsilon)}{2\pi s} \int_{-\ell/2}^{\ell/2} m(x'_a) \tilde{G}^{NS}(x, x'_a; s) dx'_a \quad (2.15)$$

$$\tilde{G}^{NS}(x, x'_a; s) = \frac{e^{-\gamma R_a}}{R_a} \quad (2.16)$$

$$R_a = \left[(x - x'_a)^2 + \left(\frac{w}{4}\right)^2 \right]^{\frac{1}{2}} \quad (2.17)$$

A point to note at this stage, is the duality^{15,22} of the problem. In fact the expressions (2.4) and (2.5) are the dual equations of a rectangular plate,^{13,23} while the expression (2.10) is the dual equation of a narrow strip scattering problem.

C. Narrow Multiple Slots

The case of diffraction by narrow finite multiple slots, figure 2.2, in a conducting screen can still be analyzed based on the integral equation (2.10) since all the slots considered form an array and are oriented parallel. But the electric vector potential \tilde{A}_{m_x} in the expression (2.10) should be redefined to take into account the mutual interaction between the adjacent slots. Hence, the integral equation for narrow finite multiple slots is given by the integral equation (2.10) with \tilde{A}_{m_x} replaced by the total electric vector potential $\tilde{A}_{m_x}^N$ due to N slots,

$$\tilde{A}_{m_x}^N(\vec{r}, s) = \frac{(\sigma + s\epsilon)}{2\pi s} \sum_{n=1}^N \iint_{S_a^n} \tilde{J}_{s_{m_x}}^n(\vec{r}'_{a_n}, s) \tilde{G}(\vec{r}, \vec{r}'_{a_n}; s) dx'_{a_n} dy'_{a_n} \quad (2.18)$$

where $\tilde{J}_{s_{m_x}}^n$ is the magnetic current distribution in the n^{th} slot and the Green's function

$$\tilde{G}(\vec{r}, \vec{r}'_{a_n}; s) = \frac{e^{-\gamma |\vec{r} - \vec{r}'_{a_n}|}}{|\vec{r} - \vec{r}'_{a_n}|} \quad (2.19)$$

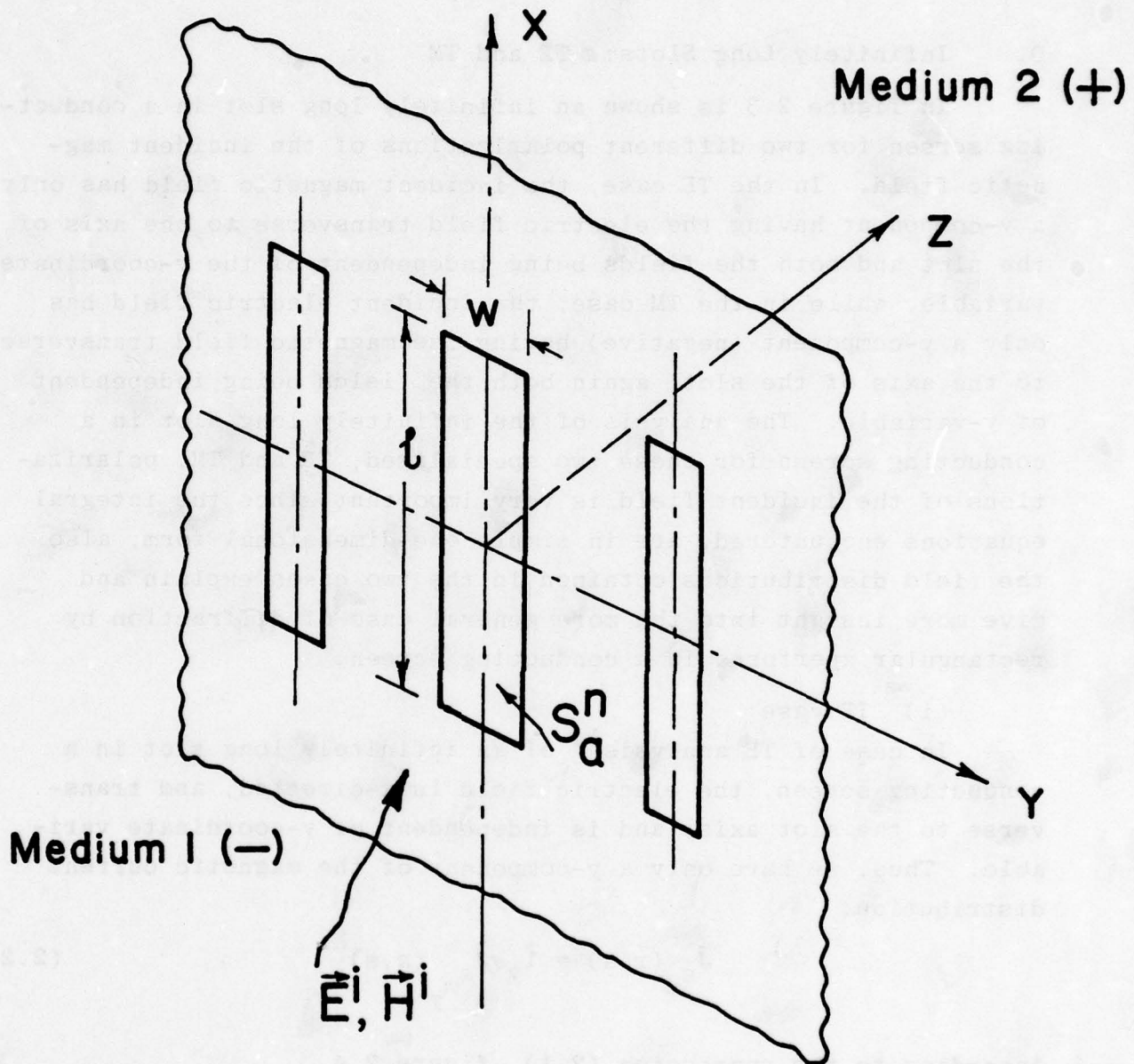


Figure 2.2 Multiple Narrow Slots in a Conducting Screen

$$|\vec{r} - \vec{r}'_{a_n}| = \left[(x - x'_{a_n})^2 + (y - y'_{a_n})^2 \right]^{\frac{1}{2}}$$

D. Infinitely Long Slots: TE and TM

In figure 2.3 is shown an infinitely long slot in a conducting screen for two different polarizations of the incident magnetic field. In the TE case, the incident magnetic field has only a y-component having the electric field transverse to the axis of the slot and both the fields being independent of the y-coordinate variable; while in the TM case, the incident electric field has only a y-component (negative) having the magnetic field transverse to the axis of the slot, again both the fields being independent of y-variable. The analysis of the infinitely long slot in a conducting screen for these two specialized, TE and TM, polarizations of the incident field is very important since the integral equations encountered, are in simple one-dimensional form; also the field distributions obtained in the two cases explain and give more insight into the more general case of diffraction by rectangular apertures in a conducting screen.

(i) TE case:

In case of TE analysis¹⁴ of an infinitely long slot in a conducting screen, the electric field is x-directed, and transverse to the slot axis, and is independent of y-coordinate variable. Thus, we have only a y-component of the magnetic current distribution,

$$\tilde{J}_{s_m}(\vec{r}, s) = I_y \tilde{J}_{s_m}(x, s) \quad (2.21)$$

According to the expression (2.1), figure 2.4,

$$s \left[\tilde{A}_{m_{y_-}}(x, s) + \tilde{A}_{m_{y_+}}(x, s) \right] = 2 \tilde{H}_y^i(x, s) \quad (2.22)$$

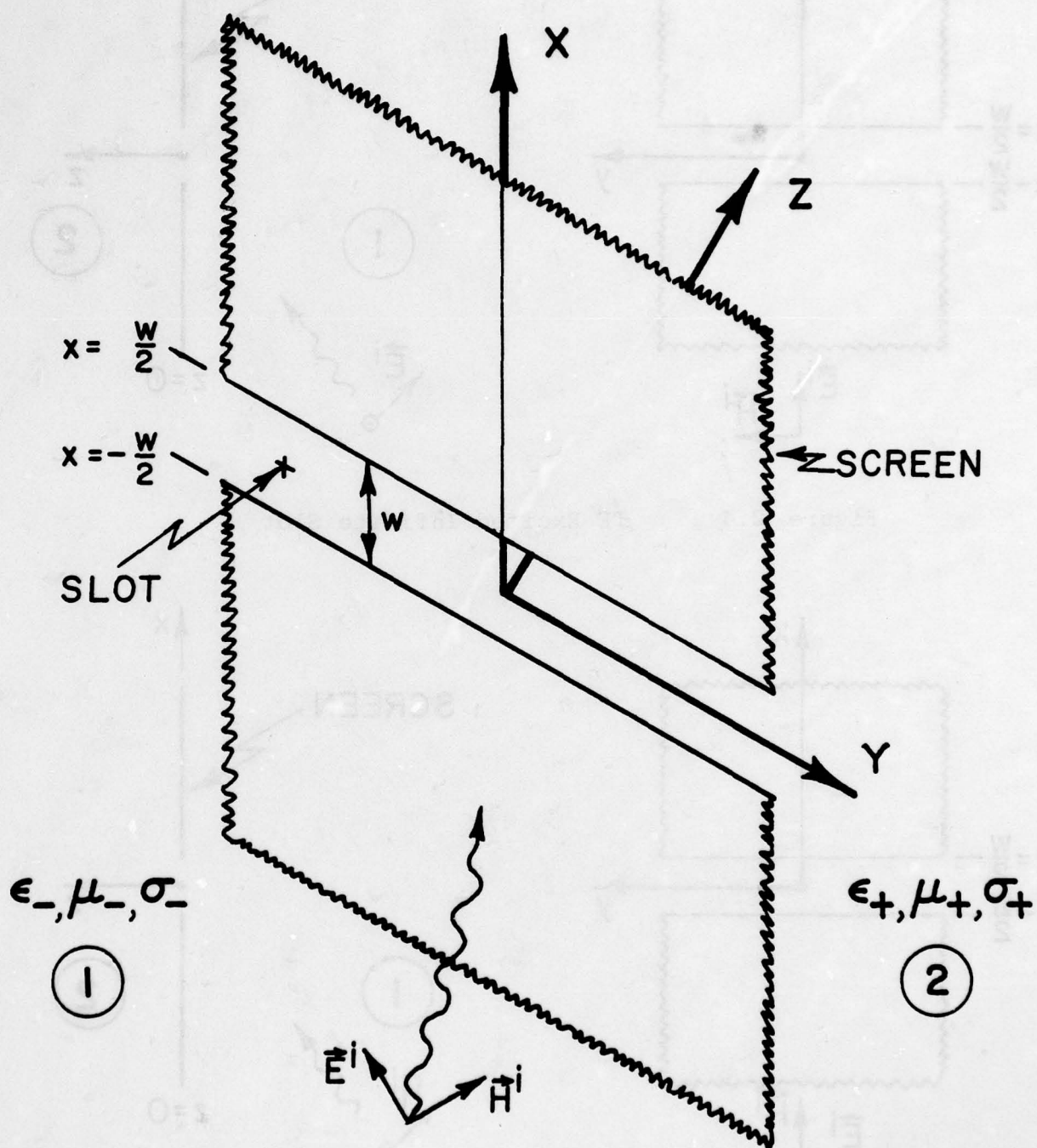
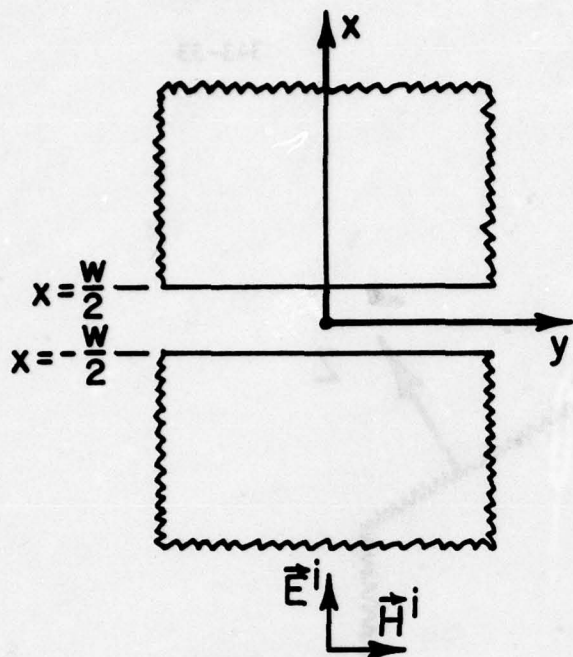


Figure 2.3 Infinite Slot in a Conducting Screen

343-34



EMP 3-38

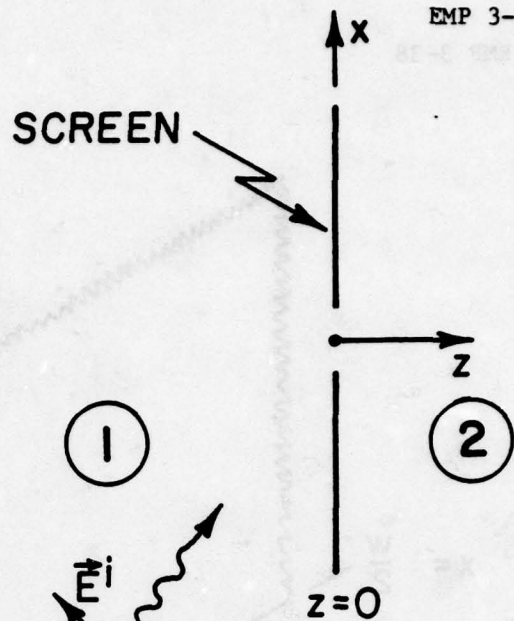


Figure 2.4 TE Excited Infinite Slot

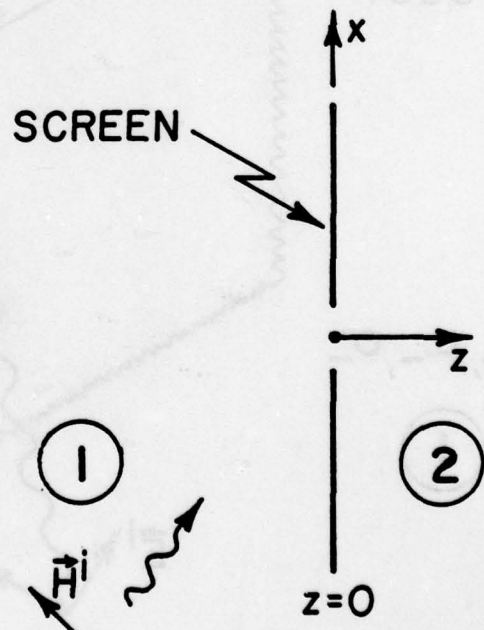
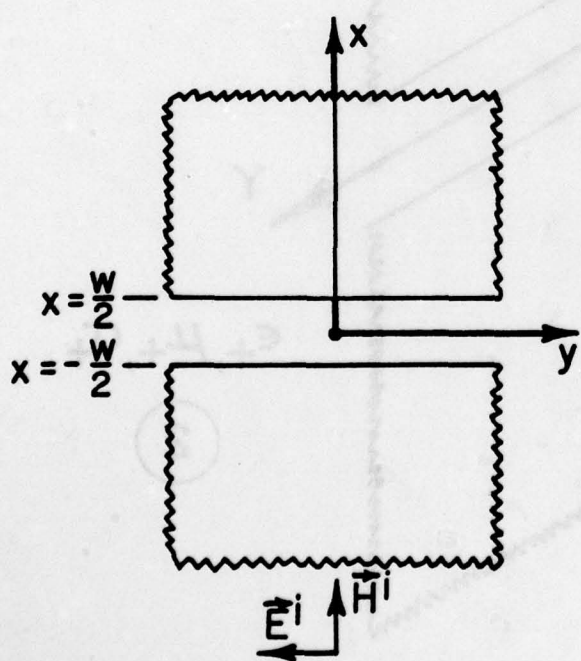


Figure 2.5 TM Excited Infinite Slot

and since $\tilde{A}_{m_y_-}$ and $\tilde{A}_{m_y_+}$ are independent of y , selecting $y = 0$ in the expression (1.5), we have

$$\begin{aligned}\tilde{A}_{m_{y_\pm}}(x, s) &= \frac{(\sigma_\pm + s\epsilon_\pm)}{2\pi s} \iint_{\text{SLOT}} \tilde{J}_{s_m_y}(\vec{r}'_a, s) \tilde{G}_\pm(\vec{r}, \vec{r}'_a; s) dx'_a dy'_a \\ &= \frac{(\sigma_\pm + s\epsilon_\pm)}{j2s} \int_{x'_a = -\frac{w}{2}}^{\frac{w}{2}} \tilde{J}_{s_m_y}(x'_a, s) H_0^{(2)}[-j\gamma_\pm |x - x'_a|] dx'_a\end{aligned}\quad (2.23)$$

where $H_0^{(2)}$ is the Hankel function of the second kind and zero order. If both sides of the media are having the same medium characteristics (μ , ϵ , σ), the expressions (2.22) and (2.23) yield

$$\int_{x'_a = -\frac{w}{2}}^{\frac{w}{2}} \tilde{J}_{s_m_y}(x'_a, s) H_0^{(2)}[-j\gamma |x - x'_a|] dx'_a = \frac{j2}{(\sigma + s\epsilon)} \tilde{H}_y^i(x, s) \quad (2.24)$$

$-\frac{w}{2} < x < \frac{w}{2}$

(ii) TM case:

A similar analysis is followed for TM excitation¹⁴ of the infinitely long slot in a conducting screen, the electric field in the slot is y -directed and independent of y -coordinate variable. We have only an x -component of the magnetic current distribution,

$$\tilde{J}_{s_m}(r, s) = I_x \tilde{J}_{s_m_x}(x, s) \quad (2.25)$$

According to the expression (2.1), figure 2.5,

$$\frac{s}{\gamma_-^2} \left[\frac{\partial^2}{\partial x^2} - \gamma_-^2 \right] \tilde{A}_{m_{x_-}}(x, s) + \frac{s}{\gamma_+^2} \left[\frac{\partial^2}{\partial x^2} - \gamma_+^2 \right] \tilde{A}_{m_{x_+}}(x, s) = -2\tilde{H}_x^i(x, s) \quad (2.26)$$

and further $\tilde{A}_{m_{x_\pm}}$ and $\tilde{A}_{m_{x_+}}$ are independent of the y-coordinate variable, selecting $y = 0$, we have from the expression (1.5),

$$\tilde{A}_{m_{x_\pm}}(x, s) = \frac{(\sigma_\pm + s\epsilon_\pm)}{j2s} \int_{x'_a = -\frac{w}{2}}^{\frac{w}{2}} \tilde{J}_{s_{m_x}}(x'_a, s) H_0^{(2)}[-j\gamma_\pm |x-x'_a|] dx'_a \quad (2.27)$$

Again, for the special case of same medium characteristics (μ , ϵ , σ), we have the integral equation,

$$\left[\frac{\partial^2}{\partial x^2} - \gamma^2 \right] \int_{x'_a = -\frac{w}{2}}^{\frac{w}{2}} \tilde{J}_{s_{m_x}}(x'_a, s) H_0^{(2)}[-j\gamma |x-x'_a|] dx'_a = -j2s\mu \tilde{H}_x^i(x, s) \quad (2.28)$$

$-\frac{w}{2} < x < \frac{w}{2}$

It is quite academic at this point to look at the duality of the equations (2.24) and (2.28). In fact, one obtains similar equations for an infinitely long strip scatterer, the equation (2.24) for a TM strip and the equation (2.28) for a TE excited strip in a homogeneous medium.

E. Numerical Results

A few of the canonical types of aperture shapes were discussed in the previous sections and the pertinent integral equations were derived in terms of the unknown aperture magnetic current distribution. Once these distributions are determined for a given type of incident excitation, the complete fields both in the illuminated and the shadow region can be determined using the field expressions (1.1) to (1.4). One of the powerful techniques available to obtain the solution of the integral equations is based on the method of moments.¹⁶ This involves the process of converting the operator type equations to the corresponding matrix type equations, which can further be analyzed numerically.²³

In figures 2.6 to 2.9, numerical results¹⁴ are presented for the case of an infinitely long slot, based on the integral expressions (2.22) and (2.26), in which the slot is in a conducting screen, figures 2.4 and 2.5, separating two half-spaces of different electrical properties. Figures 2.6 and 2.7 give the slot distribution for the TE excitation and figures 2.8 and 2.9 for the TM excitation. The left side (-) medium is assumed to be free space in which a plane wave propagates and illuminates the infinite slot. The figures depict both the real and imaginary parts of the slot magnetic current distribution as a function of the permittivity ϵ_+ figures 2.6 and 2.8, and as a function of the conductivity σ_+ figures 2.7 and 2.9. The TE slot distribution has the right type of singular behavior at the edges, while in the TM distribution it goes to zero at the edges. These results are quite valuable to understand what happens for the distribution in the case of a finite rectangular slot or aperture. Based on these solutions, the fields scattered can be calculated. In figure 2.10 is shown the far-field magnetic-field variation due to the TE excited slot and in figure 2.11 is shown the far-field electric-field distribution due to the TM excitation of the slot as a function of right half-space permittivities. The results of the far-field do exhibit wavelength contraction as the permittivity is increased.

The solution of the coupled integral equations (2.4) and (2.5) for a rectangular aperture is more involved from the numerical point of view.^{9,10,13} For electrically very small apertures, the solution procedure⁹ based on Rayleigh series can be conveniently employed so that the zero-order and first-order solutions represent to a fair degree of accuracy the distribution in small apertures. In figure 2.12 is shown the $J_{S\text{m}_X}(x,y)$ component of the magnetic current distribution in a small square aperture for a normal plane wave excitation. Similarly in figure 2.13 is shown the distribution of the $J_{S\text{m}_X}(x,y)$ component in a narrow rectangular aperture in the presence of a conducting ground plane

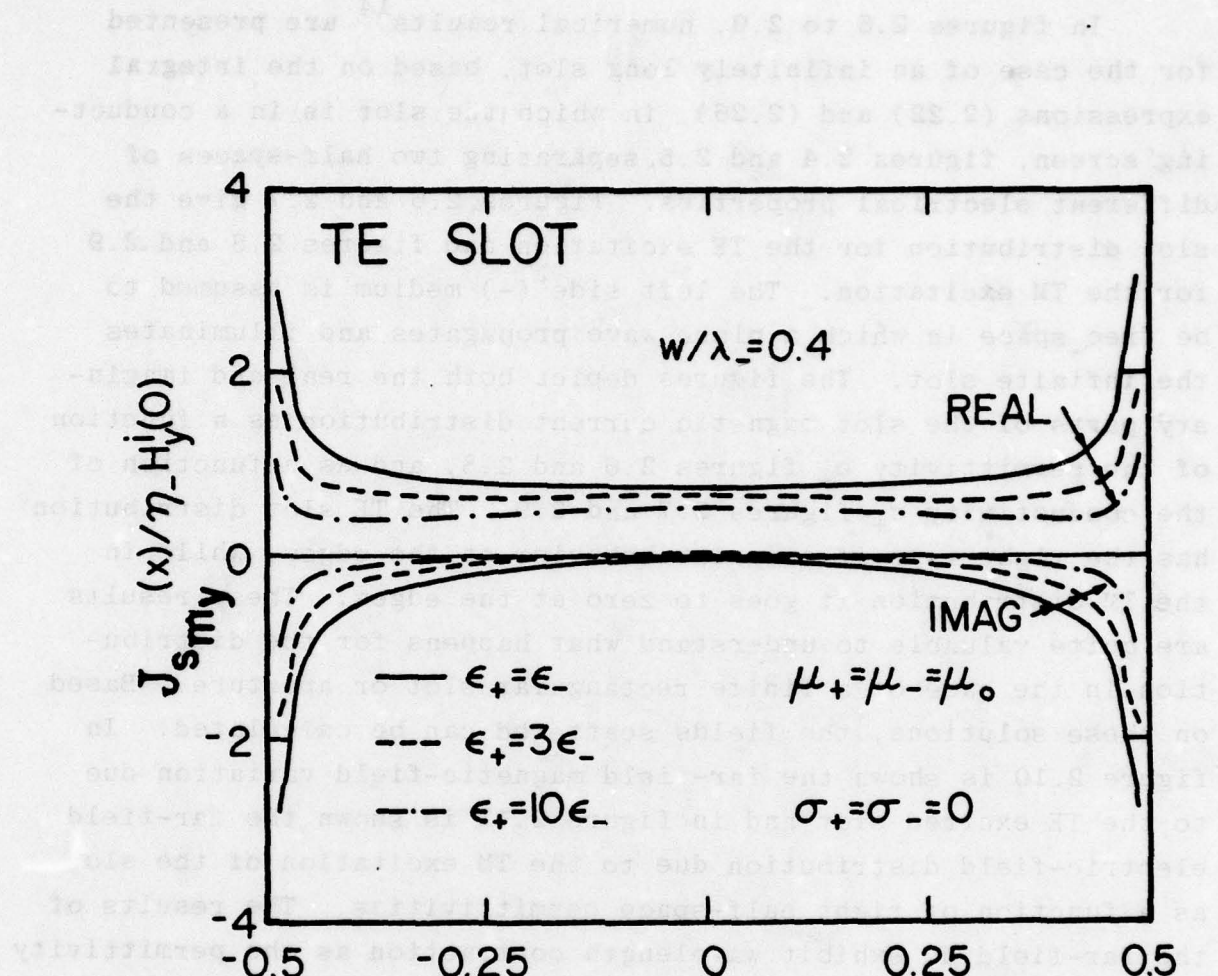


Figure 2.6 TE Magnetic Current in 0.4-Wavelength Slot for Different ϵ_+

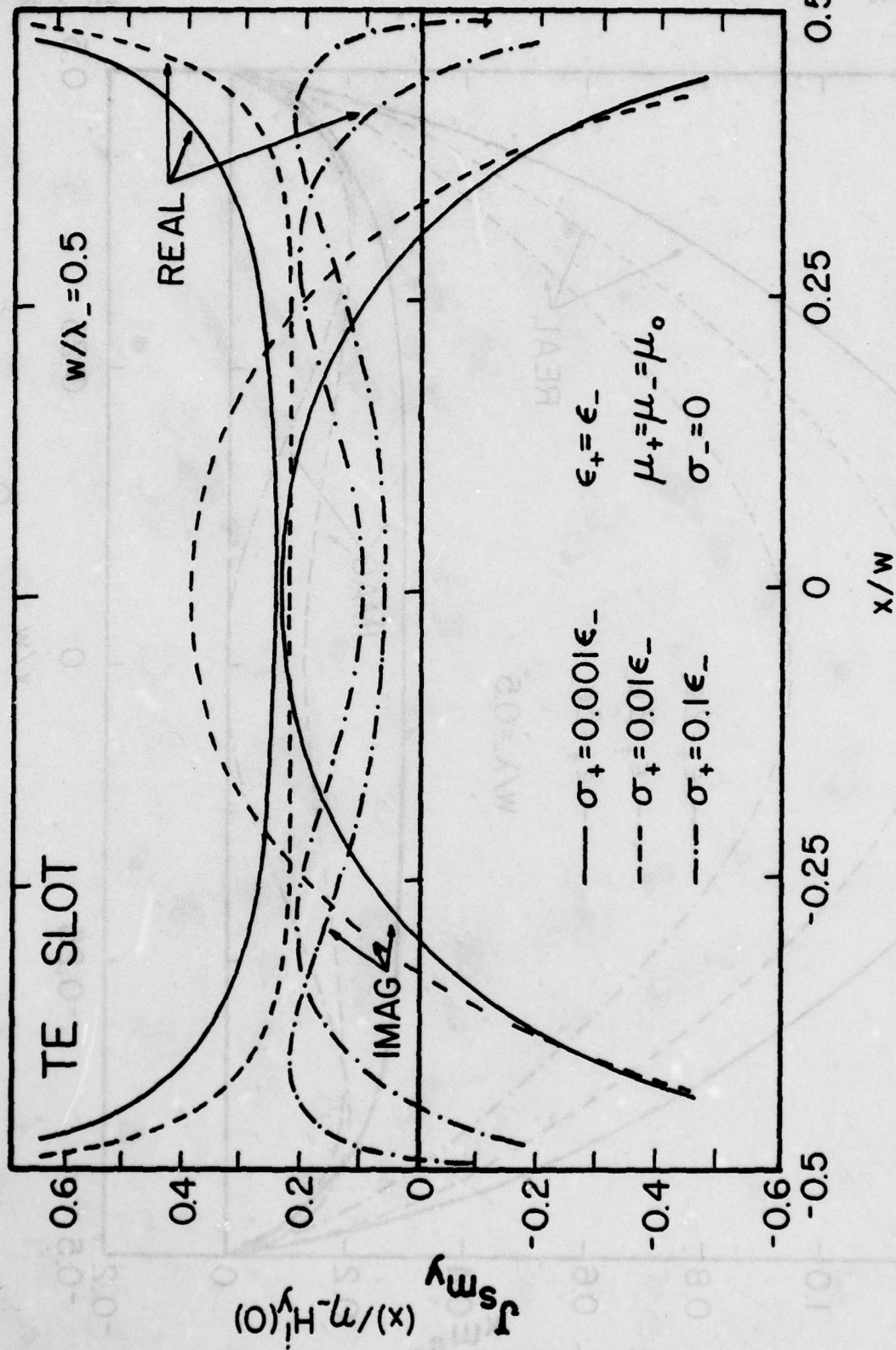


Figure 2.7 TE Magnetic Current in 0.5-Wavelength Slot for Different σ_+

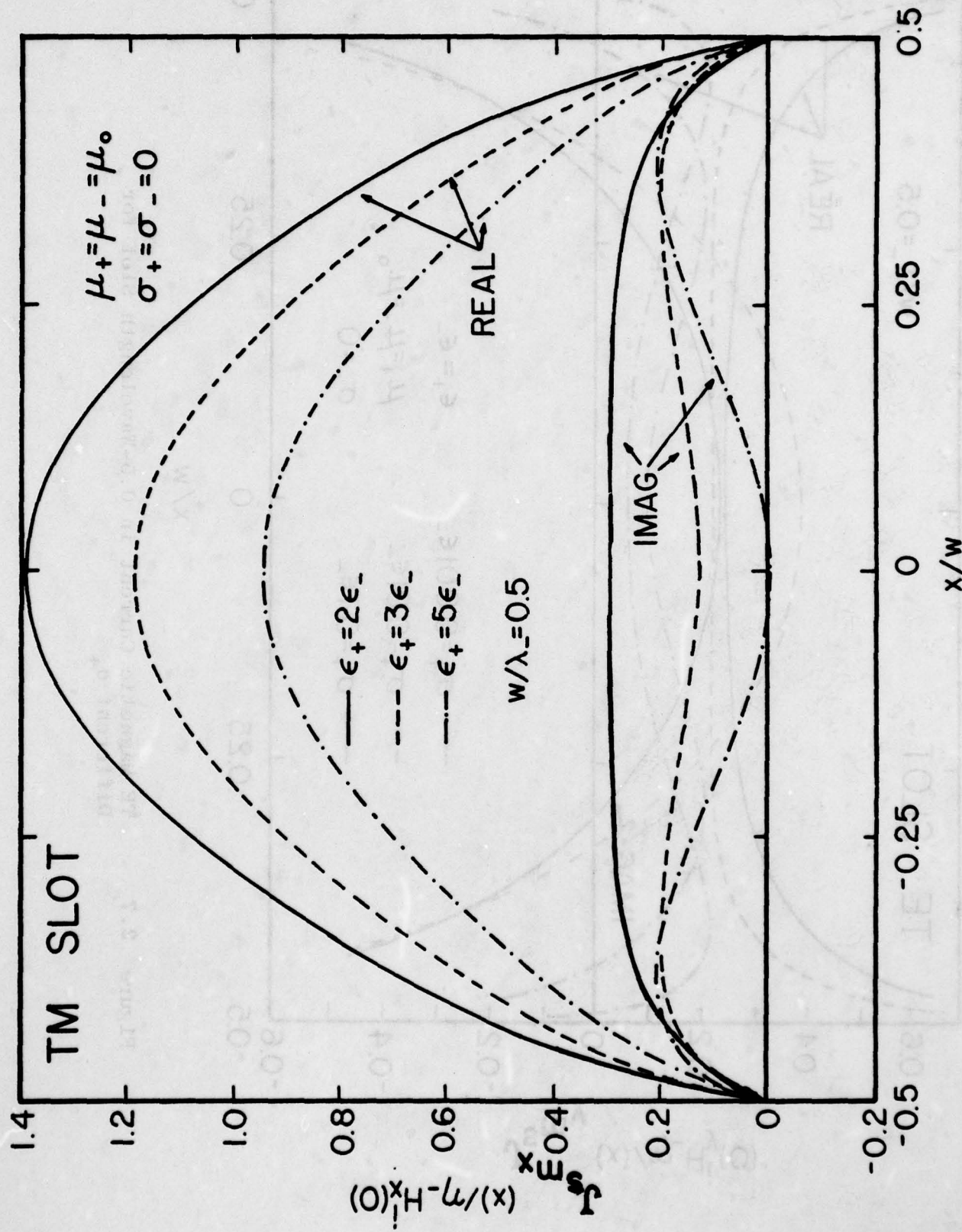


Figure 2.8 TM Magnetic Current in 0.5-Wavelength Slot for Different ϵ_+

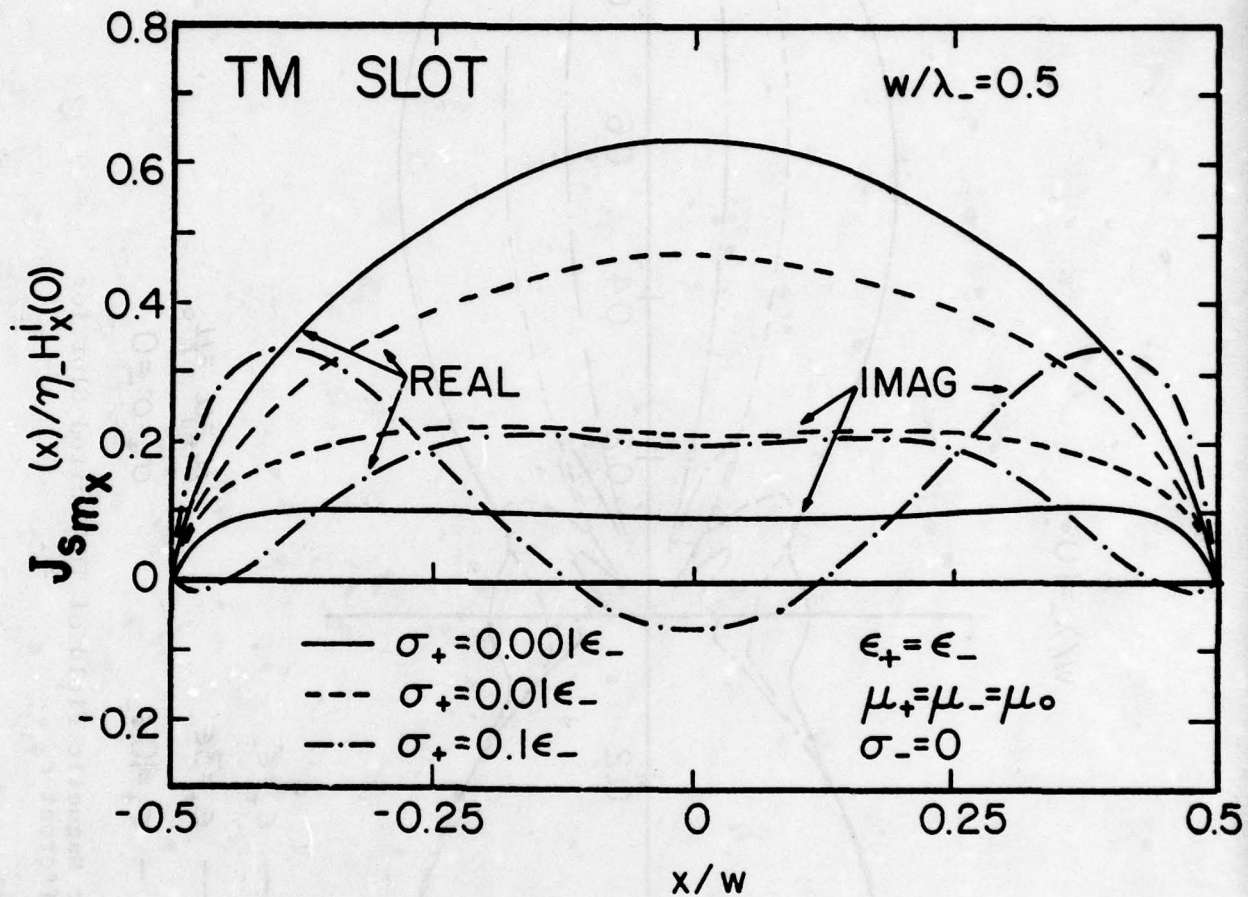


Figure 2.9 TM Magnetic Current in 0.5-Wavelength Slot for Different σ_+

TE SLOT
 $w/\lambda_- = 1.0$

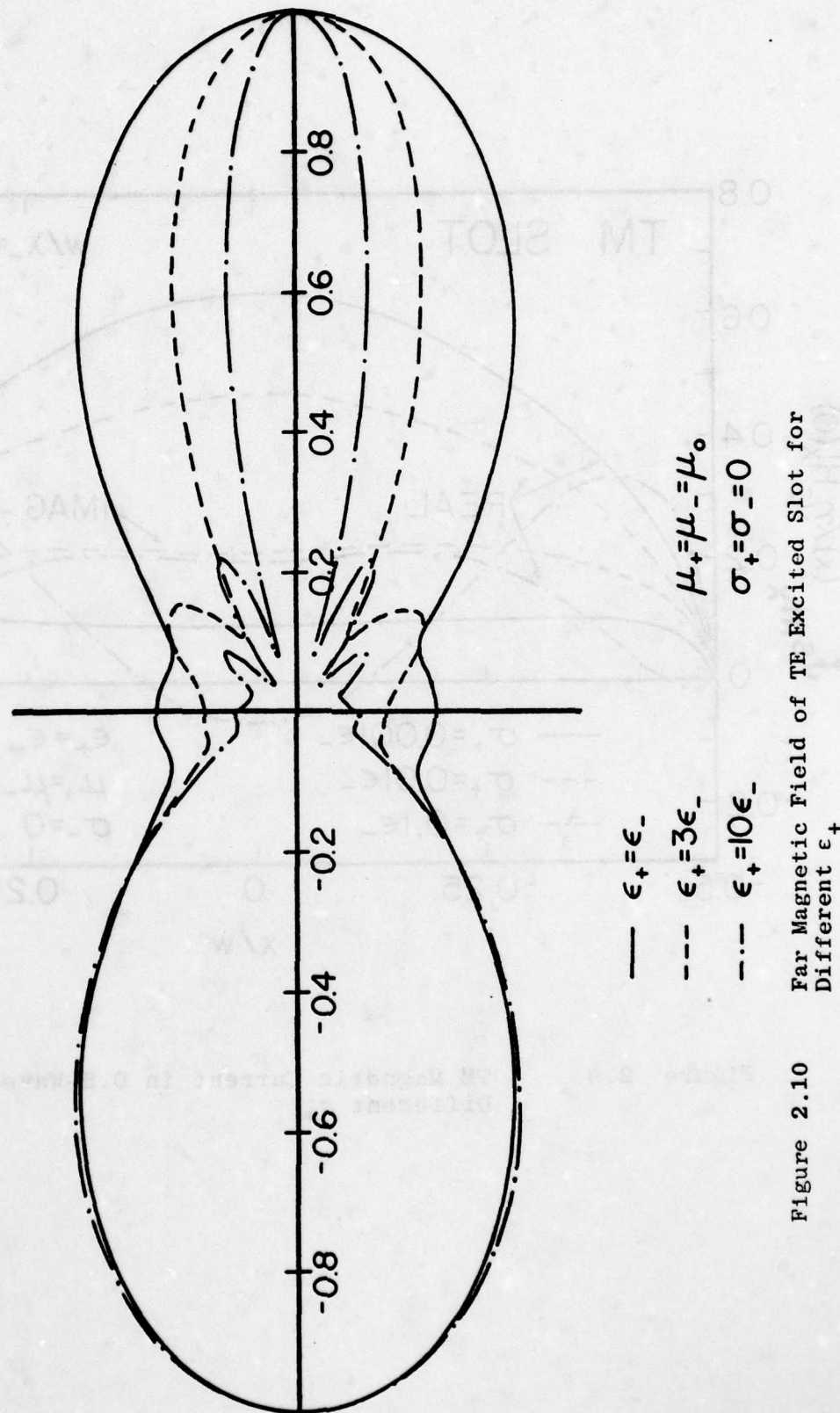


Figure 2.10 Far Magnetic Field of TE Excited Slot for Different ϵ_+

TM SLOT

$w/\lambda_- = 1.0$

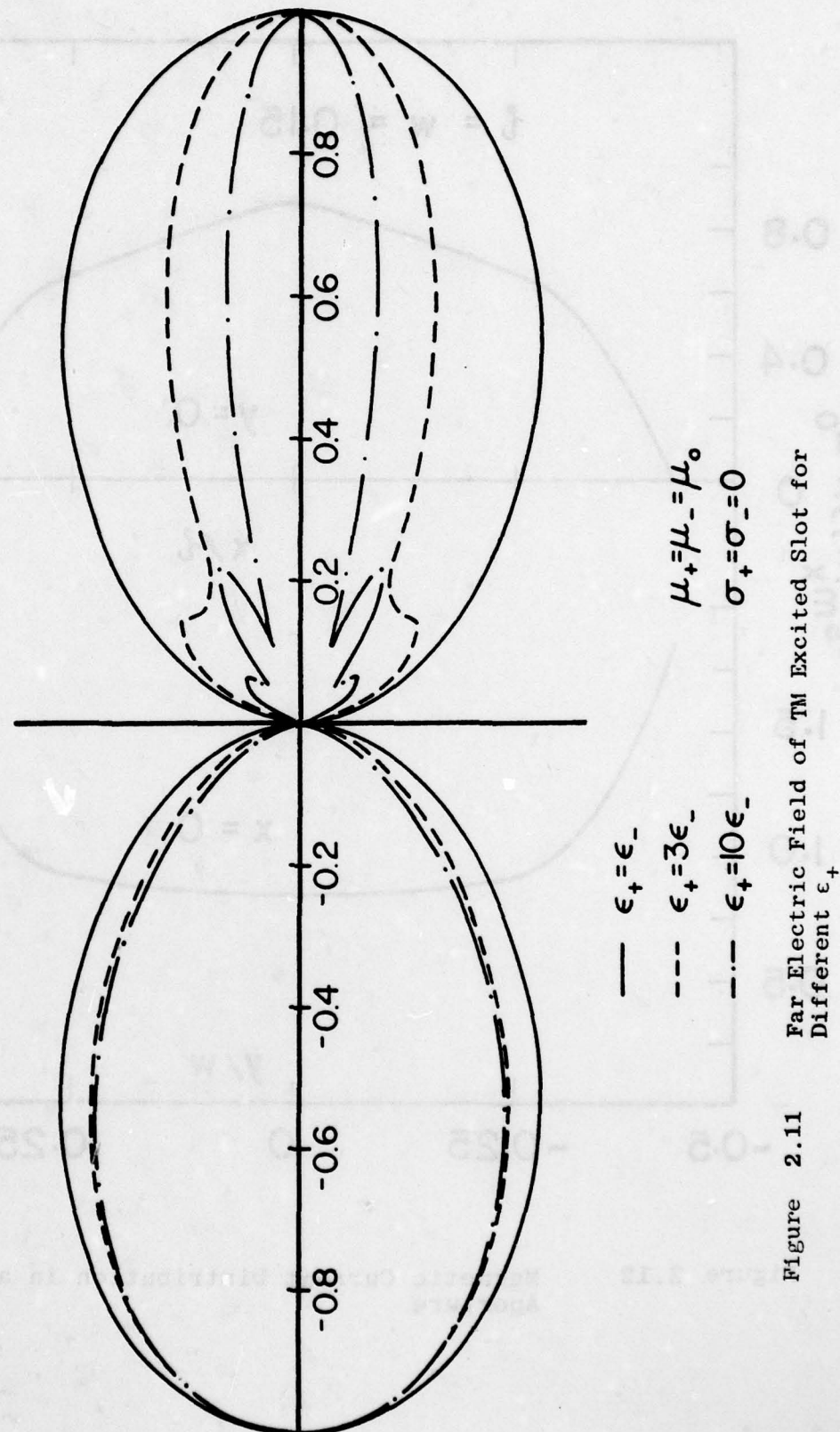


Figure 2.11 Far Electric Field of TM Excited Slot for Different ϵ_+

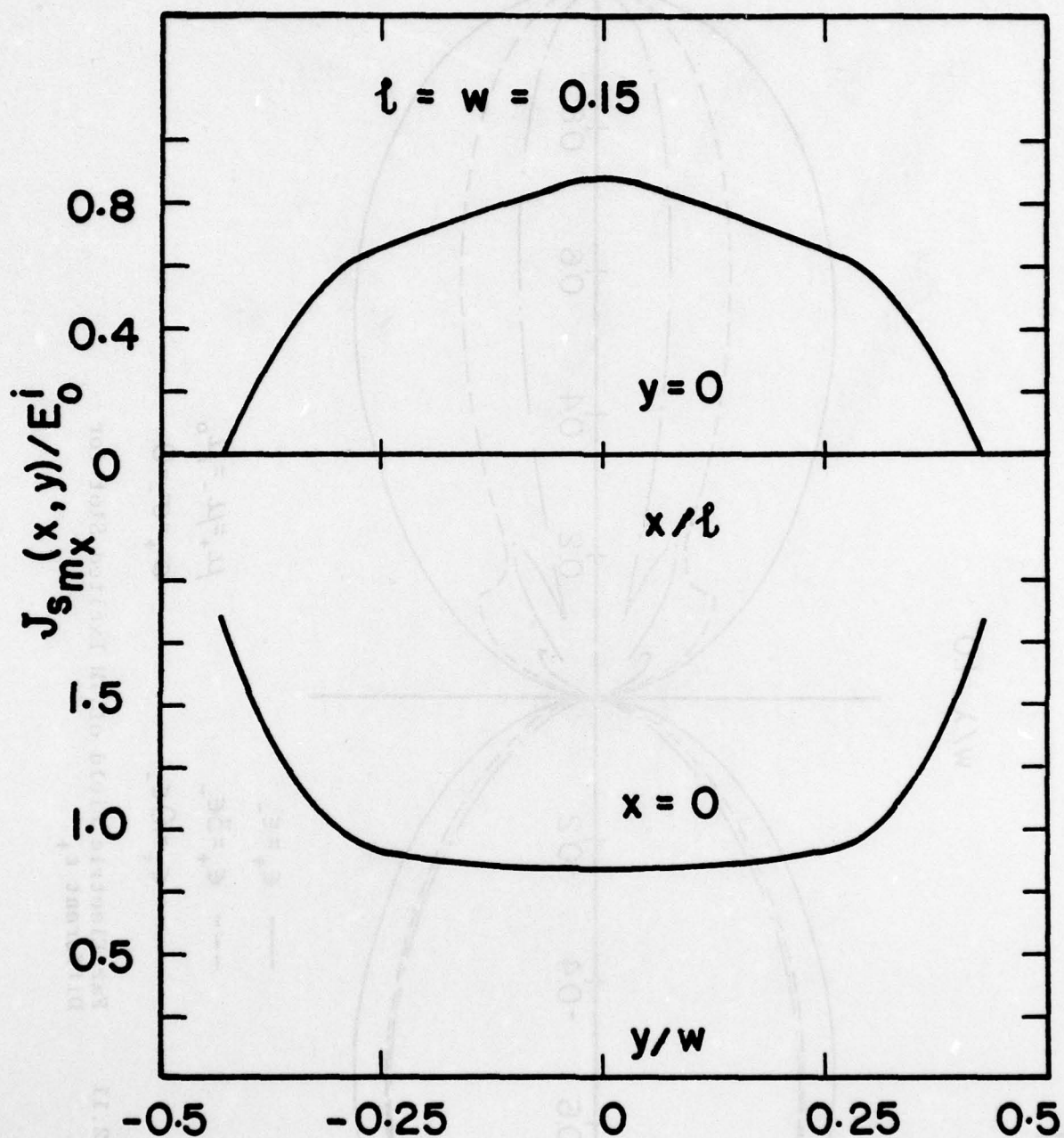


Figure 2.12 Magnetic Current Distribution in a Square Aperture

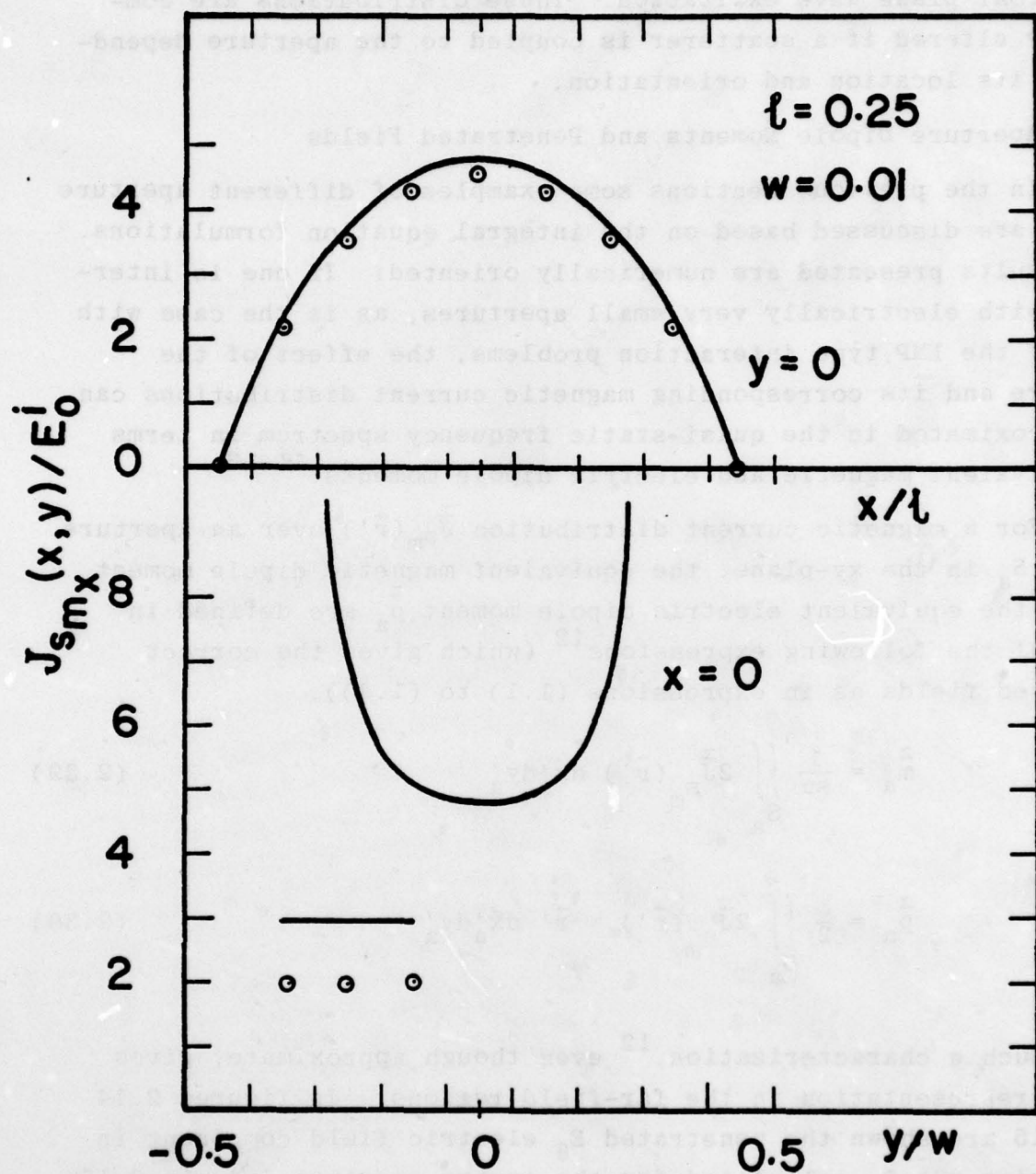


Figure 2.13 Magnetic Current Distribution in a Narrow Rectangular Slot

for normal plane wave excitation. These distributions are completely altered if a scatterer is coupled to the aperture depending on its location and orientation.

F. Aperture Dipole Moments and Penetrated Fields

In the previous sections some examples of different aperture shapes are discussed based on the integral equation formulations. The results presented are numerically oriented. If one is interested with electrically very small apertures, as is the case with many of the EMP type interaction problems, the effect of the aperture and its corresponding magnetic current distributions can be approximated in the quasi-static frequency spectrum in terms of equivalent magnetic and electric dipole moments.¹¹⁻¹³

For a magnetic current distribution $\tilde{J}_{S_m}(\vec{r}')$ over an aperture region S_a in the xy-plane, the equivalent magnetic dipole moment \tilde{m}_a and the equivalent electric dipole moment \tilde{p}_a are defined in terms of the following expressions¹² (which gives the correct scattered fields as in expressions (1.1) to (1.4)),

$$\tilde{m}_a = \frac{1}{8\mu} \iint_{S_a} 2\tilde{J}_{S_m}(\vec{r}') dx'_a dy'_a \quad (2.29)$$

and

$$\tilde{p}_a = \frac{\epsilon}{2} \iint_{S_a} 2\tilde{J}_{S_m}(\vec{r}') \times \vec{r}' dx'_a dy'_a \quad (2.30)$$

Such a characterization,¹² even though approximate, gives a good representation in the far-field regions. In figures 2.14 and 2.15 are shown the penetrated E_θ electric field component in the region $z > 0$, calculated for the square aperture $l = w = 0.15$ wavelength with the incident field oriented normally (fig. 2.14) and edge on incidence (fig. 2.15).

AD-A073 770

AIR FORCE WEAPONS LAB KIRTLAND AFB NM
ELECTROMAGNETIC PULSE INTERACTION NOTES -- EMP 3-38. (U)

F/G 20/14

MAY 79 C E BAUM
AFWL-TR-79-401

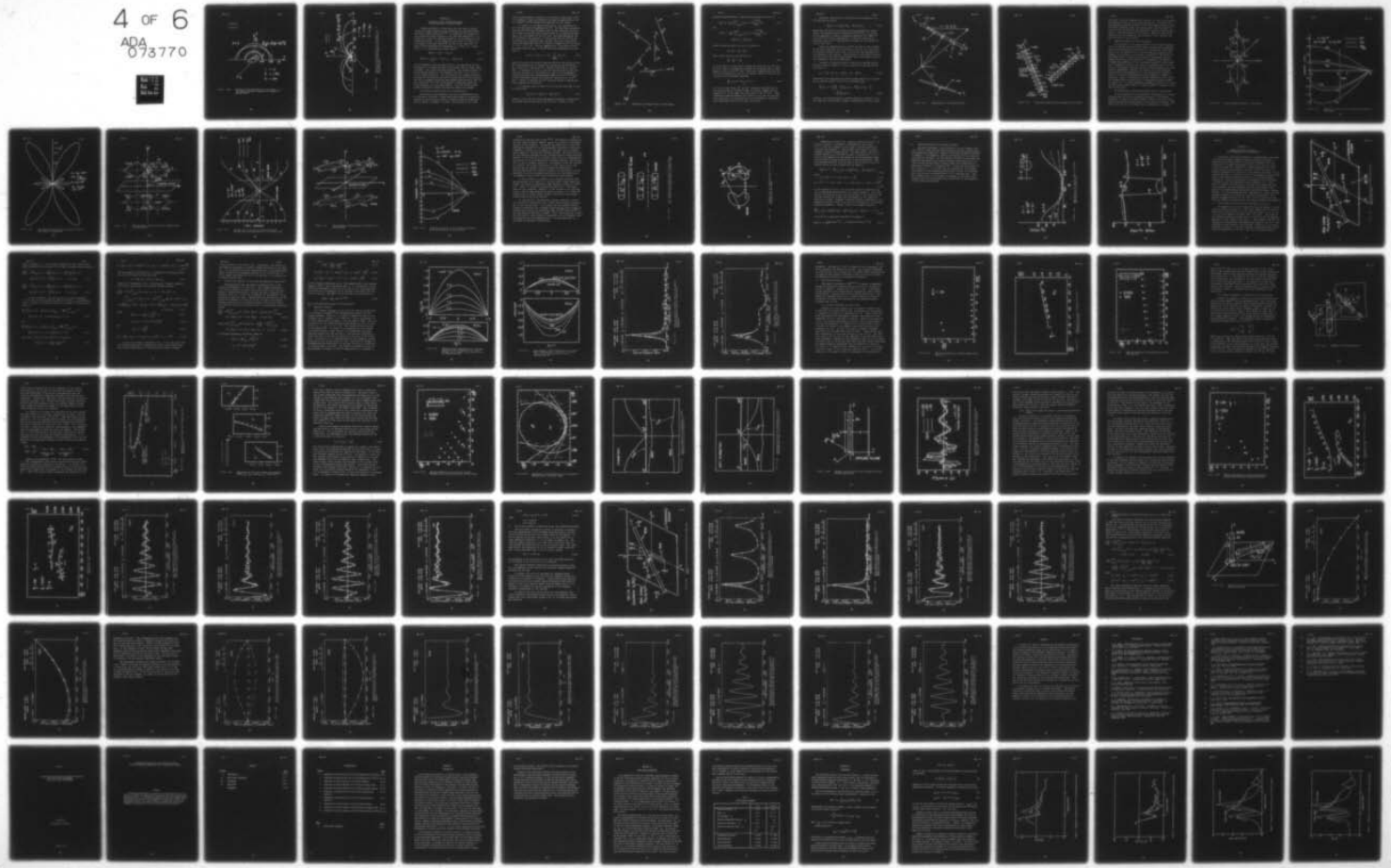
SBIE -AD-E200 329

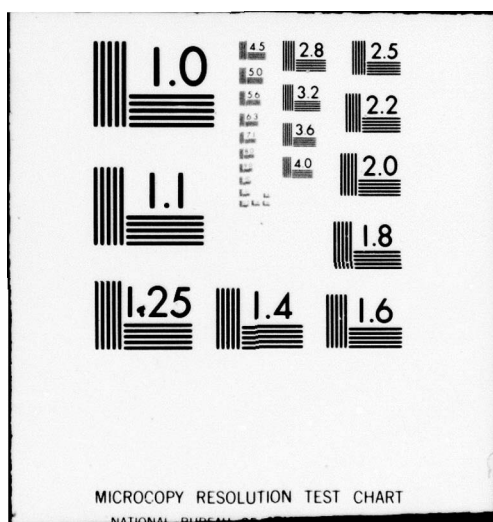
NL

UNCLASSIFIED

4 OF 6
ADA
093770

REF ID:
A79-401





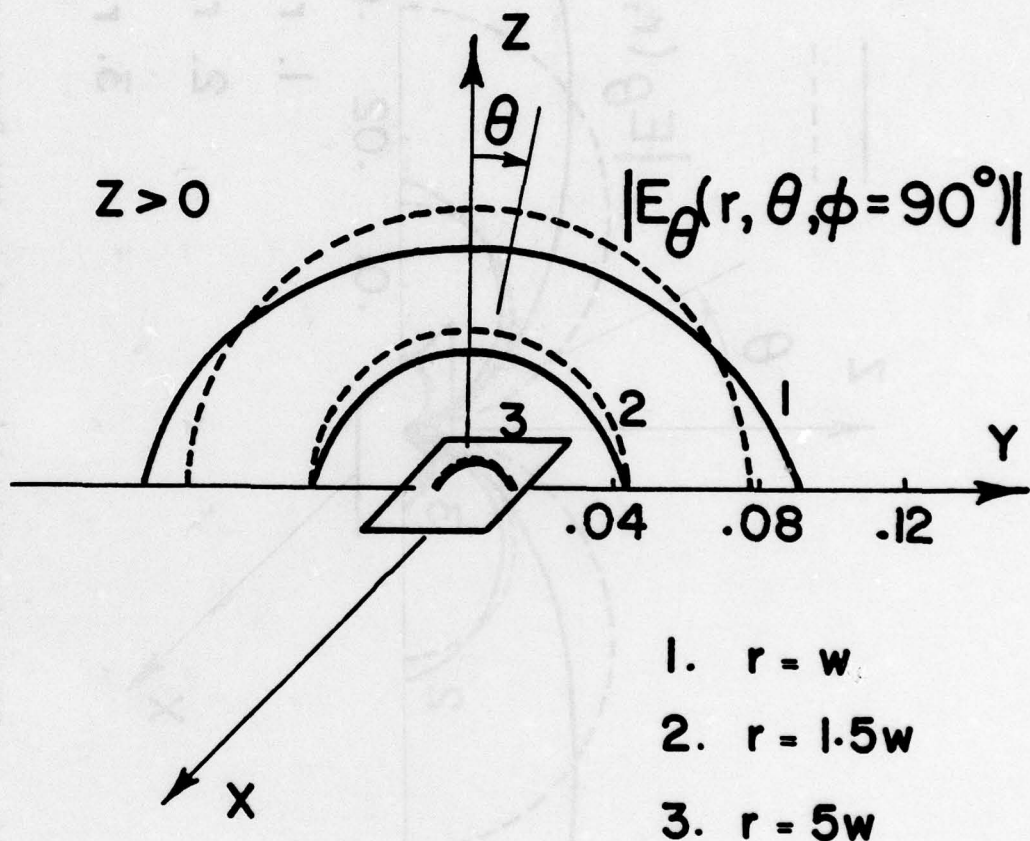


Figure 2.14 Electric Field Penetrated in the Region $z > 0$ for Square Aperture Compared with Magnetic Dipole Moment

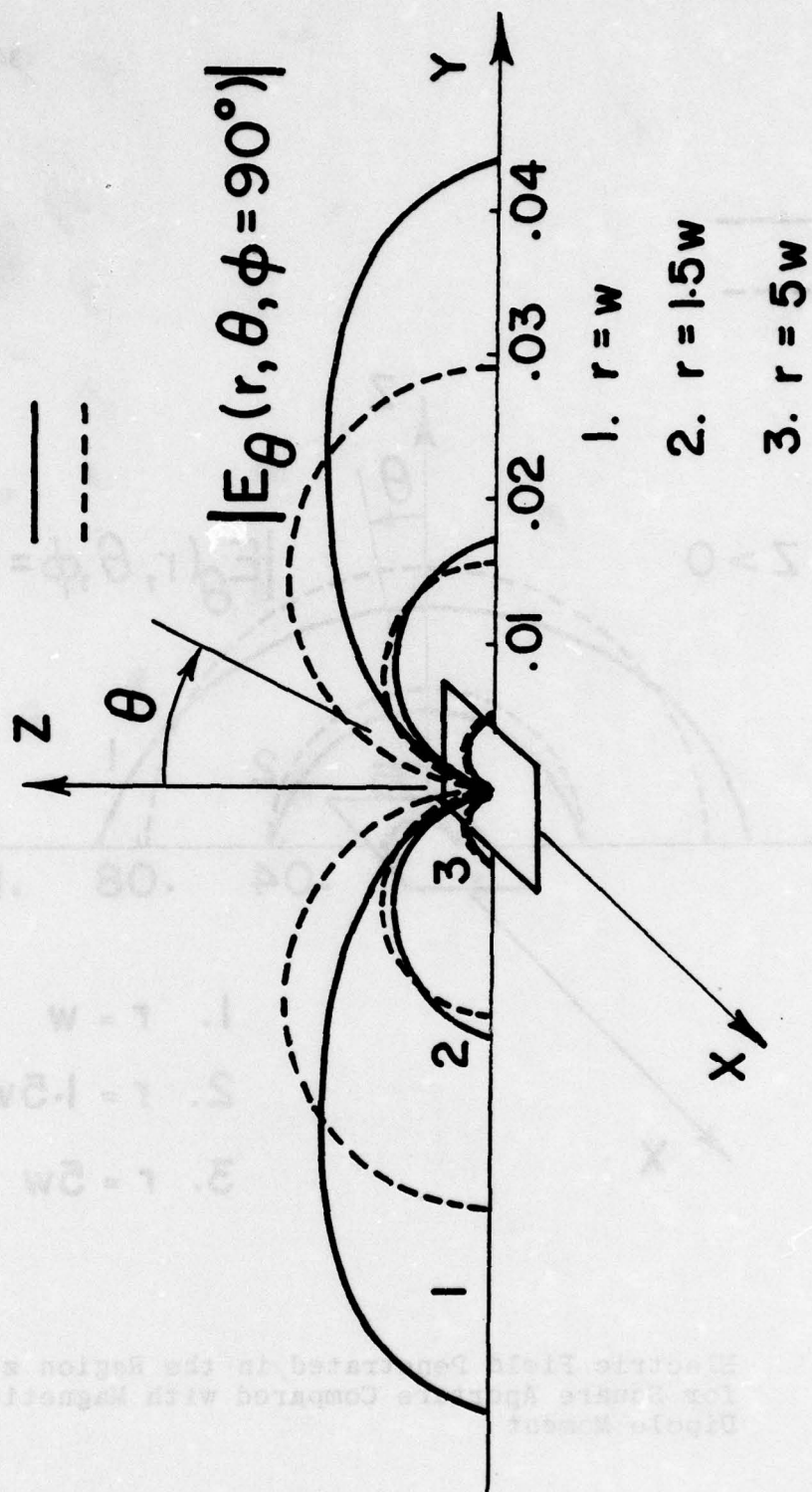


Figure 2.15 Electric Field Penetrated in the Region $z > 0$ for Square Aperture Compared with Electric Dipole Moment

CHAPTER III

Analysis of the Conducting Bodies
in the Presence of Ground Screen

Conducting bodies in free space and also above a ground screen are widely treated in the literature for analyzing their scattering characteristics.^{24,25} To understand the response of the objects and their coupling to the aperture geometries, it is essential to know the scattering behavior in the presence of the conducting screen. If the aperture S_a is absent in figure 1.1, the complete scattered fields \tilde{H}_+^c and \tilde{E}_+^c in the right half (+) space can be determined by expressions (1.3) and (1.4). Hence for $z > 0$, in the right half space medium,

$$\tilde{H}_+^c(\vec{r}, s) = \frac{1}{\mu_+} \nabla \times \tilde{A}_+(\vec{r}, s) \quad (3.1)$$

$$\tilde{E}_+^c(\vec{r}, s) = \frac{s}{\gamma_+^2} \left[\nabla(\nabla \cdot \tilde{A}_+(\vec{r}, s)) - \gamma_+^2 \tilde{A}_+(\vec{r}, s) \right] \quad (3.2)$$

and the magnetic vector potential $\tilde{A}_+(\vec{r}, s)$ is again given by the expression (1.8) which has both the scatterer and its image terms included. For a given scatterer geometry, the induced current can be determined subject to the boundary condition (1.14) for perfectly conducting bodies. In fact many of the integral equations obtained in the previous sections for apertures and slots separating two half spaces having the same medium characteristics are the dual equations²¹ for the two-dimensional conducting plate and strip problems in a free-space medium. With the ground screen present appropriate image contributions should be included.

A. Arbitrarily Oriented Thin-Wire Configurations

Arbitrarily oriented general thin-wire configurations both in free space and above a conducting ground plane are extensively studied in the literature based on integral equation techniques and the method of moments. As such, the analysis of the wires

above a ground plane is similar to the wires in free space, since the concept of images and properties of matrix symmetrization can be invoked²³ and the ground plane replaced by wire images.

In figure 3.1 are shown several wires, one designated the p^{th} wire and another designated the q^{th} . We focus major attention upon the p^{th} wire and investigate how one may calculate the electric field on this wire due to the current \tilde{I}_p on itself plus that due to \tilde{I}_q , the current on the q^{th} wire. The contribution on the p^{th} wire due to the presence of wires other than the q^{th} may be calculated in an identical way, and then the total contribution from wires other than the p^{th} is simply a summation over all wires $q = 1, 2, \dots, N (q \neq p)$. Written symbolically, the electric field directed along the axis of the p^{th} wire and evaluated on its surface is

$$\tilde{E}_\zeta(\zeta, s) = \tilde{E}_{p_\zeta}(\zeta, s) + \tilde{I}_p \cdot \sum_{\substack{q=1 \\ (q \neq p)}}^N \tilde{E}_q(\zeta, s) \quad (3.3)$$

where \tilde{E}_ζ is the total axially directed field on the surface of the p^{th} wire produced by all charges and currents on the structure, \tilde{E}_{p_ζ} is that due to the current \tilde{I}_p , and \tilde{E}_q is that due to the q^{th} wire. In equation (3.3) \tilde{I}_p is the unit vector along the p^{th} wire (and has the sense of the current \tilde{I}_p), and ζ is an independent variable denoting axial displacement along \tilde{I}_p of the p^{th} wire in a local coordinate system with origin at the center of the p^{th} wire. Figure 3.2 depicts the two wires and serves to define geometric quantities of interest.

At a general point in space (x, y, z) one may write \tilde{E}_{p_ζ} in the following form:

$$\tilde{E}_{p_\zeta}(\vec{r}, s) = -s \tilde{A}_p(\vec{r}, s) - \frac{\partial}{\partial \zeta} \tilde{\phi}_p(\vec{r}, s) \quad (3.4)$$

where \tilde{A}_p and $\tilde{\phi}_p$ are the vector and scalar potentials, respectively, calculated from the sources on the p^{th} wire. Subject to the

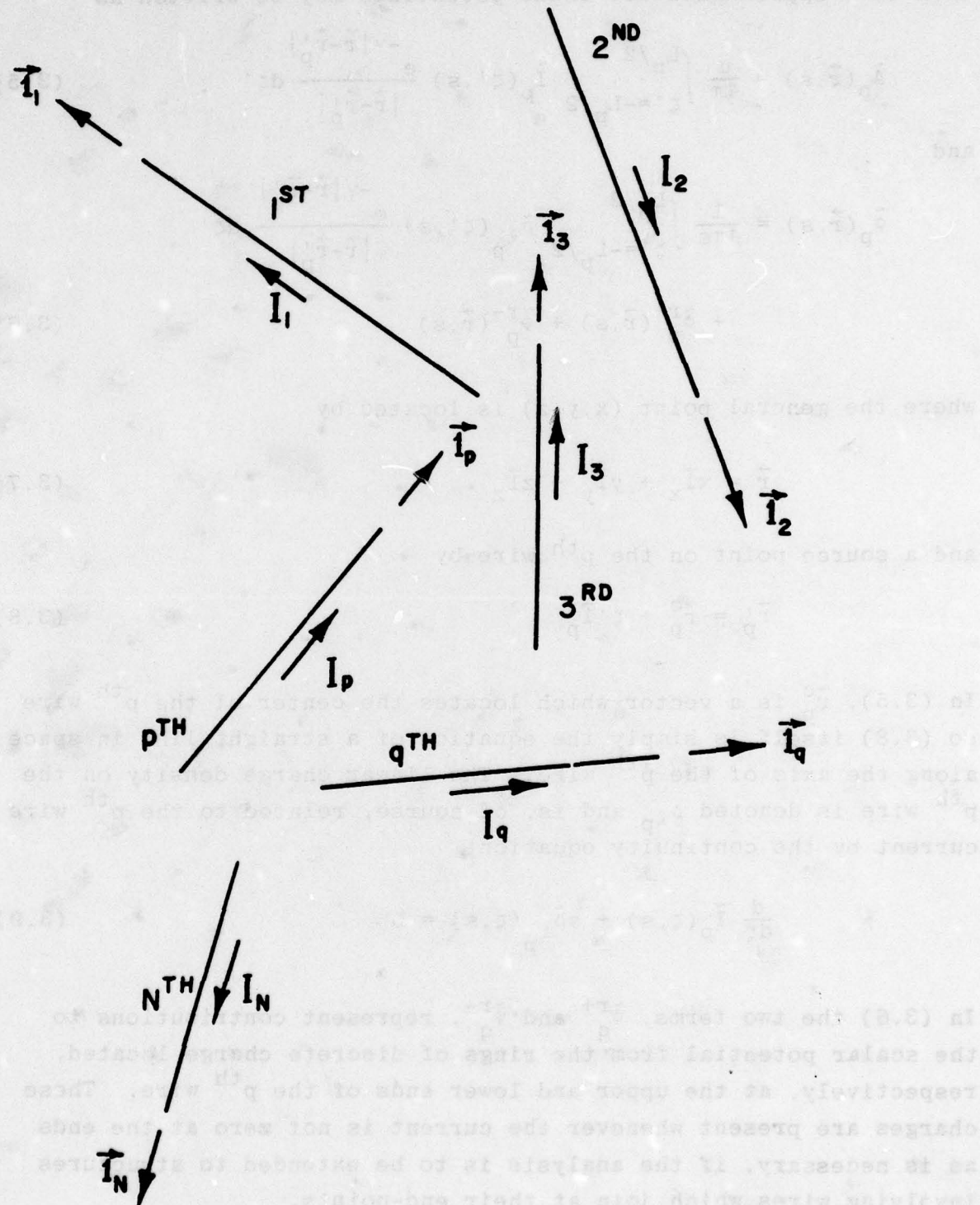


Figure 3.1 Arbitrarily Oriented Wires in Free Space

thin-wire approximations, these potentials may be written as

$$\tilde{A}_p(\vec{r}, s) = \frac{\mu}{4\pi} \int_{\zeta' = -L_p/2}^{L_p/2} \tilde{I}_p(\zeta', s) \frac{e^{-\gamma |\vec{r} - \vec{r}'_p|}}{|\vec{r} - \vec{r}'_p|} d\zeta' \quad (3.5)$$

and

$$\begin{aligned} \tilde{\phi}_p(\vec{r}, s) &= \frac{1}{4\pi\epsilon} \int_{\zeta' = -L_p/2}^{L_p/2} \tilde{\rho}_{\ell p}(\zeta', s) \frac{e^{-\gamma |\vec{r} - \vec{r}'_p|}}{|\vec{r} - \vec{r}'_p|} d\zeta' \\ &\quad + \tilde{\phi}_p^{r+}(\vec{r}, s) + \tilde{\phi}_p^{r-}(\vec{r}, s) \end{aligned} \quad (3.6)$$

where the general point (x, y, z) is located by

$$\vec{r} = x\hat{1}_x + y\hat{1}_y + z\hat{1}_z \quad (3.7)$$

and a source point on the p^{th} wire by

$$\vec{r}'_p = \vec{r}_p^c + \zeta' \hat{1}_p \quad (3.8)$$

In (3.5), \vec{r}_p^c is a vector which locates the center of the p^{th} wire so (3.8) itself is simply the equation of a straight line in space along the axis of the p^{th} wire. The linear charge density on the p^{th} wire is denoted $\tilde{\rho}_{\ell p}$ and is, of course, related to the p^{th} wire current by the continuity equation,

$$\frac{d}{d\zeta} \tilde{I}_p(\zeta, s) + s\tilde{\rho}_{\ell p}(\zeta, s) = 0 \quad (3.9)$$

In (3.6) the two terms, $\tilde{\phi}_p^{r+}$ and $\tilde{\phi}_p^{r-}$, represent contributions to the scalar potential from the rings of discrete charge located, respectively, at the upper and lower ends of the p^{th} wire. These charges are present whenever the current is not zero at the ends as is necessary, if the analysis is to be extended to structures involving wires which join at their end-points.

Similarly, the electric field $\tilde{\mathbf{E}}_q(\vec{r})$ due to sources on the q^{th} wire may be written

$$\tilde{\mathbf{E}}_q(\vec{r}, s) = -s\tilde{\mathbf{A}}_q(\vec{r}, s)\hat{\mathbf{l}}_q - \text{grad } \tilde{\phi}_q(\vec{r}, s) \quad (3.10)$$

where $\tilde{\mathbf{A}}_q$ and $\tilde{\phi}_q$ are the vector and scalar potentials, respectively, calculated from the sources on the q^{th} wire. $\tilde{\mathbf{A}}_q$ and $\tilde{\phi}_q$ can be expressed in terms of potential integrals like those of (3.5) and (3.6) with p replaced by q . The unit vector $\hat{\mathbf{l}}_q$ is directed along the q^{th} wire and has the sense of the defined current on this wire.

Since the contributions on the p^{th} wire due to the currents on the other wires are all of the form of (3.10), only two wires are tested in general below (fig. 3.3) so that the discussion is not rendered overly complex. The extension to more than two wires is quite direct and can be done readily after the present two-wire case foundation has been established.

The axially directed electric field on the surface of the p^{th} wire shown in figure 3.2, due to sources on both the p^{th} and q^{th} wires, is

$$\tilde{\mathbf{E}}_\zeta = -s\tilde{\mathbf{A}}_p - \frac{\partial}{\partial \zeta} \tilde{\phi}_p - s\tilde{\mathbf{A}}_q(\hat{\mathbf{l}}_q \cdot \hat{\mathbf{l}}_q) - \frac{\partial}{\partial \zeta} \tilde{\phi}_q \quad (3.11)$$

Retaining $\tilde{\phi}_q$ but employing the Lorentz gauge explicitly to eliminate $\tilde{\phi}_p$ one may convert (3.11) to an alternate form:

$$\begin{aligned} \frac{\gamma^2}{s} \tilde{\mathbf{E}}_\zeta(\zeta, s) &= \left(\frac{\partial^2}{\partial \zeta^2} - \gamma^2 \right) \tilde{\mathbf{A}}_p(\zeta, s) - \gamma^2 \tilde{\mathbf{A}}_q(\zeta, s)(\hat{\mathbf{l}}_q \cdot \hat{\mathbf{l}}_q) \\ &\quad - \frac{\gamma^2}{s} \frac{\partial}{\partial \zeta} \tilde{\phi}_q(\zeta, s) \end{aligned} \quad (3.12)$$

Actually, the Lorentz gauge is invoked implicitly relative to $\tilde{\phi}_q$, for otherwise the potential integral representation of the scalar

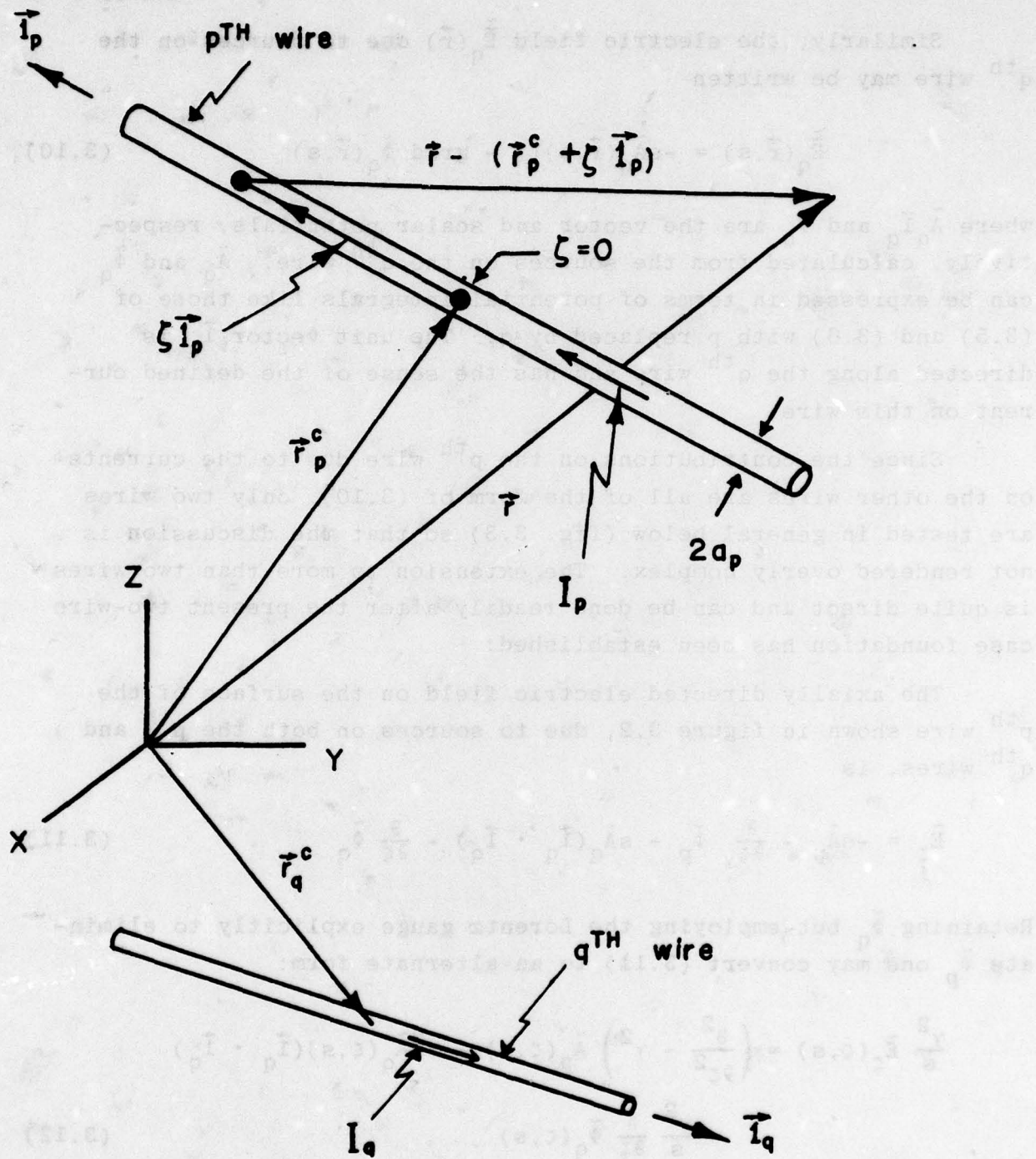
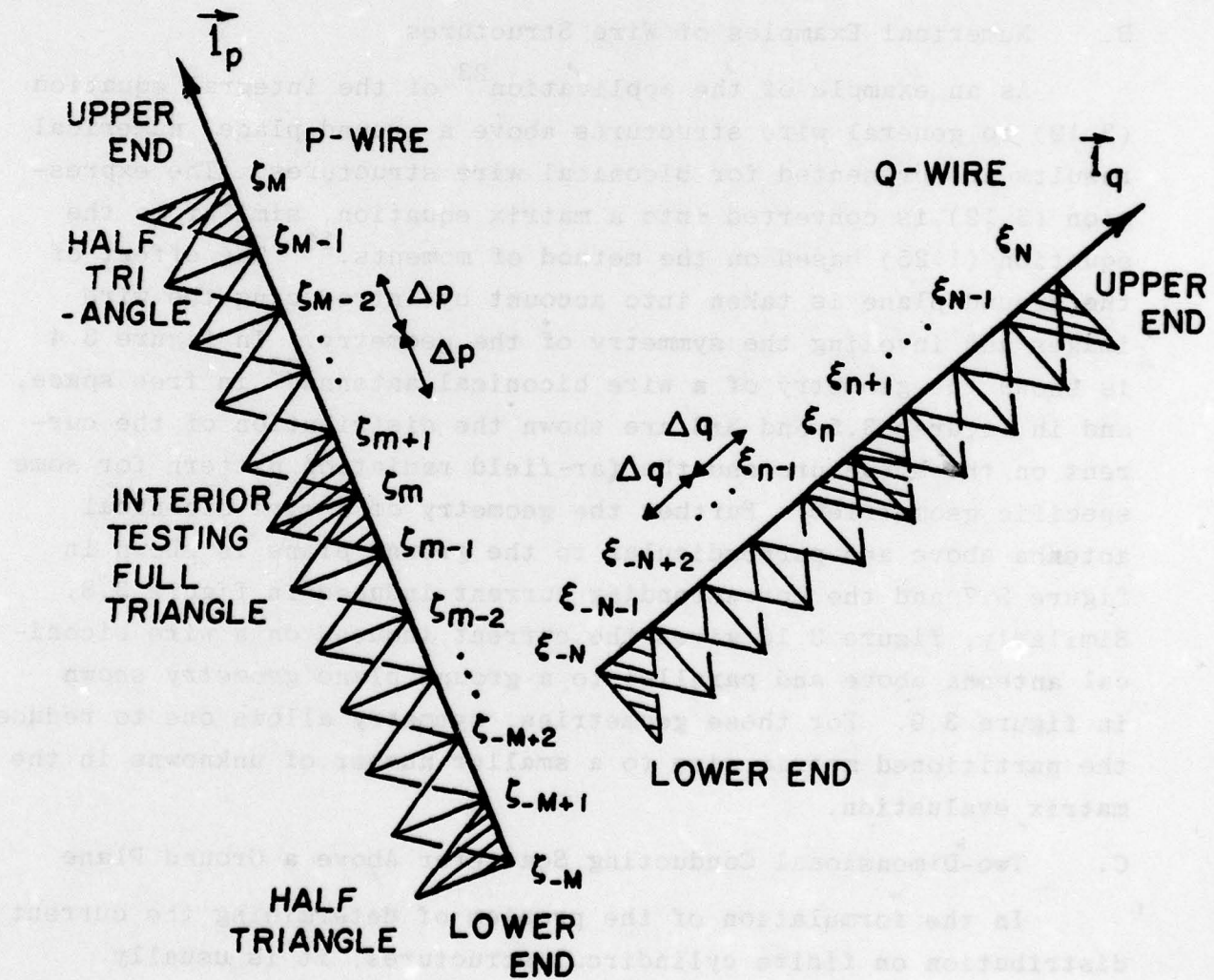


Figure 3.2 Coordinates of Two Coupled Wires

-selected into (S.I.C) at increased test frequencies and lower frequencies
 -adj to value of ω - which deformation at ω has a reduced side
 -tubes needed reinforcement and to avoid post-tensioning unconsolidation
 -saturation from zero values required and when saturated values has
 -using as constant amplitude vibrations to oscillate bridge so that
 -axial stress and each stress point no cracks and more of safety
 -need frequency (D.F) necessary and to deconsolidating, at an ratio
 -increasing side of review of some



potential, would be inappropriate; however, in (3.12) the relationship between $\tilde{\Phi}_q$ and \tilde{A}_q is not invoked directly. In view of the heterogeneous application above of the relationship between vector and scalar potential under the Lorentz gauge, one must exercise care to avoid violation of the continuity equation, when he calculates Φ_q from the charge on the q^{th} wire. When this wire joins others, as is anticipated by the expression (3.6), special heed must be given to this caution.

B. Numerical Examples of Wire Structures

As an example of the application²³ of the integral equation (3.12) to general wire structures above a ground plane, numerical results are presented for biconical wire structures. The expression (3.12) is converted into a matrix equation, similar to the equation (1.25) based on the method of moments.¹⁶ The effect of the ground plane is taken into account by introducing the wire images and invoking the symmetry of the geometry. In figure 3.4 is shown the geometry of a wire biconical antenna²³ in free space, and in figures 3.5 and 3.6 are shown the distribution of the current on the structure and the far-field radiation pattern for some specific geometries. Further the geometry of a wire biconical antenna above and perpendicular to the ground plane is shown in figure 3.7 and the corresponding current induced in figure 3.8. Similarly, figure 3.10 gives the current induced on a wire biconical antenna above and parallel to a ground plane geometry shown in figure 3.9. For these geometries, symmetry allows one to reduce the partitioned matrix size to a smaller number of unknowns in the matrix evaluation.

C. Two-Dimensional Conducting Scatterer Above a Ground Plane

In the formulation of the problem of determining the current distribution on finite cylindrical structures, it is usually necessary to assume that the cylinder is thin so that the current density around the circumference of the cylinder is uniform. When this is not the case, one must solve a coupled set of integral

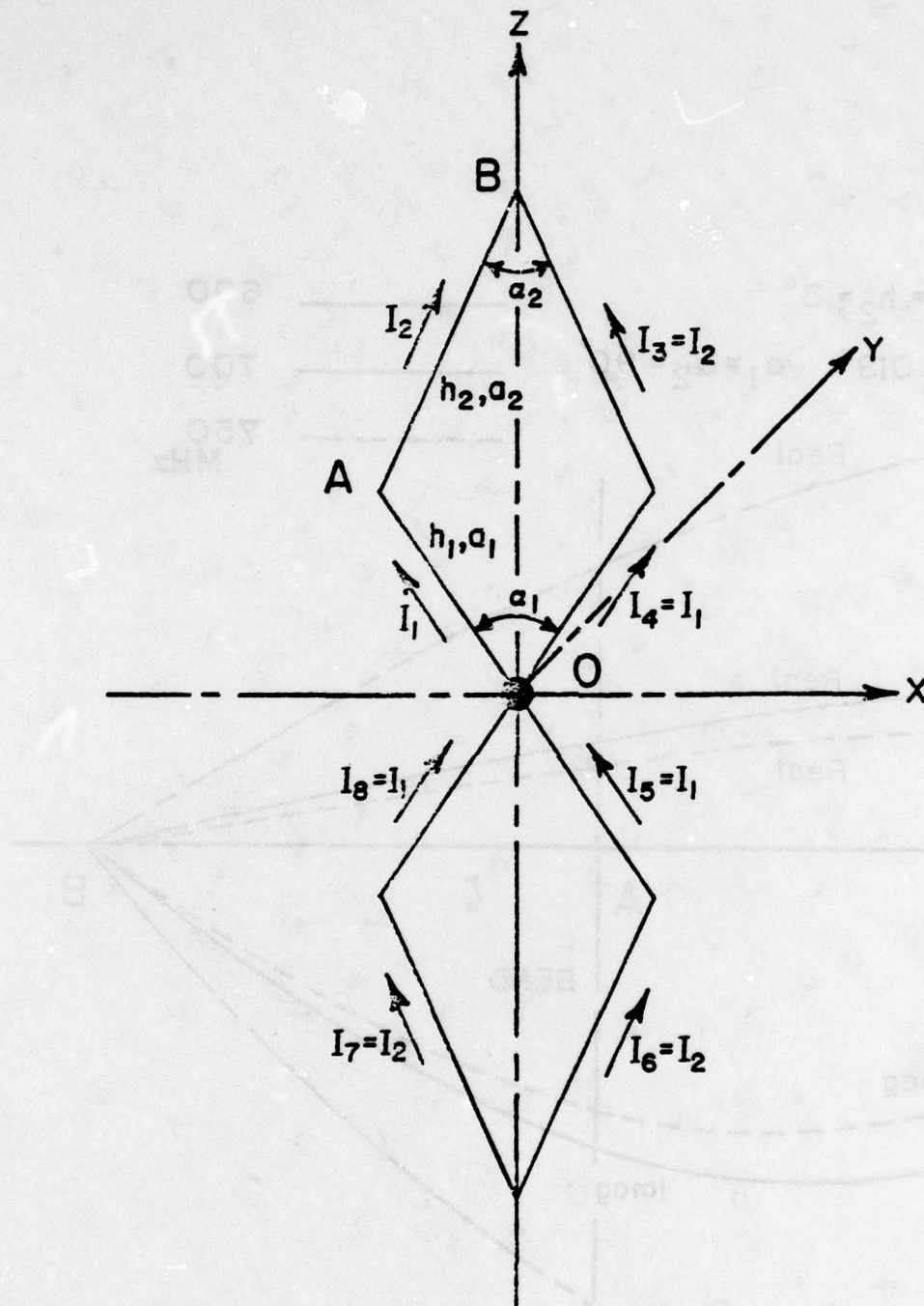


Figure 3.4 Wire Biconical Antenna in Free Space

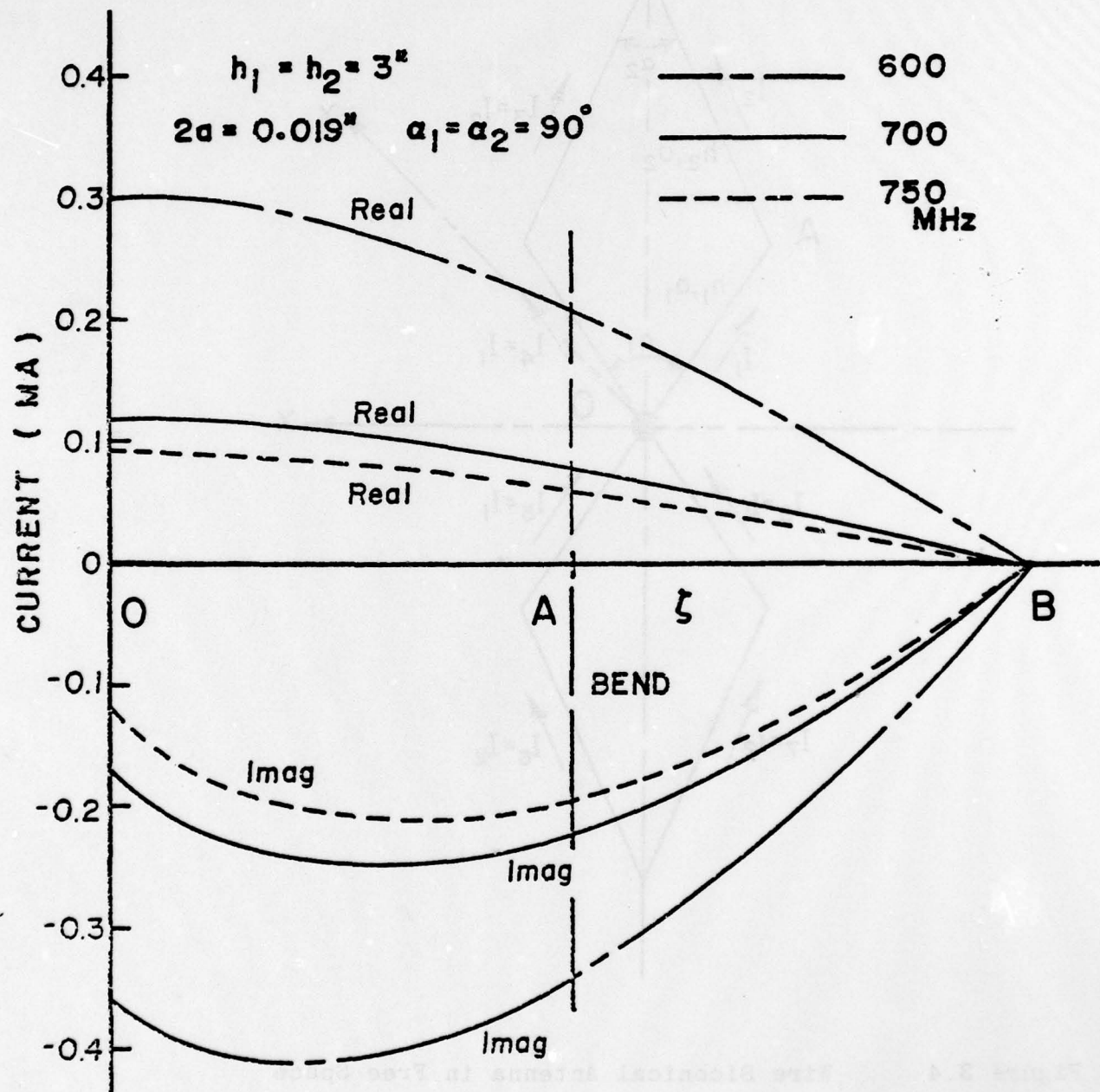


Figure 3.5 Currents I_1 and I_2 on Wire Biconical Antenna in Free Space

EMP 3-38

343-59

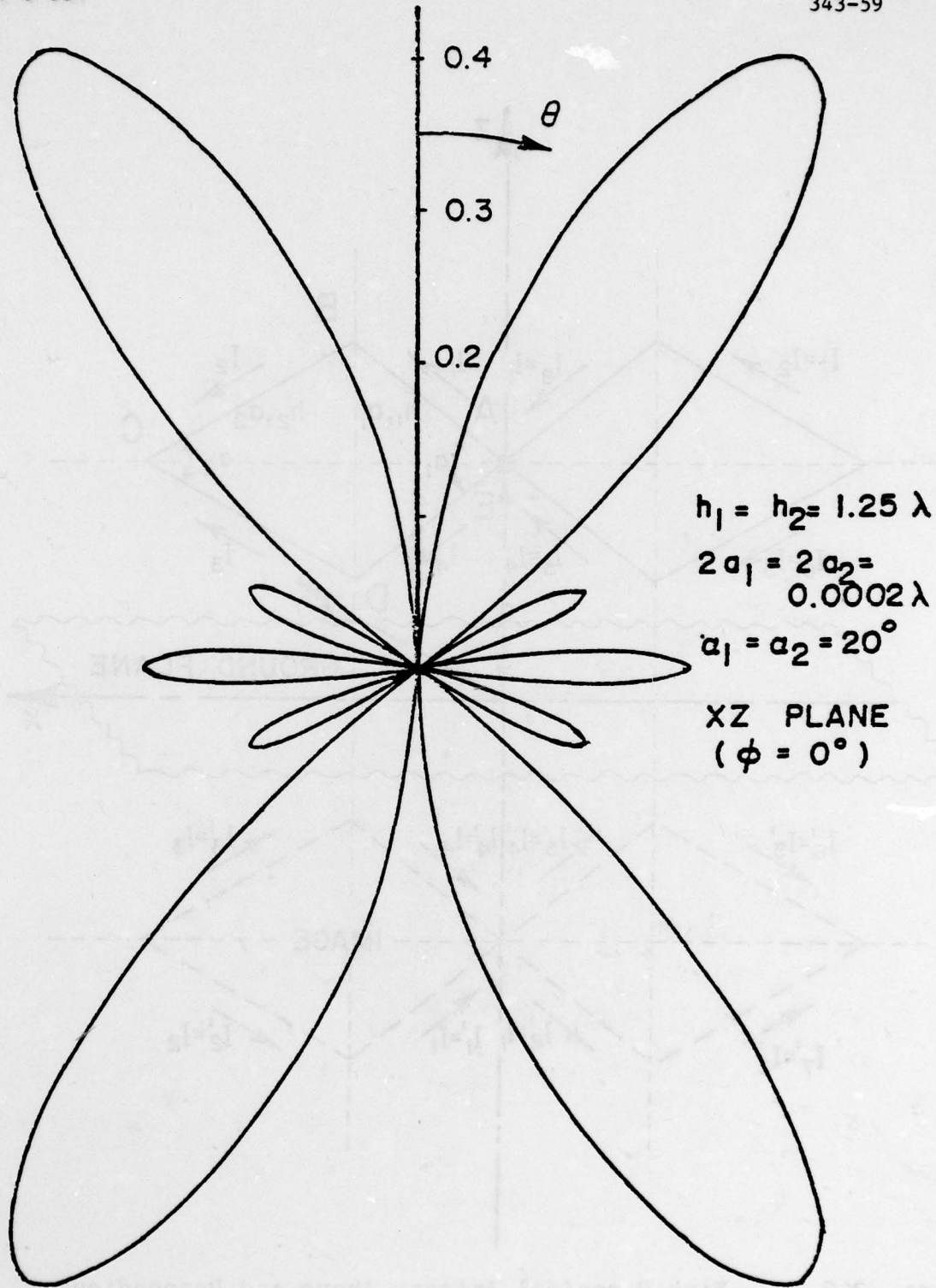


Figure 3.6

Far Field Pattern of Wire Biconical Antenna in Free Space, E_θ -Component

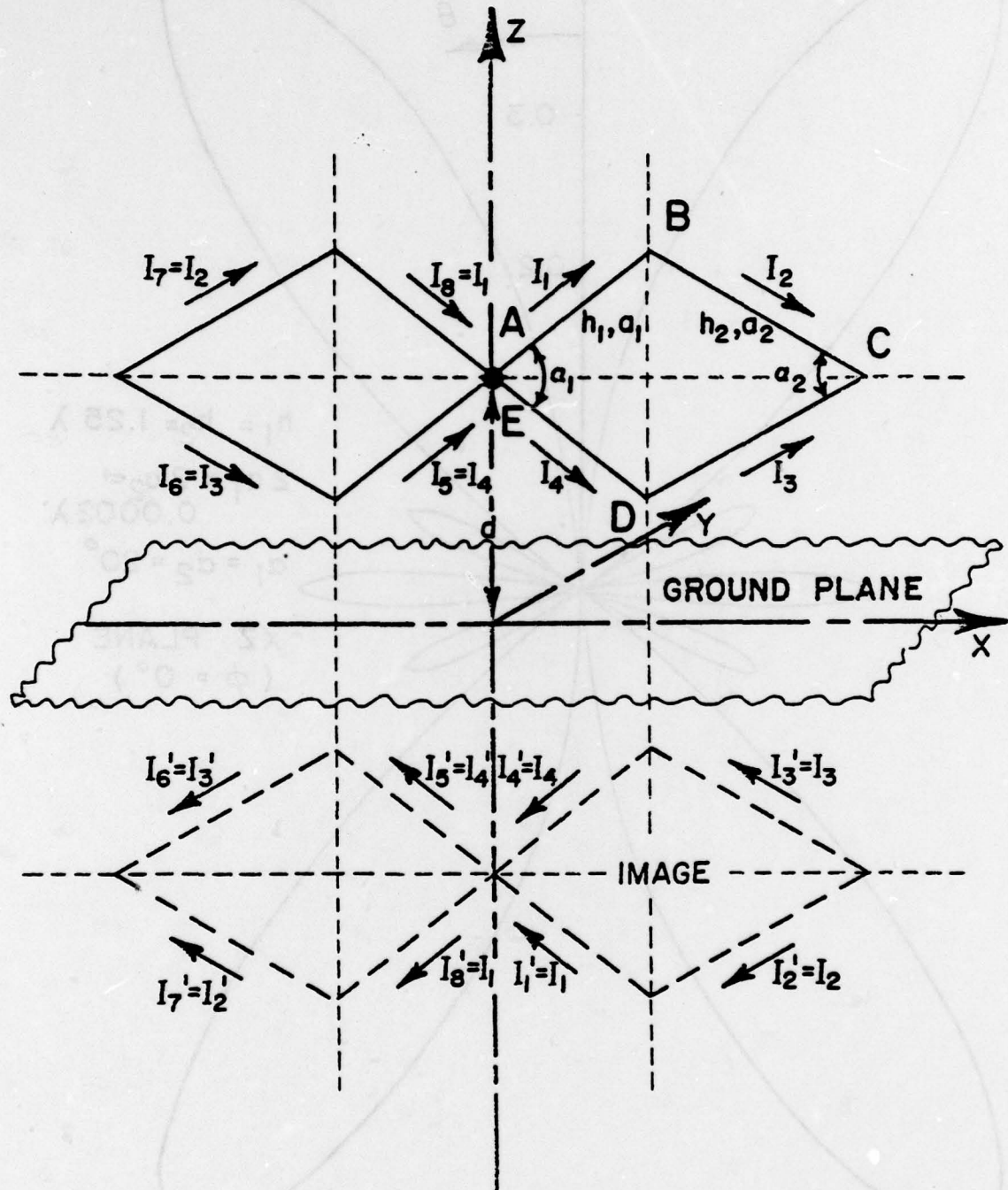


Figure 3.7

Wire Biconical Antenna Above and Perpendicular
to Ground Plane

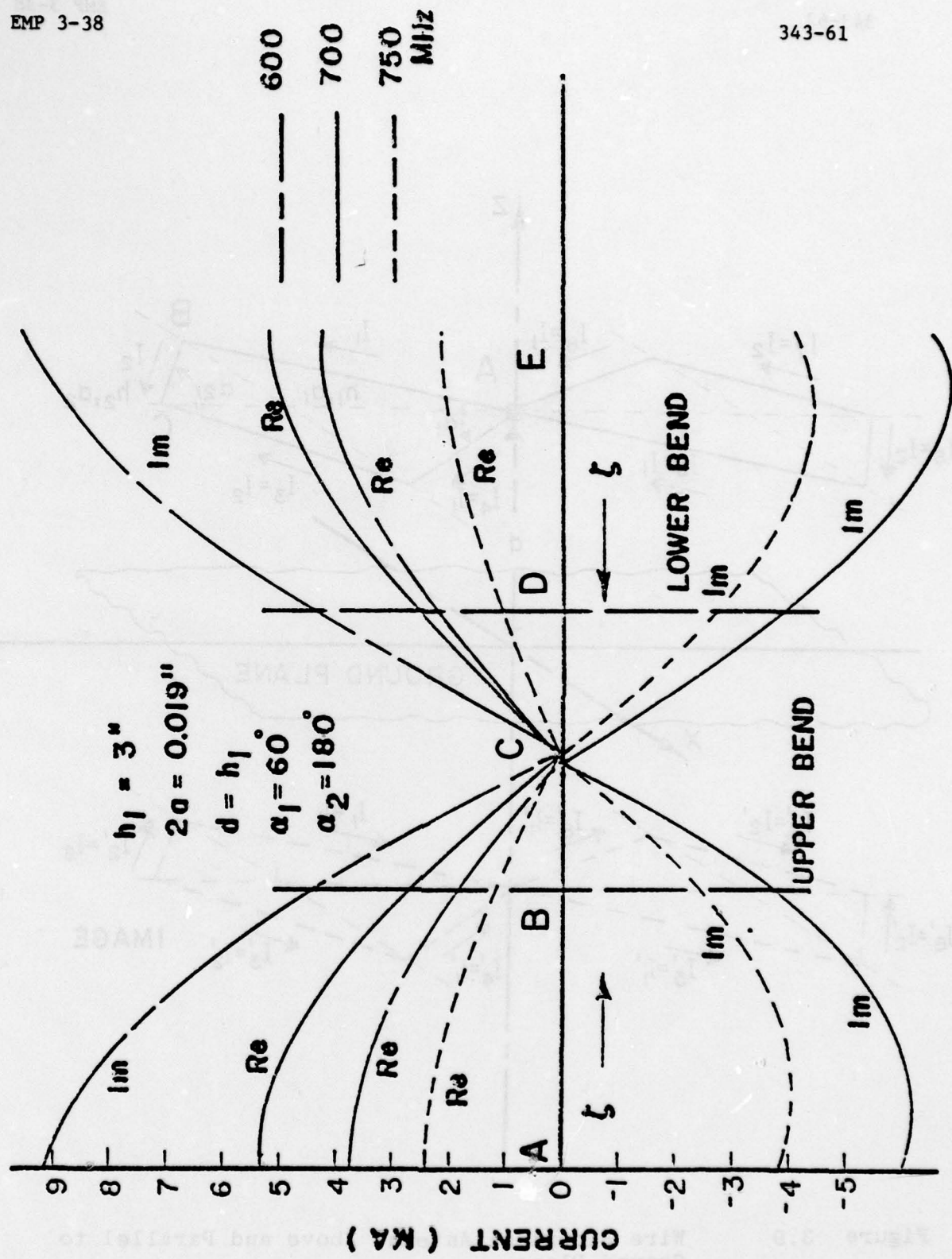


Figure 3.8

Currents I_1, I_2 and I_3, I_4 on Wire Biconical Antenna Above and Perpendicular to Ground Plane

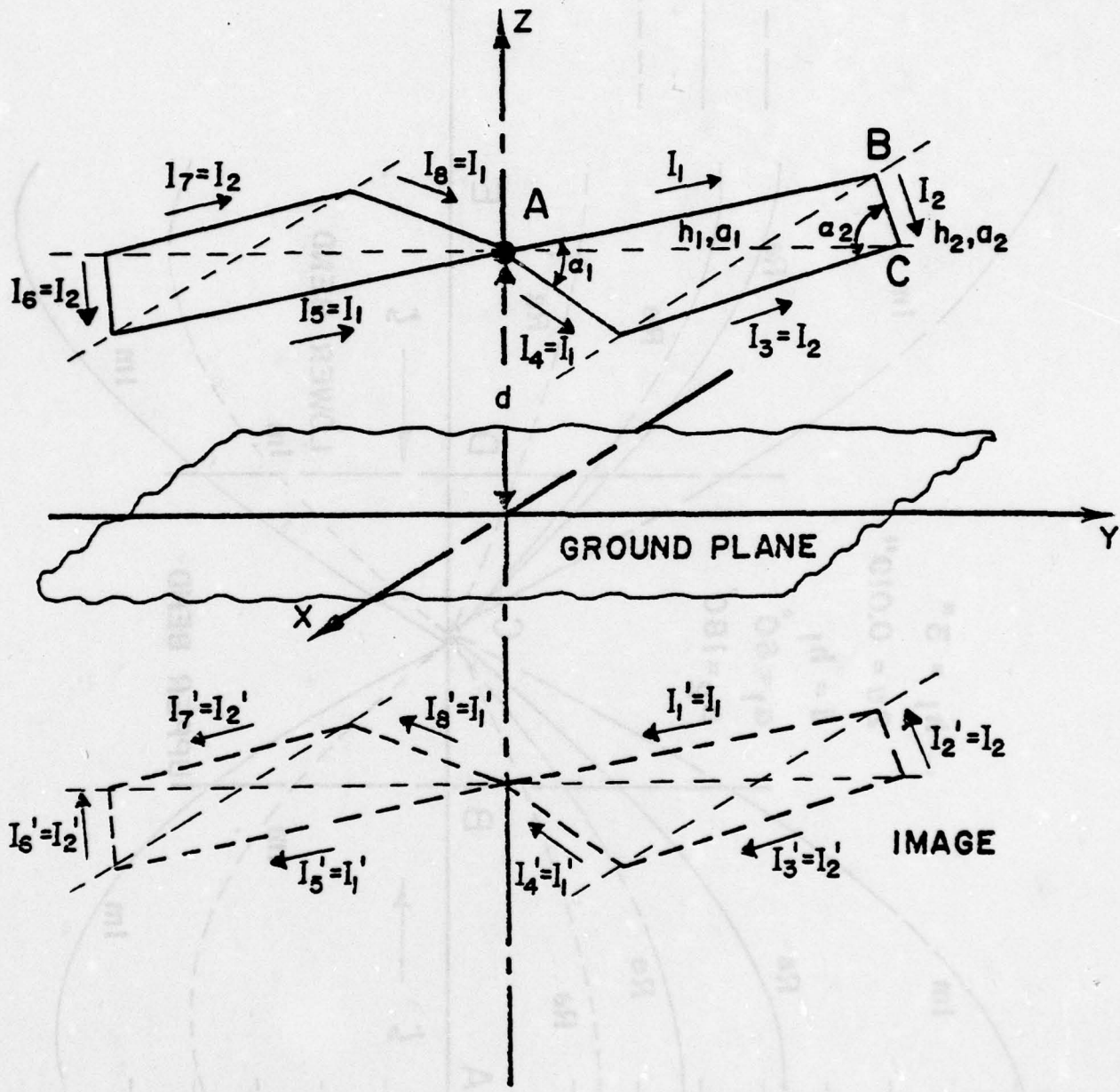


Figure 3.9 Wire Biconical Antenna Above and Parallel to Ground Plane

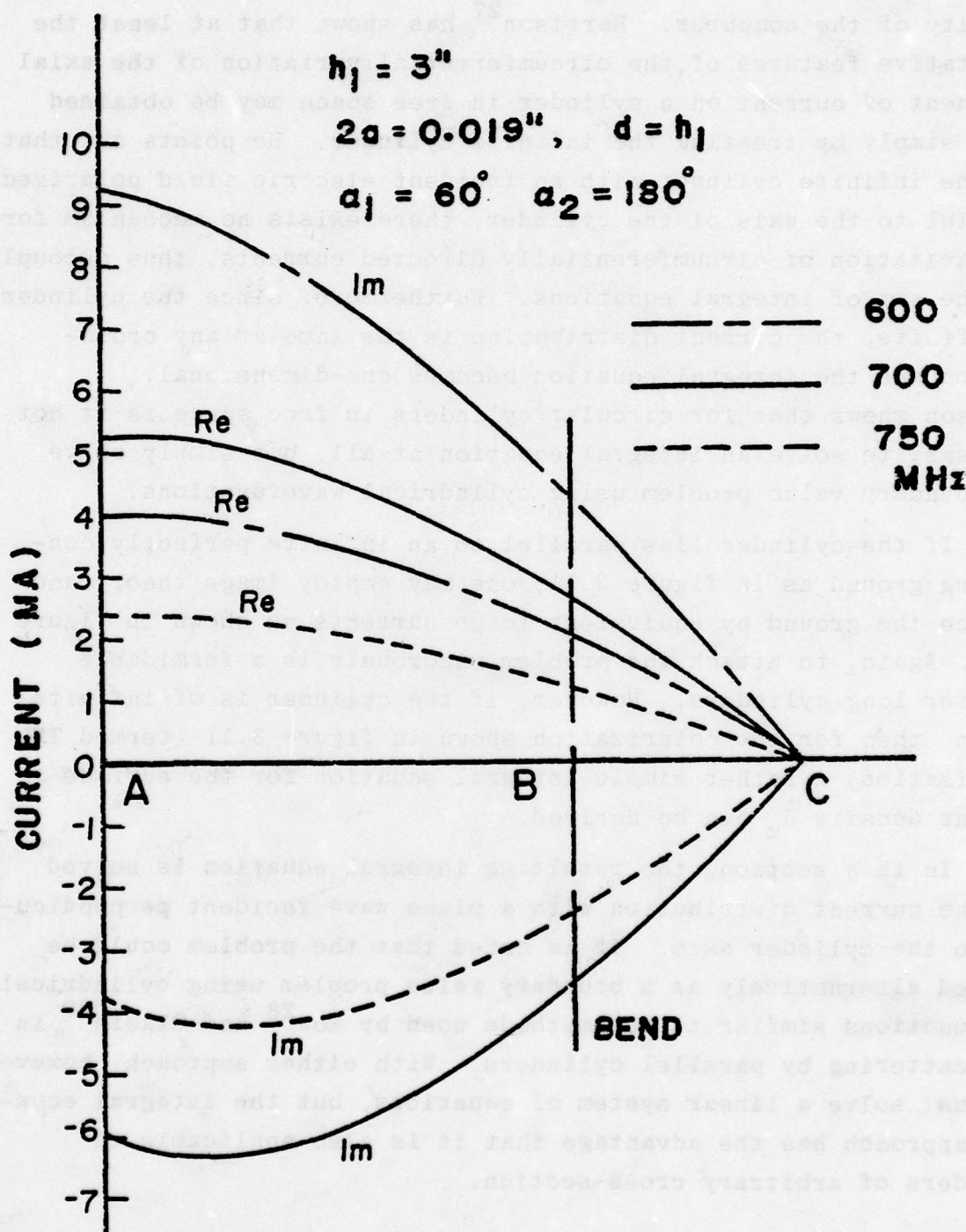


Figure 3.10 Currents I_1 and I_2 on Wire Biconical Antenna Above and Parallel to Ground Plane

equations as has been done by Kao.²⁴⁻²⁶ This method is impractical for very long cylinders, however, as one is limited by the storage capacity of the computer. Harrison²⁷ has shown that at least the qualitative features of the circumferential variation of the axial component of current on a cylinder in free space may be obtained quite simply by treating the infinite cylinder. He points out that for the infinite cylinder with an incident electric field polarized parallel to the axis of the cylinder, there exists no mechanism for the excitation of circumferentially directed currents, thus decoupling the set of integral equations. Furthermore, since the cylinder is infinite, the current distribution is the same at any cross-section and the integral equation becomes one-dimensional. Harrison shows that for circular cylinders in free space it is not necessary to solve an integral equation at all, but simply solve the boundary value problem using cylindrical wavefunctions.

If the cylinder lies parallel to an infinite perfectly conducting ground as in figure 3.11, one may employ image theory and replace the ground by equivalent image currents as shown in figure 3.12. Again, to attack the problem rigorously is a formidable task for long cylinders. However, if the cylinder is of infinite extent, then for the polarization shown in figure 3.11 (termed TM polarization) a rather simple integral equation for the surface current density \tilde{J}_z can be derived.

In this section, the resulting integral equation is solved for the current distribution with a plane wave incident perpendicular to the cylinder axis. It is noted that the problem could be treated alternatively as a boundary value problem using cylindrical wavefunctions similar to the methods used by Row²⁸ and Olaofe²⁹ in the scattering by parallel cylinders. With either approach, however, one must solve a linear system of equations, but the integral equation approach has the advantage that it is also applicable to cylinders of arbitrary cross-section.

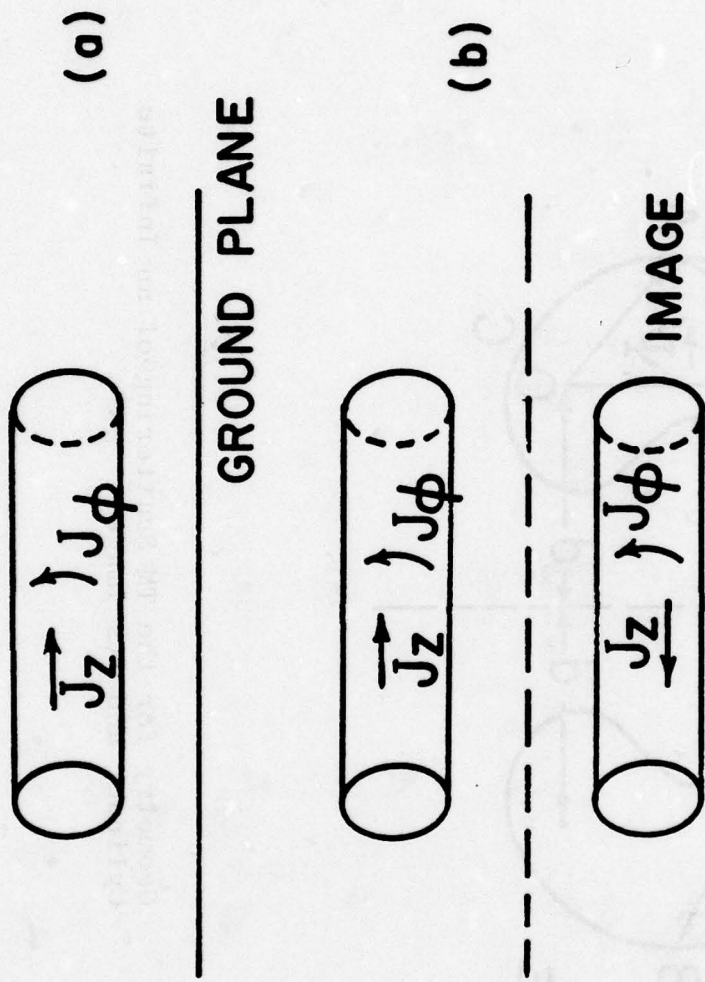


Figure 3.11 (a) Conducting Cylinder Above a Ground Plane
 (b) Ground Plane Replaced by a Cylinder Image

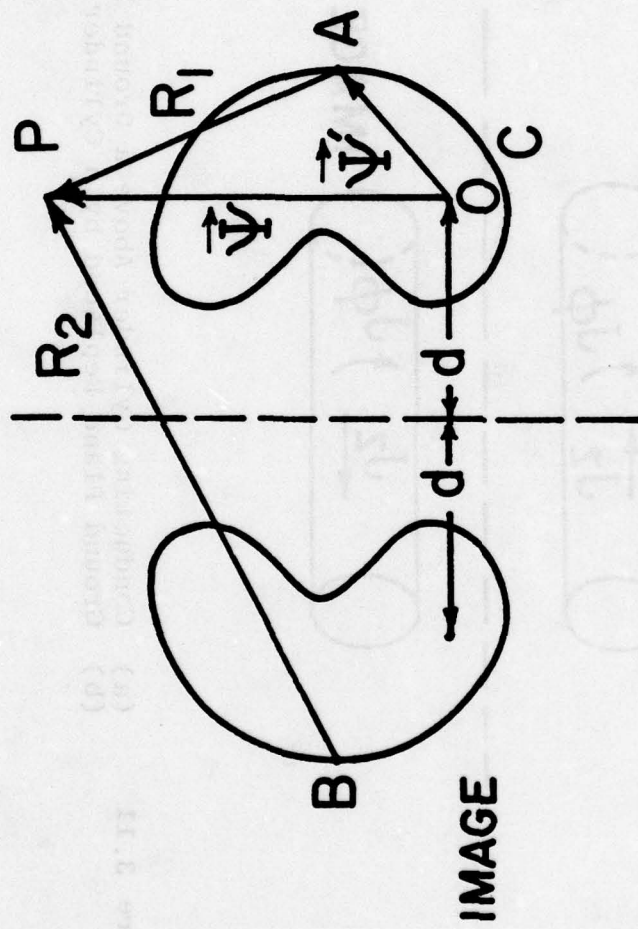


Figure 3.12 Geometry for the TM Scattering of an Infinite Cylinder and Its Image

Figure 3.12

Referring to figure 3.12, a general observation point P in space is located in cylindrical coordinates by the vector $\vec{r} = (\psi, \phi, z=0)$ with respect to the origin O located inside the cylinder with boundary C. The cylinder lies parallel to and a distance d above the ground plane. By image theory, the axial current density \tilde{J}_z on the body at point A located by $\vec{r}' = (\psi', \phi', z'=0)$ is the negative of the current at the corresponding image point B which is found by reflection in the ground plane. Thus, the scattered electric field at point P may be written from the surface current on the cylinder and its image as

$$\tilde{E}_z^s(\psi, j\omega) = -\frac{k\eta}{4} \int_C \tilde{J}_z(\psi', j\omega) [H_o^{(2)}(kR_1) - H_o^{(2)}(kR_2)] dl' \quad (3.13)$$

where

$$R_1 = [\psi^2 + \psi'^2 - 2\psi\psi' \cos(\phi - \phi')]^{\frac{1}{2}} \quad (3.14)$$

$$R_2 = [\psi^2 + \psi'^2 + 2\psi\psi' \cos(\phi + \phi') + 4d(\psi \cos\phi + \psi' \cos\phi') + 4d^2]^{\frac{1}{2}} \quad (3.15)$$

In the expression (3.13), k is the free space wave number and Z_o the corresponding characteristic free space impedance. The first term in the brackets is the contribution due to the current on the cylinder whereas the second term corresponds to the fields produced by the image. Boundary conditions require, expression (1.14), tangential electric field to be zero on the surface of the cylinder along the boundary C. Hence, we have the integral equation,

$$\frac{kZ_o}{4} \int_C \tilde{J}_z(\vec{r}', j\omega) [H_o^{(2)}(kR_1) - H_o^{(2)}(kR_2)] dl' = \tilde{E}_z^i(\vec{r}, j\omega), \quad \vec{r} \text{ on } C \quad (3.16)$$

in which for a plane wave incident at an angle ϕ^i ,

$$\tilde{E}_z^i(\vec{r}, j\omega) = \tilde{E}_o^i [e^{jk\psi \cos(\phi - \phi^i)} - e^{-jk\{2d \cos\phi^i + \psi \cos(\phi + \phi^i)\}}] \quad (3.17)$$

D. Numerical Results for Circular Cylinder

The basic advantage in the formulation of the integral equation (3.16) is that one can analyze general arbitrary-cross-section, two-dimensional geometries. Based on the matrix method¹⁷ discussed in Chapter I, the numerical results are obtained for an infinitely long circular cylinder. In the figures 3.13 and 3.14 are shown the magnitude and phase of the surface current distribution on a circular cylinder placed above a ground screen and illuminated by a plane wave incident at an angle of 45°. Curves are also shown for few values of d. It is noted that the variation of the incident field normal to the conducting ground plane is that of a standing wave, while along the ground plane it is a traveling wave. Thus the illumination on the cylinder is stronger on the side of the cylinder away from the ground plane causing some of the asymmetry in the current distribution.

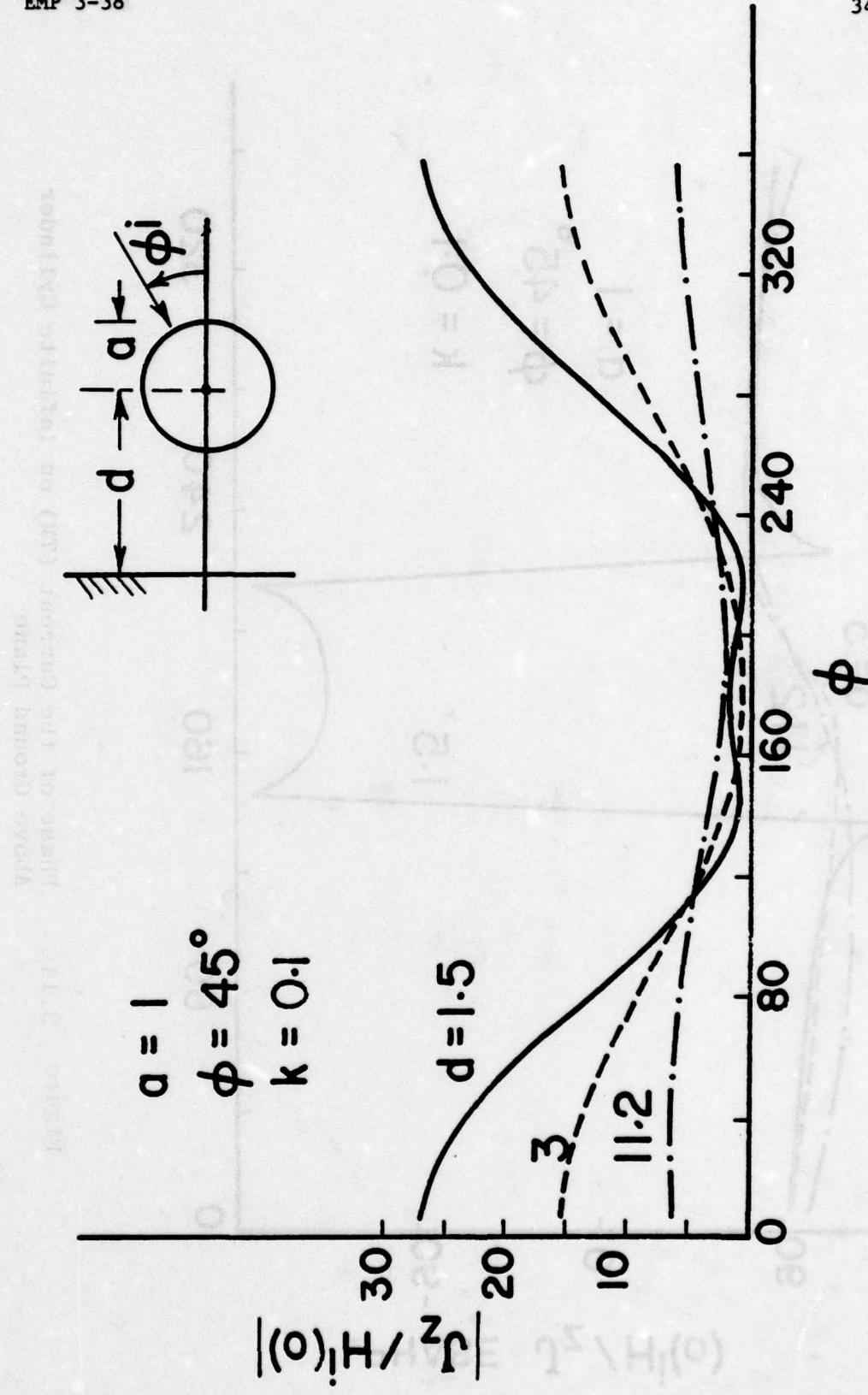


Figure 3.13 Magnitude of the Current (TM) on Infinite Cylinder Above Ground Plane

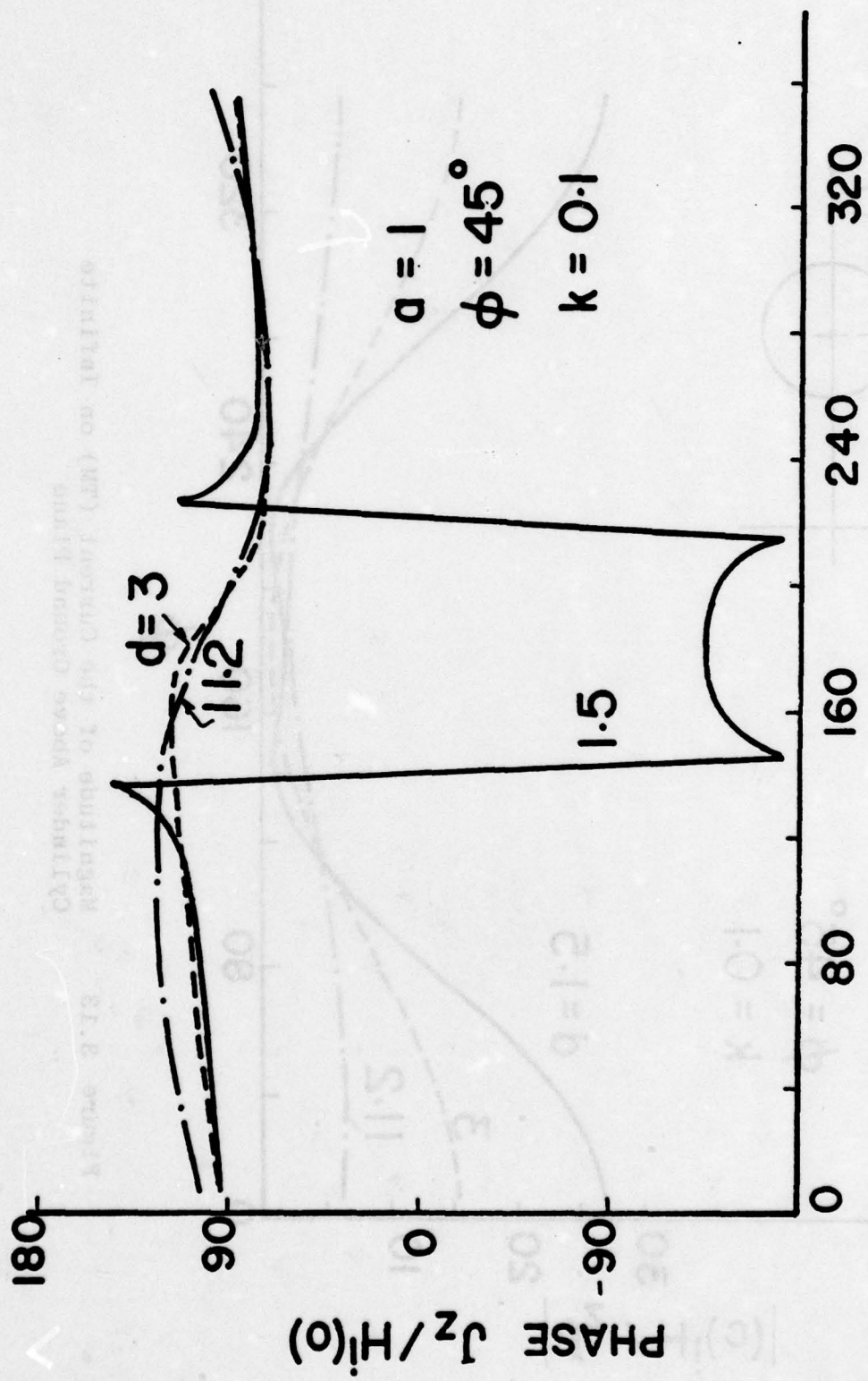


Figure 3.14

Phase of the Current (TM) on Infinite Cylinder
Above Ground Plane

CHAPTER IV

Characterization of Bodies
Behind Aperture-Perforated Screen

The general interaction problem of electromagnetic excitation of arbitrarily shaped conducting bodies through an aperture-perforated conducting screen is discussed in Chapter I and the coupled set of integro-differential equations (1.15) and (1.16), if solved for specific geometries, explain completely the interaction involved. As pointed out earlier, one has to resort to numerical methods¹⁶ for solution to the integral equations. In the previous sections, few specific cases are discussed as special geometries, individually aperture alone with no scatterers nearby (Chapter II), and also conducting wire geometries in the presence of ground screen with apertures shorted (Chapter III). These cases do explain the complexities involved in the numerical solution procedure, and the responses thus far obtained give some insight into understanding the general aperture-scatterer coupling problem. In the following sections, some specific coupled aperture-scatterer geometries of practical interest are discussed. The general integral equations (1.15) and (1.16) are specialized and both the frequency domain and the time domain responses are obtained.

A. Finite Wire Scatterer Behind a Rectangular Aperture

The geometry of a finite length wire excited through a slotted screen is shown in figure 4.1. The finite length wire is oriented arbitrarily along the unit vector $\hat{\mathbf{I}}$ with its center at (x_c, y_c, z_c) . L is the total length of the wire and a its radius. The origin of the coordinate system coincides with the center of the rectangular aperture of total length l and width w . The incident field $(\hat{\mathbf{E}}^i, \hat{\mathbf{H}}^i)$ impinging on the aperture, penetrates and couples to the wire. The treatment of this boundary value problem⁹ is similar to the theory discussed in Chapter I, and the following integral equations result from the expressions (1.15) and (1.16) for the coupled geometry

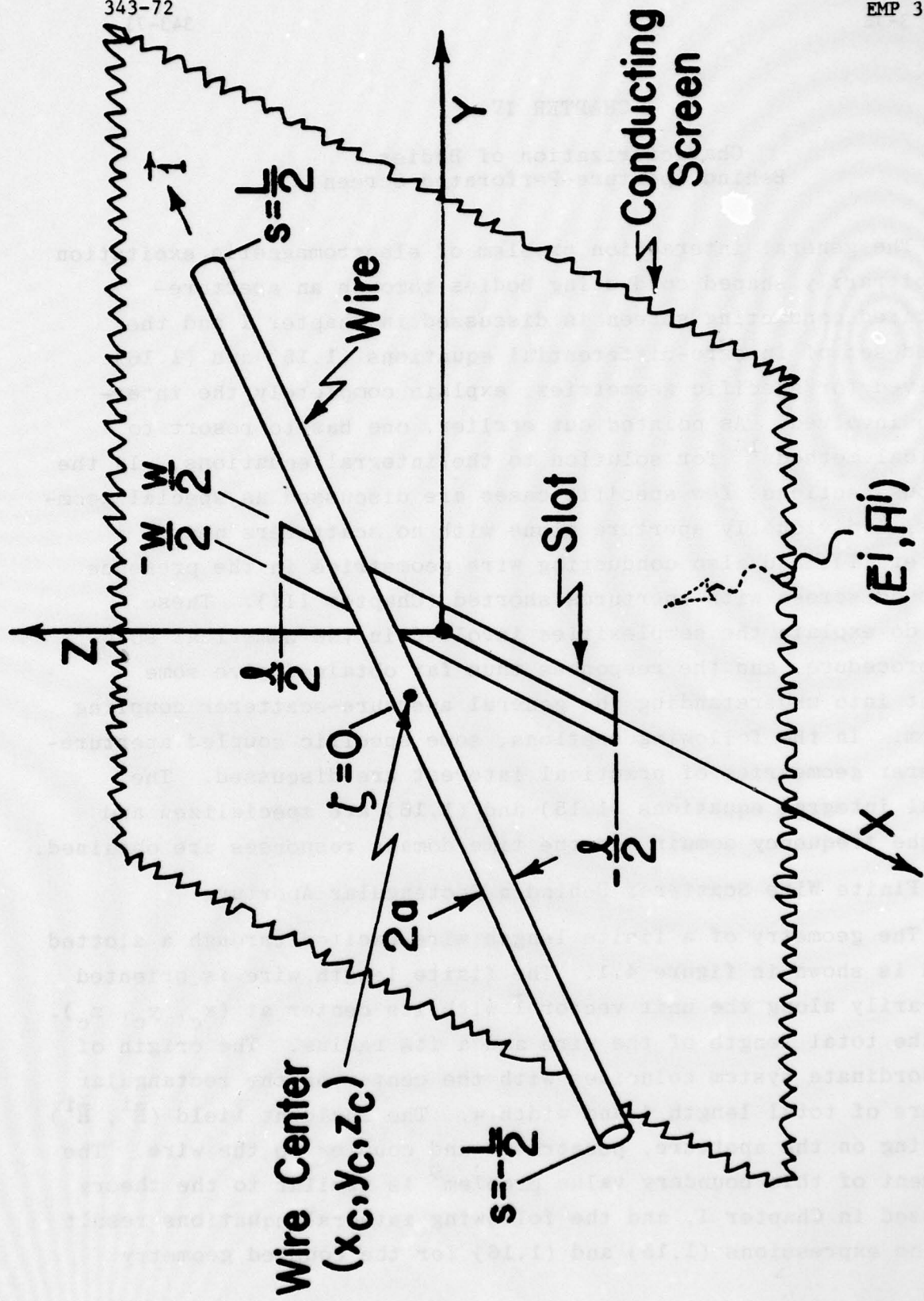


Figure 4.1 Finite Wire Scatterer Behind Narrow Slot Conducting Screen

shown in figure 4.1. It is further assumed that both sides of the media separated by the screen have the same free-space characteristics:

$$\left(\frac{\partial^2}{\partial x^2} - \gamma^2 \right) \tilde{A}_{m_x}(x, y, s) + \frac{\partial^2}{\partial x \partial y} \tilde{A}_{m_y}(x, y, s) + \frac{s\epsilon}{2} \left[\frac{\partial}{\partial z} \tilde{A}_y(x, y, s) - \frac{\partial}{\partial y} \tilde{A}_z(x, y, s) \right] = - \frac{\gamma^2}{s} \tilde{H}_x^i(x, y, s), \quad (x, y) \in S_a \quad (4.1)$$

$$\left(\frac{\partial^2}{\partial y^2} - \gamma^2 \right) \tilde{A}_{m_y}(x, y, s) + \frac{\partial^2}{\partial y \partial x} \tilde{A}_{m_x}(x, y, s) + \frac{s\epsilon}{2} \left[\frac{\partial}{\partial x} \tilde{A}_z(x, y, s) - \frac{\partial}{\partial z} \tilde{A}_x(x, y, s) \right] = - \frac{\gamma^2}{s} \tilde{H}_y^i(x, y, s), \quad (x, y) \in S_a \quad (4.2)$$

In the expressions, \tilde{A}_{m_x} and \tilde{A}_{m_y} are the x and y components of the electric vector potentials and are defined in the expression (2.6). Further the bracketed terms due to presence of the wire are given by

$$\frac{s\epsilon}{2} \left[\frac{\partial}{\partial z} \tilde{A}_y(x, y, s) - \frac{\partial}{\partial y} \tilde{A}_z(x, y, s) \right]_{z=0} = - \frac{s\mu\epsilon}{4\pi} \int_{\zeta'=-L/2}^{L/2} \tilde{I}(\zeta') \cdot \left[z_c \cos\beta + (y - y_c) \cos\nu \right] \tilde{g}_1(x, y; \zeta') d\zeta' \quad (4.3)$$

and

$$\frac{s\epsilon}{2} \left[\frac{\partial}{\partial x} \tilde{A}_z(x, y, s) - \frac{\partial}{\partial z} \tilde{A}_x(x, y, s) \right]_{z=0} = \frac{s\mu\epsilon}{4\pi} \int_{\zeta'=-L/2}^{L/2} \tilde{I}(\zeta') \cdot \left[z_c \cos\alpha + (x - x_c) \cos\nu \right] \tilde{g}_1(x, y; \zeta') d\zeta' \quad (4.4)$$

The kernel term \tilde{g}_1 in (4.3) and (4.4) is given by

$$\tilde{g}_1(x, y; \zeta') = - \left(\frac{\gamma}{D^2} + \frac{1}{D^3} \right) e^{-\gamma D} \quad (4.5)$$

$$D = \left[[x - (x_c + \zeta' \cos\alpha)]^2 + [y - (y_c + \zeta' \cos\beta)]^2 + [z_c + \zeta' \cos\nu]^2 \right]^{\frac{1}{2}} \quad (4.6)$$

and the current on the wire $\tilde{I}(\zeta')$ is assumed to be directed along unit vector \hat{I} along the wire axis, and

$$\hat{I} = \cos\alpha \hat{I}_x + \cos\beta \hat{I}_y + \cos\nu \hat{I}_z \quad (4.7)$$

Based on the expression (1.16), satisfying the boundary condition on the wire, one obtains the following integral equation

$$\begin{aligned} & \left(\frac{\partial^2}{\partial \zeta^2} - \gamma^2 \right) \int_{\zeta'=-L/2}^{L/2} \tilde{I}(\zeta') \tilde{K}(a, \zeta, \zeta') d\zeta' - \gamma^2 (2 \cos^2\nu - 1) \\ & \cdot \int_{\zeta'=-L/2}^{L/2} \tilde{I}(\zeta') \tilde{g}(\zeta, \zeta') d\zeta' - \frac{\partial}{\partial \zeta} \int_{\zeta'=-L/2}^{L/2} \frac{\partial}{\partial \zeta'} \tilde{I}(\zeta') \tilde{g}(\zeta, \zeta') d\zeta' \\ & = 4\pi s \left[\frac{\partial}{\partial z} \tilde{A}_{m_x}(\zeta) \cos\beta - \frac{\partial}{\partial z} \tilde{A}_{m_y}(\zeta) \cos\alpha + \left(\frac{\partial}{\partial x} \tilde{A}_{m_y}(\zeta) - \frac{\partial}{\partial y} \tilde{A}_{m_x}(\zeta) \right) \cos\nu \right] \\ & \quad \text{on the wire} \end{aligned} \quad (4.8)$$

where

$$\tilde{K}(a, \zeta, \zeta') = \frac{1}{2\pi} \int_{-\pi}^{\pi} \frac{e^{-\gamma r_s}}{r_s} d\psi \quad (4.9)$$

$$r_s = [(\zeta - \zeta')^2 + 4a^2 \sin^2 \frac{\psi}{2}]^{\frac{1}{2}} \quad (4.10)$$

and

$$\tilde{g}(\zeta, \zeta') = \frac{e^{-\gamma r_m}}{r_m} \quad (4.11)$$

$$r_m = [4z_c^2 + 4z_c(\zeta + \zeta') \cos\nu + 4\zeta\zeta' \cos^2\nu + (\zeta - \zeta')^2]^{\frac{1}{2}} \quad (4.12)$$

In fact the integral expressions (4.1), (4.2), and (4.8) form the coupled-coupled set of equations in terms of the unknown magnetic current distribution in the aperture and unknown induced

electric current on the finite wire. Practically, one resorts to the numerical procedures in order to obtain solutions for the problem. Let us consider a further specialization of the problem under study, and make the rectangular aperture to be a narrow slot of finite length and orient the wire to be parallel to the screen containing the narrow slot.

B. Finite Wire Parallel to the Plane and Behind the Narrow Slot

This particular case introduces a simplification of the integral expressions (4.1) and (4.8). The integral expression (4.2) can be ignored for narrow slot since we have only the axial magnetic current distribution. Further the wire is parallel to screen so that $\cos\psi = 0$ and the z-component of the magnetic vector potential \tilde{A}_z does not exist. Substituting the distribution for the narrow slot defined in (2.12) and (2.13), we have the following integral equations for the coupled problem of the finite length wire parallel and behind the narrow slot in a perforated conducting screen:

$$\left(\frac{\partial^2}{\partial x^2} - \gamma^2 \right) \int_{x'=-\ell/2}^{\ell/2} \tilde{m}(x') \tilde{K}(x-x', \frac{w}{4}) dx' + \frac{1}{2} s\mu z_c \cos\beta \int_{\zeta'=-L/2}^{L/2} \tilde{I}(\zeta') \tilde{G}(R_1) d\zeta' = - 2\pi s\mu H_x^i(x) \quad \text{on slot axis} \quad (4.13)$$

$$-2s\epsilon z_c \cos\beta \int_{x'=-\ell/2}^{\ell/2} \tilde{m}(x') \tilde{G}(D_1) dx' + \left(\frac{\partial^2}{\partial \zeta^2} - \gamma^2 \right) \int_{\zeta'=-L/2}^{L/2} \tilde{I}(\zeta') [\tilde{K}(\zeta-\zeta', a) - \tilde{K}(\zeta-\zeta', 2z_c)] d\zeta' = 0 \quad \text{on wire} \quad (4.14)$$

In the above equations, the kernel terms are

$$\tilde{K}(\zeta, a) = \frac{1}{2\pi} \int_{\psi=-\pi}^{\pi} \frac{e^{-\gamma r_1}}{r_1} d\psi \quad (4.15)$$

$$r_1 = [\zeta^2 + 4a^2 \sin^2 \frac{\psi}{2}]^{\frac{1}{2}} \quad (4.16)$$

$$\tilde{G}(R_1) = \left[\frac{1}{R_1^3} + \frac{\gamma}{R_1^2} \right] e^{-\gamma R_1} \quad (4.17)$$

$$R_1 = \left[[x - (x_c + \zeta' \cos\alpha)]^2 + [y_c + \zeta' \cos\beta]^2 + z_c^2 \right]^{\frac{1}{2}} \quad (4.18)$$

$$D_1 = \left[[(x_c + \zeta \cos\alpha) - x']^2 + [y_c + \zeta \cos\beta]^2 + z_c^2 \right]^{\frac{1}{2}} \quad (4.19)$$

In the integral expression (4.13), the component \tilde{H}_x^i is the incident magnetic field in the illuminated side $z < 0$, with electric vector polarized transverse to the slot axis, and if θ is the angle which the direction of propagation of the incident field makes with the axis of the slot, then $\tilde{H}_x^i(x)$ can be written for a plane wave as,

$$\tilde{H}_x^i(x) = \tilde{H}_{x0}^i \sin\theta e^{-\gamma \cos\theta x} \quad (4.20)$$

\tilde{H}_{x0}^i is the amplitude factor of the plane wave.

C. Numerical Results

The integral equations (4.13) and (4.14) can be solved based on the method of moments¹⁶ and representative results for the coupled geometry, figure 4.1, is shown in figures 4.2 and 4.3 for a narrow slot of length $\ell = \lambda/2$, width $w = \lambda/20$ in the presence of a finite length wire of length $L = \lambda/2$ and radius $\lambda/1000$. The wire is parallel to the screen containing the narrow slot with its center at $(x_c, y_c, z_c) = (0, 0, \lambda/4)$. The incident field is normal on the narrow slot. In figure 4.2 is indicated the wire current for various values of $\cos\beta$, where $\beta = 0$ corresponds to maximum coupling between slot and wire and $\beta = 90^\circ$ give zero coupling in which case axis of the wire is parallel to the axis of the narrow slot. In figure 4.3, is indicated the slot axial magnetic current distribution for various values of $\cos\beta$. One notes the changes in the magnitude and distribution of the slot field due to reflection of the wire back to the slot. The results of figures 4.2 and 4.3 are extended in figures 4.4 and 4.5 respectively as a function of

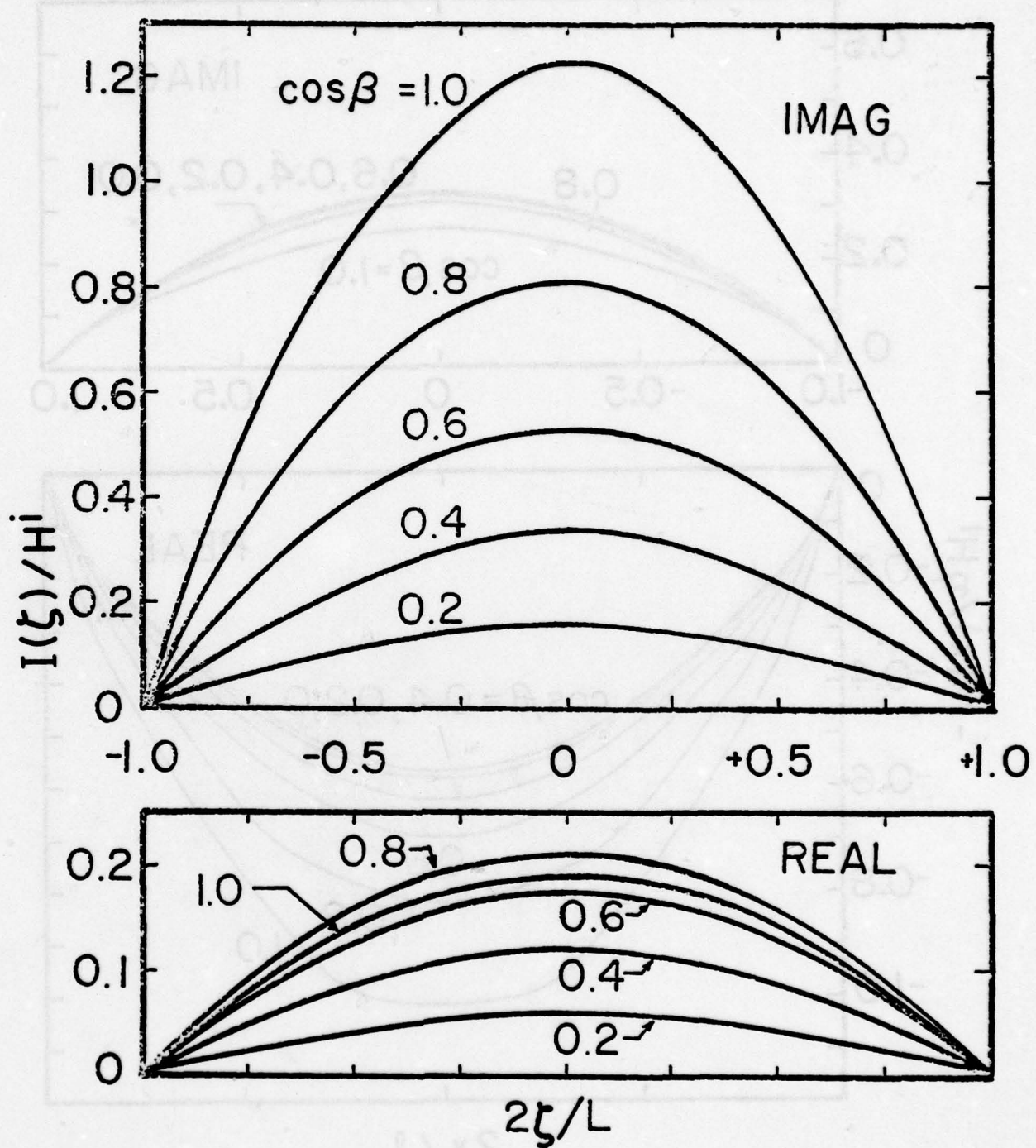


Figure 4.2

Electric Current Distribution on Finite Wire Scatterer in the Presence of Slot, $L=0.5$,
 $a=0.001$, $l=0.5$, $w=0.05$, $(x_c, y_c, z_c)=(0, 0, 0.5)$
at Frequency 300 MHz

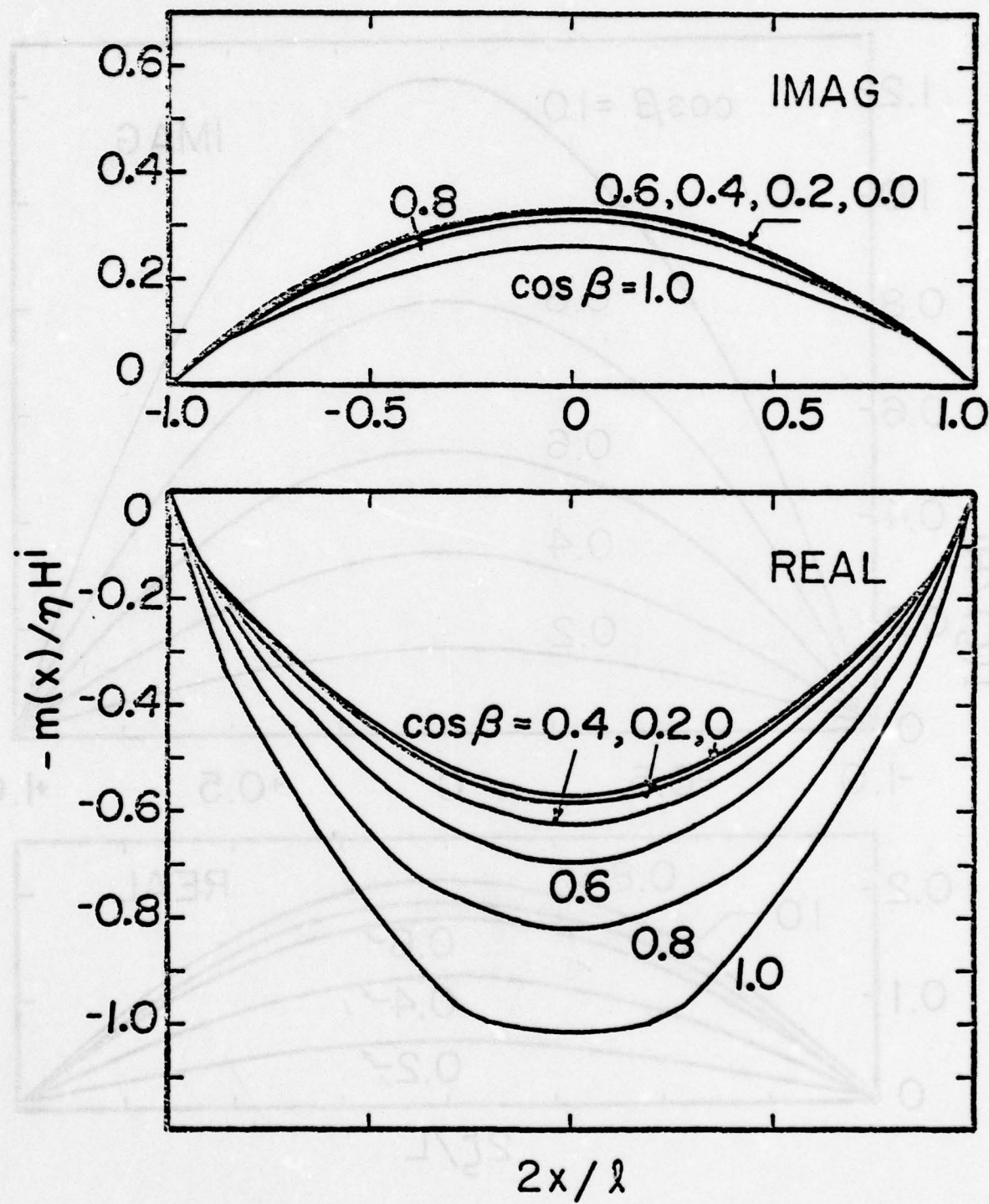


Figure 4.3 Axial Magnetic Current Distribution in a Narrow Slot in the Presence of Wire, $L=0.5$, $a=0.001$, $\ell=0.5$, $w=0.05$, $(x_c, y_c, z_c)=(0, 0, 0.5)$ at Frequency 300 MHz

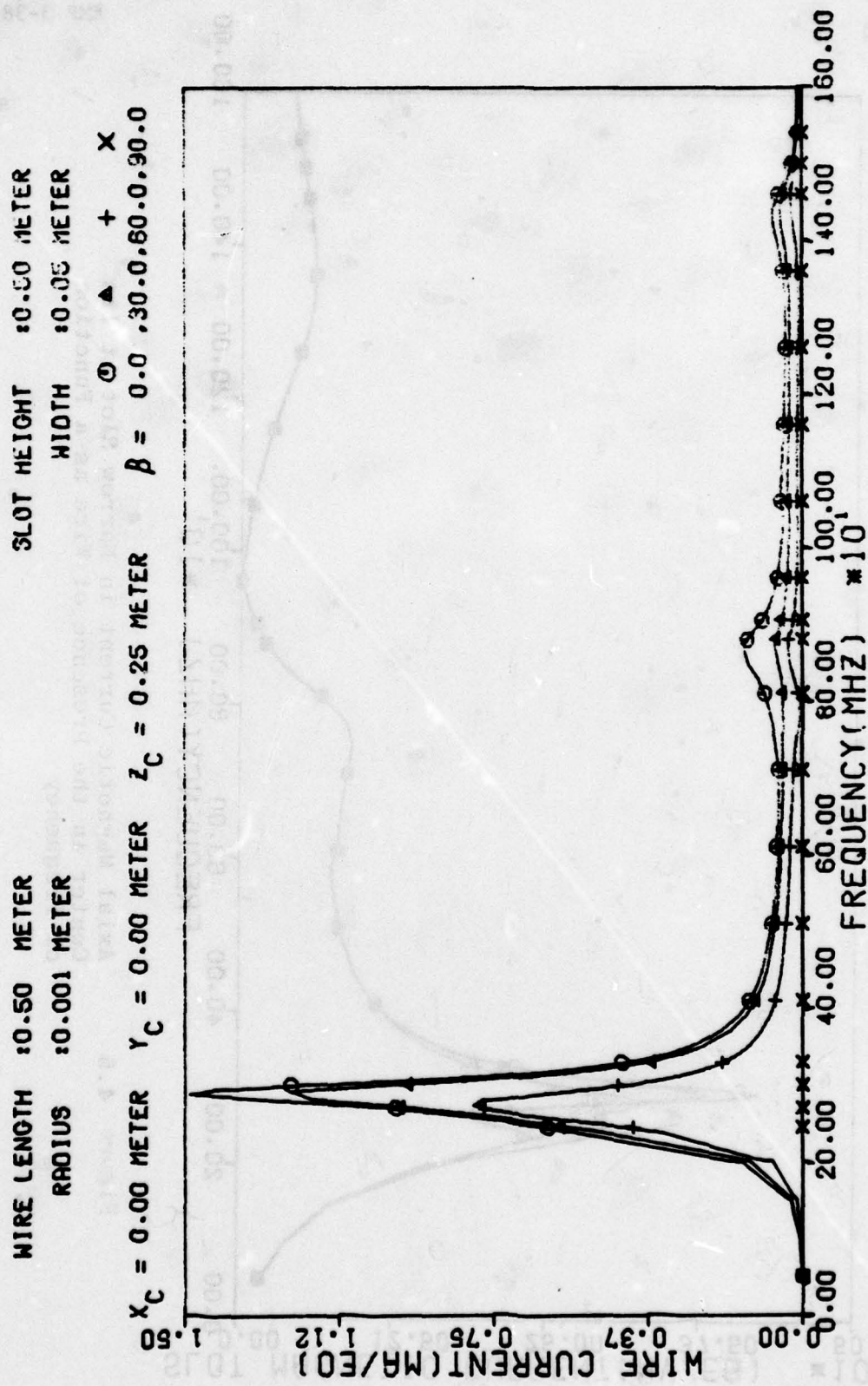


Figure 4.4
Electric Current on Finite Wire at Its Center
in the Presence of Slot as a Function of
Frequency

WIRE LENGTH : 0.50 METER
 RADIUS : 0.001 METER
 $\theta_{\text{C}} = 0.00 \text{ METER}$ $y_{\text{C}} = 0.00 \text{ METER}$ $z_{\text{C}} = 0.25 \text{ METER}$
 $\beta = 0.0 .30 .0 .60 .0 .90 .0$

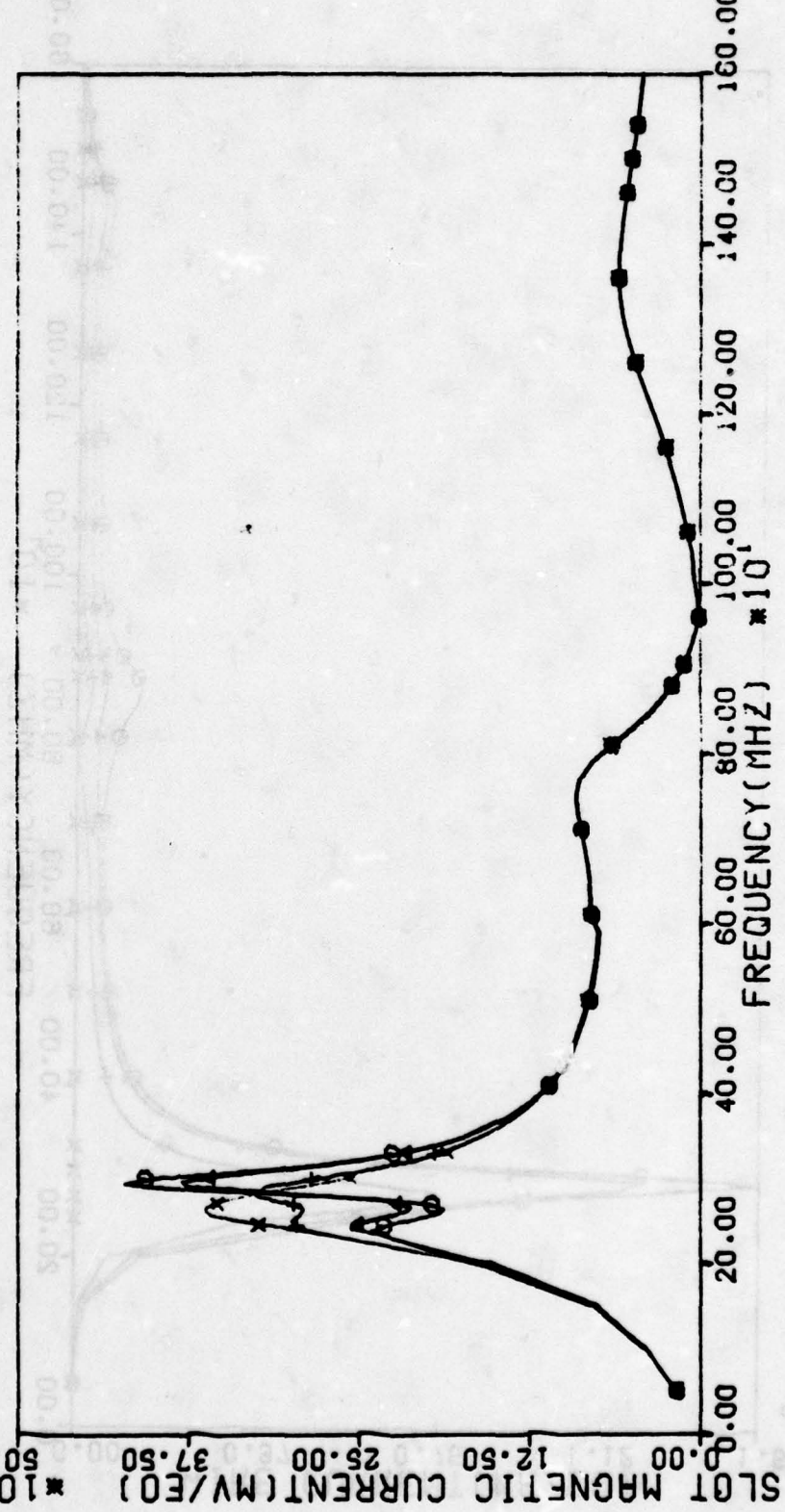


Figure 4.5 Axial Magnetic Current in Narrow Slot at Its Center in the Presence of Wire as a Function of Frequency

frequency. The case of $\beta = 90^\circ$ in figure 4.4 is an uncoupled case and no currents are induced on the wire. The frequency responses of wire and also that of narrow slot do exhibit peaks corresponding to their natural resonant frequencies which actually are a basis for SEM characterization as discussed in Chapter I.

D. SEM Characterization

The general formalism of SEM^{2,18,19} in regard to parameterization and subsequent transient characterization is briefly discussed in Chapter I, expressions (1.30) to (1.35). Accordingly, one can determine the complex natural frequencies, modal current distributions, coupling vectors and coupling coefficients. Even though this approach seems to be a direct numerically oriented procedure, care should be exercised and the problem should be analyzed step by step.

(i) Natural resonance of narrow slot

Suppose the finite length wire is completely removed, and we have only an isolated narrow slot, the equation to be analyzed is comparatively simple one, expression (2.14). There exists only axial distribution of the magnetic current, and numerically the expression (2.14) is efficient to analyze. Based on the condition (1.31), the natural frequencies or poles of the isolated narrow slot can be determined. In figure 4.6 is indicated the location of few of the poles in the complex s plane for the narrow slot dimension $l/w = 20$. In fact, they exist in complex conjugate pairs and only the upper half ones are shown. These natural resonant frequencies lie in layers parallel to the $j\omega$ -axis. The layer very close to the $j\omega$ -axis is very important in the sustained transient responses. Suppose the slot dimension ratio w/l is increased; the poles close to the $j\omega$ -axis move away from the $j\omega$ -axis exhibiting the damping behavior associated with the radiation of the slot. In figure 4.7 is shown the pole trajectory of s_{11} , the first-layer first pole close to the $j\omega$ -axis as a function of w/l . It is also academic at this stage to look at resonances of an isolated thin

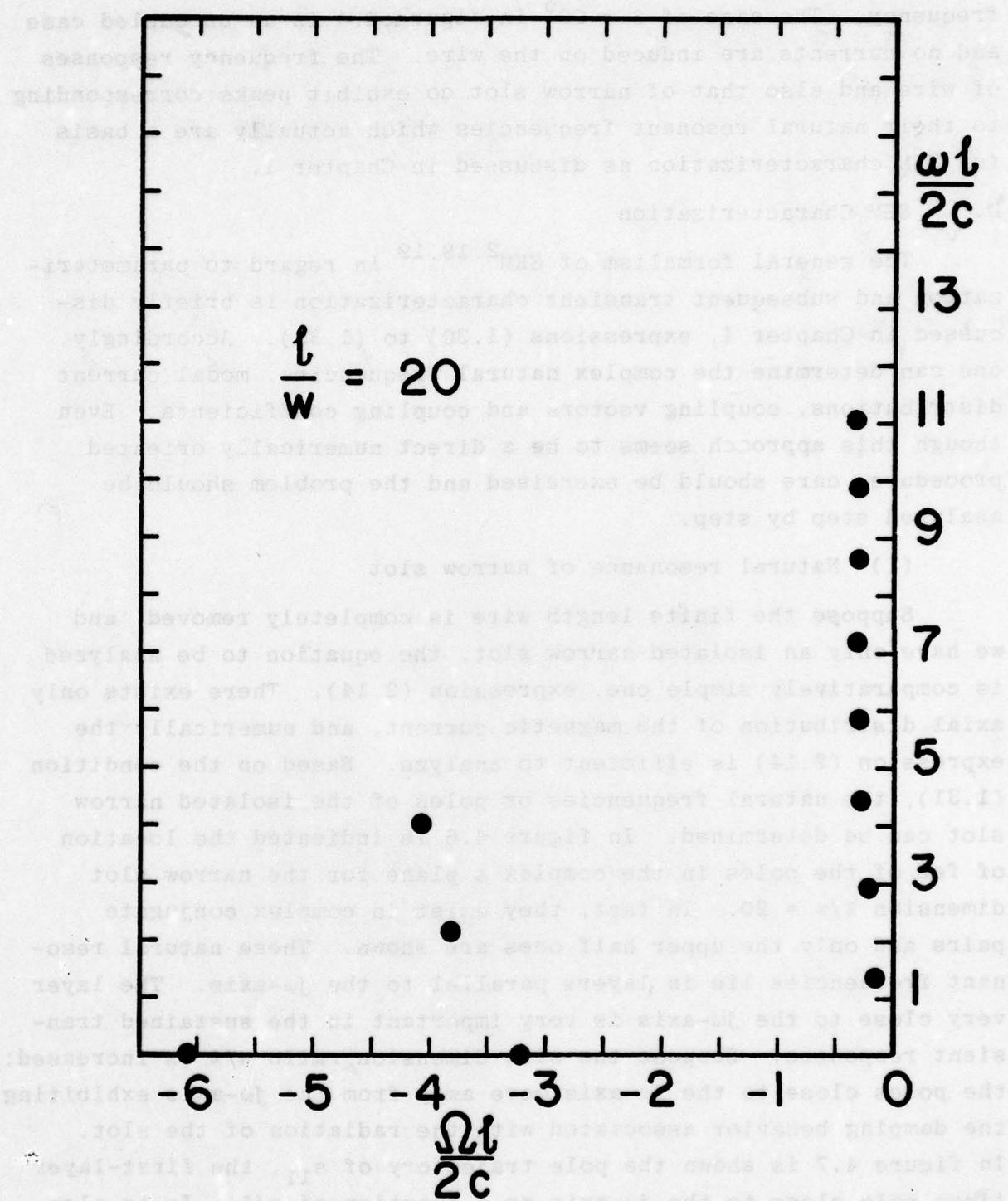


Figure 4.6 Natural Resonance of Isolated Narrow Slot,
 $l=2$, $w=0.1$

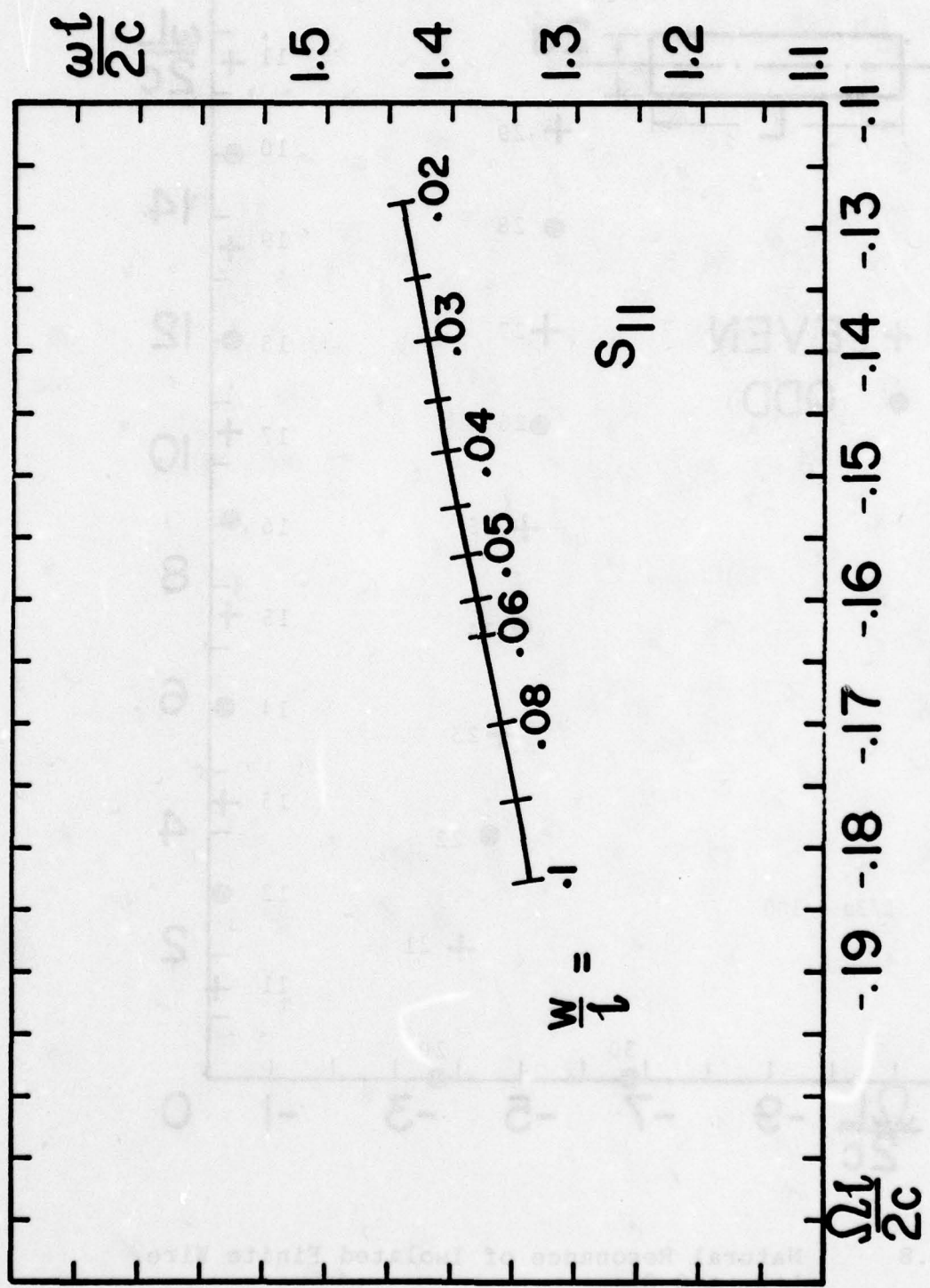


Figure 4.7 Trajectory of S_{11} as a Function of w/l of Isolated Narrow Slot

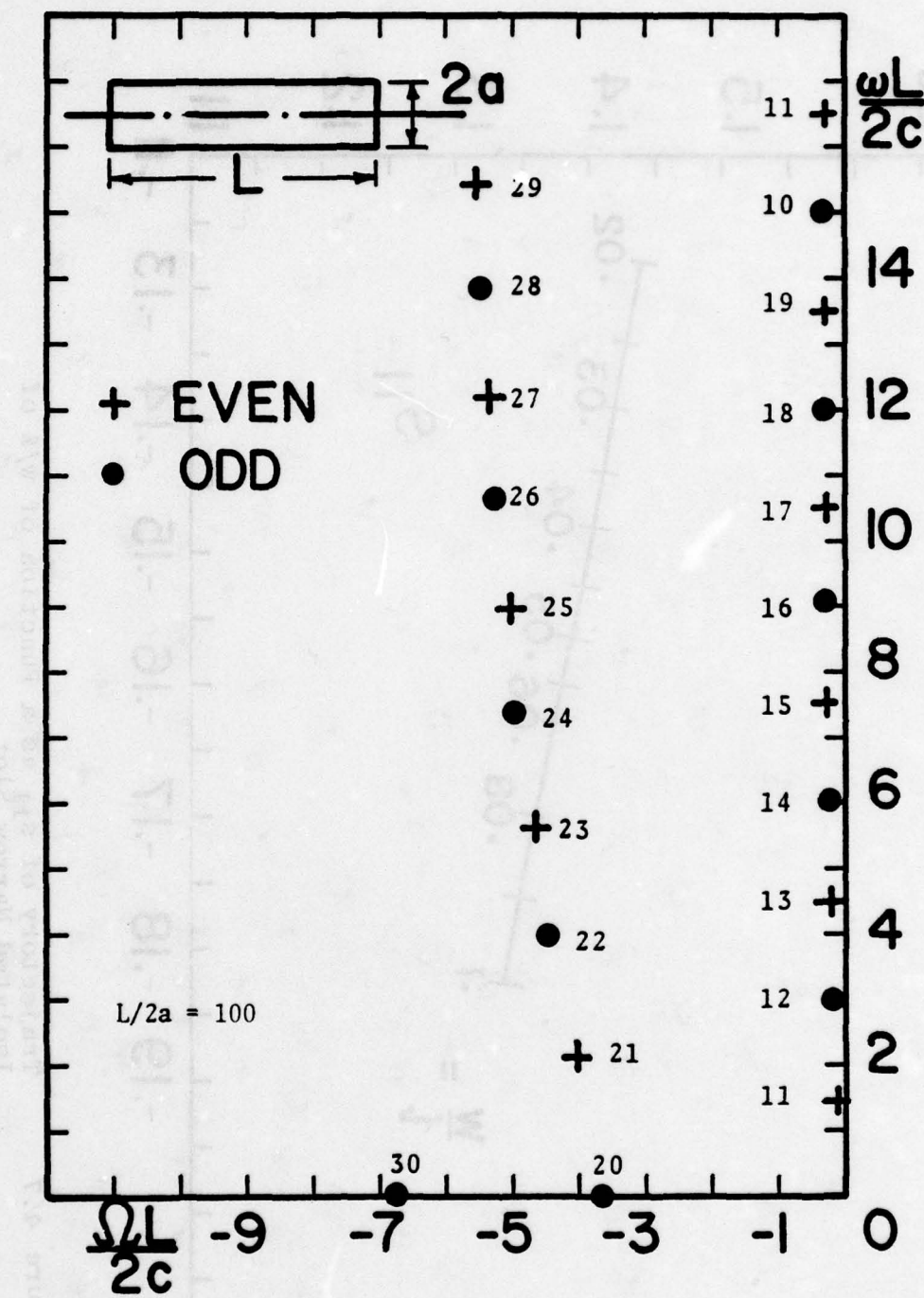


Figure 4.8 Natural Resonance of Isolated Finite Wire,
 $L=2$, $a=0.01$

finite wire.¹⁸ After all, the integral equation (2.14) is the dual of the integral equation for a narrow strip of same dimensions, and further there exists equivalence between the narrow strip and thin finite wire. If the radius of the wire $a = \frac{w}{4}$, the resonances of the narrow slot are the same as its dual narrow strip and that of a finite thin wire of radius a . In figure 4.8 is shown the various pole locations¹⁸ for an isolated finite thin wire. Thus one can also look into various trajectory plots of finite wire as a function of radius, to estimate the actual resonances of the narrow slot.

(ii) Natural resonance of finite wire over ground plane

We shall now consider a finite thin wire placed parallel and above a ground screen¹⁸ with no perforated slot. This particular problem is the special case of a more general problem of coupling between two finite wires in free space as indicated in figure 4.9, wherein two finite thin wires of lengths L_p and L_q , radii a_p and a_q are oriented in YZ at an angle ν with respect to their axis. The mutual coupling between the two wires can be studied based on the integral equation (3.12), and forming the matrix equation by applying method of moments. This procedure yields a generalized system partitioned matrix of two by two,

$$[Z_{pq}] = \begin{bmatrix} [S_p] & [C_p^q] \\ [C_q^p] & [S_q] \end{bmatrix} \quad (4.21)$$

where $[S_p]$ and $[S_q]$ are the self-partitioned matrices of p^{th} and q^{th} wires and, $[C_p^q]$ and $[C_q^p]$ are the mutual partitioned matrices corresponding to the coupling between the p^{th} and q^{th} wires. Based on the condition (1.31) the determinant of (4.21) gives the natural resonances; we expect to obtain the perturbed self-natural resonances of the p^{th} wire, the self-natural resonances of the q^{th} wire and also the mutual natural resonances between the p^{th} and q^{th} wires.

and at 1000 couplings degrees and the total number of coupled wires
coupled with the same rotation angle between them and the
base plane which has caused the coupling angles about vertical and
horizontal axis of a source field to exhibit the following effect.
that the source vector field and its derivative vector field are
not coupled with the same rotation angle as the source vector field
and the derivative vector field in the horizontal plane.

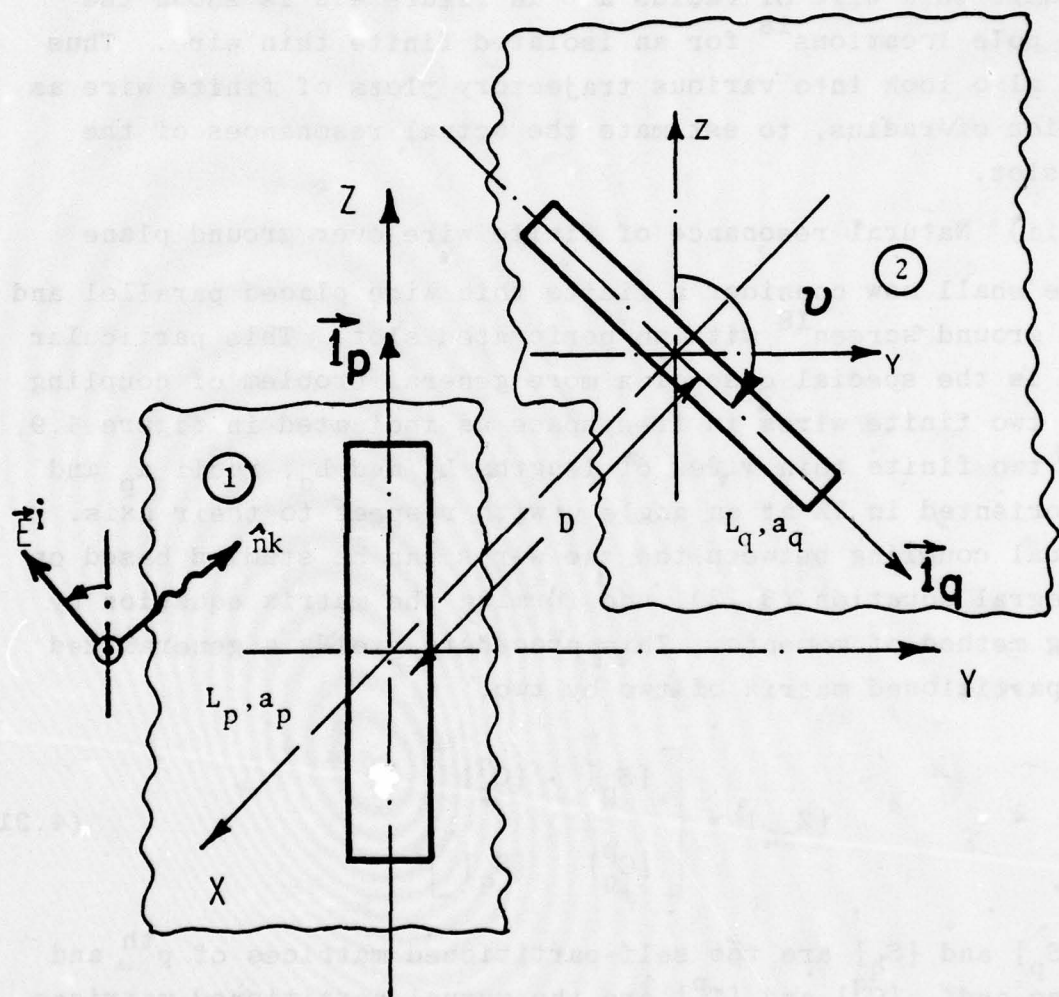


Figure 4.9 Geometry of Two Coupled Wires

These mutual resonances are in fact dependent on the relative orientation $\vec{l}_p \cdot \vec{l}_q$ of the two wires and the distance D apart. The coupling between the two wires is maximum when they are parallel and minimum or completely uncoupled when they are perpendicular. Particularly when their axes are parallel one has two different problems, viz., introducing either a perfect electric ground plane (anti-symmetric case) or a perfect magnetic ground plane (symmetric case) with respect to the distribution of the induced electric current is concerned.

In figure 4.10 is shown the trajectory of the first natural resonance close to $j\omega$ -axis as a function of the angle ν between the axes of the two wires, p^{th} and q^{th} . When their axes are perpendicular, they are uncoupled and have their own self-resonances. But if the wires are identical their individual self-resonances coincide as indicated in figure 4.10 for $\nu = 90^\circ$. As ν is varied, for every ν there exists two poles corresponding to the symmetric and the anti-symmetric modes the wires can support. The extreme case $\nu = 180^\circ$ gives poles of the wire above the electric ground plane and also the wire above the magnetic ground plane. It is possible to split the determinant of the expression (4.21) so that poles can be categorized according to their types in the complex s-plane,

$$\begin{vmatrix} [S_p] & [C_p^q] \\ [C_q^p] & [S_p] \end{vmatrix} \equiv |[[S_p] + [C_p^q]]| \cdot |[[S_p] - [C_p^q]]| \quad (4.22)$$

Symmetric Case (PMC)	Anti-Symmetric Case
-------------------------	------------------------

Based on the expression (4.22), the anti-symmetric poles ($\nu = 180^\circ$ corresponds to the case of wire over the electric ground plane) are traced as a function of the angle ν . In figure 4.11, the first three trajectories of the poles close to the $j\omega$ -axis are shown, for a fixed value of distance $D = 2.0$ between the two wires. For $\nu = 180^\circ$, the various natural resonances are obtained for the

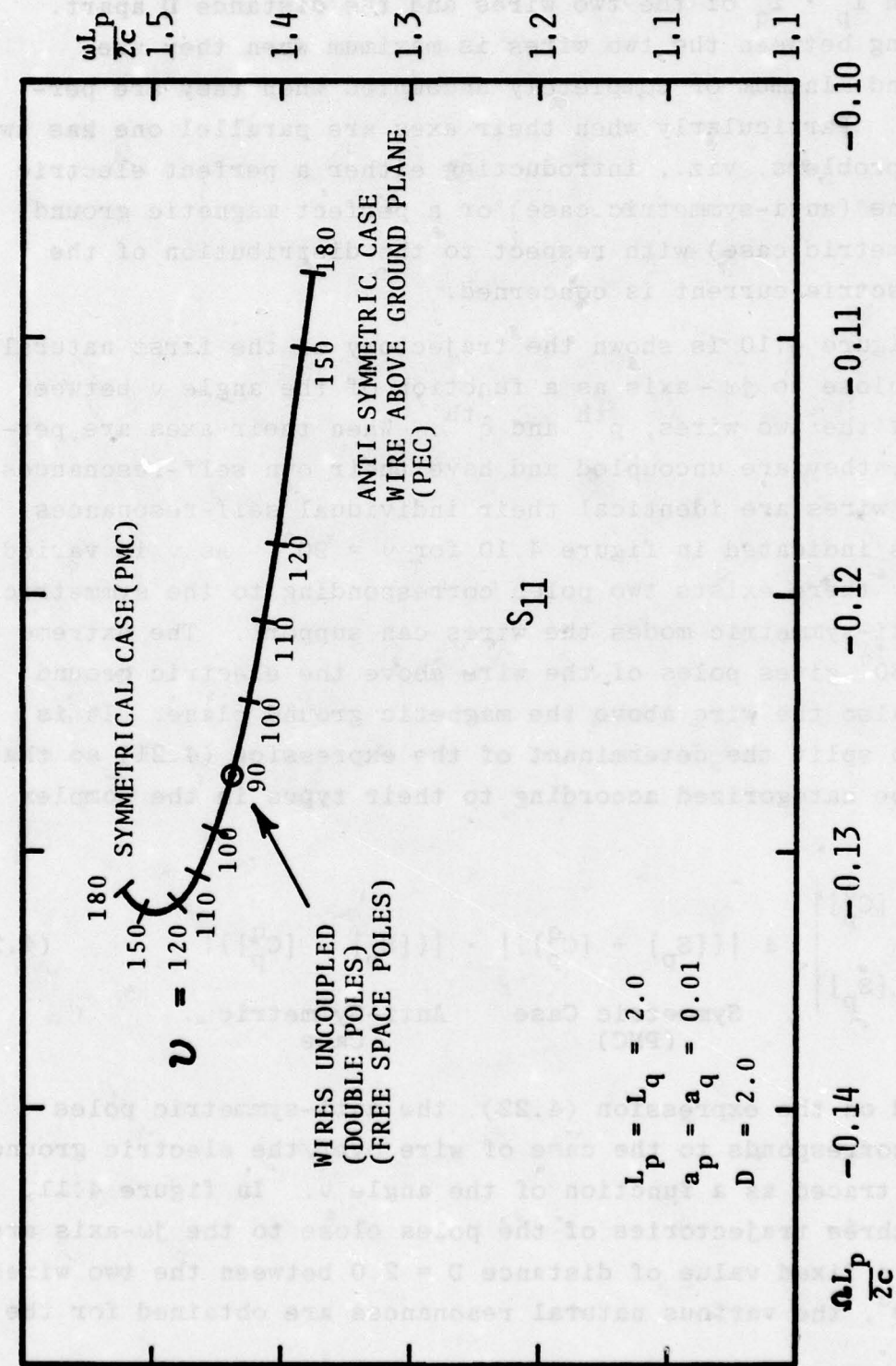


Figure 4.10 Trajectory of the First Set of Poles s_{11} as a Function of v

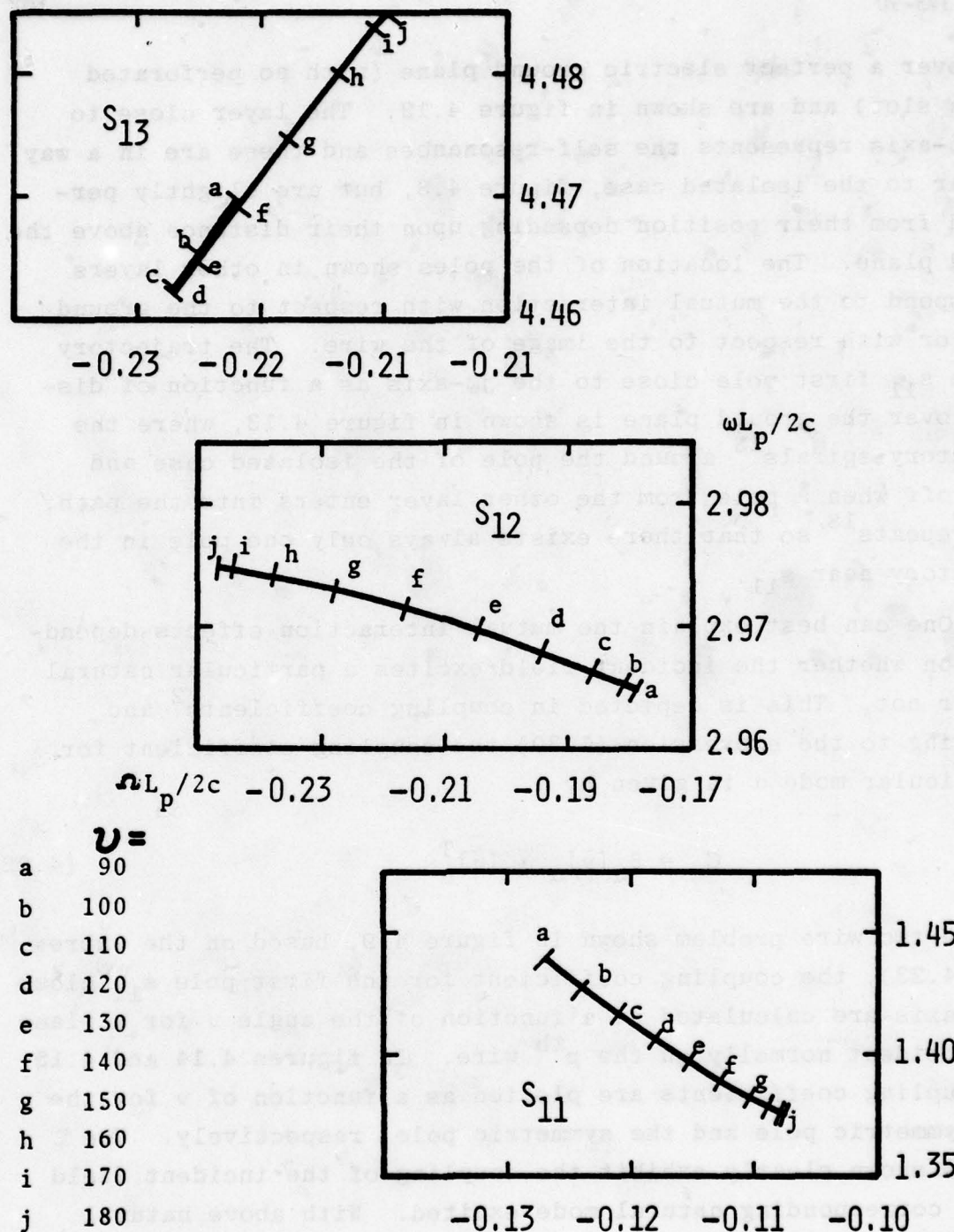


Figure 4.11 Trajectory of the First Three Anti-Symmetry Poles s_{11} , s_{12} , and s_{13} as a Function of v

wire over a perfect electric ground plane (with no perforated narrow slot) and are shown in figure 4.12. The layer close to the $j\omega$ -axis represents the self-resonances and these are in a way similar to the isolated case, figure 4.8, but are slightly perturbed from their position depending upon their distance above the ground plane. The location of the poles shown in other layers correspond to the mutual interaction with respect to the ground plane or with respect to the image of the wire. The trajectory of the s_{11} first pole close to the $j\omega$ -axis as a function of distance over the ground plane is shown in figure 4.13, where the trajectory spirals¹⁸ around the pole of the isolated case and takes off when a pole from the other layer enters into the path. This repeats¹⁸ so that there exists always only one pole in the trajectory near s_{11} .

One can best explain the mutual interaction effects depending upon whether the incident field excites a particular natural mode or not. This is depicted in coupling coefficients² and referring to the expression (1.30) the coupling coefficient for a particular mode α is given by

$$C_\alpha = \beta_\alpha [\tilde{v}]_\alpha \cdot [\tilde{\mu}]_\alpha^T \quad (4.23)$$

For the two wire problem shown in figure 4.9, based on the expression (4.23), the coupling coefficient for the first pole s_{11} close to $j\omega$ -axis are calculated as a function of the angle v for a plane wave incident normally on the p^{th} wire. In figures 4.14 and 4.15 the coupling coefficients are plotted as a function of v for the anti-symmetric pole and the symmetric pole, respectively. The results shown clearly exhibit the coupling of the incident field to the corresponding natural mode excited. With above natural resonance and coupling coefficient results, it is possible to construct the time domain response based on the expression (1.35), for the geometry of figure 4.16, a finite wire parallel to a ground plane. In figure 4.17 is shown the transient response of the

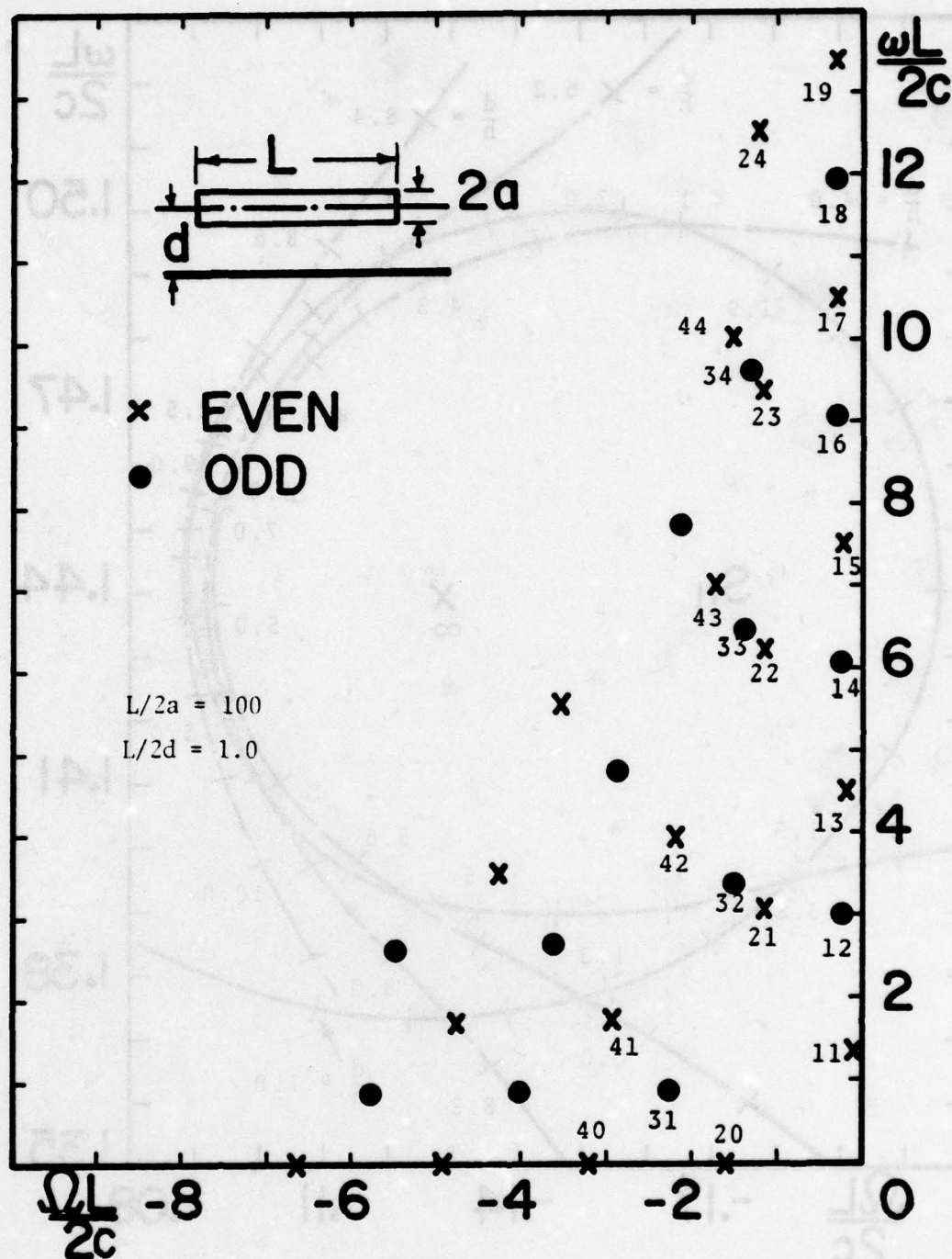


Figure 4.12 Natural Resonance of Finite Wire Placed Parallel Over a Perfect Electric Ground Plane

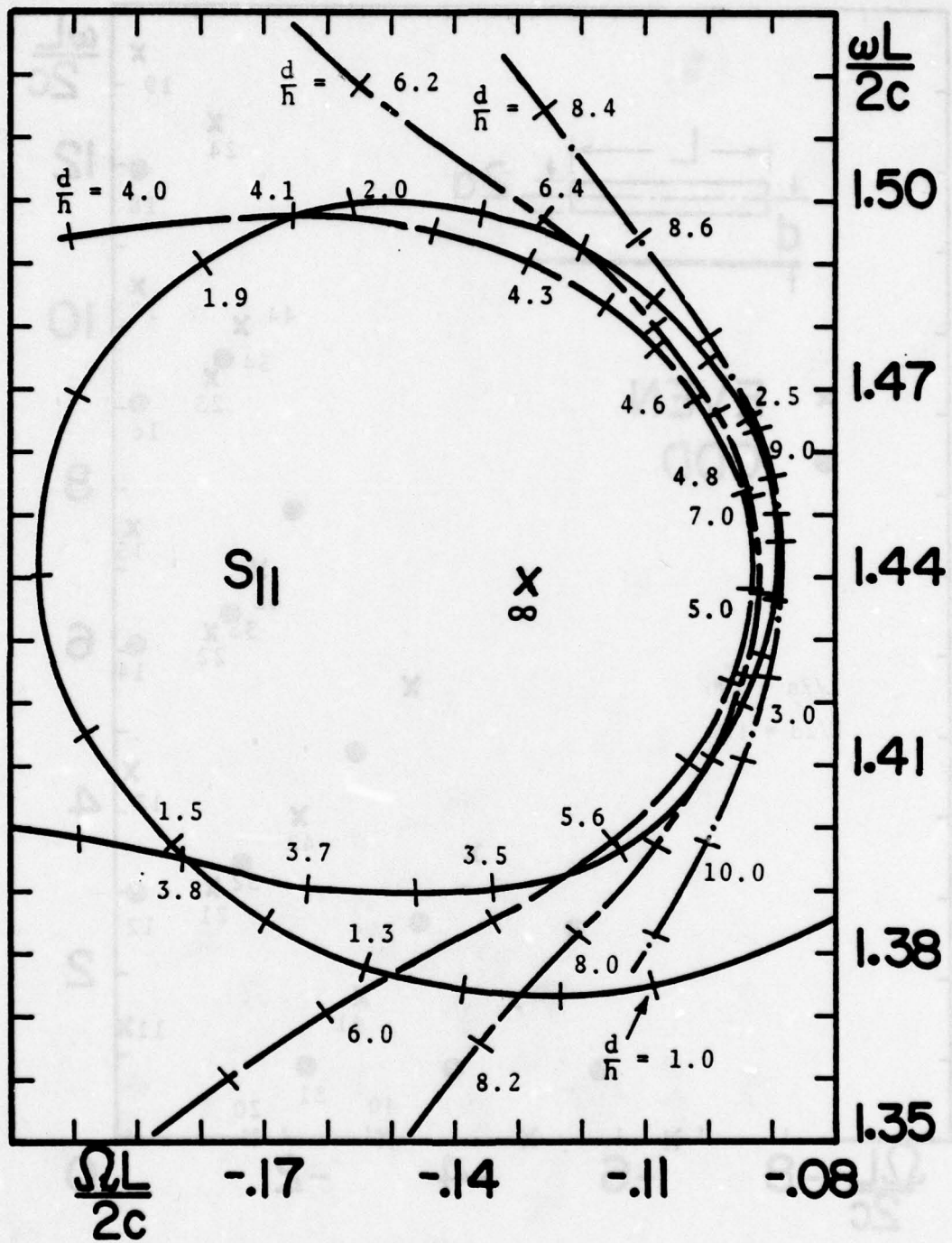


Figure 4.13 Trajectory of First Pole s_{11} as a Function of Distance Over the Ground Plane

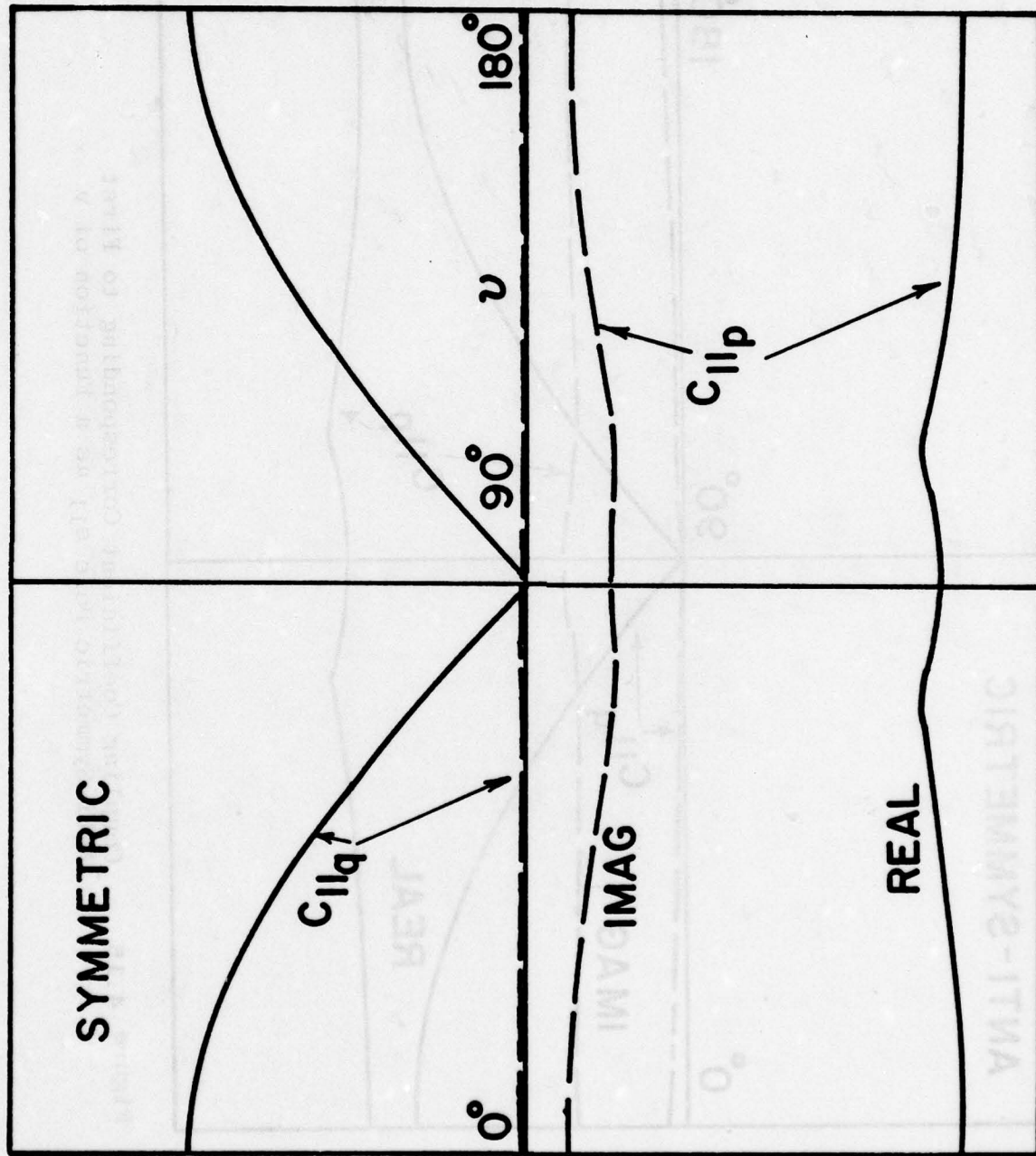


Figure 4.14 Coupling Coefficient Corresponding to First Symmetric Pole s_{11} as a Function of v

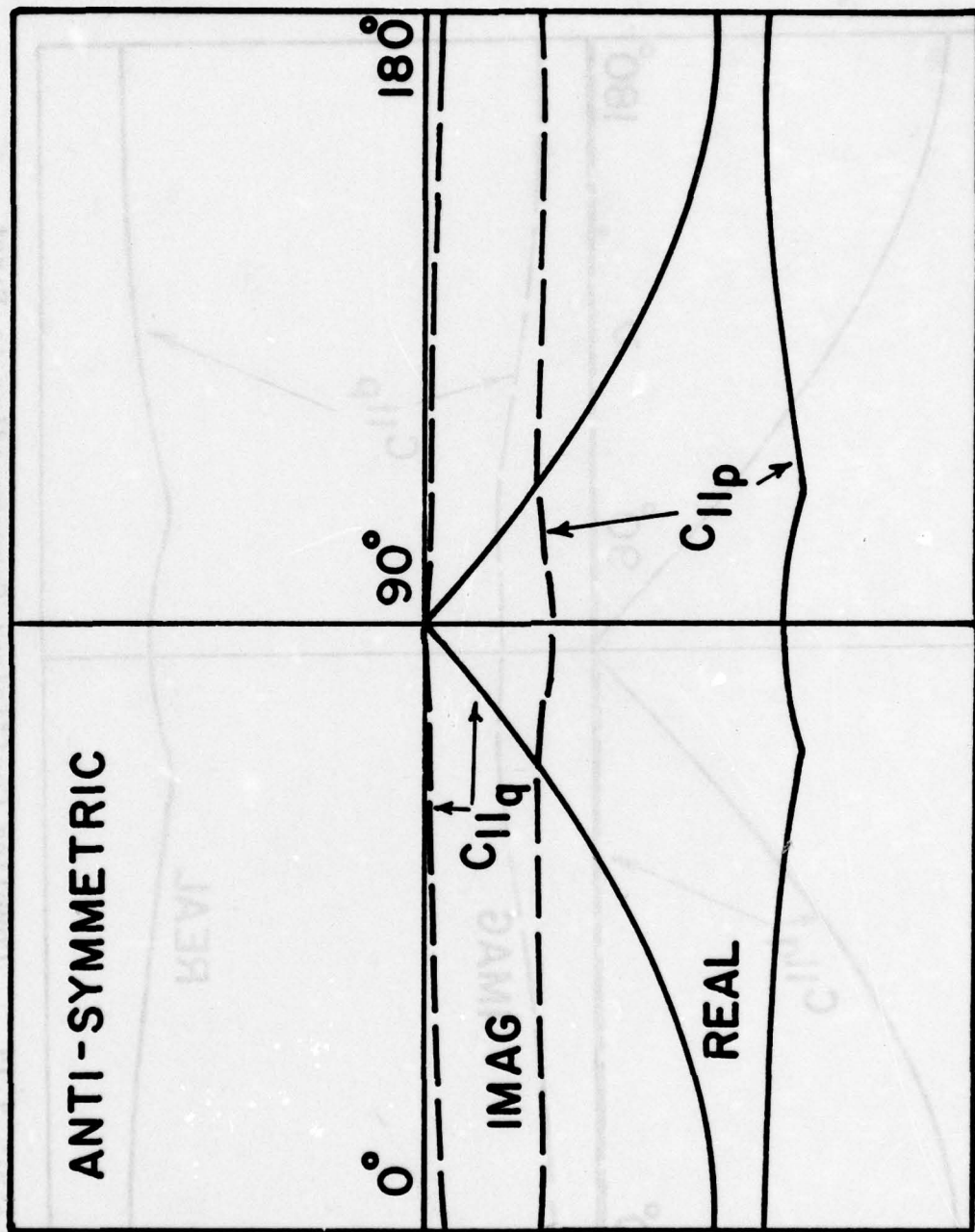


Figure 4.15 Coupling Coefficient Corresponding to First Anti-Symmetric Pole s_{11} as a Function of ν

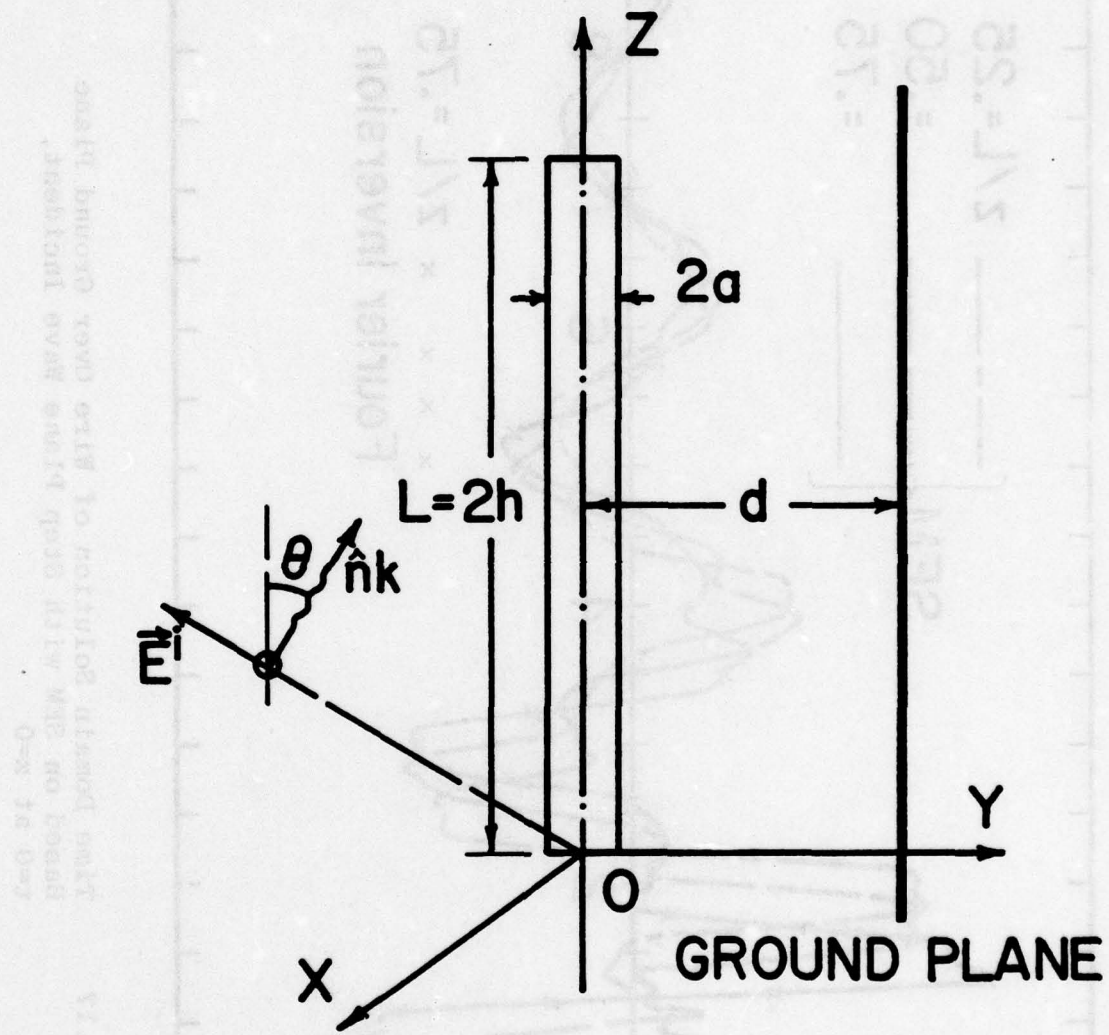


Figure 4.16 Geometry of Finite Wire Over Ground Plane with No Slot Perforated

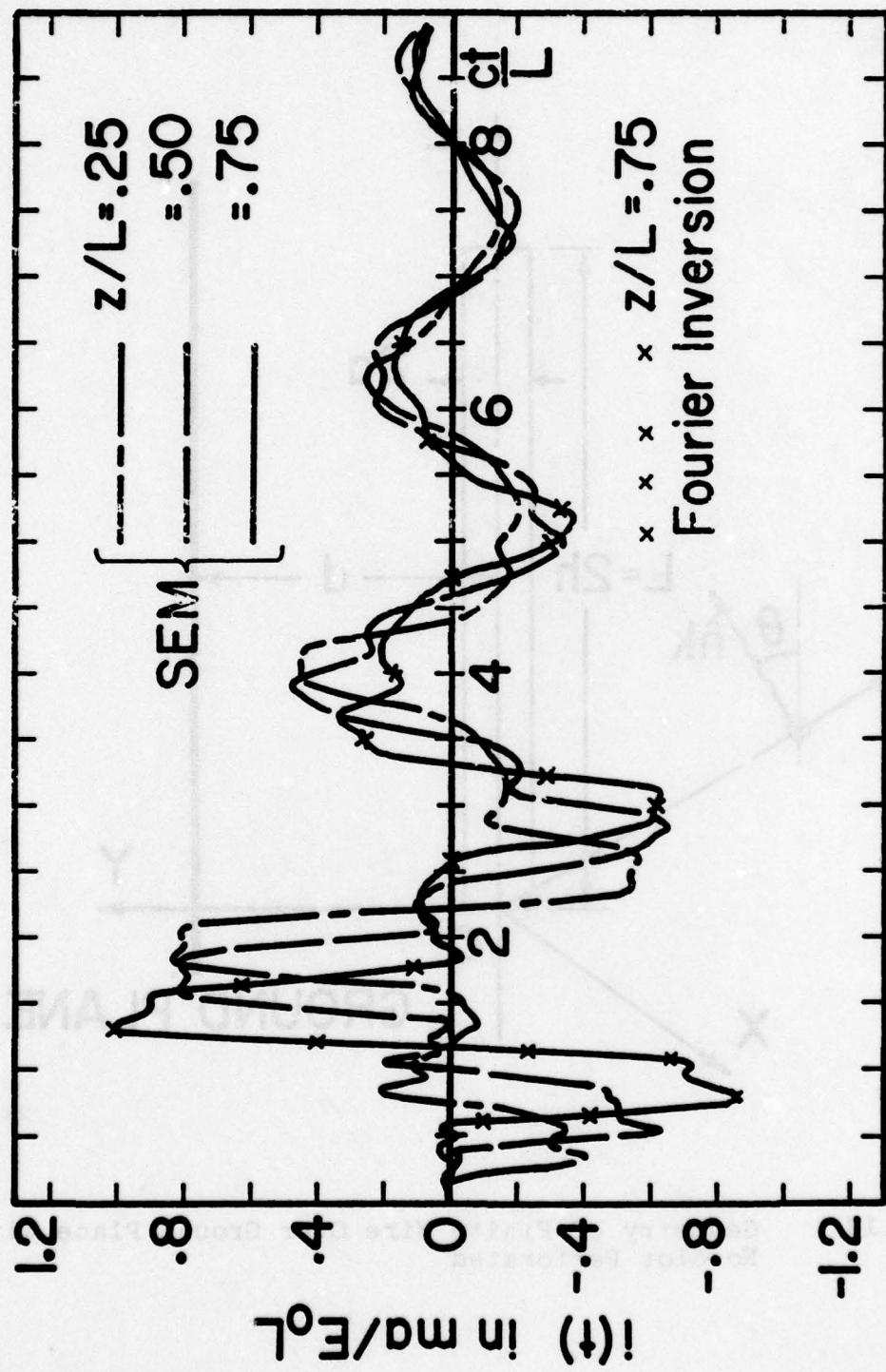


Figure 4.17 Time Domain Solution of Wire Over Ground Plane Based on SEM with Step Plane Wave Incident, $t=0$ at $z=0$

finite wire over the perfect electric ground plane, $\nu = 180^\circ$. The electric current induced is plotted as a function of time at different locations on the p^{th} wire for a step function plane wave incident at an angle of 30° to the axis of the wire. The delay in the initial response is obvious due to the delay of the step wave front excited by the wire. The time domain response gradually decays for large values of the time.

(iii) Finite wire scatterer behind a narrow-slot-perforated screen

Let us now return to the original problem of interaction with the finite wire behind a narrow slot perforated conducting screen, figure 4.1. The transient characterization and the corresponding natural resonance results obtained in section D-(i) for isolated narrow slot and in section D-(ii) for wire above ground plane are quite useful to understand and predict the results of the scatterer and narrow-slot interaction problem. Based on the coupled integro-differential equations (4.13) and (4.14), and further matrix formulation using the moment method, a matrix equation similar to the expression (1.25) is first derived. Then the various natural resonances for the coupled geometry are obtained by numerically solving the determinant equation (1.31). For this coupled problem, the natural resonances can be separated into two parts. One set of natural resonances belongs to the narrow slot geometry in the presence of the wire scatterer and the other set belongs to the finite wire scatterer over the ground plane in the presence of the narrow slot. The first set of the natural resonant frequencies belonging to the narrow slot are similar to the ones depicted in the figure 4.6, but are perturbed from their locations depending on the orientation of the wire axis with respect to the slot and distance of the wire over the ground plane. The results of the pole plot shown in figure 4.6 are for the limiting uncoupled case of $\cos\beta = 0.0$. Similarly, the second set of natural resonant frequencies belong to the finite wire scatterer

parallel and above the ground screen in the presence of the narrow slot are similar to the ones depicted in the figure 4.12, but are perturbed from their locations depending on the wire distance above the ground plane and the orientation of the wire axis with respect to the slot. The results of the figure 4.12 correspond to the uncoupled case $\cos\beta = 0.0$, so that for any other ' $\cos\beta$ ' orientation of the wire with respect to the slot axis, the new location of the poles should be determined by solving the determinant of the partitioned matrix equation obtained from the equations (4.13) and (4.14)

In figure 4.18 is shown the natural resonant frequencies of the finite wire scatterer and narrow slot geometry, figure 4.1, for the maximum coupling $\cos\beta = 1.0$. Only the first four sets of the pole locations of the first layer close to jw -axis are indicated. The pole locations are indeed perturbed to the maximum extent from their uncoupled values. The trajectory of the first set of poles close to jw -axis are shown in figure 4.19 as a function of coupling factor $\cos\beta$. The poles of the finite wire over the ground plane move away from the jw -axis while that of narrow slot move toward the jw -axis as the coupling between the wire and the slot is gradually increased. Figure 4.20 gives the trajectory results for the second set of poles close to the jw -axis. Obviously the path of the trajectory indirectly explains the coupling between the wire and the slot, and the corresponding radiation characteristics involved.

In figures 4.21 through 4.24 are shown the transient response of the wire scatterer and the narrow slot interaction problem under discussion. For the results of figures 4.21 and 4.22 a step plane wave is assumed to excite the slot normally and the origin of the coordinate system is taken as time reference $t = 0$. The same results are repeated in figures 4.23 and 4.24 but with the following EMP incident normally on the narrow slot

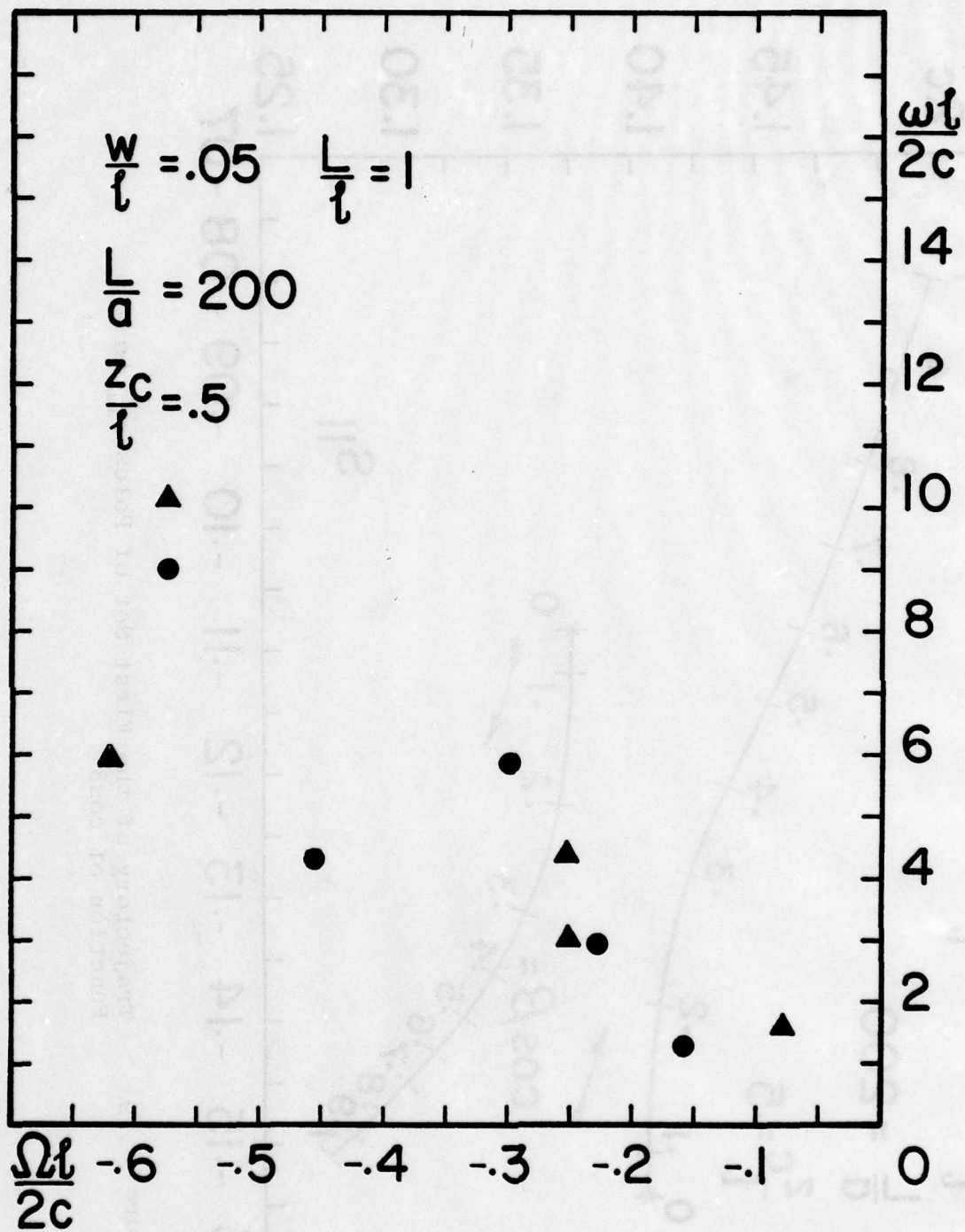


Figure 4.18 Natural Resonances of Finite Wire Behind a Narrow Slot Perforated Conducting Screen

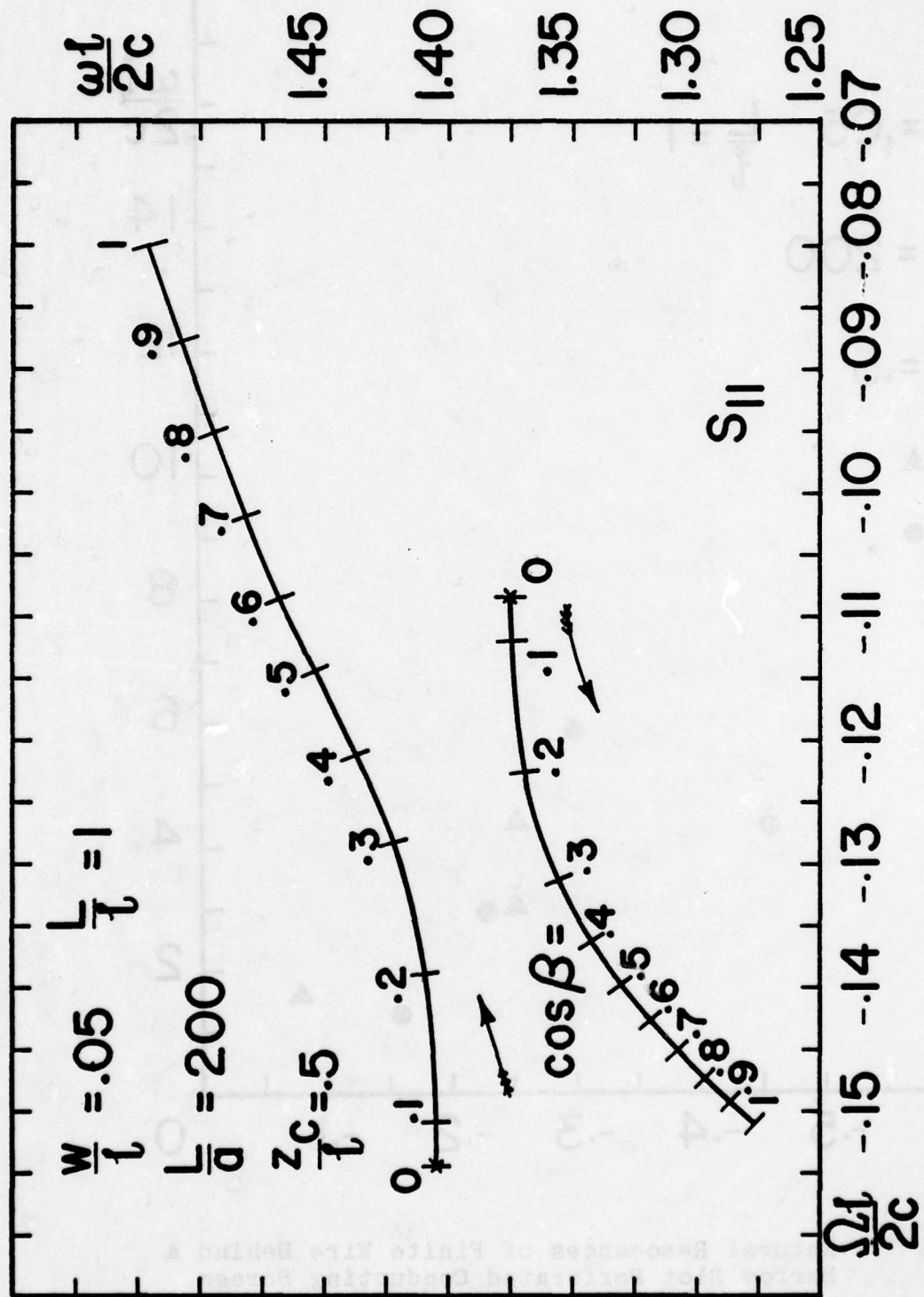
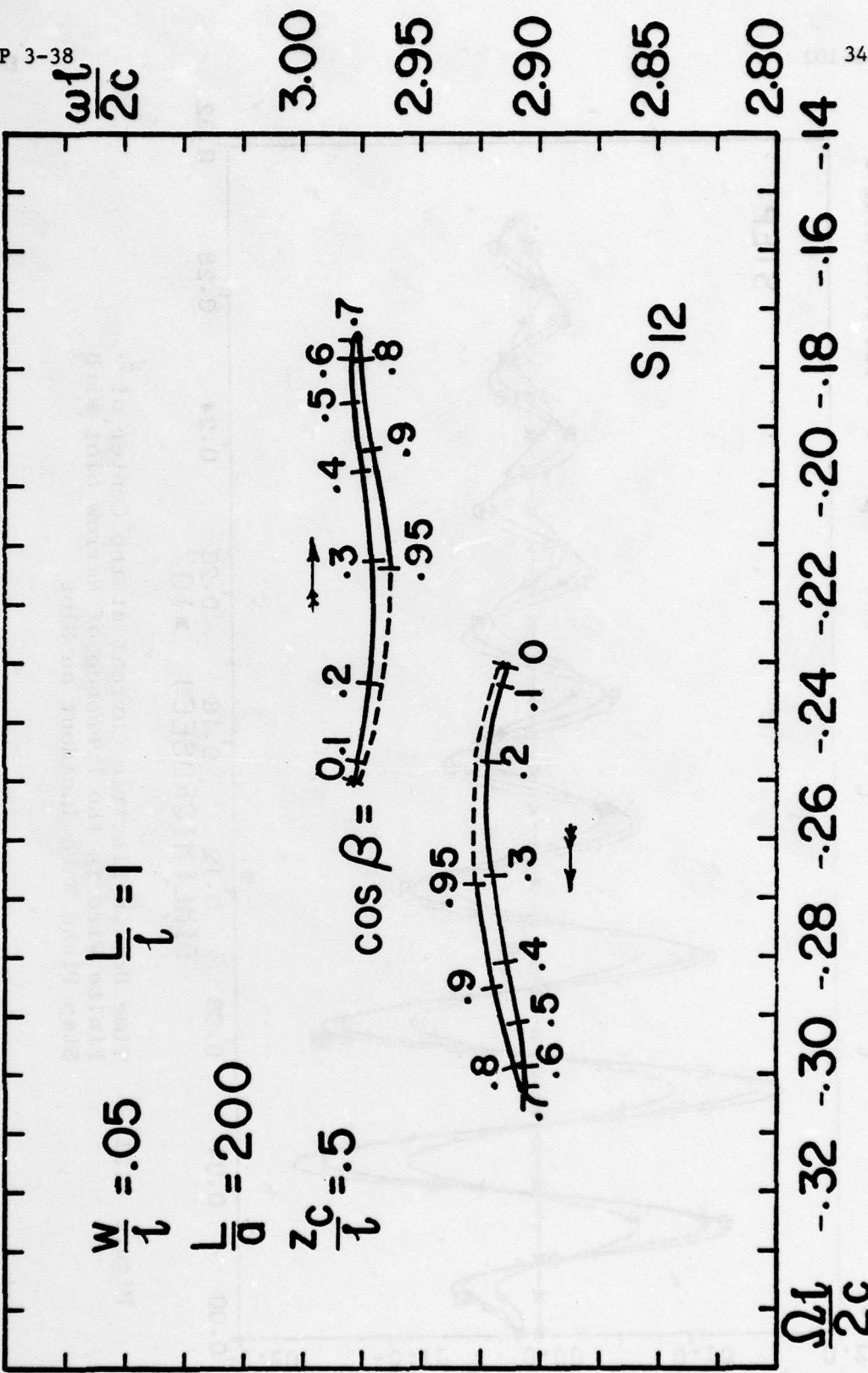


Figure 4.19 Trajectory of the First Set of Poles s_{11} as a Function of $\cos \beta$

EMP 3-38



343-101

Figure 4.20 Trajectory of the Second Set of Poles s_{12} as a Function of $\cos\beta$

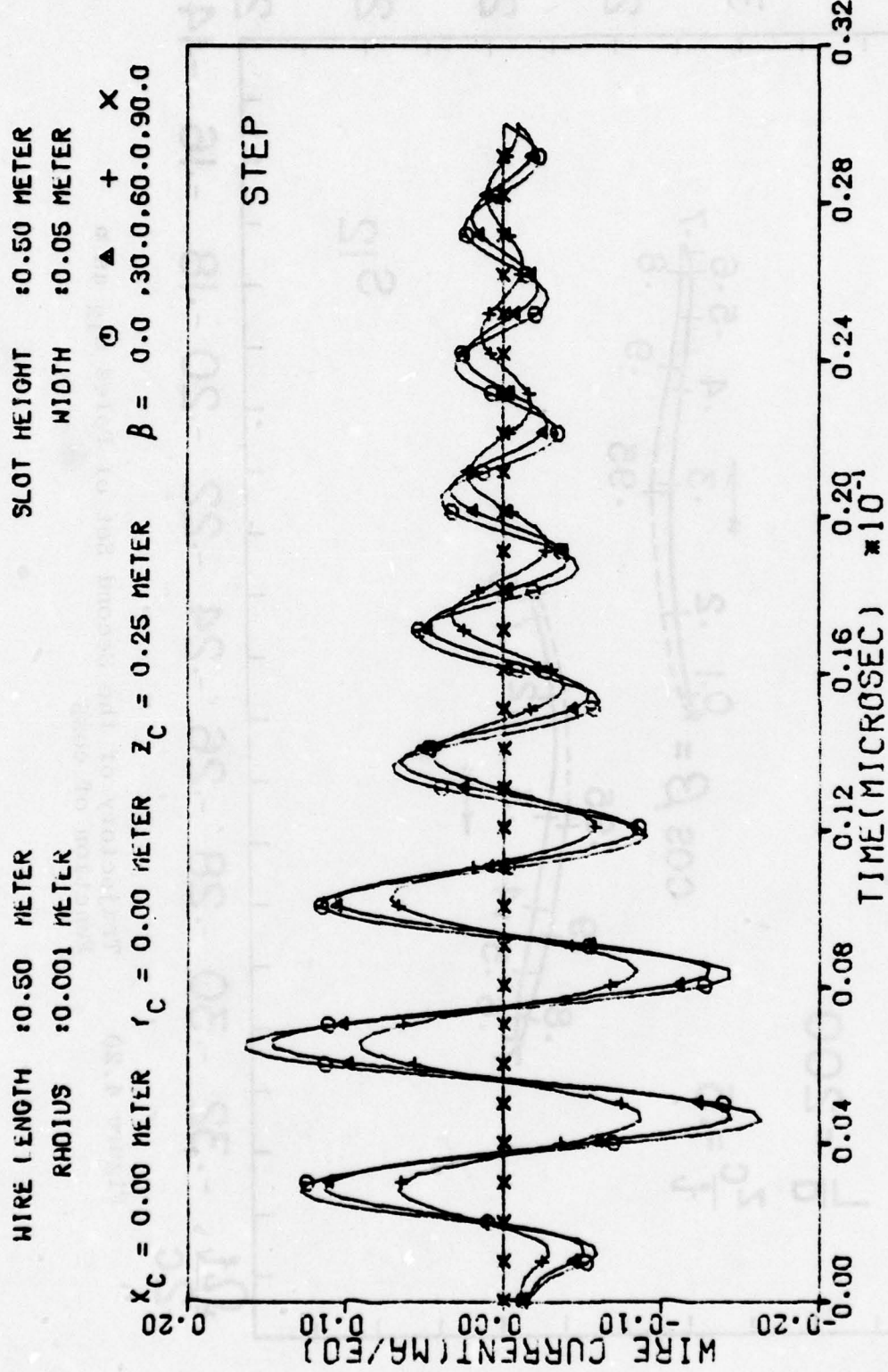


Figure 4.21 Time Domain Electric Current at the Center of Finite Wire in the Presence of Narrow Slot with Step Plane Wave Incident on Slot

341

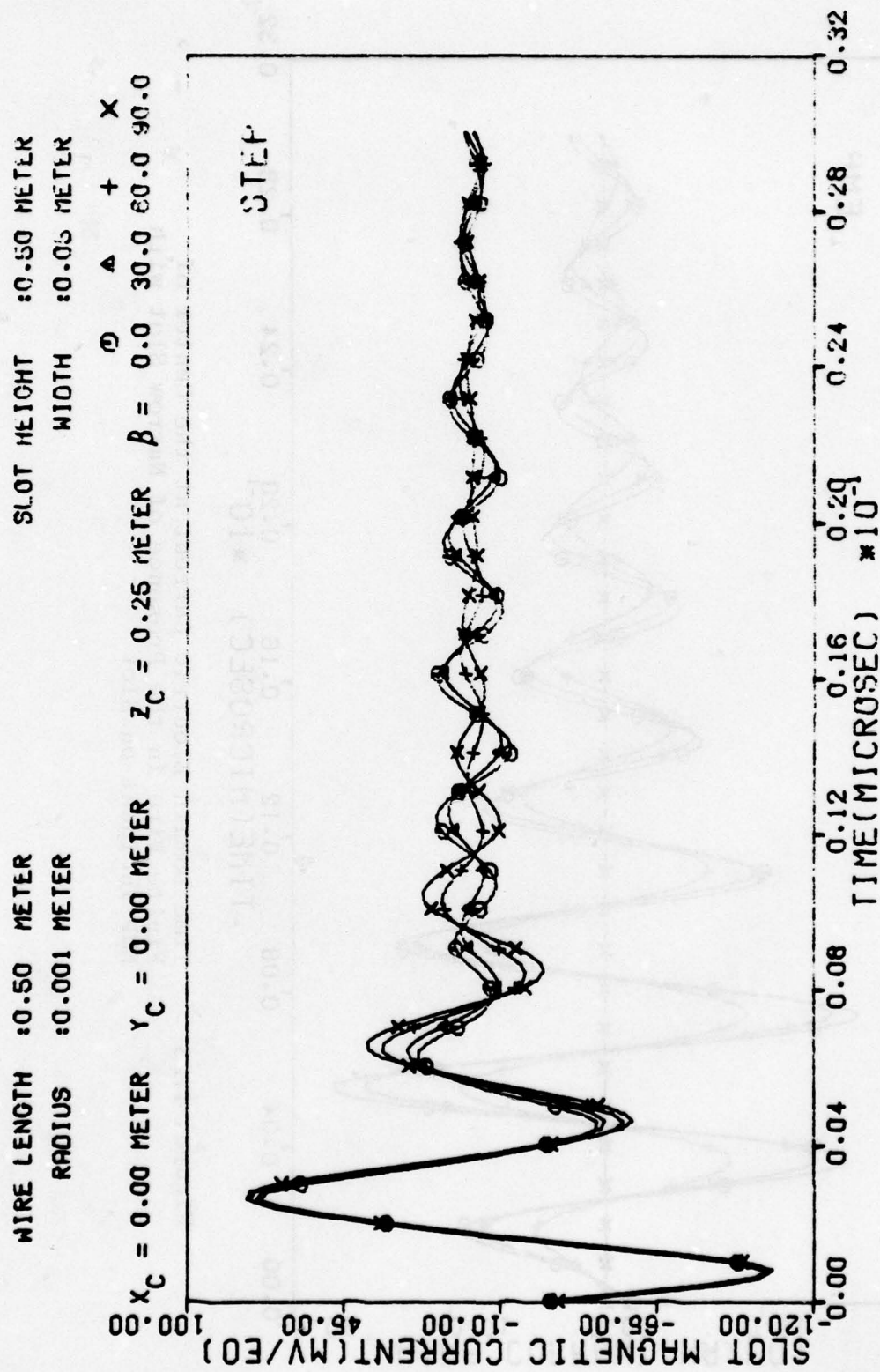


Figure 4.22 Time Domain Magnetic Current at the Center of
Narrow Slot in the Presence of Finite Wire
with Step Plane Wave Incident on Slot

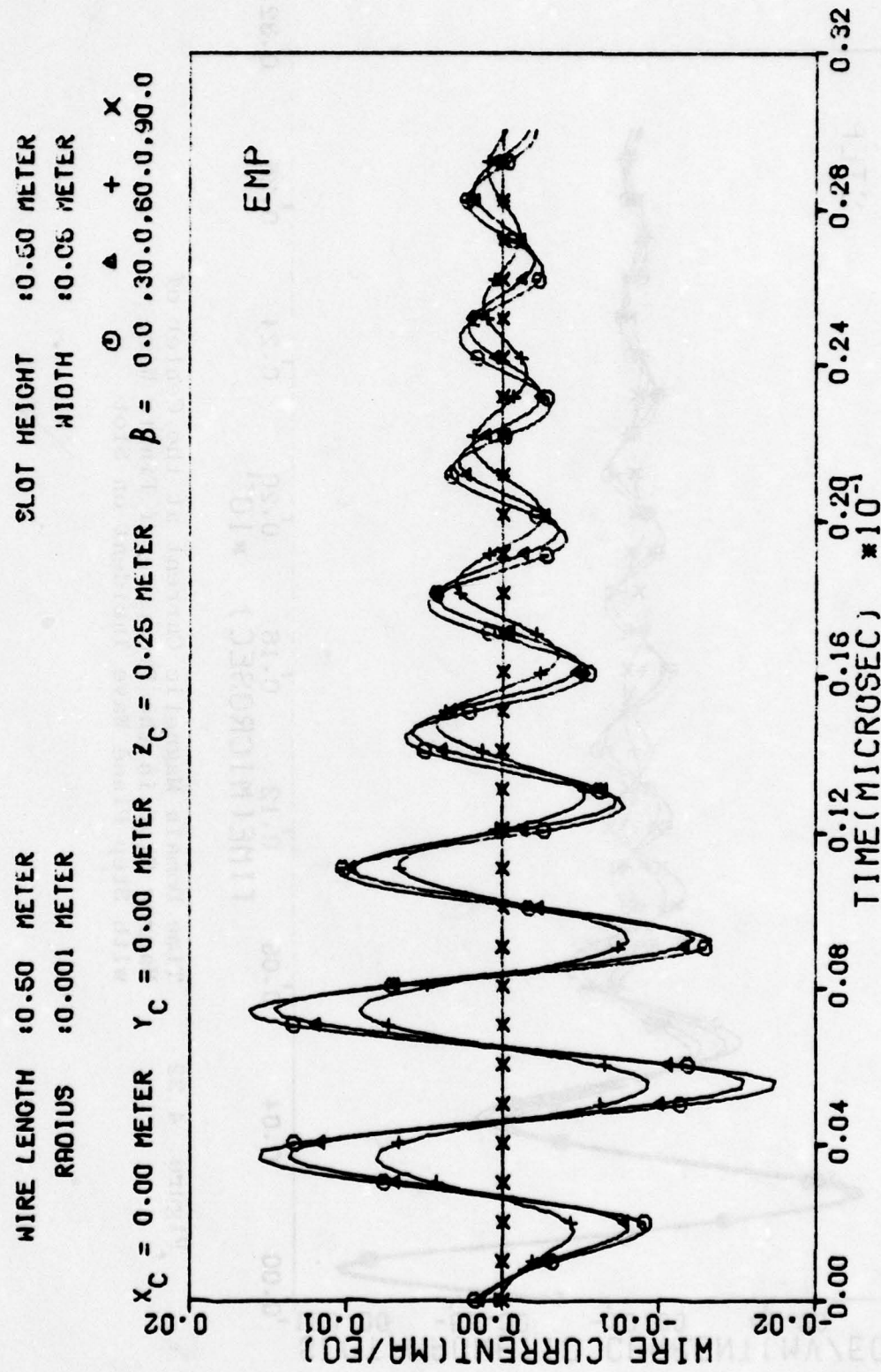
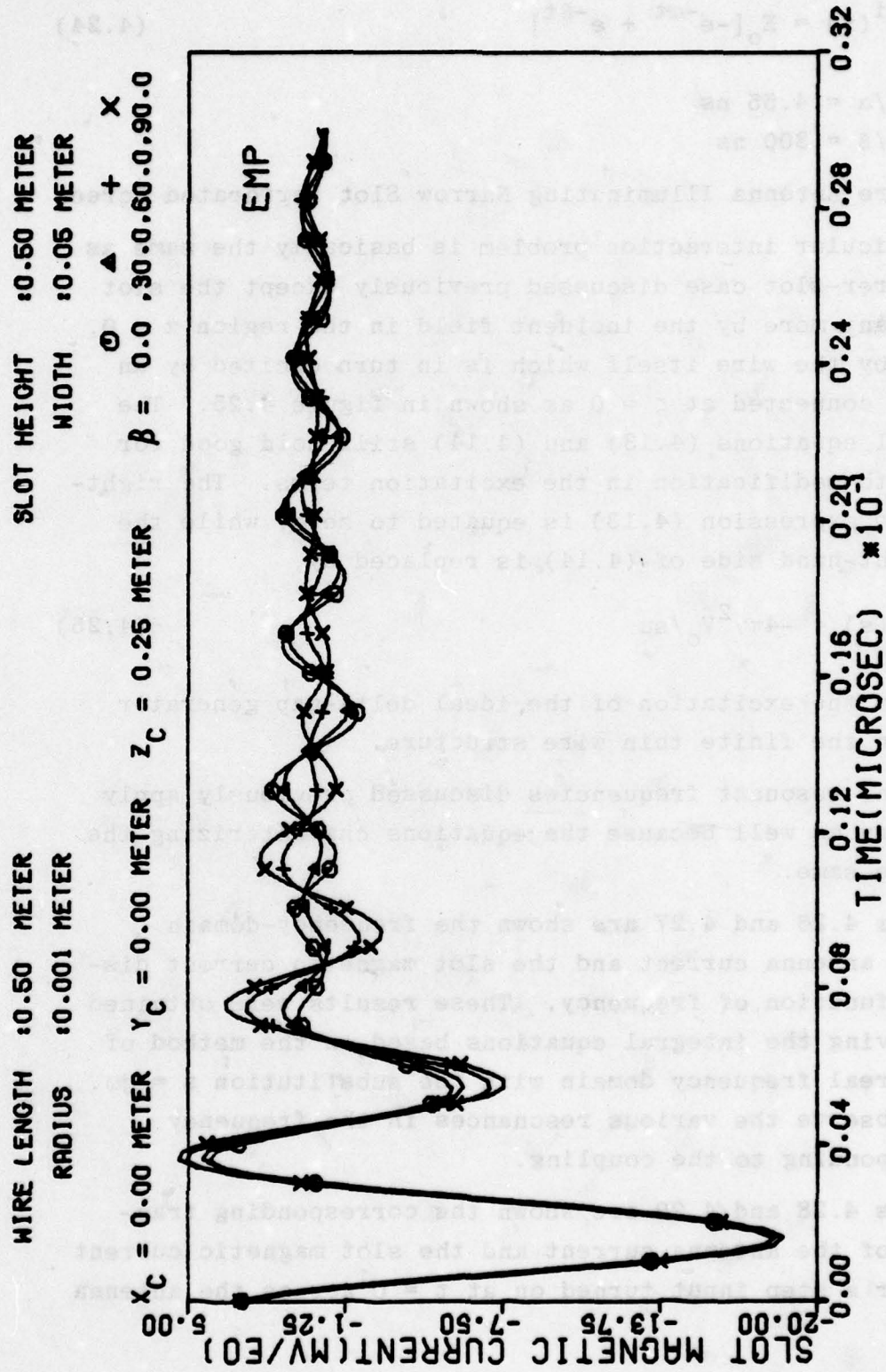


Figure 4.23

Time Domain Electric Current at the Center of
Finite Wire in the Presence of Narrow Slot with
EMP Incident on Slot



Time Domain Magnetic Current at the Center of Narrow Slot in the Presence of Finite Wire with EMP Incident on Slot

$$e^i(t) = E_0 [-e^{-\alpha t} + e^{-\beta t}] \quad (4.24)$$

where

$$1/\alpha = 4.55 \text{ ns}$$

$$1/\beta = 300 \text{ ns}$$

E. Finite Wire Antenna Illuminating Narrow Slot Perforated Screen

This particular interaction problem is basically the same as the wire scatterer-slot case discussed previously except the slot is not excited any more by the incident field in the region $z < 0$, but is excited by the wire itself which is in turn excited by an ideal generator connected at $\zeta = 0$ as shown in figure 4.25. The coupled integral equations (4.13) and (4.14) still hold good for this problem with modification in the excitation terms. The right-hand side of the expression (4.13) is equated to zero, while the zero in the right-hand side of (4.14) is replaced by,

$$\tilde{V}(s) = -4\pi\gamma^2 V_0 / s u \quad (4.25)$$

corresponding to the excitation of the ideal delta-gap generator at the center on the finite thin wire structure.

The natural resonant frequencies discussed previously apply for this geometry as well because the equations characterizing the coupling are the same.

In figures 4.26 and 4.27 are shown the frequency-domain response of the antenna current and the slot magnetic current distribution as a function of frequency. These results were obtained by directly solving the integral equations based on the method of moments in the real frequency domain with the substitution $s = j\omega$. Obviously, we observe the various resonances in the frequency response corresponding to the coupling.

In figures 4.28 and 4.29 are shown the corresponding transient response of the antenna current and the slot magnetic current respectively for a step input turned on at $t = 0$ across the antenna gap terminals.

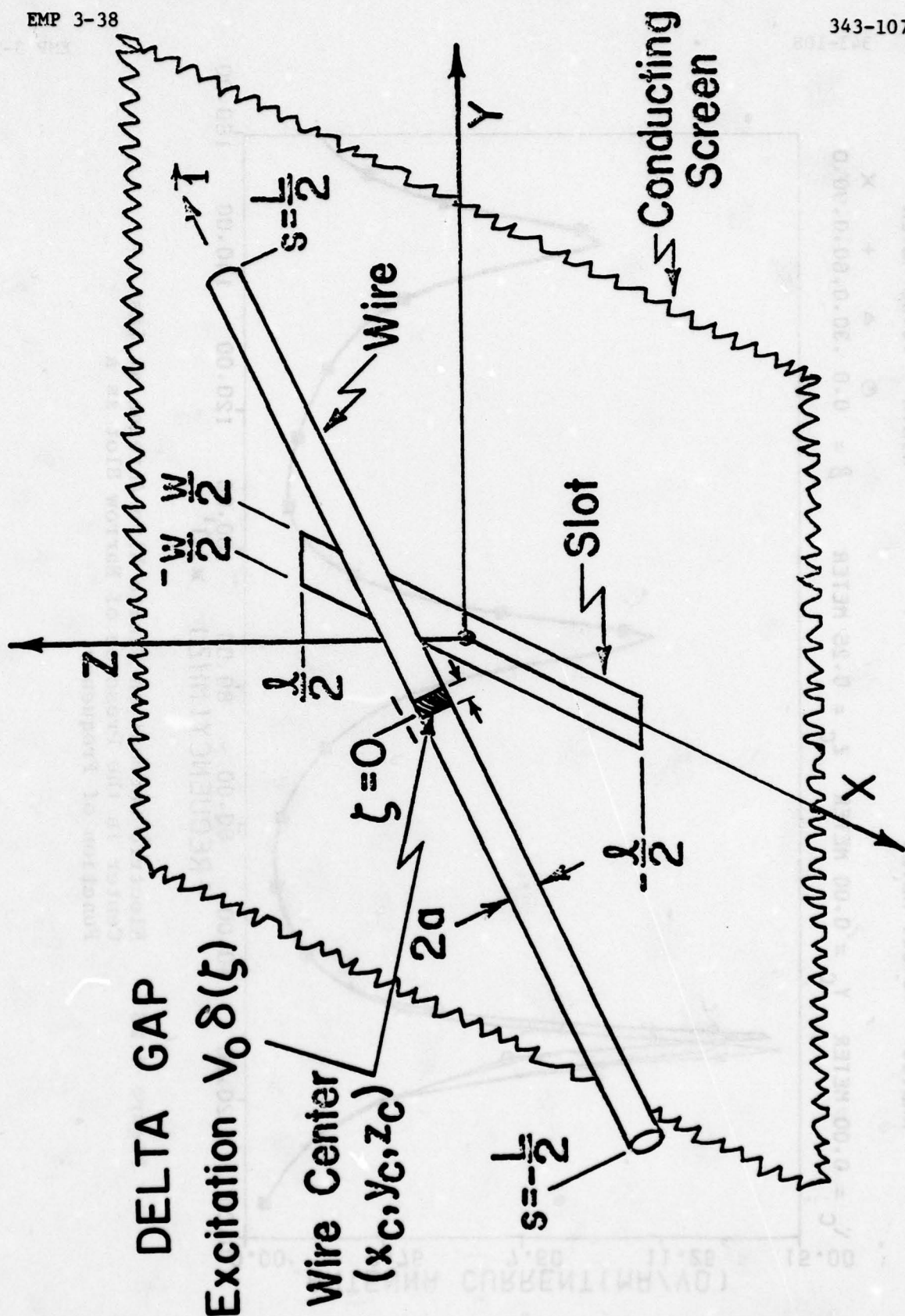


Figure 4.25 Finite Wire Antenna Behind Narrow Slot Conducting Screen

343-108

EMP 3-38

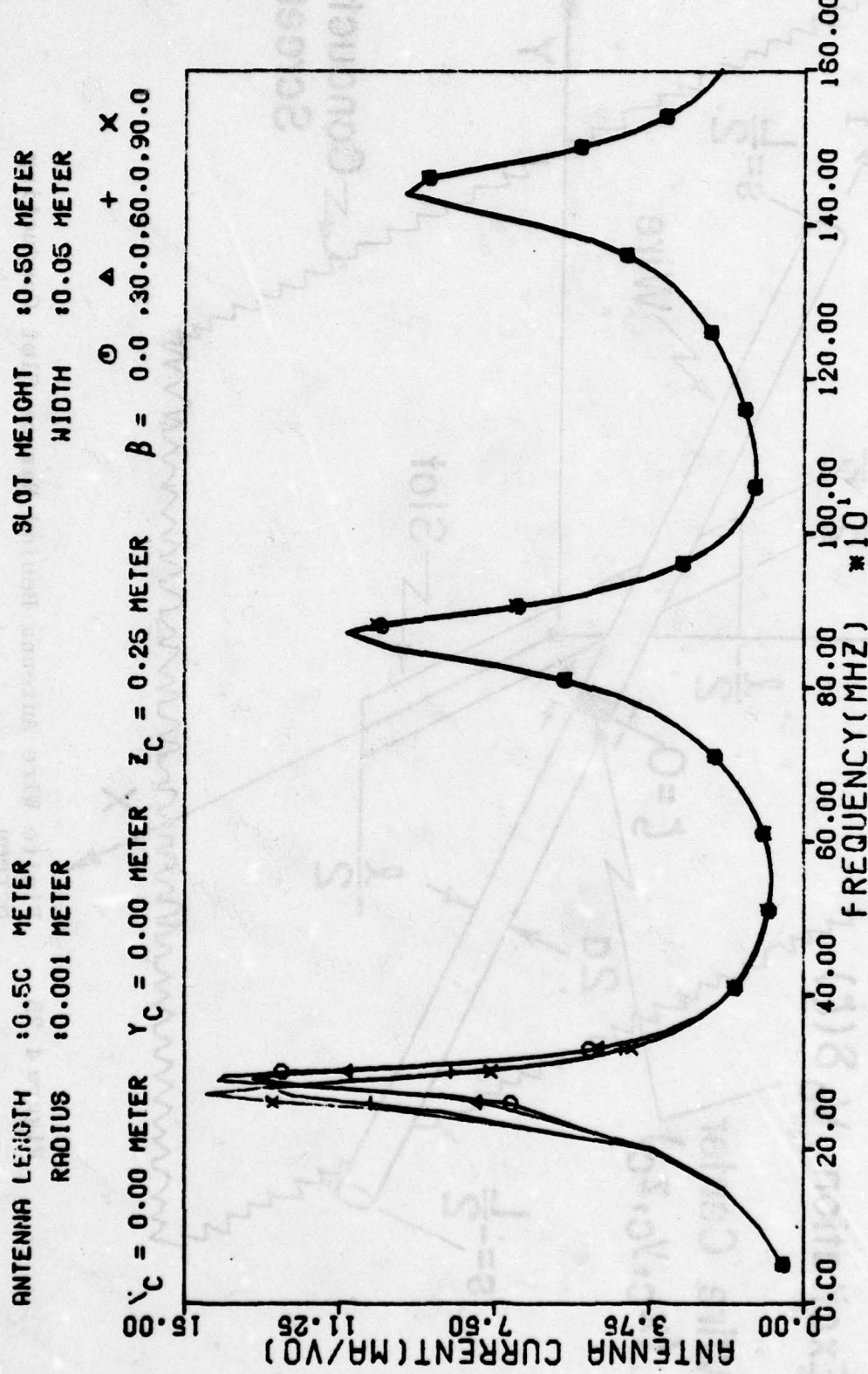


Figure 4.26 Electric Current on Finite Wire Antenna at Its Center in the Presence of Narrow Slot as a Function of Frequency

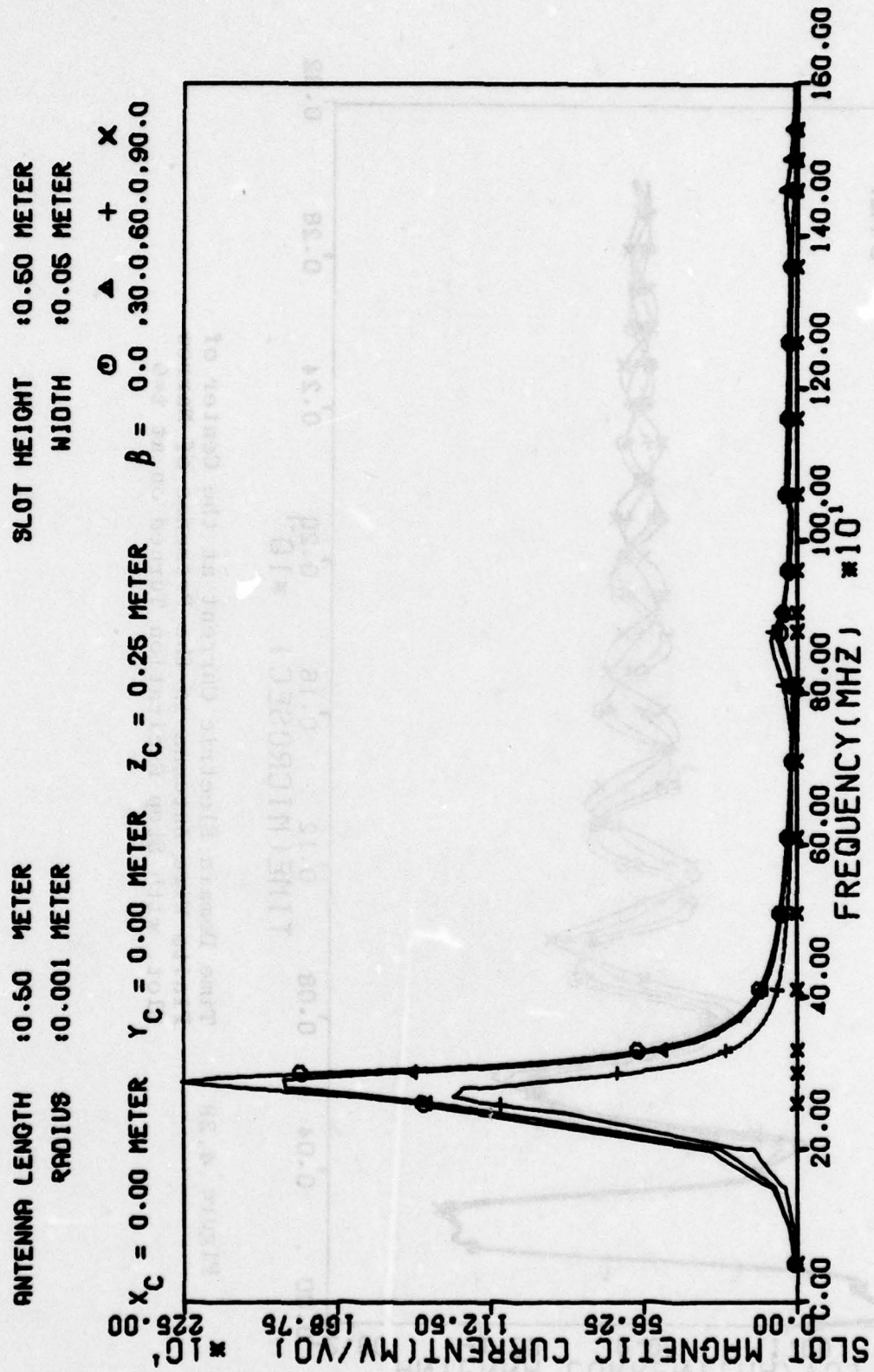


Figure 4.27 Axial Magnetic Current in Narrow Slot at Its Center in the Presence of Wire Antenna as a Function of Frequency

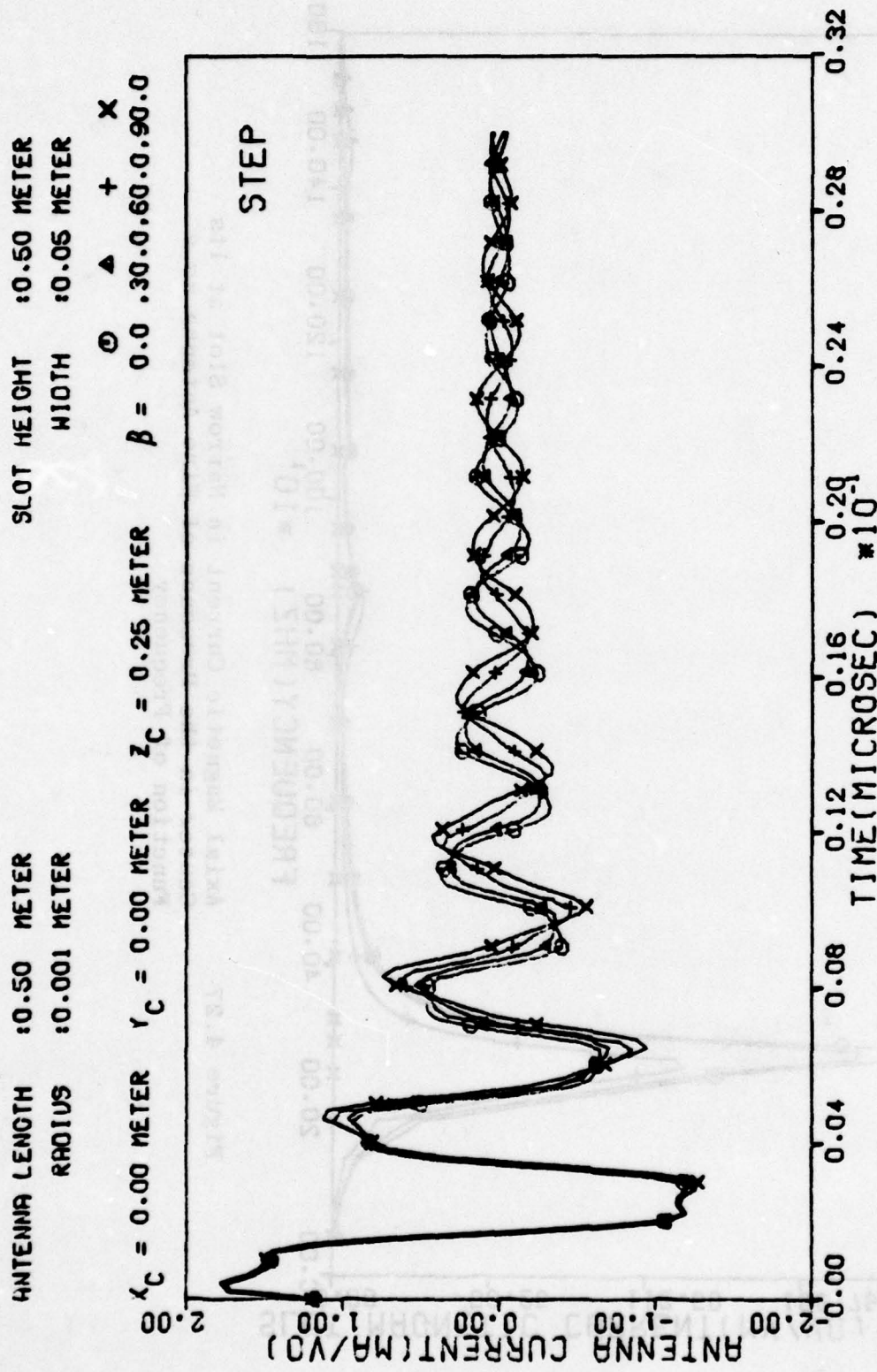


Figure 4.28 Time Domain Electric Current at the Center of Finite Wire Antenna in the Presence of Narrow Slot, with Step Excitation Turned on at $t=0$

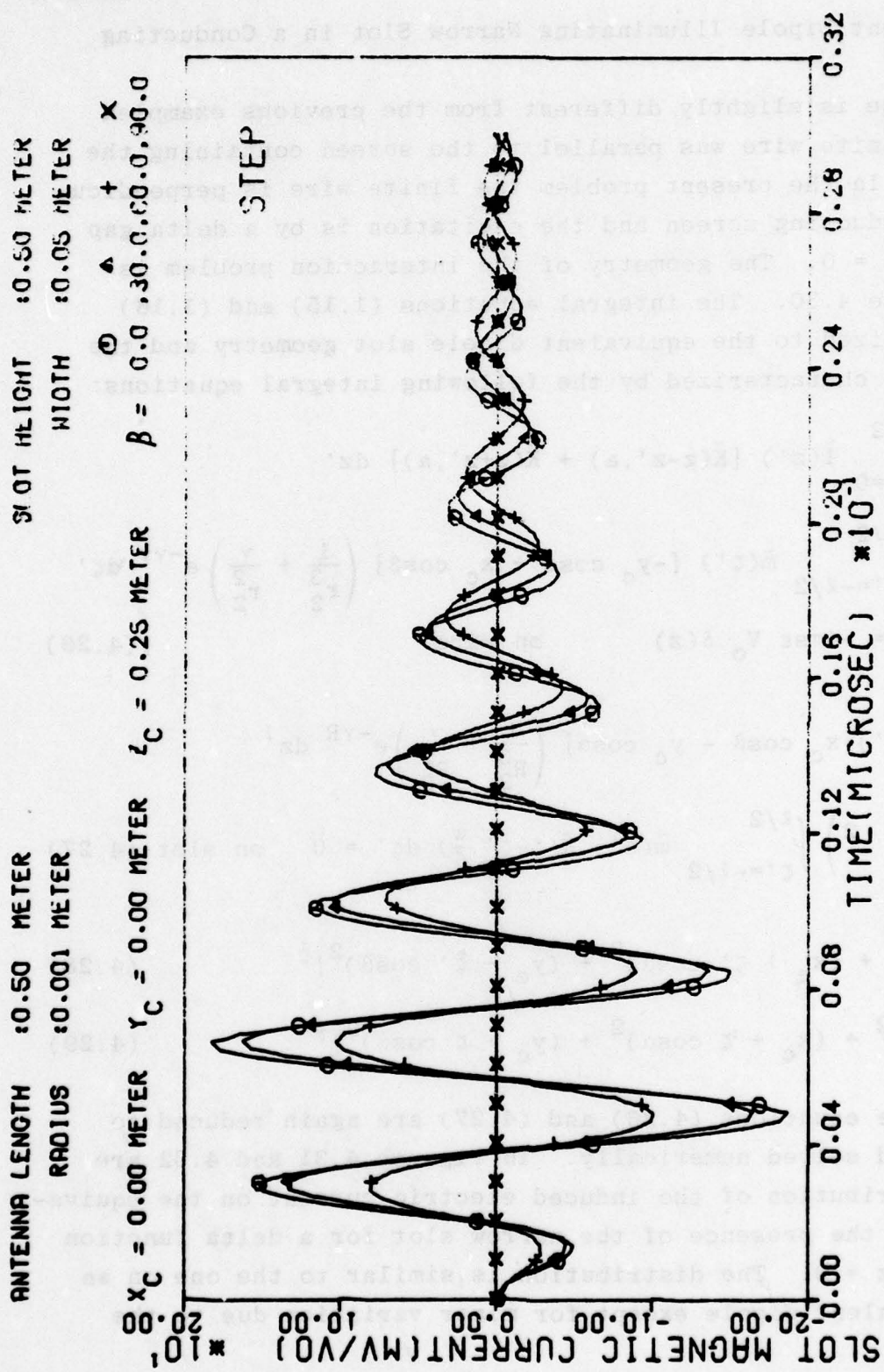


Figure 4.29 Time Domain Magnetic Current at the Center of
Narrow Slot in the Presence of Wire Antenna,
with Step Excitation Turned on at $t=0$

F. Equivalent Dipole Illuminating Narrow Slot in a Conducting Screen

This case is slightly different from the previous examples in that the finite wire was parallel to the screen containing the narrow slot. In the present problem the finite wire is perpendicular to the conducting screen and the excitation is by a delta gap generator at $z = 0$. The geometry of the interaction problem is shown in figure 4.30. The integral equations (1.15) and (1.16) can be specialized to the equivalent dipole slot geometry and the interaction is characterized by the following integral equations:

$$\begin{aligned} & \left(\frac{\partial^2}{\partial z^2} - \gamma^2 \right) \int_{z'=0}^{L/2} \tilde{I}(z') [\tilde{K}(z-z', a) + \tilde{K}(z+z', a)] dz' \\ & + 2s\epsilon \int_{\zeta'=-\ell/2}^{\ell/2} \tilde{m}(\zeta') [-y_c \cos\alpha + x_c \cos\beta] \left(\frac{1}{r_2^3} + \frac{\gamma}{r_2^2} \right) e^{-\gamma r} d\zeta' \\ & = -4\pi s\epsilon V_o \delta(z) \quad \text{on wire} \end{aligned} \quad (4.26)$$

$$\begin{aligned} & - \frac{s\mu}{2} \int_{z'=0}^{L/2} \tilde{I}(z') [x_c \cos\beta - y_c \cos\alpha] \left(\frac{1}{R_2^3} + \frac{\gamma}{R_2^2} \right) e^{-\gamma R} dz' \\ & + \left(\frac{\partial^2}{\partial \zeta^2} - \gamma^2 \right) \int_{\zeta'=-\ell/2}^{\ell/2} \tilde{m}(\zeta') \tilde{K}(\zeta-\zeta', \frac{w}{4}) d\zeta' = 0 \quad \text{on slot} \end{aligned} \quad (4.27)$$

where

$$r_2 = [z^2 + (x_c + \zeta' \cos\alpha)^2 + (y_c + \zeta' \cos\beta)^2]^{\frac{1}{2}} \quad (4.28)$$

$$R_2 = [z'^2 + (x_c + \zeta \cos\alpha)^2 + (y_c + \zeta \cos\beta)^2]^{\frac{1}{2}} \quad (4.29)$$

The above equations (4.26) and (4.27) are again reduced to matrix form and solved numerically. In figures 4.31 and 4.32 are shown the distribution of the induced electric current on the equivalent dipole in the presence of the narrow slot for a delta function excitation at $z = 0$. The distribution is similar to the one on an isolated equivalent dipole except for minor variation due to the

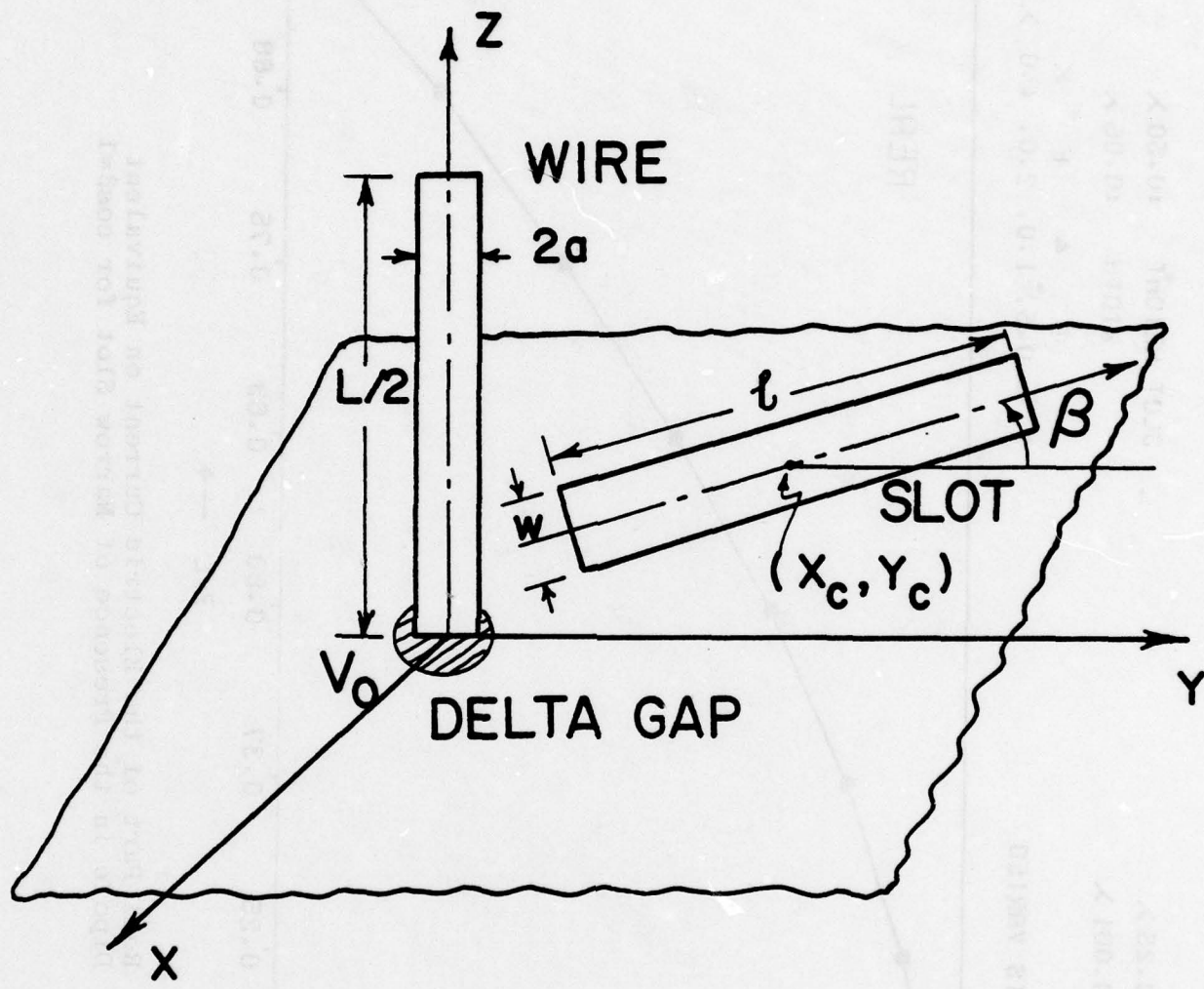


Figure 4.30 Equivalent Dipole Exciting Narrow Slot Perforated Conducting Screen

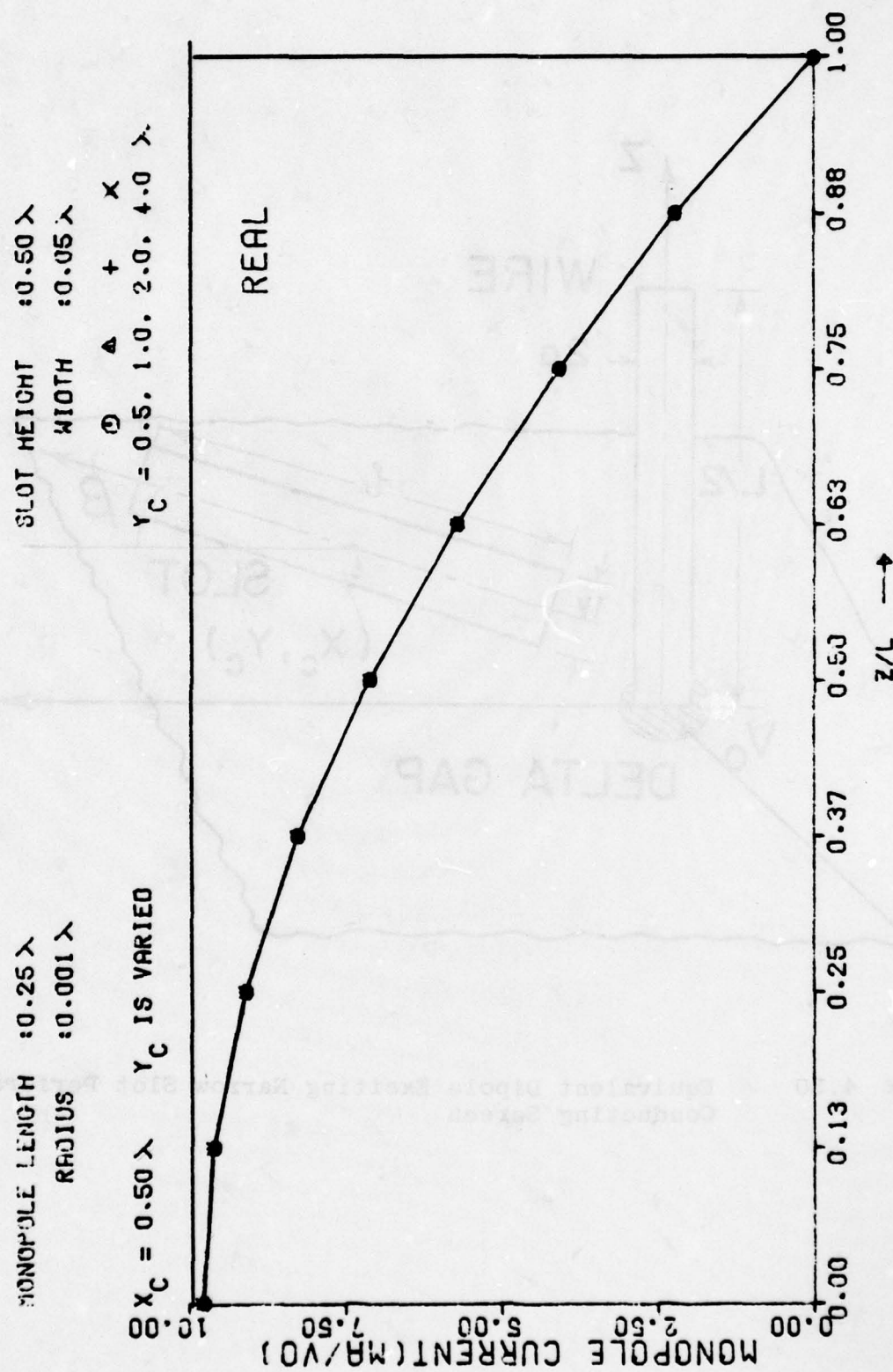


Figure 4.31 Real Part of the Electric Current on Equivalent Dipole in the Presence of Narrow Slot for $\cos\beta=1$

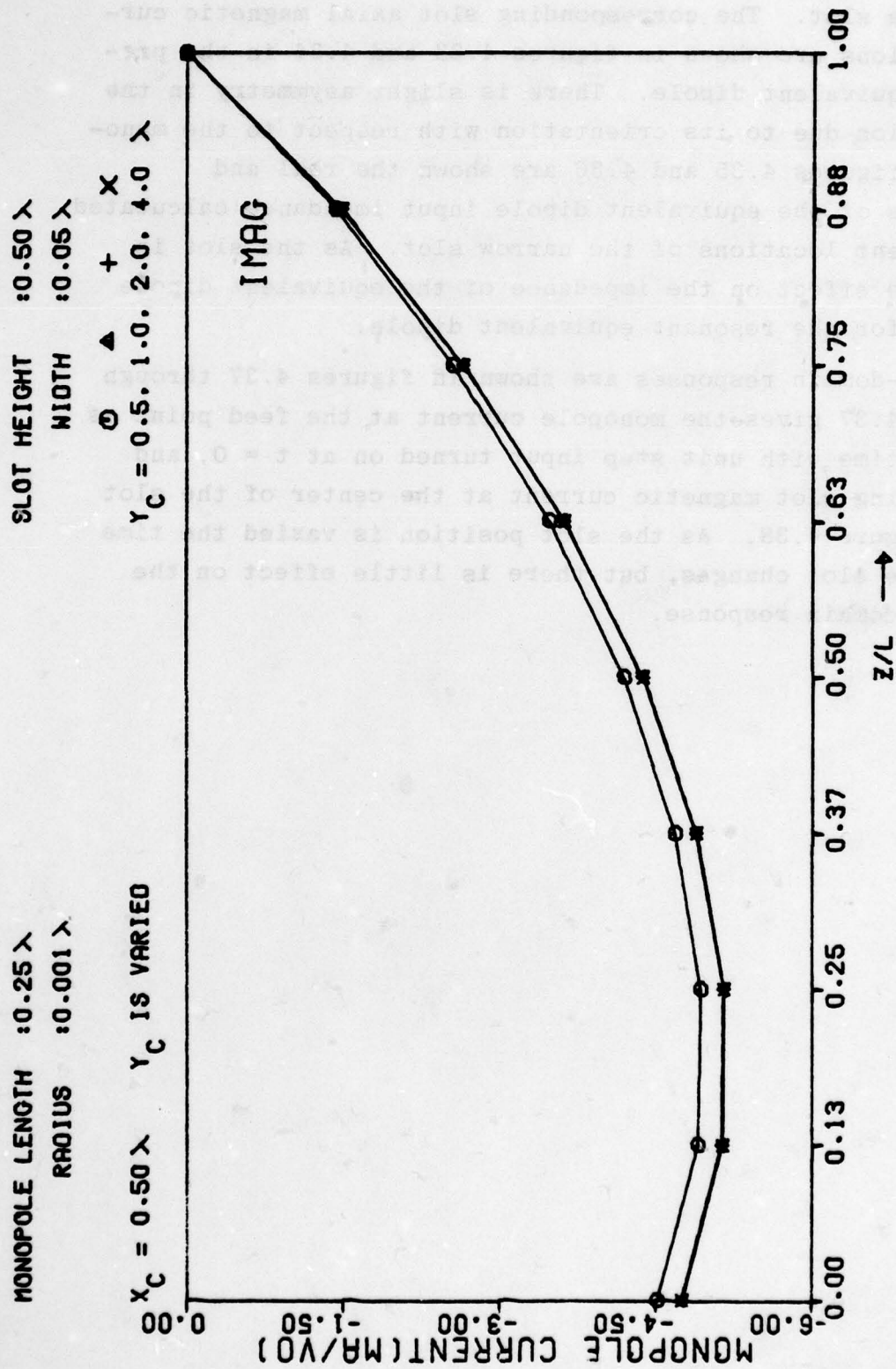


Figure 4.32 Imaginary Part of the Electric Current on Equivalent Dipole in the Presence of Narrow Slot for $\cos\beta=1$

presence of the slot. The corresponding slot axial magnetic current distributions are shown in figures 4.33 and 4.34 in the presence of the equivalent dipole. There is slight asymmetry in the slot distribution due to its orientation with respect to the monopole. In the figures 4.35 and 4.36 are shown the real and imaginary parts of the equivalent dipole input impedance calculated for the different locations of the narrow slot. As the slot is moved away, the effect on the impedance of the equivalent dipole is negligible for the resonant equivalent dipole.

The time-domain responses are shown in figures 4.37 through 4.40. Figure 4.37 gives the monopole current at the feed point as a function of time with unit step input turned on at $t = 0$, and the corresponding slot magnetic current at the center of the slot is shown in figure 4.38. As the slot position is varied the time response of the slot changes, but there is little effect on the monopole time domain response.

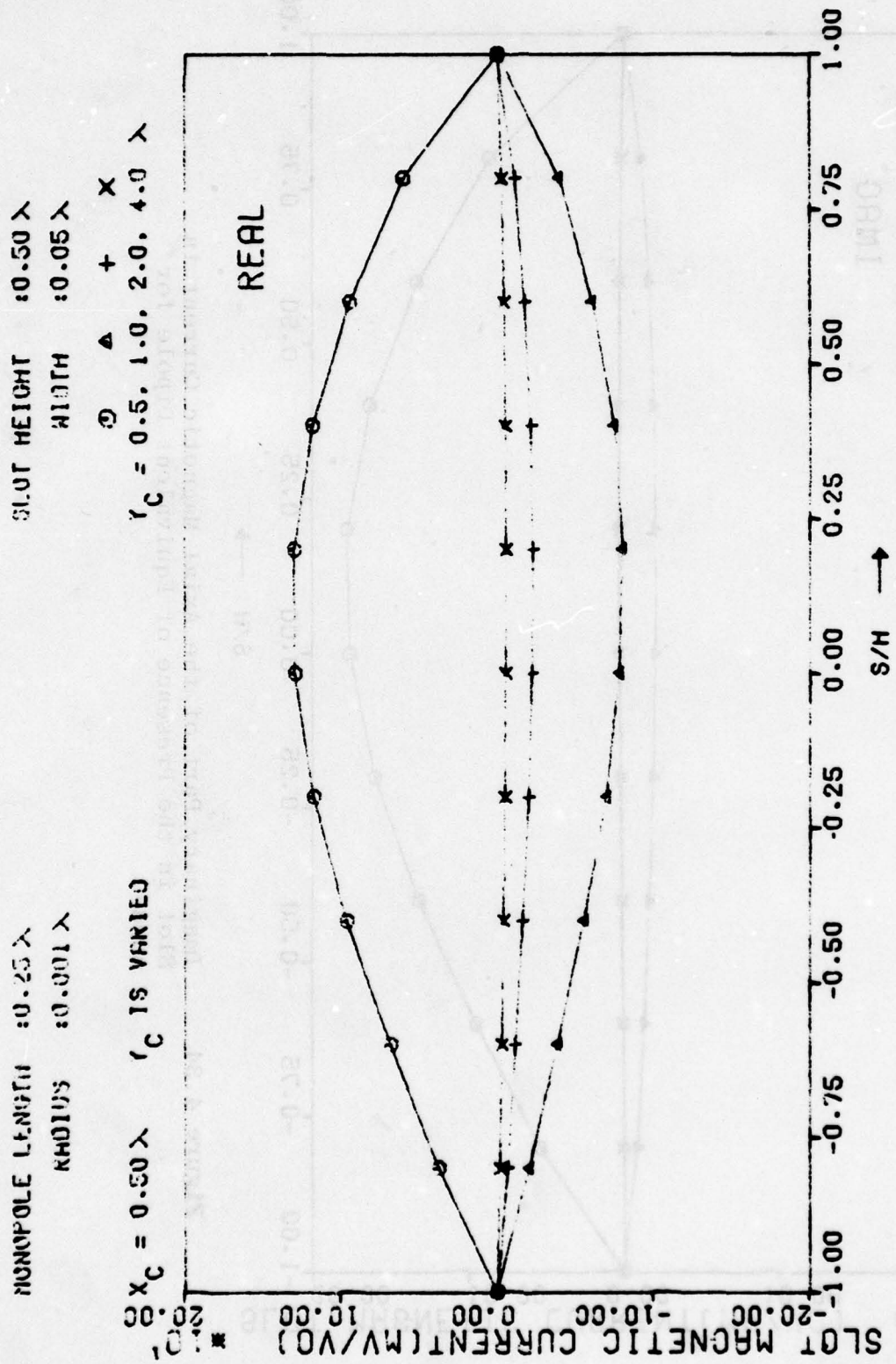


Figure 4.33 Real Part of the Axial Magnetic Current in Slot in the Presence of Equivalent Dipole for $\cos\beta=1$

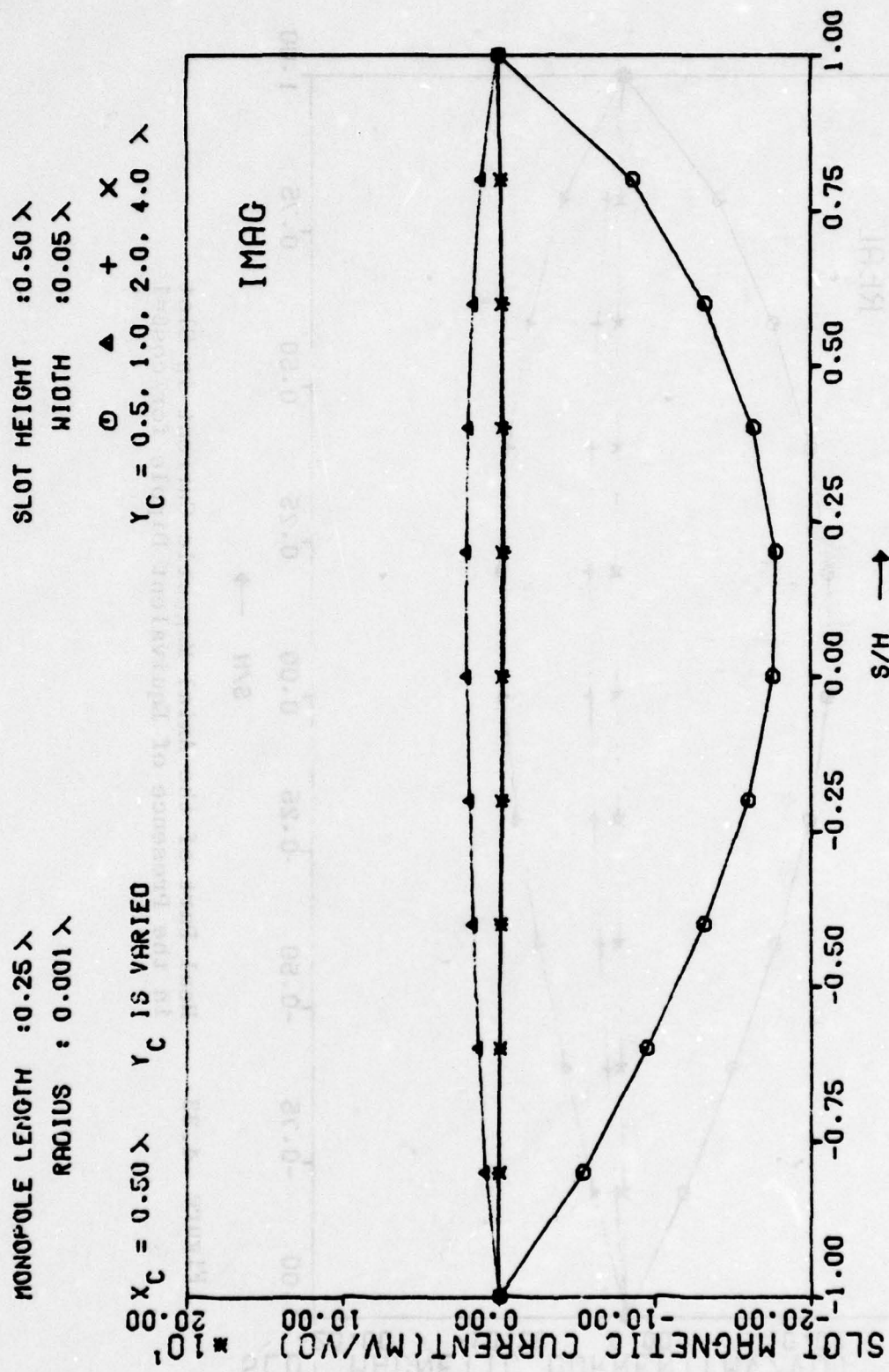


Figure 4.34
Imaginary Part of the Axial Magnetic Current in
Slot in the Presence of Equivalent Dipole for
 $\cos\beta=1$

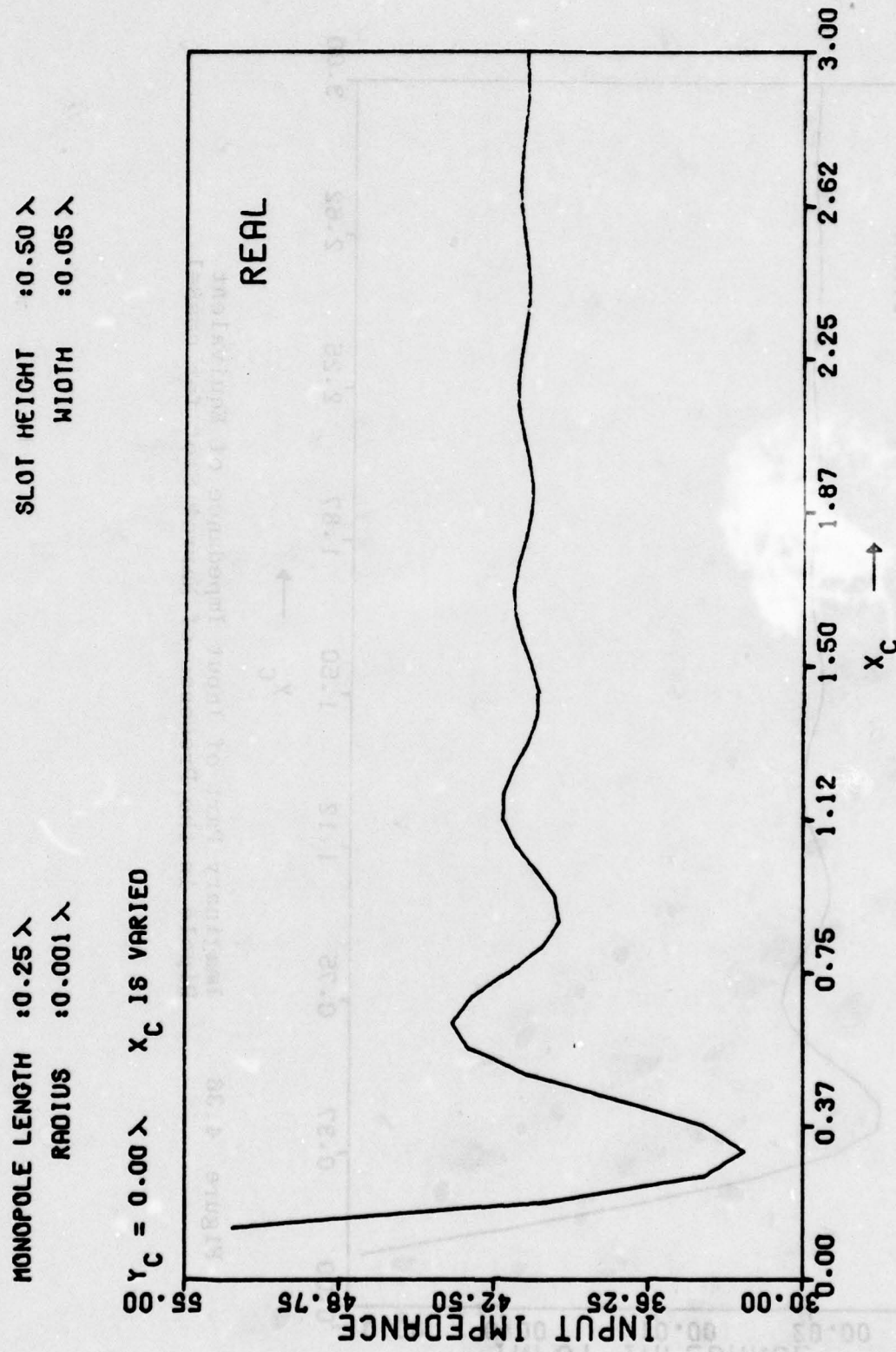


Figure 4.35 Real Part of Input Impedance of Equivalent Dipole in the Presence of Narrow Slot for $\cos\beta=1$

MONPOLE LENGTH : 0.25λ
RADIUS : 0.001λ

SLOT HEIGHT : 0.50λ
WIDTH : 0.06λ

$y_c = 0.00\lambda$ x_c IS VARIED

343-120

EMP 3-38

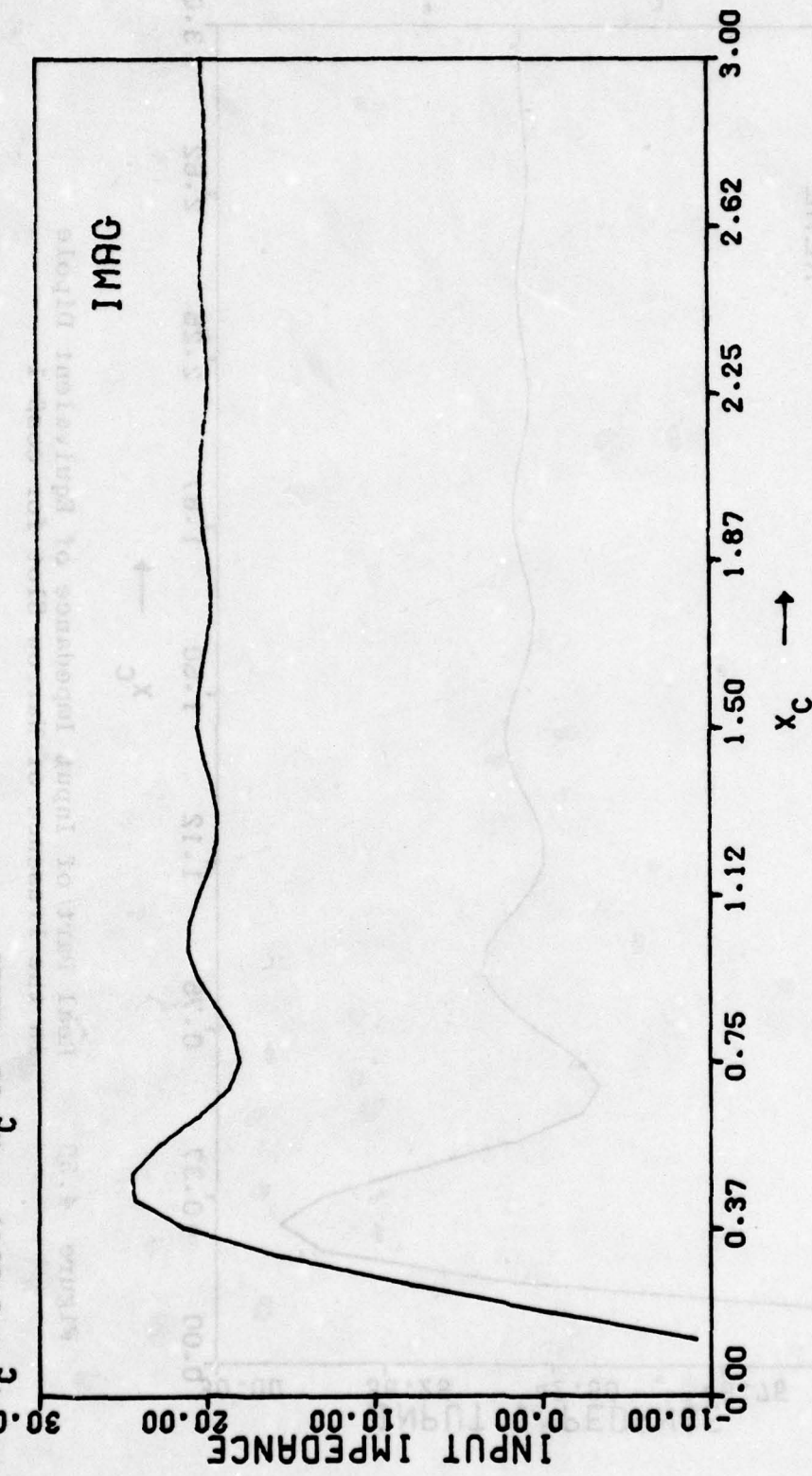


Figure 4.36 Imaginary Part of Input Impedance of Equivalent Dipole in the Presence of Narrow Slot for $\cos\beta=1$

MONPOLE LENGTH : 0.25λ x_c IS VARIED
 $y_c = 0.00\lambda$
MONPOLE LENGTH : 0.25λ x_c IS VARIED
 $y_c = 0.00\lambda$
MONPOLE LENGTH : 0.25λ x_c IS VARIED
 $y_c = 0.00\lambda$

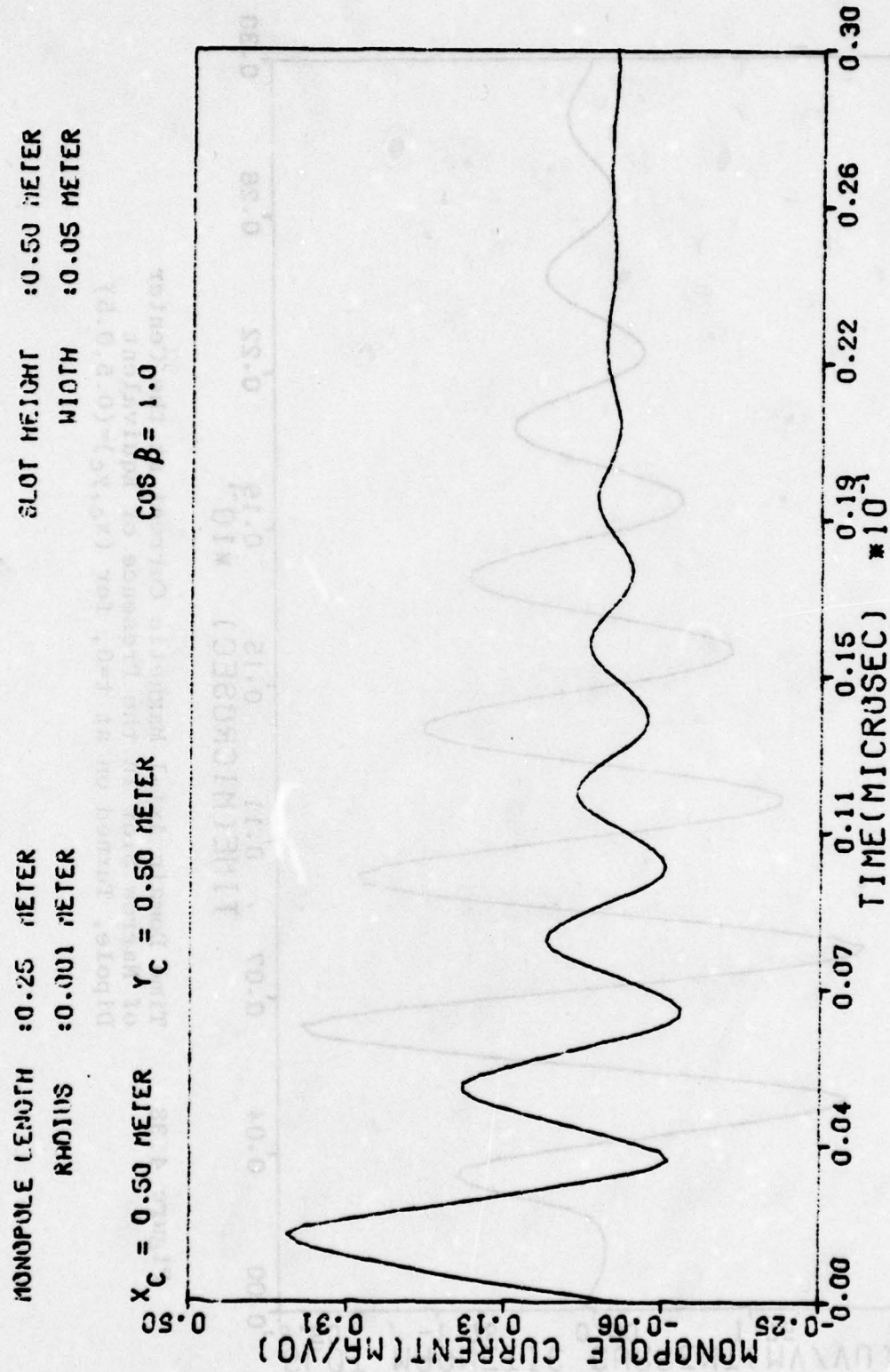


Figure 4.37 Time Domain Electric Current on Equivalent Dipole at the Feed Point in the Presence of Narrow Slot, Turned on at $t=0$, for $(x_c, y_c) = (0.5, 0.5)$

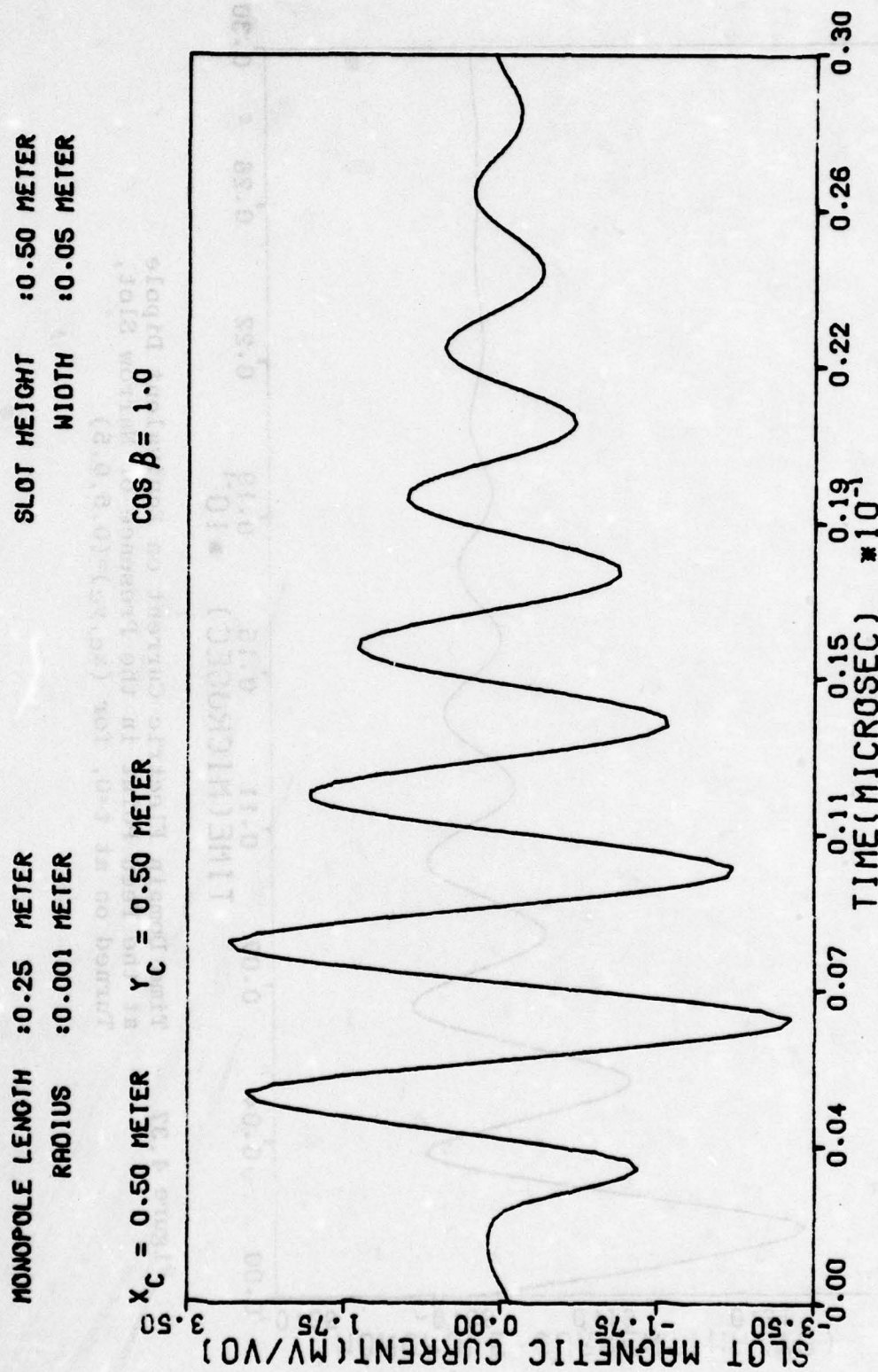


Figure 4.38 Time Domain Axial Magnetic Current at the Center of Narrow Slot in the Presence of Equivalent Dipole, Turned on at $t=0$, for $(x_c, y_c) = (0.5, 0.5)$

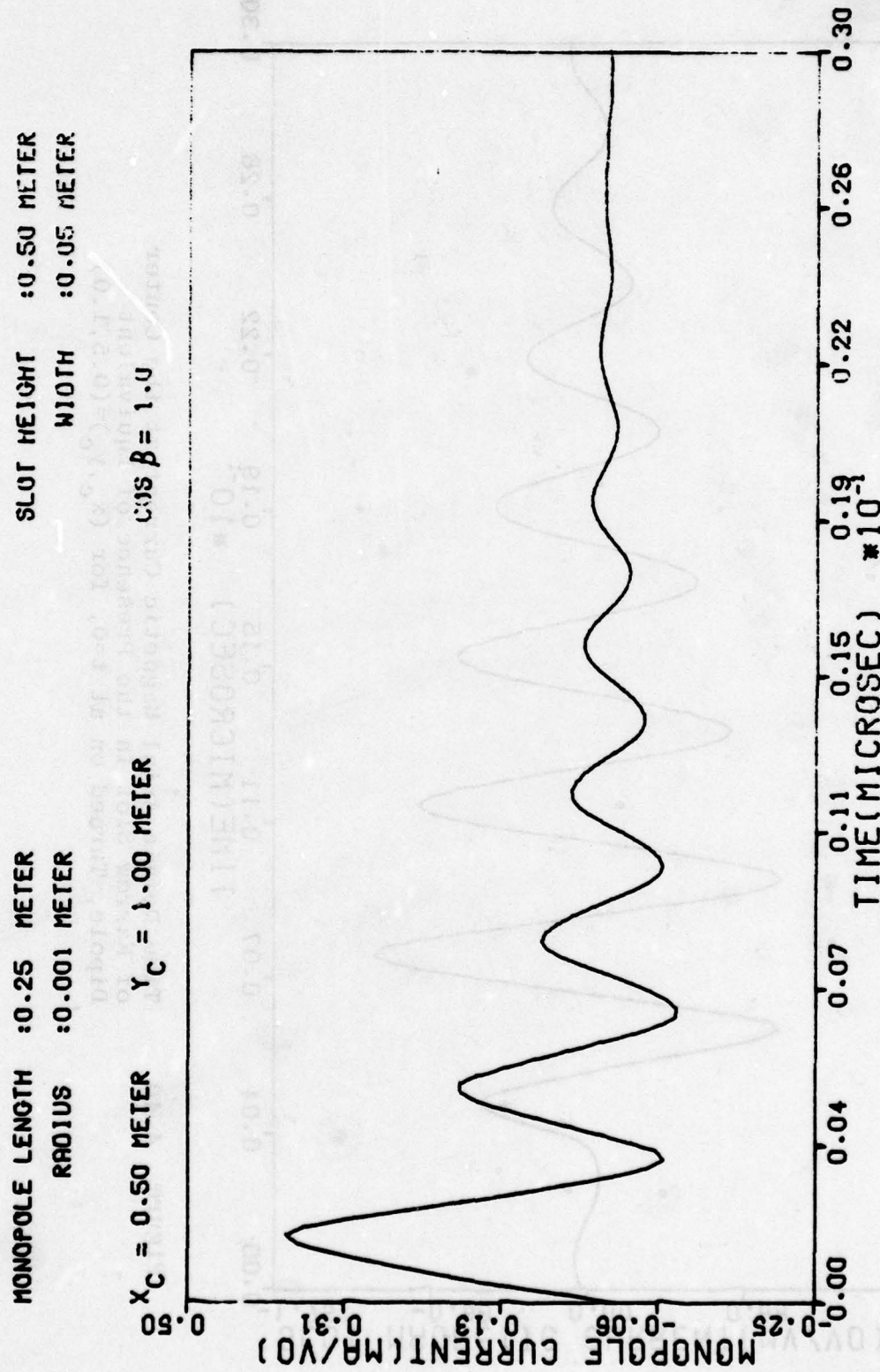


Figure 4.39 Time Domain Electric Current on Equivalent Dipole at the Feed Point in the Presence of Narrow Slot, Turned on at $t=0$, for $(x_c, y_c)=(0.5, 1.0)$

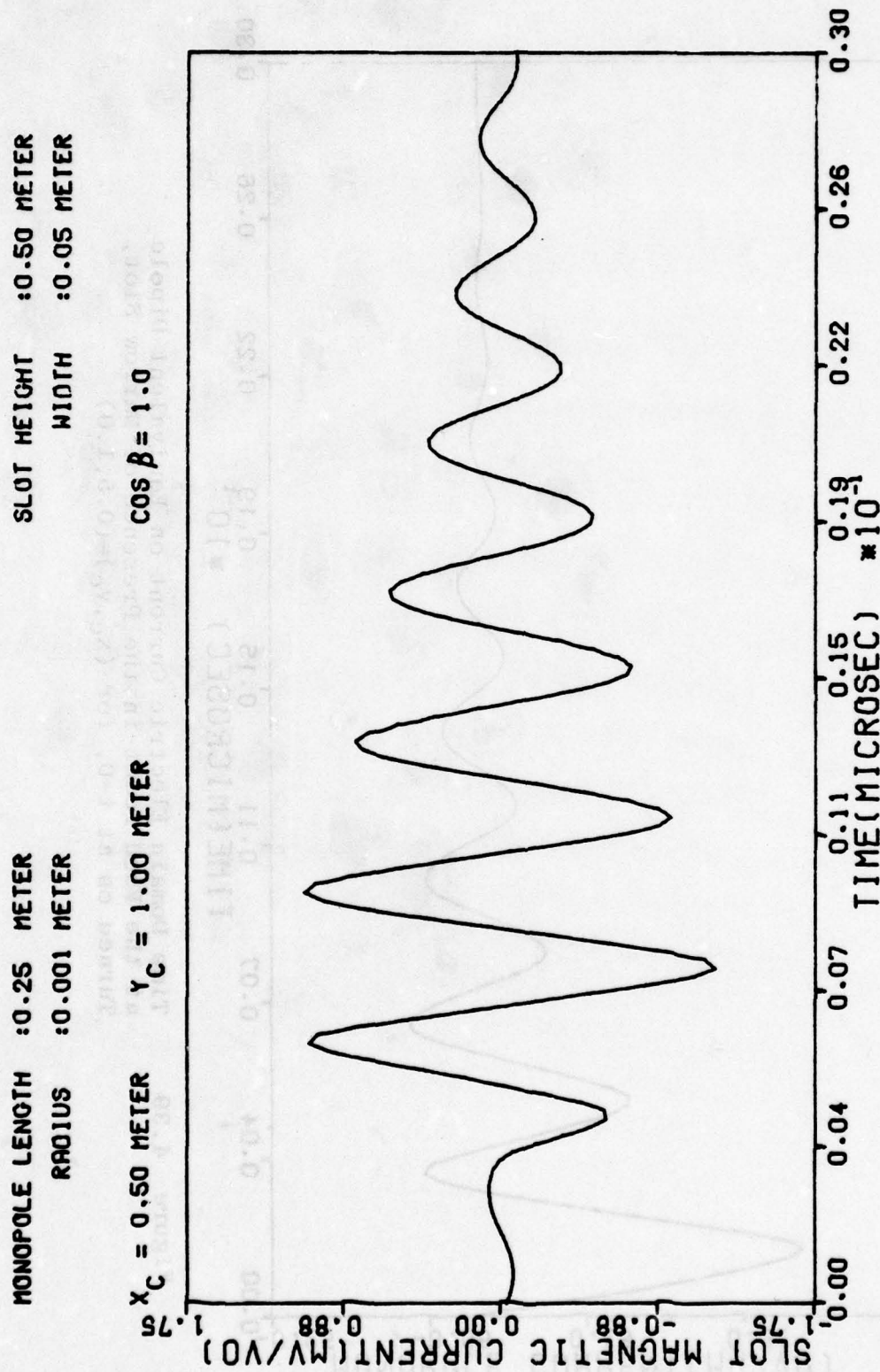


Figure 4.40 Time Domain Axial Magnetic Current at the Center of Narrow Slot in the Presence of Equivalent Dipole, Turned on at $t=0$, for $(x_c, y_c) = (0.5, 1.0)$

SUMMARY

In this note there is reported the preliminary investigation of the interaction problem of the conducting bodies behind aperture screen geometries based on the formulation of the integral equation approach and subsequent numerical analysis. To characterize the complex interaction problem step by step, apertures in the form of a narrow slot, and rectangular and square apertures are analyzed separately; similarly the finite and infinite wire geometries above conducting ground plane are treated separately and some numerical results are reported in the frequency domain. Further simple objects in the form of finite wire antenna and scatterer geometries are characterized in the presence of narrow finite slot geometry. The Singularity Expansion Method is applied for transient characterization and an attempt is made to explain the interaction between the wire and the aperture-screen. Both the narrow slot and finite wire responses are reported in the frequency and the time domains.

The reader may refer to [30] for the analysis of the infinite wire behind a narrow slot in a conducting screen. The general analysis of infinitely long multiple wires behind arbitrarily shaped apertures and the subsequent characterization of such regions in terms of an equivalent circuit including aperture resonance effects will be reported in an upcoming separate note.

REFERENCES

1. C. E. Baum, "EMP Simulators for Various Types of Nuclear EMP Environments: An Interim Categorization," Sensor and Simulation Note 151, July 1972.
2. C. E. Baum, "On the Singularity Expansion Method for the Solution of Electromagnetic Interaction Problems," Interaction Note 88, December 1971.
3. C. E. Baum, K. C. Chen, and B. K. Singaraju, "Categorization of the Types of Apertures," Interaction Note 219, January 1975.
4. C. D. Taylor, "Electromagnetic Pulse Penetration Through Small Apertures," Interaction Note 74, March 1971.
5. D. R. Wilton and O. C. Dunaway, "Electromagnetic Penetration Through Apertures of Arbitrary Shape: Formulation and Numerical Solution Procedure," Interaction Note 214, July 1974.
6. T.B.A. Senior and G. A. Desjardins, "Field Penetration into a Spherical Cavity," Interaction Note 142, August 1973.
7. K. C. Chen, "Apertures with Various Items Behind," 1974 Spring FULMEN Meeting.
8. D. Kajfez, "Excitation of a Terminated TEM Transmission Line Through Small Apertures," Interaction Note 215, July 1974.
9. C. M. Butler and K. R. Umashankar, "Electromagnetic Excitation of a Wire Through an Aperture Perforated Conducting Screen," Interaction Note 251, July 1975.
10. C. J. Bouwkamp, "Theoretical and Numerical Treatment of Diffraction Through a Circular Aperture," IEEE Trans. on Antennas and Propagation, AP-18, No. 2, March 1970.
11. K. R. Umashankar and C. M. Butler, "A Numerical Solution Procedure for Small Aperture Integral Equations," Interaction Note 212, July 1974.
12. D. R. Wilton, C. M. Butler, and K. R. Umashankar, "Penetration of Electromagnetic Fields Through Small Apertures in Planar Screens: Selected Data," Interaction Note 213, September 1974.

13. Y. Rahmat-Samii and R. Mittra, "A New Integral Equation Solution of Electromagnetic Aperture Coupling and Thin Plate Scattering Problems," Interaction Note 224, February 1975.
14. C. M. Butler and K. R. Umashankar, "Electromagnetic Penetration Through an Aperture in an Infinite Planar Screen Separating Two Half Spaces of Different Electromagnetic Properties," Radio Science, Vol. II, No. 7, July 1976.
15. C. E. Baum and B. K. Singaraju, "Generalization of Babinet's Principle in Terms of the Combined Field to Include Impedance Loaded Aperture Antennas and Scatterers," Interaction Note 217, September 1974.
16. R. F. Harrington, Field Computation by Moment Methods, MacMillan, New York, 1968.
17. C. E. Baum, "Emerging Technology for Transient and Broad-band Analysis and Synthesis of Antennas and Scatterers," Proc. of the IEEE, Vol. 64, November 1976.
18. K. R. Umashankar and D. R. Wilton, "Transient Scattering by a Thin Wire in Free Space and Above Ground Plane Using the Singularity Expansion Method," Interaction Note 236, August 1974.
19. K. R. Umashankar and D. R. Wilton, "Transient Characterization of Circular Loop Using the Singularity Expansion Method," Interaction Note 259, August 1974.
20. D. R. Wilton and K. R. Umashankar, "Parametric Study of an L-Shaped Wire Using the Singularity Expansion Method," Interaction Note 152, November 1973.
21. R. F. Harrington, Time Harmonic Electromagnetic Fields, McGraw-Hill, 1961.
22. W. L. Weeks, Electromagnetic Theory for Engineering Applications, John Wiley and Sons, New York, 1964.
23. C. M. Butler, K. R. Umashankar, and C. E. Smith, "Theoretical Analysis of the Wire Biconical Antenna," Technical Report, U. S. Army Communications-Electronics, Fort Huachuca, Arizona, January 1975.
24. C. C. Kao, "Electromagnetic Scattering from a Finite Tubular Cylinder: Numerical Solutions and Data, Pt. I; Development of Theory," USAF Cambridge Research Labs., Cambridge, Mass., Rep. AF CRL-69-0535(1), Contract F19628-68-C-0030, December 1969.

25. C. C. Kao, "Electromagnetic Scattering from a Finite Tubular Cylinder: Numerical Solutions and Data, Pt II: Tables," USAF Cambridge Research Labs., Cambridge, Mass., Rep. AFCRL-69-0535 (2), Contract F19628-68-C-0030, December 1969.
26. C. C. Kao, "Three-Dimensional Electromagnetic Scattering from a Circular Tube of Finite Length," J. Appl. Phys., Vol. 40, November 1969, pp. 4732-4740.
27. C. W. Harrison, Jr., "Missile Circumferential Current Density for Plane Wave Electromagnetic Field Illumination," Interaction Note 60, July 1970.
28. R. V. Row, "Electromagnetic Scattering from Two Parallel Conducting Circular Cylinders," Cruft Laboratory, Harvard University, Tech. Rep. No. 170, 1953.
29. G. O. Olaofe, "Scattering by Two Cylinders," Radio Science, Vol. 5, No. 11, November 1970, pp. 1351-1360.
30. K. R. Umashankar and J. R. Wait, "Electromagnetic Coupling in an Infinite Cable Placed Behind a Slot Perforated Screen," Interaction Note 330, June 1977.

NOTE 344

A COMPARISON OF STICK MODEL SKIN CURRENT PREDICTIONS
WITH SCALE MODEL MEASUREMENTS
FOR THE E-4 and EC-135 AIRCRAFT

by

G. Bedrosian

The Dikewood Corporation

January 1978

A COMPARISON OF STICK MODEL SKIN CURRENT PREDICTIONS
WITH SCALE MODEL MEASUREMENTS FOR THE E-4 AND EC-135 AIRCRAFT

ABSTRACT

Scale-model measurements of the axial skin current density on the E-4 and EC-135 aircraft are compared with predictions calculated using the six-length stick model. The stick-model predictions tend to be somewhat smaller in magnitude than the scale-model measurements except near aircraft resonances, but are otherwise in good agreement for frequencies less than or approximately equal to the second aircraft resonance and in fairly good agreement for frequencies less than the fourth aircraft resonance.

CONTENTS

<u>Section</u>	<u>Page</u>
I INTRODUCTION	344-5
II STICK MODEL PARAMETERS	344-7
III COMPARISON	344-9
IV CONCLUSION	344-21
REFERENCES	344-23

ILLUSTRATIONS

<u>Figure</u>	<u>Page</u>
1 Comparison of Measured Data for E-4 with Magnetostatic Solution.	344-11
2 Comparison of Measured Data for E-4 with Magnetostatic Solution.	344-12
3 Comparison of Total Current on E-4 Forward Fuselage.	344-13
4 Comparison of Current Density on E-4 Forward Fuselage (Top).	344-14
5 Comparison of Current Density on E-4 Forward Fuselage (Bottom).	344-15
6 Comparison of Measured Data for EC-135 with Magnetostatic Solution.	344-16
7 Comparison of Measured Data for EC-135 with Magnetostatic Solution.	344-17
8 Comparison of Total Current on EC-135 Forward Fuselage.	344-18
9 Comparison of Current Density on EC-135 Forward Fuselage (Top).	344-19
10 Comparison of Current Density on EC-135 Forward Fuselage (Bottom).	344-20

Table

<u>Page</u>	
1 STICK MODEL PARAMETERS	344-8

SECTION I

INTRODUCTION

The six-length stick model of an aircraft (refs. 1 and 2) provides a convenient method for obtaining the complex natural resonance frequencies and the natural current and charge modes on the aircraft surface, from which explicit expressions can be developed to predict the total current and total linear charge density at any position on the important aircraft sections, in either the frequency or time domain. In order to do this, it is necessary to ignore the detailed geometry of the aircraft surface and characterize the aircraft by its global length parameters, that is to say the lengths of the important aircraft sections and an overall average radius of curvature for the aircraft surface. Once the global parameters have been estimated for a particular aircraft, it is then a simple matter to predict the external coupling. The stick-model calculations assume that a linearly-polarized plane wave electromagnetic pulse (EMP), with the magnetic field along the wing axis, is incident on the aircraft in free space at some angle, θ , with respect to the fuselage. For this reason, comparisons of stick-model predictions with full scale measurements made at ground-based EMP simulators are inappropriate, since the presence of a finitely-conducting ground and other objects will change the electromagnetic characteristics of the aircraft surface. However, scale-model measurements made in the University of Michigan anechoic chamber closely simulate the same conditions that the stick-model calculations assume (refs. 3 and 4). For this reason, comparison with scale-model measurements is the best test of the accuracy of the six-length stick model.

The stick-model predictions do not give directly the current densities at the top and bottom of the aircraft sections, quantities which are measured in the scale-model experiments. On the other hand, the scale-model measurements do not give directly the total current, which is the quantity predicted by the stick model. To compare the results it is therefore necessary to invoke assumptions concerning the distribution of current around the circumference of an aircraft section, based on the magnetostatic solution

for an infinite cylinder. The validity of these assumptions can be tested using the scale-model measurements.

Because of time limitations, attention has been restricted to the current midway along the forward fuselage on the EC-135 and E-4 aircraft for $\theta = 90^\circ$ (topside) incidence. It will be seen that the agreement between calculation and measurement is good for frequencies less than or approximately equal to the second aircraft resonance frequency, and fairly good for frequencies as high as the fourth aircraft resonance frequency. Since the bulk of the energy in a typical EMP is contained in the frequency region below the second aircraft resonance, it is to be expected that the time-domain external coupling predictions based on the stick model will be accurate for all but the very earliest times. These concepts will be quantified in the discussion to follow.

SECTION II
STICK MODEL PARAMETERS

It is essential to choose the stick-model length parameters carefully so that the stick-model external coupling predictions will be as accurate as possible. As presented in references 1 and 2, there are seven length parameters in the stick model of an aircraft. The first six are the lengths of the important aircraft sections: the forward fuselage, the wings, the aft fuselage, the vertical stabilizer (bottom segment), the horizontal stabilizers, and the vertical stabilizer (top segment). On many aircraft, such as the E-4 and EC-135, the bottom segment of the vertical stabilizer has a length of zero, which simply means that the horizontal stabilizers are connected to the fuselage rather than to the vertical stabilizer. The seventh parameter, Ω , is a dimensionless quantity which is a measure of the overall radius of curvature of the aircraft surface. Since Ω depends logarithmically on the radius, it is not a critical parameter in the stick model. For most aircraft, $6 \leq \Omega \leq 7$. As $\Omega \rightarrow \infty$, the stick model becomes more accurate.

The forward fuselage length (ℓ_1) plus the aft fuselage length (ℓ_3) should be approximately the distance from just aft of the nose to the point where the vertical stabilizer joins the fuselage. The wing length (ℓ_2) is the distance from the wing root to the end of the wing, minus a few meters in case the wing has appreciable tapering. The vertical stabilizer lengths (ℓ_4 and ℓ_6) and the horizontal stabilizer length (ℓ_5) are measured from the fuselage or the junction of the vertical and horizontal stabilizers to the end of the stabilizer. Finally, the wing root must be located for the stick model, which is to say that ℓ_1 and ℓ_3 must be chosen with the constraint that $\ell_1 + \ell_3$ should remain constant. In general, increasing ℓ_1 will increase the (real) fundamental aircraft resonance frequency and decrease the (real) second aircraft resonance frequency. The exact choices for ℓ_1 through ℓ_6 are obviously somewhat arbitrary because a real aircraft is not a conjunction of very thin sticks, but a complicated structure which is only very approximately represented as thin sticks. In order to get the

best possible agreement between the stick-model predictions and the scale-model measurements, it would be desirable to make successive adjustments of ℓ_1 through ℓ_6 after comparison of the predictions with the measured data, although that was not done here.

Once the stick-model parameters are fixed, it is then a straightforward procedure to find the (complex) natural frequencies and then to estimate the total current at the same position on the forward fuselage that was used in the scale-model measurements. The mathematical details of this procedure are presented in references 1 and 2, and so will not be included here. Table 1 summarizes the stick-model parameters for the E-4 and EC-135 aircraft.

Table 1
STICK MODEL PARAMETERS

	E-4	EC-135
Forward Fuselage, ℓ_1	26 m	21 m
Wing, ℓ_2	29 m	17.5 m
Aft Fuselage, ℓ_3	27 m	14.5 m
Vertical Stabilizer (Bottom), ℓ_4	0 m	0 m
Horizontal Stabilizer, ℓ_5	11.5 m	7 m
Vertical Stabilizer (Top), ℓ_6	14 m	8.5 m
Ω	6.2	6.5
Fundamental Resonance	1.6 MHz	2.7 MHz
Second Resonance	2.8 MHz	3.8 MHz
Third Resonance	4.6 MHz	7.5 MHz
Fourth Resonance	5.7 MHz	9.3 MHz

SECTION III

COMPARISON

The stick model predicts the total axial current, I , while the scale-model measurements give the axial current density $J(\phi)$ as a function of position along the fuselage circumference ϕ . The point $\phi = 0$ corresponds to the top of the fuselage, $\phi = \pi$ to the bottom. In particular, the scale-model measurements give $J(0)$ and $J(\pi)$. It is therefore necessary to develop relationships between I and $J(\phi)$ in order to make comparisons.

Due to the symmetries of the aircraft and the exciting field, it is to be expected that the following series representation is generally valid:

$$J(\phi) = J_0 + \sum_{n=0}^{\infty} J_{2n+1} \cos[(2n+1)\phi] \quad (1)$$

Assuming that the fuselage is roughly a circular cylinder, a good estimate of the total current is given by

$$I = \int_0^{2\pi} J(\phi) a(\phi) d\phi \approx 2\pi a_{\text{eff}} J_0 \equiv I_{\text{est}} \quad (2)$$

where a_{eff} is the effective fuselage radius.

Using equation (1),

$$I_{\text{est}} = \pi a_{\text{eff}} [J(0) + J(\pi)] \quad (3)$$

In this way, the estimated total current, I_{est} , as measured for scale models can be compared with the total current predicted by the stick model.

A more restrictive assumption must be invoked to estimate the current density predicted by the stick model. If the magnetostatic circular cylinder solution is valid for the aircraft fuselage, then there is only one term in the infinite series of equation (1) which is non-zero:

$$J(\phi) = J_o + 2H_o \cos \phi \quad (4)$$

where H_o (E_o) is the strength of the incident magnetic (electric) field. In this case,

$$\Delta H \equiv [J(0) - J(\pi)] = 4H_o \quad (5)$$

Equation (5) can be checked against the scale-model data as a test of the magnetostatic assumption. As a direct consequence of equations (2) and (4),

$$J_{est}(0) = 2H_o + I/(2\pi a_{eff}) \quad (6)$$

$$J_{est}(\pi) = -2H_o + I/(2\pi a_{eff}) \quad (7)$$

In this way, the estimated top and bottom current densities, $J_{est}(0)$ and $J_{est}(\pi)$, as predicted by the stick model can be compared with the measured top and bottom current densities, $J(0)$ and $J(\pi)$.

Figures 1 through 5 use E-4 scale-model measurements which were made at the University of Michigan between August 1975 and March 1977 (ref. 3). The measurement location is STA600, roughly midway on the forward fuselage. The effective radius used for comparison is 3.5 meters. Figures 1 and 2 are tests of equation (5) in magnitude and phase. Figure 3 is a comparison of measured and predicted total current using equation (3), while figures 4 and 5 are comparisons of measured and predicted current density using equations (6) and (7).

Figures 6 through 10 are analogous to figures 1 through 5, using EC-135 scale-model measurements which were made at the University of Michigan in 1977 (ref. 3). The measurement location is STA550, again about midway on the forward fuselage. The effective radius is 2.1 meters. The EC-135 models were equipped with model high frequency (HF) antennas, which appreciably affected the measurements at STA550 only in a narrow frequency band near 3.5 MHz (full scale). The resonance region of the model HF antennas can be clearly seen in figures 6 through 10.

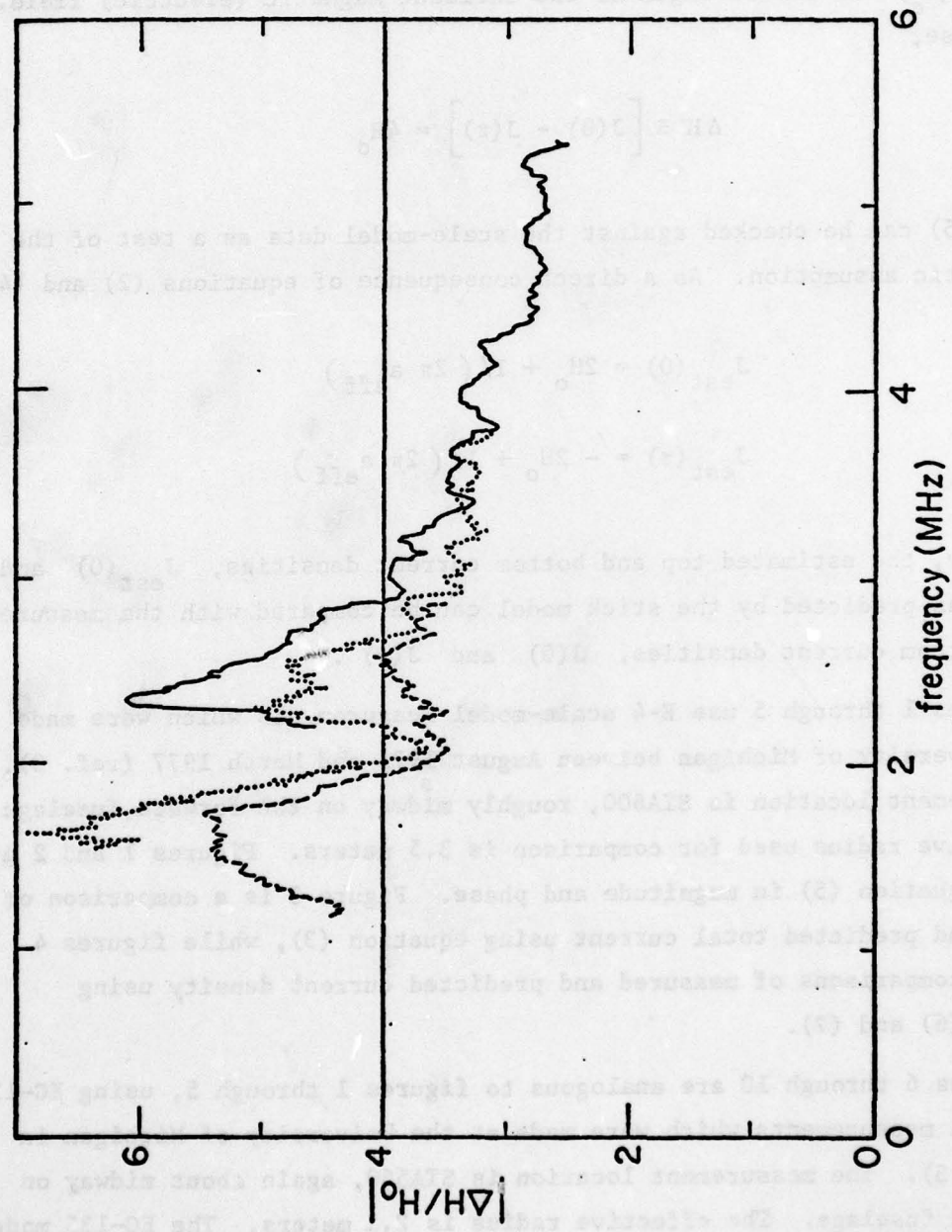


Figure 1. Comparison of Measured Data for E-4 with Magnetostatic Solution.

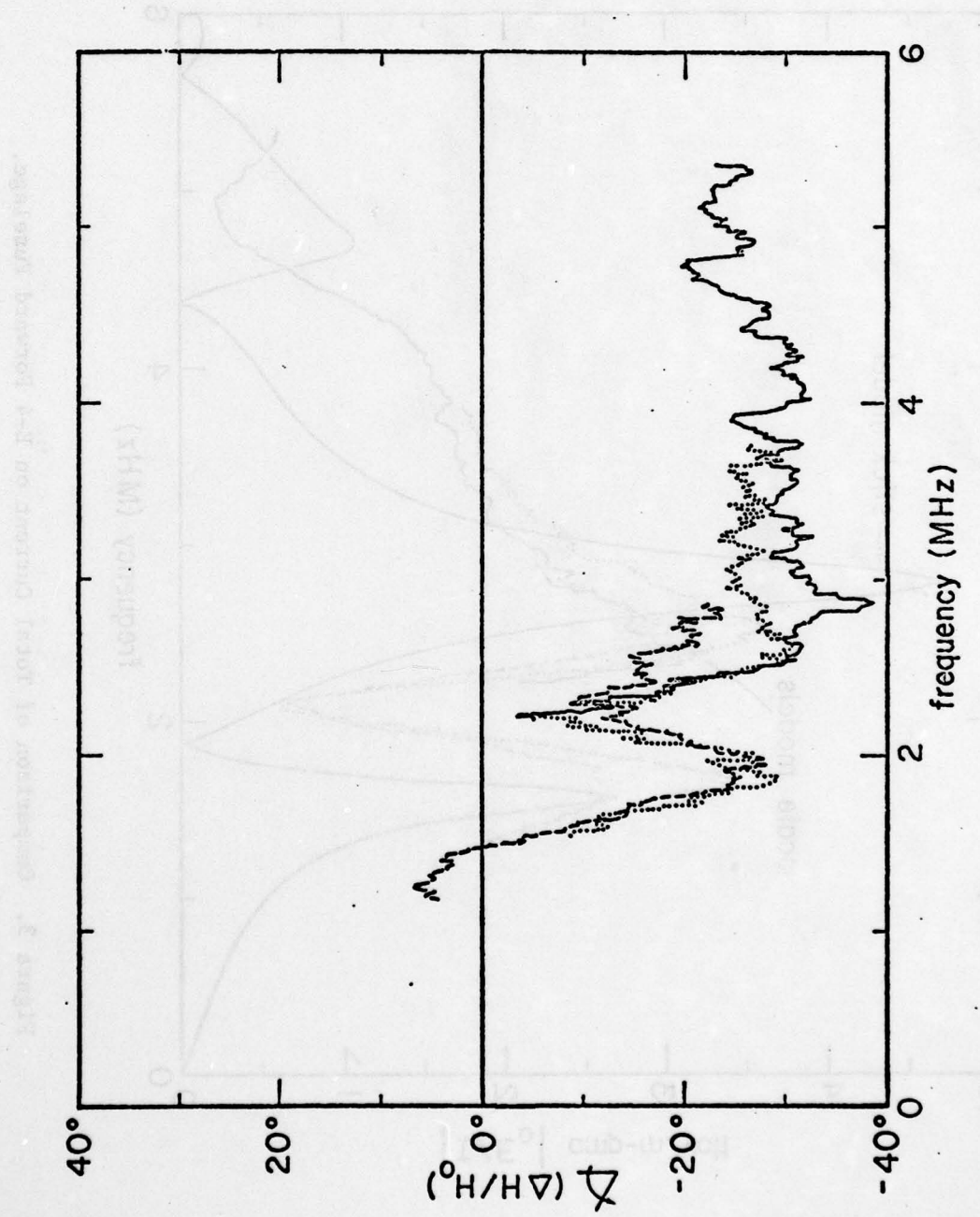


Figure 2. Comparison of Measured Data for E-4 with Magnetostatic Solution.

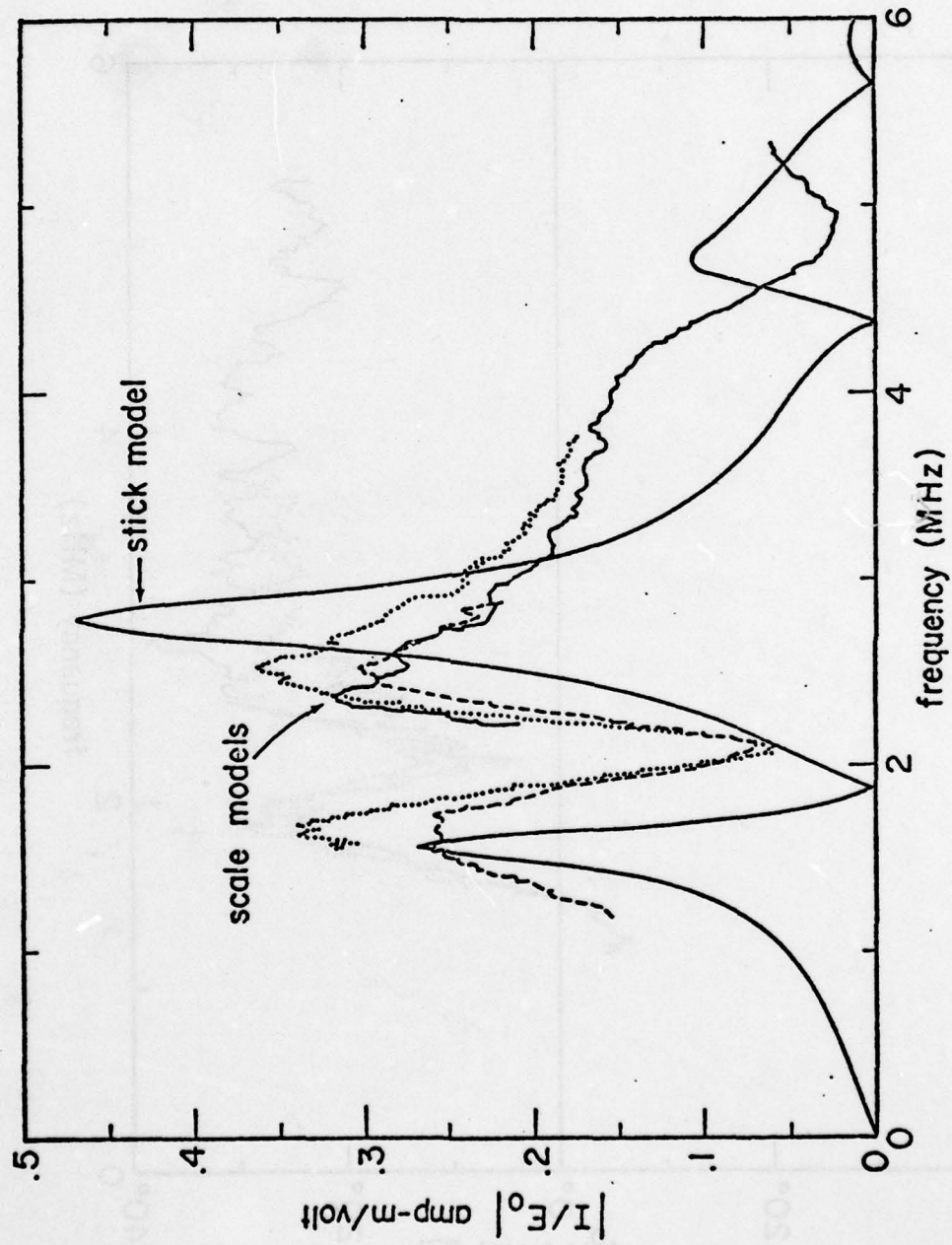


Figure 3. Comparison of Total Current on E-4 Forward Fuselage.

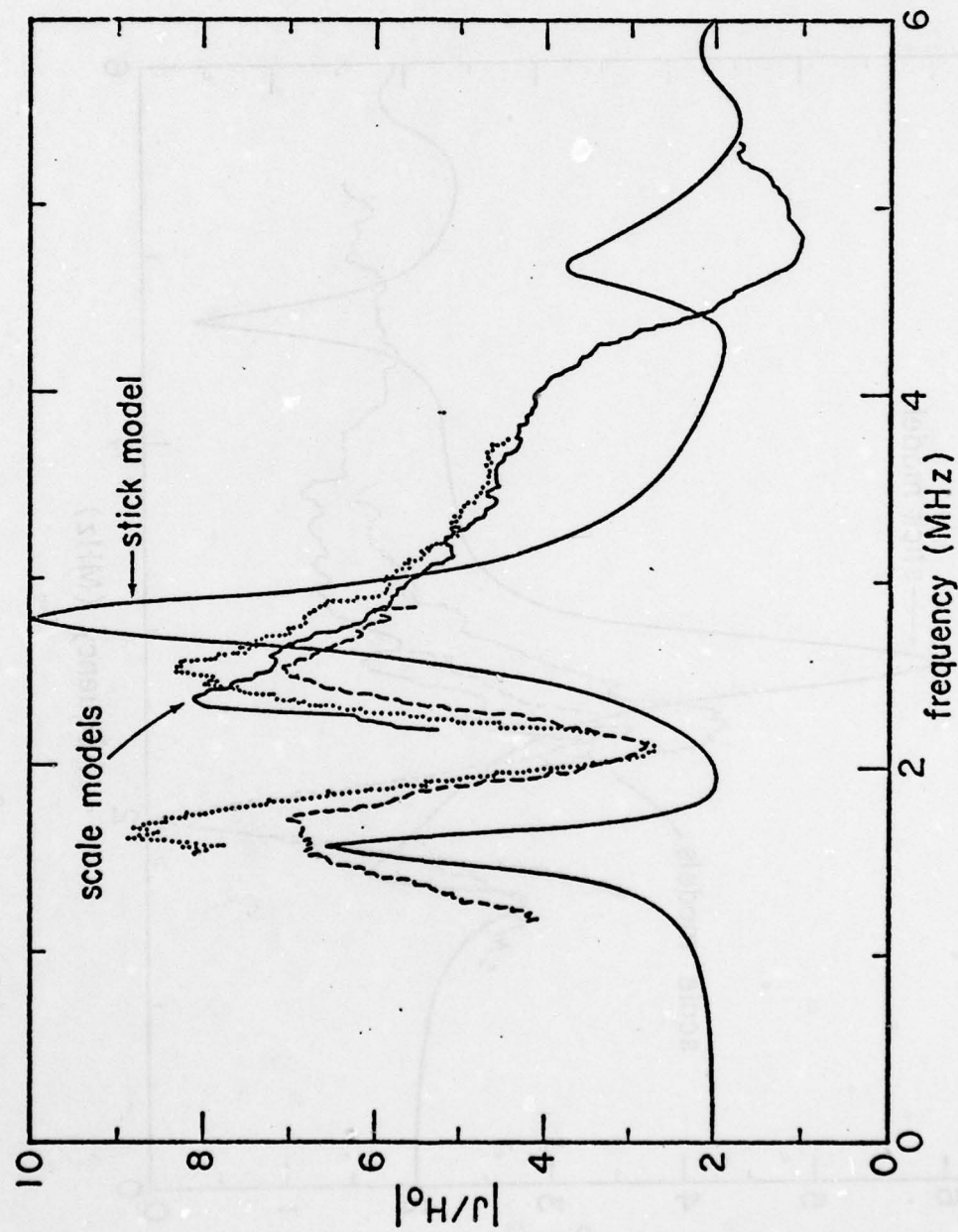


Figure 4. Comparison of Current Density on E-4 Forward Fuselage (Top).

AD-A073 770

AIR FORCE WEAPONS LAB KIRTLAND AFB NM
ELECTROMAGNETIC PULSE INTERACTION NOTES -- EMP 3-38. (U)

F/G 20/14

MAY 79 C E BAUM

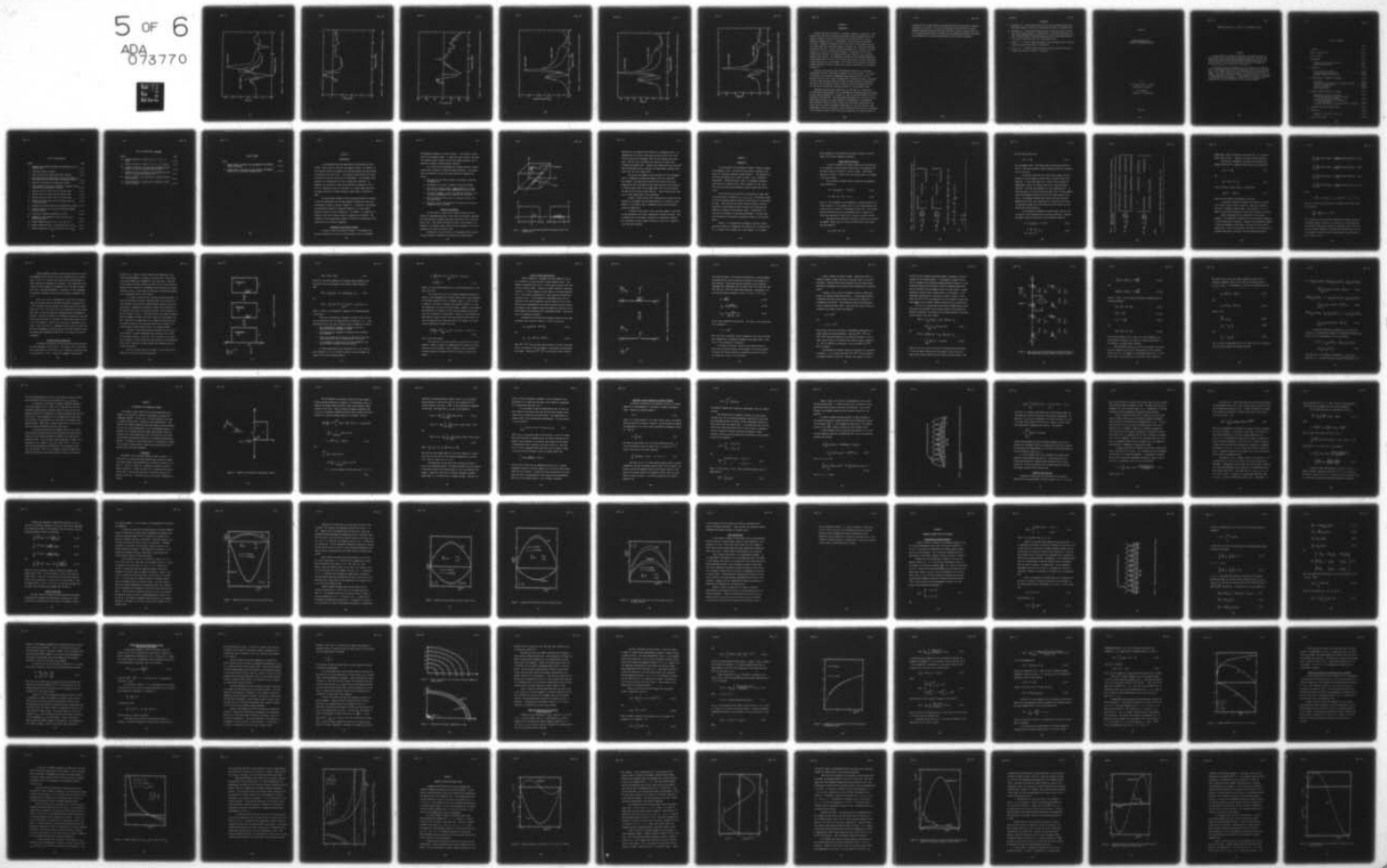
UNCLASSIFIED

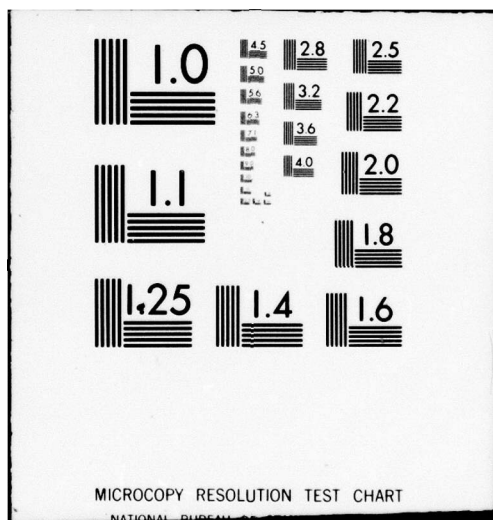
AFWL-TR-79-401

SBIE -AD-E200 329

NL

5 OF 6
ADA 093770





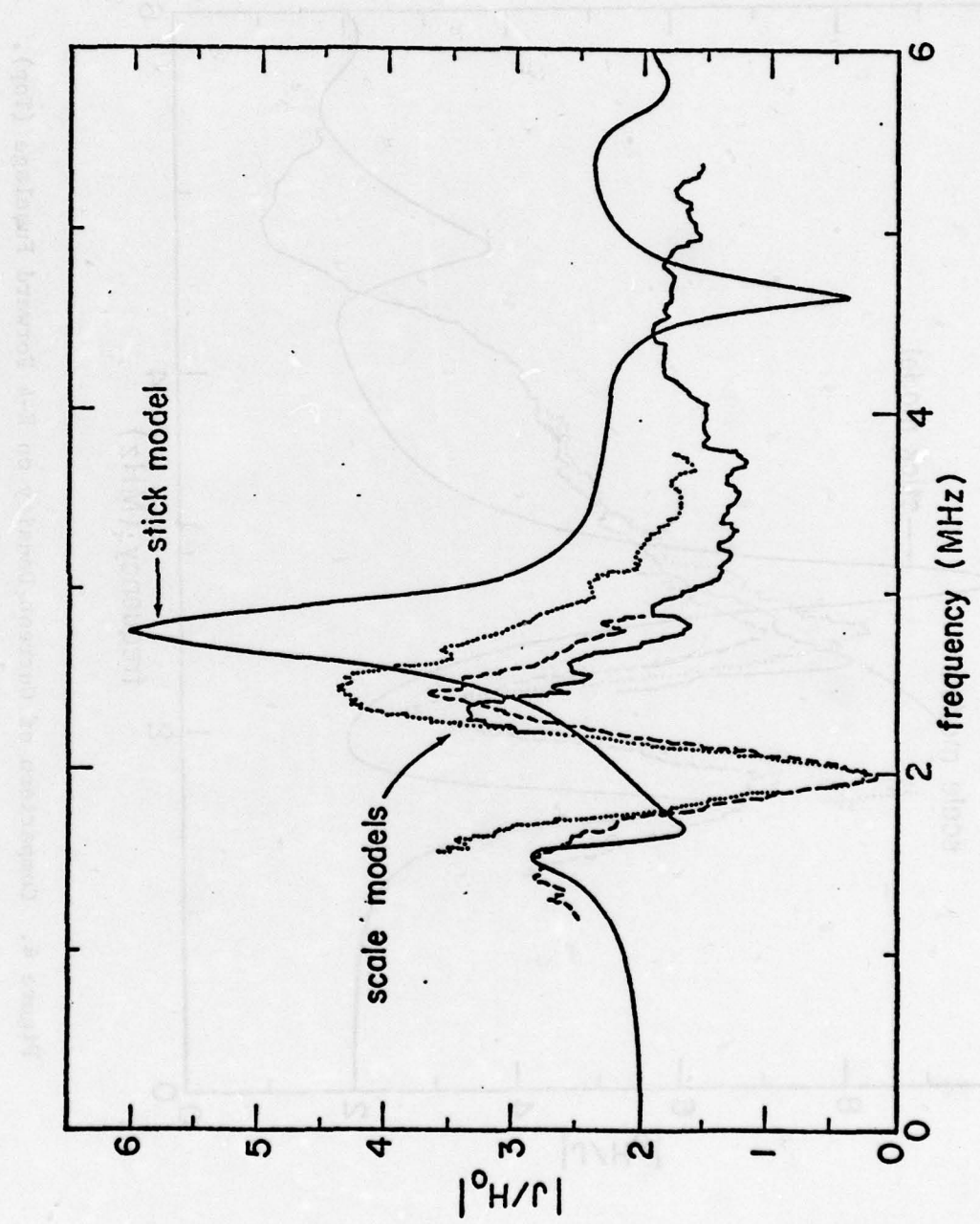


Figure 5. Comparison of Current Density on E-4 Forward Fuselage (Bottom).

344-16

EMP 3-38

Figure 6. Comparison of Measured Data for EC-135 with Magnetostatic Solution.

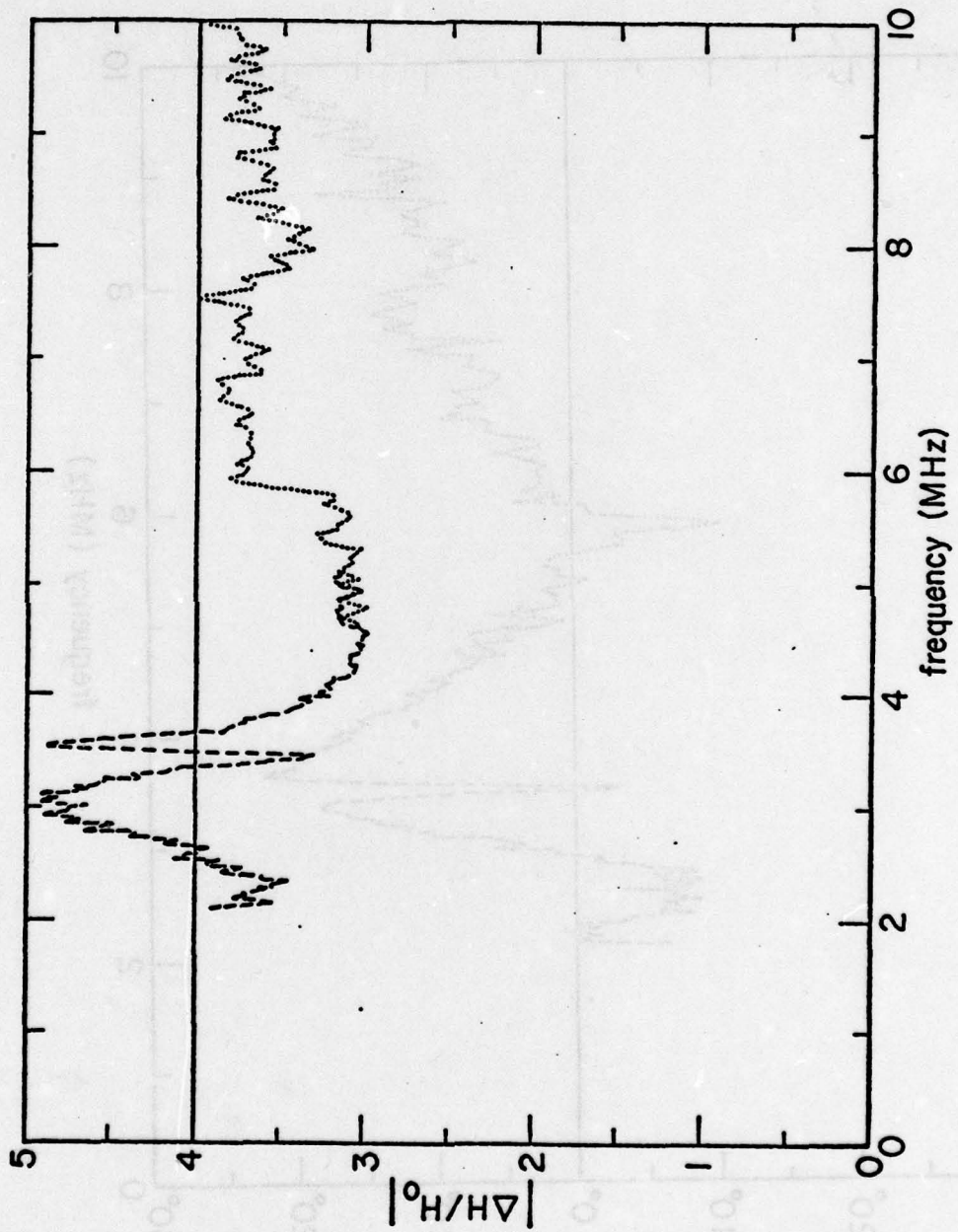


Figure 6. Comparison of Measured Data for EC-135 with Magnetostatic Solution.

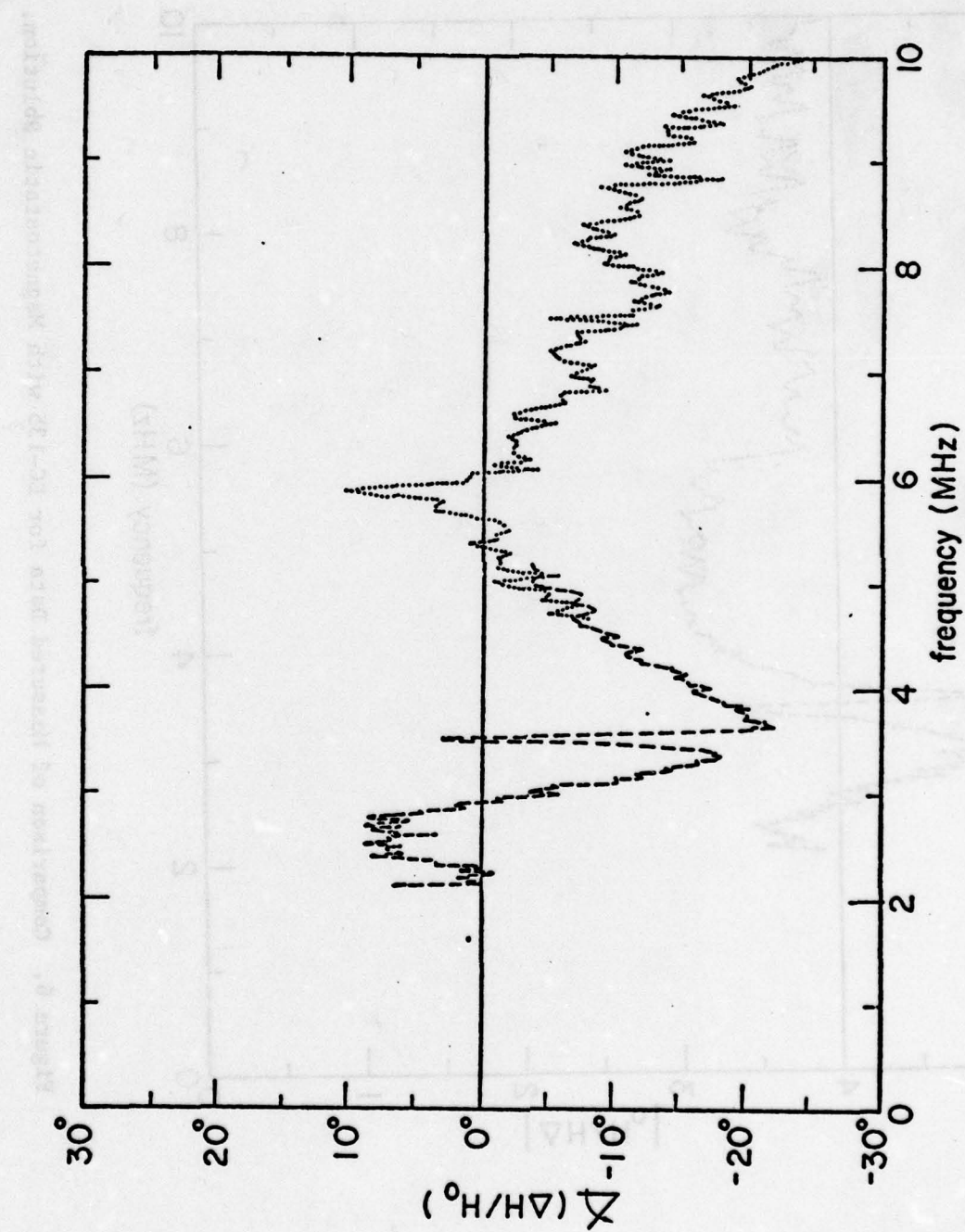
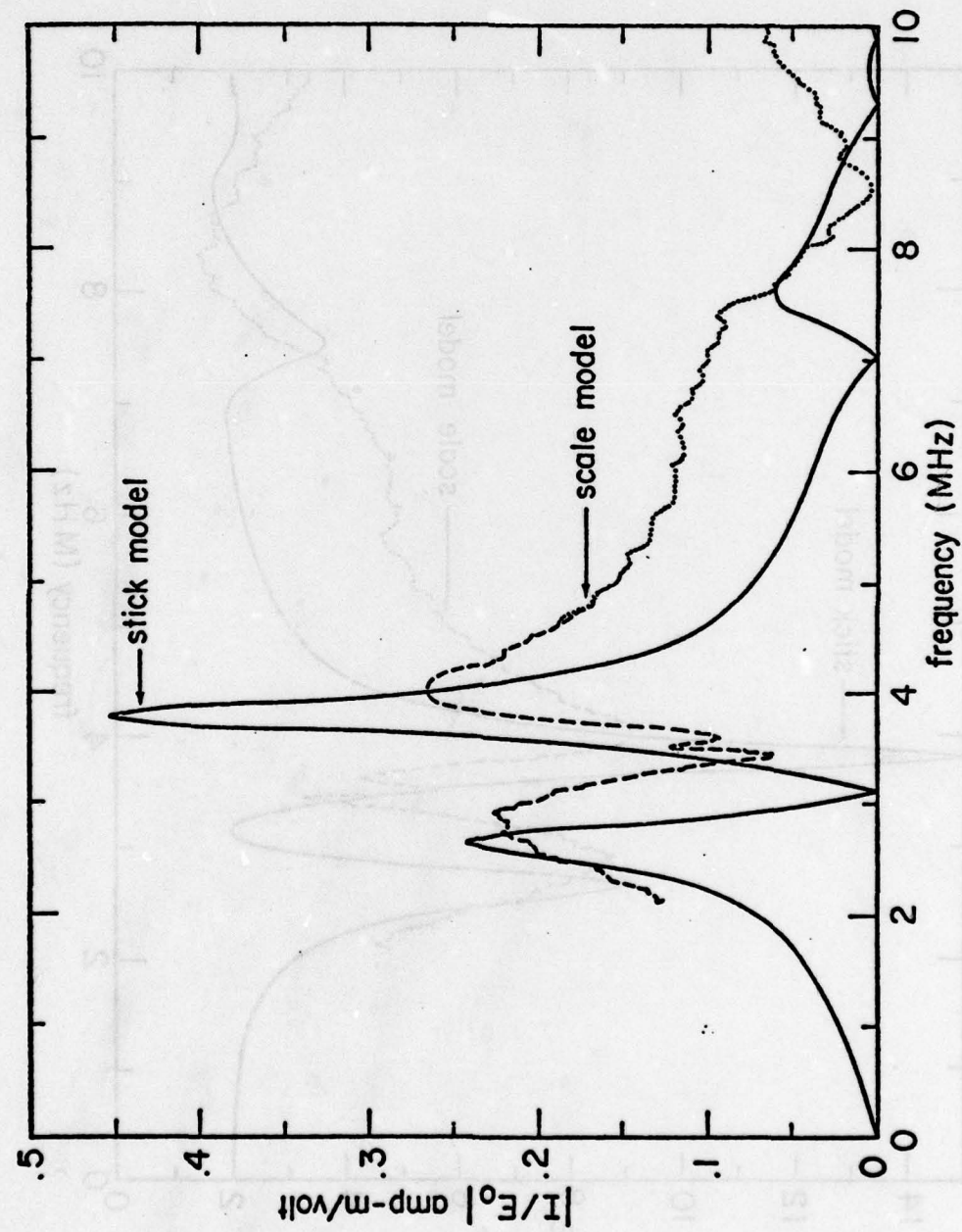


Figure 7. Comparison of Measured Data for EC-135 with Magnetostatic Solution.

Figure 8. Comparison of Currents (amp-m/Volt) on EC-135 Forward Fuselage.



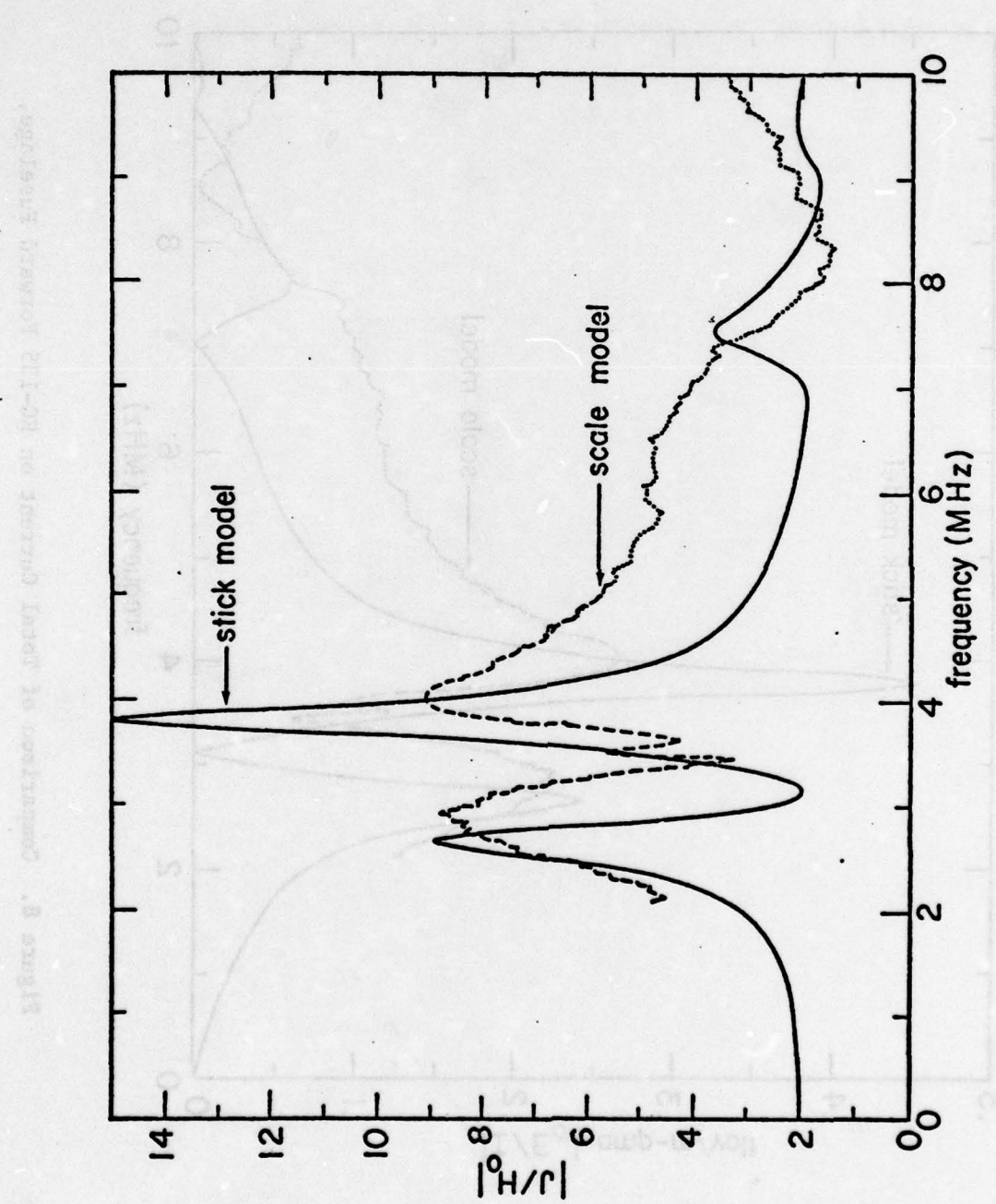


Figure 9. Comparison of Current Density on EC-135 Forward Fuselage (Top).

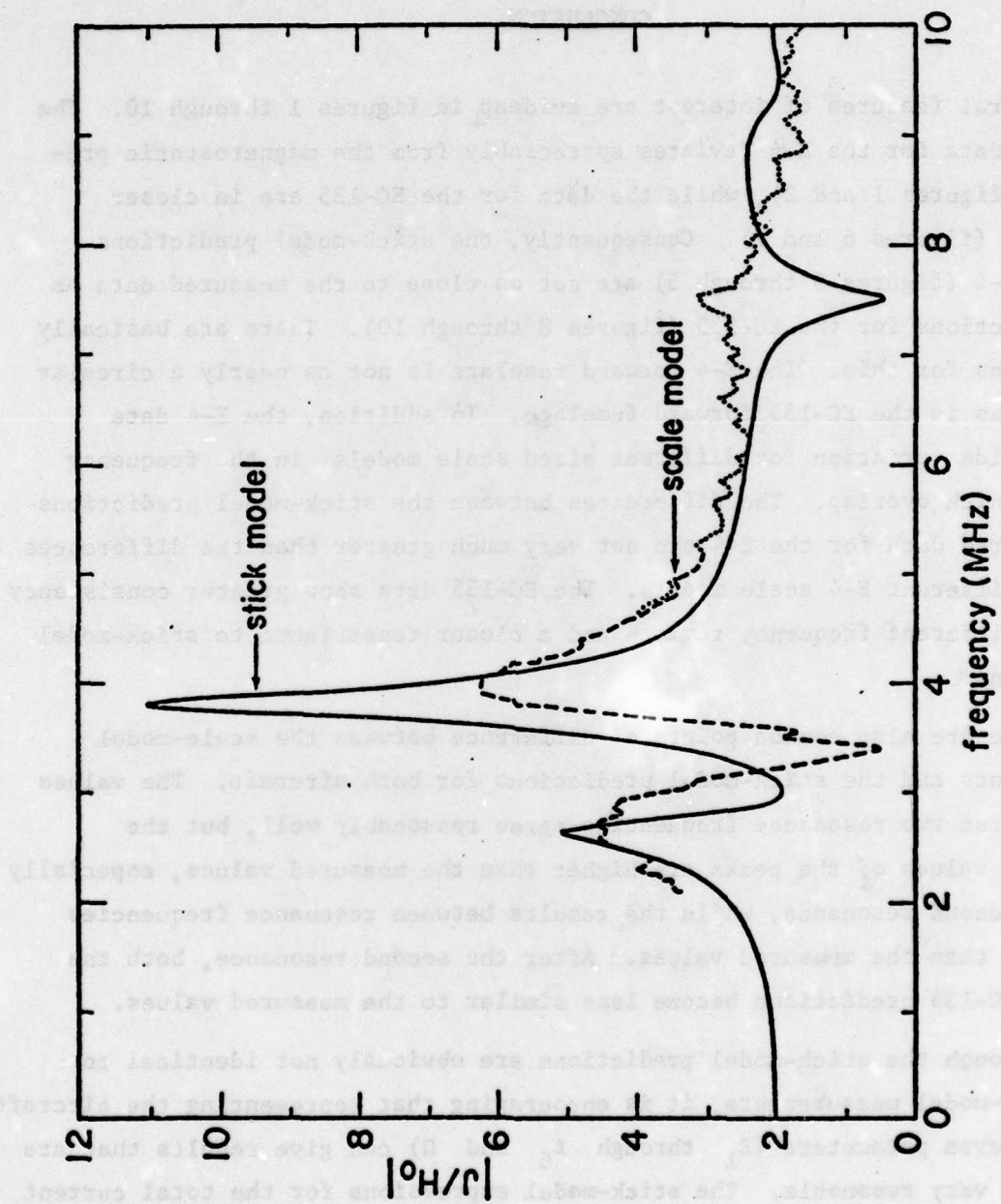


Figure 10. Comparison of Current Density on EC-135 Forward Fuselage (Bottom).

SECTION IV

CONCLUSION

Several features of interest are evident in figures 1 through 10. The measured data for the E-4 deviates appreciably from the magnetostatic prediction (figures 1 and 2), while the data for the EC-135 are in closer agreement (figures 6 and 7). Consequently, the stick-model predictions for the E-4 (figures 3 through 5) are not as close to the measured data as the predictions for the EC-135 (figures 8 through 10). There are basically two reasons for this. The E-4 forward fuselage is not as nearly a circular cylinder as is the EC-135 forward fuselage. In addition, the E-4 data exhibit wide variation for different sized scale models, in the frequency regions which overlap. The differences between the stick-model predictions and measured data for the E-4 are not very much greater than the differences between different E-4 scale models. The EC-135 data show greater consistency between different frequency regions and a closer resemblance to stick-model predictions.

There are also common points of difference between the scale-model measurements and the stick-model predictions for both aircraft. The values of the first two resonance frequencies agree reasonably well, but the predicted values of the peaks are higher than the measured values, especially for the second resonance, while the results between resonance frequencies are lower than the measured values. After the second resonance, both the E-4 and EC-135 predictions become less similar to the measured values.

Although the stick-model predictions are obviously not identical to the scale-model measurements, it is encouraging that representing the aircraft by only seven parameters (ℓ_1 through ℓ_6 and Ω) can give results that are generally very reasonable. The stick-model expressions for the total current (and charge density) are simple enough to be evaluated on a programmable desk calculator (which was done to obtain the stick-model predictions used here), and are readily transformed analytically to the time domain in case time-domain results are required. Since scale-model results are not available in the frequency region below 1 MHz, which constitutes an important part of

the spectrum of a typical EMP, the stick-model predictions provide a valuable supplement to the data. As long as the spectrum of the EMP does not have important components beyond the second aircraft resonance, which is the case for a typical EMP and typical aircraft, the time domain stick-model prediction can be expected to be a good approximation of the transient response.

REFERENCES

1. Bedrosian, G., "Stick Model Characterization of the Natural Frequencies and Natural Modes of Aircraft," Interaction Note 326, 14 September 1977
2. Bedrosian, G., "Stick Model Characterization of the Total Axial Current and Linear Charge Density on the Surface of an Aircraft Subjected to an EMP: Frequency-Domain External-Interaction Current and Charge Transfer Functions," Interaction Note 327, 13 September 1977
3. Liepa, V. V., "Surface Field Measurements on Scale Model EC-135 Aircraft," Interaction Application Memo 15, August 1977
4. Liepa, V. V., "Surface Field Measurements on Scale Model E-4 Aircraft," Interaction Application Memo 17, March 1977

NOTE 345

**APERTURE EXCITATION OF
A WIRE IN A RECTANGULAR CAVITY**

by

**D. B. Seidel and D. G. Dudley
University of Arizona**

**C. M. Butler
University of Mississippi**

June 1977

APERTURE EXCITATION OF A WIRE IN A RECTANGULAR CAVITY

ABSTRACT

In this work, the problem of determining the currents excited on a wire enclosed within a rectangular cavity is considered. The wire and cavity interior are excited by electromagnetic sources exterior to the cavity which couple to the cavity interior through a small aperture in the cavity wall. It is assumed that the wire is thin, straight and oriented perpendicular to one of the cavity walls.

An integral equation is formulated for the problem in the frequency domain using imaged dipole moments to approximate the effects of the aperture. This integral equation is then solved numerically by the method of moments. The dyadic Green's functions for this problem are difficult to compute numerically; consequently extensive numerical analysis is necessary to render the solution tractable. Sample numerical results are presented for representative configurations of cavity, wire and aperture, and suggestions for future extensions of this work are discussed.

TABLE OF CONTENTS

	Page
ABSTRACT	345-1
LIST OF ILLUSTRATIONS	345-3
LIST OF TABLES	345-5
1. INTRODUCTION	345-6
Modeling of the Physical Problem	345-6
Historical Background	345-7
2. FORMULATION	345-10
Dyadic Green's Functions	345-11
Integral Equation Formulation	345-17
Aperture Imaged Dipole Moments	345-22
3. A PRELIMINARY TWO-DIMENSIONAL PROBLEM	345-32
Formulation	345-32
Reduction to Matrix Equation by Method of Moments	345-37
Numerical Considerations	345-41
Sample Calculations	345-45
Final Observations	345-52
4. NUMERICAL METHODS FOR CAVITY PROBLEM	345-54
Approximation by Matrix Equation	345-54
An Efficient Method of Computing the Sums Outside the Source Region	345-60
Numerical Evaluation of the Integral of the Singular Sum	345-64
Numerical Evaluation of the Deleted Green's Functions .	345-72
5. NUMERICAL RESULTS FOR SAMPLE CASES	345-77
6. CONCLUSION	345-89
Suggested Extensions of this Work	345-90
LIST OF REFERENCES	345-92

LIST OF ILLUSTRATIONS

Figure	Page
1. Geometry for Aperture-Perforated Rectangular Cavity with Interior Wire	345-8
2. Equivalent Interior Problems	345-19
3. Small Aperture/Dipole Moment Equivalent Problems	345-23
4. Equivalent Interior Problem Which Accounts for Effects of Wall Reflections and Wire Currents on Aperture Dipoles	345-27
5. Geometry for Analogous Two-Dimensional Problem	345-33
6. Pulse Expansion Functions and Piecewise Sinusoidal Testing Functions for Two-Dimensional Problem	345-40
7. Aperture Field for Cavity with No Interior Wires	345-47
8. Aperture Field for Cavity with One Interior Wire	345-49
9. Aperture Field for Cavity with Two Interior Wires	345-50
10. Aperture Field for Cavity with One Interior Wire and .4λ Aperture Width	345-51
11. Expansion and Testing Functions for Unknown Wire Currents	345-56
12. Choice of Contours in m-n Plane for Efficient Summing of Double Series	345-63
13. Terms Used in Numerical Computation of Sums	345-63
14. Comparison of the Integrals of the Free Space Exact and Reduced Kernels	345-67
15. Example Computed Values of $\psi(z)$, $\psi_r(z)$ and $\psi_s(z)$	345-71
16. Example Computation for $G_{A_{zz}}$ and the Real Part of $\hat{G}_{A_{zz}}$	345-74
17. Example Computation of $g_{F_{yy}}$ and the Real Part of $\hat{g}_{F_{yy}}$	345-76

LIST OF ILLUSTRATIONS--Continued

Figure	Page
18. Currents Excited on $.2\lambda$ Wire for a $.2\lambda \times .25\lambda \times .3\lambda$ Cavity	345-78
19. Currents Excited on 1λ Wire in $.4\lambda \times .6\lambda \times 1.3\lambda$ Cavity	345-80
20. Currents Excited on $.5\lambda$ Wire for Slot Perpendicular and Parallel to <u>z</u> Directed Incident Electric Field	345-82
21. Currents Excited on $.5\lambda$ Wire for Slot Perpendicular and Parallel to <u>$-y$</u> Directed Electric Field	345-84
22. Current Excited on $.55\lambda$ Wire Which Is Attached to Cavity Wall at One End	345-86
23. Current Excited on $.8\lambda$ Wire Which Is Attached to Cavity Wall at Both Ends	345-87

LIST OF TABLES

Table	Page
1. Dyadic Green's Functions for the Magnetic and Electric Vector Potentials	345-12
2. Dyadic Green's Functions for the Electric and Magnetic Fields Due to an Electric Current Source	345-14

CHAPTER 1

INTRODUCTION

An investigation has been undertaken of the problem of a wire inside a cavity which is excited by an external source. The effects of this external source are coupled to the cavity interior and wire through an aperture in the cavity wall. The currents excited upon the wire and the fields within the cavity are to be determined. This boundary value problem is an idealization of a wire in some metal enclosure. As examples, the wire may be inside the shielding or housing of an electronic or mechanical unit on an aircraft, or it might simply pass from one metal partition to another through a region which is essentially empty.

This paper deals primarily with the problem formulation (Chapter 2) and the consideration of the many numerical difficulties which are encountered in obtain a solution (Chapter 4). In addition, an analogous two-dimensional problem is considered (Chapter 3) and some sample numerical results are given (Chapter 5). In Chapter 6, in addition to a summary of this work, several possible extensions are discussed. The remainder of this introductory chapter is devoted to the modeling of the problem and its historical background.

Modeling of the Physical Problem

In order to model the system of interest, a rectangular box having an aperture in a side wall and enclosing a wire is considered.

The appropriate geometry is shown in Figure 1. The problem is formulated in the frequency domain. It should be noted, however, that given the frequency domain solution, desired time domain quantities can be obtained by numerical inverse Fourier transform.

As is usual in the investigation of complex problems, simplifications must be invoked to render the problem tractable. The assumptions and conditions of the cavity/wire problem are summarized as follows:

1. The cavity is the interior region of a perfectly conducting rectangular box.
2. The material in the box is uniform, linear and isotropic.
3. The cavity is excited through a small aperture in a cavity wall such that aperture dipole approximations may be used.
4. The wire is straight, circular and perfectly conducting, and is oriented perpendicular to a side wall of the cavity.
5. The wire ends may or may not be in electrical contact with the cavity walls.
6. The wire is thin at the frequency of operation and thin-wire assumptions can be utilized.

Historical Background

In recent years, a great deal of work has been done on the problem of scattering from wires in free space and efficient techniques have been developed to handle them (Butler and Wilton 1975, Wilton and Butler 1976). More recently problems for which a wire couples to an aperture in an infinite planar screen have been considered (Butler and Umashankar 1976; Seidel and Butler 1976).

Historically, the work done on the rectangular cavity problem has been primarily concerned with formulating the dyadic Green's

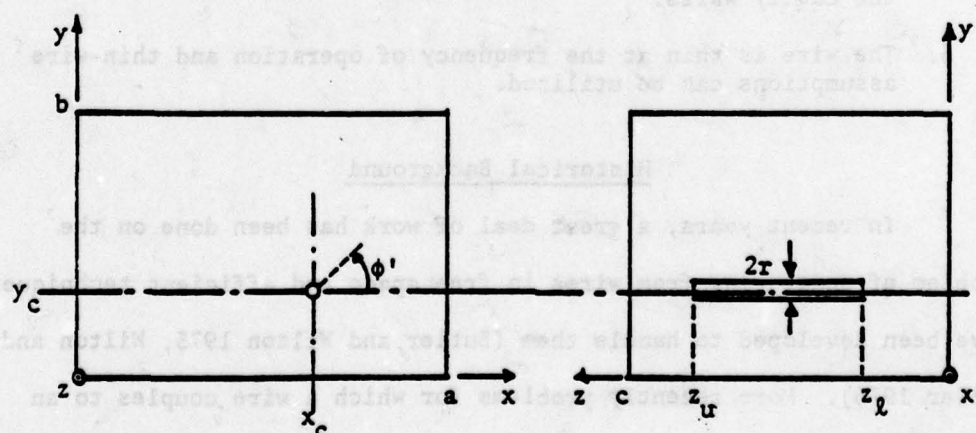
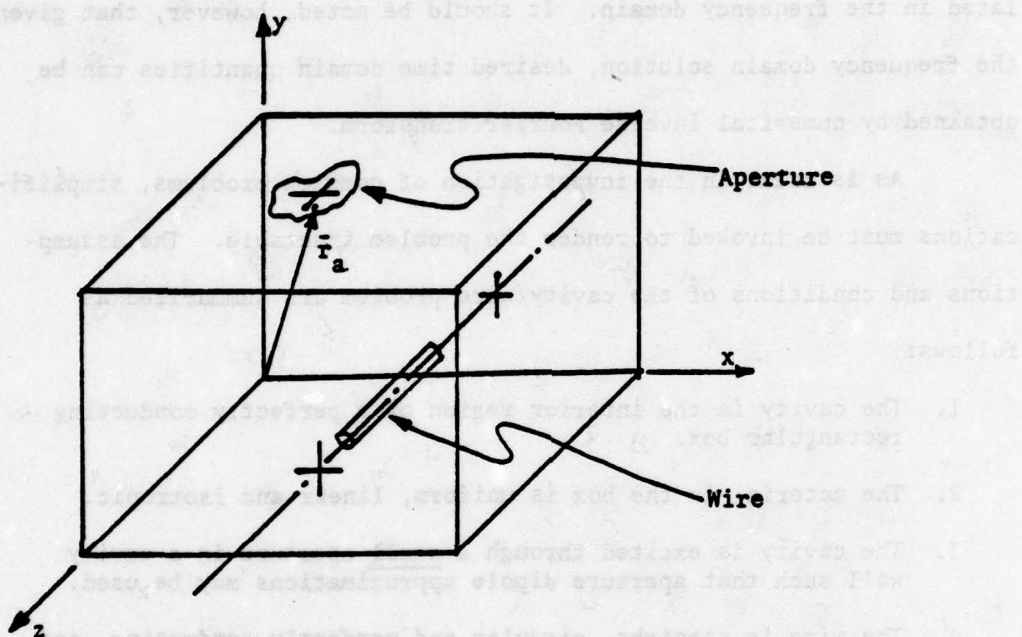


Figure 1. Geometry for Aperture-Perforated Rectangular Cavity with Interior Wire.

functions for the potentials and fields for a rectangular cavity. An expansion for the electric field dyad was found by Weyl (1913, 1915). It was pointed out by Teichmann (1952) that the expansion was incomplete. This was later corrected by the addition of another term (Teichmann and Wigner 1953). Several other authors have also shown that that the additional term is necessary for completeness (Kurokawa 1958; Collin 1973; Tai 1973; Howard 1974).

The dyad for the magnetic vector potential for the rectangular cavity is formulated in Morse and Feshbach (1953, pp. 1849-1851). More recently, this dyad and the dyad for the electric field were formulated by Tai and Rozenfeld (1976) using the vector wave functions \bar{L} , \bar{M} and \bar{N} (Hansen 1935) and by Rahmat-Samii (1975) who also derives the dyad for the electric vector potential. Both of these authors took care to insure completeness of the expansions.

Recently, Cheng and Chen (1975) formulated the solution for the problem of a rectangular cavity-backed aperture in an infinite screen. However, at the present time, no numerical data has been presented using this formulation.

It should be noted that at this time there appears to have been no work performed on the cavity containing an interior scatterer. This is probably due to the present uncertainty of computational methods for evaluating the dyadic Green's functions in the cavity, especially in or near source regions.

CHAPTER 2**FORMULATION**

For the purposes of this problem, consider a perfectly conducting rectangular cavity. One corner of this cavity is located at the origin of a cartesian coordinate system (Figure 1). The dimensions of the cavity are denoted by a , b and c in the x , y and z directions, respectively. Within this cavity, there is a perfectly conducting, round thin wire of radius r ($r \ll \lambda$) which is parallel to the z -axis. This wire may or may not be attached to either or both walls of the cavity.

One of the walls of the cavity is perforated by a small aperture whose center is located at $\bar{r}_a = (x_a, y_a, z_a)$. The exterior region to which the aperture couples the cavity interior may be of two different types. The cavity may be located behind an infinite, perfectly conducting, planar screen such that the cavity wall containing the aperture is a portion of the infinite screen. Alternatively, the cavity may be situated in a free space environment. In either case, the excitation for the problem is provided by sources in the exterior region.

Finally, it is assumed that the medium in both the interior and exterior regions is homogeneous and isotropic and is characterized by (ϵ, μ) where ϵ can be complex for a lossy medium. It is assumed

that the problem is time harmonic with angular frequency ω and the factor $e^{j\omega t}$ has been suppressed throughout.

Dyadic Green's Functions

In order to formulate an integral equation for this problem, it is necessary to know the Green's functions for the potentials and the fields within the interior, or cavity, region. These Green's functions are dyadic in nature and, as one would expect, are singular in the source region.

One can define the dyadic Green's function for the magnetic vector potential by

$$(\nabla^2 + k^2) \bar{G}_A(\bar{r}, \bar{r}') = - \bar{I} \delta(\bar{r} - \bar{r}'), \quad (2.1a)$$

$$\hat{n} \times (k^2 \bar{I} + \nabla \nabla) \cdot \bar{G}_A = 0 \text{ on } S \quad (2.1b)$$

where k is the wavenumber of the homogeneous, isotropic medium of the cavity interior, \bar{I} is the identity dyad, \hat{n} is an inward-directed unit normal vector on S where S is the surface of the cavity. This Green's dyad has been derived by Tai and Rozenfeld (1976) in terms of the vector wave functions \bar{L} , \bar{M} and \bar{N} and is shown as a matrix in Table 1.

Once \bar{G}_A has been determined, the Green's dyads for the electric and magnetic fields due to an electric current source can be found.

They are defined by

$$\bar{G}_e = (k^2 \bar{I} + \nabla \nabla) \cdot \bar{G}_A \quad (2.2)$$

Table 1. Dyadic Green's Functions for the Magnetic and Electric Vector Potentials.

$$\bar{G}_A = \frac{1}{abc} \sum_{m,n,l=0}^{\infty} \frac{\epsilon_m \epsilon_n \epsilon_l}{k_{mn\ell}^2 - k^2}$$

$$\left\{ \begin{array}{c} (cc)_x (ss)_y (ss)_z \\ 0 \\ (ss)_x (cc)_y (ss)_z \end{array} \right\}$$

$$\left\{ \begin{array}{c} 0 \\ 0 \\ (ss)_x (ss)_y (cc)_z \end{array} \right\}$$

$$\bar{g}_P = \frac{1}{abc} \sum_{m,n,\mu=0}^{\infty} \frac{\epsilon_m \epsilon_n \epsilon_\mu}{k_{mn\ell}^2 - k^2}$$

$$\left\{ \begin{array}{c} (ss)_x (cc)_y (cc)_z \\ 0 \\ (cc)_x (ss)_y (cc)_z \end{array} \right\}$$

$$\left\{ \begin{array}{c} 0 \\ 0 \\ (cc)_x (cc)_y (ss)_z \end{array} \right\}$$

where

$$(cc)_x (ss)_y (ss)_z = \cos k_x x' \cos k_y y' \sin k_z z' \sin k_y y' \sin k_z z' , \text{ etc.}$$

$$k_x = \frac{m\pi}{a}, \quad k_y = \frac{n\pi}{b}, \quad k_z = \frac{l\pi}{c}, \quad k_{mn\ell}^2 = k_x^2 + k_y^2 + k_z^2$$

and

$$\epsilon_i = \begin{cases} 1, & i=0 \\ 2, & i \neq 0 \end{cases}$$

for the electric field and

$$\bar{G}_h = \nabla \times \bar{G}_A \quad (2.3)$$

for the magnetic field. The matrix forms of \bar{G}_e and \bar{G}_h are given in Table 2. They were obtained by simply operating upon \bar{G}_A as prescribed by (2.2) and (2.3).

It should be noted that this result for \bar{G}_e agrees with that derived by Tai and Rozenfeld (1976) directly using the vector wave functions. It also would agree with a similar result obtained by Rahmat-Samii (1975) if an obvious sign error in that paper were corrected. Note that this agreement is a most important point. In these two papers, the authors have taken great care to insure completeness of the expansion functions for \bar{G}_e in the source region of the cavity. The agreement between their results and that given here demonstrates the fact that completeness is insured when the problem is formulated through use of the potentials and the fields are then derived from those potentials.

It now remains to determine the dyadic Green's function for the electric vector potential and its related field dyads. Consider the Green's dyad for the electric vector potential defined by

$$(\nabla^2 + k^2) \bar{g}_F(\bar{r}, \bar{r}') = - \bar{I} \delta(\bar{r} - \bar{r}') \quad (2.4a)$$

$$\left. \begin{array}{l} \hat{n} \cdot \bar{g}_F = 0 \\ \hat{n} \times \nabla \times \bar{g}_F = 0 \end{array} \right\}, \text{ on } S. \quad (2.4b)$$

Table 2. Dyadic Green's Functions for the Electric and Magnetic Fields Due to an Electric Current Source.

$$\bar{G}_e = \frac{1}{abc} \sum_{m,n,l=0}^{\infty} \frac{\epsilon_m \epsilon_n \epsilon_l}{k^2 m n l - k^2} \left\{ \begin{array}{l} (k^2 - k_x^2) (cc)_x (ss)_y (ss)_z - k_x k_y (cs)_x (sc)_y (ss)_z - k_x k_z (cs)_x (ss)_y (sc)_z \\ - k_x k_y (sc)_x (cs)_y (ss)_z (k^2 - k_y^2) (ss)_x (cc)_y (ss)_z - k_y k_z (ss)_x (cs)_y (sc)_z \\ - k_x k_z (sc)_x (ss)_y (cs)_z - k_y k_z (ss)_x (sc)_y (cs)_z (k^2 - k_z^2) (ss)_x (ss)_y (cc)_z \end{array} \right\}$$

$$\bar{G}_h = \frac{1}{abc} \sum_{m,n,l=0}^{\infty} \frac{\epsilon_m \epsilon_n \epsilon_l}{k^2 m n l - k^2} \left\{ \begin{array}{l} 0 \quad - k_z (ss)_x (cc)_y (cs)_z \quad k_y (ss)_x (cs)_y (cc)_z \\ k_z (cc)_x (ss)_y (cs)_z \quad 0 \quad - k_x (cs)_x (ss)_y (cc)_z \\ - k_y (cc)_x (ss)_z \quad k_x (cs)_x (cc)_y (ss)_z \quad 0 \end{array} \right\}$$

where

$$(cs)_x (ss)_y (sc)_z = \cos k_x x \sin k_x x' \sin k_y y \sin k_y y' \sin k_z z \cos k_z z' , \text{ etc.}$$

Rahmat-Samii (1975) has obtained a solution for \tilde{g}_F . It is given in matrix form in Table 1. Again the sign error has been corrected.

Now that \tilde{g}_F is determined, the dyads for the electric and magnetic fields due to a magnetic current source can be defined by

$$\tilde{g}_e = - \nabla \times \tilde{g}_F \quad (2.5)$$

and

$$\tilde{g}_h = (k^2 \tilde{I} + \nabla \nabla) \cdot \tilde{g}_F . \quad (2.6)$$

If \tilde{g}_e is written in matrix form, it is found that

$$\tilde{g}_e(\bar{r}, \bar{r}') = - \tilde{\mathbf{G}}_h(\bar{r}', \bar{r}) \quad (2.7)$$

where the tilde denotes the transpose of the dyad.

As a matter of notation, an upper case G denotes a dyad due to an electric current source; similarly a lower case g denotes a dyad due to a magnetic current source. The subscript A, F, e or h denotes the particular potential or field which is given by the dyad.

Before proceeding with the formulation of the integral equation, it is worthwhile to consider a few of the general properties of these dyadic Green's functions. Probably the most apparent property is that each component of each dyad is in itself a triply infinite Fourier sum. It can be seen, however, that any one of the sums can be performed analytically using one of the following relationships:

$$\sum_{m=1}^{\infty} \frac{1}{k_x^2 + \alpha^2} \text{sink}_x x \text{ sink}_{x'} x' = \frac{a}{2 \sinh \alpha a} \sinh \alpha x \sinh \alpha (a-x) \quad (2.8a)$$

$$\sum_{m=0}^{\infty} \frac{\epsilon_m}{k_x^2 + \alpha^2} \text{cosk}_x x \text{ cosk}_{x'} x' = \frac{a}{\alpha \sinh \alpha a} \cosh \alpha x \cosh \alpha (a-x) \quad (2.8b)$$

$$\sum_{m=1}^{\infty} \frac{k_x}{k_x^2 + \alpha^2} \text{cosk}_x x \langle \text{sink}_x x' \rangle = \frac{a}{2 \sinh \alpha a} \cosh \alpha x \sinh \alpha (a-x) \quad (2.8c)$$

$$\sum_{m=1}^{\infty} \frac{k_x}{k_x^2 + \alpha^2} \text{sink}_x x \langle \text{cosk}_x x' \rangle = \frac{-a}{2 \sinh \alpha a} \sinh \alpha x \cosh \alpha (a-x) \quad (2.8d)$$

where

$$k_x = \frac{m\pi}{a}, \quad x_< = \min(x, x'), \quad x_> = \max(x, x'), \quad 0 \leq x, x' \leq a.$$

Equations (2.8) are easily derived by considering the ordinary differential equation

$$\left(\frac{d^2}{dx^2} + k_x^2 \right) g(x, x') = \delta(x - x')$$

on the interval (0, a) with various combinations of unmixed Dirichlet and Neumann boundary conditions. The function g is then obtained by a closed form construction to obtain the right-hand side of (2.8) and also by a spectral expansion [to produce the left-hand side of (2.8)]. An alternative technique to derive these equations has been given by Collin (1960, p. 581).

Another important property of these triple sums can be seen if one remembers that both $\sinh x$ and $\cosh x$ approach $\pm \frac{1}{2} e^x$ for large x . Thus, if $|\bar{r}-\bar{r}'| \neq 0$, any one of the triple sums can be reduced to a double sum which is exponentially convergent. This demonstrates that outside the source region, all components of all the dyads converge, and in fact, converge exponentially. Therefore, all dyad components are uniformly convergent outside the source region (Titchmarsh 1939, p. 4).

Since it is valid to differentiate a series term by term provided the resulting series is uniformly convergent (Titchmarsh 1939, p. 37), the method used to construct the Green's dyads for the fields using (2.2), (2.3), (2.5) and (2.6) is valid outside the source region. This leads to the next observation regarding relative convergence of the sums. Note that the effect of a differential operator on each term of any one of the sums is to introduce a multiplicative factor of m , n , or ℓ in the numerator. This will slow the rate of convergence of the series. Thus, for $|\bar{r}-\bar{r}'| \neq 0$, components of $\bar{\bar{G}}_A$ and $\bar{\bar{g}}_F$ will exhibit the most rapid convergence, whereas $\bar{\bar{G}}_e$ and $\bar{\bar{g}}_h$, which are constructed using the second order differential operator $\nabla\nabla\cdot$, will exhibit the slowest convergence.

Integral Equation Formulation

To formulate the problem, one first uses the theories advanced for small apertures by Bethe (1944). This theory allows a small aperture, whose center is at the point \bar{r}_a , in a perfectly conducting screen to be replaced by imaged electric and magnetic dipole moments

located at \bar{r}_a . Figure 2 (a and b) depicts this equivalence. The electric dipole moment \bar{P}_e is normal to the cavity wall, and the magnetic dipole moment \bar{P}_m is tangential to the cavity wall. Note that now the aperture has been shorted, and thus one has in this equivalent problem a wire scatterer in a rectangular cavity excited by the dipole sources \bar{P}_e and \bar{P}_m . (A more precise definition of these dipole moments will be considered later in this chapter.)

It is useful to make use of yet another equivalent problem. By using the equivalence principle (Harrington 1961) one can replace the wire scatterer in the cavity by unknown surface currents \bar{J}_s which are located upon a mathematical cylindrical surface which coincides with the surface of the wire in the original problem. This equivalence is shown in Figure 2 (b and c). Now one must force the boundary condition that the tangential electric field must vanish on the cylindrical surface. When this is accomplished the two problems are equivalent and the surface currents in the equivalent problem will be equal to the surface currents induced upon the wire in the original problem.

Note that in this second equivalent problem one has a cavity whose interior is entirely homogeneous and isotropic, and is driven by the unknown sources \bar{J}_s , \bar{P}_e and \bar{P}_m . Thus the fields in the cavity may be obtained by simply taking the scalar products of the appropriate dyadic Green's functions and these sources and integrating over the volume of the cavity.

The total electric field at the point \bar{r} in the cavity can be broken into two parts in the following manner:

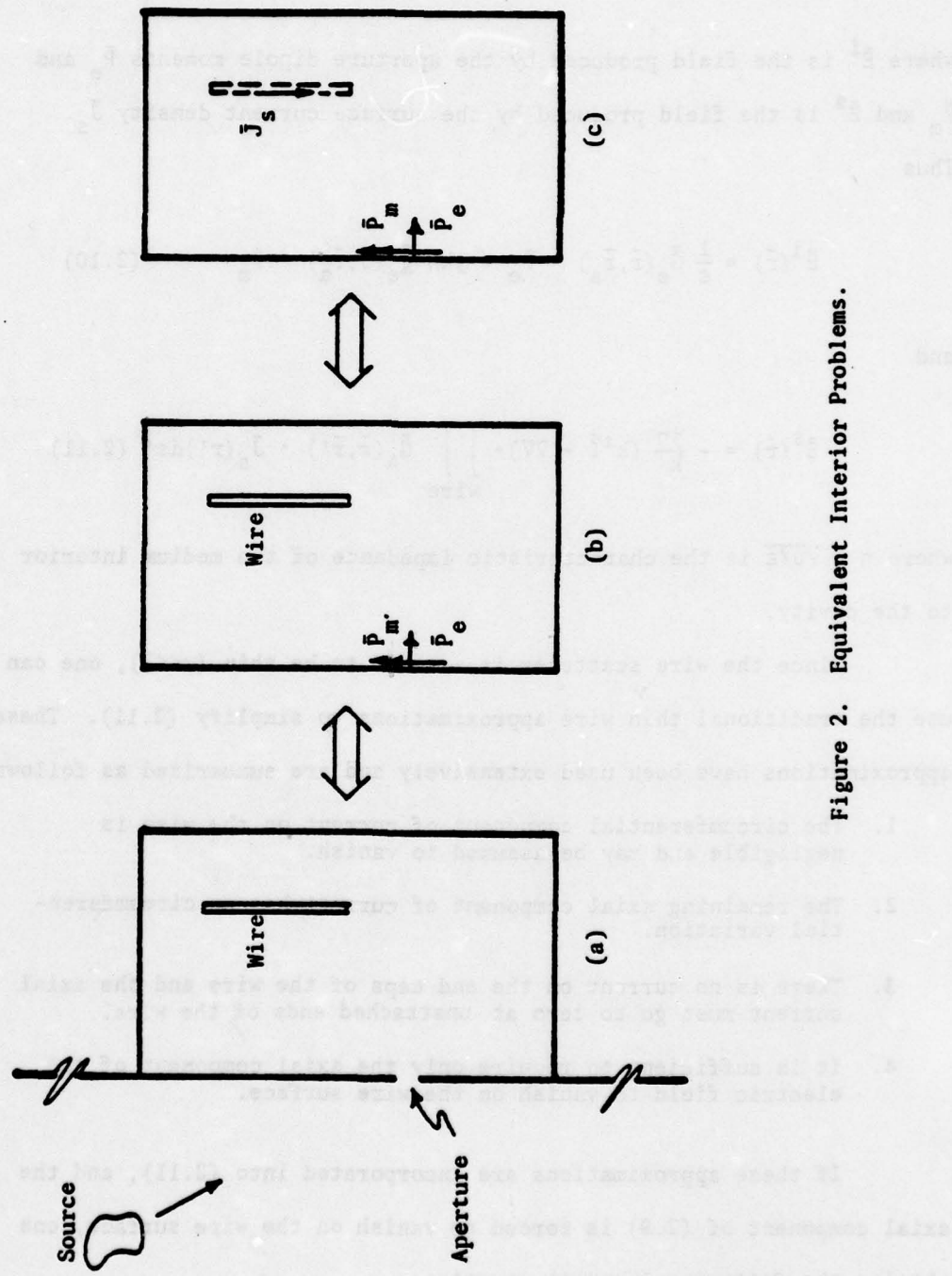


Figure 2. Equivalent Interior Problems.

$$\bar{E}(\bar{r}) = \bar{E}^i(\bar{r}) + \bar{E}^s(\bar{r}) \quad (2.9)$$

where \bar{E}^i is the field produced by the aperture dipole moments \bar{p}_e and \bar{p}_m and \bar{E}^s is the field produced by the surface current density \bar{J}_s .

Thus

$$\bar{E}^i(\bar{r}) = \frac{1}{\epsilon} \bar{G}_e(\bar{r}, \bar{r}_a) \cdot \bar{p}_e + jkn \bar{G}_e(\bar{r}, \bar{r}_a) \cdot \bar{p}_m \quad (2.10)$$

and

$$\bar{E}^s(\bar{r}) = - \frac{jn}{k} (k^2 I + \nabla V) \cdot \int \int_{\text{wire}} \bar{G}_A(\bar{r}, \bar{r}') \cdot \bar{J}_s(r') ds' \quad (2.11)$$

where $n = \sqrt{\mu/\epsilon}$ is the characteristic impedance of the medium interior to the cavity.

Since the wire scatterer is assumed to be thin ($r \ll \lambda$), one can use the traditional thin wire approximations to simplify (2.11). These approximations have been used extensively and are summarized as follows:

1. The circumferential component of current on the wire is negligible and may be assumed to vanish.
2. The remaining axial component of current has no circumferential variation.
3. There is no current on the end caps of the wire and the axial current must go to zero at unattached ends of the wire.
4. It is sufficient to require only the axial component of the electric field to vanish on the wire surface.

If these approximations are incorporated into (2.11), and the axial component of (2.9) is forced to vanish on the wire surface, one obtains the following integral equation:

$$\hat{w} \cdot \left[\frac{-jn}{k} (k^2 \mathbb{I} + \nabla \nabla) \cdot \int \int_{\text{wire}} G_A(\bar{r}, \bar{r}') \cdot \hat{w} J_w(\bar{r}') ds' + \bar{E}^i(\bar{r}) \right] = 0 \quad (2.12)$$

where \bar{r} is on the wire surface and \hat{w} is a unit vector parallel to the axis of the wire.

It is seen that (2.12) is an integro-differential equation in which all three components of the dyadic kernel and all nine components of the dyadic operator $\nabla \nabla$ will, in general, couple. As will be seen in Chapter 4, the Green's functions are extremely difficult to calculate numerically in or near the source region. Because of this problem, the feasibility of solving (2.12) for the most general case of arbitrary wire orientation is questionable. However, if one considers the case where \hat{w} is equal to one of the three cartesian unit vectors (let that unit vector be \hat{z} by convention) then (2.12) reduces to a scalar integro-differential equation as follows:

$$\frac{-jn}{k} \left(\frac{d^2}{dz^2} + k^2 \right) \int \int_{\text{wire}} G_{Azz}(\bar{r}, \bar{r}') J_z(z') ds' + \hat{z} \cdot \bar{E}^i(\bar{r}) = 0 \quad (2.13)$$

for \bar{r} on the wire surface.

Note that if (2.13) can be inverted, a solution for J_z will be obtained. However it should be remembered that \bar{E}^i contains \bar{p}_e and \bar{p}_m , which as of yet are unknown. Thus it remains to obtain additional constraints which will uniquely specify the values of these dipole moments.

Aperture Imaged Dipole Moments

Before attempting to determine the dipole moments \bar{P}_e and \bar{P}_m , it is necessary to review the basis of small aperture theory. This summary is patterned after that in a recent paper by Butler (1976) and the work of Collin (1960). Consider an infinite perfectly conducting screen at $z = 0$ which separates two half spaces of the same properties (μ, ϵ). This screen is perforated by a small aperture centered about the point $(0, 0, 0)$. If the aperture is sufficiently small and \bar{r} is sufficiently far from the aperture, then the fields at \bar{r} due to the aperture can be approximated by the radiation from an electric dipole with moment \bar{P}_e and a magnetic dipole with moment \bar{P}_m located at $(0, 0, 0)$ which radiate in the presence of the unperforated screen. This equivalence is illustrated in Figure 3.

The moments of the electric and magnetic dipoles for the right half-space ($z > 0$), which are located at $(0, 0, 0+)$ are given by

$$\bar{P}_e = \epsilon \alpha_e (E_z^{sc-}(\vec{\delta}) - E_z^{sc+}(\vec{\delta})) \hat{z} \quad (2.14a)$$

and

$$\bar{P}_m = -\bar{\alpha}_m \cdot (H^{sc-}(\vec{\delta}) - H^{sc+}(\vec{\delta})) \quad (2.14b)$$

where (E^{sc-}, H^{sc-}) are the short circuit fields in the left half-space, that is, the fields in left half-space in the presence of the unperforated screen. Similarly, (E^{sc+}, H^{sc+}) are the short circuit fields in

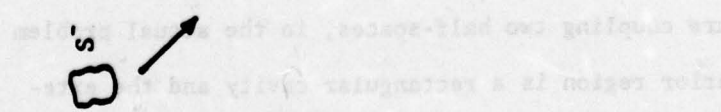
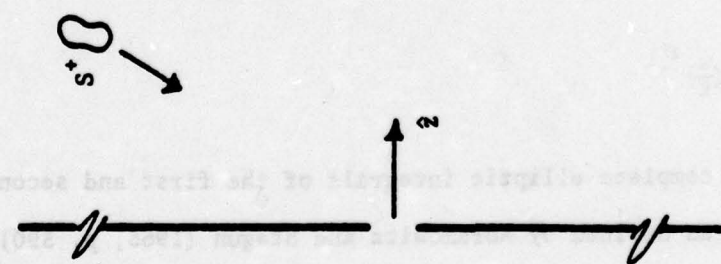
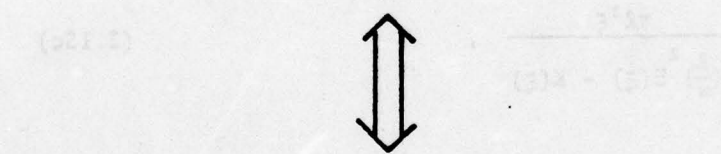
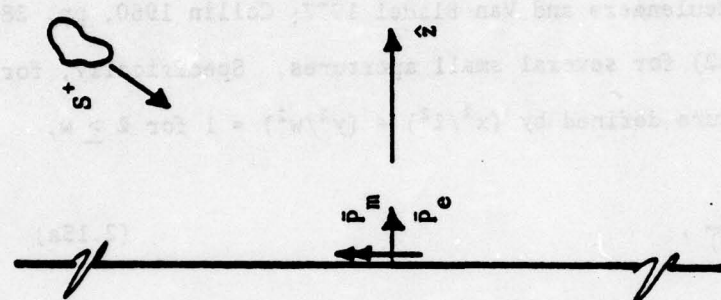


Figure 3. Small Aperture/Dipole Moment Equivalent Problems.

the right half-space. The electric polarizability α_e and the magnetic polarizability $\tilde{\alpha}_m$ relate the specific excitation to the moments for a given aperture. Polarizabilities are available in the literature (Bouwkamp 1954; DeMeulenaere and Van Bladel 1977; Collin 1960, pp. 285-302; Cohn 1951, 1952) for several small apertures. Specifically, for an elliptical aperture defined by $(x^2/l^2) + (y^2/w^2) = 1$ for $l \geq w$,

$$\alpha_e = \frac{\pi w^2 l}{3E(\xi)} , \quad (2.15a)$$

$$\alpha_{m_{xx}} = \frac{1}{3} \frac{\pi l^3 \xi}{K(\xi) - E(\xi)} , \quad (2.15b)$$

$$\alpha_{m_{yy}} = \frac{1}{3} \frac{\pi l^3 \xi}{\left(\frac{l}{w}\right)^2 E(\xi) - K(\xi)} , \quad (2.15c)$$

and all other components of $\tilde{\alpha}_m$ are zero. The square of the eccentricity (ξ) is defined by

$$\xi = 1 - \left(\frac{w}{l}\right)^2$$

and K and E are the complete elliptic integrals of the first and second kind, respectively, as defined by Abramowitz and Stegun (1965, p. 590), where ξ is the parameter of the modulus.

It should be noted that, where the small aperture theory is based upon an aperture coupling two half-spaces, in the actual problem of interest the interior region is a rectangular cavity and the exterior region may or may not be a half-space.

First, consider the exterior region. Suppose the cavity is behind an infinite screen, such that the exterior region is actually a half-space. Then the short circuit exterior fields are easily determined from a knowledge of the incident field by application of physical optics.

However, if the cavity is not behind a perfectly conducting screen, the problem becomes more difficult. It now becomes necessary to determine the short circuit fields on the exterior surface of a rectangular box scatterer. This problem has been solved numerically by Tsai, Dudley and Wilton (1974). Since the short circuit fields are related to the surface current and charge by

$$\bar{J}_s = \hat{n} \times \bar{H}^{sc-}$$

and

$$q_s = \epsilon \hat{n} \cdot \bar{E}^{sc-},$$

these values could also be provided by experimental measurements of surface charge and current densities. Note that $(\bar{E}^{sc-}, \bar{H}^{sc-})$ and $(\bar{E}^{sc+}, \bar{H}^{sc+})$ have been defined for the problem of interest to be the short circuit fields in the exterior and interior regions, respectively. For the remainder of this paper it will be assumed that $(\bar{E}^{sc-}, \bar{H}^{sc-})$ are known.

Now consider the interior region of the problem as illustrated in Figure 2c. It is readily seen that $(\bar{E}^{sc+}, \bar{H}^{sc+})$ will be driven by the surface currents on the wire. However, this region is a cavity,

and the use of yet another equivalent problem is necessary in order to account for this problem properly. If the method of images (Collin 1960) is applied to the equivalent problem depicted by Figure 2c, a new equivalent problem can be obtained in which the aperture dipoles and the wire currents have been imaged in such a way that there is a three-dimensional infinite array of image sources in a half-space. A two-dimensional cross-section of that array is given in Figure 4. This means that $(\hat{E}^{sc+}, \hat{H}^{sc+})$ are produced by all of the sources in that half-space except for the original aperture dipoles \bar{P}_e and \bar{P}_m located at \bar{r}_a .

Now if it is realized that these arrays of image sources in the half-space are equivalent to the original sources in the cavity (the problem of Figure 2c), one obtains the following relations for the short circuit fields in the cavity region:

$$\begin{aligned} E_n^{sc+}(\bar{r}) &= \hat{G}_{e_{nn}}(\bar{r}, \bar{r}_a) P_{e_n} + jk\hat{n} \cdot \hat{\mathbf{g}}_e(\bar{r}, \bar{r}_a) \cdot \bar{P}_m \\ &\quad - \frac{jn}{k} \int \int_{\text{wire}} G_{e_{nz}}(\bar{r}, \bar{r}') J_z(\bar{r}') ds' \end{aligned} \quad (2.16a)$$

and

$$\begin{aligned} \hat{H}^{sc+}(\bar{r}) &= \frac{jk}{n} \hat{\mathbf{g}}_h(\bar{r}, \bar{r}_a) \cdot \hat{n} P_{e_n} + \hat{\mathbf{g}}_h(\bar{r}, \bar{r}_a) \cdot \bar{P}_m \\ &\quad + \int \int_{\text{wire}} \hat{\mathbf{G}}_h(\bar{r}, \bar{r}') \cdot \hat{z} J_z(\bar{r}') ds' \end{aligned} \quad (2.16b)$$

where \hat{n} is the unit vector in the wall of the aperture and the symbol $(^*)$ over the dyads indicates that the original or self term of the image series (Green's function for half-space) has been deleted. Thus

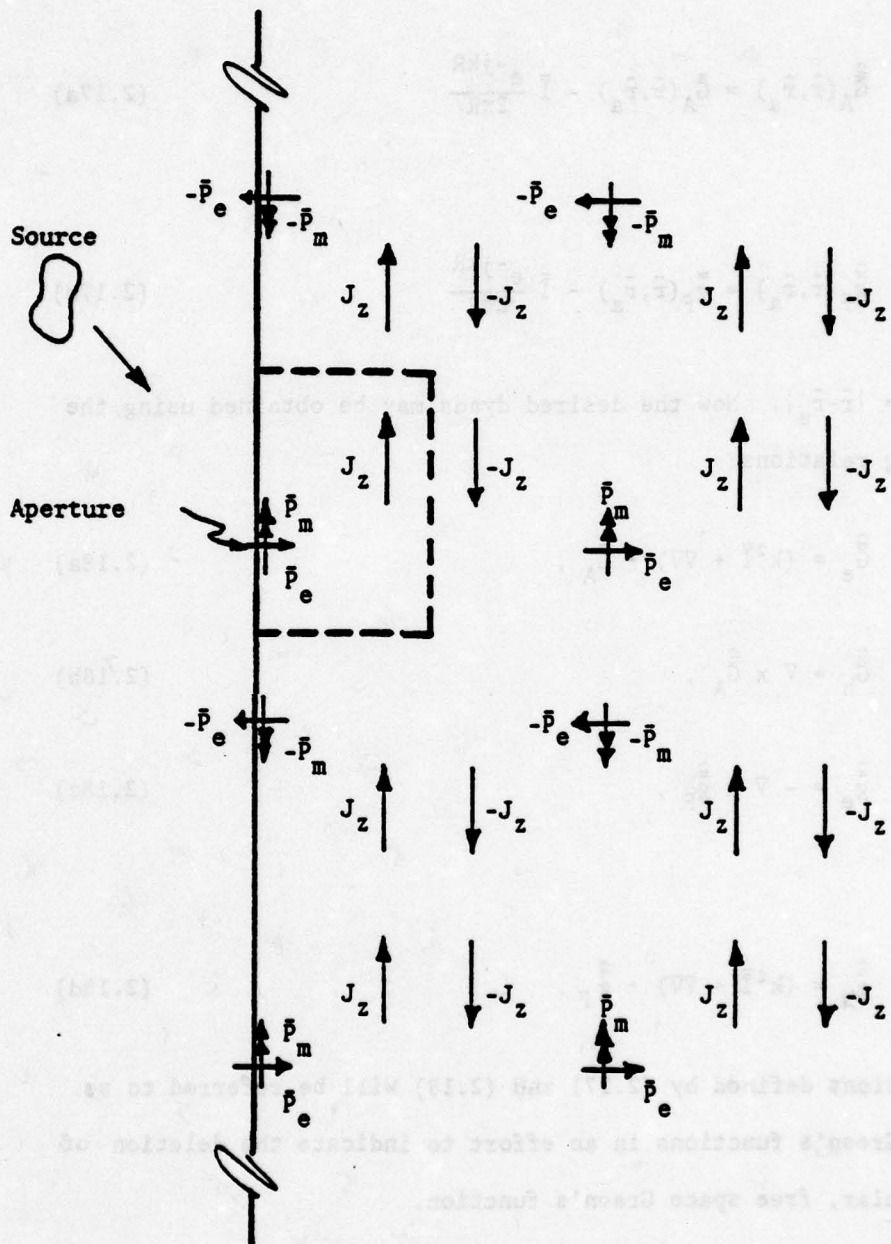


Figure 4. Equivalent Interior Problem Which Accounts for Effects of Wall Reflections and Wire Currents on Aperture Dipoles.

$$\hat{\mathbf{G}}_A(\bar{\mathbf{r}}, \bar{\mathbf{r}}_a) = \bar{\mathbf{G}}_A(\bar{\mathbf{r}}, \bar{\mathbf{r}}_a) - \bar{\mathbf{I}} \frac{e^{-jkR}}{2\pi R} \quad (2.17a)$$

and

$$\hat{\mathbf{g}}_F(\bar{\mathbf{r}}, \bar{\mathbf{r}}_a) = \bar{\mathbf{g}}_F(\bar{\mathbf{r}}, \bar{\mathbf{r}}_a) - \bar{\mathbf{I}} \frac{e^{-jkR}}{2\pi R} \quad (2.17b)$$

where $R = |\bar{\mathbf{r}} - \bar{\mathbf{r}}_a|$. Now the desired dyads may be obtained using the following relations:

$$\hat{\mathbf{G}}_e = (k^2 \bar{\mathbf{I}} + \nabla \nabla) \cdot \hat{\mathbf{G}}_A , \quad (2.18a)$$

$$\hat{\mathbf{G}}_h = \nabla \times \hat{\mathbf{G}}_A , \quad (2.18b)$$

$$\hat{\mathbf{g}}_e = - \nabla \times \hat{\mathbf{g}}_F , \quad (2.18c)$$

and

$$\hat{\mathbf{g}}_h = (k^2 \bar{\mathbf{I}} + \nabla \nabla) \cdot \hat{\mathbf{g}}_F . \quad (2.18d)$$

The functions defined by (2.17) and (2.18) will be referred to as deleted Green's functions in an effort to indicate the deletion of the singular, free space Green's function.

One now defines $\hat{\mathbf{a}}_1$ and $\hat{\mathbf{a}}_2$ to be the two cartesian unit vectors which are tangential to the wall of the aperture in such a fashion that $\hat{\mathbf{a}}_1 \times \hat{\mathbf{a}}_2 = \hat{\mathbf{n}}$. For example, if the aperture were in the $y = 0$ wall of the cavity, then $\hat{\mathbf{a}}_1$ would be $\hat{\mathbf{z}}$, $\hat{\mathbf{a}}_2$ would be $\hat{\mathbf{x}}$ and $\hat{\mathbf{n}}$ would be $\hat{\mathbf{y}}$.

Note that since \bar{P}_e has only a normal component and \bar{P}_m has only a tangential component, there are only three non-vanishing unknowns:

P_{e_n} , P_{m_1} and P_{m_2} . If new unknowns E_{T_n} and \bar{H}_T are introduced such that

$$E_{T_n} = E_n^{sc-}(\bar{r}_a) - E_n^{sc+}(\bar{r}_a) \quad (2.19a)$$

and

$$\bar{H}_T = \bar{H}^{sc-}(\bar{r}_a) - \bar{H}^{sc+}(\bar{r}_a) \quad (2.19b)$$

then by (2.14)

$$\frac{P_e}{\epsilon} = \alpha_e E_{T_n}, \quad (2.20a)$$

$$P_{m_1} = -\alpha_{m_{11}} H_{T_1} \quad (2.20b)$$

and

$$P_{m_2} = -\alpha_{m_{22}} H_{T_2}. \quad (2.20c)$$

Now, if (2.20) is substituted into (2.16), which in turn is substituted into (2.19) one obtains the following equations:

$$[1 + \alpha_e \hat{G}_{e_{nn}}(\bar{r}_a, \bar{r}_a)] E_{T_n} - jk\eta [\alpha_{m_{11}} \hat{g}_{e_{n1}}(\bar{r}_a, \bar{r}_a) H_{T_1} + \alpha_{m_{22}} \hat{g}_{e_{n2}}(\bar{r}_a, \bar{r}_a) H_{T_2}]$$

$$- \frac{j\eta}{k} \int \int_{\text{wire}} G_{e_{nz}}(\bar{r}_a, \bar{r}') J_z(\bar{r}') ds' = E_n^{\text{sc-}}(\bar{r}_a) , \quad (2.21a)$$

$$\frac{jk}{\eta} \alpha_e \hat{G}_{h_{1n}}(\bar{r}_a, \bar{r}_a) E_{T_n} + [1 - \alpha_{m_{11}} \hat{g}_{h_{11}}(\bar{r}_a, \bar{r}_a)] H_{T_1} - \alpha_{m_{22}} \hat{g}_{h_{12}}(\bar{r}_a, \bar{r}_a) H_{T_2}$$

$$+ \int \int_{\text{wire}} G_{h_{1z}}(\bar{r}_a, \bar{r}') J_z(\bar{r}') ds' = H_1^{\text{sc-}}(\bar{r}_a) , \quad (2.21b)$$

$$\frac{jk}{\eta} \alpha_e \hat{G}_{h_{2n}}(\bar{r}_a, \bar{r}_a) E_{T_n} - \alpha_{m_{11}} \hat{g}_{h_{21}}(\bar{r}_a, \bar{r}_a) H_{T_1} + [1 - \alpha_{m_{22}} \hat{g}_{h_{22}}(\bar{r}_a, \bar{r}_a)] H_{T_2}$$

$$+ \int \int_{\text{wire}} G_{h_{2z}}(\bar{r}_a, \bar{r}') J_z(\bar{r}') ds' = H_2^{\text{sc-}}(\bar{r}_a) . \quad (2.21c)$$

It should be noted that the unknowns E_{T_n} , H_{T_1} and H_{T_2} are related to the unknown dipole moments by the aperture polarizabilities.

Thus if (2.20) is substituted into (2.10) one obtains

$$\begin{aligned} \hat{z} \cdot \vec{E}^i(r) &= \alpha_e G_{e_{zn}}(\bar{r}, \bar{r}_a) E_{T_1} - jk\eta \alpha_{m_{11}} g_{e_{z1}}(\bar{r}, \bar{r}_a) H_{T_1} \\ &\quad - jk\eta \alpha_{m_{22}} g_{e_{z2}}(\bar{r}, \bar{r}_a) H_{T_2} \end{aligned} \quad (2.22)$$

This means that (2.13) contains the unknowns E_{T_n} , H_{T_1} and H_{T_2} in addition to J_z . The three additional constraints provided by (2.21)

when solved simultaneously with (2.13) will provide a unique solution for the currents on the wire and the quantities E_{T_n} , H_{T_1} and H_{T_2} .

It is helpful at this point to attempt to describe physically the various terms in (2.21). First, it is noted that the terms containing the deleted Green's functions account for the fact that the aperture dipoles will be affected by the fields reflected back from the cavity walls. This is apparent if it is remembered that these terms are the fields in the aperture due to the array of the images of the aperture dipole. These virtual sources account for all of the reflections and multiple reflections from the cavity walls.

It can also be noted that the integral term in (2.21) represents the field scattered back into the aperture by the wire and thus accounts for the coupling between the currents on the wire and the aperture dipoles. If all of these coupling effects are assumed to be negligible, (2.21) reduces to $(E_{T_n}, \bar{H}_T) = (E_n^{SC-}, \bar{H}_n^{SC-})$. If on the other hand these effects are not neglected, the difference between (E_{T_n}, \bar{H}_T) and $(E_n^{SC-}, \bar{H}_n^{SC-})$ will in some way reflect the degree to which the cavity walls and the wire scatterer couple to the aperture.

CHAPTER 3

A PRELIMINARY TWO-DIMENSIONAL PROBLEM

In an effort to gain insight for the three-dimensional cavity problem, it is helpful to consider an approximately analogous two-dimensional problem. For this case, the kernel functions would also be singular Fourier series, although of lower dimensionality. Thus where in the original problem the sums were doubly and triply-infinite, they are one- and two-dimensional in this two-dimensional analog. In addition to any insights which this effort might provide toward the solution of the three-dimensional cavity, the solution to this analogous problem may provide data pertinent to the physical problem being modeled. For example, in this simpler model, it is feasible to account for the actual coupling through a large aperture rather than use the aperture dipoles for small apertures.

Formulation

The geometry of the analogous problem is shown in Figure 5. It consists of an incident plane wave impinging upon a perfectly conducting infinite planar screen perforated by an infinite z-directed slot of width d . The slot is backed by a rectangular cylindrical cavity of depth a and width b . Within the cavity are L z-directed thin wires of various radii. The incident plane wave is polarized such that \bar{E} is parallel to the slot. Thus only the E_z , H_x and H_y field components are excited.

Explain how field and force readings will be affected when and where the "E" probe is moved from its initial position near the center of the rectangular loop to various positions along the left side of the loop. Assume that the probe is a thin wire with negligible cross section and no current flow and that no deflection of the magnetic field occurs except at the point where the probe is moved.

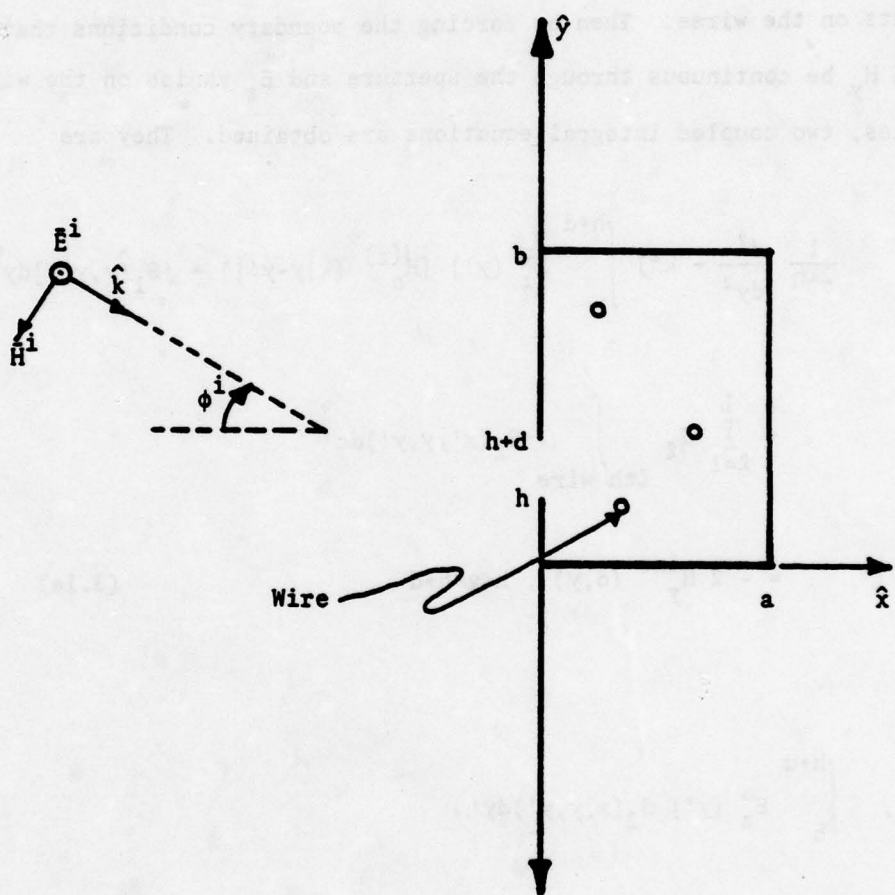


Figure 5. Geometry for Analogous Two-Dimensional Problem.

One now formulates the problem, using the thin wire approximations described previously in Chapter 2, by expressing E_z and H_y in terms of the unknown aperture electric field and the unknown surface currents on the wires. Then by forcing the boundary conditions that E_z and H_y be continuous through the aperture and E_z vanish on the wire surfaces, two coupled integral equations are obtained. They are

$$\begin{aligned} & \frac{1}{2kn} \left(\frac{d^2}{dy^2} + k^2 \right) \int_h^{h+d} E_z^a(y') [H_0^{(2)}(k|y-y'|) + jS_1(y,y')] dy' \\ & + \sum_{l=1}^L J_l \int_{\text{sth wire}} S_2(x',y,y') dc' \\ & = -2 H_y^{\text{inc}}(0,y), \quad h < y < h+d \end{aligned} \quad (3.1a)$$

and

$$\begin{aligned} & \int_h^{h+d} E_z^a(y') S_2(x,y,y') dy' \\ & - jkn \sum_{l=1}^L J_l \int_{\text{sth wire}} S_3(x,x',y,y') dc' \\ & = 0, \quad (x,y) \text{ on surface of the sth wire, for } s = 1, 2, \dots, L \end{aligned} \quad (3.1b)$$

where E_z^a is the unknown aperture electric field, J_l is the surface current density on the l th wire, H_y^{inc} is the y -component of the incident magnetic field and $\eta = \sqrt{\mu/\epsilon}$ is the characteristic impedance of the space. The functions S_1 , S_2 , and S_3 are defined by

$$S_1(y, y') = \frac{2}{ab} \sum_{m,n=0}^{\infty} \frac{\epsilon_m}{k_{mn}^2 - k^2} \sin k_y y \sin k_y y' \quad (3.2a)$$

$$S_2(x, y, y') = \frac{4}{ab} \sum_{m,n=1}^{\infty} \frac{k_x}{k_{mn}^2 - k^2} \sin k_x x \sin k_y y \sin k_y y' \quad (3.2b)$$

and

$$S_3(x, x', y, y') = \frac{4}{ab} \sum_{m,n=1}^{\infty} \frac{1}{k_{mn}^2 - k^2} \sin k_x x \sin k_x' x' \sin k_y y \sin k_y y' \quad (3.2c)$$

where $k_{mn}^2 = k_x^2 + k_y^2$, $k_x = \frac{m\pi}{a}$ and $k_y = \frac{n\pi}{b}$.

Note that any of the double sums in (3.2) can be reduced to a single sum by use of (2.8) and will thus converge exponentially as long as $\bar{r} \neq \bar{r}'$ [that is, when $(x, y) \neq (x', y')$].

Now assume that no two wires touch one another and that no wire is in the aperture region. This means then that with the exception of the first sum all of the infinite sums in (3.1a) are uniformly convergent. Indeed this first sum is uniformly convergent everywhere except when $y = y'$ in which case it diverges like $\frac{1}{n}$. Similarly, all

sums in (3.1b) are uniformly convergent, with the exception of the term where $\ell=s$, in which case one point on the surface of integration will coincide with the point (x,y) .

It is now useful to make the approximation that the wire current resides at the center of the wire and that field boundary conditions are still enforced at the wire surface. This approximation is commonly known as the reduced kernel approximation. For this problem it can be stated by

$$\int_{\text{wire}} S_3(x, x', y, y') dc' \approx 2\pi r S_3(x, x_c, y, y_c) \quad (3.3)$$

where (x_c, y_c) is the center point of the wire and r is the wire radius. This can be justified by noting that S_3 , the Green's function for the magnetic vector potential in the cavity, must contain the free space two-dimensional Green's function, which goes as $\ln|\bar{r}-\bar{r}'|$. Note that $\ln|\bar{r}-\bar{r}'|$ can be integrated analytically over the wire surface, where \bar{r} is also on the wire surface, to give the desired result that

$$\int_{-\pi}^{\pi} \ln(2r \sin \frac{|\theta'|}{2}) r d\theta' = 2\pi r \ln r .$$

Since the wire is thin and the remaining portion of S_3 is a smooth, homogeneous solution to the wave equation, it too can be validly approximated by this technique. It should be noted that given the wire radii small but finite, the application of the reduced kernel approximation makes all of the infinite sums in (3.1b) uniformly convergent.

Reduction to Matrix Equation by Method of Moments

An effective technique for the numerical solution of integral equations in electromagnetics is the method of moments (Harrington 1968). Consider the operator equation

$$L\bar{u} = \bar{f} \quad (3.4)$$

where L is a linear operator, \bar{f} is a known vector, and \bar{u} is an unknown vector for which the solution is desired. Using the method of moments, one approximates \bar{u} by a finite linear combination of expansion vectors \bar{u}_n . Thus let

$$\bar{u} = \sum_{q=1}^N a_q \bar{u}_q . \quad (3.5)$$

Now take the inner product of (3.4) with N testing vectors \bar{w}_p . If (3.5) is substituted into this result, and it is noted that L is linear, one arrives at the matrix equation

$$\sum_{q=1}^N \langle \bar{w}_p, L\bar{u}_q \rangle a_q = \langle \bar{w}_p, \bar{f} \rangle , \quad p = 1, 2, 3, \dots, N . \quad (3.6)$$

Note that (3.1a) is a linear operator equation with an integro-differential operator and unknown function $E_z^a(y)$ and the unknowns $\{J_\lambda\}$. Further, one has the boundary condition that E_z^a must vanish at each edge of the aperture because the tangential electric field (E_z) must vanish at these two points. If the inner product for this space is defined to be

$$\langle u, v \rangle = \int_h^{h+d} u(y)v(y)dy$$

the method of moments may be applied to approximate (3.1a) by a matrix equation.

The optimum choice of expansion functions (\bar{u}_p) and testing functions (\bar{w}_p) for this integro-differential operator and these boundary conditions has been the subject of many examinations (Butler and Wilton 1975; Wilton and Butler 1976). It has been shown that one efficient choice (Wilton and Butler 1976) is that of pulse, or piecewise-constant, expansion functions and piecewise-sinusoidal testing functions, denoted p_q and Λ_p^s respectively and defined in the coordinate system of this problem by

$$p_q(y) = \begin{cases} 1, & |y-y_q| < \frac{\Delta}{2} \\ 0, & |y-y_q| > \frac{\Delta}{2} \end{cases} \quad (3.7)$$

and

$$\Lambda_p^s(y) = \begin{cases} \sin(\Delta - |y-y_p|), & |y-y_p| < \Delta \\ 0, & |y-y_p| > \Delta \end{cases} \quad (3.8)$$

where $\Delta = d/(N+1)$ and $y_q = h+q\Delta$. Thus the unknown aperture field is approximated by

$$E_z^a(y) = \sum_{q=1}^N E_q p_q(y). \quad (3.9)$$

Figure 6 shows a plot of such an approximation as well as the testing functions $\Lambda_p^s(y)$. It should be noted that a half-pulse of zero amplitude has been placed at each end of the aperture. This is done because of the boundary condition that E_z^a vanish at each end of the aperture.

In order to perform the inner product one takes advantage of the piecewise-sinusoidal testing functions and the differential portion of the operator, $\frac{d^2}{dy^2} + k^2$, and integrates by parts twice. The integral portion of the result vanishes, leaving only three boundary terms.

If these expansion and test functions are applied to (3.1a) and the same expansion functions are substituted into (3.1b), the following equations are obtained

$$\begin{aligned} \frac{1}{2\pi} \sum_{q=1}^N E_q [F_q(y_{p-1}) - 2\cos k\Delta F_q(y_p) + F_q(y_{p+1})] \\ + C \sum_{l=1}^L I_l S_2(x_l, y_p, y_l) = -2C H_y^{inc}(o, y_p) \end{aligned} \quad (3.10a)$$

for $p = 1, 2, \dots, N$ and

$$\sum_{q=1}^N E_q \int_{\Delta q} S_2(x_s, y_s, y') dy' - jk\pi \sum_{l=1}^L I_l S_3(x_s, x_l, y_s, y_l) = 0 \quad (3.10b)$$

for $s = 1, 2, \dots, L$ where

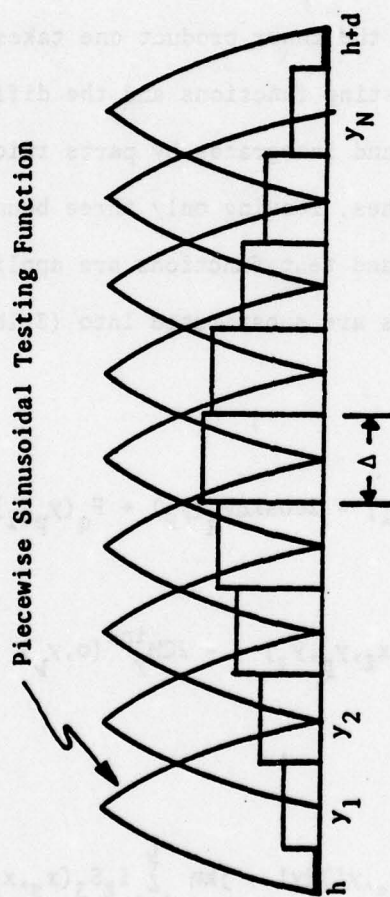


Figure 6. Pulse Expansion Functions and Piecewise Sinusoidal Testing Functions for Two-Dimensional Problem.

$$F_q(y) = \int_{\Delta q} H_0^{(2)}(k|y-y'|)dy' + j \int_{\Delta q} S_1(y,y')dy'. \quad (3.11)$$

In (3.10), $I_\ell = 2\pi r_\ell J_\ell$ is the current due to the uniform surface current density on the ℓ th wire and Δq is the interval $(y_q - \frac{\Delta}{2}, y_q + \frac{\Delta}{2})$. The point $\bar{r}_\ell = (x_\ell, y_\ell)$ is the centerpoint of the ℓ th wire and $\bar{r}_s = (x_s, y_s)$ is a point on the surface of the s th wire. However, for thin wires, this distinction is important only when $\ell=s$. The constant

$$C = \int_{y_p - \Delta}^{y_p + \Delta} A_p^s(y)dy = 2(1 - \cos k\Delta)$$

results from assuming that both the incident magnetic field at the aperture and the magnetic field in the aperture excited by the currents on the wires can be approximated over the range of pth testing function by their respective values at y_p .

It is now observed that (3.10) represents two coupled matrix equations for the unknowns $\{E_q\}$ and $\{I_\ell\}$. These equations can be solved simultaneously by standard matrix techniques, such as Gauss elimination, to find the solution for the unknown aperture field and the currents excited on the interior wires.

Numerical Considerations

Although the problem has been formulated and the integral equations have been approximated by matrix equation (3.10), it is noted

that one must be able to calculate the infinite sums S_2 and S_3 , possibly near the source where convergence is poor. The sums S_1 and S_2 must be integrated, S_1 over the source region (3.11). Consequently, it becomes necessary to develop techniques for handling these situations.

First it should be noted that in (3.10b) it is valid to integrate S_2 term by term since S_2 will always be uniformly convergent over the range of the integration (Titchmarsh 1939, p. 36). It can be shown that S_1 in (3.11) can also be integrated term by term, even though at $y=y'$, S_1 diverges. Because S_1 is uniformly convergent at every other point in the range of integration, and because the series that results if S_1 is integrated term by term is absolutely convergent, it is valid to integrate S_1 term by term (Titchmarsh 1939, pp. 44-45). This is an important result since as a general rule it is numerically more efficient to integrate the series term by term.

It remains to develop a technique for efficiently summing these series, even when $|\bar{r}-\bar{r}'|$ is small. It is expected that the convergence will be poor from a numerical standpoint. To demonstrate the method which is used to make this improvement, consider the special case of S_3 (3.2c). By applying (2.8a) to (3.2c) one finds that

$$S_3 = \frac{2}{a} \sum_{m=1}^{\infty} \text{sink}_x x \text{ sink}_{x'} x' \frac{\sinhy_b y < \sinhy_b (b-y')}{Y_b \sinhy_b b} \quad (3.12)$$

where $\gamma_b^2 = k_x^2 - k^2$.

Note that just as easily the double sum could have been reduced by eliminating the sum over m . Thus, there is always a choice of which sum to remove analytically by (2.8). Let S_3^{asy} be defined as the asymptotic series of S_3 such that its terms are the limit of the terms in (3.12) for large m . Thus

$$S_3^{\text{asy}} = \frac{1}{\pi} \sum_{m=1}^{\infty} \frac{1}{m} \sin m \frac{x}{a} \sin \frac{m \pi x'}{a} e^{-m \pi \frac{|y-y'|}{a}}. \quad (3.13)$$

Series S_3 has exponential convergence, the rapidity of which increases as $|y-y'|/a$ increases. It can easily be seen that if the sum over m were removed analytically, S_3 would converge exponentially like $|x-x'|/b$. It is reasonable to assume from this that as a general rule $|y-y'|/a$ should be compared to $|x-x'|/b$ and (3.2) should be reduced to a single sum in that way which maximizes this exponential convergence. For example, if $|y-y'|/a > |x-x'|/b$, then (3.2c) should be reduced to (3.12). Indeed, the validity of this general rule can be substantiated by the results of numerical testing.

Now return to (3.12). Suppose, however, that although $|y-y'|/a$ is larger than $|x-x'|/b$, it too is small, and (3.12) remains poorly convergent. Convergence of such a series can often be greatly improved if a closed form expression can be found for the corresponding asymptotic series (Lewin 1975). This means that if $S = \sum_n s_n$, $s_n \rightarrow s'_n$ as $n \rightarrow \infty$, and $S' = \sum_n s'_n = h$ where h is a closed form expression, then $D = \sum_n (s_n - s'_n)$ will converge more rapidly than S . Consequently, S

can be evaluated by $S = h + D$. Thus if (3.13) can be evaluated in closed form, the convergence of (3.12) could be improved.

For this particular sum, S_3 , one rewrites (3.13) as

$$S_3^{\text{asy}} = \frac{1}{2\pi} \sum_{m=1}^{\infty} \frac{e^{-ma}}{m} (\cos m\beta_1 - \cos m\beta_2) \quad (3.14)$$

where

$$\alpha = \frac{\pi|y-y'|}{a}, \beta_1 = \frac{\pi|x-x'|}{a} \text{ and } \beta_2 = \frac{\pi(x+x')}{a}.$$

But it is known that (Jolley 1961, pp. 110-111)

$$\sum_{n=1}^{\infty} \frac{e^{-nx}}{n} \cos n\lambda = \frac{x}{2} - \frac{1}{2} \ln(\cosh x - \cos \lambda) - \frac{1}{2} \ln 2. \quad (3.15)$$

With the use of (3.14) and (3.15), (3.12) becomes

$$S_3 = \frac{2}{a} \sum_{m=1}^{\infty} \sin k_x x \sin k_x x' \left[\frac{\sinh \gamma_b y < \sinh \gamma_b (b-y) >}{\gamma_b \sinh \gamma_b b} \right. \\ \left. - \frac{1}{2} \frac{e^{-ma}}{k_x} \right] + \frac{1}{4\pi} \ln \left(\frac{\cosh a - \cos \beta_2}{\cosh a - \cos \beta_1} \right). \quad (3.16)$$

It should be noted that numerically the sum in (3.16) is rapidly convergent regardless of how small $|\bar{r}-\bar{r}'|$ is, so long as it is not zero. Indeed at $|\bar{r}-\bar{r}'| = 0$, α and β_1 go to zero and from (3.16) it is seen that S_3 possesses the expected logarithmic singularity.

Although this procedure is demonstrated here only for S_3 , it can also be successfully applied to any sum or term-by-term integration of a sum which is needed in this problem. One will, however, need the following asymptotic series in closed form:

$$\sum_{n=1}^{\infty} \frac{e^{-nx}}{n} \sin n\lambda = \tan^{-1} \left(\frac{\sin \lambda}{e^x - \cos \lambda} \right), \quad (3.17a)$$

$$\sum_{n=1}^{\infty} e^{-nx} \sin n\lambda = \frac{\sin \lambda}{2(\cosh x - \cos \lambda)}, \quad (3.17b)$$

$$\sum_{n=1}^{\infty} e^{-nx} \cos n\lambda = \frac{\cos \lambda - e^{-x}}{2(\cosh x - \cos \lambda)}, \quad (3.17c)$$

and

$$\sum_{n=1}^{\infty} \frac{e^{-nx}}{n^2} = \frac{\pi^2}{6} + x \ln x - x - \frac{x^2}{4} + \sum_{n=1}^{\infty} \frac{B_{2n} x^{2n+1}}{2n(2n+1)!} \quad (3.17d)$$

where B_i is the i th Bernoulli number as defined by Abramowitz and Stegun (1965, p. 804). In the literature, (3.17a) can be found in Jolley (1961, p. 110-111), (3.17b) and (3.17c) are found in Wheelon (1968, p. 38), and finally, (3.17d) is found in Lewin (1958, p. 246) or Lindelöf (1947, p. 140). In (3.17d), the left side converges well for large x and the right side converges well for small x .

Sample Calculations

Now that the matrix equation has been formulated and methods of computing its elements have been devised, solutions for various cavity and wire configurations can be obtain via numerical solution

on a digital computer. In this section, a few representative solutions are presented.

It should be noted that a similar problem in which the infinite screen is omitted can be solved using a formulation and computer code previously developed (Seidel 1974) to calculate the currents on an array of cylindrical scatters in free space. From these currents, one can easily calculate the electric field in the aperture. Therefore, in addition to solutions of the problem at hand, solutions to the similar problem are presented. These problems are referred to as the flanged and unflanged solutions, respectively, flange meaning the infinite planar screen of the initial problem.

First consider the case of a cavity with a depth (a) of $.6\lambda$ and a width (b) of $.8\lambda$. This cavity has an aperture width of $.6\lambda$ which is centered in the cavity wall ($d = .6\lambda$, $h = .1\lambda$). The cavity is excited by a plane wave with unit magnitude electric field which impinges on the cavity from the negative x direction. Figure 7 shows a plot of aperture field for this cavity for the case of no internal wires. It is seen that the difference between the flanged solution and the unflanged solution is relatively small. Since the interior fields are uniquely determined by the aperture fields, this indicates that the presence of the flanges has little effect upon these interior fields. Note also that the aperture fields go to zero at the edges of the aperture and that they have a maximum magnitude of slightly less than unity. The fields are symmetric about the center of the aperture because of the symmetry of the cavity itself and the symmetry of the incident field.

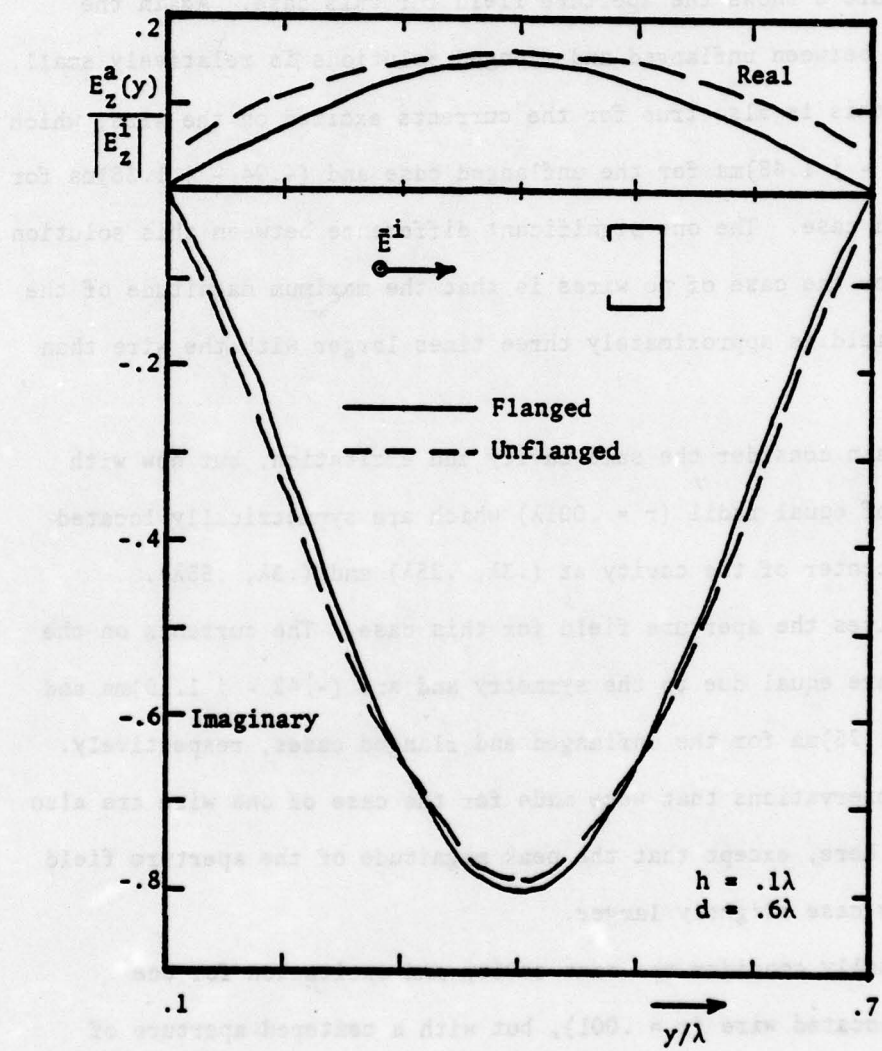


Figure 7. Aperture Field for Cavity with No Interior Wires.

Consider now the same cavity and excitation, but with a wire of radius $.001\lambda$ located at the geometric center of the cavity, $(.3\lambda, .4\lambda)$. Figure 8 shows the aperture field for this case. Again the difference between unflanged and flanged solutions is relatively small. Note that this is also true for the currents excited on the wire, which are $(-1.00 - j 1.48)\text{ma}$ for the unflanged case and $(-.94 - j 1.38)\text{ma}$ for the flanged case. The one significant difference between this solution and that for the case of no wires is that the maximum magnitude of the aperture field is approximately three times larger with the wire than without.

Again consider the same cavity and excitation, but now with two wires of equal radii ($r = .001\lambda$) which are symmetrically located about the center of the cavity at $(.3\lambda, .25\lambda)$ and $(.3\lambda, .55\lambda)$. Figure 9 gives the aperture field for this case. The currents on the two wires are equal due to the symmetry and are $(-.42 - j 1.19)\text{ma}$ and $(-.42 - j 1.25)\text{ma}$ for the unflanged and flanged cases, respectively. The same observations that were made for the case of one wire are also applicable here, except that the peak magnitude of the aperture field is for this case slightly larger.

Finally consider the same cavity and excitation for one centrally located wire ($r = .001$), but with a centered aperture of width $.4\lambda$. The aperture fields for this case are shown in Figure 10. The wire currents are $(.82 - j 1.71)\text{ma}$ and $(.98 - j 1.48)\text{ma}$ for the unflanged and flanged cases respectively. By comparison to Figure 8, it is seen that as a result of shortening the aperture, the magnitudes

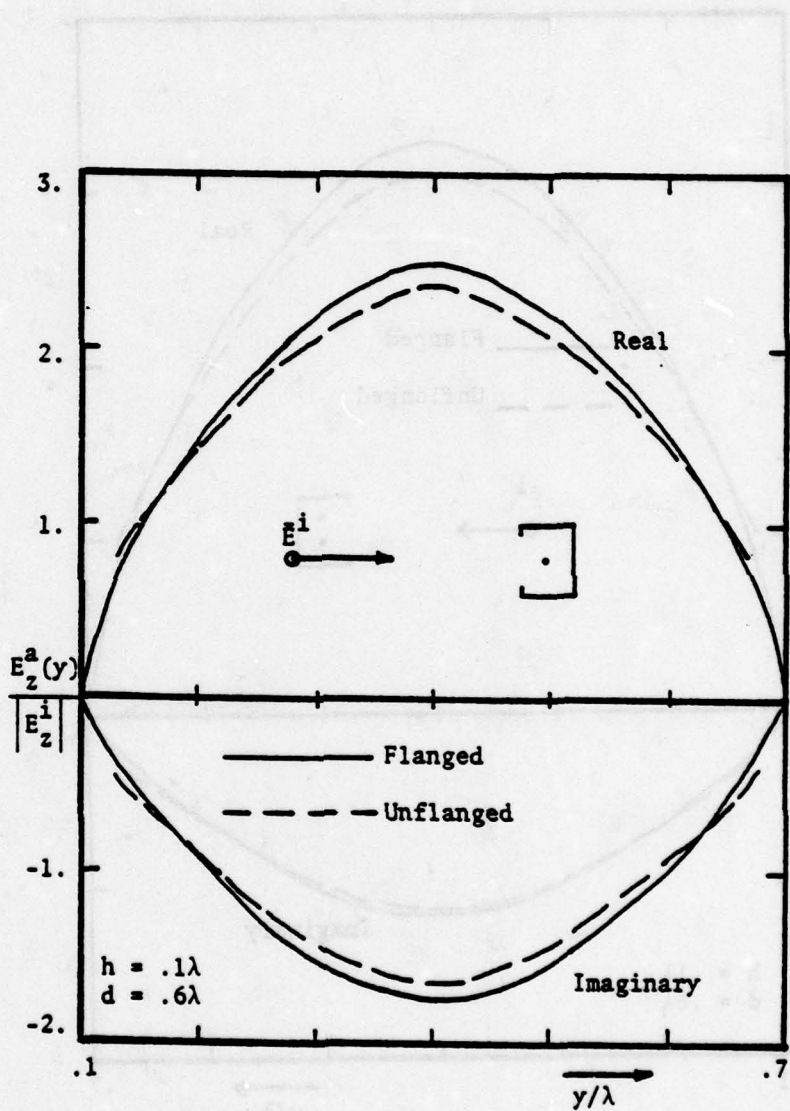


Figure 8. Aperture Field for Cavity with One Interior Wire.

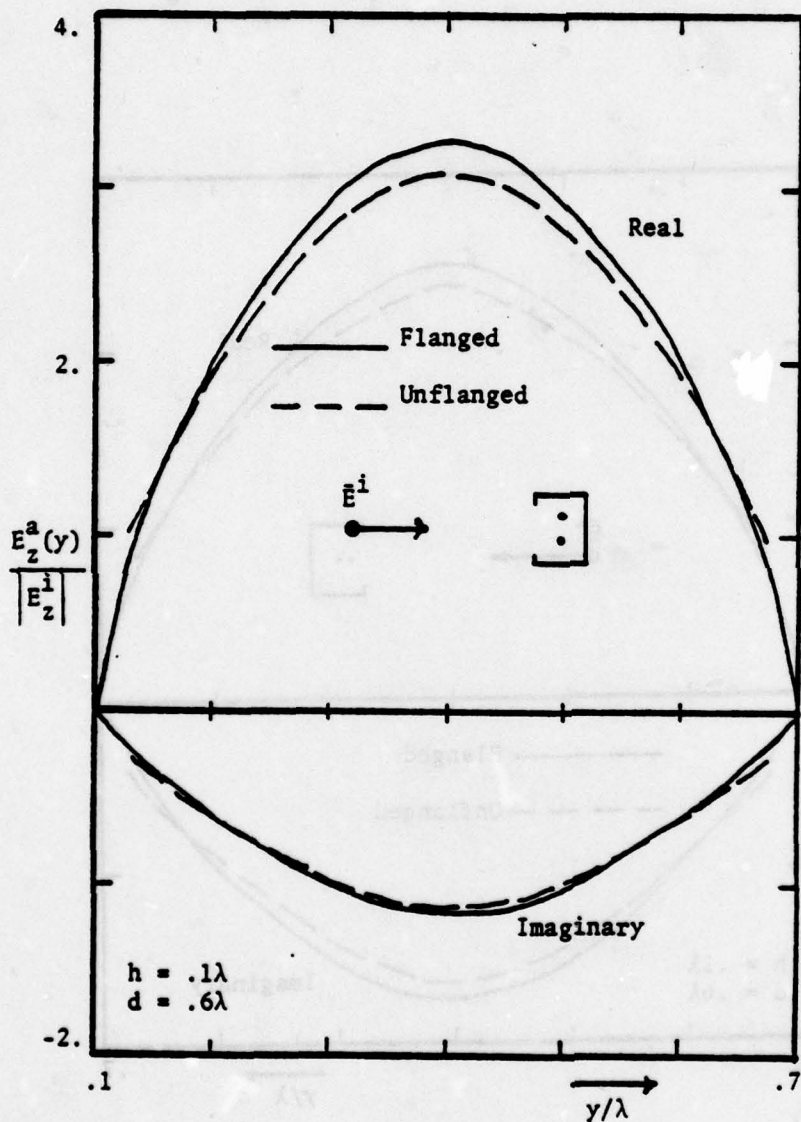


Figure 9. Aperture Field for Cavity with Two Interior Wires.

and the resonance voltage over current has been observed and is measured separately and can occur at high frequencies beyond the range of the visibility of the two begins? has been found.

Measurement will be carried out in various frequency and is dependent on the frequency and the distance between the two wires.

Figure 10 shows the aperture field for a cavity with one interior wire and .4λ aperture width.

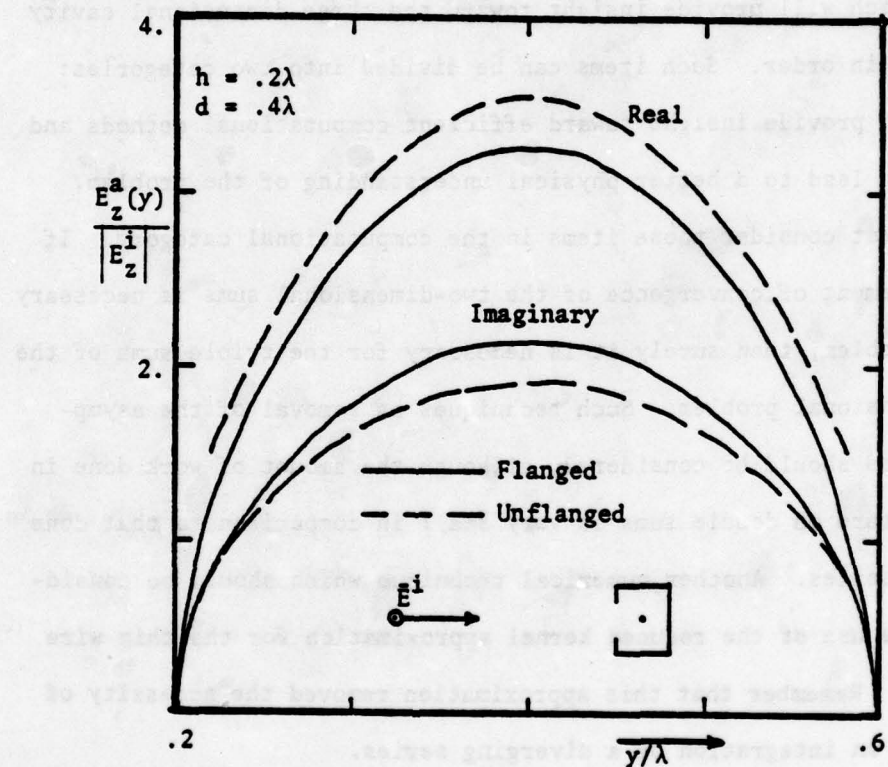


Figure 10. Aperture Field for Cavity with One Interior Wire and .4λ Aperture Width.

of the aperture field and current have slightly increased and the phase has changed considerably. Again note that the difference between unflanged and flanged solutions is relatively small.

Final Observations

At this point a summary of the portions of this two-dimensional problem which will provide insight toward the three-dimensional cavity problem is in order. Such items can be divided into two categories: those which provide insight toward efficient computational methods and those which lead to a better physical understanding of the problem.

First consider those items in the computational category. If the improvement of convergence of the two-dimensional sums is necessary in this problem, then surely it is necessary for the triple sums of the three-dimensional problem. Such techniques as removal of the asymptotic series should be considered, although the amount of work done in the literature on double sums is very small in comparison to that done on single series. Another numerical technique which should be considered is the use of the reduced kernel approximation for the thin wire scatterer. Remember that this approximation removed the necessity of performing an integration of a diverging series.

Secondly, physical insight into the effects of modeling approximations can be gained by noting the one overwhelming result of the data presented. Except for electrically small cross-section or grazing incidence, the interior cavity fields and the wire currents are relatively insensitive to the presence of the infinite screen in

this two-dimensional analog. It is quite reasonable to assume that this will also be true for the three-dimensional problem, and thus provides valuable information relating to modeling the three-dimensional cavity problem with or without the infinite screen. This finding is important because it is much easier to consider the problem with an infinite screen than without a screen.

CHAPTER 4

NUMERICAL METHODS FOR CAVITY PROBLEM

Approximation by Matrix Equation

In order to obtain a solution to the integral equation (2.13) for the three-dimensional cavity (with the coupled constraints in (2.21)), it is possible to approximate the integral equation numerically by a matrix equation. This is generally accomplished by the application of the method of moments, which was outlined in Chapter 3.

Consider the integro-differential equation (2.13) for the unknown current $J_z(z)$. It is seen that the differential portion of the operator is the harmonic operator $(\frac{d^2}{dz^2} + k^2)$, which was encountered in (3.1a). Since by thin wire approximations one also knows that the current must vanish at z_u and z_l (the z-coordinates of the wire endpoints, with $z_u > z_l$), the use of piecewise sinusoidal testing functions and pulse expansion functions is indicated (Wilton and Butler 1976), as was the case in the two-dimensional problem. For this problem, these functions are defined by

$$P_q(z) = \begin{cases} 1, & |z-z_q| < \frac{\Delta}{2} \\ 0, & |z-z_q| > \frac{\Delta}{2} \end{cases} \quad (4.1)$$

and

$$\Lambda_p^s(z) = \begin{cases} \sin(\Delta - |z-z_p|), & |z-z_p| < \Delta \\ 0, & |z-z_p| > \Delta \end{cases} \quad (4.2)$$

where $\Delta = (z_u - z_\ell)/(N+1)$ and $z_q = z_\ell + q\Delta$.

Figure 11 illustrates these expansion and test functions. It is important to note that if the wire is attached to the cavity at one or both ends, this choice must be slightly modified because the wire current does not necessarily vanish at the attached end. To rectify this problem, the zero half-pulse at an attached end is replaced by a half-pulse of unknown amplitude. Consequently, a new testing function, which is a half-piecewise sinusoidal function, must be introduced. These are shown in Figure 11 by dashed lines. In the subsequent development of the matrix equation, it is assumed that the wire is unattached. However, the extension to attached wires is straightforward.

Since J_z is assumed to be uniform about the circumference of the wire it is helpful to define the current to be the integral of the current density about circumference of the wire. By this assumption

$$I_z(z) = 2\pi r J_z(z). \quad (4.3)$$

Now approximate I_z by

$$I_z(z) = \sum_{q=1}^N I_q p_q(z). \quad (4.4)$$

Piecewise Sinusoidal Testing Function

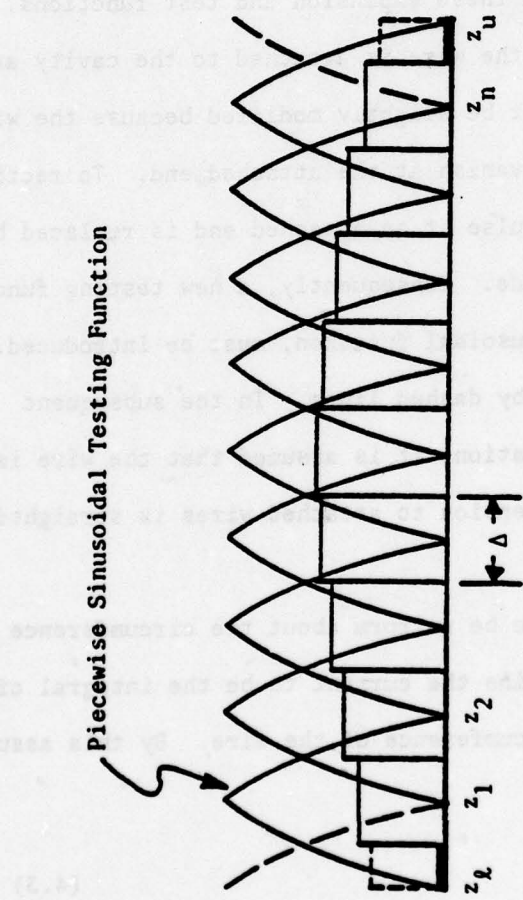


Figure 11. Expansion and Testing Functions for Unknown Wire Currents.

If this is substituted into (2.13) and (2.21) and the inner product defined by

$$\langle u, v \rangle = \int_{z_2}^{z_u} u(z)v(z)dz$$

is taken of (2.13) with the functions Λ_p^s , the following coupled matrix equations are obtained:

$$\sum_{q=1}^N Q_{pq}^a I_q + \sum_{q=1}^3 Q_{pq}^b t_q = 0 , \quad (4.5a)$$

$p = 1, 2, \dots, N$, and

$$\sum_{q=1}^N Q_{pq}^c I_q + \sum_{q=1}^3 Q_{pq}^d t_q = E_p , \quad (4.5b)$$

$p = 1, 2, 3$. These functions provide the solution for the unknown current amplitudes $\{I_q\}$ and the unknown aperture fields $(t_1, t_2, t_3) = (E_{T_n}, H_{T_1}, H_{T_2})$ driven by the exterior short circuit fields $(E_1, E_2, E_3) = (E_n^{sc-}(\bar{r}_a), H_1^{sc-}(\bar{r}_a), H_2^{sc-}(\bar{r}_a))$. The matrices in (4.5) are defined by

$$Q_{pq}^a = -j\eta [A_q(z_{p+1}) - 2\cos k\Delta A_q(z_p) + A_q(z_{p-1})] , \quad (4.6)$$

$$Q_{p1}^b = C\alpha_e G_{e_{zn}}(\bar{r}_p, \bar{r}_a) , \quad (4.7a)$$

$$Q_{p2}^b = -jCk\eta\alpha_{m_{11}} g_{e_{z1}}(\bar{r}_p, \bar{r}_a) , \quad (4.7b)$$

$$Q_{p3}^b = - jCkn\alpha_{m_{22}} g_{e_{z2}}(\bar{r}_p, \bar{r}_a) , \quad (4.7c)$$

$$Q_{1q}^c = - \frac{jn\Delta}{k} G_{e_{nz}}(\bar{r}_a, \bar{r}_p) , \quad (4.8a)$$

$$Q_{2q}^c = \Delta G_{h_{1z}}(\bar{r}_a, \bar{r}_p) , \quad (4.8b)$$

$$Q_{3q}^c = \Delta G_{h_{2z}}(\bar{r}_a, \bar{r}_p) , \quad (4.8c)$$

and

$$\bar{Q}^d = \begin{bmatrix} 1 + \alpha_e \hat{G}_{e_{nn}} & - jk n \alpha_{m_{11}} \hat{g}_{e_{n1}} & - jk n \alpha_{m_{22}} \hat{g}_{e_{n2}} \\ \frac{jk}{n} \alpha_e \hat{G}_{h_{1n}} & 1 - \alpha_{m_{11}} \hat{g}_{h_{11}} & - \alpha_{m_{22}} \hat{g}_{h_{12}} \\ \frac{jk}{n} \alpha_e \hat{G}_{h_{2n}} & - \alpha_{m_{11}} \hat{g}_{h_{21}} & 1 - \alpha_{m_{22}} \hat{g}_{h_{22}} \end{bmatrix} \quad (4.9)$$

where the deleted Green's functions in (4.9) are evaluated at (\bar{r}, \bar{r}')
 $= (\bar{r}_a, \bar{r}_a)$. Define

$$A_q(z_p) = \int_{\Delta q} K(z_p, z') dz' \quad (4.10)$$

where Δq is the interval $(z_q - \frac{\Delta}{2}, z_q + \frac{\Delta}{2})$ and

$$K(z_p, z') = \frac{1}{2\pi} \int_{-\pi}^{\pi} G_{A_{zz}}(\bar{r}_p, \bar{r}') d\phi' , \quad (4.11)$$

where ϕ' is the angular coordinate of a cylindrical coordinate system about the wire axis (Figure 1). Also, $C = 2(1-\cos k\Delta)$ and \bar{r}_p and \bar{r}' are on the wire surface. Note that to obtain (4.8), the integral over the qth tubular surface segment on the wire has been approximated by the product of the surface area of the segment and the integrand evaluated at a point on the center of the segment.

In order to solve the coupled matrix equations (4.5), one need only obtain a numerical solution to the partitioned matrix equation

$$\begin{pmatrix} \bar{Q}^a & \bar{Q}^b \\ \bar{Q}^c & \bar{Q}^d \end{pmatrix} \begin{pmatrix} \bar{I} \\ \bar{t} \end{pmatrix} = \begin{pmatrix} \bar{0} \\ \bar{E} \end{pmatrix} \quad (4.12)$$

Note that if the effects upon the aperture field of the fields scattered by the wires are ignored, $\bar{Q}^c = \bar{0}$. On the other hand, if the effects of the cavity wall reflections upon the aperture field are ignored $\bar{Q}^d = \bar{I}$, the identity matrix.

However, as in the two-dimensional problem, difficulty arises in attempting to compute the elements of the matrix, each of which contains one of the triply-infinite sums defined in Tables 1 and 2. The computations which exhibit this difficulty can be categorized into three basic types, the first of which is computation of any one of the sums outside the source region. The second category is that of the integral of $G_{A_{zz}}$ over the surface of the wire, for which at one point of the integration $G_{A_{zz}}$ will be divergent. Finally, the deleted Green's functions must be computed at the aperture. The remainder of this chapter attempts to deal with precisely these difficulties.

An Efficient Method of Computing the Sums
Outside the Source Region

As was noted in Chapter 2, each of the Green's functions (Tables 1 and 2) can be reduced from a triple sum to a double sum which is exponentially convergent for $|r-r'| \neq 0$ using (2.8). Indeed, it is easily shown that the asymptotic series associated with any one of these exponentially convergent series is of the form

$$S^{\text{asy}} = \sum_{m,n} f(m,n) \frac{e^{-k_c|z-z'|}}{k_c^\alpha} \quad (4.13)$$

where $k_c^2 = \left(\frac{m\pi}{a}\right)^2 + \left(\frac{n\pi}{b}\right)^2$, $\alpha = 0, 1, 2$ and $f(m,n)$ is a non-exponential function of m and n .

As was found in Chapter 3, it is a good general rule to reduce the triple sum in such a way as to produce the double sum with the most rapid exponential convergence. For example, if

$$\left(\frac{1}{a^2} + \frac{1}{b^2}\right)(z-z')^2$$

is greater than both

$$\left(\frac{1}{b^2} + \frac{1}{c^2}\right)(x-x')^2 \quad \text{and} \quad \left(\frac{1}{a^2} + \frac{1}{c^2}\right)(y-y')^2$$

then the sum over ℓ should be reduced.

Following the lead from the two-dimensional problem in Chapter 3, one would now attempt to find the closed forms of (4.13)

for the various $f(m,n)$ and α . It turns out, however, that the list of double sums for which a closed form is known is painfully short, and does not seem to include (4.13) for any α and $f(m,n)$ of interest in this problem.

Another method which has been suggested is to remove the known singularity from the series by expanding the singularity in the same expansion functions as the series itself. Both Tai and Rozenfeld (1976) and Rahmat-Samii (1975) have removed a delta function singularity from their series for \bar{G}_e in this way. However, this serves little purpose because the known singularity of \bar{G}_e is not the delta function. In fact, as shown by Howard (1974), the singularity of \bar{G}_e is actually the longitudinal portion of $\bar{I}\delta(\bar{r}-\bar{r}')$.

The third alternative, and the one that is used for this work, is to simply sum the double series in an efficient manner. Note that because of the exponential convergence, as one attempts to make this computation nearer and nearer the source, the series will become more and more poorly convergent. Thus one should expect to reach a point such that for $|\bar{r}-\bar{r}'|$ less than some minimum value, numerical computation of the sum in this fashion becomes unfeasible.

However, some things can be done which make this method more efficient. Because of the exponential convergence in the asymptotic series (4.13), one would expect an efficient ordering of terms to be in order of increasing k_c . This takes advantage of the exponential convergence as well as the k_c^α in the denominator. At this point, it is useful to partition the $m-n$ plane with successive curves

(Bromwich, 1926, p.83). If the sum of all terms lying between two successive curves is called s_q , then the double series can be converted into the single series of the form

$$S = \sum_{q=1}^{\infty} s_q.$$

By the proper selection of these curves, the most efficient ordering of terms can be determined.

For this problem such a choice would be that of ellipses with semi-axes in m of $\alpha_q a$ and semi-axes in n of $\alpha_q b$, where α_q is a monotonically increasing sequence of constants. Such a partitioning is shown in Figure 12. Note that for such a choice, each successive partition contains terms for which k_c is larger than in the preceding partition. Also note that since the sum of terms in the q th partition is the q th term of a single infinite series, methods used for determining the convergence of single series can be applied.

To test this method, the sums were numerically computed via digital computer. Figure 13 shows the notation used for the sum.

Note that it is assumed without loss of generality that $a \leq b$.

Numerically the series was truncated to include only those terms within C_M . The maximum value of m was M . Note that the total number of terms is approximately the area within C_M or $N_T \approx \frac{\pi b}{4a} M^2$. Let $S_p = \sum_{q=1}^p s_q$ and $R_p = \sum_{q=p+1}^{\infty} s_q$. Then R_M is the error resulting from truncation. R_M can be crudely bounded from above with an integral bound. However, for actual computation, convergence was defined to have been

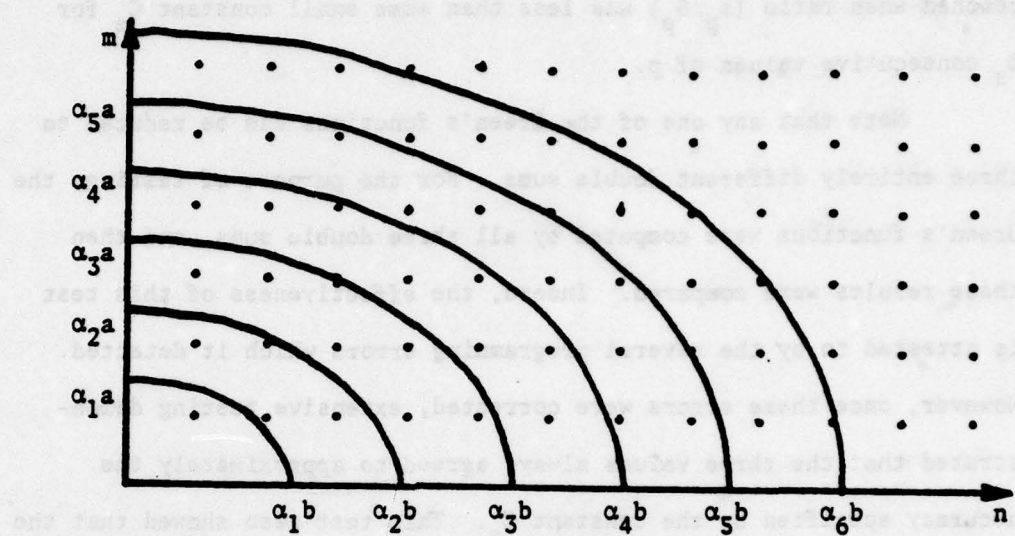


Figure 12. Choice of Contours in $m-n$ Plane for Efficient Summing of Double Series.

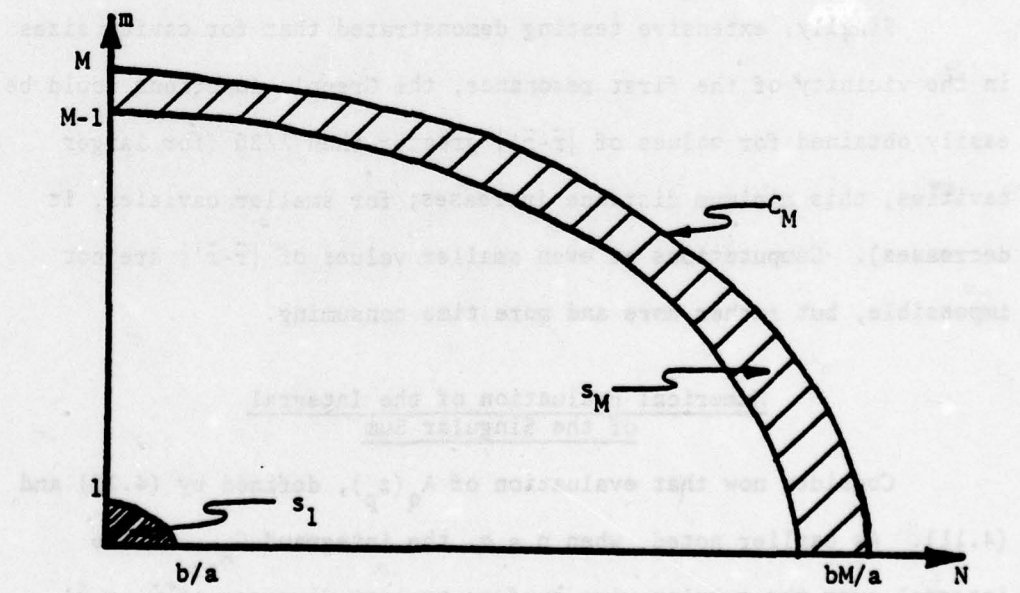


Figure 13. Terms Used in Numerical Computation of Sums.

reached when ratio (s_p/S_p) was less than some small constant C_s for ℓ_s consecutive values of p .

Note that any one of the Green's functions can be reduced to three entirely different double sums. For the purpose of testing, the Green's functions were computed by all three double sums, and then these results were compared. Indeed, the effectiveness of this test is attested to by the several programming errors which it detected. However, once these errors were corrected, extensive testing demonstrated that the three values always agreed to approximately the accuracy specified by the constant C_s . This test also showed that the general rule of reducing the sum so as to give the most rapid exponential convergence did, in fact, produce the particular one of the three possible double sums which required the fewest number of terms.

Finally, extensive testing demonstrated that for cavity sizes in the vicinity of the first resonance, the Green's functions could be easily obtained for values of $|\bar{r}-\bar{r}'|$ greater than $\lambda/20$ (for larger cavities, this minimum distance increases; for smaller cavities, it decreases). Computations at even smaller values of $|\bar{r}-\bar{r}'|$ are not impossible, but rather more and more time consuming.

Numerical Evaluation of the Integral of the Singular Sum

Consider now that evaluation of $A_q(z_p)$, defined by (4.10) and (4.11). As earlier noted, when $p = q$, the integrand $G_{A_{zz}}$ of the integral over the tubular wire surface segment diverges at $\bar{r}_p = \bar{r}'$. Even for $p \neq q$, if p is near q then the integrand will converge poorly. These two difficulties must be overcome.

In order to sidestep the first problem, it would be helpful to apply the reduced kernel approximation (assume all current resides at center of wire). With this approximation, when $p = q$ the integrand would never diverge and, in fact, would be uniformly convergent everywhere on the surface of integration because $|\bar{r} - \bar{r}'| \geq r$. However, one very important consideration is the validity of using the reduced kernel approximation for the kernel (4.11). This kernel is known to include the singularity of the free space kernel plus a remaining smooth homogeneous solution. If $r \ll \lambda$, it is justifiable to assume that the smooth part of K is essentially the same at the center of the wire and at points on the wire surface. Thus one needs a like comparison for the singular portion.

Define K_o and K_r to be the free space exact and reduced kernels, respectively, given by

$$K_o(\xi) = \frac{1}{2\pi} \int_{-\pi}^{\pi} [\xi^2 + 4r^2 \sin^2 \frac{\phi}{2}]^{-1/2} d\phi \quad (4.14a)$$

and

$$K_r(\xi) = [\xi^2 + r^2]^{-1/2}. \quad (4.14b)$$

Since ultimately integrals of the kernels over ξ are needed, such integrals will be compared. Let

$$\psi_o(z) = \int_0^z K_o(\xi) d\xi = I_o \quad (4.15a)$$

and

$$\psi_r(z) = \int_0^z K_r(\xi) d\xi = \ln \left[\frac{z}{r} + \left\{ \left(\frac{z}{r} \right)^2 + 1 \right\}^{1/2} \right] \quad (4.15b)$$

where I_0 has been defined by Butler (1975). Figure 14 shows a comparison of these two functions. It is readily apparent that such an approximation is valid for the singular part of the kernel and thus valid for the kernel (4.11).

Using the equation for $G_{A_{zz}}$ from Table 1 (reducing it to a double sum by (2.8b)) and applying the reduced kernel approximation to (4.11), one obtains

$$K(z_p, z') = \frac{4}{ab} \sum_{m,n=1}^{\infty} \frac{\cosh \gamma_c z \cosh \gamma_c (c-z)}{\gamma_c \sinh \gamma_c} F(x_c, y_c) \quad (4.16)$$

where $\gamma_c^2 = k_x^2 + k_y^2 - k^2$,

$$F(x_c, y_c) = \text{sink}_{x_c} x_c \text{sink}_{x_p} x_p \text{sink}_{y_c} y_c \text{sink}_{y_p} y_p, \quad (4.17)$$

(x_c, y_c) is the location of the center of the wire and $\bar{r}_p = (x_c + r \cos \phi, y_c + r \sin \phi, z_p)$ is a point on the wire surface. By using a hyperbolic trigonometric identity, one can express (4.16) as the sum of two terms by

$$K(z_p, z') = S(|z_p - z'|) + S(z_p + z') \quad (4.18)$$

where

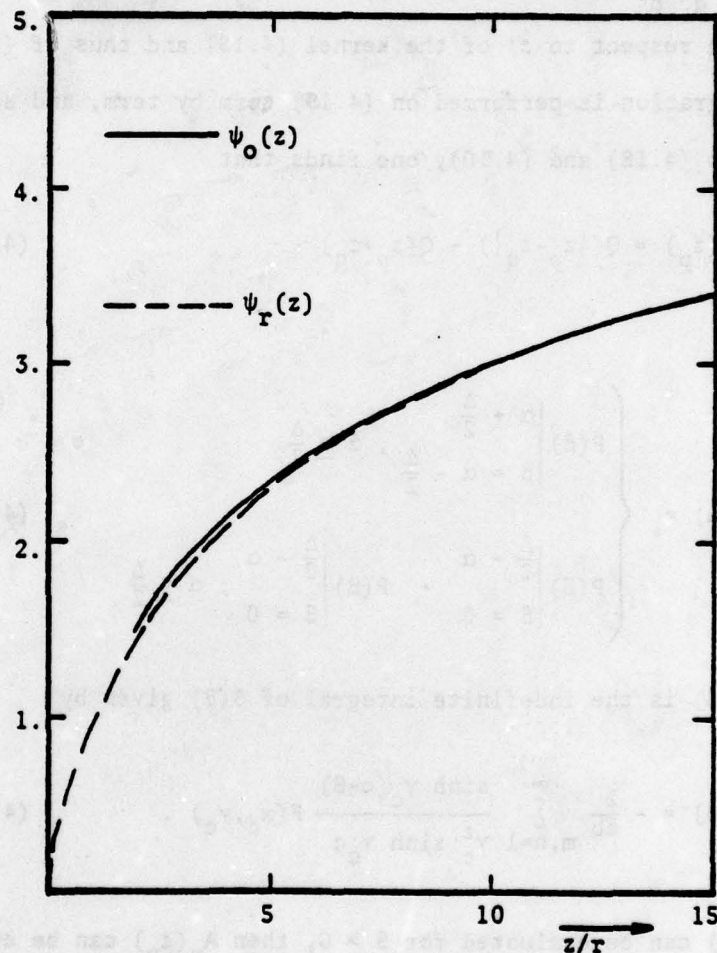


Figure 14. Comparison of the Integrals of the Free Space Exact and Reduced Kernels.

$$S(\beta) = \frac{2}{ab} \sum_{m,n=1}^{\infty} \frac{\cosh \gamma_c(c-\beta)}{\gamma_c \sinh \gamma_c c} F(x_c, y_c) \quad (4.19)$$

To evaluate $A_q(z_p)$ defined by (4.10), one needs to calculate the integral with respect to z' of the kernel (4.18) and thus of (4.19). If this integration is performed on (4.19) term by term, and substituted into (4.18) and (4.10), one finds that

$$A_q(z_p) = Q(|z_p - z_q|) + Q(z_p + z_q) \quad (4.20)$$

where

$$Q(\alpha) = \begin{cases} P(\beta) & \left| \begin{array}{l} \alpha + \frac{\Delta}{2} \\ \beta = \alpha - \frac{\Delta}{2} \end{array} \right. , \alpha \geq \frac{\Delta}{2} \\ P(\beta) & \left| \begin{array}{l} \frac{\Delta}{2} + \alpha \\ \beta = 0 \end{array} \right. + P(\beta) & \left| \begin{array}{l} \frac{\Delta}{2} - \alpha \\ \beta = 0 \end{array} \right. , \alpha \leq \frac{\Delta}{2} \end{cases} \quad (4.21)$$

and where $P(\beta)$ is the indefinite integral of $S(\beta)$ given by

$$P(\beta) = -\frac{2}{ab} \sum_{m,n=1}^{\infty} \frac{\sinh \gamma_c(c-\beta)}{\gamma_c^2 \sinh \gamma_c c} F(x_c, y_c) . \quad (4.22)$$

Thus, if $P(\beta)$ can be evaluated for $\beta \geq 0$, then $A_q(z_p)$ can be evaluated on the wire using the reduced kernel.

Consider the case where $\beta = 0$. Note that the hyperbolic sine functions in (4.22) cancel, leaving

$$P(0) = -\frac{2}{ab} \sum_{m,n=1}^{\infty} \frac{\sin k_x x_c \sin k_x x_p \sin k_y y_c \sin k_y y_p}{k_x^2 + k_y^2 - k^2} \quad (4.23)$$

It is now recognized that

$$P(0) = -\frac{1}{2} S_3(x_c, x_p, y_c, y_p) \quad (4.24)$$

where S_3 is defined by (3.2c). Thus $P(0)$ can be readily evaluated numerically using (3.16) for $r > 0$. Note that in (4.22), because the hyperbolic sine is an odd function,

$$P(2c - \beta) = -P(\beta) . \quad (4.25)$$

Thus by (4.24) and (4.25) it is also true that

$$P(2c) = \frac{1}{2} S_3(x_c, x_p, y_c, y_p) . \quad (4.26)$$

For $\beta \neq 0$ or $2c$, there appears to be no alternative other than to perform the two-dimensional sum by the methods of the previous section. Note that asymptotically P is of the following form:

$$P_{\text{asy}} \sim \sum_{m,n=1}^{\infty} F \frac{e^{-k_c \beta}}{k_c^2}, \quad 0 < \beta \leq c .$$

Thus for β near zero (or near $2c$, as indicated by (4.25)), poor convergence is expected.

It is known that the reduced kernel (4.16) must contain the singular portion free-space reduced kernel (4.14b) plus a smooth

homogeneous function. By (4.18), $S(\beta)$ must also contain that singularity. If a function $\psi(z)$ is defined similar to (4.15b) by

$$\psi(z) = \int_0^z S(\beta) d\beta = P(z) - P(0) \quad (4.27a)$$

and $\psi_s(z)$ is defined by

$$\psi_s(z) = \psi(z) - \psi_r(z) \quad (4.27b)$$

then ψ_s is the integral of a smooth function and thus itself is smooth.

Since $P(0)$ is readily computed, $\psi(z)$ can be computed numerically for z greater than some minimum value z_o . Note that the function $\psi_r(z)$ can be calculated by using (4.15b) for any z . Thus $\psi_s(z)$ can be numerically evaluated for $z > z_o$. Note that if ψ_s is smooth and z_o is sufficiently small, $\psi_s(z)$ can be interpolated for $0 < z < z_o$. Then if $\psi_r(z)$ is added to these interpolated values of $\psi_s(z)$, $\psi(z)$ can be found for $0 < z < z_o$.

To demonstrate the practicality of this technique, consider the curves of Figure 15. They show the functions $\psi(z)$, $\psi_r(z)$ and $\psi_s(z)$ for $0 \leq z \leq .5\lambda$. The cavity dimensions are $a = .7\lambda$, $b = .8\lambda$ and $c = .8\lambda$ with a wire of radius $4 = .001\lambda$ located at $x_c = .35\lambda$ and $y_c = .4\lambda$. Note that for $z < .2\lambda$, ψ_s is almost linear and could be interpolated quite accurately. The utility of this method is appreciated if it is noted that for this example the calculation of $P(z)$ took 98 terms at $z = .2\lambda$, 242 terms at $z = .1\lambda$ and 2189 terms at $z = .025\lambda$. In each case, the convergence criteria was $C_s = 10^{-5}$ and $\ell_s = 3$.

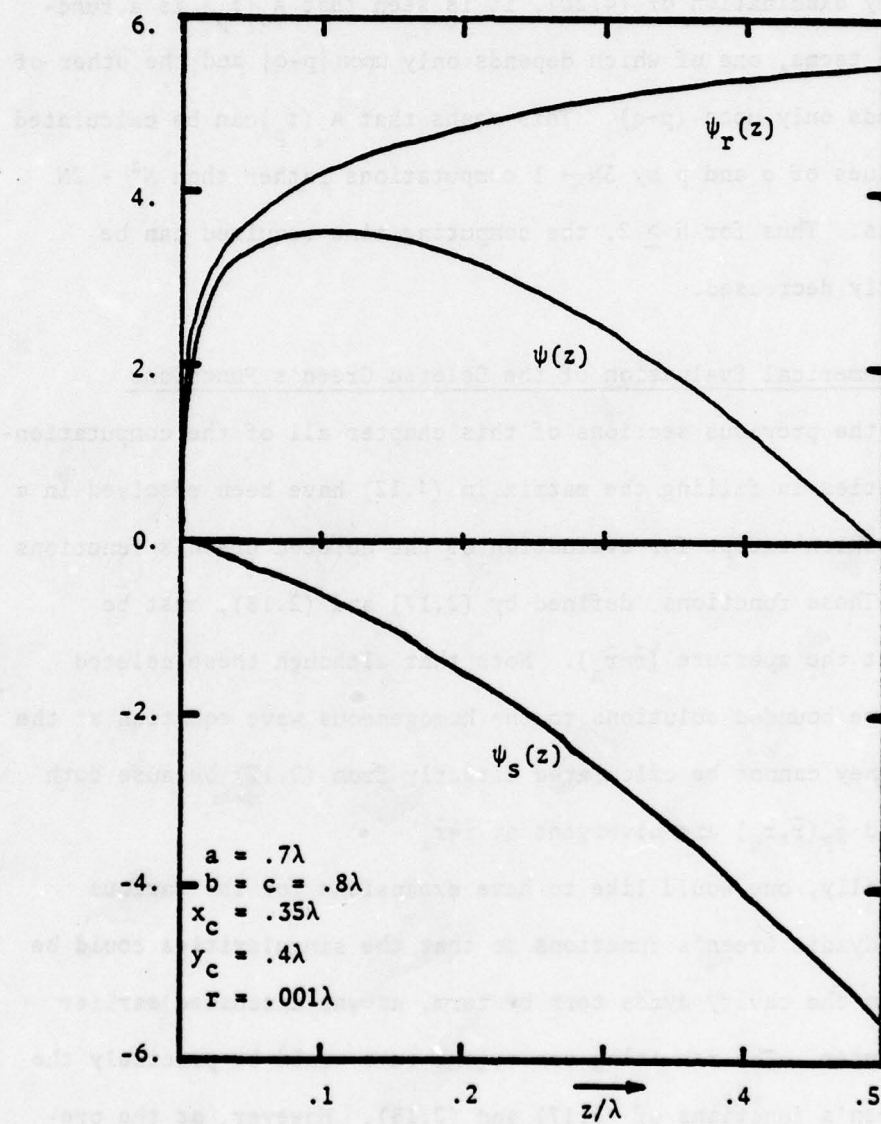


Figure 15. Example Computed Values of $\psi(z)$, $\psi_r(z)$ and $\psi_s(z)$.

Before leaving this section, one important observation should be made. By examination of (4.20), it is seen that $A_q(z_p)$ is a function of two terms, one of which depends only upon $|p-q|$ and the other of which depends only upon $(p+q)$. This means that $A_q(z_p)$ can be calculated for all values of q and p by $3N + 1$ computations rather than $N^2 + 2N$ calculations. Thus for $N \geq 2$, the computing time required can be significantly decreased.

Numerical Evaluation of the Deleted Green's Functions

In the previous sections of this chapter all of the computational difficulties in filling the matrix in (4.12) have been resolved in a workable fashion except for evaluation of the deleted Green's functions in (4.9). These functions, defined by (2.17) and (2.18), must be evaluated at the aperture ($\bar{r}=\bar{r}_a$). Note that although these deleted functions are bounded solutions to the homogeneous wave equation at the point \bar{r}_a , they cannot be calculated directly from (2.17) because both $\bar{G}_A(\bar{r},\bar{r}_a)$ and $\bar{\bar{g}}_F(\bar{r},\bar{r}_a)$ are divergent at $\bar{r}=\bar{r}_a$.

Ideally, one would like to have expansions for the various free-space dyadic Green's functions so that the singularities could be removed from the cavity dyads term by term, as was discussed earlier in this chapter. The resulting convergent sums would be precisely the deleted Green's functions of (2.17) and (2.18). However, at the present time, practical techniques of employing this method are not available.

In this work, a different approach was taken that relies upon some of the earlier observations of this chapter. Since the deleted Green's functions are homogeneous solutions to the wave equation, it is logical to expect that they could be found by using an interpolation method similar to that employed in the previous section to evaluate $A_q(z_p)$.

Note that such an interpolation scheme would require the evaluation of several different components of the various cavity dyads at points near the source. If it is assumed that the accuracy of the interpolations would improve as the points move nearer the source, increased accuracy would require increased computation time.

Since the double sums in the dyads for the vector potentials converge more rapidly than those for the fields, it is advantageous to compute only the components of \tilde{G}_A and $\tilde{\bar{g}}_P$ at several points near the source. Then by (2.17), the associated deleted Green's functions for the vector potentials could be subsequently computed. To find the values of \hat{G}_A and $\hat{\bar{g}}_P$ in the aperture, an interpolation scheme was employed. To find the values of the other deleted Green's dyads, the differential operators in (2.18) were approximated by finite difference techniques. Note that the points at which the dyads are computed should be chosen carefully so that they provide the proper information for the interpolation and finite difference techniques.

A crucial criterion for the success of this method is the smoothness of the deleted Green's functions. Figure 16 shows plots of $G_{A_{zz}}$ and $\text{Re}(\hat{G}_{A_{zz}})$ as a function of distance from the aperture. Note

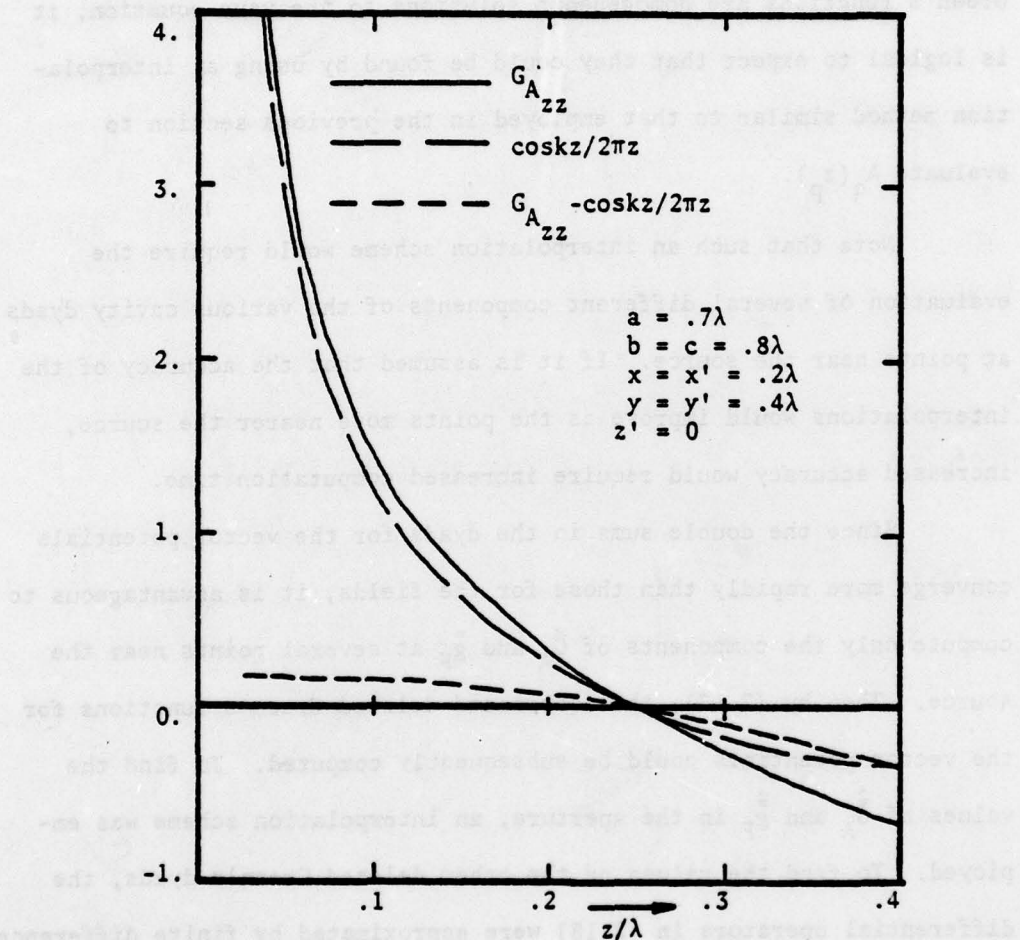


Figure 16. Example Computation for G_{Azz} and the Real Part of \hat{G}_{Azz} .

that the deleted function is indeed smooth and could be approximated near the source by interpolation techniques. Figure 17 shows similar plots of $g_{F_{yy}}$ and $\text{Re}(\hat{g}_{F_{yy}})$ and the same observations can be made.

This method has been tested numerically for several aperture location/cavity size configurations. For each configuration, the computations were made with the distances between the aperture and the points at which the computations were made becoming successively smaller. The calculated values of the deleted Green's functions for the successively smaller distances were then compared in order to determine if the process was convergent. In all cases tested, it was indeed convergent. Although error bounds are not available, based upon the numerical testing, accuracy to within 10 to 15 percent is estimated for distances from aperture to computation points being approximately $.05\lambda$ to $.1\lambda$.

It should be noted that these values for the deleted Green's functions are computed with less accuracy than any other terms in the matrix of (4.12). Nonetheless, their computation requires far more computer time than any of the other terms in the matrix. In addition, because these functions are always multiplied by the aperture polarizabilities (which are small for small apertures) in (4.9), they manifest themselves primarily as perturbations and have only a slight effect upon the solution, as will be seen in the following chapter.

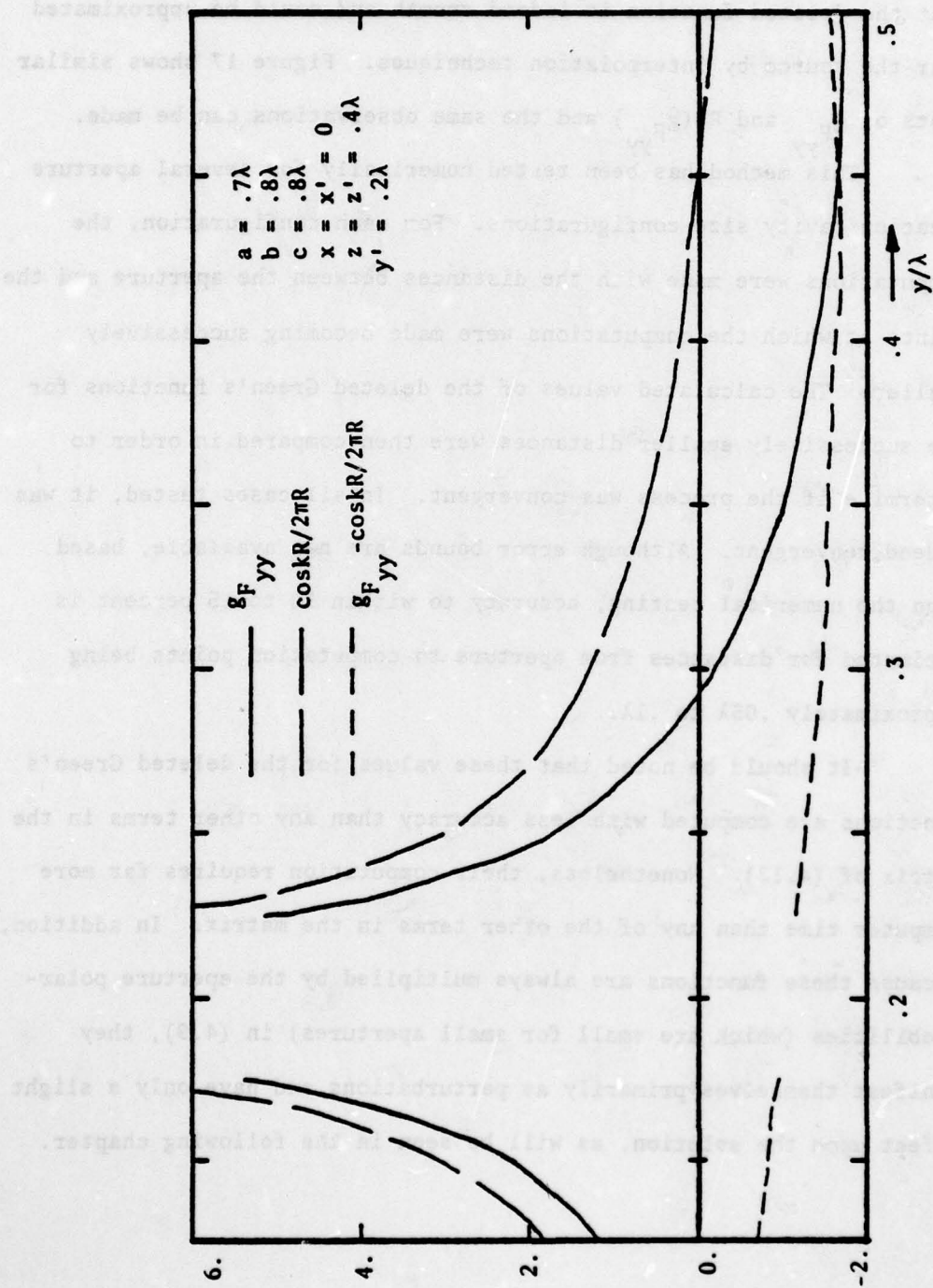


Figure 17. Example Computation of $\hat{g}_{F_{yy}}$ and the Real Part of $\hat{g}_{F_{yy}}$.

CHAPTER 5

NUMERICAL RESULTS FOR SAMPLE CASES

A computer code has been written which implements the numerical formulation presented in the previous chapter. In this chapter, selected numerical results are presented which demonstrate the capabilities of this numerical code. The program allows for an elliptic aperture in any one of the three walls defined by $x = 0$, $y = 0$ or $z = 0$, and assumes that the wall containing the aperture is an infinite planar screen. For all cases presented here, the aperture was chosen to perforate the $x = 0$ wall of the cavity. Also note that all lengths are in units of wavelength λ .

As a first example, consider a relatively small cavity whose dimensions are defined by $a = .2$, $b = .25$ and $c = .3$ which encloses a wire of length .2 and radius .001. The wire is exactly centered in the cavity ($z_l = .05$, $z_u = .25$, $x_c = .1$, $y_c = .125$). The aperture is circular with a radius of .01 and has its center at $\bar{r}_a = (0., .125, .15)$. The exterior excitation is a plane wave which impinges from the $-z$ direction and is polarized such that the electric field is in the $-x$ direction.

Figure 18 shows the current excited upon the wire for this configuration. Since both aperture and wire are symmetric about the plane $z = \frac{c}{2}$, one would expect to observe symmetric properties in the

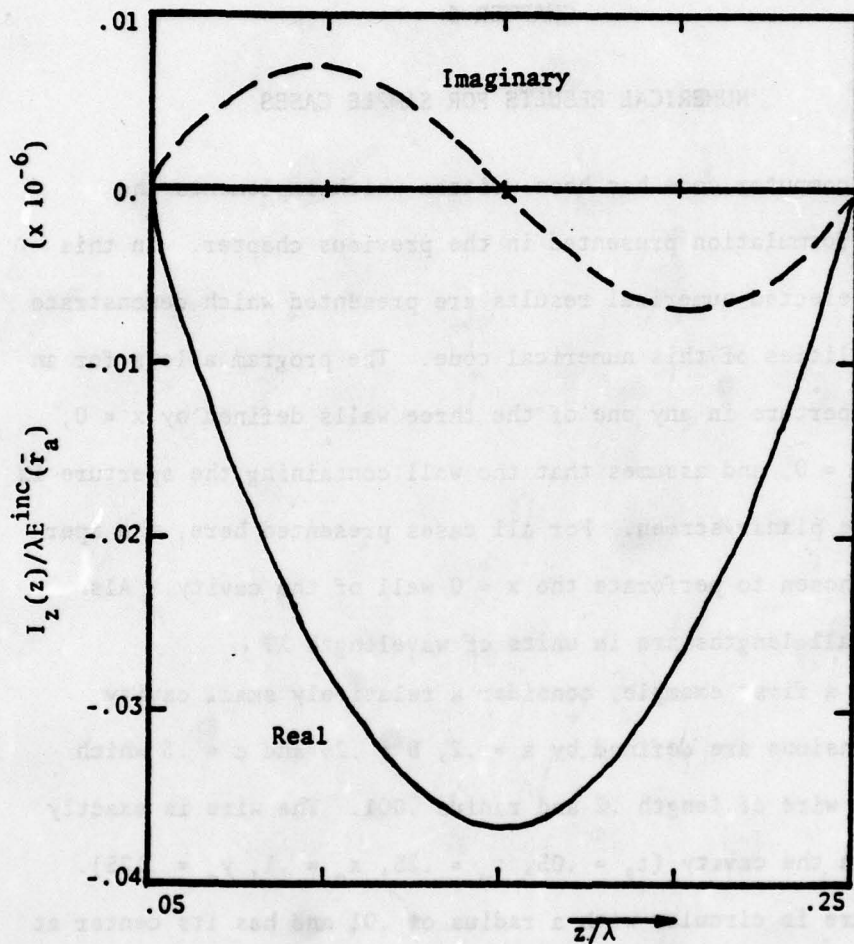


Figure 18. Currents Excited on $.2\lambda$ Wire for a $.2\lambda \times .25\lambda \times .3\lambda$ Cavity.

wire currents. This is indeed the case. The real part of the current, which is excited by the magnetic aperture dipole moment, possesses even symmetry, where the imaginary part, which is excited by \bar{P}_e , has odd symmetry about $z = .15$. This relationship between the real and imaginary parts of the current and \bar{P}_m and \bar{P}_e respectively can be seen by examination of (4.5a), (4.6) and (4.7). Also note the magnitude of the current which peaks at approximately .04 μ a. One would expect currents on the order of 1 ma for the same wire in a free space environment. Thus the shielding of the cavity reduces currents by approximately five orders of magnitude.

Next consider the case of a much larger cavity containing a longer wire. For this case, $a = .4$, $b = .6$ and $c = 1.3$, which is larger than the first several cavity resonances. Again the wire is centered in the cavity ($z_l = .15$, $z_u = 1.15$, $x_c = .2$, $y_c = .3$) and is one wavelength long with radius $r = .001$. The elliptic aperture has semiaxes of .05 and .01 in the y and z directions, respectively and is located at $\bar{r}_a = (0, .2, .4)$. Again, the incident plane wave impinges from the $-z$ direction with a $-x$ directed electric field.

Since the wire is of resonant length, one would expect to excite resonant currents. Indeed, as shown in Figure 19, this is the case. Also, note that the current magnitude now peaks at approximately 10 μ a. This increase over the previous case can be attributed to three causes. First, the aperture is larger and thus more energy is coupled. Second, the wire is of resonant length. Finally,

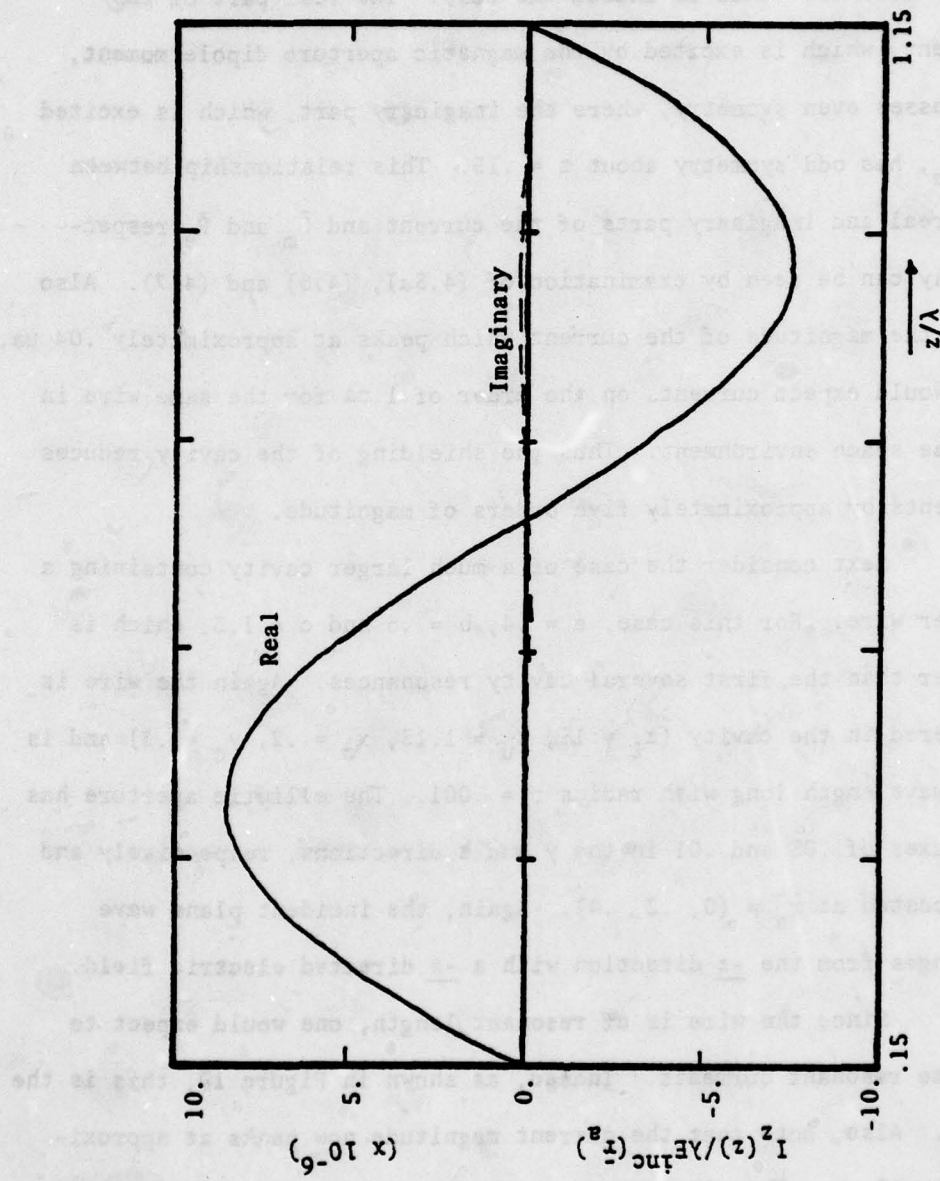


Figure 19. Currents Excited on 1 λ Wire in .4 λ x .6 λ x 1.3 λ Cavity.

the smaller cavity is considerably below the lowest cavity resonance, whereas the larger cavity is near several resonances.

Note that if one semiaxis of the aperture is much larger than the other, the aperture begins to look like a short slot. One would expect that the strongest coupling would occur when the slot is perpendicular to the wire and the incident electric field is perpendicular to the slot. To test this, consider a cavity with dimensions $.7 \times .7 \times .8$ (a, b and c respectively) with a one-half wavelength wire of radius $r = .001$ which is located in the cavity at $z_l = .15$, $z_u = .65$, $x_c = .35$, $y_c = .4$. The aperture is located in the $x = 0$ wall [$\bar{r}_a = (0., .4, .4)$], and has semiaxes of .07 and .01. The plane wave is incident from the -x direction (normal to wall of aperture) and has a z directed electric field.

Consider two cases: that where the slot is perpendicular to the incident electric field, and that where the slot is parallel to the incident electric field; that is, where the major semiaxis of the aperture is in the y or z direction, respectively. Figure 20 shows the current excited upon the wire for these two cases. It is readily seen that the current excited when the slot is perpendicular to E^{inc} is approximately twenty times larger than that excited when the slot and E^{inc} are parallel. Thus the expected effects are observed.

Now consider the same case except change the polarization of the incident plane wave such that the electric field is in the -y direction. Whereas in the previous case the incident electric field was perpendicular to the slot, it is now parallel to the slot, and

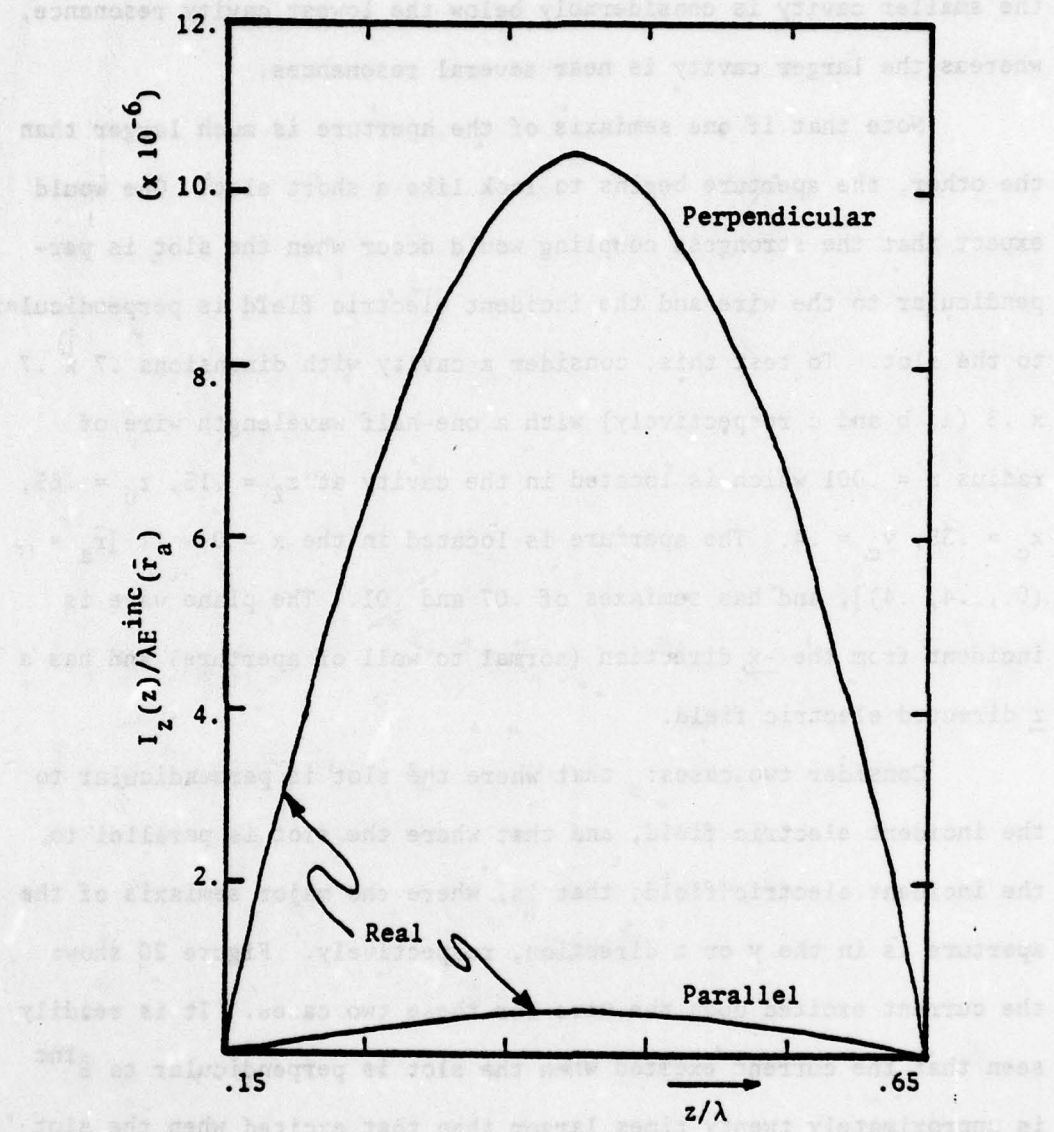


Figure 20. Currents Excited on $.5\lambda$ Wire for Slot Perpendicular and Parallel to \underline{z} Directed Incident Electric Field.

consequently one would expect the excited currents to be much smaller. As shown in Figure 21 this is the case. Again the currents are shown for both the slot perpendicular and parallel to the incident electric field. Note that the currents are again related by a factor of approximately twenty, but are over five orders of magnitude less than the currents shown in Figure 20. However, for the same wire and excitation in free space, if thin wire approximations are used, there will be no current excited upon the wire.

An examination of (4.5) shows the small, but nonetheless nonzero current in Figure 21 is due to the depolarizing effects of the cavity wall reflections. Indeed, if one lets $\bar{Q}^d = \bar{I}$ in (4.5), this polarization will not excite the wire in the cavity. Since for small apertures, these effects manifest themselves as perturbations, one does expect the currents excited by this depolarizing effect to be small.

Another effect of the cavity wall reflections is seen by noting that for the case in Figure 20, since the excitation is normally incident, $E_n^{SC-}(\bar{r}_a)$ is zero, and thus if the wall reflections are neglected, \bar{P}_e would be zero. However, the wall reflections produce a small but nonzero \bar{P}_e and thus a small imaginary current. Although not shown in Figures 20 or 21, there was actually an imaginary part of the current, which in all cases was more than two orders of magnitude less than the corresponding real portion.

At this point it is helpful to ascertain the size of this perturbation effect. In order to accomplish this, solutions were

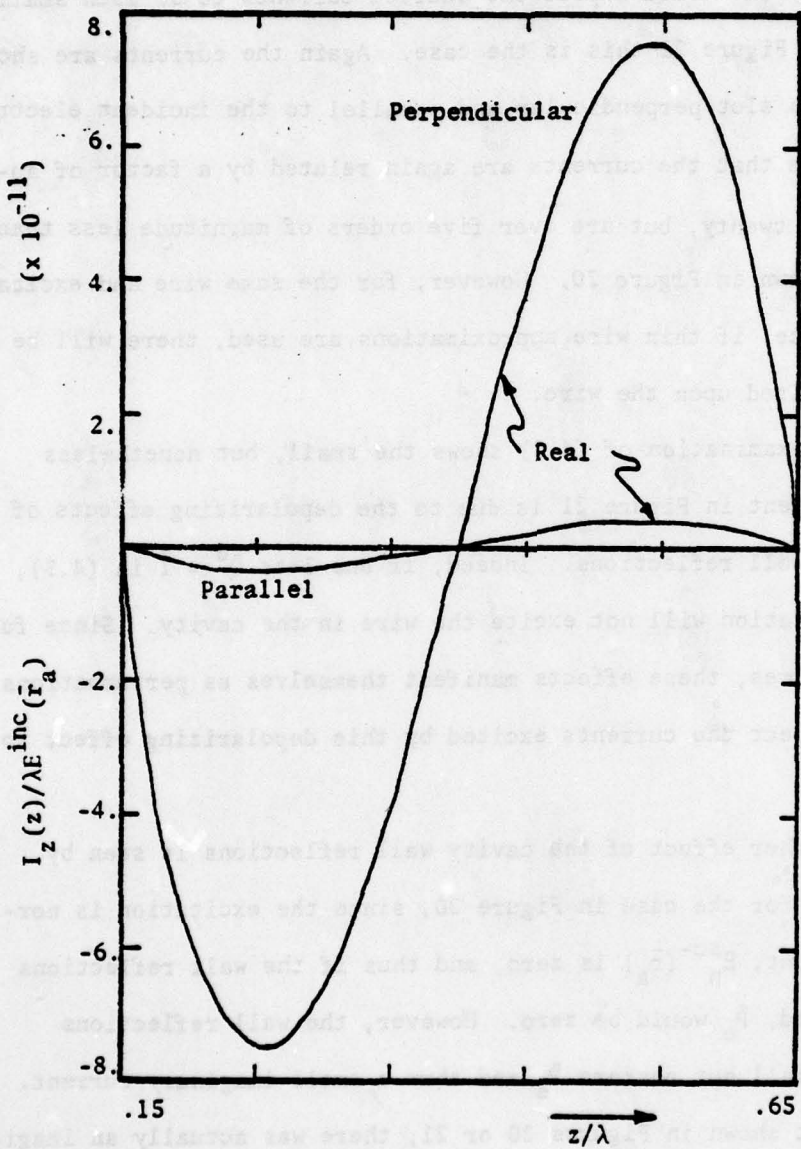


Figure 21. Currents Excited on $.5\lambda$ Wire for Slot Perpendicular and Parallel to -y Directed Electric Field.

obtained in two additional manners. In the first, the cavity wall reflections were neglected ($\bar{Q}^d = \bar{I}$). In the second, the wire scattering effects at the aperture were also ignored ($\bar{Q}^c = \bar{0}$, $\bar{Q}^d = \bar{I}$). These solutions were then compared for several cases, including those presented in this chapter. It was found that the difference between solutions increased as the aperture size increased. This is expected as the perturbation is on the order of the aperture polarizabilities, which increase as the size of the aperture increases. However, in no case did the difference between the original solution and the first additional solution exceed one percent (largest aperture considered was circular with radius .05) and the difference was much less for smaller apertures. The difference between the two additional solutions was even smaller.

It is apparent that for these small apertures, a solution closely approximating the exact one can be obtained by simply neglecting these perturbation effects. Since for apertures much larger than those considered, the applicability of small aperture theory becomes increasingly questionable anyway, this result is quite significant. Since the computation of these perturbations are very time-consuming, their omission would substantially decrease computing time.

Finally, consider the case of wires connected to the cavity at one or both ends. Figures 22 and 23 show the wire currents for these two cases respectively. The cavity size is .7 x .8 x .8 and the wire axis is at $(x_c, y_c) = (.15, .5)$ with a wire radius $r = .001$.

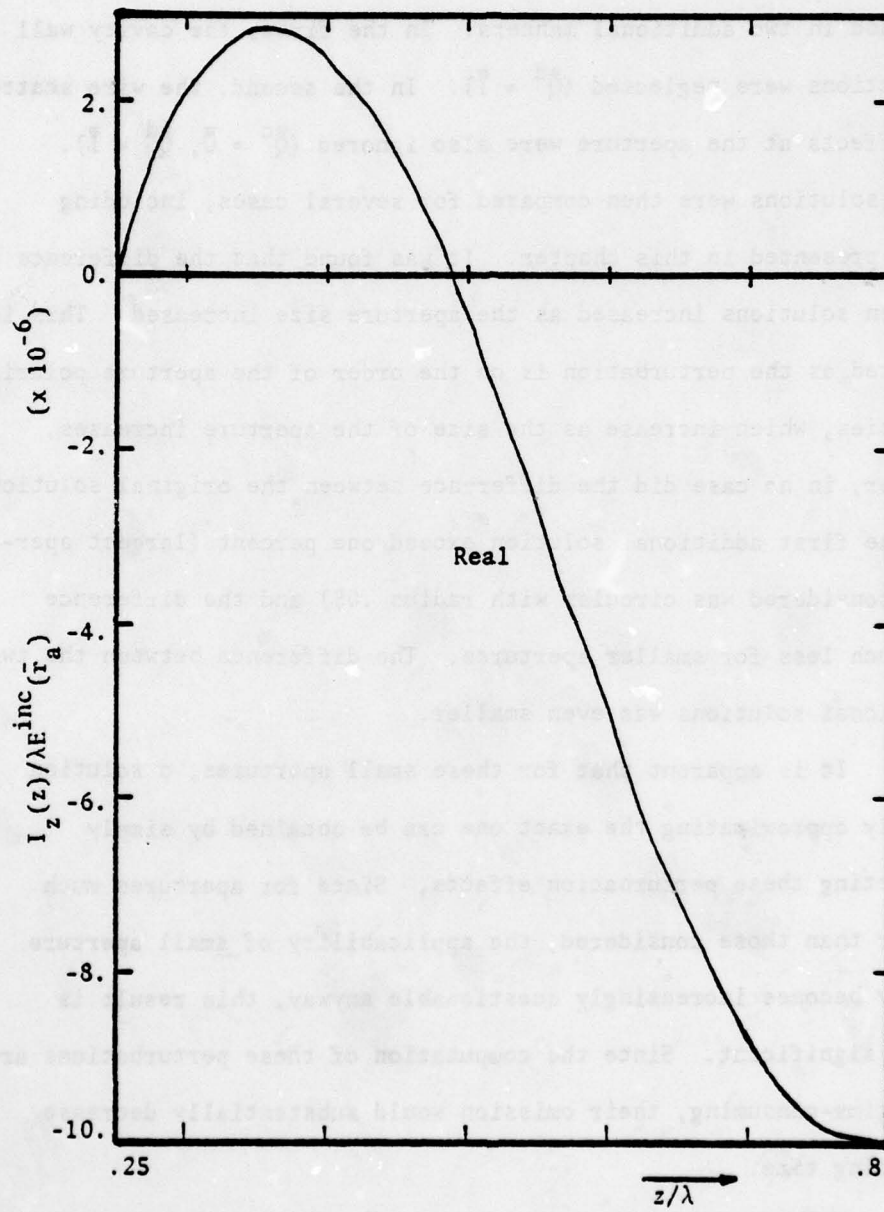


Figure 22. Current Excited on $.55\lambda$ Wire Which Is Attached to Cavity Wall at One End.

AD-A073 770

AIR FORCE WEAPONS LAB KIRTLAND AFB NM
ELECTROMAGNETIC PULSE INTERACTION NOTES -- EMP 3-38. (U)
MAY 79 C E BAUM

F/G 20/14

UNCLASSIFIED

AFWL-TR-79-401

SBIE -AD-E200 329

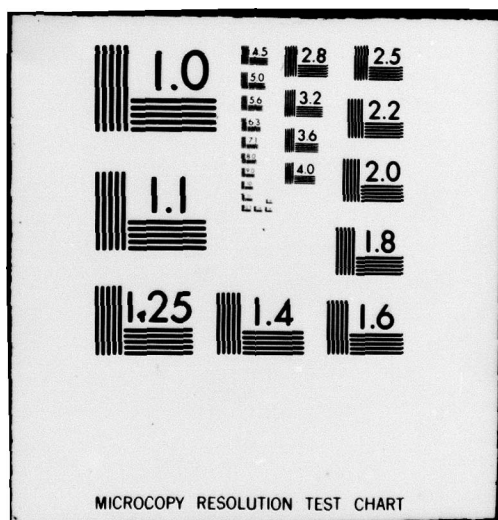
NL

6 OF 6
ADA
073770

10/12
40%



END
DATE
FILMED
10-79
DDC



MICROCOPY RESOLUTION TEST CHART

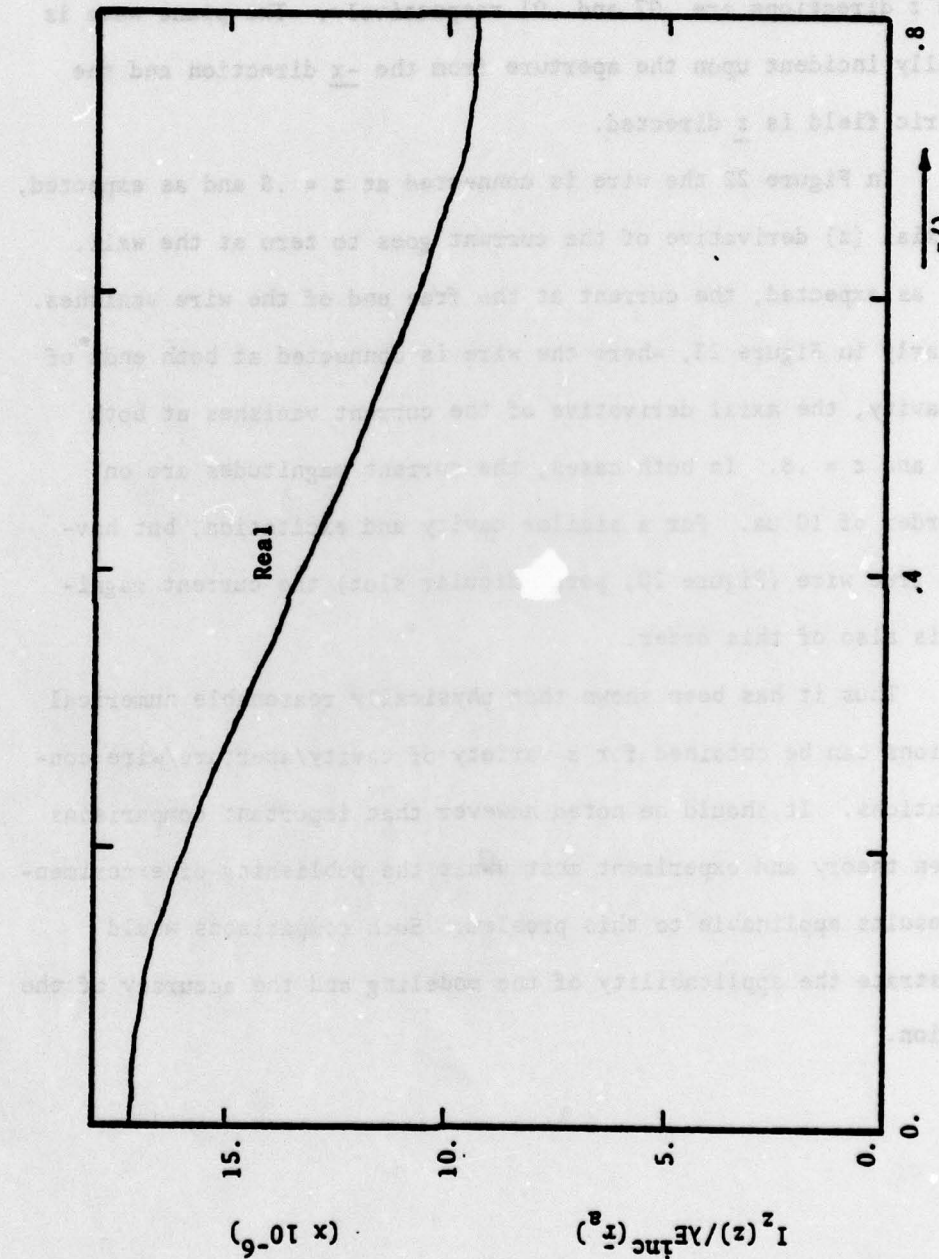


Figure 23. Current Excited on $.8\lambda$ Wire Which Is Attached to Cavity Wall at Both Ends.

The aperture is located at $\bar{r}_a = (0., .3, .6)$ and its semiaxes in the y and z directions are .07 and .01 respectively. The plane wave is normally incident upon the aperture from the -x direction and the electric field is z directed.

In Figure 22 the wire is connected at $z = .8$ and as expected, the axial (z) derivative of the current goes to zero at the wall. Also, as expected, the current at the free end of the wire vanishes. Similarly in Figure 23, where the wire is connected at both ends of the cavity, the axial derivative of the current vanishes at both $z = 0$ and $z = .8$. In both cases, the current magnitudes are on the order of 10 μ a. For a similar cavity and excitation, but having a free wire (Figure 20, perpendicular slot) the current magnitude is also of this order.

Thus it has been shown that physically reasonable numerical solutions can be obtained for a variety of cavity/aperture/wire configurations. It should be noted however that important comparisons between theory and experiment must await the publishing of experimental results applicable to this problem. Such comparisons would demonstrate the applicability of the modeling and the accuracy of the solution.

CHAPTER 6**CONCLUSION**

In this paper, the task was undertaken to formulate and numerically solve the problem of an aperture excited wire scatterer in a rectangular cavity. The formulation in Chapter 2, although tedious, was relatively straightforward. It was found that the major difficulties of the problem lay in the numerical evaluation of the infinite double sum Green's functions for the cavity interior.

By considering the preliminary two-dimensional problem in Chapter 3, valuable insight was obtained toward resolving the numerical difficulties of the three-dimensional problem. It is important to realize that the two-dimensional problem is also a significant problem in and of itself. Two-dimensional problems in many cases provide adequate models for more complex three-dimensional structures. In addition, solutions to this problem have the advantage of being applicable to large apertures whereas the major solution herein is restricted to small apertures only.

The real significance of this work is contained in Chapter 4. Here it was demonstrated that the dyadic Green's functions for the cavity problem can be calculated (although in some cases, only with considerable effort). This finding is particularly essential in or near the source region. This is because the treatment of the singular

kernel of an integral equation in the source region is crucial to its numerical solution. Thus the ability to numerically solve the integral equation for a scatterer in a cavity is demonstrated, and indeed, numerical results can be provided as found in Chapter 5.

Suggested Extensions of this Work

Perhaps more important than what this work has accomplished is rather what extensions and applications can be found for it. In general, the most immediate extensions of this work would be to eliminate some of the restrictions caused by the initial assumptions of the problem. The relevance of an extension can thus be measured by asking how restrictive is the assumption which the extension eliminates.

A very important extension would be to allow a large aperture in the cavity wall. It should be noted that in order to do this an aperture field integral equation must be formulated and solved simultaneously with the integral equation for the wire (2.13). In general, the aperture fields must be divided into a two-dimensional array of surface patches, requiring large amounts of computer storage and time. However if the aperture is small in one dimension (a slot), it need only be divided into a one-dimensional array of surface patches.

A second extension of the present work would be to account for more complex scattering geometries. This might include uniformly or lumped loaded wires, more than one wire, or wires which are not parallel to one of the coordinate axes. The first two of these suggestions would be relatively straightforward (but only if each wire remains

parallel to one of the coordinate axes) and would primarily require extensive logic for their numerical implementation.

It should be noted, however, that the consideration of a wire which is not parallel to one of the coordinate axes would require considerable effort. First of all, integral equation (2.12) would have to be used, and thus all nine components of the dyads would be needed. In addition, the benefits of piecewise-sinusoidal testing (namely, the removal of the differential operator) are no longer applicable. Probably the most important problem this extension would cause is that the methods outlined in Chapter 4 for evaluating the integral of the kernel could no longer be applied. Careful examination reveals that this technique is crucially dependent upon the fact that the wire is z-directed.

Finally, consider the application of this work to the case of a time dependent excitation (such as EMP). The corresponding time-dependent solution can be obtained by inverse Fourier transformation. Note that this would involve the use of the time-harmonic solution at many angular frequencies ω over the spectrum of the excitation. It should be noted that for many transient excitations (including EMP) the low frequency portion of the spectrum is dominant. Thus for such excitations, a quasi-static solution for the problem is needed for small ω in order to perform the inverse Fourier transform numerically. Alternatively, transient results could be obtained by finding the poles of the system in the complex s-plane ($s=i\omega$) using the singularity expansion method (Baum 1976).

LIST OF REFERENCES

Abramowitz, M. and I. Stegun. Handbook of Mathematical Functions, New York: Dover, 1965.

Baum, C. E. "The Singularity Expansion Method," in Topics in Applied Physics, Vol. 10, Transient Electromagnetic Fields, L. B. Felsen, Ed., New York: Springer-Verlag, 1976.

Bethe, H. A. "Theory of Diffraction by Small Holes," Phys. Revs., Vol. 66, pp. 163-182, Oct. 1944.

Bouwkamp, C. J. "Diffraction Theory," Repts. Prog. in Phys., Vol. 17, pp. 35-100, 1954.

Bromwich, T. J. I'A. An Introduction to the Theory of Infinite Series, 2nd Ed., London: MacMillan, 1926.

Butler, C. M. "Evaluation of Potential Integral at Singularity of Exact Kernel in Thin-Wire Calculations," IEEE Trans. on Ant. and Prop., Vol. AP-23, pp. 293-295, March 1975.

_____. "Excitation of a General Scatterer in the Vicinity of an Aperture in a Planar, Conducting Screen," in preparation, University of Mississippi, University of Mississippi.

_____. and K. R. Umashankar. "Electromagnetic Excitation of a Wire Through an Aperture-Perforated, Conducting Screen," IEEE Trans. Ant. Prop., Vol. AP-24, pp. 456-462, July 1976, and also AFWL Interaction Note 251, June 1975.

_____. and D. R. Wilton. "Analysis of Various Numerical Techniques Applied to Thin-Wire Scatterers," IEEE Trans. on Ant. and Prop., Vol. AP-23, pp. 534-540, July 1975.

Cheng, D. K. and C. A. Chen. "On Transient Electromagnetic Excitation of a Rectangular Cavity Through an Aperture," AFWL Interaction Note 237, February 1975.

Cohn, S. B. "Determination of Aperture Parameters by Electrolytic-Tank Measurements," Proc. IRE, Vol. 39, pp. 1416-1421, Nov. 1951.

_____. "The Electric Polarizability of Apertures of Arbitrary Shape," Proc. IRE, Vol. 40, pp. 1069-1071, Sept. 1952.

Collin, R. E. Field Theory of Guided Waves, New York: McGraw-Hill, 1960.

_____. "On the Incompleteness of E and H Modes in Wave Guides," Can. J. Phys., Vol. 51, pp. 1135-1140, June 1973.

DeMeulenaere, F. and J. Van Bladel. "Polarizability of Some Small Apertures," IEEE Trans. Ant. Prop., Vol. AP-25, pp. 198-205, March 1977.

Hansen, W. W. "A New Type of Expansion in Radiation Problems," Phys. Rev., Vol. 47, pp. 139-143, 1935.

Harrington, R. F. Time-Harmonic Electromagnetic Fields, New York: McGraw-Hill, 1961.

_____. Field Computation by Moment Methods, New York: MacMillan, 1968.

Howard, A. Q., Jr. "On the Longitudinal Component of the Green's Function Dyadic," Proc. IEEE (Lett.), Vol. 62, pp. 1704-1705, Dec. 1974.

Jolley, L. B. W. Summation of Series, 2nd Ed., New York: Dover, 1961.

Kurokawa, K. "The Expansion of Electromagnetic Fields in Cavities," IRE Trans. MTT, Vol. MTT-6, pp. 178-187, April 1958.

Lewin, L. Dilogarithms and Associated Functions, London: MacDonald, 1958.

_____. Theory of Waveguides, New York: Halsted Press, 1975.

Lindelöf, Ernst. Le Calcul des Résidus et ses Applications à la Théorie des Fonctions, New York: Chelsea, 1947.

Morse, P. M. and H. Feshbach. Methods of Theoretical Physics, Part II, New York: McGraw-Hill, 1953.

Rahmat-Samii, Y. "On the Question of Computation of the Dyadic Green's Function at the Source Region in Waveguides and Cavities," IEEE Trans. on MTT, Vol. MTT-23, pp. 762-765, Sept. 1975.

Seidel, D. B. "A New Method for the Detection and Correction of Errors Due to Interior Resonance for the Problem of Scattering from Cylinders of Arbitrary Cross-Section," Master's thesis, Department of Electrical Engineering, University of Arizona, Tucson, Arizona, Dec. 1974.

_____. and C. M. Butler. "Determination of Current on a Wire which Passes Through a Hole in a Planar Screen," URSI Annual Meeting, Amherst, Massachusetts, Oct. 1976.

Tai, C. T. "On the Eigenfunction Expansion of Dyadic Green's Functions," Proc. IEEE (Lett.), Vol. 61, pp. 480-481, April 1973.

_____ and P. Rozenfeld. "Different Representations of Dyadic Green's Functions for a Rectangular Cavity," IEEE Trans. on MTT, Vol. MTT-24, pp. 597-601, Sept. 1976.

Teichmann, T. "Completeness Relations for Loss-Free Microwave Junctions," J. Appl. Phys., Vol. 23, pp. 701-710, July 1952.

_____ and E. P. Wigner. "Electromagnetic Field Expansions in Loss-Free Cavities Excited Through Holes," J. Appl. Phys., Vol. 24, pp. 262-267, March 1953.

Titchmarsh, E. C. The Theory of Functions, 2nd Ed., London: Oxford University Press, 1939.

Tsai, L. L., D. G. Dudley and D. R. Wilton. "Electromagnetic Scattering by a Three-Dimensional Conducting Rectangular Box," J. Appl. Phys., Vol. 45, Oct. 1974.

Weyl, H. "Über Die Randwertaufgabe der Strahlungstheorie und Asymptotische Spektralgesetze," J. F. Reine Ange. Math., Vol. 143, pp. 177-202, 1913.

_____ . "Das Asymptotische Verzalungsgesetz der Eigenschwingen Eines Beliebig Gestalteten Elastischen Körpers," Rend. d. Circ. Math. Palermo, Vol. 39, pp. 1-49, 1915.

Wheelon, Albert D. Tables of Summable Series and Integrals Involving Bessel Functions, San Francisco: Holden-Day, 1968.

Wilton, D. R. and C. M. Butler. "Efficient Numerical Techniques for Solving Pocklington's Equation and Their Relationships to Other Methods," IEEE Trans. Ant. and Prop., Vol. AP-24, pp. 83-86, January 1976.